ASME
SETTING THE STANDARD
1880 2005

Transactions of the ASME, Journal of Fluids Engineering (ISSN 0098-2202) is published bimonthly (Jan., Mar., May, July, Sept., Nov.) by The American Society of Mechanical Engineers, Three Park Avenue, New York, NY 10016. Periodicals postage paid at New York, NY and additional mailing offices.
POSTMASTER: Send address changes to Transactions of the ASME, Journal of Fluids Engineering, c/o THE AMERICAN SOCIETY OF MECHANICAL ENGINEERS, 22 Law Drive, Box 2300, Fairfield, NJ 07007-2300.
CHANGES OF ADDRESS must be received at Society headquarters seven weeks before they are to be effective. Please send old label and new address.
STATEMENT from By-Laws. The Society shall not be responsible for statements or opinions advanced in papers or ... printed in its publications (B7.1, Par. 3).

Journal of Fluids Engineering

Published Bimonthly by ASME

VOLUME 127 • NUMBER 4 • JULY 2005

EDITORIAL

SPECIAL SECTION ON CFD METHODS

TECHNICAL PAPERS

(Contents continued on inside back cover)

This journal is printed on acid-free paper, which exceeds the ANSI Z39.48-1992 specification for permanence of paper and library materials. ♾™
♻ 85% recycled content, including 10% post-consumer fibers.

Journal of Fluids Engineering Volume 127, Number 4 JULY 2005

TECHNICAL BRIEF

The ASME Journal of Fluids Engineering is abstracted and indexed in the following:

Applied Science & Technology Index, Chemical Abstracts, Chemical Engineering and Biotechnology Abstracts (Electronic equivalent of Process and Chemical Engineering), Civil Engineering Abstracts, Computer & Information Systems Abstracts, Corrosion Abstracts, Current Contents, Ei EncompassLit, Electronics & Communications Abstracts, Engineered Materials Abstracts, Engineering Index, Environmental Engineering Abstracts, Environmental Science and Pollution Management, Excerpta Medica, Fluidex, Index to Scientific Reviews, INSPEC, International Building Services Abstracts, Mechanical & Transportation Engineering Abstracts, Mechanical Engineering Abstracts, METADEX (The electronic equivalent of Metals Abstracts and Alloys Index), Petroleum Abstracts, Process and Chemical Engineering, Referativnyi Zhurnal, Science Citation Index, SciSearch (The electronic equivalent of Science Citation Index), Shock and Vibration Digest, Solid State and Superconductivity Abstracts, Theoretical Chemical Engineering

Journal of Fluids Engineering

Editorial

Recent Advances in Numerical Methods for Fluid Dynamics and Heat Transfer

Computational fluid dynamics (CFD) tools are the key for modern understanding of many physical, electrochemical, and biological processes. They not only help explain complex events involving disparate temporal and spatial scales, but also allow us to peer at the heart of breakthrough science. This special section of the Journal of Fluids Engineering is a collection of select papers presented at the ASME 2004 Fluids Engineering Division Summer Meeting in Charlotte, North Carolina in the symposium on "Algorithmic Developments in CFD" sponsored by the Fluids Engineering and Heat Transfer Divisions. They represent an excellent cross section of research and developments crucial to issues both in fundamental progress and industrial applications. The symposium on algorithmic developments started in the 1990s and is intended to provide means for presenting novel and enhanced numerical algorithms for computational fluid dynamics (CFD) applications, direct numerical simulation, Monte Carlo methods, iterative and segregated solvers, shearing interface algorithms, exploitation of parallel architecture, and adaptive techniques. Specific topics of interest include, but are not limited to, laminar and turbulent flows, reacting flows, compressible and incompressible flows, and non-Newtonian flows. The symposium is led by Subrata Roy from Kettering University, along with co-organizers Dhanireddy R. Reddy from NASA Glenn Research Center and Miguel Visbal from the Air Force Research Laboratory at Wright Patterson. The ongoing concurrent series of these symposia epitomize excellent cutting edge numerical research from an international representation of applied mathematicians, numerical physicists, fluid dynamicists, as well as industrial practitioners. The diffusion of knowledge that sprouts from the syntheses of ideas of these leading scientists and engineers usher in new technological breakthroughs and developments.

The seven papers selected for this collection are divided into two loosely formed groups. The first four papers present fundamental algorithm developments with underlying important practical applications. Three papers in the following group focus on novel implementations of developed numerical techniques for a wide range of flow simulations.

In the first group, Issa from Texas A&M University and Yao from Carnegie Mellon University develop a new numerical recipe for modeling the dynamics of the droplet-wall interaction and heat transfer mechanisms at subatmospheric to elevated ambient pressures, and for surface temperatures ranging from nucleate to film boiling. This has applications in a wide range of problems, including mist cooling of thin-strip casting, gas turbine airfoils, glass tempering, and electronic chips where misting jets show a better cooling efficiency and control of the material temperature. Simulation results for their method compares well against available test data for single stream of droplets at nonatmospheric conditions. The next paper is on multilevel Boundary Element Methods (BEM) for fast and accurate solutions of steady Stokes flows. A major problem dragging the progress of BEM is its high memory overhead and efficiency concerns for a general class of problems. The novel formulation proposed by Dargush and Grigoriev of the State University of New York at Buffalo shows promise in significantly overcoming that problem. For a test case in an irregular pentagon, the new formulation reduces the CPU times by a factor of nearly 700,000 while the memory requirements are shown to reduce by more than 16,000 times. The third paper in this category is the development of a meshless local Petrov-Galerkin control volume algorithm for fluid thermal system applications by Arefmanesh et al. from Islamic Azad University of Tehran. The accuracy and applicability of their method have been benchmarked for the transient heat conduction, potential flow over a block, and convection-diffusion-type non-self-adjoint problems. The Fourier series along with a modified upwinding relation has been utilized for optimal (artificial) diffusion in convective flow cases. The fourth paper by Celik et al. from West Virginia University investigates the limitations of the well-known Richardson extrapolation method focusing on the origin of oscillatory convergence in finite difference methods and demonstrates statistical performances of some possible remedies based on the modeled error equation. A new method based on the extrapolation of approximate error is also proposed.

The next set of papers begins with "An Adaptive Wavelet Method for Incompressible Flows in Complex Domains" by Wirasaet and Paolucci of the University of Notre Dame. They overcome the well-known difficulty of applying such a method for complex domains by using the Navier-Stokes/Brinkman equations, which take into account solid obstacles by adding a penalty term in the momentum equation. The method is based on interpolating wavelets and has been tested for incompressible flows over obstacles. Stolz from the Institute of Fluid Dynamics, Zürich, Switzerland has applied the newly developed high-pass filtered Smagorinsky models for large-eddy simulations of wall-bounded compressible flows. Specifically, the simulation of a spatially developing supersonic turbulent boundary layer at a Mach number of 2.5 and momentunm-thickness Reynolds numbers at inflow of approximately 4500 is validated with experimental data. The numerical method uses entropy splitting along with a finite difference approximation for the diffusive flux. In recent days, there has been a flurry of research on the level set methods. The final paper in this anthology is by collaborators from Switzerland and the USA on the Streamline-Upwind/Petrov-Galerkin (SUPG) finite-element based level set method. Shepel and Smith from the Paul Scherrer Institut in Switzerland and Paolucci from the University of Notre Dame implemented the level set interface tracking method in the commercial FIDAP and CFX-4 codes. The procedure can be used for both structured and unstructured grids. Two formulations encompassing the single phase liquids and the coupled

motion of the gas-liquid phases are given and tested for large density and viscosity ratios.

I would like to congratulate the authors of the papers in this special section of the Journal of Fluids Engineering for their staunch efforts in preparing and improving their manuscripts in response to the reviews. The anonymous referees contributed a lot of their time and expertise. They deserve special thanks. I also thank Laurel Murphy for providing consistent support and help throughout the progress of this collection. Finally, Reddy and Visbal did more than their share in organizing the series of symposia that culminated into this special section. I most certainly acknowledge their help.

Subrata Roy
Associate Editor

A Numerical Model for the Mist Dynamics and Heat Transfer at Various Ambient Pressures

Roy J. Issa
Assistant Professor
e-mail: rissa@mail.wtamu.edu
Department of Mathematics, Physical Sciences and Engineering, Mechanical Engineering Division,
West Texas A&M University, Canyon, TX

S. C. Yao
Professor
e-mail: sy0d@andrew.cmu.edu
Department of Mechanical Engineering,
Carnegie Mellon University, Pittsburgh, PA

A numerical model is developed to simulate the dynamics of the droplet-wall interaction and heat transfer mechanisms at sub-atmospheric to elevated ambient pressures, and for surface temperatures ranging from nucleate to film boiling. This is the first time a general model is developed to study these phenomena over a wide range of ambient pressures. The model provides insight to the optimal flow conditions, and droplet size distribution for best heat transfer enhancement. Simulations are provided for single stream droplet impactions, and for full conical sprays using nozzles that dispense a spectrum of non-uniform droplets. The model simulation was compared against available test data for single stream of droplets at non-atmospheric conditions, and the simulation compared favorably well with the test data. [DOI: 10.1115/1.1976743]

1 Introduction

Intense cooling methods have been widely used in many industrial applications, especially those requiring rapid cooling from high temperatures. In applications where mist cooling is performed at atmospheric conditions, such as thin strip casting, glass tempering, and electronic chip cooling [1–4], cooling by misting jets provides high efficiency of cooling and a better control of the material temperature. Mist cooling has also found use in high pressure applications such as gas turbines [5–7]. Experiments have been conducted on the internal cooling of gas turbine airfoils by injecting mist with the compressed air. The results show significant enhancement in the cooling process, whereas an injection of 5% water mist into air can enhance the heat transfer by about 20–30% [5] and reduce the consumption of the compressed air conventionally required to cool the airfoils by almost 50%.

In water spray cooling, a limited number of experiments [8–11] have been performed at either high or sub-atmospheric ambient pressures. Unfortunately, none of those experiments were conducted for full spray conditions. They have been performed either for single droplet impactions, or for a single sessile (stationary) droplet on a hot surface. In the diesel spray impingement onto the cylinder walls, experiments [12–14] have been conducted using high-speed photography to examine the distribution pattern of the spray and fundamental parameters such as the wall-spray height, and the wall-spray radius. The common disadvantage made by those researchers is that their studies were mostly conducted at room surface temperatures.

Very few models that predict the spray behavior have been developed. The existing models do not consider the droplet bouncing behavior at the wall, but only track the droplets up to the point where they make contact without calculating the partial evaporation and the heat transfer effectiveness at impaction. In addition, the existing models were often based on experiments conducted at atmospheric pressure. Therefore, a model that can handle the effect of a wide range of ambient pressures is of tremendous value to the spray cooling research.

The objective of this paper is to simulate high and sub-atmospheric pressures based on the model developed earlier for atmospheric applications [15] with a proper account of the droplet-wall interaction and air-mist heat transfer mechanism. Understanding of the droplet contact heat transfer at high and sub-atmospheric pressures is scarce. The challenges behind this research are to obtain a valuable basic understanding of the parameters that affect the heat transfer enhancement over a wide range of operating pressures.

2 Droplet Dynamics

Experiments conducted for single droplet impingements on heated surfaces at atmospheric pressures show that during impaction, the droplet spreads in the form of a flattened disk along the surface, and then recoils as a result of the droplet surface tension before rebounding. The droplet will rebound without breaking up as long as the impinging droplet Weber number is less than the critical Weber number at which the droplet disintegrates. There are several factors that influence the droplet impaction mode at the wall such as surface thermal conductivity, surface roughness, surface temperature, and droplet impingement angle. However, one factor, which is the Weber number, is considered to be the governing parameter for the droplet deformation. Data gathered from several sources for water droplet impaction at atmospheric conditions [16–19] (and at about Leidenfrost temperature) show the relationship between the droplet normal coefficient of restitution and the normal impinging Weber number (Fig. 1) [15]:

$$e_n = 1 - 0.1630 We_n^{0.3913} \tag{1}$$

where

$$We_n = \frac{\rho_d v_{i,n}^2 d}{\sigma_d} \tag{2}$$

According to Chandra and Avedisian [20], the droplet maximum spread was theoretically shown to be directly proportional to the square root of the Weber number. Experimental data [20] show the maximum droplet spread to decrease as the wall temperature increases (as shown in Fig. 2). Therefore, the momentum loss of the impacting droplet also decreases with temperature. As a result, it is expected that the droplet coefficient of restitution at temperatures lower than the Leidenfrost is slightly lower than that presented in Fig. 1.

As the ambient pressure increases, both the droplet density and surface tension decrease with the rate of decrease in the surface tension much larger than that of the droplet density. As a result, at high pressure, the droplet will deform and spread more. However, the change in the droplet spread is not very significant resulting only in about 16% increase at 20 atm and 7% decrease at about 0.01 atm [21]. Therefore, the correlation between the droplet coefficient of restitution and the droplet Weber number developed

Contributed by the Fluids Engineering Division for Publication in the JOURNAL OF FLUIDS ENGINEERING. Manuscript received by the Fluids Engineering Division August 23, 2004. Final manuscript received: April 9, 2005. Associate Editor: Subrata Roy

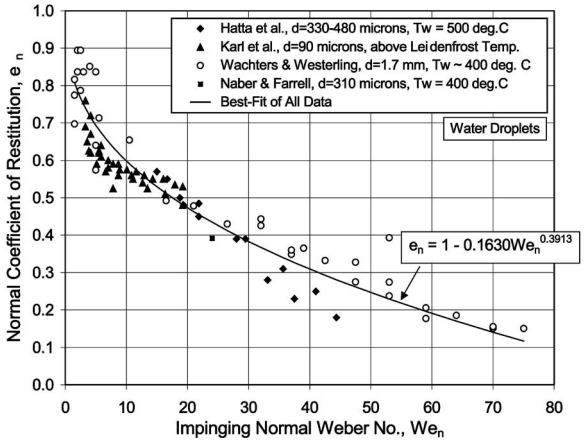

Fig. 1 Droplet coefficient of restitution as function of We_n at about Leidenfrost temperature (1 atm) [15]

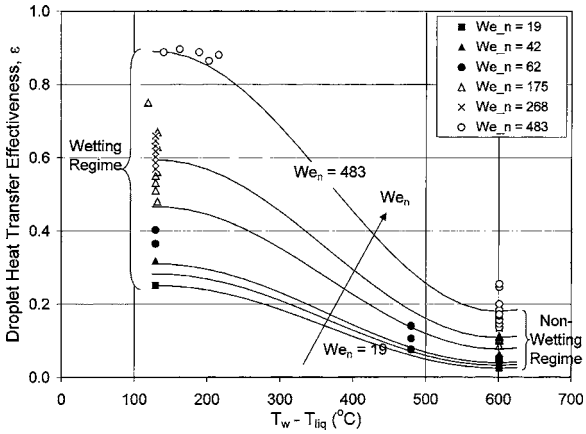

Fig. 4 Droplet contact heat transfer effectiveness in the transition to film boiling region (at 1 atm) [15]

for atmospheric conditions [15] can still be applicable with sufficient accuracy for higher ambient pressures, and for sub-atmospheric pressures.

3 Droplet Heat Transfer

The various modes of heat transfer associated with the droplet heat transfer consist of (Fig. 3) [22]: 1) conduction through wall contact, 2) convection associated with the bulk air flow and the droplet cooling of the thermal boundary layer, and 3) wall radiation. Contact heat transfer can be further classified into two types:

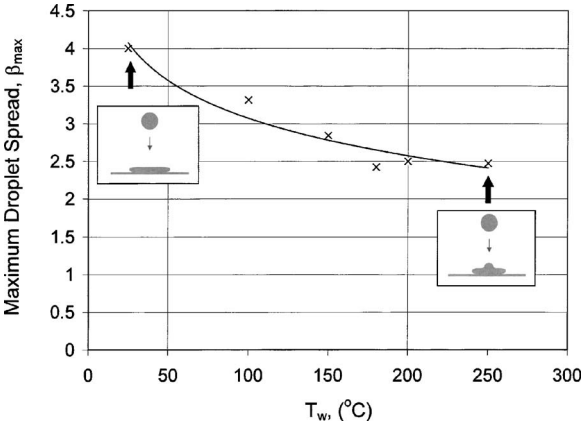

Fig. 2 Water droplet maximum spread versus wall temperature (Adapted from Chandra and Avedisian [20])

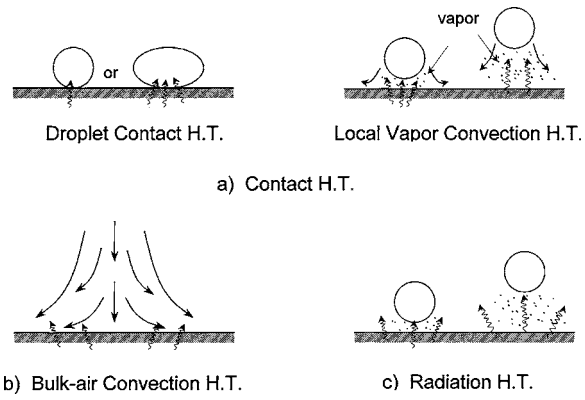

Fig. 3 Basic mechanisms for spray heat transfer [22]

a) heat transfer by wet-contact in which the droplets are in continuous or semi-continuous contact, and b) heat transfer by non-wet contact where after a short period of contact, a film layer is generated between the droplet and the wall preventing direct contact.

The droplet contact heat transfer effectiveness is defined as the ratio of the actual heat transfer by the droplet to the maximum possible heat transfer that can be achieved. The maximum release of heat consists of: 1) the pre-boiling cooling potential when the droplet arrives to the surface at a temperature lower than the saturation temperature, 2) the release of heat when the droplet completely vaporizes at the saturation temperature, and 3) the superheating of the droplet to the surface temperature. The droplet heat transfer effectiveness can be expressed as

$$\varepsilon = \frac{q_c}{G[h_{fg} + c_{p,l}(T_{sat} - T_{liq}) + c_{p,v}(T_w - T_{sat})]} \tag{3}$$

In an earlier study [15], it was shown that the heat transfer effectiveness is strongly dependent on the normal impinging droplet Weber number and the wall temperature. There are also other secondary factors influencing the heat transfer effectiveness but not as influential as the preceding ones, such as the droplet impingement frequency, surface inclination angle, surface material and roughness. Heat transfer effectiveness versus the wall temperature and droplet impinging Weber number is shown in Fig. 4 [15]. The data are based on experiments conducted by Pedersen [23], Senda et al. [24], and McGinnis and Holman [25] at atmospheric pressure conditions and for a wide temperature range.

As the ambient pressure increases, the effect of the pressure on the enthalpy of vaporization and the specific heat constant for water becomes significant. As shown in Fig. 5, when the pressure increases, h_{fg} reduces significantly while $c_{p,l}$ and T_{sat} increase. A large portion of the heat absorbed is now being used to increase the droplet temperature towards the saturation temperature. Therefore, at high ambient pressures, the effect of droplet subcooling becomes more evident and the decrease in the enthalpy of vaporization makes the evaporation of the liquid droplets much easier.

3.1 Effect of Ambient Pressure on Non-Wet Cooling. High-pressure conditions significantly alter the droplet cooling efficiency on heated surfaces. The effect of pressure on the evaporation time and on the Leidenfrost temperature of discrete water droplets deposited on metallic plates such as stainless steel, brass and monel have been studied by Emmerson and Snoek [10,11]. The chamber pressure ranged from 1 to 5.1 atm, and the water droplet size on the plate was estimated to be 3.8 mm. Testa and Nicotra [9] studied the influence of sub-atmospheric pressures on the Leidenfrost temperature for a single stream of water droplets impinging on a molybdenum strip. The droplet size was about 2

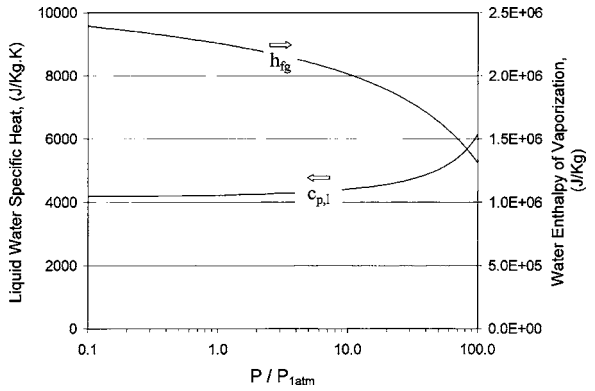

Fig. 5 Effect of pressure on water enthalpy of vaporization and specific heat constant

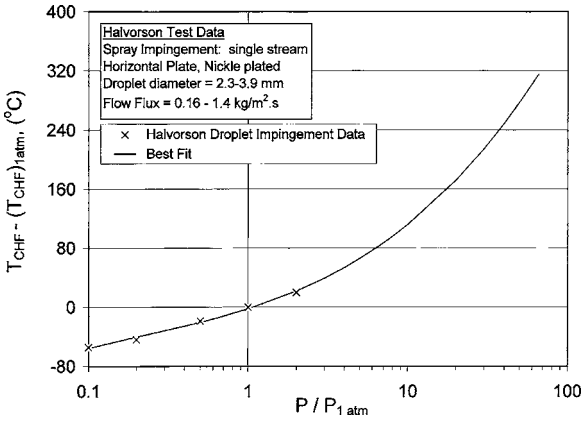

Fig. 8 Variation in the temperature at the critical heat flux with ambient pressure

mm, and the pressure in the vacuum chamber ranged from 1 atm down to 0.065 atm. Figure 6 shows the variation in the Leidenfrost temperature as function of the normalized ambient pressure for a wide range of pressures. The data demonstrate that the minimum heat flux corresponds to the maximum lifetime of the droplet. Figure 7 shows the effect of the ambient pressure on the minimum heat flux.

3.2 Effect of Ambient Pressure on Wet Cooling. Halvorson conducted experiments on the droplet impact cooling using a sealed chamber with ambient pressures of 0.1, 0.2, 0.5, 1.0, and 2.0 atm [8]. He used three different sizes of gauge needles that produced droplet diameters ranging from 2.3 to 3.9 mm. The droplet frequencies ranged from 2 to 15 droplets per second, and the droplet impact velocity was about 1.3 m/s. In all the experiments, the droplet mass flux ranged from 0.15 to 1.6 kg/m^2 s. The heated surface was a nickel-plated end of a copper cylinder placed vertically and heated to temperatures where critical heat fluxes from the droplets impaction were obtained. The temperature at which the critical heat flux occurred ranged between 75 and 150 °C, with the lowest temperatures occurring at the lowest pressures. Figure 8 shows the variation in the critical heat flux temperature as function of the normalized ambient pressure for a wide range of pressures, and Fig. 9 shows the variation in the critical heat flux.

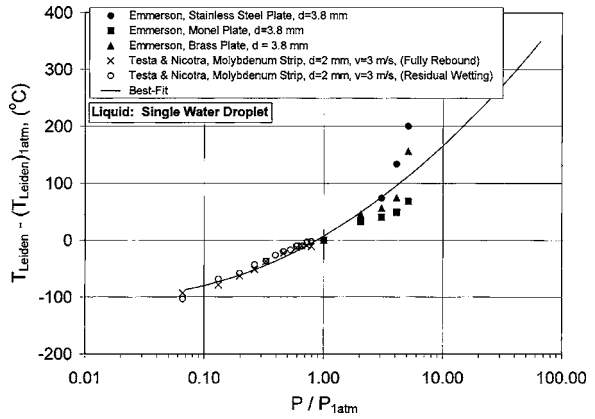

Fig. 6 Variation in the Leidenfrost temperature with ambient pressure

3.3 Contact Heat Transfer Effectiveness for Different Ambient Pressures. An understanding and predictability of the droplet-wall contact heat transfer effectiveness is needed for high pressure spraying environments. Using the results from Figs. 6–9 and applying them to Fig. 4, the predictability of the droplet contact heat transfer effectiveness can be extended from atmospheric pressure conditions to higher pressures, and also to sub-atmospheric pressures. At high ambient pressures, film boiling regime for droplet cooling would be shifted further to a high temperature range as the pressure increases. As a result, a heat transfer mode that would be in the film boiling at atmospheric pressure would now occur closer to the nucleate boiling region for high ambient pressures. The high pressure would then significantly increase the droplet heat transfer effectiveness. At sub-atmospheric pressures, film boiling region would be shifted further to a lower temperature region as the pressure decreases, and the droplet heat

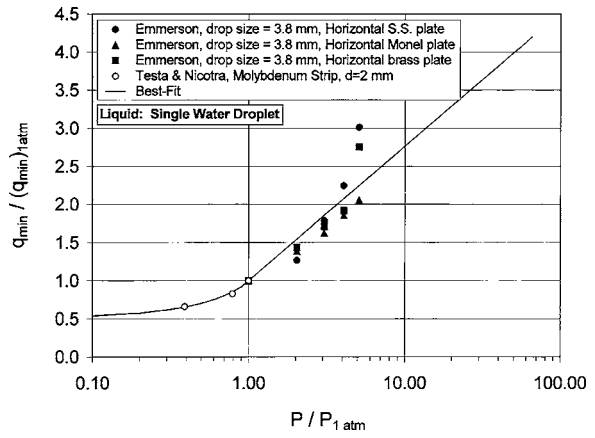

Fig. 7 Minimum heat flux as function of ambient pressure

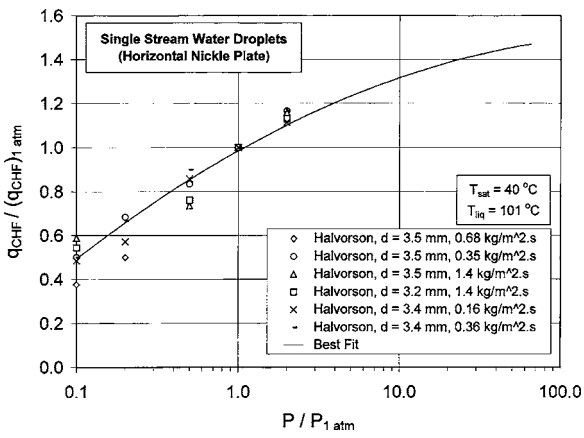

Fig. 9 Critical heat flux as function of ambient pressure

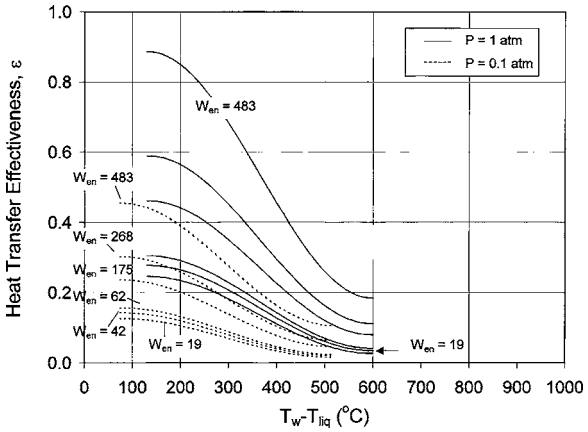

Fig. 10 Comparison in droplet contact heat transfer effectiveness between 1 and 0.1 atm ambient pressures

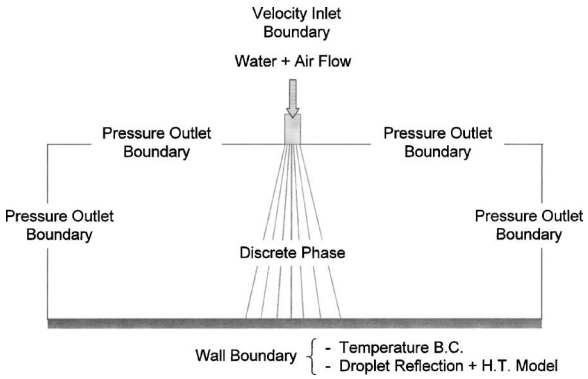

Fig. 12 Model boundary conditions (shown here for the case of full spray injection)

transfer effectiveness would significantly decrease. A new set of droplet contact boiling curves similar to that shown in Fig. 4 (for atmospheric pressure condition [15]) can be obtained for different operating pressures as shown in Figs 10 and 11 for the case of 0.1 and 50 atm, respectively.

4 Computation Scheme

Numerical computations are performed using FLUENT software. The modeling of the spray consists of a mixture of two phases: an air medium referred to as the continuous phase, and the water droplets referred to as the discrete phase. The droplets are dispersed in the continuous phase and are traced stochastically in the Lagrangian reference frame. The trajectory of the droplet is solved by integrating the force balance on the droplet, where the inertial force is balanced by the drag force and the gravitational force. The droplet temperature is calculated by applying an energy balance on the droplet. The sensible heat change in the droplet is balanced by the convective, radiative, and latent heat transfer between the droplet and the gas phase medium. The turbulence continuous phase model uses the two equations in the k-ϵ method expressed in Eulerian coordinates. The effect of the gas turbulence on the droplets is obtained by adding a velocity fluctuation to the mean gas velocity while tracing the droplets. A control volume based approach is used to convert the governing equations into algebraic equations that can be then numerically solved.

In this model [21], steady state flow conditions are simulated. It is assumed that no droplets interaction occurs, and dilute spray conditions prevail. Also it is assumed that the droplet impinging

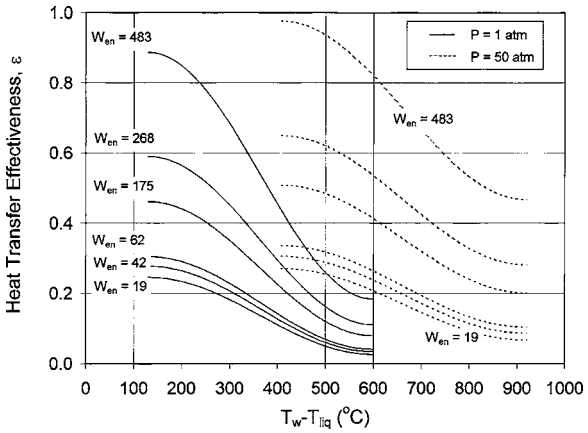

Fig. 11 Comparison in droplet contact heat transfer effectiveness between 1 and 50 atm ambient pressures

Weber number is small enough so that the droplets do not to splatter. An axisymmetric model is developed to simulate the spray flow over a heated plate that is 101.6 mm in diameter. The nozzle is situated at the center of the plate at a distance of 40 mm above the plate. Weighing factors are used to concentrate the grid mesh at the center of the computation domain, and also near the plate surface. Sufficient grid refinement at the wall is necessary to capture the wall interaction event and to ensure computational stability. For dilute spray conditions (water mass flux <2 kg/s m^2) a quadrilateral grid mesh of 75×60 provided acceptable numerical accuracy. However, for higher water mass fluxes, a more refined grid mesh was needed. Therefore, the accuracy of the simulation results was grid size dependent, and the grid size that was needed was in turn dependent on the water mass flux. A grid independence study was conducted where the density of the nodes near the wall was increased until the solution no longer changed with further grid refinement. To achieve this, an enhanced wall treatment using the Two-Layer Zonal Model was enabled in FLUENT, where value of $y^+(=\rho u_\tau y/\mu)$ at the wall-adjacent cells was kept close to 1.

During impaction, the droplet mass is recalculated based on the droplet contact heat transfer empirical correlations, and the excess mass that is the difference between the incoming droplet mass and the re-calculated mass is released as saturated vapor at the nearest cells to the wall. The created vapor mass has the same momentum and energy of the phase from which it is created. The calculations for the droplet dynamic interaction with the wall, and the droplet-wall contact heat transfer effectiveness are introduced into FLUENT through user-defined functions which are compiled and linked to FLUENT executable software during runtime. The coupling between the discrete phase and continuous phase is accomplished as follows. The equations for the gas phase (continuity, momentum, energy) are solved prior to the injection of droplets. The equations for the liquid droplet phase are then introduced, and the trajectories for the droplets are calculated. The effect of the discrete droplets onto the gas phase is then considered by resolving the gas phase equations with the newly calculated source terms associated with the presence of the droplets. The droplets trajectories are then recalculated based on the modified results of the gas phase equations. The procedure is repeated until solution convergence is achieved.

The boundary conditions for the computation domain are as follows (Fig. 12). Velocity inlet boundaries are applied for the water droplets and air. The injection plane is considered to be at a small distance below the nozzle exit plane where the droplets are released. It is assumed that the water stream at this location has been fully atomized. This simplification is necessary to avoid the need for a complicated nozzle model where flow conditions are difficult to simulate. At the vertical edges of the computation do-

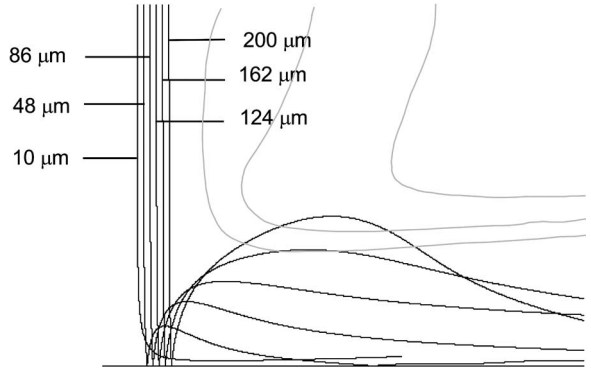

Fig. 13 Droplet-wall interaction using multiple streams of droplets at 0.5 atm ambient pressure

main, pressure outlet boundaries are applied. The wall boundary represented by the strip is assumed to be at a fixed temperature.

5 Results and Discussion

5.1 Droplet-Wall Interaction Using Multiple Stream Injections. A stream of water droplets with diameters of 10, 48, 86, 124, 162 and 200 μm were injected into an air stream (where the injected droplet and air velocity is 3 m/s each). The air and water mass flow rates were 0.028 and 1.2×10^{-3} kg/s, respectively. The surface was heated to 525 °C. Simulations were generated for 0.5, 1, and 5 atm ambient pressures. Figures 13–15 show the interaction between the droplets and the heated wall. In all the cases, the 10 μm droplet was too small to make it to the surface and drifted away until completely evaporated. During

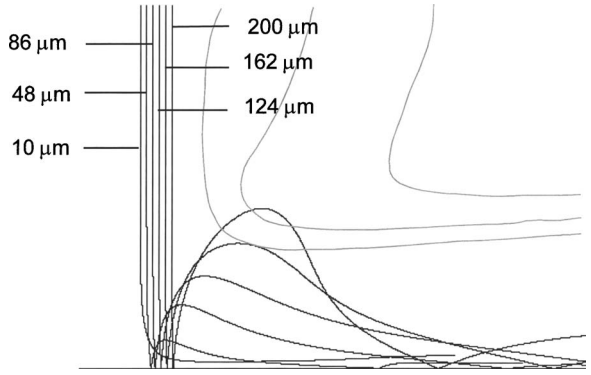

Fig. 14 Droplet-wall interaction using multiple streams of droplets at 1 atm ambient pressure

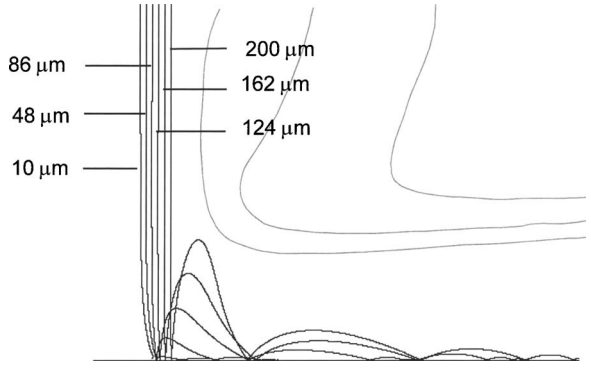

Fig. 15 Droplet-wall interaction using multiple streams of droplets at 5 atm ambient pressure

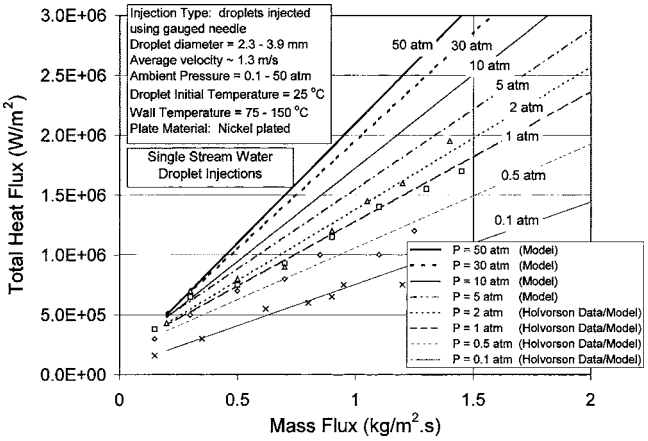

Fig. 16 Comparison between the total heat flux at various ambient pressures

their trajectory, the droplets underwent transient heating, and the evaporation occurred faster as the pressure increased due to the decrease in the latent heat of vaporization. More vapor was also generated from impaction at higher pressure due to the shift in the droplet contact boiling regime. This resulted in an increase in the droplet heat transfer effectiveness. It was shown that for all the droplets, the rebound height decreased with the increase in pressure due to the higher vapor density and higher dynamic viscosity of the air causing an increase in the drag force. The droplets were therefore closer to the wall.

5.2 Heat Transfer Using Single Stream Impingements. In order to check the sensitivity and the validity of the model to various operating pressure conditions, the spray experiment conducted by Halvorson [8] was simulated. In this experiment, a single stream of water droplets ranging from 2.3 to 3.9 mm impinged on a heated nickel plate with wetting contact. The impinging droplet average velocity was about 1.3 m/s and the maximum droplet mass flux was about 2 kg/m^2 s. The model was simulated for the following chamber pressures: 0.1, 0.5, 1, 2, 5 10, 30 and 50 atm. Experimental data by Halvorson were only available for comparison at 0.1, 0.5, 1, and 2 atm ambient pressures (chamber pressures). At 5, 10, 30 and 50 atm, the presented results were based on the model predictions at high operating ambient pressure conditions. Figure 16 shows the droplet total heat flux (at the critical heat flux point) as function of the mass flow flux. The total heat flux accounts for the mist heat flux, radiation, and air convection arising from the local evaporation at the surface. The results reveal a good agreement between Halvorson's experimental data and the model predictions. The almost linear relationship between the critical heat flux and the mass flux shows the spray to behave like an ideal one. The likelihood of the droplets interaction and the flooding on the surface is very small at those relatively low mass fluxes.

Figure 17 shows the total heat flux and the droplet contact heat transfer effectiveness at 2 kg/m^2 s. This mass flux corresponds to the stagnation point in the spray at the wall. The 0.1 atm ambient pressure produces a 60% decrease in the critical heat flux from that at atmospheric pressure for the same mass flux, while the 50 atm ambient pressure produces a 73% increase in the critical heat flux. At 50 atm, the peak in the droplet contact heat flux is close to the maximum that can be possibly achieved [21]. This trend is similar to the experimental data for pool boiling of water [26] where the peak in the critical heat flux was found to occur somewhere between 1/4 to 1/3 of the critical pressure for water (which is between 54 and 73 atm). At pressures above 73 atm, data for pool boiling of water [26] shows a decrease in the critical pool heat flux until it vanishes at the critical pressure. With the lack of experimental data at extreme pressures, it is expected that the

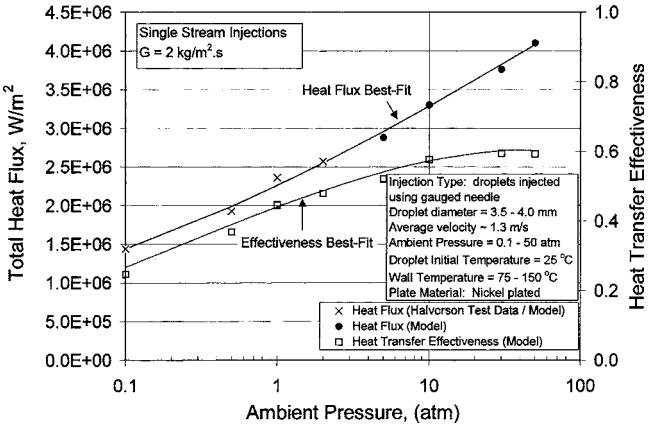

Fig. 17 Total heat flux and droplet contact heat transfer effectiveness at 2 kg/m² s for various ambient pressures

droplet heat flux would follow a similar trend.

The droplet contact heat transfer effectiveness is shown to increase with pressure. There was no noticeable change in the heat transfer effectiveness from 30 to 50 atm. The reason for this is that based on our definition of the effectiveness, the actual droplet heat transfer and the maximum possible heat removal by the droplet have both increased in similar proportions at these high pressures. At high pressures, the sub-cooling of the droplet has a significant effect on the absorption of heat. This is because of the fact that with the increase in pressure, the saturation temperature and the liquid specific heat constant also increase, and therefore a large portion of heat is needed to increase the droplet temperature towards the saturation temperature. Results are shown in Fig. 18 for Halvorson's data and the model predictions at high pressures. The figure shows that at 50 atm, the droplet sub-cooling accounts for 35% of the maximum possible heat removal by the droplet, compared to 11% at atmospheric pressure and to 3% at a sub-atmospheric pressure of 0.1 atm.

5.3 Heat Transfer Using a Full Spray. One of the challenges in air mist cooling is to understand the effect of the droplet size on the heat transfer enhancement and on the uniformity of cooling. The droplet size is an important factor because it affects the amount of deposition on the surface. It will be shown that the desirable droplet size to be used in the spray depends strongly on the system pressure. Figures 19–21 show the spray mist at 0.5, 1, and 10 atm. In this case a full conical spray type is injected onto a stainless steel plate at 525 °C. The initial air and droplet temperature is 27 °C. For all ambient pressures cases, the air and water mass flow rates are 2×10^{-3} and 10^{-4} kg/s (20:1 ratio), respectively. The nozzle is situated at a distance of 40 mm above

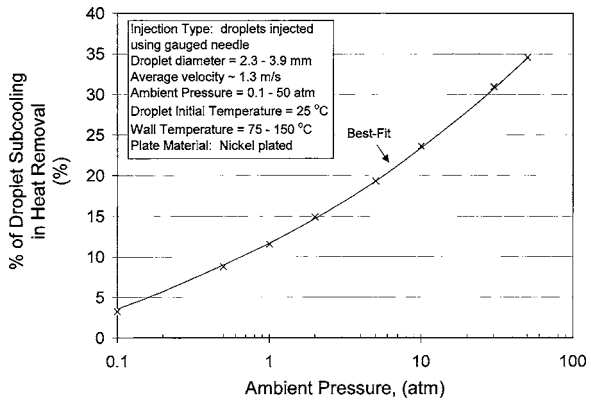

Fig. 18 Droplet sub-cooling versus ambient pressure

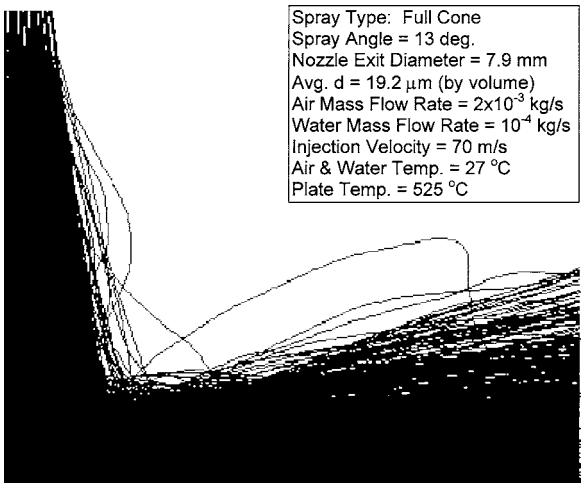

Fig. 19 Mist spray pattern at 0.5 atm ambient pressure (Avg. d=19.2 μm by volume)

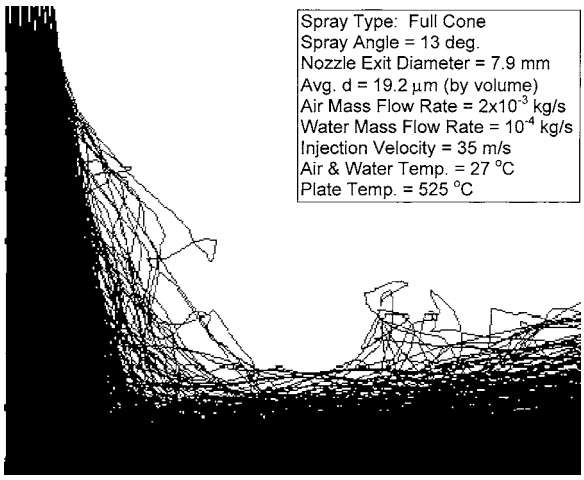

Fig. 20 Mist spray pattern at 1 atm ambient pressure (Avg. d =19.2 μm by volume)

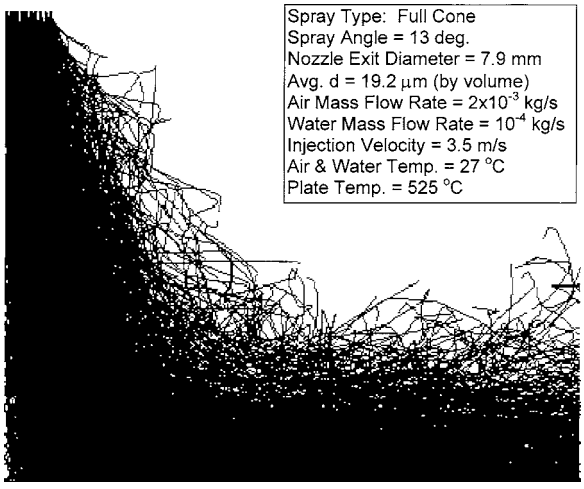

Fig. 21 Mist spray pattern at 10 atm ambient pressure (Avg. d=19.2 μm by volume)

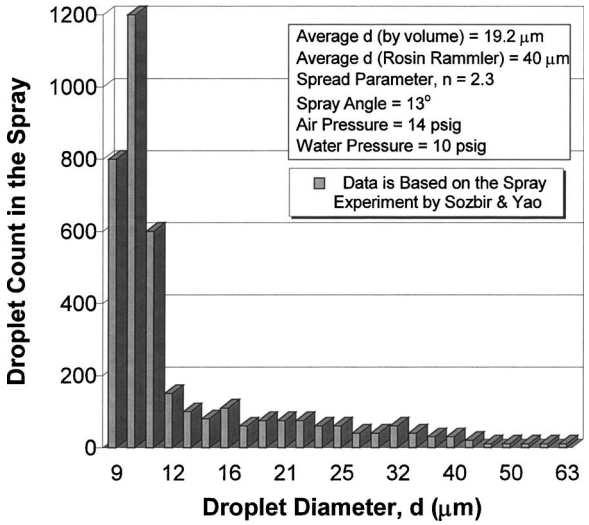

Fig. 22 Droplet count distribution based on the experiment by Sozbir and Yao [2]

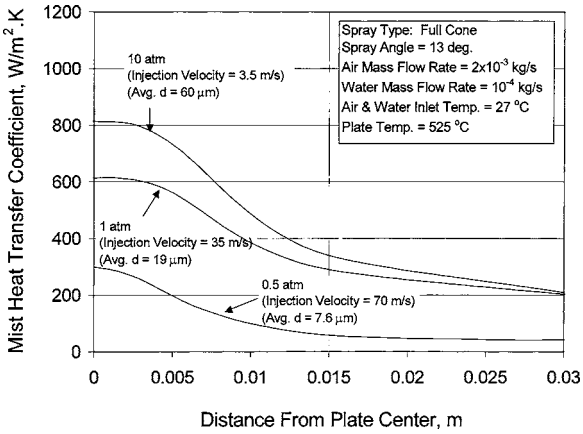

Fig. 24 Mist spray heat transfer coefficient versus ambient pressure using different droplet size spectrum

the plate. The air velocity exiting the air chamber is about 35 m/s. The air-mist nozzle consists of a liquid chamber surrounded by an air chamber with operating water and air gauge pressures of 10 and 14 psig, respectively. The exit diameter of the water chamber is about 1 mm and that of the nozzle system is about 7.9 mm. The liquid flow flux at the plate center (stagnation point) is 2.5 kg/m^2 s at 1 atm ambient pressure. For these flow parameters, the nozzle spray angle was 13°. The spray has a spectrum of droplet diameters with an average diameter of 19.2 μm by volume, a minimum of 9 μm, and a maximum of 63 μm as shown in Fig. 22. The data presented in this figure are based on the experiment conducted by Sozbir and Yao [2].

For the low sub-atmospheric pressure of 0.5 atm, and for the same air and water mass flow rate as the 1 atm case, the droplets are injected with a velocity two times greater than that at 1 atm. With much less air drag acting on the droplets, the droplets reach the surface with a much higher velocity than the case at 1 atm. This causes a drastic increase in the droplet momentum, and the droplets hit mostly at the jet impingement point. The result is a non-uniform cooling of the surface, with high cooling at the plate center, and a sharp decrease in the cooling further away from the center. Compared to the case at 1 atm, and for the same air and water mass flow rate, simulation of the spray at 10 atm ambient pressure shows the droplets to impinge on the surface at a much-reduced velocity due to the ten times increase in the air density. The reduction in the droplet speed causes the droplets to scatter over a wide area with more droplets drifting away. Simulation also shows that at 10 atm the droplets evaporate much easier than at 1 atm. Therefore, droplets that make it to the surface, impinge with a much lower velocity and smaller diameter compared to the case at 1 atm. As a result, the droplet impinging Weber number decreases sharply causing a drastic decrease in the droplet heat transfer effectiveness. Figure 23 shows a comparison in the heat transfer coefficient between the three cases. Simulation shows that 9.4% of the original spray mass evaporated at 0.5 atm, compared to 15% at 1 atm, and 65% at 10 atm.

Figure 24 shows the mist heat transfer coefficient at 0.5, 1, and 10 atm, whereas in this case, finer droplets are used at 0.5 atm and larger droplets are used in the spray at 10 atm, with a spread in the droplet spectrum equivalent to that in Fig. 22. The spray at 0.5 atm has an average droplet size of 7.6 μm (min d=3.6 μm, max d=25 μm), while the spray at 10 atm has an average droplet size by volume of 60 μm (min d=28 μm, max d=198 μm). The decrease in the droplets average size from 19.2 to 7.6 μm for the 0.5 atm case (same water and air mass flow rates) causes the spray to have a higher droplet number density but a lower droplet momentum. As a result, the droplets would hit at the jet impingement point with lower impacting Weber numbers. Therefore, the cooling will be less at the center but more uniform and spreads out to a larger area (as seen in Fig. 25). The decrease in the droplet

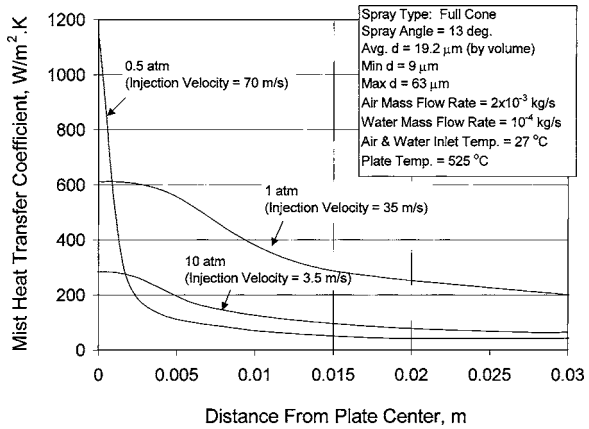

Fig. 23 Mist spray heat transfer coefficient profile versus ambient pressure using the same droplet size spectrum

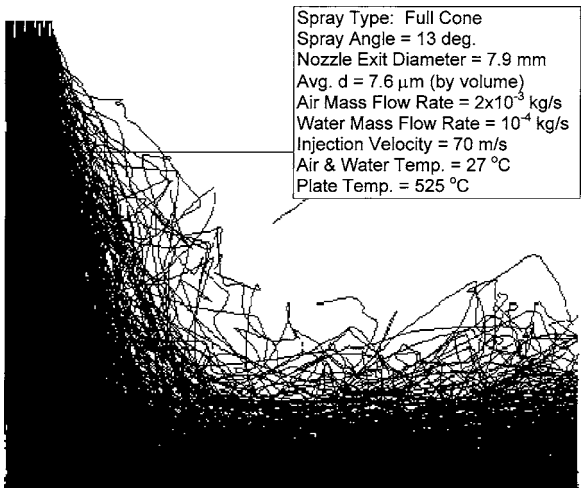

Fig. 25 Mist spray pattern at 0.5 atm ambient pressure (Avg. d=7.6 μm by volume)

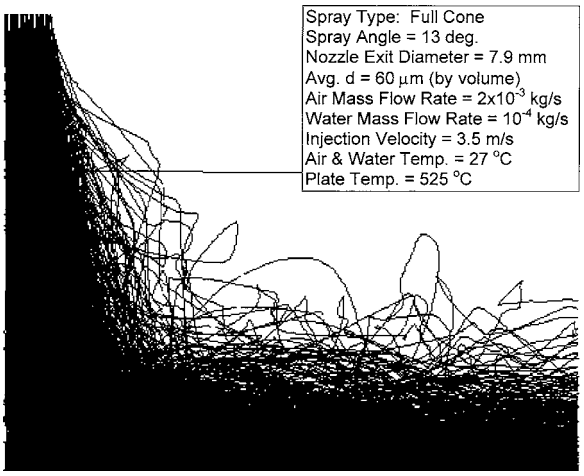

Fig. 26 Mist spray pattern at 10 atm ambient pressure (Avg. d=60 μm by volume)

Weber number at the jet impingement point would cause a decrease in the heat transfer effectiveness. This can be seen by comparing Fig. 24 with Fig. 23.

At 10 atm ambient pressure, for the same amount of air and water mass flow rate used earlier, and with larger droplets (60 μm compared to 19.2 μm), the spray has a lower droplet number density but a higher droplet momentum. Figure 26 shows the spray mist at 10 atm. More droplets make impact at the plate center (Fig. 26) than when finer droplets are used (Fig. 21), and the number of drifting droplets decreases sharply. With larger droplets, the impinging Weber number increases, and the chances that the droplets would make multiple impingements also increase. This causes an increase in the droplet contact heat transfer effectiveness.

6 Conclusions

A numerical model was developed to study the mist cooling on metallic surfaces heated in the temperature range between nucleate and film boiling at various ambient pressures. The model, which was initially developed for simulating atmospheric pressure conditions, was expanded to simulate high and sub-atmospheric pressure conditions by properly accounting for the droplet-wall impaction and the air-mist heat transfer mechanism as function of the ambient pressure. The model was tested against available experiments for single stream droplet impactions and compared favorably well. Spray simulation conducted for a wide range of pressures (using nozzles that dispense a spectrum of non-uniform droplets) reveals the following primary key issues regarding droplet dynamics, heat transfer, and vaporization:

1) *Droplet dynamics*. At higher pressures, the larger the droplet size, the better is the droplet-wall impaction. Larger droplets are able to hit the surface and better spread at impaction. At sub-atmospheric pressures, larger droplets have a detrimental effect due to their ballistic and localized impaction near the stagnation point. This is caused by the much reduced air resistance due to the lower ambient density. For all ranges of pressure, a spray dispersing a spectrum of non-uniform droplets always has the larger droplets impinging closer to the center while the smaller droplets impinging further away.
2) *Droplet heat transfer*. At higher pressures, the Leidenfrost point shifts to a higher temperature. This leads to an increase in the wetting capability of the droplets at impaction, and therefore, to a higher droplet contact heat transfer effectiveness. For the same amount of liquid loading, and for low-pressure applications, larger droplets result in non-uniform cooling because the ballistic impaction of larger droplets causes a sharp increase in the heat transfer near the stagnation point. On the other hand, for high-pressure applications, larger droplets result in uniform cooling due to better impact at the wall.
3) *Droplet vaporization*. At high ambient pressures, more vapor is generated at each droplet impaction at the wall. This is due to the much-reduced latent heat of vaporization at higher pressures. The result is an increase in the droplet contact heat transfer effectiveness.

Nomenclature

$c_{p,l}$ = liquid specific heat constant (J/kg K)
$c_{p,v}$ = vapor specific heat constant (J/kg K)
d = droplet diameter (μm)
e_n = normal coefficient of restitution
G = liquid mass flux (kg/m^2 s)
h_{fg} = latent heat of vaporization (J/kg)
P = ambient pressure (N/m^2)
q_c = surface heat flux (W/m^2)
q_{CHF} = critical heat flux (W/m^2)
q_{Min} = minimum heat flux (W/m^2)
T_{CHF} = temperature at critical heat flux (°C)
T_{Lieden} = Leidenfrost temperature (°C)
T_{liq} = liquid temperature (°C)
T_{sat} = liquid saturation temperature (°C)
T_w = wall temperature (°C)
u_τ = shear velocity at the wall (m/s)
$v_{i,n}$ = droplet impinging normal velocity at the surface (m/s)
v_a = air velocity (m/s)
We_n = normal impinging droplet Weber number
y = distance from the wall (m)
y^+ = normalized distance from the wall (m)
ε = droplet contact heat transfer effectiveness
ρ = density of the liquid-vapor mixture (kg/m^3)
ρ_d = droplet density (kg/m^3)
μ = dynamic viscosity of the liquid-vapor mixture (kg/s m)
σ_d = droplet surface tension (N/m)

References

[1] Chang, Y. W., and Yao, S. C., 2000, "Studies of Water Mist Cooling on Heated Metal Surfaces," *Proceedings of NHTC'00, 34th National Heat Transfer Conference*.
[2] Sozbir, N., and Yao, S. C., 2002, "Experimental Investigation of Water Mist Cooling for Glass Tempering," ASME-IMECE Conference.
[3] Yao, S. C., et al., 1989, "Impact Spray Boiling for Thermal Control of Electronic Systems," ASME HTD-Heat Transfer in Electronics, **111**, pp. 129–133.
[4] Yao, S. C., et al., 2001, "MEMS Enabled Micro Spray Cooling System for Thermal Control of Electronic Chips," ASME, IMECE.
[5] Nirmalan, N. V., et al., 1998, "An Experimental Study of Turbine Vane Heat Transfer with Water-Air Cooling," J. Turbomach., **120**, pp. 50–62.
[6] Li, X., et al., 2003, "Mist/Steam Heat Transfer with Jet Impingement onto a Concave Surface," J. Heat Transfer, **125**(3), pp. 438–446.
[7] Bohn, D., et al., 2002, "Experimental and Numerical Investigation of a Steam-Cooled Vane," *Proceedings of ASME Turbo Expo 2002*, Amsterdam, The Netherlands, June 3–6, 2002.
[8] Halvorson, P. J., 1994, "On the Heat Transfer Characteristics of Spray Cooling," Ph.D. thesis, Georgia Institute of Technology.
[9] Testa, P., and Nicotra, L., 1986, "Influence of Pressure on the Leidenfrost Temperature and on Extracted Heat Fluxes in the Transient Mode and Low Pressure," J. Heat Transfer, **108**, pp. 916–921.
[10] Emmerson, G. S., and Snoek, C. W., 1978, "The Effect of Pressure on the Leidenfrost Point of Discrete Drops of Water and Freon on a Brass Surface," Int. J. Heat Mass Transfer, **21**, pp. 1081–1086.
[11] Emmerson, G. S., 1975, "The Effect of Pressure and Surface Material on the Leidenfrost Point of Discrete Drops of Water," Int. J. Heat Mass Transfer, **18**, pp. 381–386.
[12] Sakane, A., et al., 1988, "Behaviour of Diesel Spray Impinging on a Wall," Trans. of JSME, **54–503(B)**, pp. 1861–1865 (in Japanese).

[13] Mirza, R., 1991, "Studies of Diesel Spray Interacting with Cross-Flow and Solid Boundaries," Ph.D. thesis, University of Manchester, Manchester, UK.
[14] Senda, J., et al., 1994, "Modeling of Diesel Spray Impingement on a Flat Wall," SAE Paper No. 941894, pp. 1918–1931.
[15] Issa, R. J., and Yao, S. C., 2003, "Numerical Simulation of Sprays Impinging on Heated Surfaces," *Sixth ASME-JSME Thermal Engineering Joint Conference*, March 16–20.
[16] Wachters, L. H. J., and Westerling, N. A. J., 1966, "The Heat Transfer from a Hot Wall to Impinging Water Drops in the Spheroidal State," Chem. Eng. Sci., **21**, pp. 1047–1056.
[17] Naber, J. D., and Farrell, P. V., 1993, "Hydrodynamics of Droplet Impingement on a Heated Surface," SAE Publ. No. 930919.
[18] Hatta, N., et al., 1995, "Collision Dynamics of a Water Droplet Impinging on a Rigid Surface above the Leidenfrost Temperature," ISIJ Int., **35**, pp. 50–55.
[19] Karl, A., et al., 1996, "Comparison of New Numerical Results for Droplet Wall Interactions with Experimental Results," The American Society of Mechanical Engineers, 1996 Fluids Engineering Division Conference, 1.
[20] Chandra, S., and Avedisian, C. T., 1991, "On the Collision of a Droplet with a Solid Surface," Proc. R. Soc. London, Ser. A, **432**, pp. 13–41.
[21] Issa, R. J., 2003, "Numerical Modeling of the Dynamics and Heat Transfer of Impacting Sprays for a Wide Range of Pressures," Ph.D. dissertation, University of Pittsburgh.
[22] Deb, S., and Yao, S. C., 1989, "Analysis on Film Boiling Heat Transfer of Impacting Sprays," Int. J. Heat Mass Transfer, **32**, pp. 2099–2112.
[23] Pedersen, C. O., 1970, "An Experimental Study of the Dynamic Behavior and Heat Transfer Characteristics of Water Droplets Impinging Upon a Heated Surface," Int. J. Heat Mass Transfer, **13**, pp. 369–380.
[24] Senda, J., et al., 1988, "The Heat Transfer Characteristics of a Small Droplet Impinging upon a Hot Surface," JSME Int. J., Ser. II, **31**, pp. 105–111.
[25] McGinnis, F. K. III, and Holman, J. P., 1969, "Individual Droplet Heat Transfer Rates for Splattering on Hot Surfaces," Int. J. Heat Mass Transfer, **12**, pp. 95–108.
[26] Cichelli, M. T., and Bonilla, C. F., 1946, "Heat Transfer to Liquids Boiling Under Pressure," AIChE J., **42**, pp. 755–787.

Fast and Accurate Solutions of Steady Stokes Flows Using Multilevel Boundary Element Methods

G. F. Dargush

M. M. Grigoriev
e-mail: mmg3@eng.buffalo.edu

Department of Civil Engineering,
State University of New York at Buffalo,
Amherst, New York 14260 USA

Most recently, we have developed a novel multilevel boundary element method (MLBEM) for steady Stokes flows in irregular two-dimensional domains (Grigoriev, M.M., and Dargush, G.F., Comput. Methods. Appl. Mech. Eng., 2005). The multilevel algorithm permitted boundary element solutions with slightly over 16,000 degrees of freedom, for which approximately 40-fold speedups were demonstrated for the fast MLBEM algorithm compared to a conventional Gauss elimination approach. Meanwhile, the sevenfold memory savings were attained for the fast algorithm. This paper extends the MLBEM methodology to dramatically improve the performance of the original multilevel formulation for the steady Stokes flows. For a model problem in an irregular pentagon, we demonstrate that the new MLBEM formulation reduces the CPU times by a factor of nearly 700,000. Meanwhile, the memory requirements are reduced more than 16,000 times. These superior run-time and memory reductions compared to regular boundary element methods are achieved while preserving the accuracy of the boundary element solution. [DOI: 10.1115/1.1949648]

Keywords: Stokes Flows, Multilevel Boundary Element Methods

Introduction

Boundary element methods (BEM) have become one of the most powerful and attractive tools to solve linear Stokes flow problems because of their inherent accuracy and a boundary-only discretization of the computational domain. A standard BEM technique requires two major steps to obtain a numerical solution. During the first step, a global boundary element matrix is formed, which necessitates an integration of the Stokeslets over each of the boundary elements. The global matrix solution constitutes the second step to obtain an unknown vector of boundary velocities and tractions. Although the first step requires N^2 operations, the complexity of the second step is of order N^3 when using Gauss elimination. For relatively small numbers of degrees of freedom N (e.g., $N<10^4$), the regular boundary element methods are fast and practical, even on a single-processor computer, since the integration over the boundary elements dominates over the matrix solution. However, most problems of practical importance, especially in three dimensions, require fine boundary element meshes leading to very large numbers of degrees of freedom $N>10^5$. For these boundary element discretizations, the conventional BEM algorithms become prohibitively expensive even on state-of-the-art supercomputers due to both memory and run-time requirements.

To extend the applicability of regular boundary element methods to larger numbers of degrees of freedom, several fast algorithms have been proposed in the past two decades. These techniques include Barnes-Hut [1,2], wavelets [3,4], fast multipole [5–12], and multilevel multi-integration [13–19] algorithms. The fast multipole methods (FMM), first introduced by Rokhlin [5], are currently the most popular of the fast algorithms. These reduce the computational complexity of the matrix-vector multiplication to order $N \ln N$ per iteration loop. When integral equations of the second kind are considered, an overall complexity of iterative solutions using the fast multipole algorithms is of order $N \ln N$.

Although FMM and wavelet-based approaches have been extensively developed, multilevel multi-integration (MLMI) methods have not enjoyed a wide acceptance in computational practice despite the great potential of the methods. The MLMI method was proposed by Brandt and Lubrecht [13] for fast evaluation of multi-integrals involving both smooth and singular-smooth kernels. The MLMI requires that the kernels are asymptotically smooth, implying they can be accurately represented by the approximate kernel functions from coarser meshes when the points of interest are located at a some distance from the source points. This, in turn, requires a correction only within the singularity zone, and thus facilitates finer-to-coarser inter-level transfers with essentially no loss in accuracy of the original BEM formulation. We note that the modern MLMI algorithms utilize interpolating polynomials to represent the kernel functions and are directly applicable to almost all types of nonoscillatory kernels that exhibit asymptotical smoothness (fortunately, most physically relevant kernels do!). This is in sharp contrast to the fast multipole algorithms, where each type of kernel requires specific expansion.

Following the pioneering work [13], Lubrecht and Ioannides [14], Polonsky and Keer [18,20] and Venner and Lubrecht [21] extended the MLMI methods to the solution of elastohydrodynamic lubrication and rough surface contact problems. Recently, Grigoriev and Dargush [15] extended the MLMI algorithm to two-dimensional solutions of the Laplace equation in a unit square with mixed boundary conditions giving a rise to a multilevel boundary element method (MLBEM). Then, the authors extended the MLBEM algorithm to the solution of the Helmholtz equation using an integral form that involves asymptotically decaying oscillatory log-singular and strongly singular kernels [16]. Most recently, the MLBEM algorithm was extended to solve steady two-dimensional Stokes flows in more complex geometries [19]. The multilevel algorithm permitted boundary element solutions using as many as 16,392 degrees of freedom. While preserving the accuracy of the original BEM solutions, the authors demonstrated a

Contributed by the Fluids Engineering Divison for Publication in the JOURNAL OF FLUIDS ENGINEERING. Manuscript received by the Fluids Engineering Division August 29, 2004; Final manuscript received February 23, 2005; Associate Editor: Subrata Roy.

speed-up factor of ~40 for the fast MLBEM algorithm compared to a conventional Gauss elimination approach. The sevenfold memory savings were attained for the multilevel algorithm.

Similar to our previous studies [15–17,19] on the MLBEM, we consider a direct boundary element method for mixed Dirichlet-Neumann boundary conditions, leading to boundary integral formulations of the first kind. In general, this results in slow convergence of the iterations as the boundary element meshes are refined and no preconditioning is used. In this paper, we utilize C-cycle multigrid iterations [22] to accelerate convergence. The alternative approaches can include the use of other types of preconditioners or the use of indirect boundary element formulations [23,24]. However, discussions of these formulations go beyond the scope of this paper.

In this presentation, we extend the MLBEM formulation [19] to dramatically improve the performance of the numerical approach. First, we preevaluate the singular corrections $C_i^{(k)}$ for both matrix-vector and matrix-transpose-vector multiplication. Next, the centered correction stencils are also preevaluated for an internal source point and then applied to any other source point except for the patch-end points. These two modifications in the original algorithm lead to tremendous reductions in run-time and memory requirements. In order to demonstrate the performance of the proposed method, we consider an example problem with the exact solution.

Multilevel Boundary Element Methods

Governing Equations and Integral Formulation. The steady Stokes flow is governed by the well-known dimensionless continuity

$$\frac{\partial u_i}{\partial x_i} = 0 \tag{1}$$

and momentum

$$\nu \frac{\partial^2 u_i}{\partial x_j \partial x_j} - \frac{\partial p}{\partial x_i} = 0 \tag{2}$$

equations. In Eqs. (1) and (2), u_i is the velocity of the flow, p is the pressure, ν is the viscosity. Both velocities $\bar{u}_i(x)$ on $x \in \Gamma_u$ and tractions $\bar{t}_i(x)$ on $x \in \Gamma_t$ may be specified as Dirichlet and Neumann boundary conditions, respectively. Note that $\Gamma_u \cap \Gamma_t = 0$ and $\Gamma_u \cup \Gamma_t = \Gamma$, where the surface Γ bounds the computational domain Ω. The corresponding integral form of the boundary value problem is given by

$$c(\xi)u_k(\xi) + \int_\Gamma u_i(x) f_{ik}(x-\xi) d\Gamma(x) = \int_\Gamma t_i(x) g_{ik}(x-\xi) d\Gamma(x) \tag{3}$$

Here,

$$g_{ik}(x-\xi) = \frac{1}{4\pi\nu}\left(\frac{y_i y_k}{r^2} - \delta_{ik} \ln r\right) \tag{4}$$

and

$$f_{ik}(x-\xi) = -\frac{y_i y_k y_j n_j}{\pi r^4} \tag{5}$$

are two-dimensional Stokeslets representing single- and double-layer potentials, respectively. In (3), $t_i = \sigma_{ij} n_j$ is the boundary traction, n_i is the unit outward normal to the surface $\Gamma(x)$, ξ stands for the collocation point $\xi \in \Omega$, $y_i = x_i - \xi_i$, and $r = \sqrt{y_i y_i}$ is the distance from the collocation point ξ_i to the field point x_i. The stress tensor is defined as usual

$$\sigma_{ij} = \nu\left(\frac{\partial u_i}{\partial x_j} + \frac{\partial u_j}{\partial x_i}\right) - p\,\delta_{ij}$$

The geometric function $c(\xi) = 0.5$ when the source point ξ is on a smooth portion of the boundary.

Boundary Element Discretization. Let us introduce P smooth nonoverlapping boundary patches Γ_p for $p = 1, 2, \ldots, P$ and assume that the variation of boundary velocity $u_i(x)$ and traction $t_i(x)$ over every patch Γ_p is smooth. Then, Eq. (3) may be written as follows:

$$c(\xi)u_k(\xi) + \sum_{p=1}^{P} \int_{\Gamma_p} u_i(x) f_{ik}(y) d\Gamma(x) = \sum_{p=1}^{P} \int_{\Gamma_p} t_i(x) g_{ik}(y) d\Gamma(x) \tag{6}$$

Introducing linear boundary elements over all boundary patches, we discretize the integral equation (6) to the form

$$c(\xi)u_k(\xi) + \sum_{p=1}^{P} \sum_{n=1}^{N_p} u_i^{(\alpha)} F_{ikmn}^{(\alpha)} = \sum_{p=1}^{P} \sum_{n=1}^{N_p} t_i^{(\alpha)} G_{ikmn}^{(\alpha)} \tag{7}$$

The algorithm of accurate evaluation of discrete coefficients $G_{ikmn}^{(\alpha)}$ and $F_{ikmn}^{(\alpha)}$ is detailed in Ref. [19]. Here, to facilitate the MLBEM algorithm, we apply boundary conditions and recast the discrete integral equation (7) into the following matrix form:

$$\boldsymbol{A} \cdot \boldsymbol{\nu} = \boldsymbol{b} \tag{8}$$

where $\boldsymbol{\nu}$ is the generalized vector of unknown velocities and tractions, and $\boldsymbol{b}$ is the known force vector. Note that the global matrix $\boldsymbol{A}$ of size $N \times N$ is dense.

Similar to our earlier work [15,16,19], we utilize a biconjugate gradient method [25] to solve the matrix equation (8). Since this iterative approach requires both matrix-vector $\boldsymbol{A\nu}$ and matrix transpose-vector $\boldsymbol{A}^T\boldsymbol{\nu}$ multiplications at any iteration, we use fast multilevel multi-integration [13] for these operations. In the following two subsections, we briefly outline the MLMI algorithm that was detailed in Grigoriev and Dargush [19], and discuss modifications introduced in the fast matrix-vector operations that allow tremendous savings in computational resources.

MLMI for Block-Matrix-Vector Multiplication. For every patch Γ_p, we introduce a sequence of L boundary element meshes $M^0, M^1, \ldots, M^L$, where M^0 is the finest level mesh and M^L is the coarsest boundary element mesh. For the sake of simplicity, our consideration is restricted to uniform boundary element segmentations over the patches; however, the mesh sizes on M^0 can differ from patch to patch. On the finest level mesh, the block-matrix-vector multiplication $\boldsymbol{A\nu}$ can be represented as the following multisummation over every patch:

$$w_i^{(0)} = h_0 \sum_{j=0}^{N_0} H_{i,j}^{(0)} v_j^{(0)} - R_i \quad \text{for } i = 0, 1, \cdots, N_0 \tag{9}$$

In (9), the multisummation is performed over index j representing the set of boundary elements on M^0, h_0 is the scaled boundary element mesh size on the finest level mesh, $v_j^{(0)}$ stands for the generalized vector of unknown velocities or tractions at any iteration on the finest level mesh, and $H_{i,j}^{(0)}$ is the generalized form of assembled coefficients associated with $G_{ikmn}^{(\alpha)}$ and $F_{ikmn}^{(\alpha)}$. Note that mesh M^0 has N_0 linear boundary elements and N_0+1 collocation nodes. The patch end correction R_i in (9) ensures a smooth variation of the coefficients $H_{i,j}^{(0)}$ within the patch on the finest level, and its definition can be found in Ref. [19].

Following the approach presented earlier by the current authors [19], we introduce a coarse-to-fine level interpolation of the generalized kernels that permits a fine-to-coarse-level transfer of the multisummation (9). Furthermore, owing to the asymptotic

smoothness of the kernels, we restrict correction of the interpolated kernels only to a small area at the vicinity of the source point. In doing so, all corrections outside the singularity zone are neglected because these are smaller than the error due to a boundary element discretization. Therefore, the multi-integrals on any coarse level $k=1,2,\ldots,L$ can be written in the following form:

$$w_i^{(k)} \cong h_k \sum_{j=0}^{N_k} H_{i,j}^{(k)} v_j^{(k)} + C_i^{(k)} \tag{10}$$

Here, the total correction $C_i^{(k)}$ includes both the singular and patch-end corrections [19]. Note that although Eq. (10) allows an evaluation of the multi-integral $w_i^{(k)}$ on any level mesh, the complexity of the matrix-vector operation can be reduced to $O(N \log N)$ if the multi-integral is recursively evaluated from the coarsest to the finest levels using the following equation [19]:

$$w_i^{(k)} \cong [\hat{\mathbf{\Pi}}_{k+1}^k w_\cdot^{(k+1)}]_i + h_k \sum_{|i-j|\leqslant m}^{N_k} [H_{i,j}^{(k)} - \hat{H}_{i,j}^{(k)}] v_j^{(k)} + C_i^{(k)} - \hat{C}_i^{(k)} \tag{11}$$

We should note that the evaluation of the correction $\hat{C}_i^{(k)}$ requires a sequential evaluation of coefficients $C_i^{(k)}$ for stencil nodes adjacent to the current source node i. Obviously, the computational load as well as storage requirements are reduced significantly provided that the corrections $C_i^{(k)}$ are preevaluated. Moreover, note that these preevaluations are not needed to be performed for all levels. This approach recently implemented for heat diffusion problems [15] leads to a dramatic reduction of the computational complexity compared to the original developments for the acoustics problems [16] and steady Stokes flows [19].

In this study, the computer requirements are reduced even to a more dramatic extent beyond those achieved in our earlier research on steady heat diffusion [15]. Here, the centered correction stencils are preevaluated for an internal source point and then applied to any other source point for which the correction stencil is not affected by the patch ends. Indeed, several source points close to the patch ends require reevaluation of the individual correction stencils. However, as the boundary mesh gets refined, the additional computations become insignificant.

MLMI for Block-Matrix-Transpose-Vector Multiplication. A block-matrix-transpose-vector multiplication on the finest level mesh M^0 can be given by the following multisummation over each patch:

$$w_j^{(0)} = h_0 \sum_{i=0}^{N_0} H_{i,j}^{(0)} v_i^{(0)} - R_j \quad \text{for } j = 0,1,\cdots,N_0 \tag{12}$$

Note that the summation in (12) is now performed over index i representing the collocation point ξ_i. In (12), the patch-end corrections R_j on the finest level boundary element mesh are again defined in Ref. [19]. Following our earlier work [19], we transfer the multisummation (12) defined on level $k=0$ to any coarse level $k>0$ as follows:

$$w_j^{(k)} \cong h_k \sum_{i=0}^{N_k} H_{i,j}^{(k)} v_i^{(k)} + C_j^{(k)} \quad \text{for } k = 0,1,\cdots,L \tag{13}$$

The total correction $C_j^{(k)}$ involving the patch-end corrections R_j and a sum of singular corrections from each finer level can also be found in [19]. Although the multi-integrals $w_j^{(k)}$ can be evaluated using expression (13) on each level, we perform the fast multisummation only on the coarsest level boundary element mesh M^L

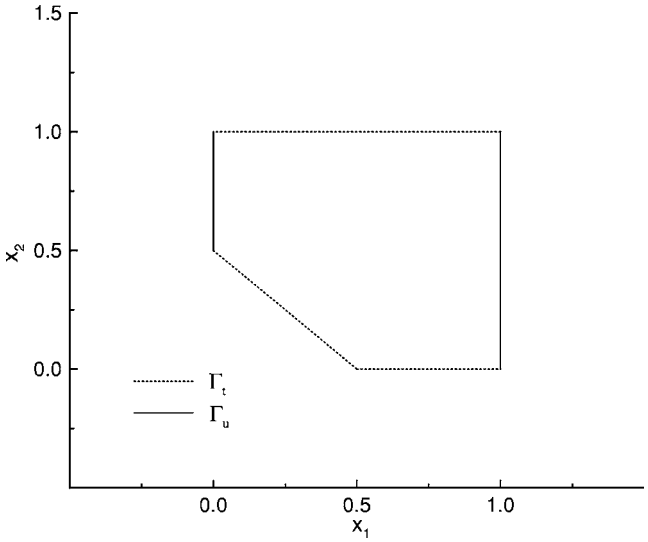

Fig. 1 Problem definition for the irregular pentagon domain

$$w_j^{(L)} \cong h_L \sum_{i=0}^{N_L} H_{i,j}^{(L)} v_i^{(L)} + C_j^{(L)} \tag{14}$$

as the direct application of (14) to the finer levels $k<L$ will require even more operations than the original multisummation (12) on the finest level mesh. The multi-integrals (14) on the finer level mesh points can be represented as follows:

$$w_j^{(k)} \cong [\tilde{\mathbf{\Pi}}_{k+1}^k w_\cdot^{(k+1)}]_j + h_k \sum_{|i-j|\leqslant m}^{N_k} (H_{i,j}^{(k)} - \tilde{H}_{i,j}^{(k)}) v_i^{(k)} + C_j^{(k)} - \tilde{C}_j^{(k)} \tag{15}$$

Again, we preevaluate $\tilde{C}_j^{(k)}$ and the centered correction stencils to dramatically reduce the complexity of the computations similar to the fast matrix-vector operation described above.

C-Cycle Multigrid. Since the biconjugate gradient method [25] used in this work requires $O(N^{1/2})$ iterations on the boundary element mesh M^0, we utilize the multigrid technique proposed by Brandt [22] to accelerate the convergence. Although several multigrid algorithms are readily available, we restrict our consideration to the C-cycle multigrid [22], as it provides good convergence acceleration for the problems considered in this presentation.

Numerical Results

Introduction. The MLBEM code developed earlier for the fast solution of the heat diffusion [15], acoustics scattering [16], and Stokes flows [19] has been extended to accommodate the modifications outlined above. All runs have been performed on a Sun Ultra-Enterprise workstation with quadruple UltraSparc-II 336 MHz processors. In this presentation, we consider an example problem for steady Stokes flow that possesses an analytical solution. The model problem is formulated in a pentagon of irregular shape that is split into five boundary patches. We consider two multilevel boundary element methods, namely, one presented earlier in [19] and the algorithm modified here. The run-time and memory requirements for both MLBEM formulations are investigated for the model problem to highlight an exceptional performance of the fast MLBEM formulation proposed in this paper.

Example Problem. We consider Stokes flow in the pentagonal domain of irregular shape as shown in Fig. 1. The exact velocity

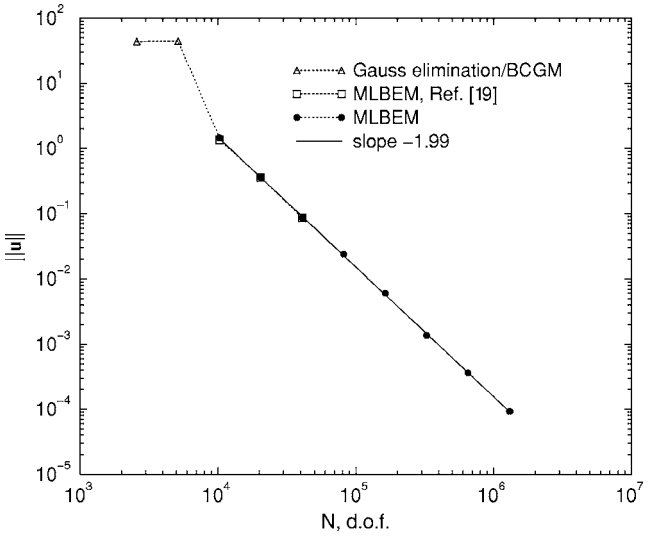

Fig. 2 Convergence of the numerical errors for the conventional and fast boundary element methods with the boundary mesh refinement

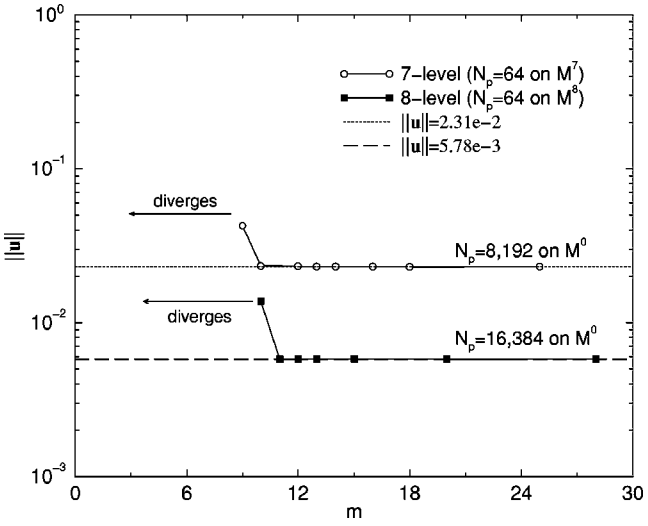

Fig. 3 MLMI errors with respect to the number of singular zone points

and pressure fields satisfying the governing equations (1) and (2) are defined as follows:

$$u_1(x_1,x_2) = \cos(kx_1)\frac{\exp(kx_2)}{\exp(k)} + \sin(kx_2)\frac{\exp(kx_1)}{\exp(k)} \tag{16}$$

$$u_2(x_1,x_2) = \sin(kx_1)\frac{\exp(kx_2)}{\exp(k)} + \cos(kx_2)\frac{\exp(kx_1)}{\exp(k)} \tag{17}$$

$$p(x_1,x_2) = \text{const} \tag{18}$$

respectively. For the boundary value problem, we specify velocities on Γ_u, and tractions on Γ_t directly from (16)–(18). Note that Γ_u includes two boundary patches, while Γ_t has three patches (Fig. 1). In this study, we consider high wave parameter $k = 10^3\pi$; thus, the solution is very oscillatory in space along both directions and involves extremely sharp velocity gradients at $x_1 \to 1$ and $x_2 \to 1$. Therefore, very sharp boundary element discretizations are needed to obtain a proper resolution.

An L_∞ error norm $\|\boldsymbol{u}\|$ is used to monitor the numerical solution error throughout the paper. Thus,

$$\|\boldsymbol{u}\| = \max|\boldsymbol{u}^{(num)} - \boldsymbol{u}^{(ex)}| \text{ for } \zeta \in \Gamma_t. \tag{19}$$

We note that one of our objectives is to demonstrate that the multilevel BEM formulation allows extremely fast solutions, while retaining the same level of accuracy as the direct boundary element method on mesh M^0. Figure 2 shows the numerical error norm $\|\boldsymbol{u}\|$ with respect to the total number of degrees of freedom N on M^0. We emphasize that, for a relatively small number of degrees of freedom, both multilevel boundary element methods presented earlier [19] and in this paper result in the same accuracy as the direct Gauss elimination and the direct application of the iterative BCGM algorithm. Note that the direct BEM algorithms are not applicable to boundary element discretizations of $N_p = 2048$ or finer due to memory restrictions. As evident from Fig. 2, much finer boundary element meshes are needed to obtain sufficiently accurate numerical solutions for $k = 10^3\ \pi$. We emphasize that the MLBEM approach permits very fine mesh resolutions. On the current workstation, we have been able to obtain solutions on the BEM mesh as fine as $N_p = 131,072$ on M^0 resulting in as many as 1,310,730 degrees of freedom. Meanwhile, the multilevel boundary element method presented in [19] permits numerical solutions with only $N_p = 4096$ elements or coarser per patch. Note that the MLBEM algorithms using the linear boundary elements provide a quadratic rate of convergence with respect to the mesh size for the entire range of mesh discretizations; that is, error of order $O(h_0^2)$ for the velocity vector (Fig. 2).

Next, we investigate the MLMI errors for six-noded interpolation stencils considered in this paper. These centered and noncentered stencils lead to quintic interpolation functions that are presented in [16]. Figure 3 shows the MLMI errors $\|\boldsymbol{u}\|$ for different level transfers for meshes involving $N_p = 8192$ and $N_p = 16,384$ boundary elements per patch on M^0. The number of boundary elements on the coarsest MLMI levels is shown in the parentheses with the legends. We should note that the MLMI approach allows accurate results even when the number of correction points within the singularity zone m is significantly fewer than the optimal values given by Brandt and Lubrecht [13]. However, the accuracy of the MLMI approach deteriorates quickly when m becomes too small (Fig. 3). No converged solutions are possible when the number of correction points is insufficient to retain accuracy of the solution. Note again that for both mesh discretizations, the conventional BEM methods are not realizable on the workstation due to memory requirements. Also, the coarsest level mesh of $N_p = 64$ boundary elements are too coarse to provide any meaningful results for $k = 10^3\ \pi$.

Figure 4 presents the number of points m that should be retained in the singular zone to preserve the accuracy of the MLMI transfers. For the example problem considered in this paper involving a very oscillatory solution, the number of correction points is significantly fewer than the optimal number of points for the quintic interpolation stencils recommended by Brandt and Lubrecht [13]. We note that m is greatly dependent on the smoothness of the problem. Generally, the smoother the problem, the greater the number of singular points needed to maintain the accuracy of the MLBEM algorithm. For the hypothetical case of linear temperature fields, the MLBEM formulation using linear boundary elements would require the singular zone to extend to include all nodal points. Fortunately, only a single linear boundary element per patch will provide a solution with machine precision for this kind of problem and fast methods are not needed. On the other hand, when the solution has greater variability, m may be maintained at moderate levels with no loss in accuracy.

In this presentation, we consider multigrid method results when the initial vector on mesh M^0 is obtained using the interpolation of the coarsest multigrid level BEM mesh solution since this provides us with extremely rapid convergence. The evolution of the error norm $\|\boldsymbol{u}\|$ with respect to the iterations on the M^0 -mesh is shown in Fig. 5. Here, we consider one-, two-, and three-level

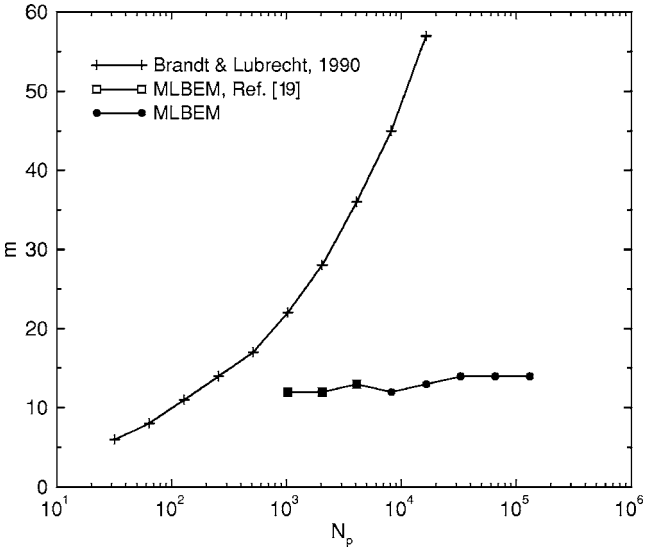

Fig. 4 The number of singular zone points *m* needed to retain a desired level of accuracy

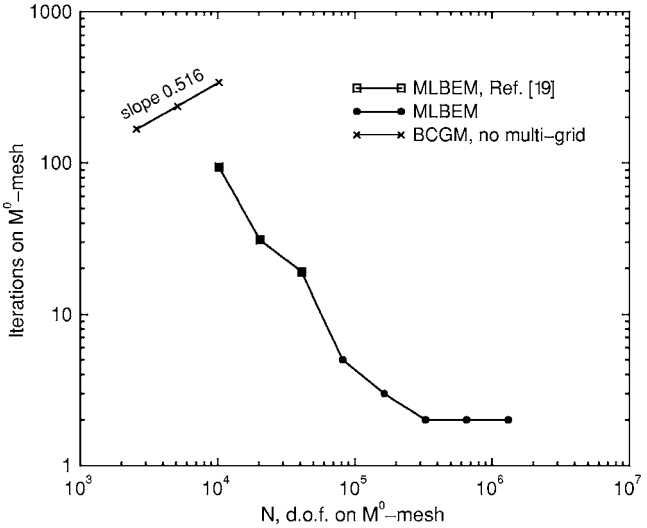

Fig. 6 The number of iterations on the finest level mesh to achieve convergence; One-level multi-grid versus no multi-grid

multigrid iterations. For one-level multigrid (i.e., $\Lambda=1$), the numerical error reduces dramatically for the first two iterations on the finest level mesh reaching the desired level in just two C-cycles. Then, the numerical error remains on the desired level if the iterations are continued. For $\Lambda=2$ and $\Lambda=3$, the numbers of iterations required to reduce the error norm to the desired level are slightly higher (Fig. 5). Additionally, the performance of the multigrid for $\Lambda>1$ degrades slightly compared to a single-level multigrid iterations due to increased number of iterations on the coarser multigrid levels. Thus, we adopt $\Lambda=1$ hereafter in this work to analyze the performance of the MLBEM algorithm.

Figure 6 suggests that almost 100 iterations on the finest level mesh are needed for a relatively coarse boundary element discretization when using the C-cycle multigrid. As the finer BEM meshes are considered, the number of multigrid cycles reduce dramatically and become independent of the mesh discretization for fine meshes. Note that starting from $N_p=32,768$ boundary elements per patch, only two C-cycles are required to reduce the numerical errors to the desired levels (Fig. 6). Meanwhile, the non-multigrid solutions require dramatically larger number of iterations with iteration counts following nearly the anticipated $O(N^{1/2})$ behavior. Again, the MLBEM algorithm presented in [19] allows to obtain solutions only for meshes with $N_p=4096$ elements or coarser per patch. Note that the iteration numbers for both fast multilevel algorithms are the same, as expected (Fig. 6).

Finally, we compare the CPU times and memory requirements for the conventional and fast multilevel boundary element methods for the example problem. Figures 7 and 8 show that the fast multilevel boundary element method developed and presented in [19] reduces run-time and memory requirements approximately by an order of magnitude compared to the conventional BEM formulations for $N\leqslant 4096$. Meanwhile, the current MLBEM approach requires almost two orders of magnitude less CPU times and memory even for a moderate number of degrees of freedom. For larger values of N, the efficiency of the fast method increases even further as anticipated. At $N=10,250$, a speed-up factor of approximately 88, and 54 is obtained for the fast algorithm compared to a conventional Gauss elimination and BCGM approaches, respectively. Note that for larger number of degrees of

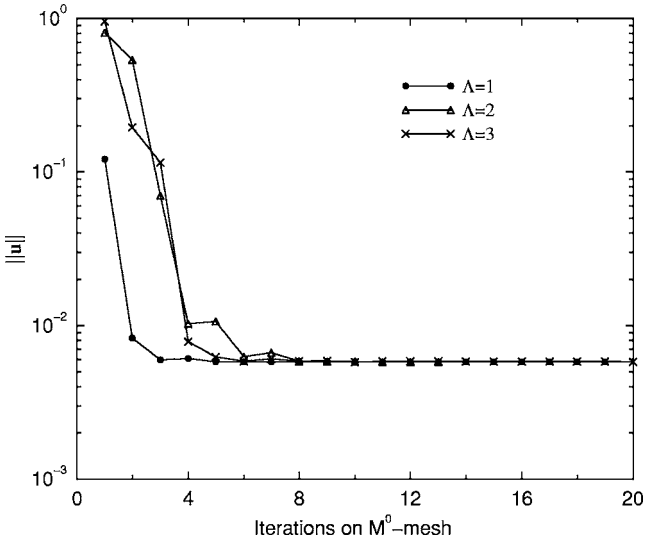

Fig. 5 Convergence history for mesh of *Np*=16,384 boundary elements for various number of multi-grid levels

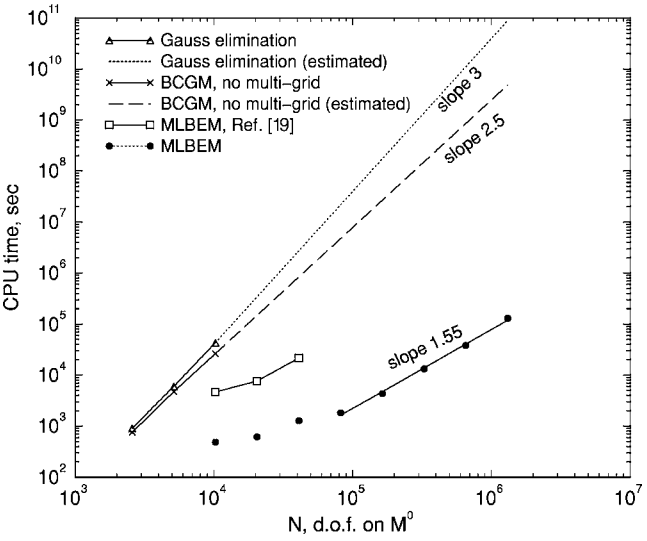

Fig. 7 Comparisons of the CPU requirements for the conventional BEM and MLBEM algorithms

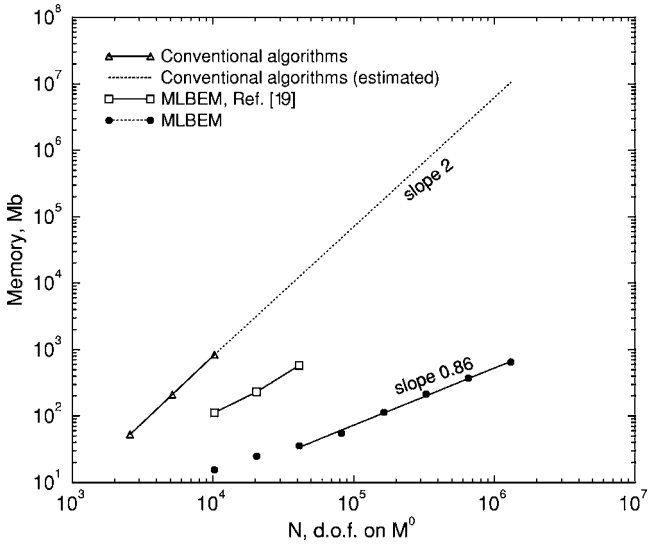

Fig. 8 Comparisons of the memory requirements for the conventional BEM and MLBEM algorithms

freedom on the finest level mesh, the conventional formulations are not even realizable on the current workstation when using double precision arithmetic. Thus, for illustration purposes, we have extrapolated the CPU and memory requirements for the conventional algorithms assuming that the matrix solution dominates its formation (Fig. 7 and 8). Furthermore, we assume that the BCGM approach will converge in order $O(N^{1/2})$ iterations. For $N=1,310,730$ involving a boundary element mesh 128 times finer than the finest BEM mesh possible for the conventional algorithms, the speed-up factors are 685,632 and 185,364 for Gauss elimination and BCGM approaches, respectively. We note that the Gauss elimination would require almost three millennia to provide a solution for this mesh, whereas the current MLBEM approach requires slightly more than 36 hr on the workstation. Finally we should like to emphasize that the conventional methods would require more than 10 Tb of memory to store the global matrix using double-precision arithmetic. Accordingly, the MLBEM reduces this burden by a factor of 16,384 and requires just 647 Mb of memory which, of course, can easily be stored in core.

Conclusions

A multilevel boundary element solver [19] recently developed for Stokes flows in two-dimensions has been extended to provide an extremely robust, efficient, and fast computational tool. We introduced two important modifications into the code, namely, implemented a preevaluation of the total correction from the fine level meshes, and facilitated fast matrix-vector multiplications using a sliding correction stencil for the discrete coefficients. These amendments have led to dramatic improvements of the modified multilevel algorithm and permitted solutions on boundary element meshes that are 32 times finer than those possible using our previous formulation [19].

In this study, we investigate performance of the MLBEM on a model Stokes flow problem. The numerical example shows conservation of numerical accuracy even for multilevel transfers. We compare the CPU time and memory requirements for the fast multilevel and conventional boundary element methods and demonstrate exceptional performance of the fast boundary element method. We have been able to model the example Stokes flow problem involving more than one million degrees of freedom on a workstation, for which we achieved almost a million-fold speed-up compared to the direct Gauss elimination algorithm.

Acknowledgment

The work described in this paper was partially supported by the National Science Foundation under Grant No. CMS 0084632 The authors gratefully acknowledge this support.

Nomenclature

$\boldsymbol{g}, \boldsymbol{f}$ = Stokeslets
h = boundary element mesh size
m = number of singular correction points
$\boldsymbol{n}$ = unit outward normal
p = pressure
$\boldsymbol{t}$ = traction
$\boldsymbol{u}$ = velocity of the flow
w = multi-integral
x = Eulerian coordinate
y = relative distance from source point
C = total correction
$\boldsymbol{G}, \boldsymbol{F}$ = coefficients
$\boldsymbol{H}$ = generalized coefficients
L = number of MLMI levels
M = boundary element mesh
N = number of degrees of freedom
P = number of boundary patches
R = patch end correction
Γ = domain boundary
Ω = domain of interest
$\|\boldsymbol{u}\|$ = velocity error norm
σ = stress tensor
ν = viscosity
Λ = number of multigrid levels

References

[1] Barnes, J., and Hut, P., 1986, "A Hierarchical Force Calculation Algorithm," Nature (London) **324**, pp. 446–449.
[2] Grama, A., Kumar, A., and Sameh, A., 1998, "Parallel Hierarchical Solvers and Preconditioners for Boundary Element Methods," SIAM J. Sci. Comput. (USA) **20**, pp. 337–358.
[3] Beylkin, G., Coifman, R., and Rokhlin, V., 1991, "Fast Wavelet Transforms and Numerical Algorithms: 1," Commun. Pure Appl. Math. **44**, pp. 141–183.
[4] Alpert, B., Beylkin, G., Coifman, R., and Rokhlin, V., 1993, "Waveletlike Bases for the Fast Solution of Second-Kind Integral Equations," SIAM J. Sci. Comput. (USA) **14**, pp. 159–184.
[5] Rokhlin, V., 1985, "Rapid Solution of Integral Equations of Classical Potential Theory," J. Comput. Phys. **60**, pp. 187–207.
[6] Greengard, L., and Rokhlin, V., 1987, "A Fast Algorithm for Particle Simulations," J. Comput. Phys. **73**, pp. 325–348.
[7] Nabors, K., Korsmeyer, F. T., Leighton, F. T., and White, J., 1994, "Preconditioned, Adaptive, Multipole-Accelerated Iterative Methods for Three-Dimensional First-Kind Integral Equations of Potential Theory," SIAM J. Sci. Comput. (USA) **15**, pp. 713–735.
[8] Rahola, J., 1996, "Diagonal Forms of the Translation Operators in the Fast Multipole Algorithm for Scattering Problems," BIT **36**, pp. 333–358.
[9] Cheng, H., Greengard, L., and Rokhlin, V., 1999, "A Fast Adaptive Multipole Algorithm in Three Dimensions," J. Comput. Phys. **155**, pp. 468–498.
[10] Koc, S., Song, J., and Chew, W. C., 1999, "Error Analysis for the Numerical Evaluation of the Diagonal Forms of the Scalar Spherical Addition Theorem," SIAM (Soc. Ind. Appl. Math.) J. Numer. Anal. **36**, pp. 906–921.
[11] Darve, E., 2000, "The Fast Multipole Method: Numerical Implementation, J. Comput. Phys. **160**, pp. 195–240.
[12] Darve, E., 2000, "The Fast Multipole Method 1: Error Analysis and Asymptotic Complexity," SIAM (Soc. Ind. Appl. Math.) J. Numer. Anal., **38**, pp. 98-128.
[13] Brandt, A., and Lubrecht, A. A., 1990, "Multilevel Matrix Multiplication and Fast Solution of Integral Equations," J. Comput. Phys. **90**, pp. 348–370.
[14] Lubrecht, A., and Ioannides, E., 1991, "A Fast Solution of the Dry Contact Problem and the Associated Subsurface Stress Field Using Multilevel Techniques," ASME J. Tribol. **113**, pp. 128–133.
[15] Grigoriev, M. M., and Dargush, G. F., 2004, "A Multi-Level Boundary Element Method for Two-Dimensional Steady Heat Diffusion," Numer. Heat Transfer, Part B **46**, pp. 329–356.
[16] Grigoriev, M. M., and Dargush, G. F., 2004, "A Fast Multi-Level Boundary Element Method for the Helmholtz Equation," Comput. Methods Appl. Mech. Eng. **193**, pp. 165–203.
[17] Wang, C. H., Grigoriev, M. M., and Dargush, G. F., 2005, "A Fast Multi-Level Convolution Boundary Element Method for Transient Diffusion Problems,"

Int. J. Numer. Methods Eng. **62**, pp. 1895–1926.
[18] Polonsky, I. A., and Keer, L. M., 1999, "A Numerical Method for Solving Rough Contact Problems Based on the Multi-Level Multi-Summation and Conjugate Gradient Techniques," Wear **231**, pp. 206–219.
[19] Grigoriev, M. M., and Dargush, G. F., 2005, "A Multi-Level Boundary Element Method for Stokes Flows in Irregular Two-Dimensional Domains," Comput. Methods Appl. Mech. Eng. **194**, pp. 3553–3581.
[20] Polonsky, I. A., and Keer, L. M., 2000, "Fast Methods for Solving Rough Contact Problems: A Comparative Study, ASME J. Tribol. **122**, pp. 36–41.
[21] Venner, C. H., and Lubrecht, A. A., 2000, *Multi-level Methods in Lubrication*, Elsevier, Amsterdam.
[22] Brandt, A., 1977, "Multi-level Adaptive Solutions to Boundary-Value Problems," Math. Comput. **31**, pp. 333–390.
[23] Costabel, M., 1988, "Boundary Integral Operators on Lipschitz Domains: Elementary Results," SIAM J. Math. Anal., **19**, pp. 613–626.
[24] Laubin, P., 2001, "Optimal Order Collocation for the Mixed Boundary Value Problem on Polygons," Math. Comput. **70**, pp. 607–636.
[25] Press, W. H., Teukolsky, S. A., Vetterling, W. T., and Flannery, B. P., 1992, *Numerical Recipes in C, The Art of Scientific Computing*, Cambridge University Press, Cambridge.

A Meshless Local Petrov-Galerkin Method for Fluid Dynamics and Heat Transfer Applications

Ali Arefmanesh
e-mail: a_aref32@yahoo.com

Mohammad Najafi
e-mail: m_njafi36@yahoo.com

Hooman Abdi
e-mail: hoomanabdi@softhome.net

Islamic Azad University, Science & Research Division, Mechanical Engineering Department, Tehran 14155-4933, IRAN, Tel: 4817170, Fax: 4817175

The meshless local Petrov-Galerkin method has been modified to develop a meshless numerical technique to solve computational fluid dynamics and heat transfer problems. The theory behind the proposed technique, hereafter called "the meshless control volume method," is explained and a number of examples illustrating the implementation of the method is presented. In this study, the technique is applied for one- and two-dimensional transient heat conduction as well as one- and two-dimensional advection-diffusion problems. Compared to other methods, including the exact solution, the results appear to be highly accurate for the considered cases. Being a meshless technique, the control volumes are arbitrarily chosen and possess simple shapes, which, contrary to the existing control volume methods, can overlap. The number of points within each control volume and, therefore, the degree of interpolation, can be different throughout the considered computational domain. Since the control volumes have simple shapes, the integrals can be readily evaluated. [DOI: 10.1115/1.1949651]

Keywords: Meshless, Control Volume, Advection-Diffusion, Least-Squares

Introduction

The finite element and finite volume methods [1–3] are among the most frequently used numerical techniques in computational fluid dynamics and heat transfer applications that require mesh generation on the computational domain. Generating a good mesh is a prerequisite to obtaining accurate numerical solutions. An acceptable mesh should have no excessively distorted elements and no elemental high aspect ratio. These and other constraints render the mesh generation, despite recent advances in this field [4], still arduous and problematic.

To circumvent these difficulties, considerable research has been devoted in recent years to develop numerical methods for solving differential equations that do not require mesh generation. Among these so-called meshless techniques is "the diffuse element method" proposed by Nayroles et al. [5] in which a collection of nodes and a boundary description are sufficient to obtain the Galerkin equations. However, in this method an auxiliary grid is still necessary to evaluate the integrals that result from applying the Galerkin method to the differential equations. Subsequently, Belytschko et al. [6] and Lu et al. [7] proposed the element-free Galerkin method in which a regular cell structure is employed as an auxiliary grid and high-order quadratures are used to evaluate the integrals on this background grid. An extensive review of these mesh-free techniques can be found in Belytschko et al. [8].

Based on the work of Batina [9], Oňate et al. [10,11] introduced another category of meshless techniques called "the finite point method." In this method, a collection of points is selected in the domain and an interpolation cloud is then chosen around each of the points. Subsequently, the interpolations of the unknown function within the clouds are substituted into the weighted residual formulation of the problem and the resulting integrals are evaluated using the point collocation. Hence, no background grid is needed, and the method is truly meshless.

Recently, two other meshless schemes—the meshless local boundary equation method, and the meshless local Petrov-Galerkin method—have been proposed for solving differential equations [12–17]. Both methods employ a local weak form of the differential equation over a local subdomain and the shape functions from the moving least-squares interpolation together with numerical quadrature to obtain the discretized equations. A comprehensive review of the meshless methods, in general, and the meshless local Petrov-Galerkin (MLPG) method, in particular, can be found in two recent monographs by Atluri and Shen [18] and Atluri [19]. These works focus on various interpolation schemes, different types of test functions, as well as discretization of boundary integral equations. A number of three-dimensional solid mechanics problems and their solutions with singularities are also considered in these works.

In recent years, other truly meshless methods have been proposed, among them are the method of finite spheres by De and Bathe [20], the local point interpolation method by Gu and Liu [21], the local radial point interpolation method by Liu and Gu [22], and the regular hybrid boundary method by Zhang et al. [23,24] and Zhang and Yao [25].

In the method of finite spheres, subdomains of spherical shapes are generated around every point in the domain. Subsequently, the dependant variables are interpolated within the spheres using the partition-of-unity paradigm [26]. The discretized equations are obtained by substituting the interpolations in the Galerkin weak form of the partial differential equations for the subdomains. Some improved numerical integration schemes for the method of finite spheres have been presented in Ref. [27].

In the local point interpolation method, which is based on the MLPG, a technique is proposed to construct polynomial interpolation with Kronecker delta property for a group of arbitrarily distributed points. Therefore, contrary to the other meshless schemes that employ moving least-squares interpolation for the dependent variable, in this method essential boundary conditions can be applied rather easily. On the other hand, the regular hybrid boundary node method, which is based on coupling a modified functional with the moving least-squares approximations, only requires discrete nodes construction on the boundary of a domain.

In this study, an amended meshless local Petrov-Galerkin method, the meshless control volume method (MCVM), is introduced for solving computational fluid dynamics and heat transfer problems. In this method, similar to the finite point method

Contributed by the Fluids Engineering Division for Publication in the JOURNAL OF FLUIDS ENGINEERING. Manuscript received by the Fluids Engineering Division August 18, 2004. Final manuscript received April 18, 2005: Associate Editor: Surya P. Vanka.

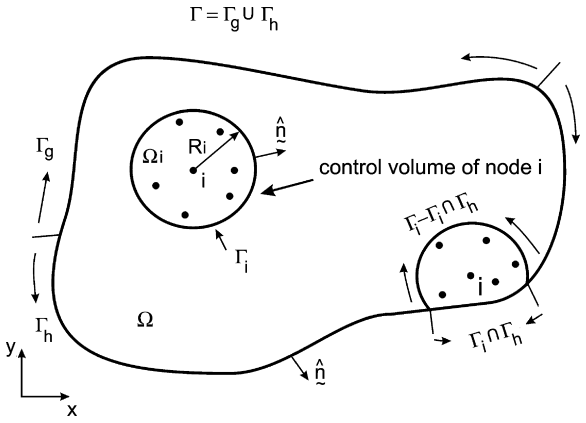

Fig. 1 Domain Ω with two circular control volumes

(FPM), a collection of points is chosen in the domain. Subsequently, a control volume is generated around each of the points. The control volumes have simple shapes and, contrary to the usual control volume methods [28,29], they can intersect each other and overlap. Substituting the interpolation of the unknown function within each control volume into the weak form of the differential equation and using unity as the test function yield the discretized equation of a control volume. Because of the simple shapes of the control volumes, the integrals in the discretized equation are easily evaluated. Among the main differences between the MCVM and the other meshless techniques is that in the MCVM there is neither a need for an auxiliary grid nor for numerical integration on the auxiliary grid. Also, the MCVM, unlike the existing meshless techniques, such as the FPM, possesses flux conservation properties.

Meshless Control Volume Method

To develop the theory of the MCVM, consider a bounded region Ω with the boundary $\Gamma=\Gamma_g\cup\Gamma_h$ in the two-dimensional space (Fig. 1). The transient convection-diffusion equation in Ω written in terms of temperature, $T(\vec{x},t)$, is

$$T_{,t}+\vec{\nabla}\cdot(\vec{u}T)=\alpha\nabla^2T+S \tag{1}$$

where $\vec{u}$ is the divergence-free velocity field, $\alpha=K/\rho C_p$, and S is a source term. Boundary and initial conditions for Eq. (1) are

$$T=T_g \text{ on } \Gamma_g \tag{2}$$

$$\hat{n}\cdot(K\vec{\nabla}T)+H(T-\tilde{T})=q \text{ on } \Gamma_h \tag{3}$$

$$T(\vec{x},0)=T_0(\vec{x}) \text{ in } \bar{\Omega} \tag{4}$$

where T_g is a given function of position, $\tilde{T}$ is the free-stream temperature, $\hat{n}$ is the unit normal to Γ_h, H is the heat transfer coefficient, q is the known heat flux, $T_0(\vec{x})$ is the given initial temperature, and $\bar{\Omega}=\Omega\cup\Gamma$.

In this MCVM, similar to the other meshless techniques [10,11], a collection of points is selected in the domain. Subsequently, a control volume is generated around each of the points. The control volume is a line segment in the one-dimensional space and can be a circle or rectangle in the two-dimensional space. A typical circular control volume Ω_i with radius R_i and boundary Γ_i, which is generated around point i, is shown in Fig. 1. The number of points belonging to a control volume and their distribution can, in general, vary from one control volume to another, and, contrary to the commonly used control volume techniques [29], in this method control volumes can intersect one another and overlap.

Multiplying Eq. (1) by the weighting function w, integrating the resulting expression over Ω_i, and employing the integration by parts yields

$$\int_{\Omega_i}wT_{,t}d\Omega-\int_{\Omega_i}\vec{\nabla}w\cdot(\vec{u}T-\alpha\vec{\nabla}T)d\Omega+\int_{\Gamma_i}w(\vec{u}T-\alpha\vec{\nabla}T)\cdot\hat{n}d\Gamma=\int_{\Omega_i}Swd\Omega \tag{5}$$

Choosing a weighting function equal to unity in Eq. (5) results in the following equation for a control volume Ω_i, which has no boundary in common with the domain boundary:

$$\int_{\Omega_i}T_{,t}d\Omega+\int_{\Gamma_i}(\vec{u}T-\alpha\vec{\nabla}T)\cdot\hat{n}d\Gamma=\int_{\Omega_i}Sd\Omega \tag{6}$$

In case the boundary Γ_i of the control volume Ω_i has an intersection with Γ_h, the equation of the control volume changes to

$$\int_{\Omega_i}T_{,t}d\Omega+\int_{\Gamma_i}\vec{u}T\cdot\hat{n}d\Gamma-\int_{\Gamma_i\cap\Gamma_h}\frac{H(T-\vec{T})+q}{\rho C_p}d\Gamma-\int_{\Gamma_i-\Gamma_i\cap\Gamma_h}\alpha\frac{\partial T}{\partial n}d\Gamma=\int_{\Omega_i}Sd\Omega \tag{7}$$

where $\Gamma_i\cap\Gamma_h$ represents the intersection of Γ_i with Γ_h.

To obtain the discretized equation of the control volume Ω_i, which contains n points, the unknown temperature field is approximated within Ω_i by [10]

$$T(\vec{x},t)\cong\bar{T}^{(i)}(\vec{x},t)=\sum_{l=1}^{m}P_l(\vec{x})\alpha_l(t)=\mathbf{P}^T(\vec{x})\boldsymbol{\alpha}(t) \tag{8}$$

where $\boldsymbol{\alpha}(t)=[\alpha_1(t),\alpha_2(t),\ldots,\alpha_m(t)]^T$ and the elements of vector $\mathbf{P}(\vec{x})$ are, in general, monomials. For example, in a one-dimensional case for $m=3$, the vector $\mathbf{P}(\vec{x})$ is given by $[1,x,x^2]^T$, and in a two-dimensional case for $m=3$, it is expressed as $[1,x,y]^T$.

Setting the approximation (8) equal to the value of the function $T(\vec{x},t)$ at the n points belonging to the control volume yields

$$\mathbf{T}=\begin{Bmatrix}T_1\\T_2\\\vdots\\T_n\end{Bmatrix}=\begin{Bmatrix}\mathbf{P}_1^T\\\mathbf{P}_2^T\\\vdots\\\mathbf{P}_n^T\end{Bmatrix}\boldsymbol{\alpha}=\mathbf{C}\boldsymbol{\alpha} \tag{9}$$

where $T_j=T(\vec{x}_j,t)$ is the magnitude of $T(\vec{x},t)$ at the point $\vec{x}_j$ and $\mathbf{P}_j=\mathbf{P}(\vec{x}_j)$. If the number of points belonging to the control volume n is equal to the number of monomials of the vector $\mathbf{P}(\vec{x})$, m, the performed interpolation will be exact at the points (i.e., it will be equal to the value of the unknown function at the points), and the vector $\boldsymbol{\alpha}$ will be given by

$$\boldsymbol{\alpha}=\begin{Bmatrix}\mathbf{P}_1^T\\\mathbf{P}_2^T\\\vdots\\\mathbf{P}_n^T\end{Bmatrix}^{-1}\mathbf{T}=\mathbf{C}^{-1}\mathbf{T} \tag{10}$$

The approximation $\bar{T}^{(i)}(\vec{x},t)$, in this case, is expressed as

$$\bar{T}^{(i)}(\vec{x},t)=\sum_{j=1}^{n}\phi_j^{(i)}T_j(t) \tag{11}$$

where $\phi_j^{(i)}(\vec{x})$, $j=1(1)n$, are the usual interpolation functions (i.e., Lagrange polynomials) and T_j, $j=1(1)n$, are the nodal values of the unknown function at the points. The interpolation functions,

which satisfy the standard condition $\phi_j^{(i)}(\vec{x}_l)=\delta_{jl}$, δ_{jl} being the Kronecker delta, are given by [30]

$$\phi_j^{(i)}(\vec{x})=\sum_{l=1}^{m} P_l(\vec{x})C_{lj}^{-1}, \quad j=1(1)n \tag{12}$$

If the number of points belonging to the control volume is greater than the number of monomials of the vector $\mathbf{P}(\vec{x})$ (i.e., $n>m$), the approximation will be obtained using a least-squares fit. The approximation is still given by (11), however, the interpolation functions are now written as follows [30]:

$$\phi_j^{(i)}(\vec{x})=\sum_{l=1}^{m} P_l(\vec{x})D_{lj}^{-1}, \quad j=1(1)n \tag{13}$$

where

$$\mathbf{D}^{-1}=\mathbf{A}^{-1}\mathbf{B}, \quad \mathbf{A}=\sum_{j=1}^{n}\mathbf{P}(\vec{x}_j)\mathbf{P}^T(\vec{x}_j) \text{ and}$$

$$\mathbf{B}=[\mathbf{P}(\vec{x}_1),\mathbf{P}(\vec{x}_2),\ldots,\mathbf{P}(\vec{x}_n)]$$

Substituting the approximation $\bar{T}^{(i)}(\vec{x},t)$ into Eq. (6) or (7) yields the discretized equation for Ω_i. Using the same procedure for every control volume yields the system of the discretized equations for all the points within the domain. Solving the system of algebraic equations gives the unknown variables at the points. The following examples illustrate the new method implementation.

Transient Conduction and Potential Flow Application of the Method

Consider a one-dimensional transient heat conduction equation given by

$$T_{,t}=\alpha T_{,xx} \quad 0<x<1 \tag{14a}$$

$$T(0,t)=0 \tag{14b}$$

$$T(1,t)=0 \tag{14c}$$

$$T(x,0)=x(1-x) \tag{14d}$$

The analytical solution of the equation is [31]

$$T(x,t)=\sum_{n=1,3,5}^{\infty}\left(\frac{2}{n\pi}\right)^3 \sin(n\pi x)e^{-n^2\pi^2\alpha t} \tag{15}$$

To solve Eqs. (14*a*)–(14*d*) with the MCVM, a collection of N equally spaced points is selected in the domain. A control volume is generated around each of the points. Each control volume, in this case, contains three points, Fig. 2(*a*) for uniform and Fig. 2(*b*) for nonuniform point distribution. The equation of the control volume Ω_i is given by

$$\frac{\partial}{\partial t}\int_{x_{i-1}}^{x_{i+1}} T(x,t)dx=\alpha[T_{,x}(x_{i+1},t)-T_{,x}(x_{i-1},t)] \tag{16}$$

Using a second-order approximation $\bar{T}^{(i)}(x,t)=\Sigma_{j=i-1}^{i+1}\phi_j^{(i)}(x)T_j(t)$ within the control volume in Eq. (16) and discretizing the time derivative by a first-order implicit scheme, yields

$$\left(\frac{1}{3}-\frac{2\alpha\Delta t}{\Delta x^2}\right)T_{i-1}^{n+1}+\left(\frac{4}{3}+\frac{4\alpha\Delta t}{\Delta x^2}\right)T_i^{n+1}+\left(\frac{1}{3}-\frac{2\alpha\Delta t}{\Delta x^2}\right)T_{i+1}^{n+1}$$
$$=\frac{1}{3}T_{i-1}^{n}+\frac{4}{3}T_i^{n}+\frac{1}{3}T_{i+1}^{n} \tag{17}$$

where Δx is the distance between two consecutive points (for the uniform case), Δt is the time step, and n and $n+1$ represent two consecutive time steps. Different methods have been developed to impose the essential boundary conditions while using least-squares interpolations for the trial functions [10,16]. Following the scheme used in [10], in this work $T_i(x_j)$ is set equal to $T_g(x_j)$ at the points located on Γ_g.

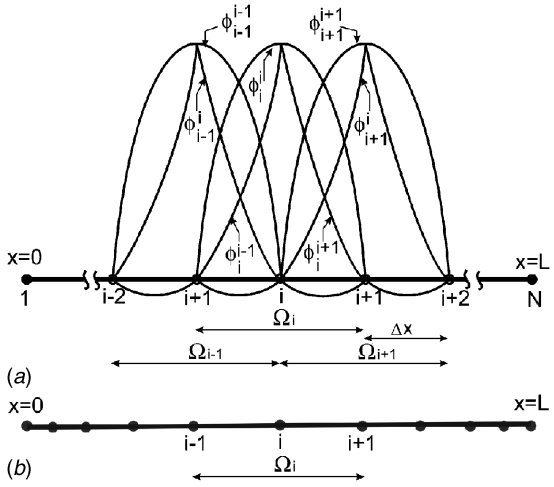

Fig. 2 One-dimensional control volumes for (*a*) uniform point distribution with second-order interpolation function and (*b*) nonuniform point distribution

Similar discretized equations are obtained for other control volumes whose solutions yield T_j, $j=1(1)N$. In case Ω_i contains five points and a fourth-order approximation of the temperature is employed, the discretized equation will be given by

$$\frac{1}{\Delta t}\sum_{j=i-2}^{i+2} T_j^{n+1}\left(\int_{i-2}^{i+2}\phi_j dx-\alpha\phi_{j,x}\Big|_{i-2}^{i+2}\right)=\frac{1}{\Delta t}\sum_{j=i-2}^{i+2} T_j^{n} \tag{18}$$

Figure 3 shows the change of temperature with time at $x=0.5$ for $\alpha=1$ obtained by the MCVM using control volumes with three points and second-order approximation together with the analytical solution and the numerical results obtained by the FVM [2]. Eleven equally spaced points have been selected in the domain with $\Delta t=0.001$ s. It is seen from the figure that the results are quite accurate even for the small number of control volumes generated in the domain, with a maximum relative error of $<3\%$.

Figure 4 shows the temperature distribution in the domain at three different times for the one-dimensional transient conduction problem. Three types of control volumes, namely, control volumes containing three points with second-order approximation, containing five points with third-order least-squares, and fourth-order ex-

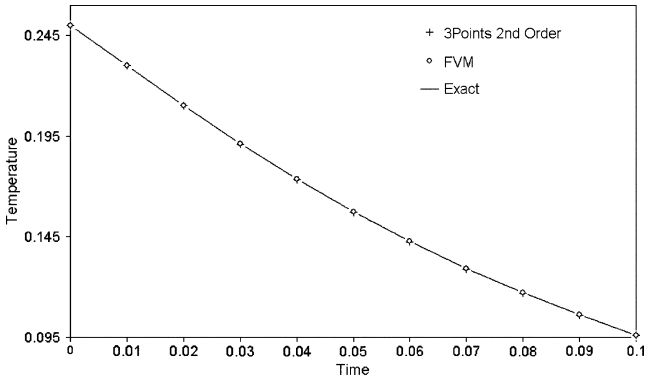

Fig. 3 Temperature variation with time at $x=0.5$ for the one-dimensional transient conduction with uniform point distribution

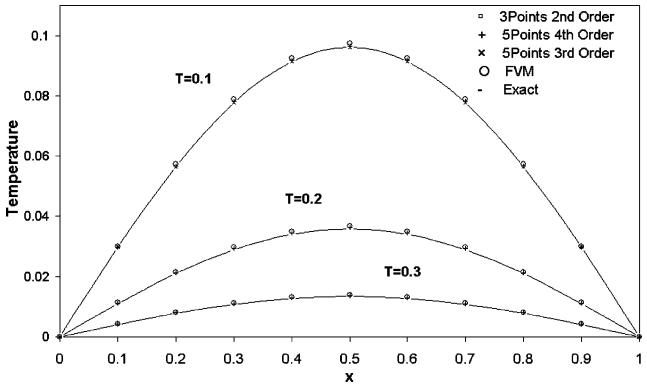

Fig. 4 Temperature distribution in the domain at three different times for the one-dimensional transient conduction with uniform point distribution

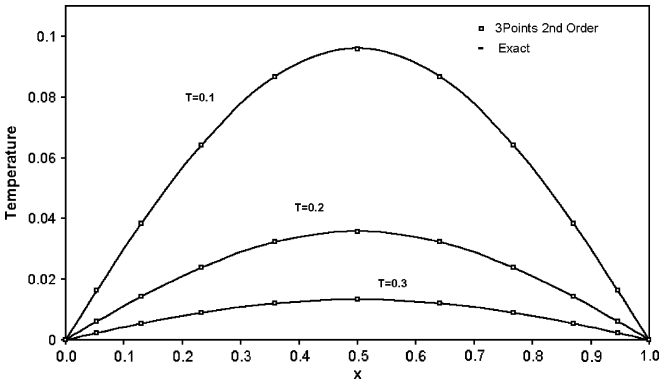

Fig. 5 Temperature distribution in the domain at three different times for the one-dimensional transient conduction with nonuniform point distribution

act approximations have been employed. Other conditions are similar to those used in Fig. 3. As Fig. 4 shows, the results obtained by the MCVM, FVM, and the exact solution coincide. The percent relative error for the cases shown in Fig. 4 for $\Delta t = 0.001$ s are presented in Table 1. From Fig. 4 and the results illustrated in Table 1, the MCVM accuracy is apparent. Obviously, the magnitude of Δt governs the percent error for the MCVM as well as FVM with respect to the analytical solution.

Equation (17) has the following modified equation:

$$\frac{\partial T}{\partial t} - \alpha\frac{\partial^2 T}{\partial x^2} = \left(\alpha\Delta t - \frac{\Delta x^2}{6}\right)\frac{\partial^4 T}{\partial x^4} + O(\Delta t^2, \Delta t^2 \Delta x^2) \tag{19}$$

which shows that Eq. (17) is, in the limit, consistent with Eq. (14*a*). On the other hand, an implicit stable scheme has been employed to discretize the time derivative. Therefore, according to the Lax's equivalence theorem [32,33], convergence is assured.

To analyze the effect of nonuniformity in the size of the control volumes on the results, 11 unequally spaced points have been selected within the domain (Fig. 2(*b*)). In this regard, Fig. 5 shows the temperature distribution at three different times for the one-dimensional transient conduction for which control volumes containing three points with the second-order approximation have been employed. Comparing Fig. 4 to Fig. 5, the results show similar accuracies.

Next, the following two-dimensional transient heat conduction equation in a square domain is considered:

$$T_{,t} = \alpha\nabla^2 T \quad \text{in} \quad \Omega = (1 \times 1) \tag{20a}$$

$$T(0,y,t) = 0, \quad T(1,y,t) = 0 \tag{20b}$$

$$T(x,0,t) = 0, \quad T(x,1,t) = 0 \tag{20c}$$

$$T(x,y,0) = (x - x^2)(y - y^2) \tag{20d}$$

The exact solution of Eqs. (20*a*)–(20*d*) is [31]

$$T(x,y,t) = \sum_{m=1,3,5}^{\infty}\sum_{n=1,3,5}^{\infty}\frac{64}{(m\pi)^3(n\pi)^3}\sin(m\pi x) \times \sin(n\pi y)e^{-\alpha(m^2+n^2)\pi^2 t}. \tag{21}$$

To solve the equation by the MCVM, a collection of regular square 11×11 points is selected in the domain. A typical control volume containing nine points, which is used in this case, is shown in Fig. 6(*a*) for uniform and Fig. 6(*b*) for nonuniform point distribution. Using biquadratic approximation and discretizing the time derivative by a first-order implicit scheme yields the following discretized equation for an internal control volume:

$$\sum_{j=1}^{4}\left(1 - \frac{12\alpha\Delta t}{h^2}\right)T_{ij}^{n+1} + \sum_{j=5}^{8}\left(4 - \frac{12\alpha\Delta t}{h^2}\right)T_{ij}^{n+1} + \left(16 + \frac{96\alpha\Delta t}{h^2}\right)T_i^{n+1} = \sum_{j=1}^{4}T_{ij}^{n} + 4\sum_{j=5}^{8}T_{ij}^{n} + 16T_i^{n} \tag{22}$$

where h ($h = \Delta x = \Delta y$) is the distance between two consecutive points in either x or y direction (for the uniform case).

Figure 7 shows the temperature distribution in the domain obtained by the MCVM at time equal to 0.025 s for $\alpha = 1$. A regular square of 11×11 points has been selected in the domain, and control volumes containing nine points with biquadratic approxi-

Table 1 MCVM and FVM percent relative error comparison for the one-dimensional conduction (uniform point distribution)

	MCVM											
	3 points–second order			5 points–fourth order			5 points–third order			FVM		
x	T=0.1	0.2	0.3	0.1	0.2	0.3	0.1	0.2	0.3	0.1	0.2	0.3
0	0	0	0	0	0	0	0	0	0	0	0	0
0.1	0.33	0.65	0.97	0.51	1.01	1.52	0.29	0.25	0.21	1.30	2.60	3.93
0.2	0.33	0.65	0.97	0.47	0.98	1.49	0.05	0.09	0.13	1.29	2.60	3.93
0.3	0.33	0.65	0.97	0.47	0.98	1.49	0.22	0.26	0.30	1.29	2.60	3.93
0.4	0.33	0.65	0.97	0.49	1.00	1.51	0.07	0.03	0.01	1.29	2.60	3.93
0.5	0.33	0.65	0.97	0.50	1.01	1.52	0.09	0.13	0.17	1.29	2.60	3.93
0.6	0.33	0.65	0.97	0.49	1.00	1.51	0.17	0.21	0.25	1.29	2.60	3.93
0.7	0.33	0.65	0.97	0.47	0.98	1.49	0.01	0.02	0.06	1.29	2.60	3.93
0.8	0.33	0.65	0.97	0.47	0.98	1.49	0.38	0.35	0.31	1.29	2.60	3.93
0.9	0.33	0.65	0.97	0.51	1.01	1.52	1.40	1.36	1.32	1.30	2.60	3.93
1	0	0	0	0	0	0	0	0	0	0	0	0

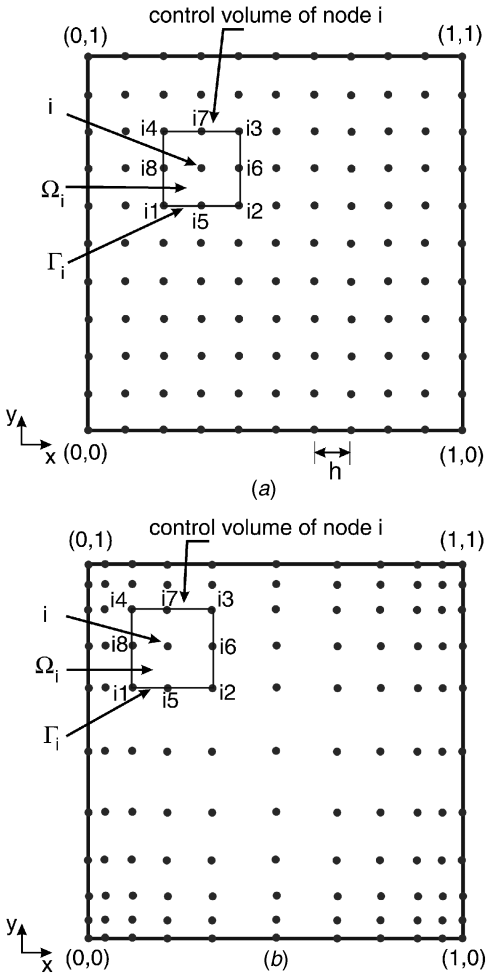

Fig. 6 Domain and a typical control volume for the two-dimensional problems with (*a*) uniform point distribution (*b*) nonuniform point distribution

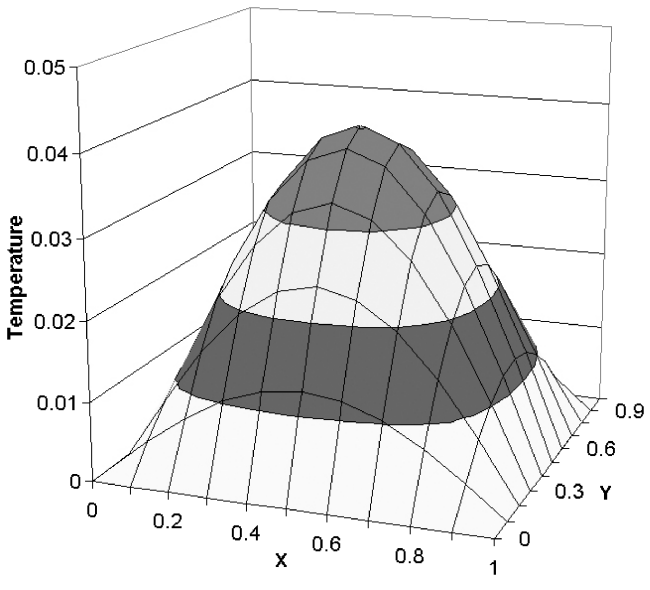

Fig. 7 Temperature distribution in the domain at $t=0.025$ s for the two-dimensional transient conduction with uniform point distribution

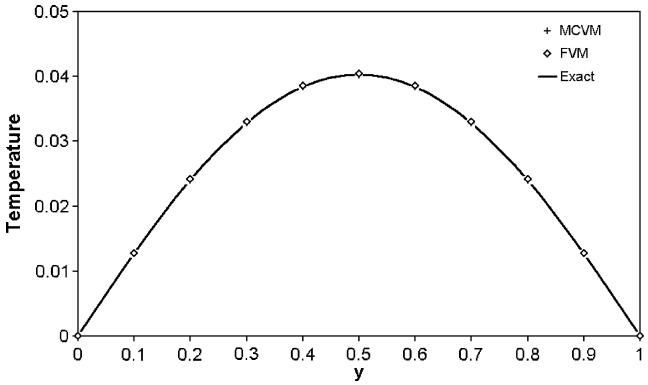

Fig. 8 Temperature distribution along the *y*-axis at $x=0.5$ for the two-dimensional transient conduction with uniform point distribution

mation have been used. The temperature distribution along the y-axis at $x=0.5$ and for time equal to 0.025 s obtained by the MCVM is shown in Fig. 8. Other conditions are similar to those in Fig. 7. The time step Δt is again set to be 0.001 s. As the figure shows, for the two-dimensional case similar to the one-dimensional, the MCVM, FVM, and exact solution coincide with one another. The percent relative error in Table 2, however, for both the MCVM and FVM are mainly $<1\%$. This insignificant error for numerical and engineering purposes, in turn, approves the MCVM accuracy.

The modified equation of the discretized Eq. (22) is

$$\frac{\partial T}{\partial t}-\alpha\nabla^2 T=\left(\alpha\frac{\Delta t}{2}-\frac{h^2}{12}\right)\left(\frac{\partial^4 T}{\partial x^4}+\frac{\partial^4 T}{\partial y^4}\right)+\alpha\Delta t\frac{\partial^4 T}{\partial x^2\partial y^2}+O(\Delta t^2,h^2\Delta t) \tag{23}$$

Considering the above modified Eq. (22) is, in the limit, consistent with the original differential equation (Eq. (20*a*)). Furthermore, an implicit stable scheme has been employed to discretize the time derivative. Hence, according to the Lax's equivalence theorem the method is convergent [32,33].

Next, the two-dimensional transient heat conduction problem is solved using the nonuniform point distribution. The temperature distribution along the y-axis at $x=0.5$ and for time equal to 0.025 s for the nonuniform point distribution is shown in Fig. 9. An overall comparison of Figs. 8 and 9 show a higher accuracy for the nonuniform point distribution.

As a final example in this section, fluid flow over a square block (potential flow) is considered. Figure 10 shows the domain and the point distribution using the control volume similar to the one in Fig. 6 for this case. The streamlines profile obtained through the MCVM using the nonuniform point distribution for this potential flow is illustrated in Fig. 11.

Table 2 MCVM and FVM percent relative error comparison for the two-dimensional conduction (uniform point distribution at $x=0.5$)

y	MCVM	FVM
0	0	0
0.1	0.03	1.14
0.2	0.06	0.97
0.3	0.09	0.78
0.4	0.11	0.64
0.5	0.12	0.59
0.6	0.11	0.64
0.7	0.09	0.78
0.8	0.06	0.97
0.9	0.03	1.14
1	0	0

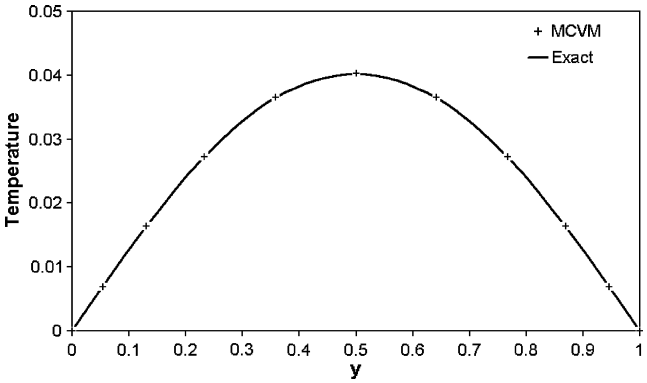

Fig. 9 Temperature distribution along the *y*-axis at *x*=0.5 for the two-dimensional transient conduction with nonuniform point distribution

Convection-Diffusion, Application of the Method

As a further implementation of the method, consider the MCVM used to solve differential equations with non-self-adjoint operators, such as those that generally occur in convective heat transfer and fluid dynamics. A typical example is the following one-dimensional advection-diffusion equation:

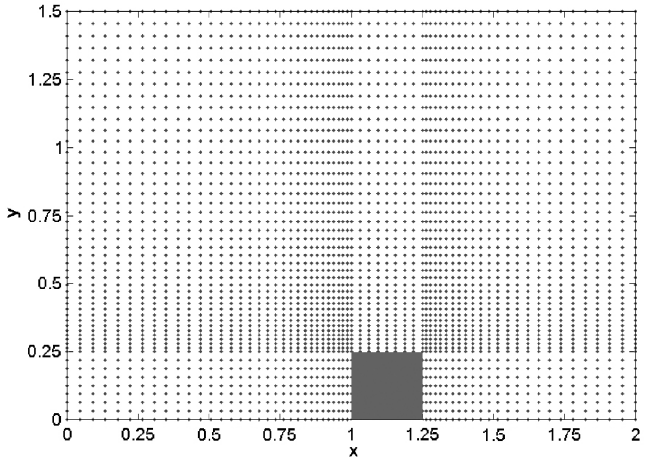

Fig. 10 Domain and nonuniform point distribution for the potential flow over a square block

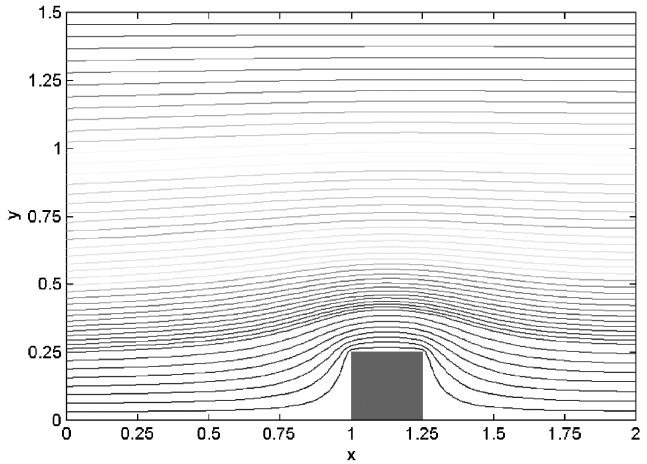

Fig. 11 MCVM solution of the streamlines for a potential flow over a block

$$T_{,\bar{x}} = (1/\mathrm{Pe})T_{,\bar{x}\bar{x}} \quad 1 > \bar{x} > 0 \tag{24a}$$

$$T(\bar{x}=0) = 0, \quad T(\bar{x}=1) = 1 \tag{24b}$$

where $\mathrm{Pe}=\rho cuL/K$ is the Peclet number, u is the fluid velocity, L is the length of the domain, and $\bar{x}=x/L$. The analytical solution of Eqs. (24*a*) and (24*b*) is [29]

$$T(\bar{x}) = (1 - e^{\mathrm{Pe}\bar{x}})/(1 - e^{\mathrm{Pe}}). \tag{25}$$

Applying the MCVM to Eqs. (24*a*) and (24*b*) yields the following discretized equation for a control volume Ω_i containing three points with second-order approximation:

$$\left(\frac{1}{\bar{\mathrm{Pe}}} + \frac{1}{2}\right)T_{i-1} - \frac{2}{\bar{\mathrm{Pe}}}T_i + \left(\frac{1}{\bar{\mathrm{Pe}}} - \frac{1}{2}\right)T_{i+1} = 0 \tag{26}$$

where $\bar{\mathrm{Pe}}=\rho cu\Delta x/K$ is the local Peclet number. Equation (26) is not stable for $\bar{\mathrm{Pe}}>2$, and severe oscillations may appear in the numerical solutions under these circumstances. There exist different standard techniques to stabilize discretized form of the convection-diffusion equation in the finite difference, finite element, and finite volume methods [28,29,34,35].

To stabilize the numerical solution in this study, a balancing diffusion $\bar{k}$ is added to Eq. (24*a*), whereupon the discretized equation for Ω_i changes to

$$\left(\frac{1}{\bar{\mathrm{Pe}}} + \frac{1}{2} + \frac{\bar{k}}{\overline{\Delta x}}\right)T_{i-1} - \left(\frac{2}{\bar{\mathrm{Pe}}} + \frac{\bar{k}}{\overline{\Delta x}}\right)T_i + \left(\frac{1}{\bar{\mathrm{Pe}}} - \frac{1}{2} + \frac{\bar{k}}{\overline{\Delta x}}\right)T_{i+1} = 0 \tag{27}$$

The magnitude of $\bar{k}$ is now evaluated such that the solution of Eq. (27) be nodally exact. To this end, the solution of Eq. (27) is considered as a term of the Fourier series, $T_j=e^{iK_mL\bar{x}_j}$, with K_m being the wave number. Substituting the Fourier series solution into Eq. (27) and setting the truncation error to zero yields the optimal $\bar{k}$ for a control volume with three points and second-order approximation

$$\bar{k} = \frac{\overline{\Delta x}}{2}\left[\coth\left(\frac{\bar{\mathrm{Pe}}}{2}\right) - \frac{2}{\bar{\mathrm{Pe}}}\right] \tag{28}$$

It should be noted that the above $\bar{k}$ is similar to the optimal balancing diffusion, which has been obtained previously by Brooks and Hughes [34] and Lewis et al. [35]. Now, using a similar approach, the following new expression is obtained for the optimal balancing diffusion for the control volumes with five points and fourth-order approximation

$$\frac{\bar{k}}{\overline{\Delta x}} = \frac{14[\cosh(2\bar{\mathrm{Pe}}) - 1] - 32[\cosh(\bar{\mathrm{Pe}}) - 1] - 6(\bar{\mathrm{Pe}})\sinh(2\bar{\mathrm{Pe}})}{32[\cosh(\bar{\mathrm{Pe}}) - 1] - 14[\cosh(2\bar{\mathrm{Pe}}) - 1]} \tag{29}$$

Figure 12 shows the numerical solution of Eqs. (24*a*) and (24*b*) obtained by the MCVM for a range of Peclet numbers together with the analytical solution in each case. Twenty-one equally spaced points have been selected in the domain, and control volumes containing three points with a second-order approximation have been used in each case. It is clear from the figure that the numerical results, in all the cases, are coincident with the exact solutions.

To analyze the effect of changing the number of points and varying the order of approximation within control volumes on the numerical results, the solution was obtained using control volumes with five points and fourth-order approximation. The results for 21 equally spaced points are presented in Fig. 13 with virtually no changes compared to Fig. 12. Figure 14 shows a comparison of the solution obtained by the MCVM with the exact and the FVM solutions for Pe=50. The previously used control volumes with

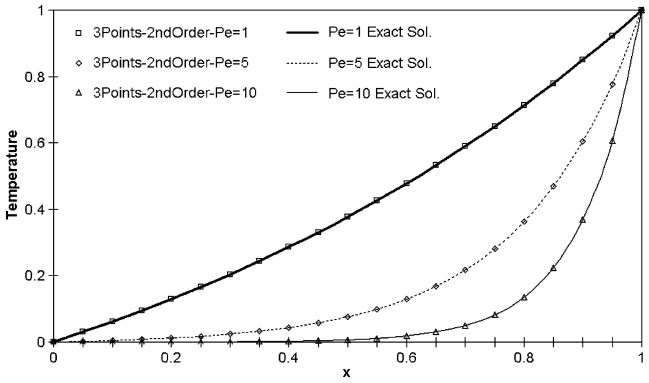

Fig. 12 MCVM solutions of the one-dimensional steady advection-diffusion equation for uniform point distribution

the second- and fourth-order approximations have been employed. The number of points is the same as that in Fig. 12. The numerical solutions are wiggle-free and coincident with the exact solutions for a wide range of Peclet numbers, which demonstrates that the optimal balancing diffusion is predicted correctly by the relations (28) and (29).

As a final example, the following two-dimensional convection-diffusion equation in a square domain is considered:

$$T_{,x} + T_{,y} = \frac{1}{\mathrm{Pe}}\nabla^2 T \quad \text{in} \quad \Omega = (1 \times 1) \tag{30a}$$

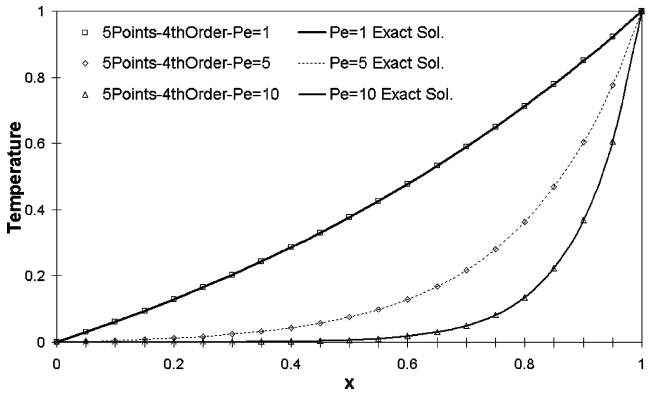

Fig. 13 MCVM solutions of the one-dimensional steady advection-diffusion equation for uniform point distribution

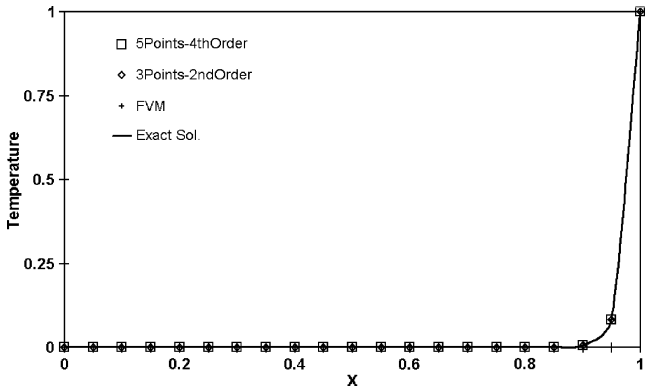

Fig. 14 MCVM solution of the one-dimensional steady advection-diffusion equation for Pe=50 with uniform point distribution

$$T(x,0) = \frac{1 - \exp[(x-1)\mathrm{Pe}]}{1 - \exp(-\mathrm{Pe})}, \quad T(x,1) = 0 \tag{30b}$$

$$T(y,0) = \frac{1 - \exp[(y-1)\mathrm{Pe}]}{1 - \exp(-\mathrm{Pe})}, \quad T(1,y) = 0 \tag{30c}$$

The exact solution of the equation is [36]

$$T(x,y) = \left\{\frac{1 - \exp[(x-1)\mathrm{Pe}]}{1 - \exp(-\mathrm{Pe})}\right\}\left\{\frac{1 - \exp[(y-1)\mathrm{Pe}]}{1 - \exp(-\mathrm{Pe})}\right\} \tag{31}$$

To solve the equation by the MCVM, a collection of regular square 11×11 points is selected in the domain. A typical control volume, in this case, contains nine points, Fig. 6(*a*). Using a bi-quadratic approximation, the discretized equation for a typical control volume is given by

$$\frac{1}{\mathrm{Pe}}\sum_{j=1}^{4} T_{ij} + \left(\frac{1}{\mathrm{Pe}} + \frac{4h}{3}\right)T_{i5} + \left(\frac{1}{\mathrm{Pe}} - \frac{4h}{3}\right)T_{i6} + \left(\frac{1}{\mathrm{Pe}} + \frac{4h}{3}\right)T_{i7} + \left(\frac{1}{\mathrm{Pe}} - \frac{4h}{3}\right)T_{i8} - \frac{8}{\mathrm{Pe}}T_i = 0 \tag{32}$$

where h ($h=\Delta x=\Delta y$) is the distance between two consecutive points (for the uniform case).

Figure 15 demonstrates the solution of Eqs. (30*a*)–(30*c*) obtained by the MCVM. The numerical results, in this case, agree with the exact solution with a maximum relative error of $<3\%$.

Conclusions

A modified meshless local Petrov-Galerkin method is proposed and illustrated to numerically solve one- and two-dimensional transient heat conduction, fluid flow, and convection-diffusion problems.

Being inherently meshless, the technique offers choosing the control volumes arbitrarily. In this technique, the control volumes have simple shapes and can overlap one another. The number of points within each control volume, hence, the degree of interpolation, can be different from one control volume to another. This makes the old and never-ending problem of "noncontrollability of the interpolation degree" no longer a numerical technique drawback. Integrals over each control volume and along its boundary, which arise from integrating the differential equation within the control volume and applying Gauss's theorem to the resulting expression, can now be easily evaluated. Therefore, there is no need for a background grid; hence, the method would truly be a meshless one.

Application of the method to the transient heat conduction, potential flow over a block, and convection-diffusion problems shows the accuracy and diverse applicability of the method even with a coarse distribution of points. A procedure based on the Fourier series has been introduced to determine the optimal balancing diffusion for convection-dominated situations. Using this technique, a new upwinding relation is presented whose accuracy is validated through numerical examples.

The results of this study, in turn, show that the meshless local Petrov-Galerkin method can be well tailored so that the outcome numerical technique—the proposed MCVM—can be implemented to solve a variety of computational fluid dynamics and heat transfer problems.

Nomenclature

C_p = specific heat
H = heat transfer film coefficient
h = distance between two consecutive points
K = thermal conductivity
$\bar{k}$ = balancing diffusion
K_m = wave number
L = domain length

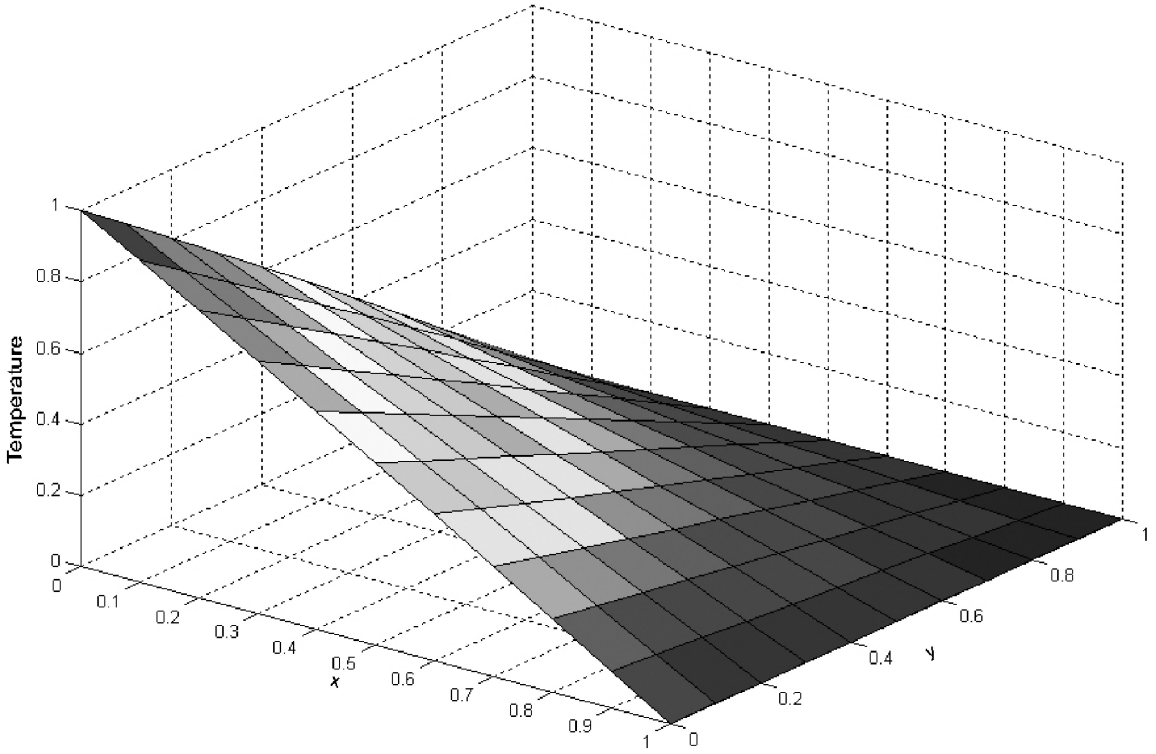

Fig. 15 MCVM solution of the two-dimensional advection-diffusion equation for uniform point distribution

N = total number of points
n = number of points within a control volume, time-step sequence
O = order of magnitude
Pe = Peclet number
q = heat flux
R = radius
S = source
T = temperature
$\tilde{T}$ = free-stream temperature
T_g = a given position function
t = time
u = velocity
w = weighting function

Greek Symbols

α = thermal diffusivity
ϕ = interpolation function
Γ = boundary
Γ_g, Γ_h = boundary segments
ρ = density
Ω = domain

Subscripts

, = derivative
i = point or control volume number

Superscripts

$-$ = dimensionless variable
$\wedge$ = unit vector
$\rightarrow$ = vector

References

[1] Zienkiewicz, O. C., and Oñate E., 1991, "*Finite Elements Versus Finite Volumes. Is There a Choice?*" in Non Linear Computational Mechanics. State of the Art, P. Wriggers and W. Wagner eds., Springer, Berlin.

[2] Versteeg, H. K., and Malalasekera, W., 1995, *An Introduction to Computational Fluid Dynamics, the Finite Volume Method*, Longman, Loughborogh, England.

[3] Oñate, E., Cervera, M., and Zienkiewicz, O. C., 1994, "A Finite Volume Format for Structural Mechanics," Int. J. Numer. Methods Eng., **37**, pp. 181–201.

[4] Thompson, J. F., Bharat, K. S., and Weatherill, N. P., editors, 1999, *Handbook of Grid Generation*, CRC Press, New York.

[5] Nayroles, B., Touzot, G., and Villon, P., 1992, "Generalizing the FEM: Diffuse Approximation and Diffuse Elements," Comput. Mech., **10**, pp. 307–318.

[6] Belytschko, T., Lu, Y., and Gu, L., 1994, "Element Free Galerkin Methods," Int. J. Numer. Methods Eng., **37**, pp. 229–256.

[7] Lu, Y. Y., Belytschko, T., and Gu, L., 1994, "A New Implementation of the Element Free Galerkin Method," Comput. Methods Appl. Mech. Eng., **113**, pp. 397–414.

[8] Belytschko, T., Krongauz, Y., Organ, D., Fleming, M., and Krysl, P., 1996, "Meshless Methods: An Overview and Recent Developments," Comput. Methods Appl. Mech. Eng., **139**, pp. 3–47.

[9] Batina, J., 1993, "A Gridless Euler/Navier Stokes Solution Algorithm for Complex Aircraft Applications," AIAA 93-0333, Reno, NV.

[10] Oñate, E., Idelsohn, S., Zienkiewicz, O. C., and Taylor, R., 1996, "A Finite Point Method in Computational Mechanics: Applications to Convective Transport and Fluid Flow," Int. J. Numer. Methods Eng., **39**, pp. 3839–3866.

[11] Oñate, E., Idelsohn, S., Zienkiewicz, O. C., Taylor, R. L., and Sacco, C., 1996, "A Stabilized Finite Point Method for Analysis of Fluid Mechanics Problems," Comput. Methods Appl. Mech. Eng., **139**, pp. 315–346.

[12] Zhu, T., Zhang, T. D., and Atluri, S. N., 1998, "A Local Boundary Integral Equation (LBIE) Method in Computational Mechanics, and a Meshless Discretization Approach," Comput. Mech., **21**, pp. 223–235.

[13] Zhu, T., Zhang, T. D., and Atluri, S. N., 1998, "A Meshless Local Boundary Integral Equation (LBIE) Method for Solving Nonlinear Problems," Comput. Mech., **22**, pp. 174–186.

[14] Atluri, S. N., and Zhu, T., 1998, "A New Meshless Local Petrov-Galerkin (MLPG) Approach for Nonlinear Problems in Computer Modeling and Simulation," Comput. Model. Simul. Eng., **3**, pp. 187–196.

[15] Zhu, T., 1999, "A New Meshless Regular Local Boundary Integral Equation (MRLBIE) Approach," Int. J. Numer. Methods Eng., **46**, pp. 1237–1252.

[16] Atluri, S. N., and Cho, J. Y., 1999, "A Critical Assessment of the Truly Meshless Local Petrov-Galerkin (MLPG) and Local Boundary Integral Equation (LBIE) Methods," Comput. Mech., **24**, pp. 348–372.

[17] Atluri, S. N., and Zhu, T., 2000, "The Local Petrov-Galerkin (MLPG) Approach for Solving Problems in Elasto-Statics," Comput. Mech., **25**, pp. 169–179.

[18] Atluri, S. N., and Shen, S., 2002, *The Meshless Local Petrov-Galerkin (MLPG) Method*, Tech. Science Press.

[19] Atluri, S. N., 2004, *The Meshless Method (MLPG) for Domain and Bie Discretizations*, Tech. Science Press.

[20] De, S., and Bathe, K. J., 2000, "The Method of Finite Spheres" Comput.

Mech., **25**, pp. 329–45.
[21] Gu, Y. T., and Liu, G. R., 2001, "A Local Point Interpolation Method for Static and Dynamic Analysis of Thin Beams," Comput. Methods Appl. Mech. Eng., **190**, pp. 5515–5528.
[22] Liu, G. R., and Gu, Y. T., 2001, "A Local Radial Point Interpolation Method (LRPIM) for Free Vibration Analysis of 2-D Solids" J. Sound Vib., **246**(1), pp. 29–46.
[23] Zhang, J. M., Yao, Z. H., and Li, H., 2002, "A Hybrid Boundary Node Method," Int. J. Numer. Methods Eng., **53**, pp. 751–63.
[24] Zhang, J., Yao, Z., and Tanaka, M., 2003, "The Meshless Regular Hybrid Boundary Node Method for 2D Linear Elasticity," Eng. Anal. Boundary Elem., **27**, pp. 259–268.
[25] Zhang, J., and Yao, Z., 2004, "The Regular Hybrid Boundary Node Method for Three-Dimensional Linear Elasticity," Eng. Anal. Boundary Elem., **28**, pp. 525–534.
[26] Melenk, J. M., and Babuška, I., 1996, "The Partition of Unity Finite Element Method: Basic Theory and Applications" Comput. Methods Appl. Mech. Eng., **139**, pp. 289–314.
[27] De, S., and Bathe, K. J., 2001, "The Method of Finite Spheres with Improved Numerical Integration," Comput. Struct., **79**, pp. 2183–2196.
[28] Hoffman, K. A., and Chiang, S. T., 1993, *Computational Fluid Dynamics for Engineers*, Engineering Education System, Wichita, Kan.
[29] Gresho, P. M., and Sani, R. L., 2000, *Incompressible Flow and the Finite Element Method, Volume 1: Advection-Diffusion*, Wiley, Ltd, Chichester, England.
[30] Zienkiewiz, O. C., and Taylor, R. L., 1986 "*The Finite Element Method. Vol. 1: Basic Formulation and Linear Problems*," 4th Edition, McGraw-Hill, London, England.
[31] Greenberg, M. D., 1978, *Foundations of Applied Mathematics*, Prentice-Hall, Englewood Cliffs, N.J.
[32] Richtmyer, R. D., and Morton, K. W., 1967, *Difference Methods for Initial-Value Problems*, Interscience Publishers, New York.
[33] Hirsch, C., 1992, *Numerical Computation of Internal and External Flows, Volume 1: Fundamentals of Numerical Discretization*, Wiley, New York.
[34] Brooks, A. N., and Hughes, T. J. R., 1982, "Streamline Upwind/Petrov-Galerkin Formulation for Convection Dominated Flows With Particular Emphasis on the Incompressible Navier-Stokes Equations," Comput. Methods Appl. Mech. Eng., **32**, pp. 199–258.
[35] Lewis, R. W., Morgan, K., Thomas, H. R., and Seetharamu K. N., 1996, *The Finite Element Method in Heat Transfer Analysis*, Wiley, Chichester, England.
[36] Anderson, D. A., Tannehill, J. C., and Pletcher, R. H., 1984, *Computational Fluid Mechanics and Heat Transfer*, Hemisphere, New York.

Adaptive Wavelet Method for Incompressible Flows in Complex Domains

Damrongsak Wirasaet
e-mail: dwirasae@nd.edu

Samuel Paolucci
e-mail: paolucci@nd.edu

Department of Aerospace and Mechanical Engineering, University of Notre Dame
Notre Dame, Indiana 46556

An adaptive wavelet-based method provides an alternative means to refine grids according to local demands of the physical solution. One of the prominent challenges of such a method is the application to problems defined on complex domains. In the case of incompressible flow, the application to problems with complicated domains is made possible by the use of the Navier-Stokes–Brinkman equations. These equations take into account solid obstacles by adding a penalized velocity term in the momentum equation. In this study, an adaptive wavelet collocation method, based on interpolating wavelets, is first applied to a benchmark problem defined on a simple domain to demonstrate the accuracy and efficiency of the method. Then the penalty technique is used to simulate flows over obstacles. The numerical results are compared to those obtained by other computational approaches as well as to experiments. [DOI: 10.1115/1.1949650]

Introduction

In dealing with unsteady incompressible flows, one often encounters problems whose solutions contain localized features, or sharp variations, in which their locations vary with time. Accurate numerical simulations of such problems using uniform grids require a large number of degrees of freedom, since a high-resolution discretization is necessary to resolve sharp variations. In order to reduce the required number of degrees of freedom and, at the same time, obtain solutions with similar accuracy, an adaptive discretization method that reflects the local demands of the solutions becomes necessary.

We discuss the use of an adaptive wavelet-based method, as an alternative to adaptive mesh refinement methods (e.g., [1]) and adaptive finite element methods (e.g., [2]). In the adaptive wavelet method, the numerical solution is represented by a multiscale basis called wavelets. Such a basis is localized in both physical and Fourier spaces [3]. It is this feature that allows one to design a dynamically adaptive algorithm for solving problems of evolution type [4–9]. These algorithms take advantage of the fact that the local regularity of a function is provided by the magnitude of wavelet coefficients. A large magnitude implies that locally the function or one of it derivatives changes rapidly. On the other hand, coefficients with small magnitude imply that the function varies smoothly. Thus, examining the wavelet coefficients suggests which regions should be refined and which can be coarsened. Existing adaptive wavelet-based methods are based on either wavelet-Galerkin [4,5] or wavelet-collocation approaches [6–10]. Despite the generality that the Galerkin approach provides, evaluation of integrals of nonlinear terms poses a challenge in obtaining an algorithm that is both efficient and accurate. This is not an issue for the collocation approach. An additional issue, which wavelet-based methods have to address, deals with the fact that higher-dimensional wavelets are conventionally constructed by employing the tensor product of the one-dimensional wavelets. Thus, the use of these methods in higher dimensions has been primarily limited to solving problems defined on rectangular domains.

In [9,11], a wavelet-based adaptive multiresolution representation algorithm has been developed for problems defined in three-dimensional parallelepiped domains. The method is based on the interpolating wavelet basis and the collocation formulation. The algorithm utilizes the connection between the interpolation properties of interpolating wavelets and the semi-structured dyadic collocation points in order to obtain a fast wavelet transform on irregular grids. This, and the use of an efficient data structure [11], results in a relatively inexpensive grid adaption procedure. In addition, a fast algorithm for derivative calculations via finite differences has also been developed. Other features of the adaptive wavelet algorithm include the ability of handling boundary conditions of type other than periodic and the capability of coping with any order of the interpolating wavelet basis chosen.

In this work, the primary goal is to investigate the application of the adaptive wavelet algorithm to incompressible flow problems defined on complicated domains. The task may be accomplished by the use of a generalized coordinate transformation to map the physical domain to a simple Cartesian computational domain and, subsequently, solve the transformed equation in the simple domain. When a problem is such that it involves either irregularly shaped (possibly moving) objects immersed in a fluid or a flow within complicated domain boundaries, the following alternative approaches (and variants) are used: (i) the fictitious domain method [12,13], (ii) the immersed boundary technique [14–16], and (iii) the Brinkman penalization method [17]. These techniques share one common idea in that the original domain is embedded into an artificial simple domain, a box in either two or three dimensions. Subsequently, governing equations are reformulated so that they are valid for the complete new simple domain. In the fictitious domain method, the problem is reformulated in weak form where the original boundary conditions are taken into account by the introduction of an auxiliary variable and a Lagrange multiplier. In the immersed boundary technique, appropriate external surface-forcing terms represented by Dirac δ functions are added to the momentum equation to simulate the presence of objects. In the Brinkman penalization technique, instead of adding a surface force, the objects are taken into account by adding a Darcy volumetric drag term in the momentum equation; thus, one considers the Navier-Stokes–Brinkman equations. Since our discretization relies on a collocation formulation, either the immersed boundary or the Brinkman penalization techniques are suitable to incorporate in our procedure. Although proven successful in handling complicated moving boundaries, especially in biological fluid flows [14,15,18], the immersed boundary technique yields only first-order accurate solutions near objects due to the

Contributed by the Fluids Engineering Division for Publication in the JOURNAL OF FLUIDS ENGINEERING. Manuscript received by the Fluids Engineering Division September 22, 2004 Conference acknowledgement: 2004 ASME Heat Transfer/Fluids Engineering Summer Conference (HT-FED2004), July 11, 2004 - July 15, 2004, Charlotte, North Carolina, USA Final manuscript received: April 6, 2005 Associate Editor: Subrata Roy

singularities of the surface forcing terms [18]. Mathematical estimates and numerical evidence [17,19] suggest that solutions using the Brinkman penalization approach converge with respect to the Darcy drag parameter, which is independent of the spatial and temporal discretization. Because of this, in this work the Brinkman penalization approach is used.

In the following, we provide a brief summary of the adaptive wavelet collocation algorithm. Subsequently, the Navier-Stokes-Brinkman equations and their time discretization via a fractional step method are described. The method is then first applied to the lid-driven cavity problem in a square domain to demonstrate the accuracy and efficiency of the method. Thereafter, the method is used to simulate the flow past two circular cylinders with horizontal tandem arrangements. Conclusions are given in the last section.

Adaptive Wavelet-Based Algorithm

We discuss the adaptive wavelet-based multiresolution representation algorithm, which is based on the use of the interpolating wavelets on a finite interval introduced in [20]. Below, we first give a brief introduction of the one-dimensional basis and the generalization to higher dimensions. This is followed by a description of the dynamically adaptive grid strategy for time-dependent problems.

One-Dimensional Interpolating Wavelet Basis. We define the space $\{V_j[0,1]\}$, $j \geqslant j_0$, which is the span of $\{\phi_{j,k}, k=0,\ldots,2^j\}$. We denote the function $\phi_{j,k}$ as the scaling function on level of resolution j and location k. Such basis functions of order p ($p \in \mathbf{N}$, p even) are defined as the follows [8,20] for $j \geqslant \log_2(p)+1$,

$$\phi_{j,k}(x) = \phi(2^j x - k) + \sum_{n=-p+2}^{-1} a_{nk}\phi(2^j x - n), \quad k = 0, \ldots, p-1 \tag{1}$$

$$\phi_{j,k}(x) = \phi(2^j x - k), \quad k = p, \ldots, 2^j - p \tag{2}$$

$$\phi_{j,k}(x) = \phi(2^j x - k) + \sum_{n=2^j+1}^{2^j+p-2} b_{nk}\phi(2^j x - n), \quad k = 2^j - p + 1, \ldots, 2^j \tag{3}$$

where $\phi(x)$ is the interpolating scaling function of order p [20–22]. The weights a_{nk} and b_{nk} are defined as

$$a_{nk} = l^l_{jk}(x_{j,n}) \text{ and } b_{nk} = l^r_{jk}(x_{j,n})$$

where $x_{j,k} = 2^{-j}k$ denotes a dyadic grid and l^l_{jk} and l^r_{jk} represent, respectively, the Lagrange polynomials of order $p-1$ relative to the p-tuples of $\{x_{j,0}, x_{j,1}, \ldots, x_{j,p-1}\}$ and $\{x_{j,2^j-p+1}, x_{j,2^j-p+2}, \ldots, x_{j,2^j}\}$ i.e.,

$$l^l_{jk}(x) = \prod_{\substack{i=0 \\ i\neq k}}^{p-1} \frac{x - x_{j,i}}{x_{j,k} - x_{j,i}} \text{ and } l^r_{jk}(x) = \prod_{\substack{i=2^j-p+1 \\ i\neq k}}^{2^j} \frac{x - x_{j,i}}{x_{j,k} - x_{j,i}}$$

The scaling function $\phi_{j,k}$ has the following properties:

1. Since $\phi(n) = \delta_{0,n}$, the function $\phi_{j,k}$ satisfies the so-called interpolation property, i.e., $\phi_{j,k}(x_{j,l}) = \delta_{k,l}$.
2. The support of $\phi_{j,k}$ is compact, i.e., $|\text{supp } \phi_{j,k}(x)| \sim O(2^{-j})$, due to the fact that supp $\phi(x) = [-p+1, p-1]$.
3. The function $\phi_{j,k}(x)$ is the solution of the scaling relation

$$\phi_{j,k}(x) = \sum_l h^{j,k}_l \phi_{j+1,l}(x) \tag{4}$$

where the coefficients $\{h^{j,k}_l\}$ can be easily obtained by making use of the fact that $\phi(x)$ satisfies the scaling relation relation $\phi(x) = \sum_{k=-p+1}^{k=p-1} h_k \phi(2x-k)$, and the coefficients $\{h_k\}$ are filters that determine the interpolating scaling function [20,22]. We note that the set of coefficients $\{h^{j,k}_l\}$ has compact support.

4. Polynomials of degree less than p on [0,1] can be written as linear combinations of $\{\phi_{j,k}, k=0,\ldots,2^j\}$.

As a consequence of property 3, the spaces V_j (here, we drop the span [0,1] for notational simplicity) form a sequence of ladder spaces $V_j \subset V_{j+1}$. We now define the complementary space W_j such that

$$V_{j+1} = V_j \oplus W_j \tag{5}$$

The basis functions of W_j, denoted by $\psi_{j,k}$, are called wavelets. In this particular setting, wavelets can be simply chosen as

$$\psi_{j,k}(x) = \phi_{j+1,2k+1}(x), \quad k = 0, \ldots, 2^j - 1 \tag{6}$$

The decomposition of V_{j+1} until V_{j_0} is reached, where V_{j_0} denotes the space associated with the coarsest scale, yields the multiresolution analysis (MRA) of V_{j+1},

$$V_{j+1} = V_{j_0} \oplus \left(\bigoplus_{l=j_0}^{j} W_l \right) \tag{7}$$

Because of the interpolation property of the basis, we can define the interpolation operator I_j that maps the continuous function $f \in C^0[0,1]$ to the space V_j

$$(I_j f)(x) = \sum_{k=0}^{k=2^j} f_{j,k}\phi_{j,k}(x) \tag{8}$$

where $f_{j,k} = f(x_{j,k})$. Let us denotes $(I_j f)$ by f^j. Equation (7) implies immediately that f^j can also be written in the multiscale representation

$$f = \sum_{k=0}^{2^{j_0}} c_{j_0,k}\phi_{j_0,k}(x) + \sum_{l=j_0}^{j-1}\sum_{k=0}^{2^l-1} d_{l,k}\psi_{l,k}(x) \tag{9}$$

where $d_{j,k}$ is called the wavelet coefficient. Consider the difference of the approximations of f in the two successive spaces V_j and V_{j+1}

$$w^j = f^{j+1} - f^j = \sum_{k=0}^{2^{j+1}} f_{j+1,k}\phi_{j+1,k} - \sum_{k=0}^{2^j} f_{j,k}\phi_{j,k} = \sum_{k=0}^{2^j-1} d_{j,k}\psi_{j,k}$$

From Eqs. (4) and (6), and the interpolation property, it can be seen that the wavelet coefficients, obtained by evaluating $w^j(x_{j+1,2k+1})$, are given by

$$d_{j,k} = f_{j+1,2k+1} - \sum_{l=0}^{2^j} h^{j,l}_{2k+1} f_{j,l} \tag{10}$$

It is immediately evident that the wavelet coefficient $d_{j,k}$ provides a measure of the error of the approximation of f by f^j at the point $x_{j+1,2k+1}$. The wavelet coefficient is large when the function $\psi_{j,k}$ is located in the vicinity of a singularity or near singularity of f. Therefore, the number of wavelets required to represent the function f, having near-singular behavior within a desired accuracy, can be substantially reduced if we use the wavelet representation instead of the scaling function representation. It is noted that in Eq. (10), for each k, only a small number of $h^{j,l}_{2k+1}$ (precisely p) have nonzero values. Consequently, to compute the particular wavelet coefficient $d_{j,k}$, we require only $f_{j+1,2k+1}$ and those $f_{j,l}$ with l such that the value of $h^{j,l}_{2k+1}$ is nonzero. The fast algorithm of the interpolating wavelet transform on irregular grids takes advantage of such observation (see [9] for details).

To this end, let us note that it has been shown in [20] that f^j converges uniformly to f in the L_∞ norm, i.e., $\|f - f^j\|_\infty \to 0$, as j

$\rightarrow\infty$ (see the estimate for the Sobelov norm in [23]). Analytical properties of wavelets, such as norm equivalences in different functional spaces, can be found in [20,23,24].

Two-Dimensional Interpolating Wavelet Basis. Higher-dimensional bases are constructed by using the tensor product of the one-dimensional basis. Particularly, the scaling function on level of resolution j in the two-dimensional case is defined by

$$\Phi_{j,\mathbf{k}}^{(x,y)} = \phi_{j,k_1}(x)\phi_{j,k_2}(y), \quad \mathbf{k} = (k_1,k_2) \in \boldsymbol{\kappa}_j = \{0,\cdots,2^j\}^2 \tag{11}$$

and two-dimensional wavelets consist of three different products

$$\Psi_{j,\mathbf{k}}^{(1,0)}(x,y) = \psi_{j,k_1}(x)\phi_{j,k_2}(y), \quad \mathbf{k} \in \boldsymbol{\kappa}_j^{(1,0)} = \{0,\cdots,2^j-1\} \times \{0,\cdots,2^j\} \tag{12}$$

$$\Psi_{j,\mathbf{k}}^{(0,1)}(x,y) = \phi_{j,k_1}(x)\psi_{j,k_2}(y), \quad \mathbf{k} \in \boldsymbol{\kappa}_j^{(0,1)} = \{0,\cdots,2^j\} \times \{0,\cdots,2^j-1\} \tag{13}$$

$$\Psi_{j,\mathbf{k}}^{(1,1)}(x,y) = \psi_{j,k_1}(x)\psi_{j,k_2}(y), \quad \mathbf{k} \in \boldsymbol{\kappa}_j^{(1,1)} = \{0,\cdots,2^j-1\} \times \{0,\cdots,2^j-1\} \tag{14}$$

As a consequence of the one-dimensional basis, the two dimensional scaling function has properties that are generalizations of properties 1–4.

To simplify the notation, let us introduce the multi-index $\lambda = (\mathbf{e},\mathbf{k})$ with $\mathbf{e} \in \{(1,0),(0,1),(1,1)\}$ and $\mathbf{k} \in \kappa_j^{\mathbf{e}}$ and set $\Psi_{j,\lambda} \equiv \Psi_{j,\mathbf{k}}^{\mathbf{e}}$. The spaces $\mathbf{V}_j$ and $\mathbf{W}_j$, which are, respectively, the span of the sets $\{\Phi_{j,\mathbf{k}}\}$ and $\{\Psi_{j,\lambda}\}$ satisfy

$$\mathbf{V}_j \subset \mathbf{V}_{j+1} \text{ and } \mathbf{V}_{j+1} = \mathbf{V}_j \oplus \mathbf{W}_j = \mathbf{V}_{j_0} \oplus \left(\bigoplus_{l=j_0}^{j} \mathbf{W}_l \right)$$

The multiscale approximation of a function $f(x,y) \in C^0[0,1]^2$ at level of resolution j is given by

$$f^j(x,y) = \sum_{\mathbf{k}} f_{j_0,\mathbf{k}} \Phi_{j_0,\mathbf{k}}(x,y) + \sum_{l=j_0}^{j-1} \sum_{\lambda} d_{l,\lambda} \Psi_{l,\lambda} \tag{15}$$

where $f_{j_0,\mathbf{k}} = f(x_{j_0,k_1}, y_{j_0,k_2})$ and $d_{j,\lambda}$ represents the wavelet coefficients. Analogous to the one-dimensional case, wavelet coefficients $d_{l,\mathbf{k}}^{(1,0)}$, $d_{l,\mathbf{k}}^{(0,1)}$, and $d_{l,\mathbf{k}}^{(1,1)}$ measure the singular behavior along horizontal, vertical, and diagonal directions respectively. Because of the nature of the tensor product, the calculation of wavelet coefficients $d_{j,\lambda}$ on each level of resolution reduces to the application of the one-dimensional transform, first to the column and then to the row of $\{f_{j+1,\mathbf{k}}\}$ (or vice versa).

Sparse Wavelet Representation and Irregular Grids. The multiscale approximation can be rewritten as a sum of wavelets whose amplitude are above and below a certain threshold ε

$$f^J(x,y) = f_\varepsilon^J(x,y) + R_\varepsilon^J(x,y) \tag{16}$$

where

$$f_\varepsilon^J(x,y) = \sum_{\mathbf{k}} f_{j_0,\mathbf{k}} \Phi_{0,\mathbf{k}} + \sum_{l=j_0}^{J-1} \sum_{\lambda:|d_{l,\lambda}|\geqslant\varepsilon} d_{l,\lambda} \Psi_{l,\lambda} \tag{17}$$

$$R_\varepsilon^J(x,y) = \sum_{l=j_0}^{J-1} \sum_{\lambda:|d_{l,\lambda}|<\varepsilon} d_{l,\lambda} \Psi_{l,\lambda} \tag{18}$$

In order for the approximate function f^J to be within a prescribed accuracy, J must be sufficiently large. Neglect of the term R_ε results in an error, which is of the order of ε. Provided that the function f is sufficiently smooth, the error is proportional to the threshold value ε [20]

$$\|f - f_\varepsilon^J\|_\infty \leqslant [C_1 + C_2 \log(\varepsilon)]\varepsilon \leqslant C_3\varepsilon \tag{19}$$

where C_1, C_2, and C_3 are constants that depends on the function f. Furthermore, the number of basis functions in (17), denoted by N, whose amplitudes are larger than the threshold value ε, satisfies [20]

$$N^{1/d} \leqslant C_4 \varepsilon^{-1/p} \tag{20}$$

where d is the dimensionality of the problem and the constant C_4 depends on the function f. These bounds imply that f_ε^J approximates f within ε with approximately $\varepsilon^{-d/p}$ wavelet coefficients. In other words, a more accurate approximation function f_ε^J can be obtained by decreasing the value ε, however, with a commensurate increase in the number of basis functions required.

Let collocation points $x_{j,\mathbf{k}} = (2^{-j}k_1, 2^{-j}k_2)$ and $x_{j,\lambda} = x_{j+1,2\mathbf{k}+\mathbf{e}}$ denote points on the dyadic grid corresponding to the specific scaling function and wavelet, respectively. The term f_ε^J is called the *sparse wavelet representation* (SWR) of the function $f(x,y)$ [10]. The wavelets that are associated with the SWR are called *essential wavelets*. The term R_ε^J consists of wavelets whose coefficients are smaller than ε and thus is neglected. Subsequently, the associated collocation points are also omitted. This results in the irregular (semi-structured) sparse grid of *essential points* $\mathcal{G}_e = \{x_{j_0,\mathbf{k}}, \cup_{l=j_0}^{l=J-1} x_{l,\lambda} : |d_{l,\lambda}| \geqslant \varepsilon\}$.

Derivative Approximation. In order to solve partial differential equations within the collocation framework, an efficient procedure for computing the approximation of derivatives is necessary. The approximation can be computed by direct differentiation of the SWR of the function [7]. However, this approach is somewhat computationally costly because of different support sizes of wavelets on different levels. An alternative approach is to approximate derivatives using finite-differences [10,25]. This is possible due to the relationship between derivatives of the interpolating basis and finite differences. For a consistent approximation, the order of the finite difference used must be connected to the order of the wavelet. Then an approximation can obtained on a reconstructed uniform stencil [10]. Such an algorithm is less expensive than direct differentiation, but still somewhat inefficient in the case where a large number of absent points need to be reconstructed by interpolation of the sparse grid. Here, we use the more efficient approach developed in [9], which uses finite differences on nonuniform stencils (with some restrictions). Consequently, the need of interpolations is reduced substantially. In addition, the algorithm takes advantage of the fact that $\mathcal{G}_e$ is a dyadic semi-structured grid. Hence, coefficients of possible finite-difference stencils can be calculated and stored a priori. The calculation of finite-difference coefficients for a particular grid is reduced to simply fetching the stored coefficients whose stencil matches the one being considered. All three of the above methods produce derivative approximations of the same order of accuracy but have different computational cost and somewhat different robustness, which may be important in some problems.

Adaptive Algorithm for Time-Dependent Problems. In order to resolve structures appearing in the solution as they evolve, the collocation points need to be adapted dynamically to reflect the local change of the solution. The conceptual idea of the adaptive strategy, introduced in [4] (and later pursued by several others [5–10]), is that at each time step only the set of wavelets that represents the function within some prescribed accuracy is retained. To accommodate the possible advection and sharpening of solution features within a time step, wavelets that are centered in the vicinity of an essential wavelet at the same scale or smaller scale are also retained. Such wavelets are called *neighboring wavelets*. This strategy is expected to perform well when the solution changes smoothly in time, i.e., the solution is appropriately time resolved. To elaborate on the implementation of this adaptive

strategy within the present work, consider, for example, a second-order partial differential equation of the form

$$\frac{\partial u}{\partial t} = F\left(u, \frac{\partial u}{\partial x}, \frac{\partial u}{\partial y}, \frac{\partial^2 u}{\partial x^2}, \cdots\right)$$

with appropriate boundary conditions. After discretization in time by a finite-difference algorithm, the numerical solution of the problem reduces to solving a sequence of equations of the form

$$\mathcal{A}^{n+1} u^{n+1} = \mathcal{F}^{n+1} \tag{21}$$

Depending on F and the discretization scheme, $\mathcal{A}^{n+1}$ may depend on u^n and/or u^{n+1}. Given the approximate solution u^n at the previous time step t_n, the approximate solution u^{n+1} can then be computed. As proposed in [8], two threshold parameters $\varepsilon_s \leqslant \varepsilon_a$ are introduced, where the former determines whether wavelets (and their corresponding collocation points) are essential and thus must be retained, whereas the latter determines which neighborhood wavelets should be included. Roughly speaking, the threshold ε_s controls the error of the solution to be obtained, while ε_a determines the sensitivity of the adaptive refinement. Note that essential wavelets and their corresponding collocation points together with neighborhood wavelets and their associated collocation points constitute the sets of *active wavelets* and *active collocation points*, respectively. We denote the irregular sparse grids of active collocation points at t_n as $\mathcal{G}^n$. With the wavelet collocation discretization on $\mathcal{G}^n$, the combined (21) and boundary conditions reduce to a system of (linear or nonlinear) algebraic equations that can be solved by direct or iterative linear methods. The dynamically adaptive algorithm can be summarized as follows:

i. Solve the discrete system to obtain the approximate solution u^{n+1} on the irregular sparse grid $\mathcal{G}^n$ by using the solution from the previous time step as initial condition.

ii. Determine $\hat{\mathcal{G}}_e = \{x_{j_0,\mathbf{k}}, \cup_{l \geqslant j_0} x_{l,\lambda} : |d_{l,\lambda}^{n+1}| \geqslant \varepsilon_s\}$ based on thresholding of the magnitude of essential wavelet coefficients and determine the neighboring region, i.e., $\hat{\mathcal{G}}_n = \cup_{(l,\lambda)\in\Lambda_a} \mathcal{N}_{l,\lambda}$, where $\Lambda_a \equiv \{(l,\lambda) : |d_{l,\lambda}^{n+1}| \geqslant \varepsilon_a\}$ and $\mathcal{N}_{l,\lambda}$ is a set neighborhood points defined by a certain strategy, to yield the new sparse grid $\hat{\mathcal{G}} = \hat{\mathcal{G}}_e \cup \hat{\mathcal{G}}_n$.

iii. Assign a zero value to wavelet coefficients $d_{l,\lambda}^{n+1}$ associated with new collocation points, i.e., set $d_{l,\lambda}^{n+1} = 0$, for $x_{l,\lambda} \in \hat{\mathcal{G}} \backslash \mathcal{G}^n$ and compute the inverse adaptive wavelet transform to yield u^{n+1} on the new sparse grid $\hat{\mathcal{G}}$.

iv. Assign $u^{n+1} \rightarrow u^n$ and $\hat{\mathcal{G}} \rightarrow \mathcal{G}^{n+1}$ increment time and go back to step i.

The initial sparse grid $\mathcal{G}^0$ is obtained by consideration of the initial conditions. Different strategies can be employed in defining the set of neighborhood points $\mathcal{N}_{j,\lambda}$. One possibility is to include $(N_n+1)2^{N_n+1}$ $(N_n \in \mathbf{N})$ surrounding points at the same level j as well as at the next level [11]. As wavelet coefficients associated with different wavelets measure the strength of singularities in different directions, the strategy can account for this property [26]. Since $d_{j,\lambda}$ with $\mathbf{e}=(1,0)$ measures the strength of the singularity in the horizontal direction, corresponding to such wavelet we include in $N_n 2^{N_n-1}$ collocation points to the left and right at the same level as well as at the next level. The set $\mathcal{N}_{j,\lambda}$ with $\mathbf{e}=(0,1)$ can be defined in an analogous way (by simply switching left to bottom and right to top). Since the coefficient $d_{j,\lambda}$ with $\mathbf{e}=(1,1)$ measures the strength of the singularity in the diagonal directions, $\mathcal{N}_{j,\lambda}$ associated with such wavelets include $(N_n+1)2^{N_n+1}$ surrounding points in both directions at the same level as well as at the next level. Note that the collocation points associated with $\mathbf{e}$ in the three cases are centered at different locations. This strategy results in an irregular sparse grid with larger sparseness. Other possible strategies may be considered. For example, the number of points in $\mathcal{N}_{j,\lambda}$ might vary relative to the magnitude of wavelet coefficients.

Governing Equations

We consider fluid flow governed by the two-dimensional, time-dependent, Newtonian, incompressible Navier-Stokes equation in $\Omega_f \times R^+$

$$\frac{\partial \mathbf{u}}{\partial t} + (\mathbf{u} \cdot \nabla)\mathbf{u} = -\nabla p + \frac{1}{\mathrm{Re}} \nabla^2 \mathbf{u} \tag{22}$$

$$\nabla \cdot \mathbf{u} = 0, \tag{23}$$

with appropriate initial and boundary conditions. Here, Ω_f denotes the fluid domain, $\mathbf{u} = [u(x,y,t), v(x,y,t)]^T$ represents the velocity fields and p is the pressure. The dimensionless parameter Re denotes the Reynolds number.

Since the numerical method is based on the tensor product of a one-dimensional basis, it is not suited to problems where the boundary of the domain $\partial\Omega_f$ is not rectangular. However, the Brinkman penalization approach [17,19] allows one to study such a problem within a rectangular domain. In this approach, the domain $\Omega = \Omega_f \cup \Omega_s$, where Ω_s denotes solid obstacles or walls, is embedded in a rectangular domain $\hat{\Omega}$ that contains Ω, i.e., $\Omega \subseteq \hat{\Omega}$. The flow within the domain $\hat{\Omega}$ is then considered in the limit of Brinkman's porous media. More precisely, the solid and fluid regions are, respectively, characterized by small and large values of a permeability parameter K. The Navier-Stokes–Brinkman equations, obtained by adding a volumetric Darcy drag term to the Navier-Stokes equations, now governs the flow within the domain $\hat{\Omega} \times R^+$ [17,19]

$$\frac{\partial \mathbf{u}}{\partial t} + (\mathbf{u} \cdot \nabla)\mathbf{u} + \frac{1}{\mathrm{ReDa}K} \mathbf{u} = -\nabla p + \frac{1}{\mathrm{Re}} \nabla^2 \mathbf{u} \tag{24}$$

$$\nabla \cdot \mathbf{u} = 0, \tag{25}$$

where Da denotes the Darcy number. The permeability of each medium is defined by $K = K_s \rightarrow 0^+$ for $(x,y) \in \Omega_s$ and $K = K_f \rightarrow +\infty$ for $(x,y) \in \Omega_f$.

Since the Navier-Stokes–Brinkman equations are valid in the entire domain $\hat{\Omega}$, the adaptive wavelet collocation method can now be applied to the solve this reformulated problem. Note that the equations take into account the interface conditions between different media implicitly. With slightly modification, a moving boundary can also be considered (see [19]). Estimates of solution error resulting from (24) and (25) are given in [17]. The error is found to be $O(K_f^{-1} + K_s^{1/4})$ in the H_1-norm over the domain $\hat{\Omega}$, and $O(K_s^{3/4})$ in the L_2-norm over Ω_s. This implies that the solution of (24) and (25) converges to that of (22) and (23) as $K_s \rightarrow 0^+$ and $K_f \rightarrow +\infty$. Numerical verification from the solution of a specific problem shows slightly better accuracy than the estimate. However, worst accuracy is observed when K_s is smaller than some particular value.

Fractional Step Method

A fractional step method (sometimes called a projection method, a pressure correction method, etc.) [27,28] is used for the time discretization of the Navier-Stokes–Brinkman equation. In the first step, the transport step, an intermediate velocity field $\hat{\mathbf{u}}$ is calculated by using the Crank-Nicholson scheme for the viscous term and the second-order Adams-Bashforth scheme for the convective term

$$\frac{\hat{\mathbf{u}}-\mathbf{u}^n}{\Delta t}+\sum_{q=0}^{1}\gamma_q(\mathbf{u}^{n-q}\cdot\nabla)\mathbf{u}^{n-q}+\frac{1}{2\mathrm{ReDa}K}(\hat{\mathbf{u}}+\mathbf{u}^n)$$

$$=\frac{1}{2\mathrm{Re}}\nabla^2(\hat{\mathbf{u}}+\mathbf{u}^n) \tag{26}$$

where $\gamma_0=3/2$ and $\gamma_1=-1/2$. As the pressure is not used, this intermediate velocity field is not divergence-free. In the second step, the projection step, an approximation to the true velocity field $\mathbf{u}$ is obtained by solving the system

$$\frac{\mathbf{u}^{n+1}-\hat{\mathbf{u}}}{\Delta t}=-\nabla\phi \tag{27}$$

$$\nabla\cdot\mathbf{u}^{n+1}=0 \tag{28}$$

where ϕ is an auxiliary potential function. Equations (27) and (28) are equivalent to the following Poisson equation:

$$\nabla^2\phi=\frac{1}{\Delta t}\nabla\cdot\hat{\mathbf{u}} \tag{29}$$

When required, the pressure field at the new time step can be computed from

$$p^{n+1}=\phi-\frac{1}{2\mathrm{Re}}\Delta t\nabla^2\phi \tag{30}$$

Equations (26) and (29) must be augmented by boundary conditions for $\hat{\mathbf{u}}$ and ϕ, respectively. There is some disagreement in the literature on the proper choice of conditions [28–30]. In this work, the boundary conditions on $\hat{\mathbf{u}}$ are taken to be the same as those on $\mathbf{u}$. The boundary conditions for ϕ are taken to be of Neumann type and are deduced from (27) in conjunction with the condition of global mass conservation.

After discretization in space on the irregular sparse grid $\mathcal{G}^n$, (26) and (29) with their boundary conditions reduce to three linear systems of equations of the following form:

$$\mathbf{A}\mathbf{y}=\mathbf{f} \tag{31}$$

The matrix $\mathbf{A}$, of size $N_a\times N_a$ with N_a corresponding to the number of collocation points, represents the discrete Laplacian within the domain $\hat{\Omega}$ with boundary conditions incorporated. The vectors $\mathbf{y}$ and $\mathbf{f}$ are discrete representations of $\hat{u},\hat{v}$, or ϕ and corresponding nonhomogeneous terms, respectively. Spatial derivatives of $\hat{u}$ and $\hat{v}$ are approximated on a nonuniform stencil by using the fast algorithm discussed earlier [9]. However, it is found that the use of this algorithm to compute derivative approximations of ϕ sometimes results in numerical instabilities. Such instabilities are overcome by approximating these derivatives on uniform reconstructed stencils [10]. The linear system (31) is solved using the conjugate gradient squared (CGS) method with incomplete LU (ILU) preconditioning.

We note that the irregular sparse grid $\mathcal{G}^{n+1}$ is constructed from thresholding of velocity components only since pressure acts as an intermediate nonphysical variable in incompressible flows, i.e., it is a Lagrange multiplier that constrains the velocity field to be divergence-free.

Numerical Applications

In order to demonstrate the accuracy and flexibility of the adaptive wavelet method in a simple domain, we first consider the lid-driven cavity problem. The problem has served as a benchmark test for assessing the accuracy of numerical methods. For relatively low Reynolds numbers, the flow exhibits standing vortices in which their shape, size, and number are functions of Re. Subsequently, we consider the flow past two circular cylinders in a horizontal tandem arrangement as a test problem for the combined method based on Brinkman penalization and adaptive wavelets. In this flow, a variety of shedding patterns are obtained as the distance between the two cylinders is varied [31].

Lid-Driven Cavity. The physical configuration of the lid-driven cavity is that of a unit square cavity with rigid walls filled with a fluid. The equations governing the flow in dimensionless form are (24) and (25) with $\hat{\Omega}=\Omega_f=[0,1]\times[0,1]$ and $K_f\rightarrow\infty$. The fluid is set in motion by moving the top boundary (lid) at a constant velocity; thus, the boundary conditions are

$$\mathbf{u}(x,y,t)=\mathbf{g}(x,y,t)\equiv\begin{cases}(1,0)^T \text{ on } y=1,\\ (0,0)^T \text{ on } x=0,1 \text{ and } y=0\end{cases} \tag{32}$$

and the initial condition is given by $\mathbf{u}(x,y,0)=\mathbf{0}$.

The boundary conditions for $\hat{\mathbf{u}}$ are taken to be identical to those of $\mathbf{u}$

$$\hat{\mathbf{u}}=\mathbf{u}=\mathbf{g}^{n+1},\quad \text{on } \partial\hat{\Omega} \tag{33}$$

Because of this choice of boundary conditions, we now have that $\hat{\mathbf{u}}\cdot\mathbf{n}=\mathbf{g}^{n+1}\cdot\mathbf{n}$, which along with (27) results in the following homogeneous Neumann boundary conditions for ϕ:

$$\nabla\phi\cdot\mathbf{n}=0 \text{ on } \partial\hat{\Omega} \tag{34}$$

It can easily be seen from (27) that

$$\int_{\partial\hat{\Omega}}\mathbf{u}^{n+1}\cdot\mathbf{n}\,d\Gamma=\int_{\partial\hat{\Omega}}\hat{\mathbf{u}}\cdot\mathbf{n}\,d\Gamma-\Delta t\int_{\partial\hat{\Omega}}\nabla\phi\cdot\mathbf{n}\,d\Gamma \tag{35}$$

By making use of (33) and (34), we see that the global mass constraint $\int_{\partial\hat{\Omega}}\mathbf{u}^{n+1}\cdot\mathbf{n}\,d\Gamma=0$ is identically satisfied.

In all numerical calculations, we use a basis of order $p=4$ and threshold parameters $\varepsilon_s=5\times10^{-4}$ and $\varepsilon_a=2\varepsilon_s$. Consistent derivative approximations are obtained via nine-point finite-difference stencils. The number of resolution levels is set to $J-j_0=6$ with $j_0=3$ (nine points in each direction at the coarsest scale). Note that the finest grid spacing is equivalent to $\Delta x=\Delta y=1/512$. Time integrations are performed until steady state, defined by $\|\mathbf{u}^{n+1}-\mathbf{u}^n\|_\infty<5\times10^{-5}$, is reached.

Figure 1 shows streamlines and active collocation points obtained for Re=1000 at different times as well as at steady state. Formation of eddies can be observed very distinctly and the pattern agrees qualitatively quite well with that given in [32]. The distribution of collocation points clearly demonstrates that the dynamically adaptive grid is able to properly track the moving structures. As a results, the number of collocation points in $\mathcal{G}^n$, $N=\dim\mathcal{G}^n$, varies with the local demands of the solution for fixed threshold parameters. For these particular threshold values, the maximum number of collocation points required during the simulation is found to be approximately 4400. At steady state, the compression ratio (the ratio of the number of active points to that corresponding to a uniform mesh of equivalent resolution) is 60. Note that due to the velocity singularities in the upper corners, the adaptive algorithm demands a considerable number of points in confined neighborhoods of these locations. Solving the corresponding desingularized problem would reduce the number of such points substantially [33,34].

The streamlines and collocation points of the solutions at steady state for Re=400 and 3200 are shown in Fig. 2. For Re=3200, as can be seen, an additional secondary vortex appears near the upper left corner. It is worth noting that in the case of Re=400, the algorithm yields an inaccurate structure of the secondary vortex at the lower left corner. However, this is not surprising since the size of this eddy (0.1237 in width and 0.1081 in length [35]) is smaller than the coarsest resolution. In addition its strength is fairly weak as the maximum value of absolute vorticity is of the order of 0.05 (our computation with larger j_0 and [35]). Although heuristic, the issue can also be remedied by simply setting the threshold parameters such that the adaption criteria is more sensitive near the lower left corner. Specifically, adapt the grid based on $w(x_{j,\lambda})d_{j,\lambda}$

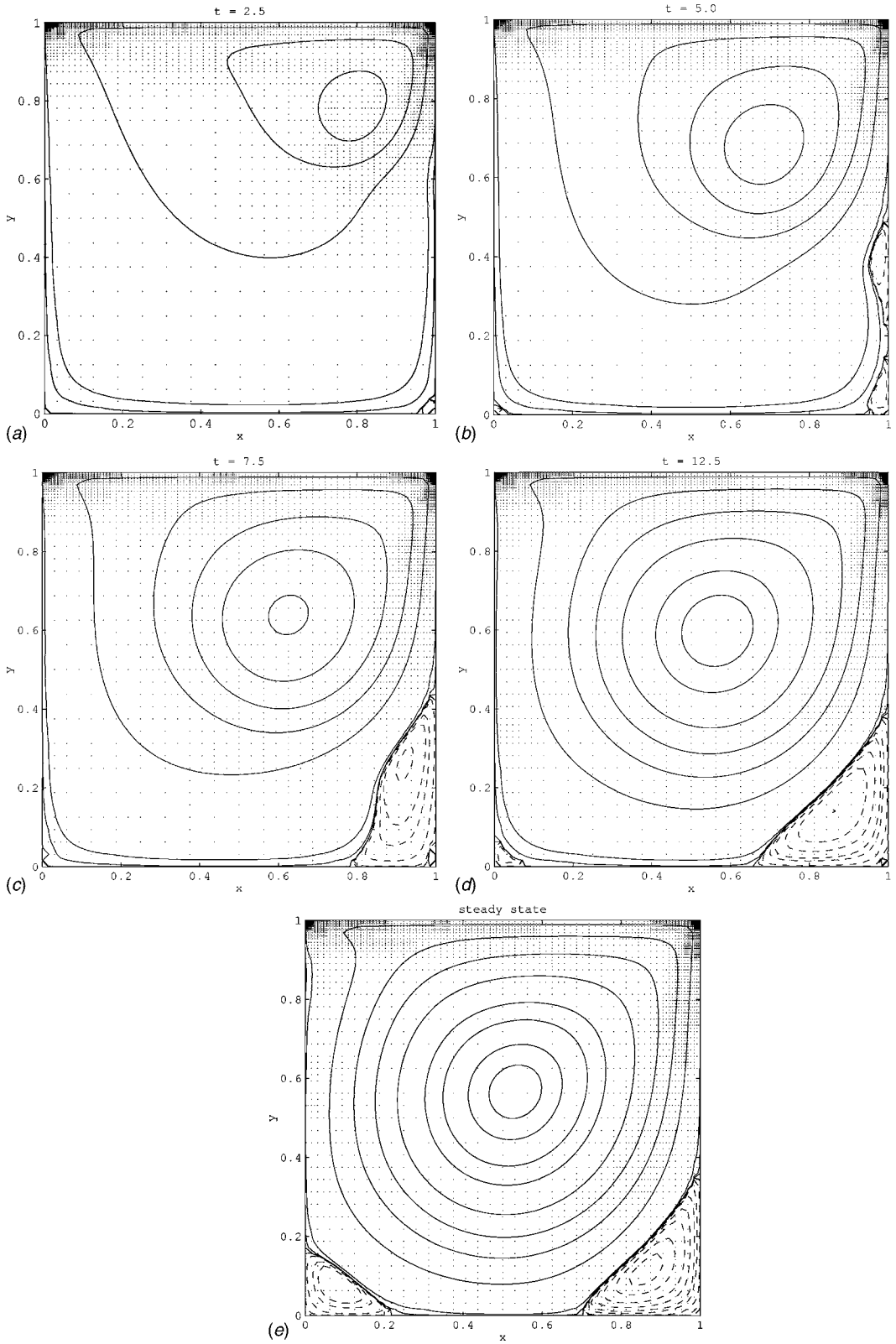

Fig. 1 Evolution of streamlines and dynamically adaptive grids for Re=1000 at *t*=2.5, 5.0, 7.5, 12.5, and steady state. The associated number of collocation points at each time are respectively *N* =3378, 3910, 4075, 4180, and 4372

instead of $d_{j,\lambda}$ with the Gaussian weight function $w(x_{j,\lambda}) = 9\exp(-25x^2_{j+1,2\mathbf{k}+\mathbf{e}})+1$. Comparisons of steady-state velocity distributions along the midsections of the cavity for Re=400, 1000, and 3200 with those of [35] are shown respectively in Figs. 3–5. Table 1 compares the intensities of the primary vortex and the lower left corner secondary vortex to those given in [35], obtained by the use of a multigrid technique, and in [34] by using a Chebyshev spectral collocation method for the desingularized

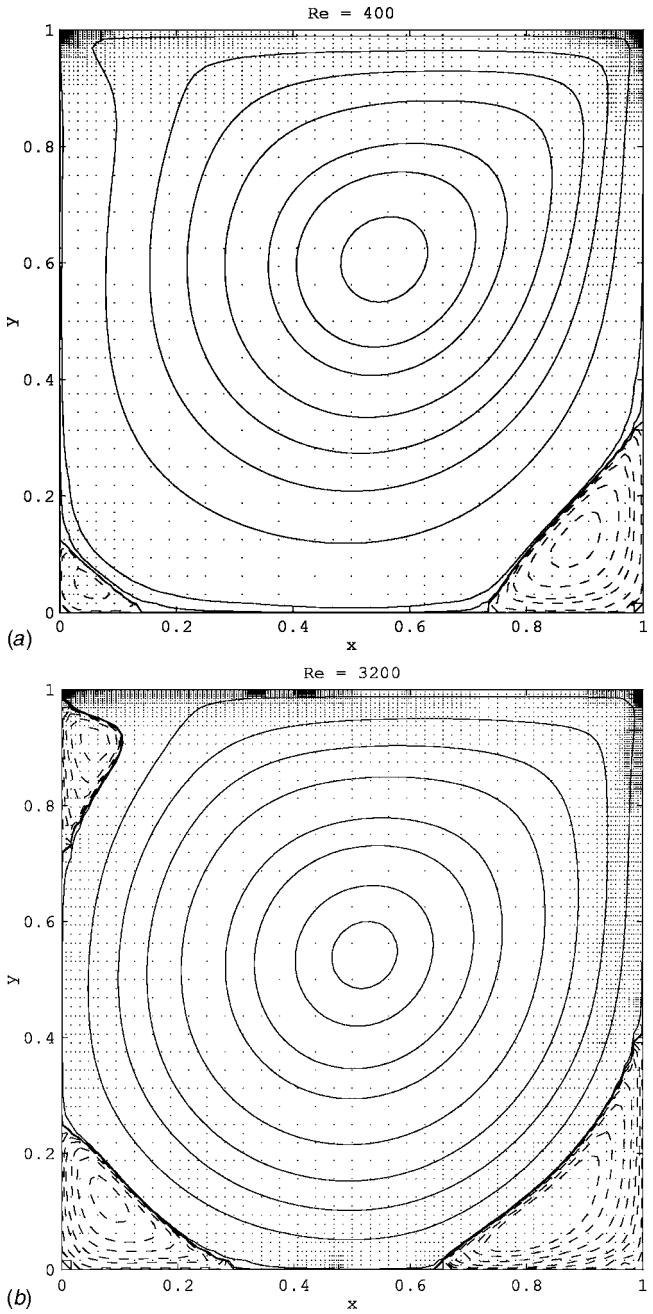

Fig. 2 Streamlines and dynamically adaptive grids at steady state for Re=1000 and 3200

problem. Note that resolutions of 257×257 grids (129×129 for Re=1000) were used in the calculations reported in [35], and 160×160 modes (and subsequently collocation points) in those in [34]. The total number of active wavelet collocation points required at steady state in the present computations are $N=3165$, 4180, and 6170 for Re=400, 1000, and 3200, respectively. Although the numbers of collocation points are relatively small, Figs. 3–5 and Table 1 indicate that the results compare favorably with the best results available in the literature.

Flow Past a Tandem Pair of Circular Cylinders. We consider the two-dimensional unsteady laminar flow of a viscous fluid past circular cylinders in tandem horizontal arrangements in an open domain. To apply the adaptive wavelet method, we use the governing equations (24) and (25). In order to solve the problem numerically, the computational domain is truncated from the open

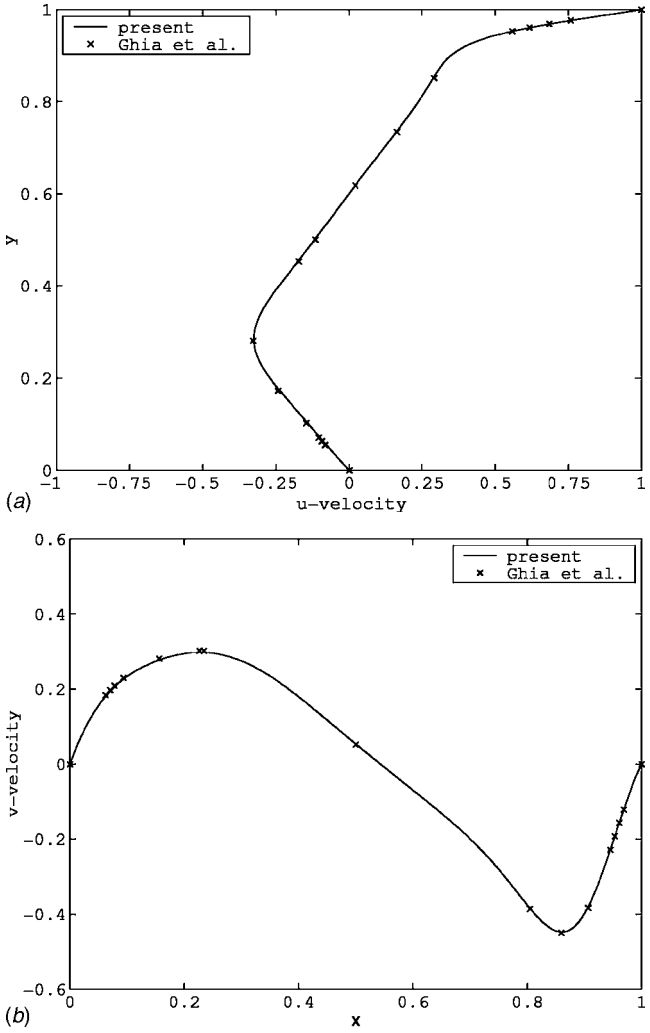

Fig. 3 Comparison of steady state velocity profiles $u(0.5,y)$ and $v(x,0.5)$ with those of [35] for Re=400

infinite domain and suitable boundary conditions are imposed. In this study, the computational domain is $[x_a,x_b]\times[y_a,y_b]=[0,35]\times[0,24]$. Two cylinders, with identical diameters $D=1$, are located at $(x,y)=(8,12)$ and $(8+L,12)$, respectively. The condition imposed on the left boundary is that of inflow, i.e., $\mathbf{u}=(1,0)^T$. Free-slip conditions are imposed at the upper and lower boundaries, i.e., on such boundaries we take $\partial u/\partial y=0$ and $v=0$. The proper outflow boundary conditions, which allows the flow to exit gracefully without producing reflections, are nontrivial and, in fact, have long been the subject of discussions in the literature [30,36,37]. In this work, we use the simple conditions

$$\frac{\partial \mathbf{u}}{\partial x}=\mathbf{0} \tag{36}$$

One may expect such conditions to perform well when the outflow boundary is located sufficiently far down-stream. Numerical studies reported in [36] indicate that these conditions produce very weak or no distortions even when the outflow boundary is located near the flow structures in unstratified flow, while some artificial distortions are observed in stratified flow (e.g., in Poiseuille-Bénard channel flow).

In the first case that we look at, we assume that the boundary conditions for $\hat{\mathbf{u}}$ and $\mathbf{u}$ are the same, as before. In the second case, since the boundaries are artificial, we take the implicit conditions $\hat{\mathbf{u}}\cdot\mathbf{n}=\mathbf{u}^{n+1}\cdot\mathbf{n}$ on the inflow, and upper and lower boundaries. On

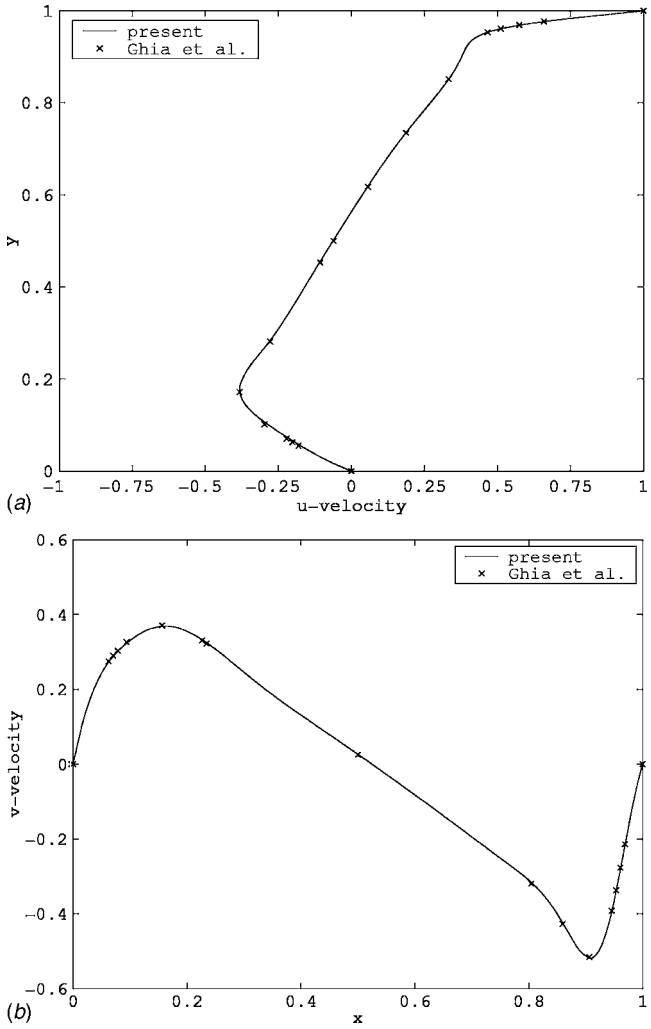

Fig. 4 Comparison of steady state velocity profiles $u(0.5, y)$ and $v(x, 0.5)$ with those of [35] for Re=1000

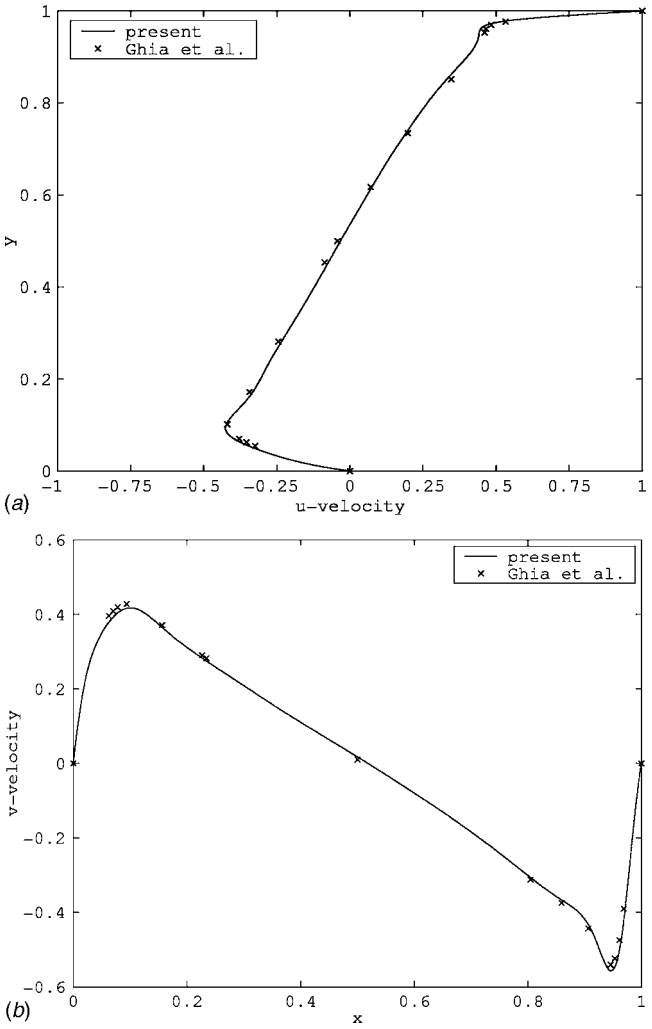

Fig. 5 Comparison of steady state velocity profiles $u(0.5, y)$ and $v(x, 0.5)$ with those of [35] for Re=3200

the outflow boundary we take $\hat{\mathbf{u}} \cdot \mathbf{n} = \mathbf{u}^{n+1} \cdot \mathbf{n} - \delta$, where δ is obtained from the global mass conservation statement

$$\int_{\partial\hat{\Omega}} \mathbf{u}^{n+1} \cdot \mathbf{n} \, d\Gamma = 0$$

and is given by

$$\delta = 1 - \frac{1}{H} \int_{\Gamma_o} \mathbf{n} \, d\Gamma \tag{37}$$

where H is the size of the outflow boundary Γ_o. Such conditions on the normal direction of $\hat{\mathbf{u}}$, with (27), suggest the homogeneous Neumann conditions

$$\nabla \phi \cdot \mathbf{n} = 0 \tag{38}$$

on the inflow, and upper and lower boundaries, and the nonhomogeneous Neumann condition

$$\nabla \phi \cdot \mathbf{n} = -\frac{\delta}{\Delta t} \tag{39}$$

on the outflow boundary for the Poisson equation (29). The above boundary conditions were originally proposed in [36].

For the calculations, we use the basis of order $p=4$ and threshold parameter $\varepsilon_s = 7.5 \times 10^{-4}$ and $\varepsilon_a = 10\varepsilon_s$. The number of resolution levels is limited to 4, and 71×49 collocation points are used in the x and y directions at the coarsest scale. This results in the finest grid spacing of 0.03125. The parameter ReDaK is set to 7.5×10^{-4} in the solid circular cylindrical domains and to 1×10^{10} in the fluid domain.

The flow with Re=200 and gap L between two cylinders with $1.5D \leqslant L \leqslant 4D$ is examined. Plots of vorticity for the flow with $L=1.5D$, $3D$, and $4D$ at $t=200$ are depicted in Figs. 6(*a*), 7(*a*), and 8(*a*), respectively. It can be observed that the vortex-shedding pattern changes when the distance between two cylinders is varied. For $L=1.5D$, the cylinders behave like a single blunt body at this Reynolds number. The vortex street forms behind the downstream cylinder. For $L=4D$, the vortex street forms behind both cylinders. The present results agree qualitatively well with experimental observations in [31] as well as with the numerical study in [38]. The corresponding irregular sparse grids resulting from the dynamically adaptive algorithm are depicted in Figs. 6(*b*), 7(*b*), and 8(*b*). It can be observed that the distribution of collocation points in the wake reflects the wake strength and pattern. The results clearly indicate that the adaptive algorithm concentrates the collocation points according to the solution features. We note that the compression ratio varies with time during each simulation. For example, for $L=3D$, the compression ratio is approximately 130 ($N \approx 6600$) in the early flow-development stage and 85 ($N \approx 10200$) when in the periodic-shedding stage. Other relevant flow quantities, such as shedding frequency as well as lift and drag coefficients, are currently being examined.

Table 1 Comparisons of the intensities of the primary vortex and the lower left corner secondary vortex

Re	Investigators	Primary vortex			Lower left corner vortex		
		$\psi_{\min}$	$\omega_{v,c}$	Location (x,y)	$\psi_{\max}$	$\omega_{v,c}$	Location (x,y)
400	Present	−0.1131	2.3087	(0.5547,0.6094)	1.5953×10^{-5}	−0.06295	(0.0547,0.0469)
	Ref [35]	−0.1139	2.2947	(0.5547,0.6055)	1.4195×10^{-5}	−0.05697	(0.0859,0.0781)
1000	Present	−0.1173	2.0476	(0.5313,0.5703)	2.2027×10^{-4}	−0.35628	(0.0859,0.0781)
	Ref [35]	−0.1179	2.0497	(0.5313,0.5643)	2.3113×10^{-4}	−0.36175	(0.0859,0.0781)
	Ref [34]	−0.1189	2.0678	(0.5384,0.5652)	2.3345×10^{-4}	−0.35228	(0.0833,0.0781)
3200	Present	−0.1171	1.8594	(0.5234,0.5390)	9.8933×10^{-4}	−1.02891	(0.0781,0.1172)
	Ref [35]	−0.1204	1.9886	(0.5117,0.5352)	9.7823×10^{-4}	−1.06301	(0.0859,0.1094)

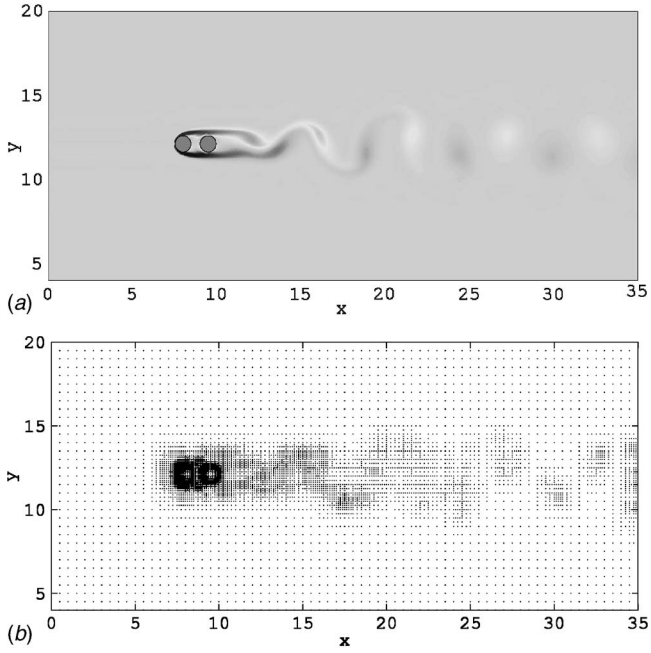

Fig. 6 (a) Vorticity field and (b) dynamically adaptive grid for flow past a tandem pair of circular cylinders with gap $L=1.5D$ at $t=200$ for Re=200

Concluding Remarks

In this work, an adaptive wavelet-based multiresolution collocation method is combined with the Brinkman penalization method using a fractional time step algorithm to solve incompressible Navier-Stokes equations.

In the lid-driven cavity problem, it is observed that the dynamically adaptive algorithm, based on thresholding of wavelet coefficients, adapts collocation points to the flow structures. As a results, the number of collocation points varies with the demand of the solution. Numerical results are found to be in good agreement with those obtained by previous investigators even with the use of a relative small number of unknowns.

As an application of the method to flow in complex domains, the external flow past a tandem pair of circular cylinders is investigated. The numerical solutions agree qualitatively well with experimental and other numerical solutions even though relatively few degrees of freedom are used. This is primarily due to the effectiveness of the adaptive algorithm in locating collocation points to reflect the shedding wake pattern of the flow.

Acknowledgment

The authors acknowledge the partial support from Los Alamos National Laboratories in the performance of this work.

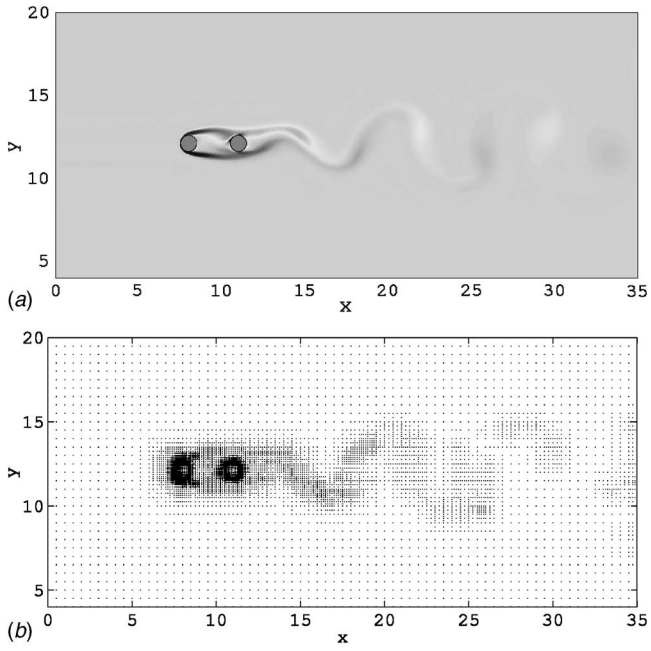

Fig. 7 (a) Vorticity field and (b) dynamically adaptive grid for flow past a tandem pair of circular cylinders with gap $L=3D$ at $t=200$ for Re=200

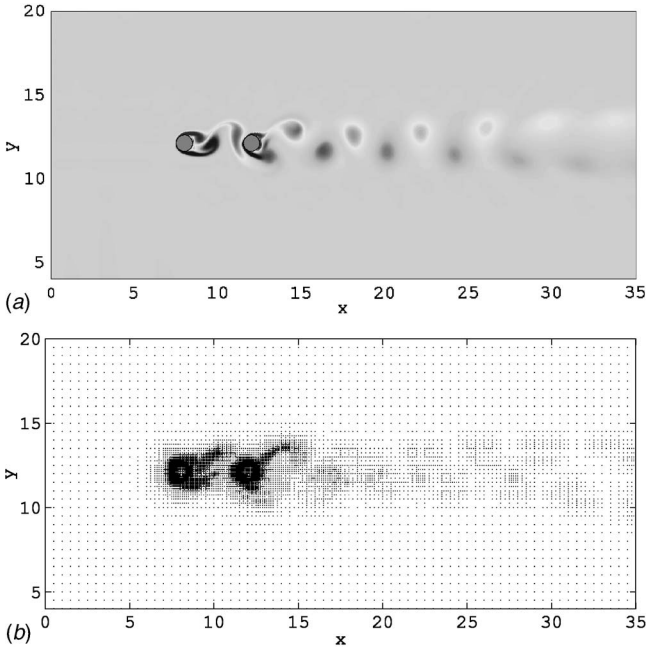

Fig. 8 (a) Vorticity field and (b) dynamically adaptive grid for flow past a tandem pair of circular cylinders with gap $L=4D$ at $t=200$ for Re=200

References

[1] Berger, M. J., and Colella, P., 1989, "Local Adaptive Mesh Refinement for Shock Hydrodynamics," J. Comput. Phys. **82**, pp. 64–68.

[2] Mackerle, J., 2001, "Error Estimates and Adaptive Finite Element Methods: A Bibliography (1990 - 2000)," Eng. Comput. **18**, pp. 802–914.

[3] Daubechies, I., 1992, *Ten Lectures on Wavelets*, SIAM, Philadelphia.

[4] Liandrat, J., and Tchamitchian, P., 1990, Resolution of the 1D Regularized Burgers Equation Using a Spatial Wavelet Approximation, ICASE Report 90—83, NASA.

[5] Fröhlich, J., and Schneider, K., 1994, "An Adaptive Wavelet Galerkin Algorithm for One-Dimensional and 2-Dimensional Flame Computations," Eur. J. Mech. B/Fluids **13**, pp. 439–471.

[6] Vasilyev, O. V., and Paolucci, S., 1996, "Dynamically Adaptive Multilevel Wavelet Collocation Method for Solving Partial Differential Equations in a Finite Domain," J. Comput. Phys. **125**, pp. 498–512.

[7] Vasilyev, O. V., and Paolucci, S., 1997, "A Fast Adaptive Wavelet Collocation Algorithm for Multidimensional PDEs," J. Comput. Phys. **138**, pp. 16–56.

[8] Bertoluzza, S., 1996, "Adaptive Wavelet Collocation Method for the Solution of Burgers Equation," Transp. Theory Stat. Phys. **25**, pp. 339–359.

[9] Rastigejev, Y., and Paolucci, S., 2003, "Wavelet Based Adaptive Multiresolution Computation of Viscous Reactive Flows," *[Submitted]*.

[10] Holmström, M., 1999. "Solving Hyperbolic PDEs Using Interpolating Wavelets," SIAM J. Sci. Comput. (USA) **21**, pp. 405–420.

[11] Rastigejev, Y., 2002, Multiscale Computations with a Wavelet Adaptive Algorithm, Ph.D. thesis, University of Notre Dame, Notre Dame, IN.

[12] Marchuck, G. I., Kuznetsov, Y., and Matsokin, A. M., 1986, "Fictitious Domain and Domain Decomposition Methods," *Sov. J. Num. Anal. Math. Model.*, 1, pp. 3–35.

[13] Glowinski, R., Pan, T. W., Hesla, T. I., Joseph, D. D., and Périaux, J., 2001, "A Fictitious Domain Approach to the Direct Numerical Simulation of Incompressible Viscous Flow Past Moving Rigid Bodies: Application to Particulate Flow," J. Comput. Phys., **169**, pp. 363–426.

[14] Peskin, C. S., 1977, "Numerical Analysis of Blood Flow in Heart," J. Comput. Phys. **25**, pp. 220–252.

[15] Beyer, R. P., 1992. "A Computational Model of the Cochlea Using the Immersed Boundary Method," J. Comput. Phys. **98**, pp. 145–162.

[16] Goldstein, D., Handler, R., and Sirovich, L., 1993, "Modeling a No-Slip Flow Boundary With an External Force Field," J. Comput. Phys. **105**, pp. 354–366.

[17] Angot, P., Bruneau, C.-H., and Fabrie, P., 1999, "A Penalization Method to Take Into Account Obstacles in Incompressible Viscous Flows," Numer. Math. **81**, pp. 497–520.

[18] Beyer, R. P., and Leveque, R. J., 1992, "Analysis of a One-Dimensional Model for the Immersed Boundary Method," SIAM (Soc. Ind. Appl. Math.) J. Numer. Anal. **29**, pp. 332–364.

[19] Khadra, K., Angot, P., Parneix, S., and Caltagirone, J.-P., 2000, "Fictitious Domain Approach for Numerical Modeling of Navier-Stokes Equations," Int. J. Numer. Methods Fluids **34**, pp. 651–684.

[20] Donoho, D., 1992, Interpolating Wavelet Transform, Report, Dep. of Statistics, Stanford University.

[21] Deslauriers, G., and Dubuc, S., 1989, "Symmetric Iterative Interpolation Processes," Constructive Approx. **5**, pp. 49–68.

[22] Saito, N., and Beylkin, G., 1993, "Multiresolution Representations Using the Auto-Correlation Functions of Compactly Supported wavelets," IEEE Trans. Signal Process. **41**, pp. 3584–3590.

[23] Bertoluzza, S., 1997, "An Adaptive Collocation Method Based on Interpolating Wavelets," in *Multiscale Wavelet Methods for Partial Differential Equations*, W. D. et al., eds., Vol. 6 of Wavelet Analysis and Its Applications, Academic, New York, pp. 109–135.

[24] Dahmen, W., 1997, "Wavelet and Multiscale Methods for Operator Equations," Acta Numerica **6**, pp. 55–228.

[25] Jameson, L., 1998, "A Wavelet-Optimized, Very High Order Numerical Method," SIAM J. Sci. Comput. (USA) **19**, pp. 1980–2013.

[26] Bertoluzza, S., 1995, "Adaptive Wavelet Collocation for the Solution of Steady-State Equations," in Wavelet Applications II: April 17-21, Orlando, Proc. SPIE **2491**, pp. 947–956.

[27] Kim, J., and Moin, P., 1985, "Application of a Fractional-Step Method to Incompressible Navier-Stokes Equation," J. Comput. Phys. **59**, pp. 308–323.

[28] Gresho, P. M., 1990, "On the Theory of Semi-Implicit Projection Methods for Viscous Incompressible Flow and Its Implementation Via a Finite Element Method That Also Introduces a Nearly Consistent Mass Matrix Part I: Theory," Int. J. Numer. Methods Fluids **11**, pp. 587–620.

[29] Timmermans, L. J. P., Minev, P. D., and Van De Vosse, F. N., 1996, "An Approximate Projection Scheme for Incompressible Flow Using Spectral Elements," Int. J. Numer. Methods Fluids **22**, pp. 673–688.

[30] Jin, G., and Braza, M., 1993, "A Nonreflecting Outlet Boundary Condition for Incompressible Unsteady Navier-Stokes Calculations," J. Comput. Phys., **107**, pp. 239–253.

[31] Zdravkovich, M. M., 1977, "Review of Flow Interference Between Two Circular Cylinders in Various Arrangements," ASME J. Fluids Eng. **99**, pp. 618–633.

[32] Griebel, M., Dornseifer, T., and Neunhoeffer, T., 1998, *Numerical Simulation in Fluid Dynamics: A Practical Introduction*, SIAM, Philadelphia, PA.

[33] Shen, J., 1991, "Hopf-Bifucation of the Unsteady Regularized Driven Cavity Flow," J. Comput. Phys. **95**, pp. 228–245.

[34] Botella, O., and Peyret, R., 1998, "Benchmark Spectral Results on the Lid-Driven Cavity Flow," Comput. Fluids **27**, pp. 421–433.

[35] Ghia, U., Ghia, K. N., and Shin, C. T., 1982, "High-Re Solutions for Incompressible Flow Using Navier-Stokes Equations and a Multigrid Method," J. Comput. Phys., **48**, pp. 387-411.

[36] Sani, R. L., and Gresho, P. M., 1994, "Résumé and Remarks on the Open Boundary Condition Minisymposium," Int. J. Numer. Methods Fluids **18**, pp. 983–1008.

[37] Ol'shanskii, M. A., and Staroverov, V. M., 2000, "On Simulation of Outflow Boundary Conditions in Finite Difference Calculations for Incompressible Fluid," Int. J. Numer. Methods Fluids, **33**, pp. 449–534.

[38] Meneghini, J. R., Saltara, F., Siqueira, C. L. R., and Ferrari Jr., J. A., 2001, "Numerical Simulation of Flow Interference Between Two Cylinders in Tandem and Side-By-Side Arrangements," J. Fluids Struct. **15**, pp. 327–350.

High-Pass Filtered Eddy-Viscosity Models for Large-Eddy Simulations of Compressible Wall-Bounded Flows

Steffen Stolz
Institute of Fluid Dynamics, ETH Zurich,
CH-8092 Zürich, Switzerland
e-mail: stolz@ifd.mavt.ethz.ch

In this contribution we consider large-eddy simulation (LES) using the high-pass filtered (HPF) Smagorinsky model of a spatially developing supersonic turbulent boundary layer at a Mach number of 2.5 and momentum-thickness Reynolds numbers at inflow of ~4500. *The HPF eddy-viscosity models employ high-pass filtered quantities instead of the full velocity field for the computation of the subgrid-scale (SGS) model terms. This approach has been proposed independently by Vreman (Vreman, A. W., 2003, Phys. Fluids,* ***15****, pp. L61–L64) and Stolz et al. (Stolz, S., Schlatter, P., Meyer, D., and Kleiser, L., 2003, in Direct and Large Eddy Simulation V, Kluwer, Dordrecht, pp. 81–88). Different from classical eddy-viscosity models, such as the Smagorinsky model (Smagorinsky, J., 1963, Mon. Weath. Rev,* ***93****, pp. 99–164) or the structure-function model (Métais, O. and Lesieur, M., 1992, J. Fluid Mech.,* ***239****, pp. 157–194) which are among the most often employed SGS models for LES, the HPF eddy-viscosity models do need neither van Driest wall damping functions for a correct prediction of the viscous sublayer of wall-bounded turbulent flows nor a dynamic determination of the coefficient. Furthermore, the HPF eddy-viscosity models are formulated locally and three-dimensionally in space. For compressible flows the model is supplemented by a HPF eddy-diffusivity ansatz for the SGS heat flux in the energy equation. Turbulent inflow conditions are generated by a rescaling and recycling technique in which the mean and fluctuating part of the turbulent boundary layer at some distance downstream of inflow is rescaled and reintroduced at the inflow position (Stolz, S. and Adams, N. A., 2003, Phys. Fluids,* ***15****, pp. 2389–2412).* [DOI: 10.1115/1.1949652]

Introduction

Fixed-coefficient eddy-viscosity subgrid-scale (SGS) models for large-eddy simulations (LESs), e.g., the Smagorinsky model [1] or the structure-function (SF) model [2], require special treatment of the viscous sublayer of wall-bounded turbulent flows. An ad hoc measure frequently used is the van Driest damping function for the model coefficient in the near-wall region, which is, however, designed for special flow situations only [3]. Ideally, the SGS model used for LES should be defined locally and fully three-dimensional, i.e., without special treatment of selected spatial directions, and it should not require ad hoc adaptation to the specific flow configuration. In general, the dynamic Smagorinsky model [4,5] is defined locally and adapts itself automatically to different flow situations (e.g., laminar, transitional, and turbulent flows). However, it does not necessarily predict a vanishing value of the model coefficient for laminar flows as it should and can be singular due to a vanishing strain rate. Furthermore, it is often used in a nonlocal formulation using averaging in homogeneous directions.

In this contribution, we consider a different approach for SGS modeling by analyzing high-pass filtered (HPF) eddy-viscosity models [6]. The HPF Smagorinsky and HPF structure-function model were shown to give good results for incompressible turbulent and transitional channel flow [6]. The concept of HPF models and the relation to the variational multiscale method [7] was proposed recently, independently by Stolz et al. [6] and by Vreman [8]. However, different from Ref. [6] and this contribution, where filtering is done with filters proposed in Ref. [9], filtering is performed in Ref. [8] using a top-hat filter. From a physical point of view, the HPF models take into account only the most important interactions between the nonresolved subgrid scales and the resolved scales, which take place between the smallest resolved scales and the largest subgrid scales, while the interactions between the large-scale flow and subgrid scales are negligible [8,10]. Compared to the classical fixed-coefficient eddy-viscosity models based on the full velocity field, the HPF models do predict a significantly reduced eddy-viscosity in the near-wall region or for laminar flow regions. For this reason, no van Driest damping or intermittency functions are necessary.

LESs with the HPF Smagorinsky model of a turbulent compressible boundary layer at high Reynolds number and a direct comparison of the results to experimental data are the subject of the present study. The configuration for the turbulent supersonic boundary layer considered here corresponds to case A in Ref. [11], where LES using the approximate deconvolution model (ADM) [12,13] have been performed. For computational efficiency, only a relatively short streamwise section of the turbulent boundary layer is included in the computational domain. Including the spatially developing boundary-layer transition region would require a significantly increased size of the computational domain. The rescaling and recycling method (RRM) as introduced by Stolz and Adams [11] for compressible flows is employed for generation of turbulent inflow data. The RRM allows for an easy control of the desired turbulent boundary-layer properties at a certain downstream station, such as the momentum thickness. Furthermore, the transient region downstream of the inflow required to recover a developed turbulent boundary layer is rather small.

Contributed by the Fluids Engineering Division for publication in the JOURNAL OF FLUIDS ENGINEERING. Manuscript received by the Fluids Engineering Division August 13, 2004; Final manuscript received February 18, 2005. Associate Editor: Ugo Piomelli.

Filtered Transport Equations

We solve the filtered Navier-Stokes equations that constitute the fundamental equations for the resolved conservative variables $\{\bar{\rho}, \bar{\rho}\bar{u}_1, \bar{\rho}\bar{u}_2, \bar{\rho}\bar{u}_3, \breve{E}\}$ being the filtered density, filtered momentum, and total resolved energy, respectively. Filtered quantities are indicated by $\bar{}$. Furthermore, Favre-filtered quantities, denoted by $\tilde{}$, are computed from a mass-weighted filtering operation $\tilde{\phi}=\overline{\rho\phi}/\bar{\rho}$. Quantities denoted by $\breve{}$ are computed according to their definition, but from filtered variables. The filtered Navier-Stokes equations are derived following Vreman [14], and commutation errors due to a variable filter width are neglected.

The filtered continuity equation is

$$\frac{\partial\bar{\rho}}{\partial t}+\frac{\partial\overline{\rho}\bar{u}_j}{\partial x_j}=0 \tag{1}$$

and the filtered momentum equations are

$$\frac{\partial\bar{\rho}\bar{u}_i}{\partial t}+\frac{\partial}{\partial x_j}(\bar{\rho}\bar{u}_i\bar{u}_j+\bar{p}\,\delta_{ij}-\breve{\tau}_{ij})=-\frac{\partial\bar{\rho}\sigma_{ij}}{\partial x_j}+\beta_i \tag{2}$$

with the viscous stress tensor and strain rate tensor

$$\breve{\tau}_{ij}=\frac{\breve{\mu}(\tilde{T})}{\mathrm{Re}}\breve{S}_{ij},\quad \breve{S}_{ij}=\frac{\partial\bar{u}_i}{\partial x_j}+\frac{\partial\bar{u}_j}{\partial x_i}-\frac{2}{3}\frac{\partial\bar{u}_l}{\partial x_l}\delta_{ij},$$

respectively. Furthermore, the viscosity $\breve{\mu}$ is computed from the Favre-filtered temperature $\tilde{T}$ according to the Sutherland's law,

$$\breve{\mu}(\tilde{T})=\tilde{T}^{3/2}\frac{1+S}{\tilde{T}+S}$$

with Sutherland constant S. The subgrid-scale stresses are

$$\bar{\rho}\sigma_{ij}=\bar{\rho}(\widetilde{u_iu_j}-\tilde{u}_i\tilde{u}_j) \tag{3}$$

and the subgrid-scale term

$$\beta_i=\frac{\partial(\bar{\tau}_{ij}-\breve{\tau}_{ij})}{\partial x_j} \tag{4}$$

arises from the nonlinearity of the viscous stresses due to the temperature dependency of the viscosity.

Furthermore, we consider the equation for the total resolved energy $\breve{E}=\bar{p}/(\gamma-1)+\frac{1}{2}\overline{\rho u_i}\overline{\rho u_i}/\bar{\rho}$ with γ being the ratio of specific heats c_p/c_v and $\bar{p}$ denoting the filtered pressure

$$\frac{\partial\breve{E}}{\partial t}+\frac{\partial}{\partial x_j}[(\breve{E}+\bar{p})\tilde{u}_j-\breve{\tau}_{ij}\tilde{u}_i+\breve{q}_j]=-\alpha_1-\alpha_2-\alpha_3+\alpha_4+\alpha_5-\alpha_6 \tag{5}$$

with the molecular heat flux

$$\breve{q}_j=\frac{\breve{\mu}(\tilde{T})}{(\gamma-1)\mathrm{Re}\,\mathrm{Pr}\,M^2}\frac{\partial\tilde{T}}{\partial x_j},$$

with Pr being the (molecular) Prandtl number and M the reference Mach number. The subgrid-scale terms occurring in the equation for the total resolved energy are

$$\alpha_1=\tilde{u}_i\frac{\partial\bar{\rho}\sigma_{ij}}{\partial x_j},\quad \alpha_2=\frac{1}{\gamma-1}\frac{\partial}{\partial x_j}(\overline{pu_j}-\bar{p}\tilde{u}_j)$$

$$\alpha_3=\overline{p\frac{\partial u_j}{\partial x_j}}-\bar{p}\frac{\partial\tilde{u}_j}{\partial x_j},\quad \alpha_4=\overline{\tau_{ij}\frac{\partial u_i}{\partial x_j}}-\bar{\tau}_{ij}\frac{\partial\tilde{u}_i}{\partial x_j}$$

$$\alpha_5=\frac{\partial}{\partial x_j}(\tilde{u}_i\bar{\tau}_{ij}-\tilde{u}_i\breve{\tau}_{ij}),\quad \alpha_6=\frac{\partial}{\partial x_j}(\bar{q}_j-\breve{q}_j)$$

where α_1 is the SGS-dissipation and α_2 is the pressure-velocity correlation, which resembles a turbulent heat flux and describes the contribution of the subgrid turbulence to the conduction of heat. The term α_3 is the pressure-dilatation correlation and α_4 can be physically interpreted as SGS molecular dissipation. The terms α_5 and α_6 represent the SGS diffusion due to the molecular transport of momentum and heat, respectively, and arise from the nonlinearity of the viscous stresses and heat flux.

High-Pass Filtered Eddy-Viscosity Models

Van Driest wall damping functions can be employed with fixed-coefficient Smagorinsky model for the SGS stresses $\bar{\rho}\sigma_{ij}$ in order to reduce too large values for the eddy-viscosity due to the velocity gradient in the near-wall region. However, such ad hoc measures are suitable for special flow situations only and require adaptation to the specific flow configuration. Instead of using ad hoc measures we consider the high-pass filtered (HPF) Smagorinsky model, which predicts a reduced eddy viscosity in the near-wall region. With the HPF eddy-viscosity model, a dynamic computation of the model coefficient is found not to be necessary to correctly predict near-wall and transitional flows [2], however, it can, in principle, also be employed for the determination of the model coefficient.

The HPF model is based on the fixed-coefficient Smagorinsky model given by

$$\bar{\rho}\sigma_{ij}-\frac{\delta_{ij}}{3}\bar{\rho}\sigma_{kk}\approx m_{ij}^S:=-2\bar{\rho}(C_S\Delta)^2|S(\tilde{\mathbf{u}})|\cdot S_{ij}(\tilde{\mathbf{u}})=-2\nu_tS_{ij}(\tilde{\mathbf{u}}) \tag{6}$$

with the strain rate

$$S_{ij}(\tilde{\mathbf{u}})=\frac{1}{2}\left(\frac{\partial\tilde{u}_i}{\partial x_j}+\frac{\partial\tilde{u}_j}{\partial x_i}-\frac{2}{3}\delta_{ij}\frac{\partial\tilde{u}_k}{\partial x_k}\right)$$

and $|S(\tilde{\mathbf{u}})|=\sqrt{2S_{ij}(\tilde{\mathbf{u}})S_{ij}(\tilde{\mathbf{u}})}$. For the filter width $\Delta=(\Delta x_1\Delta x_2\Delta x_3)^{1/3}$ is employed. Note that the grid spacing Δx_i is computed from the grid spacing in the equidistant computational space and from the Jacobian of the mapping between the physical and computational space that is employed for the solution of the differential equations on nonequidistant meshes.

The HPF eddy-viscosity models employ high-pass filtered quantities $H*\tilde{\mathbf{u}}$ instead of $\tilde{\mathbf{u}}$ for the computation of the turbulent eddy viscosity and strain rate, where H is a suitable high-pass filter operator. The HPF Smagorinsky model is then given by

$$m_{ij}^{\mathrm{HPF}}=-2\bar{\rho}(C_{S,\omega_c}^{\mathrm{HPF}}\Delta)^2|S(H*\tilde{\mathbf{u}})|\cdot S_{ij}(H*\tilde{\mathbf{u}})=-2\nu_t^{\mathrm{HPF}}S_{ij}(H*\tilde{\mathbf{u}}) \tag{7}$$

Furthermore, the turbulent heat flux α_2 in the equation for the total resolved energy is modeled by an eddy-diffusivity ansatz based on the gradient of the high-pass filtered temperature

$$\alpha_2\approx\frac{\partial}{\partial x_j}\left(\frac{\nu_t^{\mathrm{HPF}}}{(\gamma-1)\mathrm{Pr}_t\,M^2}\frac{\partial(H*\tilde{T})}{\partial x_j}\right) \tag{8}$$

where the turbulent Prandtl number Pr_t is set to 0.7. For the SGS dissipation α_1 no additional model is required as it involves filtered quantities and the subgrid-scale stress tensor only. The other SGS terms, $\alpha_3-\alpha_6$ and β_i, are neglected as they are expected to be smaller than the SGS terms that are modeled [14,15].

With suitable filters, high-pass filtered quantities are vanishing for smooth velocity profiles (e.g., low-order polynomials), and the corresponding SGS model contributions are evanescent. High-pass filtering is performed by subtracting low-pass filtered quantities from the unfiltered ones. A detailed description of the construction of the explicit five-point low-pass filter G used herein can be found in Ref. [9]. The high-pass filtered quantity is then given by

$$H * \tilde{u} = (I - G) * \tilde{u} = O(\Delta^r) \tag{9}$$

with r being the order of the low-pass filter G. For arbitrary grids $r=3$, however, for equidistant grids odd-numbered moments are vanishing and r increases to 4 [10]. $H*\tilde{u}$ is vanishing if $\tilde{u}$ is a polynomial of up to degree $r-1$. The cutoff wave number ω_c, defined arbitrarily by $|\hat{H}(\omega_c)|=1/2$ where $\hat{}$ denotes a Fourier transform, of the explicit filter employed here is $\omega_c \approx 2\pi/3$. In order to account for the dependency of the model coefficient on the cutoff wave number ω_c of the high-pass filter in the range $\omega_c \in [\pi/3, 3\pi/4]$, Stolz et al. [6] proposed an empirical correction given by

$$C_{S,\omega_c}^{\mathrm{HPF}} \approx \frac{\pi}{\pi - \omega_c} \cdot C_0, \tag{10}$$

where the recommended value for C_0 is 0.1/3, e.g., $C_{S,\omega_c}^{\mathrm{HPF}}=0.1$ for $\omega_c=2\pi/3$. For this reason the model coefficient is set to 0.1 for the LES using the explicit filter with $\omega_c \approx 2\pi/3$.

Numerical Method

To achieve stability of the LES, a high-order numerical scheme as proposed by Sandham et al. [16] is used for the solution of the conservation equations for the filtered density, filtered momentum, and total resolved energy. The main ingredients are a fourth-order central spatial difference operator satisfying a summation-by-parts condition [17], an entropy-splitting approach which splits Eulerian fluxes into conservative and nonconservative parts [18,19], and usage of fourth-order central scheme for second derivatives in the viscous term wherever possible [16,17]. For the entropy-splitting scheme a splitting parameter $\beta=6$ is used such that 6/7 of the Eulerian fluxes are computed in their conservative form and 1/7 in the entropy splitting form. The parameter is in the region $2 \leqslant \beta \leqslant 8$ as proposed in Ref. [16]. Note that the numerical scheme does not introduce artificial dissipation or employ upwinding or filtering for stabilizing of the numerical integration [16]. Note that the simulations with the HPF Smagorinsky were found not to be stable when using the same numerical scheme, i.e., without entropy splitting and with the sixth-order Padé scheme [20], employed for simulations with the approximate deconvolution model (ADM) in Ref. [11]. Conversely, LES with ADM can also be performed with the more stable numerical scheme used herein for simulations with the HPF Smagorinsky. The stabilizing mechanism of ADM can be mainly traced back to the relaxation term, which is also employed for the continuity equation in order to ensure a well-resolved representation of the filtered solution. It can also be interpreted as applying a high-order filter to the computational quantities every few time steps and is related to stabilizing of numerical schemes by means of filtering, e.g., Maeder et al. [21]. In general, the relaxation term effects scales only which are numerically not well resolved with finite-difference schemes and are physically meaningless for this reason.

In order to further reduce odd-even oscillations second derivatives for the eddy-viscosity model are discretized directly instead of using schemes for the first derivative twice. The equations are integrated in time by an explicit low-storage third-order Runge-Kutta scheme [22]. Simulations model were found not to be stable when no SGS model is used, demonstrating the necessity of the SGS model in the considered case.

Configuration and Results

We consider a spatially developing supersonic turbulent boundary layer at a free-stream Mach number of $M_\infty=2.5$ and Reynolds number based on the mean momentum thickness $\delta_{2,\mathrm{in}}$ at the inflow and the viscosity at the wall of $\mathrm{Re}_{\delta_{2,\mathrm{in}}}(u_\infty \delta_2/\nu_w) \approx 2200$; based on the momentum thickness δ_2 and the free-stream viscosity, $\mathrm{Re}_\theta = u_\infty \delta_2/\nu_\infty \approx 4500$. If not mentioned otherwise, $\delta_{2,\mathrm{in}}$ is used as reference length. The Reynolds numbers $\mathrm{Re}_{\delta_{0,\mathrm{in}}}$ and $\mathrm{Re}_{\delta_{1,\mathrm{in}}}$, based on the 99.5% boundary layer thickness $\delta_{0,\mathrm{in}}$ and the displacement thickness $\delta_{1,\mathrm{in}}$ at the inflow, respectively, and the free-stream viscosity u_∞ is given in Table 1. The Reynolds numbers are in a range where experimental data is available, e.g., collected by Fernholz and Finley in Refs. [23–25]. The size of the computational domain for all cases is $220\delta_{2,\mathrm{in}}$ in the streamwise, $22\delta_{2,\mathrm{in}}$ in the spanwise, and $55\delta_{2,\mathrm{in}}$ in the wall-normal direction. The streamwise and spanwise coordinates are denoted by x_1 and x_2, respectively.

Table 1 Parameters of the numerical simulation

	HPF Smag.	ADM	HPF Smag./ADM	
M_∞	2.5		L_{x_1}	$220\delta_{2,\mathrm{in}}$
Pr	0.72		L_{x_2}	$22\delta_{2,\mathrm{in}}$
$\mathrm{Re}_{\delta_{0,\mathrm{in}}}$	59,265	63,325	L_{x_3}	$55\delta_{2,\mathrm{in}}$
$\mathrm{Re}_{\delta_{1,\mathrm{in}}}$	15,572	17,988	x_r	$88\delta_{2,\mathrm{in}}$
$\mathrm{Re}_{\theta,\mathrm{in}}$	4535	4531	N_1	251
$\mathrm{Re}\delta_{2,\mathrm{in}}$	2200	2199	N_2	51
$\delta_{0,\mathrm{in}}$	$13.1\delta_{2,\mathrm{in}}$	$14.0\delta_{2,\mathrm{in}}$	N_3	101
T_∞^*	140 K		$\Delta_{x_1}^+$	41
T_W	$2.25T_\infty^*$		$\Delta_{x_2}^+$	21
S^*	110.4 K		$\Delta_{x_3}^{+(1)}$	1.6

A detailed description of the parameters is given in Table 1. Note that the distance of the first grid point off the wall $\Delta x_3^{+(1)}$ has to be chosen smaller than in Ref. [11] and four grid points (excluding point at the wall boundary) are contained in the range up to $x_3^+ \leqslant 10$ instead of 2 points in Ref. [11] in order to obtain a good prediction of critical boundary-layer properties. However, the same total number of grid points in the wall-normal direction is used. The reason for the necessity of an increased resolution in the near-wall region is mainly due to the different SGS model. LES with ADM on the same grid as used in Ref. [11], however, employing the numerical scheme used herein results in a deviation in the skin-friction coefficient of only about 5%, which is significantly less than the deviation due to the different SGS model (using the same grid and numerical scheme). For comparison, data obtained with ADM using the same grid and numerical scheme as employed herein for the LES with the HPF Smagorinsky are also shown.

Turbulent inflow conditions for our boundary-layer simulations are generated by a rescaling and recycling method (RRM) following that of Lund et al. [26], simplified and extended to compressible flows by Stolz and Adams [11]. The mean-flow profiles, in terms of the wall-normal coordinate x_3 and time t for the streamwise and the wall-normal velocity, density, and the temperature, and the corresponding fluctuation fields, are sampled at a reference station x_r downstream of inflow (Fig. 1). The mean value of the spanwise velocity is set to zero. The mean flow profiles for the RRM are computed with a sliding time average by employing a second-order discrete Butterworth filter with a characteristic time

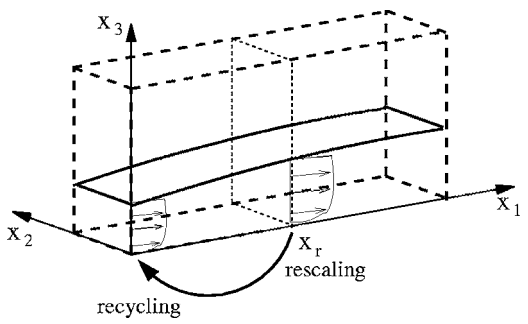

Fig. 1 Schematic of the rescaling and recycling technique

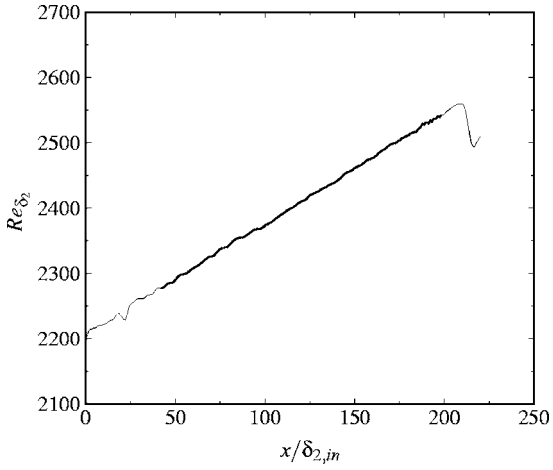

Fig. 2 Reynolds number Re_{δ_2} based on the momentum thickness δ_2 and the viscosity at the wall ν_w shown with thick lines for the LES with HPF Smagorinsky model over the downstream coordinate; thin lines indicate transient regions at the inflow due to the RRM procedure and due to the sponge-layer at outflow

scale of $T_s \simeq 8\delta_{0,\mathrm{in}}/u_\infty$ [11]. Except for the mean profiles at the reference station x_r, only the boundary-layer thicknesses $\delta_{0,r}$ and $\delta_{2,r}$ have to be determined for the generation of the turbulent inflow data. Different from the technique proposed by Lund et al. [26], it is not necessary to compute the skin friction at the reference station.

Two-point correlations for the density, velocity components, and temperature demonstrate decorrelation of the fluctuations over half the domain length in the spanwise direction and half the distance of sampling station used for RRM from the inflow x_r in the streamwise direction, which indicates that the computational domain and the downstream distance of sampling station for the RRM are chosen large enough, (see Fig. 13 and Ref. [11]).

At the outflow and the upper truncation plane a nonreflecting boundary condition is employed. Additionally, a sponge layer is used [27] near the outflow and upper truncation plane. For the latter, free-stream conditions are imposed on the density, velocity, and temperature. The wall is assumed to be isothermal, and no-slip conditions are imposed on the velocity. Furthermore, periodic boundary conditions are employed in the homogeneous spanwise direction.

Mean Flow. Statistical averaging is performed in time over a period of $\sim 100\delta_0/U_\infty$ and in space over the homogeneous spanwise direction and is indicated with angular brackets. The simulation was started with turbulent LES data of Ref. [11] and conducted for about $150\delta_0/U_\infty$, i.e., until a statistically steady state was reached, before sampling was performed. With the RRM, we did not observe a drift in the boundary-layer properties during the sampling time which can also anticipated from Fig. 2 of Ref. [11].

The streamwise evolution of the Reynolds number Re_{δ_2} based on the momentum thickness and the viscosity at the wall is shown in Fig. 2. Transient regions near the inflow and outflow boundaries where the solution is not considered to be physically meaningful are indicated by thin lines. The transient region near inflow is a consequence of the inflow-data generation procedure, whereas the one near the outflow is a result of the sponge-layer outflow boundary condition. The transient region near the inflow extends over approximately $3\delta_{0,\mathrm{in}} \approx 40\delta_{2,\mathrm{in}}$. A small kink can be observed approximately $1.8\delta_{0,\mathrm{in}} \approx 25\delta_{2,\mathrm{in}}$ downstream of the inflow plane. This kink is due to a standing pressure wave originating from the near-wall region at the inflow.

A challenging task for numerical simulations is to predict the experimentally observed skin-friction coefficient C_f

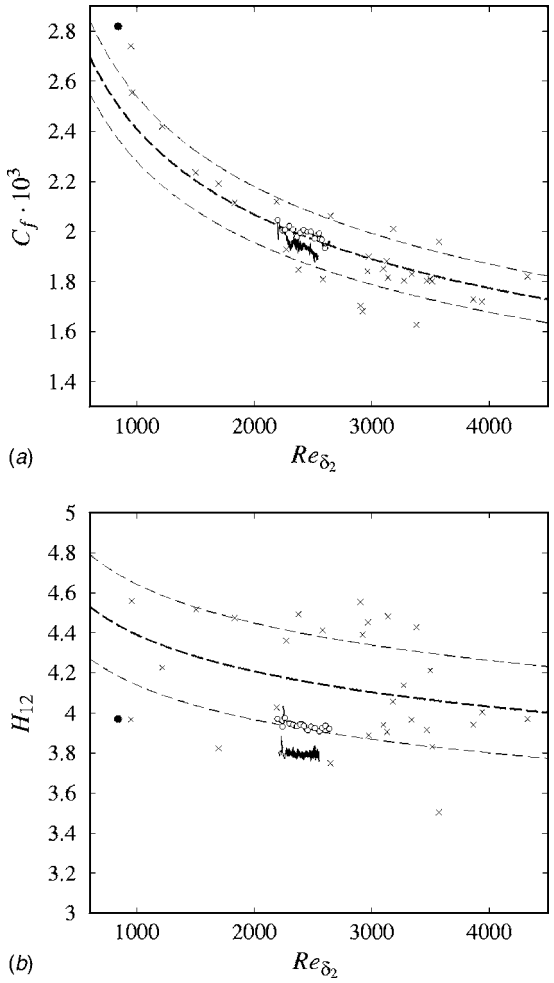

Fig. 3 (*a*) Skin friction coefficient C_F and (*b*) shape factor H_{12} over Re_{δ_2}; —HPF Smagorinsky model and —○—ADM; × experiments of Coles [23,28], Mabey [23,25] and Shutts et al. [23], ● DNS data of Guarini et al. [29], ----regression of experimental data ($C_f = 0.01026\,\mathrm{Re}_{\delta_2}^{-0.21}$, $H_{12} = 6.71\,\mathrm{Re}_{\delta_2}^{-0.062}$), ----regression ± standard deviation

$= 2\langle \breve{\mu}\partial\tilde{u}_1/\partial x_3\rangle/\mathrm{Re}$ and shape factor $H_{12} = \langle\delta_1\rangle/\langle\delta_2\rangle$. The former requires a correct representation of the near-wall turbulence phenomena, whereas the latter also requires a sufficient accuracy within the outer layer. $\tilde{u}_1 = \rho u_1/\bar{\rho}$ denotes the Favre-filtered (density-weighted) downstream velocity component, and $\breve{\mu}$ is the dynamic viscosity computed according to Sutherland's law using the temperature $\tilde{T}$. A comparison of the downstream evolution of C_f with experimental data of Coles [23,28], Mabey [23,25], and Shutts et al. [23] as function of Re_{δ_2} is shown in Fig. 3(*a*). Corresponding values of the direct-numerical simulation (DNS) of Guarini et al. [29] at $M_\infty = 2.5$ are also shown. The agreement of the skin-friction coefficient C_f predicted by LES with a regression of the experimental data is very good for both SGS models. Even within the transient region at the inflow (indicated by thin lines) C_f differs by no more than about 3% from the experimental regression, which is well within the respective standard deviations. Note that data for the region affected by the sponge layer near the outflow is omitted in Fig. 3 as they are physically meaningless. The shape factor H_{12} is underpredicted by the simulation in comparison to experimental data, by about 10% with HPF Smagorinsky and is not predicted as well as with ADM, see Fig. 3(*b*). However, the value of H_{12} is still in the range predicted by some experiments and close to the result of the DNS of Guarini et al.

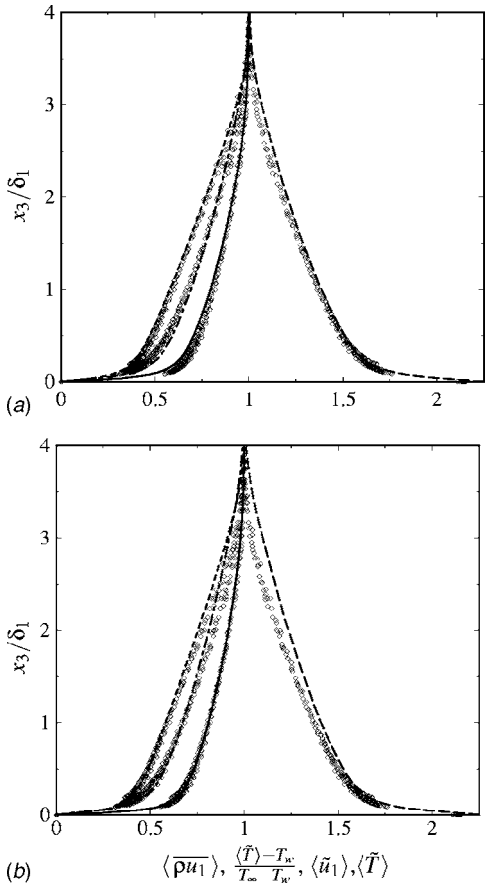

Fig. 4 Mean-flow profiles, —$\langle \tilde{u}_1 \rangle$, ····· $\langle \overline{\rho u_1} \rangle$, ----$\langle \tilde{T} \rangle$, and —·—·— $(\langle \tilde{T} \rangle - T_w)/(T_\infty - T_w)$; Lines: LES, Symbols: Experiments of Mabey [23]; (*a*) HPF Smagorinsky model and (*b*) ADM

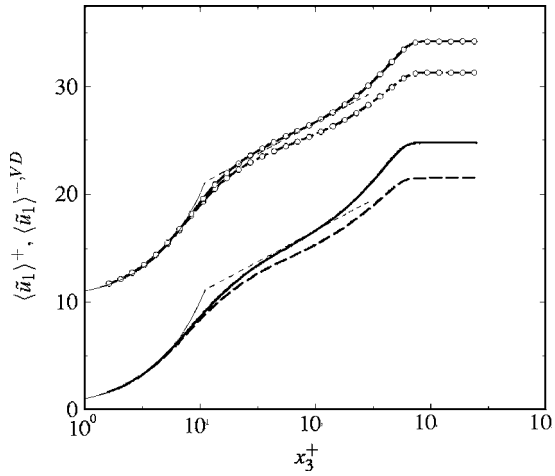

Fig. 5 Downstream-velocity profiles scaled in wall units, ----$\langle \tilde{u}_1 \rangle^+$ and —$\langle \tilde{u}_1 \rangle^{+,VD}$ for the HPF Smagorinsky model, --○--$\langle \tilde{u}_1 \rangle^+$ and —○—$\langle \tilde{u}_1 \rangle^{+,VD}$ for ADM (shifted by 10); also shown are the linear law, —and the logarithmic law with $\ln(x_3^+)/0.4+5.1$,----

[29] at a much lower Reynolds number. Note that the scatter in the experimental data for H_{12} is larger than that for C_f and the regression analysis is less reliable (the dashed lines indicate the respective standard deviations).

The mean-flow profiles for the streamwise mass flux $\langle \overline{\rho u_1} \rangle$, streamwise velocity $\langle \tilde{u}_1 \rangle$, and temperature $\langle \tilde{T} \rangle$ are shown in Fig. 4 and compared to experimental data of Mabey [23] at a Mach number of 2.5 and Reynolds numbers ranging within $3099 \leqslant \mathrm{Re}_{\delta_2} \leqslant 9095$ (cases 74020100–74020302 of Ref. [23]). Computational results are evaluated at 10 equidistantly spaced downstream stations for x_1 between $3\delta_{0,\mathrm{in}}$ and $14.5\delta_{0,\mathrm{in}}$ (region away from inflow transient and upstream of the sponge region at outflow). All data shown subsequently collapse for the different downstream stations when plotted according to the scaling laws, demonstrating that the LES data exhibits the correct spatial evolution of the boundary layer. For this reason only averaged (according to the scaling laws) profiles are shown in the corresponding figures. The agreement for the mean streamwise momentum and velocity is very good. A small difference between the computational and experimental temperature profiles is caused by the slightly different wall temperatures in the experiment ($T_w \approx 2.13$) and in the simulation ($T_w = 2.25$). Profiles compensated for this difference $(\langle \tilde{T} \rangle - T_w)/(T_\infty - T_w)$ are in good agreement.

The mean streamwise velocity profiles and the van Driest transformed velocity profiles plotted in wall units are shown in Fig. 5. The van Driest transformed velocity profiles [30] computed by

$$\langle \tilde{u}_1 \rangle^{+,VD} = \frac{1}{\kappa} \ln z^+ + \mathcal{C} \tag{11}$$

show a very good agreement with the law of the wall with the standard parameters of Fernholz and Finley [24], $\kappa = 0.40$ and $\mathcal{C} = 5.1$, for turbulent boundary layers along adiabatic walls. The linear and logarithmic regions for the parameter sets of Fernholz and Finley is indicated in Fig. 5.

For the outer-layer profiles an outer scaling using the Rotta integral length scale

$$\mathcal{L} = \frac{1}{u_\tau} \int_0^{\delta_0} (\tilde{u}_{1\infty}^{VD} - \tilde{u}_1^{VD}) dx_3 \tag{12}$$

is applied. Formulated for compressible flows the empirical law of the wake [31] is

$$\langle \tilde{u}_1 \rangle_\infty^{+,VD} - \langle \tilde{u}_1 \rangle^{+,VD} = -4.7 \ln\left(\frac{x_3}{\mathcal{L}}\right) - 6.74. \tag{13}$$

The LES results show an excellent agreement with the law of the wake for $x_3/\mathcal{L} > 0.05$ (see Fig. 6).

The Favre-averaged total temperature $\langle \rho \check{T}_0 \rangle / \langle \rho \rangle$ with

$$\check{T}_0 = \tilde{T} + (\gamma - 1) M_\infty^2 \frac{\tilde{u}_1^2 + \tilde{u}_2^2 + \tilde{u}_3^2}{2} \tag{14}$$

is almost constant across the boundary layer (see Fig. 7). As expected from experimental data the mean total temperature decreases near the wall and has its maximum slightly below the boundary layer edge [32].

Turbulence Statistics. Experimental data for the Reynolds stresses are not available for the experiments of Coles and Mabey cited above. Other experimental data show a considerable scatter, so that we follow the suggestion of Guarini et al. [29] to compare the density-weighted Reynolds stresses with DNS data for incompressible boundary layers of Spalart [33]. Comparison of density-weighted Reynolds stresses with incompressible data was also proposed by Morkovin [34] and was found to be appropriate for Mach numbers up to at least 5 [32,35]. Guarini et al. [29] found a good agreement between their supersonic DNS results and Spalart's incompressible DNS data when scaling the velocity fluctuations by the square root of the density profile. Furthermore, they have shown that when plotting the data over x_3/δ_0 (instead of x_3^+) the position of the peak strongly depends on the Reynolds num-

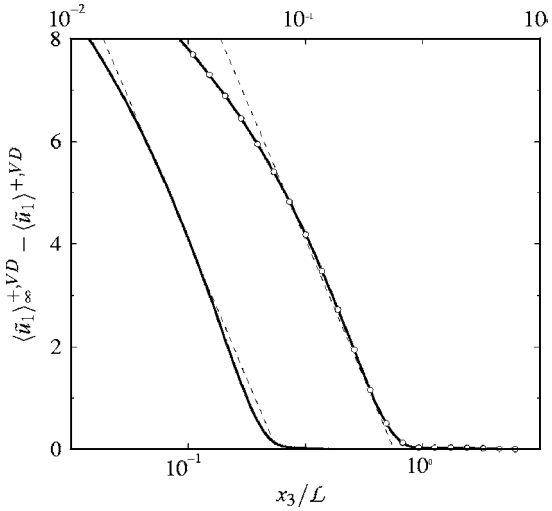

Fig. 6 Mean-flow profiles in outer scaling $\langle \tilde{u}_1 \rangle_\infty^{+,VD} - \langle \tilde{u}_1 \rangle^{+,VD}$: —HPF Smagorinsky model (scale on bottom), —○—ADM (scale on top), and ----law of the wake $-4.7 \ln(z/\mathcal{L}) - 6.74$

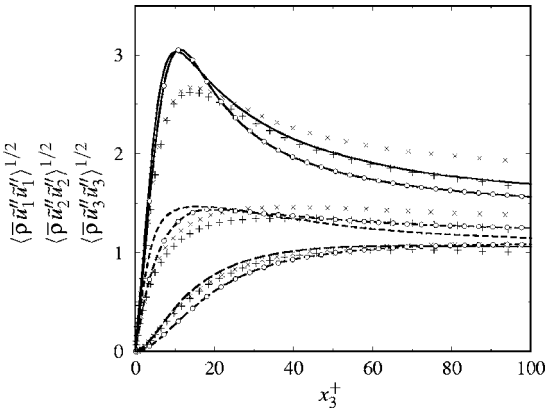

Fig. 8 Reynolds normal stresses normalized with $\sqrt{\rho_w u_\tau^2}$: solid lines $\sqrt{\langle \bar{\rho} \tilde{u}_1'' \tilde{u}_1'' \rangle}$, dashed lines $\sqrt{\langle \bar{\rho} \tilde{u}_2'' \tilde{u}_2'' \rangle}$, and long- dashed lines $\sqrt{\langle \bar{\rho} \tilde{u}_3'' \tilde{u}_3'' \rangle}$; —HPF Smagorinsky model and —○—ADM; symbols are DNS data of Spalart [33], ×Re_θ=1410 and +Re_θ=670

ber. The Reynolds normal stresses, computed as $\langle \bar{\rho} \tilde{u}_i'' \tilde{u}_i'' \rangle$, are shown in Fig. 8. The double prime indicates a fluctuation with respect to the Favre time-average $\tilde{u}_i'' = \tilde{u}_i - \langle \bar{\rho} \tilde{u}_i \rangle / \langle \bar{\rho} \rangle$. The Reynolds normal stresses for the streamwise and the wall-normal velocity components are overpredicted in comparison to the DNS data. The peak of the Reynolds normal stresses is shifted slightly toward the wall. Note that the DNS data are unfiltered, but they are also at a significantly lower Re_θ than the LES. The Reynolds normal stresses for the spanwise velocity component and the Reynolds shear stress, computed as $\langle \bar{\rho} \tilde{u}_1'' \tilde{u}_3'' \rangle$, exhibits a good agreement with Spalart's incompressible DNS data for both SGS models (see Fig. 9).

To quantify compressibility effects commonly the turbulence Mach number M_t is used

$$M_t = \frac{\langle \tilde{u}_1''^2 + \tilde{u}_2''^2 + \tilde{u}_3''^2 \rangle}{\langle c \rangle} \tag{15}$$

with c being the speed of sound. Alternatively, the fluctuating Mach number

$$M' = \langle (M - \langle M \rangle)^2 \rangle^{1/2} \tag{16}$$

with $M = M_\infty \tilde{u}_1 / \sqrt{\tilde{T}}$ can be employed (see Fig. 10). Different from the turbulence Mach number the fluctuating Mach number varies through both velocity and temperature fluctuations. The peak for both Mach numbers is located in the vicinity of the wall and reaches Mach numbers of ~0.25. The turbulence Mach number decreases faster than the fluctuating Mach number to a negligible value at the boundary-layer edge.

Figure 11 shows the root-mean-square fluctuations of the total temperature $\langle \check{T}_0''^2 \rangle$ and the fluctuations of the temperature $\langle \tilde{T}''^2 \rangle$, which have almost the same magnitude. The fluctuations of the temperature are more peaked in the near-wall region than the fluctuations of the total temperature.

Near-wall streaks can be visualized by colors of the wall-normal vorticity ω_3, which is shown in Fig. 12 in a wall-parallel plane at $x_3^+ \approx 11$. It is obvious that the computational box accommodates several streaks in the streamwise and spanwise directions. The streak spacing length. is apparent from the two-point correlations for the density, velocity components, and temperature depicted in Fig. 13 in the same wall-parallel plane. The two-point correlations in spanwise direction for wall-normal velocity w exhibit a peak at about 80–120 wall units, which corresponds to

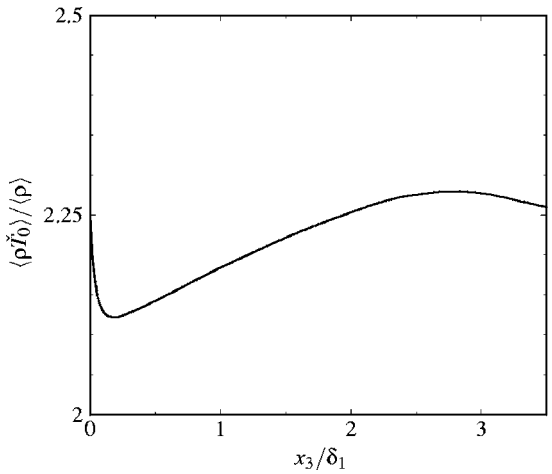

Fig. 7 Favre-averaged total temperature $\check{T}_0$, —HPF Smagorinsky model

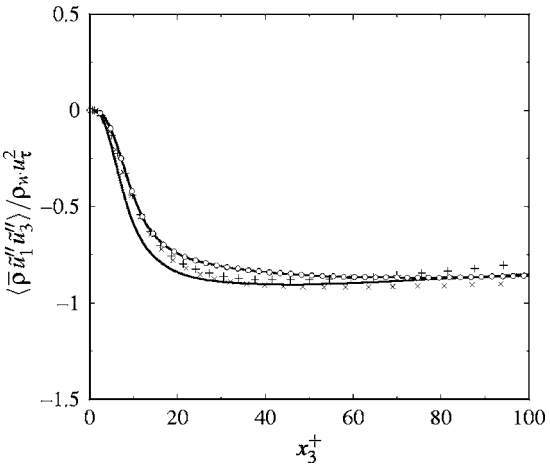

Fig. 9 Reynolds shear stress $\langle \bar{\rho} \tilde{u}_1'' \tilde{u}_3'' \rangle / u_\tau^2$, —HPF Smagorinsky model and —○—ADM; Symbols are incompressible DNS data of Spalart [33], ×Re_θ=1410 and +Re_θ=670

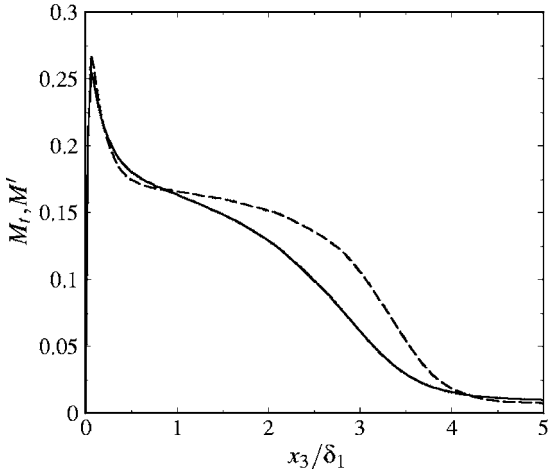

Fig. 10 Turbulence Mach number M_t for HPF Smagorinsky model, —and fluctuating Mach number M', ----

roughly five grid points.

The highly intermittent boundary-layer edge is depicted by density distributions in a longitudinal cross section (Fig. 14).

Conclusions

A compressible turbulent boundary layer at $M_\infty = 2.5$ and comparably large Reynolds numbers of $2200 \leqslant \mathrm{Re}_{\delta_2} \leqslant 2510$ has been computed by means of large-eddy simulation (LES) with the fixed-coefficient high-pass filtered (HPF) Smagorinsky model [6,8] supplemented by a HPF eddy-diffusivity ansatz for the SGS heat flux. With respect to the boundary-layer thickness and the free-stream viscosity the covered Reynolds number range is $59265 \leqslant \mathrm{Re}_{\delta_0} \leqslant 69356$. The Reynolds number range is well within that of available experimental data. The LES results are compared to experimental data of Coles [23,28], Mabey [23,25], and Shutts et al. [23]. The results obtained agree reasonably well with experimental data and theoretical results, such as the law of the wall and the law of the wake. The density-weighted Reynolds stresses are compared with the incompressible DNS data of Spalart [33]. For comparison, data of LES with the approximate deconvolution model (ADM) [12,13] is also shown.

The rescaling and recycling method [11] is employed for inflow-data generation. Using this technique, inflow data are generated concurrently with the ongoing simulation by sampling the boundary layer at some distance downstream of the inflow. For stability of the simulations a numerical method following Sandham et al. [16] based on entropy splitting, usage of finite-difference approximations for second derivatives and finite-difference operators satisfying a summation-by-parts condition has to be used.

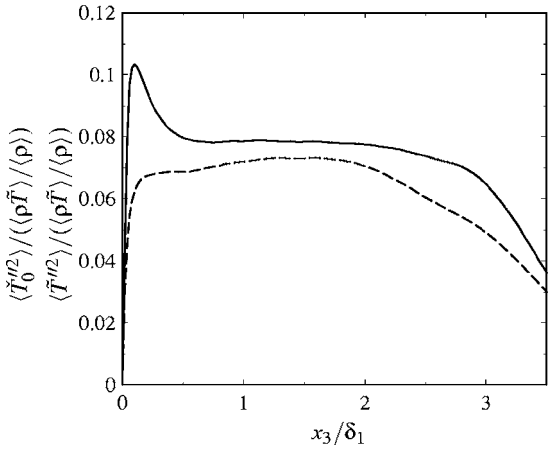

Fig. 11 Relative Favre fluctuations of the total temperature $\check{T}_0$, ----, and of the temperature $\tilde{T}$, —for HPF Smagorinsky model

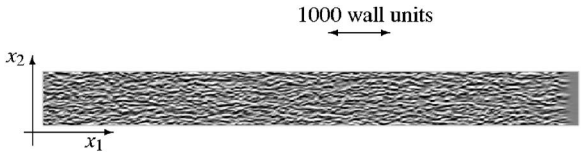

Fig. 12 Instantaneous ω_z distribution for HPF Smagorinsky model in a x_1-x_2 plane; $x_3^+ \approx 11$

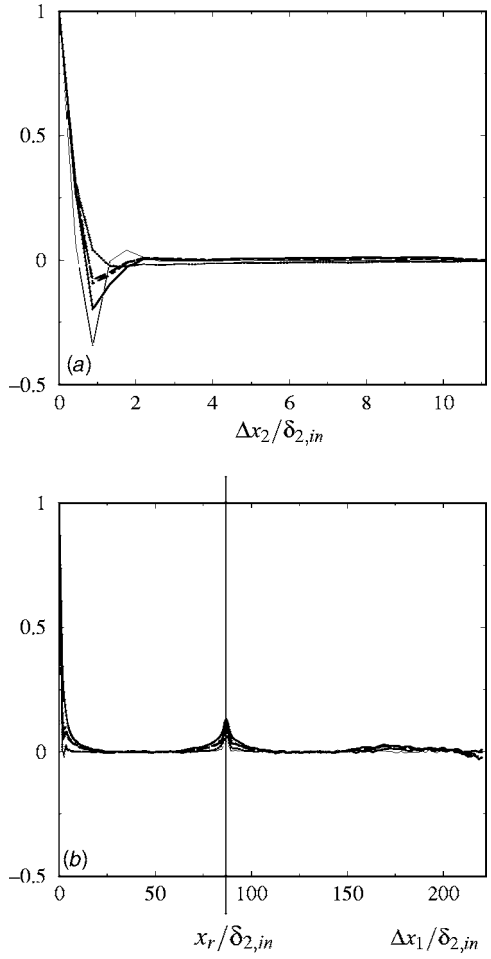

Fig. 13 Two-point correlations for HPF Smagorinsky model in (*a*) x_2 direction and x_1 direction at $x_3^+ \approx 11$; ----ρ, —u, ·····v, —w, and —·—T

Fig. 14 Instantaneous density distribution in a x_1-x_3 plane, $0.4 < \bar{\rho} < 1.1$

Acknowledgments

The author is indebted to P. Schlatter and L. Kleiser for stimulating discussions. Special thanks go to N. Sandham, University of Southampton, for helpful discussions and support concerning the implementation of the underlying numerical scheme. Calculations have been performed at the Swiss Center for Scientific Computing (CSCS).

References

[1] Smagorinsky, J., 1963, "General Circulation Experiments With the Primitive Equations," Mon. Weather Rev., **93**, pp. 99–164.
[2] Métais, O., and Lesieur, M., 1992, "Spectral Large-Eddy Simulations of Isotropic and Stably-Stratified Turbulence," J. Fluid Mech., **239**, pp. 157–194.
[3] Van Driest, E. R., 1956, "On the Turbulent Flow Near a Wall," J. Aeronaut. Sci., **23**, pp. 1007–1011.
[4] Lilly, D., 1992, "A Proposed Modification of the Germano Subgrid-Scale Closure Model," Phys. Fluids A, **4**, pp. 633–635.
[5] Germano, M., Piomelli, U., Moin, P., and Cabot, W. H., 1991, "A Dynamic Subgrid-Scale Eddy Viscosity Model," Phys. Fluids A, **3**, pp. 1760–1765.
[6] Stolz, S., Schlatter, P., Meyer, D., and Kleiser, L., 2003, "High-Pass Filtered Eddy-Viscosity Models for LES," *Direct and Large-Eddy Simulation*, V. R. Friedrich, B. J. Geurts, and O. Métais, Eds., Kluwer, Dordrecht, pp. 81–88.
[7] Hughes, T. J. R., Mazzei, L., and Jansen, K. E., 2000, "Large Eddy Simulation and the Variational Multiscale Method," Comput. Visual. Sci., **3**, pp. 47–59.
[8] Vreman, A. W., 2003, "The Filtering Analog of The Variational Multiscale Method in Large-Eddy Simulation," Phys. Fluids, **15**, pp. L61–L64.
[9] Stolz, S., Adams, N. A., and Kleiser, L., 2001, "An Approximate Deconvolution Model for Large-Eddy Simulation With Application to Incompressible Wall-Bounded Flows," Phys. Fluids, **13**, pp. 997–1015.
[10] Domaradzki, J. A., Liu, W., Härtel, C., and Kleiser, L., 1994, "Energy-Transfer in Numerically Simulated Wall-Bounded Turbulent Flows," Phys. Fluids, **6**, pp. 1583–1599.
[11] Stolz, S., and Adams, N. A., 2003, "LES of High-Reynolds-Number Supersonic Boundary Layers Using the Approximate Deconvolution Model and a Rescaling and Recycling Technique," Phys. Fluids, **15**, pp. 2389–2412.
[12] Stolz, S., and Adams, N. A., 1999, "An Approximate Deconvolution Procedure for Large-Eddy Simulation," Phys. Fluids, **11**, pp. 1699–1701.
[13] Stolz, S., Adams, N. A., and Kleiser, L., 2001, "The Approximate Deconvolution Model for LES of Compressible Flows and its Application to Shock-Turbulent-Boundary-Layer Interaction," Phys. Fluids, **13**, pp. 2985–3001.
[14] Vreman, A. W., 1995, "Direct and Large-Eddy Simulation of the Compressible Turbulent Mixing Layer," PhD thesis, University of Twente, the Netherlands.
[15] Stolz, S., Adams, N. A., and Kleiser, L., 1999, "Analysis of Sub-Grid Scales and Sub-Grid Scale Modeling for Shock-Boundary-Layer Interaction," *Turbulence and Shear Flow I*, S. Banerjee and J. Eaton, eds., Begell House, New York, pp. 881–886.
[16] Sandham, N. D., Li, W., and Yee, H. C., 2002, "Entropy Splitting for High-Order Numerical Simulation of Compressible Turbulence," J. Comput. Phys., **178**, pp. 307–322.
[17] Carpenter, M. H., Gottlieb, J., and Gottlieb, D., 1999, "A Stable and Conservative Interface Treatment of Arbitrary Spatial Accuracy," J. Comput. Phys., **148**, pp. 341–365.
[18] Harten, A., 1983, "On the Symmetric Form of Systems of Conservation Laws With Entropy," J. Comput. Phys., **49**, pp. 151–164.
[19] Gerritsen, M., and Olsson, P., 1996, "Designing an Efficient Solution Strategy for Fluid Flows," J. Comput. Phys., **129**, pp. 245–262.
[20] Lele, S. K., 1992, "Compact Finite Difference Schemes With Spectral-Like Resolution," J. Comput. Phys., **103**, pp. 16–42.
[21] Maeder, T., Adams, N. A., and Kleiser, L., 2001, "Direct Simulation of Turbulent Supersonic Boundary Layers by an Extended Temporal Approach," J. Fluid Mech., **429**, pp. 187–216.
[22] Williamson, J. H., 1980, "Low-Storage Runge-Kutta Schemes," J. Comput. Phys., **35**, pp. 48–56.
[23] Fernholz, H. H., and Finley, P. J., 1977, "A Critical Compilation of Compressible Turbulent Boundary Layer Data," Tech. Rep. AGARDograph No. 223, AGARD, Neuilly sur Seine, France.
[24] Fernholz, H. H., and Finley, P. J., 1980, "A Critical Commentary on Mean Flow Data for Two-Dimensional Compressible Turbulent Boundary Layers," Tech. Rep. AGARDograph No. 253, AGARD, Neuilly sur Seine, France.
[25] Fernholz, H. H., and Finley, P. J., 1981, "A Further Compilation of Compressible Boundary Layer Data With a Survey of Turbulence Data," Tech. Rep. AGARDograph No. 263, AGARD, Neuilly sur Seine, France.
[26] Lund, T. S., Wu, X., and Squires, K. D., 1998, "Generation of Turbulent Inflow Data for Spatially Developing Boundary Layer Simulations," J. Comput. Phys., **140**, pp. 233–258.
[27] Adams, N. A., 1998, "Direct Numerical Simulation of Turbulent Compression Corner Flow," Theor. Comput. Fluid Dyn., **12**, pp. 109–129.
[28] Coles, D., 1954, "Measurement of Turbulent Friction on a Smooth Flat Plate in Supersonic Flow," J. Aeronaut. Sci., **7**, pp. 433–448.
[29] Guarini, S. E., Moser, R. D., Shariff, K., and Wray, A., 2000, "Direct Numerical Simulation of a Supersonic Turbulent Boundary Layer at Mach 2.5," J. Fluid Mech., **414**, pp. 1–33.
[30] Bradshaw, P., 1977, "Compressible Turbulent Shear Layers," Annu. Rev. Fluid Mech., **9**, pp. 33–54.
[31] Fernholz, H. H., 1971, "Ein Halbempirisches Gesetz für die Wandreibung in Kompressiblen Turbulenten Grenzschichten bei Isothermer and Adiabater Wand," Z. Angew. Math. Mech., **51**, pp. T148–T149.
[32] Smits, A. J., and Dussauge, J.-P., 1996, *Turbulent Shear Layers in Supersonic Flow.* AIP Press, Woodbury, New York.
[33] Spalart, P. R., 1988, "Direct Simulation of a Turbulent Boundary Layer up to Re_θ=1410," J. Fluid Mech., **187**, pp. 61–98.
[34] Morkovin, M. V., 1962, "Effects of Compressibility on Turbulent Flows," *Mécanique de la Turbulence*, A. Favre, ed., CNRS, Paris, pp. 367–380.
[35] Spina, E. F., Smits, A. J., and Robinson, S. K., 1994, "The Physics of Supersonic Turbulent Boundary Layers," Annu. Rev. Fluid Mech., **26**, pp. 287–319.

Implementation of a Level Set Interface Tracking Method in the FIDAP and CFX-4 Codes

Sergey V. Shepel
e-mail: sergey.shepel@psi.ch

Brian L. Smith
e-mail: brian.smith@psi.ch

Thermal-Hydraulics Laboratory,
Paul Scherrer Institut,
CH-5232, Villigen PSI, Switzerland

Samuel Paolucci
e-mail: paolucci.1@nd.edu
Department of Aerospace and Mechanical Engineering,
University of Notre Dame,
Notre Dame, IN, 46556, USA

We present a streamline-upwind–Petrov-Galerkin (SUPG) finite element level set method that may be implemented into commercial computational fluid dynamics (CFD) software, both finite element (FE) and finite volume (FV) based, to solve problems involving incompressible, two-phase flows with moving interfaces. The method can be used on both structured and unstructured grids. Two formulations are given. The first considers the coupled motion of the two phases and is implemented within the framework of the commercial CFD code CFX-4. The second can be applied for those gas-liquid flows for which effects of the gaseous phase on the motion of the liquid phase are negligible; consequently, the gaseous phase is removed from consideration. This level set formulation is implemented in the commercial CFD code FIDAP. The resulting level set formulations are tested and validated on sample problems involving two-phase flows with density ratios of the order of 10^3 *and viscosity ratios as high as* 1.6×10^5. [DOI: 10.1115/1.1949636]

Keywords: Two-Phase Flow, Interface Tracking, Level Set, Finite Element, Finite Volume, CFX, FIDAP, Validation

Introduction

The present work is concerned with modeling of two-phase, incompressible flows with the phases separated by a distinct interface. In general, the phases are assumed to have different values for density and viscosity. Numerical modeling of such interfacial flows requires the use of special interface-tracking procedures, such as the front-tracking method [1], the boundary integral method [2], the phase-field method [3], the Second Gradient method [4], the volume-of-fluid (VOF) method [5,6], or the level set method (see, for example, Sethian [7], or the review by Osher and Fedkiw [8]). Here, we are specifically interested in developing and implementing the level set method within the framework of the commercial codes CFX-4 [9] and FIDAP [10], codes to which we have ready access.

It should be noted that both the CFX-4 and FIDAP codes have their own interface-tracking models, which are provided with the standard code configuration. The model implemented in FIDAP is of the VOF type, in which the interface geometry is approximated using the piecewise constant stair-stepped (PCSS) reconstruction procedure [10]. Although the PCSS VOF interface-tracking scheme is very robust, it is only first-order accurate [11]. Application of this model to interfacial flows with strong surface tension effects would be degraded below first order because of the numerical errors resulting from calculating the interface curvature. The CFX-4 standard interface-tracking model is also first-order accurate and is based on solving a transport equation for the phase volume fractions, combined with a simple ad hoc algorithm for regrouping these fractions (surface sharpening algorithm) [9]. As demonstrated in this paper, in addition to the above-mentioned lack of accuracy associated with calculating the interface curvature, the CFX-4 standard interface-tracking method is also very diffusive.

In order to improve the accuracy of the calculations, one would need to resort to higher-order methods that could be implemented within the framework of these codes. In the most general type of application of industrial interfacial flows, simulation needs to be performed in both two and three dimensions, using structured and/or unstructured grids. For these reasons, we choose the streamline-upwind–Petrov-Galerkin (SUPG) finite element (FE) level set method [12], because it is second-order accurate, robust, readily extended to three dimensions, may be adjusted to unstructured grids, and is easier to program compared to other advanced interface-tracking methods.

Two formulations of the SUPG FE level set method are presented here. The first considers coupled motion of the two phases. Away from the interface, the fluid properties are set to be those of the appropriate constituent phases, whereas in the vicinity of the interface they are interpolated appropriately to ensure a smooth transition from one phase to the other. We refer to this approach as the *fluid-fluid* formulation.

The second formulation considers gas-liquid flows in which the gaseous phase has a negligible effect on the motion of the liquid phase. Applications include hydraulic flows in open containers and mold-filling processes in metallurgy, provided that there is no air entrainment in the liquid phase. When modeling such flows, the gaseous phase can be considered a region of void. This approach, which we refer to as the *fluid-void* formulation, is obviously less general than the fluid-fluid approach. On the other hand, since no fluid flow equations need to be solved in the void region, the fluid-void formulation is computationally more efficient. We implement the fluid-fluid formulation within the framework of the code CFX-4, and the fluid-void formulation into FIDAP.

It should be noted that, in the traditional level set method for incompressible flows, the fluid flow and interface-tracking equations are written in the nonconservative form. This approach has been used successfully over a wide range of applications for two-phase flows (e.g., [13–19]). To our knowledge, the conservative form of the fluid flow and level set interface-tracking equations has been used and validated only once, by Sussman and Puckett [20] in the coupled level set-VOF (CLSVOF) method. The *mixed* level set formulations, which involve the conservative form of the fluid flow equations and nonconservative form of the interface-tracking equations, have been used before for compressible flow modeling (see, e.g., [21]); however, as far as the incompressible flows are concerned, there is clearly a lack of information. Nevertheless, the mixed formulation has a strong potential from the

Contributed by the Fluids Engineering Division for publication in the JOURNAL OF FLUIDS ENGINEERING. Manuscript received by the Fluids Engineering Division October 14, 2004; Final manuscript received April 12, 2005. Associate Editor: Surya P Vanka.

point of view of implementation into commercial CFD codes, since many of these incorporate conservative finite volume (FV) flow solvers. Thus, a distinctive feature of the fluid-fluid model that we implement into the code CFX-4 is the coupling of the nonconservative FE level set interface-tracking method to the conservative FV Navier-Stokes solver.

Problem Formulation

The local equations governing the motion of an unsteady, viscous, incompressible, isothermal, immiscible two-phase liquid are the Navier-Stokes equations, which in conservative form are given as

$$\frac{\partial(\rho\mathbf{u})}{\partial t} + \nabla\cdot(\rho\mathbf{u}\otimes\mathbf{u}) = \mathbf{B} - \nabla p + \nabla\cdot(2\mu\mathbf{D}) \tag{1a}$$

$$\frac{\partial\rho}{\partial t} + \nabla\cdot(\rho\mathbf{u}) = 0 \tag{1b}$$

where $\mathbf{u}$ is the velocity vector, ρ is the density, t is time, p is the pressure, $\mathbf{B}$ is the body force, μ is the dynamic viscosity, and $\mathbf{D}$ is the rate of deformation tensor, with the components $D_{ij}=\frac{1}{2}(u_{i,j}+u_{j,i})$. The total stress tensor $\boldsymbol{\tau}$ is given by $\boldsymbol{\tau}=-p\mathbf{I}+2\mu\mathbf{D}$, where $\mathbf{I}$ is the identity matrix.

The surface tension acting on the interfacial surface Γ_l, creates a jump of the normal stress across the interface, which in tensor notation is represented by

$$\left[\tau_{ij}n_j\right]\big|_{\Gamma_l} = \sigma\kappa n_i \tag{2}$$

where the notation $[\varphi]$ denotes the jump in value of φ, κ is the curvature of Γ_l, σ is the surface tension, and $\mathbf{n}$ is the unit vector normal to Γ_l.

In the level set method, the interface between the two phases is represented by a continuous scalar function $\phi(\mathbf{x},t)$, which is set to zero on the interface, is positive on one side, and negative on the other. This way both phases are identified, and the location of the physical interface is associated with the surface $\phi=0$. The function ϕ is called the level set function and is typically defined as the signed distance to the interface; i.e., $\phi=-d(\mathbf{x},t)$ on one side of the interface and $\phi=+d(\mathbf{x},t)$ on the other, where $d(\mathbf{x},t)$ is the shortest distance from the point $\mathbf{x}$ to the interface.

When the interface is advected by the flow, the evolution of the level set function is given by

$$\frac{\partial\phi}{\partial t} + \mathbf{u}\cdot\nabla\phi = 0 \tag{3}$$

In the level set fluid-fluid formulation, the density and viscosity are typically interpolated across the interface as follows:

$$\rho(\mathbf{x},t) = \rho_2 + (\rho_1-\rho_2)H_\varepsilon(\phi(\mathbf{x},t)) \tag{4a}$$

$$\mu(\mathbf{x},t) = \mu_2 + (\mu_1-\mu_2)H_\varepsilon(\phi(\mathbf{x},t)) \tag{4b}$$

where subscripts 1 and 2 denote the values corresponding, respectively, to the two different phases. Here, $H_\varepsilon(\phi)$ is a smoothed Heaviside function, which is used instead of the discontinuous function to aid numerical stability [13]. By virtue of Eq. (4*a*), we note that $\rho(\mathbf{x},t)=\rho(\phi(\mathbf{x},t))$, which together with Eqs. (1*b*) and (3), reduces to the continuity condition $\nabla\cdot\mathbf{u}=0$. In the fluid-void formulation, the interpolation procedure defined by Eq. (4) does not need to be applied, since there is only one phase present in the model.

Following the work of Sussman et al. [13], we use the following expression for $H_\varepsilon(\phi)$:

$$H_\varepsilon(\phi) = \begin{cases} 0 & \text{if} \quad \phi < -\varepsilon \\ (\phi+\varepsilon)/(2\varepsilon) + \sin(\pi\phi/\varepsilon)/(2\pi) & \text{if} \quad |\phi| \leqslant \varepsilon \\ 1 & \text{if} \quad \phi > \varepsilon \end{cases} \tag{5}$$

where ε is a small parameter of the order of the size of a mesh cell close to the interface. By using the smoothed Heaviside function defined in Eq. (5), one effectively assigns the interface a fixed finite thickness of 2ε, over which the phase properties are interpolated. Hence, the value of ε can be considered to be the half-thickness of the numerical interface.

The surface tension can be modeled numerically as a body force, $\mathbf{B}_{st}$, concentrated at the interface (see, e.g., [6,18]). Here, the distribution of $\mathbf{B}_{st}$ near the interface is approximated as

$$\mathbf{B}_{st} = \sigma\kappa(\phi)\mathbf{n}\delta_\epsilon(\phi) \tag{6}$$

where $\delta_\epsilon(\phi)$ is the smoothed delta function defined as the derivative of the $H_\epsilon(\phi)$ in Eq. (5) with respect to ϕ. The normal to the interface $\mathbf{n}$ and curvature κ are given by

$$\mathbf{n} = \frac{\nabla\phi}{|\nabla\phi|}, \quad \kappa(\phi) = \nabla\cdot\frac{\nabla\phi}{|\nabla\phi|}. \tag{7}$$

Addition of the body force $\mathbf{B}_{st}$ to the right-hand side of Eq. (1*a*) effectively removes the explicit boundary condition given by Eq. (2) from the problem formulation.

When solving the advection equation (3), the level set function $\phi(\mathbf{x},t)$ ceases to be the signed distance from the interface, even if it is properly initialized at $t=0$. However, in order to interpolate the phase properties in the fluid-fluid formulation according to Eqs. (4), it is necessary to keep the level set function equal to the signed distance function $d(\mathbf{x},t)$ at all times. As mentioned before, this interpolation is not strictly needed for the fluid-void formulation, though it is still important to keep the distribution of ϕ equal to the signed distance from the interface in order to avoid strong numerical diffusion [22]. Consequently, both level set formulations need to reinitialize ϕ regularly, preferably at every time step. An efficient method to do this was proposed by Sussman and Fatemi [15], and is based on solving for the steady-state solution of the following equation:

$$\frac{\partial\phi}{\partial\tau} + \mathrm{sign}(\phi_0)(|\nabla\phi|-1) = \lambda\delta_\varepsilon(\phi)|\nabla\phi| \tag{8}$$

where τ is a timelike variable (different from the physical time t), ϕ_0 is the initial distribution of the level set function before reinitialization, and λ is a correction coefficient calculated in such a way as to ensure mass conservation up to the first-order term in the Taylor expansion of the integral over the domain $\partial_\tau\int H_\varepsilon(\phi)d\phi$ (for details, see [15]).

Sussman and Fatemi [15] demonstrated numerically that the solution of Eq. (8) converges to the signed distance function distribution around the interface and displays good mass-conservation properties. In the original formulation, the reinitialization problem was solved using the essentially nonoscillatory (ENO) finite-difference scheme. Finite-difference schemes, however, are difficult to apply on irregular, body-fitted grids. At the same time, the nonconservative form of Eq. (8) precludes the use of FV schemes. In our work, we adapt the Sussman and Fatemi level set formulation to the second-order SUPG FE method; the latter is employed to solve both the advection equation (3) and the level set reinitialization equation (8).

Various FE formulations of the level set method have been used before by Tornberg and Engquist [19], Hetu and Ilinca [23], Pillapakkam and Singh [24], and Chessa and Belytschko [25]. In these works, the authors used the FE method to solve both the level set and fluid flow equations. We employ this approach when implementing the level set method into FIDAP. However, in the fluid-fluid model that we implement in CFX-4, we use the FE method only to solve the level set equations (3) and (8), whereas the fluid flow equations (1) are solved using the conservative finite

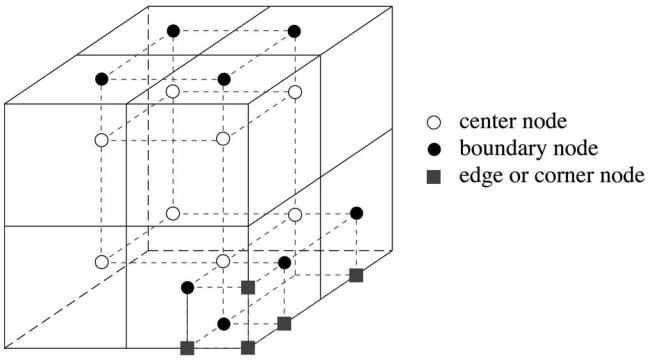

Fig. 1 Construction of the FE mesh by overlaying the FV grid. Schematic of grids, nodes, and elements. The dashed lines show the edges of the finite elements.

volume scheme. To our knowledge, this combination of FE and FV methods has never been used before in the level set modeling of two-phase flows.

Implementation of the Level Set Method Within CFX-4. In CFX-4, the Navier-Stokes equations are solved in the conservative form, as given by Eqs. (1), using the second-order FV method. The code uses structured grids, though the computational cells can be skewed. Thus, the level set (3) and (8) and fluid-flow (1) equations form a mixed FE-FV formulation. We introduce the level set interface-tracking subroutines into CFX-4 via the standard set of user subroutines, with the level set function to provide the fluid configuration and the CFX-4 solver being used to generate the flow velocity field.

In the CFX-4 two-phase solver, the properties of the two-phase mixture are approximated as

$$\rho(\mathbf{x},t) = \rho_1 F_1(\mathbf{x},t) + \rho_2 F_2(\mathbf{x},t) \tag{9a}$$

$$\mu(\mathbf{x},t) = \mu_1 F_1(\mathbf{x},t) + \mu_2 F_2(\mathbf{x},t) \tag{9b}$$

where $F_i(\mathbf{x},t)$, $i=1, 2$, are phase volume fractions. Consequently, in order to approximate the phase properties according to the level set model defined by Eqs. (4), the phase volume fractions are described in the following way:

$$F_1(\mathbf{x},t) = H_\varepsilon(\phi(\mathbf{x},t)), \quad F_2(\mathbf{x},t) = 1 - H_\varepsilon(\phi(\mathbf{x},t)) \tag{10}$$

where $H_\varepsilon(\phi)$ is the smoothed Heaviside function introduced earlier. We specify the phase volume fractions defined by Eq. (10) at every time step by overwriting the corresponding entries generated internally by CFX-4. Note that these expressions are only approximations because of the use of $H_\varepsilon(\phi)$, rather than the discontinuous Heaviside function $H(\phi)$.

In CFX-4, all variables, including velocity, pressure, and bulk body forces, are defined at cell centers. The boundary conditions are imposed by introducing so-called boundary nodes, located at the centers of the cell faces bordering the fluid domain, and by using dummy cells on the other side of the boundary. In the SUPG FE method, however, variables are defined at element vertices. If the same mesh is used to solve both the fluid flow equations (1) and the level set equations (3) and (8), then interpolation procedures would have to be invoked to transfer information between cell centers and vertices. Using such interpolation procedures would result in smearing of the interface, and the accuracy of the solution would be thereby degraded. For this reason, in addition to the FV mesh used to solve the Navier-Stokes equations, we introduce a FE mesh whose vertices are constructed from the center and boundary nodes belonging to the FV mesh. This idea is illustrated in Fig. 1. Note that construction of the FE mesh requires the introduction of new type of nodes, not present in the FV mesh. The new nodes are placed on the edges and corners of the external boundaries of the fluid domain. Velocities at such nodes are prescribed based on the appropriate (free-slip or no-slip) boundary conditions. The FE elements constructed in this way are hexahedrals, and isoparametric bilinear shape functions are employed.

In the present work, the FE mesh is constructed over the entire FV grid. This procedure requires an additional amount of computer storage; in particular, for three-dimensional problems the amount of computer memory allocated to the FE and FV grids is approximately double that occupied by the FV grid alone. However, the computer resources can be much more efficiently utilized if the finite elements are placed only in that part of the computational domain where the interface actually moves. This option will be implemented in the future.

The values of the normal to the interface $\mathbf{n}$ and curvature κ have to be calculated at the centers of the FV cells, which, as explained earlier, also are the vertices of the finite elements. In the SUPG FE method, however, the gradient of the solution $\nabla\phi$ is not uniquely defined at element nodes, since it is a discontinuous function across the element edges. Consequently, to calculate $\mathbf{n}$ and κ at a FE node, we average their corresponding values from the neighboring elements. This procedure can be employed on both structured and unstructured grids. Consider, for example, the node i and the group of elements K_j^i, $j=1,\ldots,N^e$, all sharing the same vertex i. Denote the volumes of these elements as V_j. In each element K_j^i, we first calculate the gradient of ϕ at the center of the element. The vectors $\mathbf{n}_j$ are then averaged over the elements in the selected group, K_j^i, to obtain the average normal $\langle\mathbf{n}^i\rangle$ at vertex i. Later, the nodal distribution of $\langle\mathbf{n}^i\rangle$ is used in an analogous manner to estimate the averaged curvature $\langle\kappa^i\rangle$. Thus,

$$\langle\mathbf{n}^i\rangle = \left\{\sum_{j=1}^{N^e}\frac{1}{V_j}\right\}^{-1}\sum_{j=1}^{N^e}\frac{\mathbf{n}_j}{V_j}, \quad \langle\kappa^i\rangle = \left\{\sum_{j=1}^{N^e}\frac{1}{V_j}\right\}^{-1}\sum_{j=1}^{N^e}\frac{\nabla\cdot\langle\mathbf{n}_j\rangle}{V_j} \tag{11}$$

The overlaying of FV and FE grids, as shown in Fig. 1, also offers a new way of handling the no-slip velocity boundary condition. It is known that in numerical simulations involving an interface sliding along a solid boundary with an imposed no-slip condition, the part of the interface located inside the boundary layer can remain motionless or can lag far behind the main front (e.g., [22]). In such situations, the interface experiences significant and unrealistic stretching. This numerical artifact is a result of the inconsistency of the no-slip boundary condition in the vicinity of the contact line of the interface with the wall [26]. The free surface actually rolls over the wall, but the scale of this phenomenon is too small to resolve it using standard continuum equations. Here, the Navier-Stokes equations (1) are solved together with the no-slip boundary condition, whereas the level set advection equation (3) is solved using the modified velocity field in which the tangential velocities at boundary nodes are assigned to be equal to those of the nearest inner FV nodes. For other possible ways of handling the no-slip boundary condition in the context of level set modeling (see [17]).

The flux quantities on cell boundaries are computed in CFX-4 using the Rhie-Chow algorithm [27]. Space differencing is centered, except for the advection quantities where a variety of schemes are available. Here, we use the second-order "higher upwind differencing scheme," in which velocities on control-volume faces are obtained by extrapolation from two upwind points. A second-order, backward scheme is used for the time discretization. The discretized equations are solved using a nested (inner and outer) iteration technique based on the SIMPLEC velocity-pressure coupling algorithm [28].

Implementation of the Level Set Method Within FIDAP. Our experience shows that it is not possible at the user level to overwrite the phase volume fractions in FIDAP as one does in CFX-4, since the corresponding data structures cannot be readily accessed. For this reason, it does not seem possible to implement the

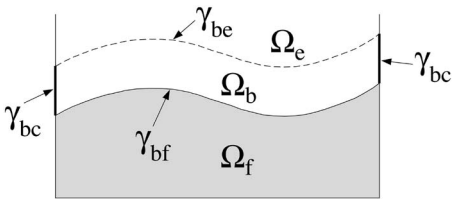

Fig. 2 Schematic of the computational domain of the level set fluid-void formulation. The domain Ω is divided into three regions: the fluid region Ω_f, the buffer zone Ω_b, and the empty region Ω_e. The surface γ_{bf} separates Ω_b from Ω_f, and γ_{be} separates Ω_b from Ω_e. The surface γ_{bc} is that part of the boundary of Ω_b located on the container walls.

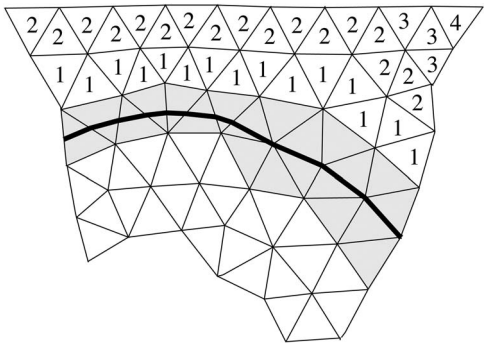

Fig. 3 Element bands built around the zero level set (shown in bold). The shaded region is the "zero-element band." The blank and shaded elements are those located in the fluid region Ω_f. Numbered elements are those located in the buffer zone Ω_b. Numbers inside elements indicate the element band number.

fluid-fluid level set formulation within FIDAP without modifying the source code or having appropriate data structures available to the user. Consequently, only the fluid-void approach, which considers the motion of only one phase, has been attempted with this code.

In the traditional fluid-void model, the computational domain consists of two regions: fluid and void [5]. However, the level set function ϕ must be continuous across the interface and, therefore, has to be defined in both the fluid and void regions. In order to advect ϕ, some "extension" velocity field has to be generated inside the void region near free surface in such a way as to be consistent with the flow velocity at the interface. To do this, a buffer zone is constructed ahead of the moving free surface [7]. A schematic of the computational domain is shown in Fig. 2. Three nonoverlapping regions are identified within the computational domain Ω: the fluid region Ω_f, the buffer zone Ω_b, and the empty region Ω_e, so that $\Omega=\Omega_f\cup\Omega_b\cup\Omega_e$. In the numerical implementation, those mesh cells that contain the interface itself are included in the fluid region Ω_f.

In the fluid region Ω_f, the flow is modeled with the Navier-Stokes equations in the nonconservative form

$$\rho_L\left(\frac{\partial \mathbf{u}}{\partial t}+\mathbf{u}\cdot\nabla\mathbf{u}\right)=\mathbf{B}-\nabla p+\nabla\cdot(2\mu_L\mathbf{D}), \tag{12a}$$

$$\nabla\cdot\mathbf{u}=0 \tag{12b}$$

where the subscript L indicates the phase properties associated with the liquid phase in Ω_f.

In the buffer zone, Ω_b, the extension velocity field is artificially generated. It should be noted that there is no unique definition of the extension velocity field, and so there is considerable freedom available in constructing it [29,30]. Certainly, the extension velocity $\mathbf{u}_b$ should, in the limit as one approaches the zero level set, yield the physical velocity of the interface itself. One way of extending the velocity field into the buffer zone, which still satisfies the continuity condition $\nabla\cdot\mathbf{u}_b=0$ and can be applied on both structured and unstructured grids, has been proposed by Hetu and Ilinca [23]. This method views the buffer zone as if it were filled with some fictitious fluid and solves the mass and momentum conservation equations for this fluid with the prescribed velocity profile on the interface. In their approach, the fluid inside the buffer zone is modeled as incompressible, and inertia and gravity terms are neglected. Thus, in the region Ω_b, the steady Stokes equations apply:

$$\mathbf{0}=-\nabla P_b+\nabla\cdot(\mu_b\nabla\mathbf{u}_b) \tag{13a}$$

$$\nabla\cdot\mathbf{u}_b=0 \tag{13b}$$

where the subscript b denotes variables defined inside the buffer zone.

Equations (13) require velocity boundary conditions. We identify three different parts of the buffer zone boundary $\partial\Omega_b$: γ_{bf}, γ_{be}, and γ_{bc}, so that $\partial\Omega_b=\gamma_{bf}\cup\gamma_{be}\cup\gamma_{bc}$ (see Fig. 2). The surface γ_{bf} separates the buffer zone Ω_b from the fluid region Ω_f, and the surface γ_{be} separates the buffer zone from the empty Ω_e region. The surface γ_{bc} is that part of the boundary $\partial\Omega_b$ which is located on the container walls. On the interface γ_{bf}, the velocity $\mathbf{u}_b$ is prescribed as a boundary condition. This velocity is found beforehand by solving Eqs. (12) for the flow of liquid in Ω_f. On γ_{be}, we impose the zero-traction boundary condition, which means that the pressure along γ_{be} is constant and the tangential stress is zero. On boundary γ_{bc}, different conditions can be applied; in this work, we employ and test the free-slip and zero-tranction conditions.

Figure 3 illustrates the idea of how the buffer zone is constructed. At each time step, we locate the band of elements containing the interface, which we refer to as the zero-element band. Then, all the element bands attached to the zero-element band on the side of the void region are located; each band is assigned a number, depending on its proximity to the interface. Finally, the buffer zone is given by the set of element bands. The thickness of the buffer zone is characterized in terms of the number of the element band N_b located the farthest from the zero level set.

We solve the Navier-Stokes (12) and Stokes (13) equations, consecutively, using the second-order SUPG FE method implemented into FIDAP [31]. First, Eqs. (12) are solved (with the zero-traction condition imposed on γ_{bf}), then Eqs. (13), and afterward the level set field is reinitialized. We have found that because of the inflexibility of FIDAP the only way to implement the fluid-void model is to solve Eqs. (12) and (13) in separate complete runs at each time step, while the level set subroutines are run outside of the FIDAP main environment. This restriction clearly results in long computation times, and we hope that it will be overcome in future releases of the code. The velocities and level set function are defined at element vertices, so that the fluid flow (12) and (13) and level set (3) and (8) equations are solved on the same mesh. After each computation, data is exchanged between the level set subroutines and FIDAP, with FIDAP providing the velocity field in $\Omega_f\cup\Omega_b$, and the level set subroutines providing the reinitialization of ϕ, and the allocation of the domains Ω_f,Ω_b, and boundary $\partial\Omega_b$. With FIDAP, both structured and unstructured grids can be used. Since all the equations are solved using the FE method, the present level set formulation may be called an FE-FE approach.

Numerical Results

In this section, we apply our numerical method to several selected problems with the purpose of testing and validating the two level set formulations. We have implemented the fluid-fluid, three-dimensional level set method into CFX-4, and the two-dimensional fluid-void level set formulation into FIDAP. The test problems that

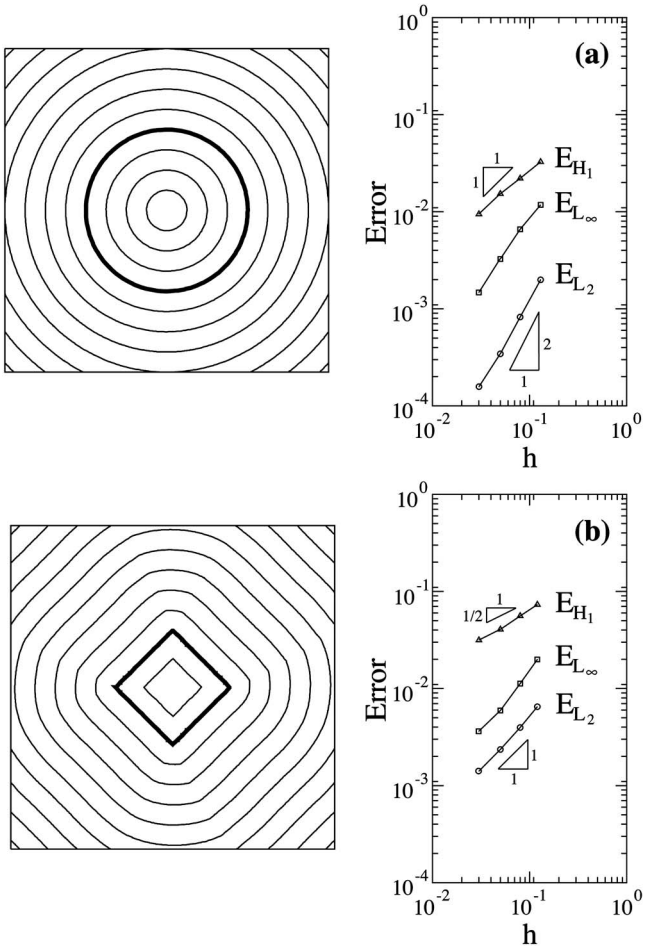

Fig. 4 First column: steady-state solutions of the reinitialization problem defined by Eq. (8) for (*a*) the unit circle and (*b*) the unit square, on the 4×4 domain. The bold line shows the zero level set; the contours of constant ϕ are spaced $\Delta x=0.25$ apart from each other. Second column: errors resulting from the convergence study. The mesh is unstructured.

we present in the next sections are all two-dimensional or axisymmetric.

Reinitialization. Barth and Sethian [12] studied, in detail, the properties of the SUPG FE method applied to the reinitialization problem defined by the homogeneous version of Eq. (8), i.e., with $\lambda=0$. The right-hand side, $\lambda\delta_\varepsilon(\phi)|\nabla\phi|$, was added later by Sussman and Fatemi [15], solely to improve numerical stability. We apply the SUPG FE method to the nonhomogeneous equation, with the coefficient λ computed using the prediction-correction procedure proposed by Sussman and Fatemi [15].

To test the SUPG FE reinitialization procedure, we solve the problem of reinitialization of the initially distorted level set field around two contours: a unit circle of radius 1 and a unit square, both located in the center of the 4×4 domain as shown by the bold line in the left column of Fig. 4. These contours are defined as the zero level sets of the function ϕ initialized as a discontinuous function (i.e., $\phi_0=-1$ inside, $\phi_0=+1$ outside, and $\phi_0=0$ on the contour itself). In both cases, we employ unstructured triangular grids, since their use is more general compared to structured grids. The average element edge is used as a measure of the mesh size h.

The steady-state solutions of Eq. (8) are visualized as level set contours of function ϕ shown by the thin lines in the left column of Fig. 4. The right column of Fig. 4 shows results of the convergence study. The error E is calculated here with respect to the exact solution; the subscript indicates the norm used: L_∞ norm, L_2 norm, and the Sobolev H_1 semi-norm. As one can see, the SUPG FE formulation is second-order accurate in the L_2 and L_∞ norms, and first-order accurate in the H_1 semi-norm in the case of the unit circle, which provides a smooth solution without shocks (by shocks we mean the regions where the characteristics of Eq. (8) cross each other). These are optimal convergence rates for linear elements. If the solution develops shocks, as is the case with the square because of the sharp angles in the zero level set contour, the SUPG FE formulation is first-order accurate in the L_2 and L_∞ norms, and one-half-order accurate in the H_1 semi-norm.

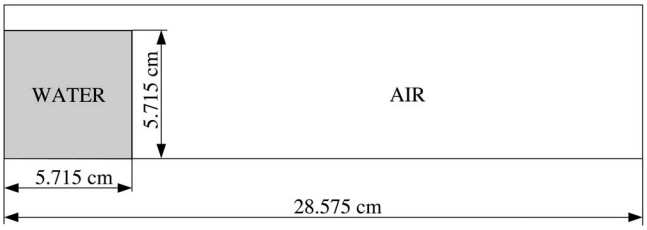

Fig. 5 Schematic diagram of the broken-dam problem.

The convergence rates agree with those obtained by Barth and Sethian [12] and show that the inclusion of the nonhomogeneous part into Eq. (8) does not reduce the accuracy of the SUPG FE level set method. Finally, we note that the convergence rate of the level set interface-tracking scheme can degrade to the first order, depending on the shape of the interface, in particular, if the shape of the interface is such that it develops shocks in the solution of Eq. (8).

Below, we present results of simulations for problems involving fluid flow. In such problems, the level set function ϕ needs to be reinitialized only in the $O(h)$ vicinity of the interface. Consequently, the level set equations (3) and (8) are solved only in a band around the interface. The half-width of the band is set to $4h$, while the time step $\Delta\tau$ for solving the reinitialization equation (8) is set to $h/2$. For flows involving surface tension effects, the level set field ϕ needs to be reinitialized with very high accuracy because of the need to calculate the interface curvature, and Eq. (8) is solved for 10 time steps for every new location of the interface (i.e., for every time step of the Navier-Stokes solver). For cases without surface tension, Eq. (8) is solved for five time steps.

Broken-Dam Problem. The broken-dam problem refers to the collapse of a water column under the effect of gravity. In the present work, we model the problem configuration used in the experiment of Martin and Moyce [32]. The two-dimensional computational domain and the initial configuration of the fluid are shown in Fig. 5. Initially, the water is at rest. At time $t=0$, the dam (right wall) supporting the water is instantaneously removed and the fluid collapses. The properties of the water are set to $\rho_L=1000\ \text{kg/m}^3$ and $\mu_L=0.001\ \text{kg/ms}$, with the water-air density and viscosity ratios being 860 and 54, respectively; the acceleration of gravity is $g=9.81\ \text{m/s}^2$. A free-slip boundary condition is imposed on all sides of the computational domain, except the top, where a pressure boundary condition is used. Surface tension effects are not important in this problem.

For convenience, we introduce the following dimensionless variables:

$$\mathbf{u}^*=\frac{\mathbf{u}}{\sqrt{gh_c}},\quad \mathbf{x}^*=\frac{\mathbf{x}}{h_c},\quad \rho^*=\frac{\rho}{\rho_L},\quad \mu^*=\frac{\mu}{\rho_L h_c\sqrt{gh_c}} \tag{14a}$$

$$t^*=\frac{t\sqrt{gh_c}}{h_c},\quad p^*=\frac{p}{\rho_L g h_c} \tag{14b}$$

where the initial height of the water column h_c is used as the length scale and the velocity scale is set equal to $\sqrt{gh_c}$. Here, and

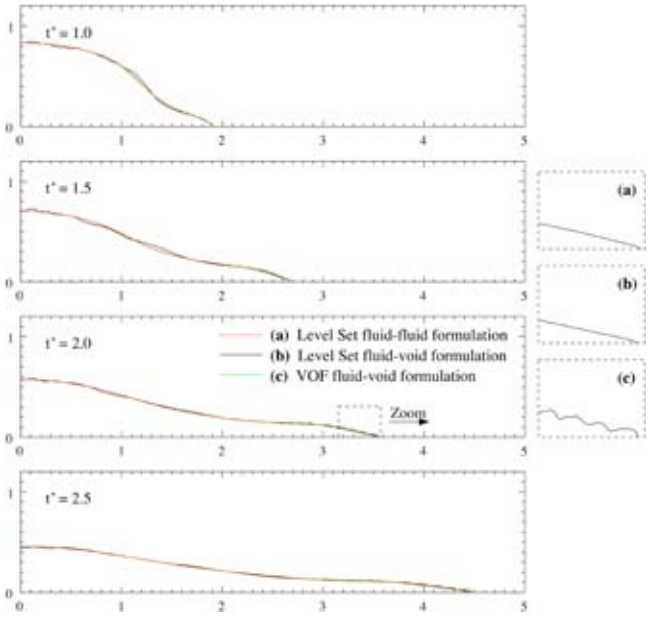

Fig. 6 Fluid configurations for the broken-dam problem at different times obtained by the two level set formulations and the PCSS VOF method. The latter solution was obtained using a regular grid. The container dimensions are nondimensionalized with the value of the initial height of the water column h_c. The average mesh size is $h^*=0.02$.

later in the text, the asterisk superscript is used to denote dimensionless values.

We solve the problem using both the fluid-void (FIDAP) and fluid-fluid (CFX-4) level set formulations. In the former case, we use an unstructured triangular grid, while a regular structured mesh is used in the latter. A constant time step of $\Delta t^*=0.2h^*$ is used in both cases, in which h^* is the dimensionless mesh size. The interfacial thickness parameter is set to $\varepsilon^*=2h^*$. In the fluid-void method, a free-slip velocity condition is imposed on boundary γ_{bc}, the dimensionless viscosity of the fictitious fluid inside the buffer zone is set to $\mu_b^*=1.0$, and the buffer zone thickness is set to $N_b=12$. We have found that increasing the buffer zone beyond $N_b=12$ results in negligibly small changes in the solution.

Figure 6 gives snapshots of the solution at different times obtained using the two level set formulations, as well as the solution obtained on a regular grid using the PCSS VOF fluid-void method (the FIDAP standard model). As one can see, the interface shapes predicted by the level set fluid-fluid formulation and the VOF fluid void method are very close, except near the container floor where the free surface obtained using VOF develops perturbations in the form of square steps. The presence of these perturbations could clearly cause difficulties in calculating the interface curvature if a surface tension model were to be applied. In the case of unstructured grids, the steplike perturbations at the interface become more pronounced and develop over the entire free surface [22]. In contrast, the use of the level set fluid-void method on the unstructured grid gives a smooth interface, with waves of small amplitude; these waves develop during the initial stages of the flow, but later tend to disappear. The level set fluid-fluid model provides the solution with no noticeable perturbations on the interface.

Table 1 shows the results of the convergence study. Three solutions were found using grids of different resolution. The position of the water front on the container floor x_{WF}^* at time $t^*=2.5$ is chosen as a target parameter, with the origin being in the lower left corner of the container. The error E_1^i between succeeding mesh resolutions is computed using the L_1^i norm, which is well suited for interfacial flow problems

Table 1 Convergence study of the two SUPG FE level set formulations for the broken-dam problem

	Level set fluid-fluid method (CFX-4)		Level set fluid-void method (FIDAP)	
h^*	$x_{WF}^*(2.5)$	$E_1^i(2.5)$	$x_{WF}^*(2.5)$	$E_1^i(2.5)$
0.08	4.29	N/A	4.17	N/A
0.04	4.40	$2.55\cdot10^{-2}$	4.38	$1.06\cdot10^{-1}$
0.02	4.49	$1.11\cdot10^{-2}$	4.46	$5.49\cdot10^{-2}$

$$E_1^i = \int_{\Omega^*} |H(\phi_r) - H(\phi_c)| d\Omega^* \tag{15}$$

where $H(\phi)$ is the discontinuous Heaviside function, and ϕ_r and ϕ_c are solutions from, respectively, refined and coarse grids. As one can see from the values of E_1^i, both level set formulations display first-order convergence, although formally the SUPG FE method is second-order accurate. To investigate this issue further, we conducted additional simulations of the broken-dam problem in which the sharp corner in the free surface at $t=0$ was replaced by smooth arcs of different radii. It was found that the convergence rate of solutions for these simulations was also first order. Thus, although the sharp angle singularity in the interface certainly degrades the accuracy of the solution, as was discussed above, it may not be the only reason for the observed lack of accuracy.

We believe that in the case of the fluid-void (FIDAP) level set formulation, the first-order convergence rate of the solution is a consequence of the insufficiently accurate treatment of the Dirichlet pressure boundary condition on the interface. Indeed, the surface γ_{bf} on which the zero-traction condition is applied is only a first-order accurate representation of the interface (see Fig. 3). Thus, to achieve optimal second-order convergence, it is necessary to enforce the pressure boundary condition on γ_{bf} to second-order accuracy (see, e.g., [30]). On the other hand, the one-order-of-magnitude reduction in the convergence rate obtained using the fluid-fluid (CFX-4) level set formulation could be caused by the large phase density ratio, as discussed by Sussman and Puckett [20].

We estimate the effect on the solution of the viscosity of the fictitious fluid inside the buffer zone in the fluid-void (FIDAP) formulation by performing simulations with different values of μ_b^* and, comparing the deviation of the solutions from the reference solution ϕ_r, obtained with $\mu_b^*=1$ and $N_b=12$. The deviation is calculated as the relative error $\tilde{E}_1^i$ given by

$$\tilde{E}_1^i = \frac{1}{\varepsilon^* L_i^*} \int_{\Omega^*} |H(\phi) - H(\phi_r)| d\Omega^* \tag{16}$$

where L_i is the length of the interface. Figure 7 shows the values of $\tilde{E}_1^i$ as a function of the Reynolds number, $\mathrm{Re}_b=1/\mu_b^*$, at different times t^*. As follows from the figure, the level set solution is fairly insensitive to the value of μ_b^*, which can be varied by orders of magnitude without having a noticeable effect on the solution.

Figure 8 shows results of the sensitivity analysis of the level set fluid-void solution to the buffer zone thickness N_b. Here again, the error $\tilde{E}_1^i$ is calculated with respect to the reference solution obtained with $\mu_b^*=1$ and $N_b=12$. We note that increasing the buffer zone thickness leads to smaller dependence of the solution on the value of N_b. Ultimately, the final choice of the value of N_b for a particular application depends on the accuracy required. It is important to note the following fact: we have found that the local

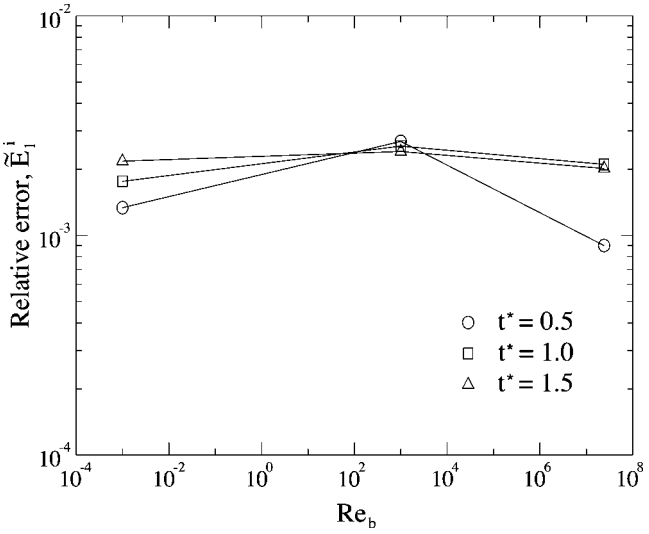

Fig. 7 Effect of the viscosity of the fictitious fluid inside the buffer zone on the level set fluid-void solution

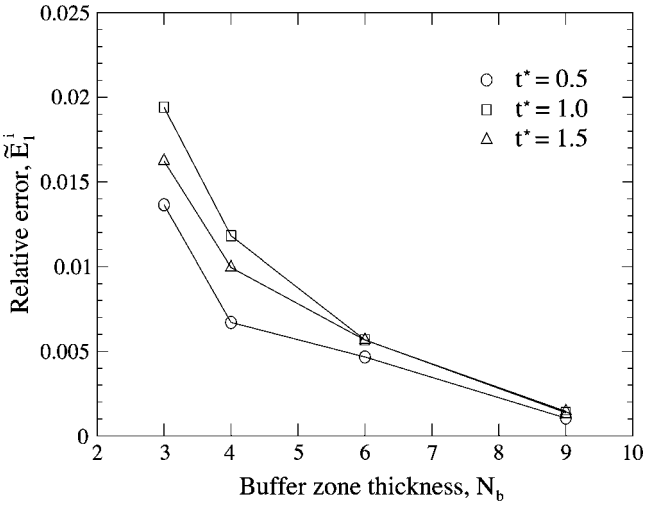

Fig. 8 Effect of the buffer zone thickness N_b on the level set fluid-void solution. The error $\tilde{E}_1^i$ is calculated in terms of the solution obtained with Re_b=1 and N_b=12.

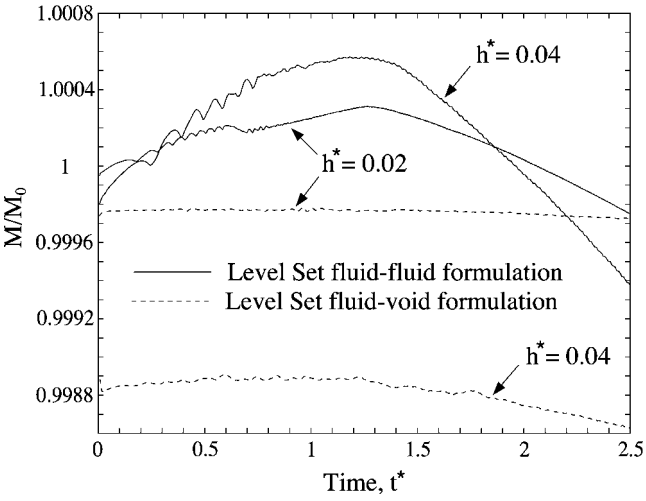

Fig. 9 Variation of the mass of water as a function of time in the level set solution of the broken-dam problem for two mesh resolutions

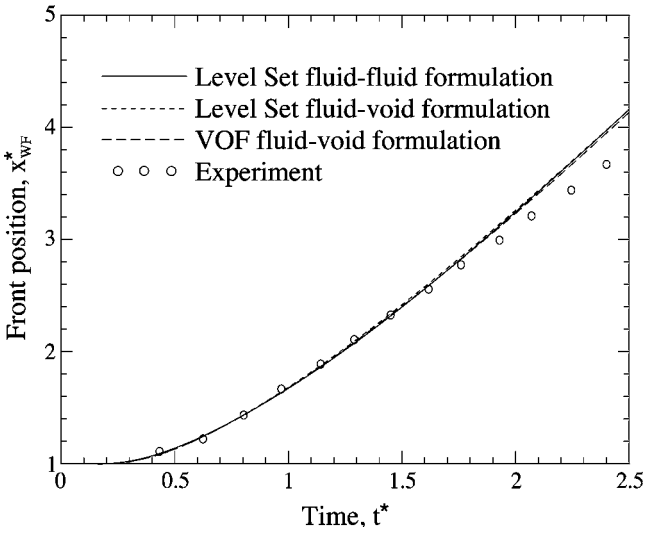

Fig. 10 Comparison of the predicted water front positions with the experimental data for the broken-dam problem.

decrease of the buffer zone thickness below N_b=3, which can occur in many practical applications, can result in localized oscillations on the interface and relatively large errors in the solution. This problem needs further investigation, and we will report on its progress in a future communication.

To investigate the effect on the solution of the boundary condition imposed on γ_{bc}, an additional simulation has been performed with the zero-traction condition imposed on γ_{bc} instead of the free-slip condition; the difference between the two solutions is measured using the error $\tilde{E}_1^i$. The results are given in Table 2. Evidently, the solution is not sensitive to which of the two boundary conditions is used for γ_{bc}.

Figure 9 shows the variation of the mass of water M as a function of time for two meshes of different resolution. The fluid-void formulation clearly demonstrates smaller mass variations (which suggests better mass conservation properties) compared to the fluid-fluid formulation.

The resulting positions of the water front on the container floor as a function of time, obtained using the two level set formulations and the VOF method, are shown in Fig. 10. This figure also

Table 2 The difference between two solutions of the broken-dam problem obtained using the FE-FE level set fluid-void formulation (FIDAP) with, respectively, the free-slip and zero-traction conditions imposed on boundary γ_{bc}. Here, we use μ_b^*=1 and N_b=12. The mesh is unstructured, with resolution h^*=0.02.

t^*	0.5	1.0	1.5	2.0	2.5
L_i^*	1.94	2.17	2.81	3.61	4.49
$\tilde{E}_1^i$	$1.76\cdot10^{-3}$	$3.46\cdot10^{-3}$	$3.60\cdot10^{-3}$	$3.61\cdot10^{-3}$	$3.35\cdot10^{-3}$

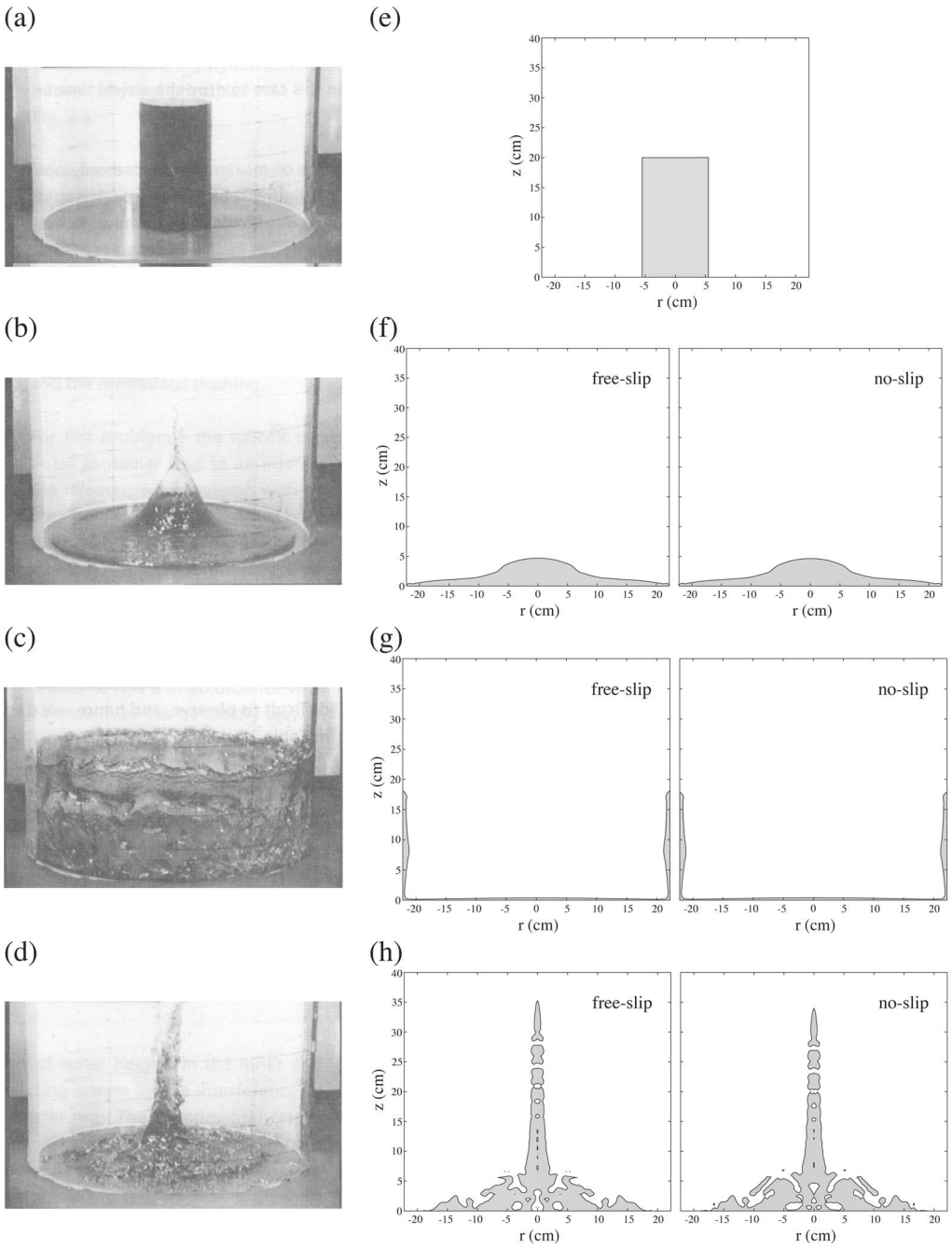

Fig. 11 Collapsing cylinder of water: left column shows pictures obtained experimentally by Munz and Maschek [33]; right column shows the numerical predictions obtained using the FE-FV level set fluid-fluid formulation (CFX-4) for the free and no-slip boundary conditions. Rows correspond to characteristic times t_0, t_1, t_2, and t_3.

Table 3 Experimental and numerical values for the characteristic times and heights of the collapsing water cylinder. Numerical data: case 1, level set CFX, free-slip condition; case 2, level set CFX, no-slip condition; case 3, PLIC VOF [34]; and case 4, CFX standard method with surface sharpening [34]. The experimental values were obtained by Munz and Maschek [33].

Case	t_1 (s)	t_2 (s)	H_2 (mm)	t_3 (s)	H_3 (mm)
1	0.19	0.39	181	0.91	355
2	0.19	0.39	179	0.90	342
3	0.23	0.36	93	0.85	>355.2
4	0.22	0.40	128	0.88	150
Exp	0.20±0.02	0.42±0.02	160±10	0.88±0.04	400±50

shows the experimental data obtained by Martin and Moyce [32]. It should be noted that Martin and Moyce normalized their experimental data for the water front positions by setting $x^*_{WF}(0.8) = 1.44$. This was done due to difficulties in recording the exact "start time" of the motion. To be consistent with their data, we have normalized our numerical results the same way. The numerical and experimental curves $x^*_{WF}(t^*)$ are in very good agreement during the initial stages of the flow, but the agreement deteriorates somewhat after $t^* = 1.8$. This could be the result of three-dimensional effects appearing in the experiment.

Collapsing Cylinder of Water. The problem of a collapsing water cylinder under gravity has been studied experimentally by Munz and Maschek [33]. A photograph of the experimental setup is shown in Fig. 11(*a*). Initially, a water column of diameter 11 cm and height 20 cm is supported by a glass cylinder and contained in a larger cylindrical container of diameter 44.4 cm. At $t_0 = 0$, the smaller cylinder is "instantaneously" removed from the top, and the water column slumps under gravity and flows across the container floor.

Because of the intensive air entrainment in the flow, the collapsing cylinder problem cannot be simulated using the level set fluid-void formulation. Consequently, we solve the problem using the FE-FV level set fluid-fluid formulation implemented into CFX-4. Due to axial symmetry, the computational domain of the size 22.2 cm $\times$ 40 cm represents only one-half of the container in cylindrical coordinates. A regular grid of cell size $h = 4.44$ mm has been used for this simulation. The chosen mesh resolution is identical to that used by Meier [34], who simulated the same problem using the second-order accurate piecewise-linear interface construction (PLIC) VOF method.

For comparison purposes, we employ both free and no-slip velocity boundary conditions on the floor and container walls, while a constant pressure boundary condition is imposed on the upper horizontal side of the computational domain. Because of small-scale air bubbles entrained in the flow, we cannot resolve the surface tension effects with our limited computer resources. Therefore, surface tension effects, though considered important in later transient stages, are not considered in this simulation. The interfacial thickness parameter ε^* is set to $2h^*$, as before.

Figures 11(*b*)–11(*d*) are snapshots of the flow taken during the experiment, and Figs. 11(*f*)–11(*h*) show numerical predictions of the free surface at the same times. In the early part of the transient, a cylindrical water wave runs outward and reaches the container wall at time t_1, as shown in Figs. 11(*b*) and 11(*f*) and reaches a maximum height on the wall H_2 at time t_2, as shown in Figs. 11(*c*) and 11(*g*). At this moment, the flow reverses, the liquid rolls back, and finally produces a large spout of height H_3 in the center of the container at time t_3 (Figs. 11(*d*) and 11(*h*)). Having formed the spout, the motion again reverses and the water falls back under gravity. Surprisingly, the front profiles obtained numerically using the free and no-slip boundary conditions are very similar up to time t_2. For $t > t_2$, the difference between the two numerical solutions starts to increase, most likely due to the developing mixing in the flow.

Comparing the water front profiles obtained in this work against those of Meier [34], one notes that the level set method predicts separation of water from the vertical container wall at $t = t_3$, as shown in Fig. 11(*h*), whereas in the Meier's PLIC-VOF method, the water stays in contact with the wall during the entire time of spout development. Of the two, the level set prediction is the one in accord with the experiment (Fig. 11(*d*)).

Table 3 shows characteristic times and dimensions observed in the experiment, together with those from numerical solutions. The data obtained by Meier [34] and those obtained with CFX-4 using the standard interface-tracking method with surface sharpening are also given in the table. It should be noted that the numerical predictions of the spout formation have to be interpreted with care, since at this stage the water front experiences fragmentation into small droplets and bubbles, and none of the methods considered can capture these phenomena accurately with the given mesh resolution. Overall, the level set formulation provides the most accurate results of the three methods discussed.

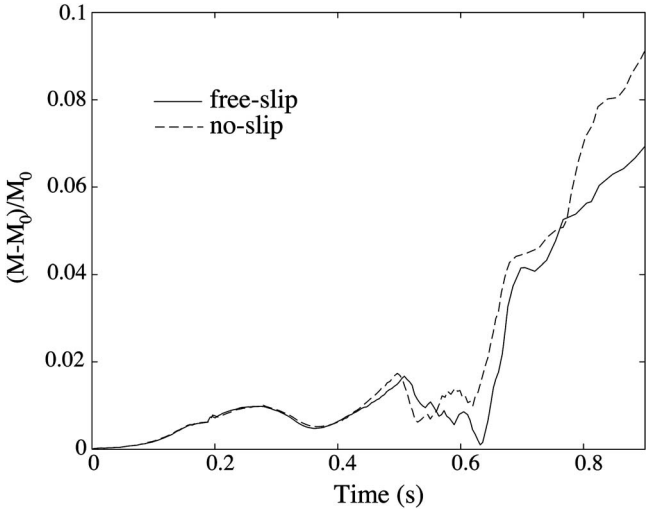

Fig. 12 Variation of mass of water as a function of time in the solution for the collapsing water cylinder obtained using the level set fluid-fluid method; the mesh size is 4.44 mm.

Figure 12 shows mass variations with time for the level set solutions. Taking into account the coarseness of the mesh we have used, the mass conservation is acceptable for $t < 0.6$ s. At later times, the flow is characterized by the formation of small, entrained air bubbles of the size of the mesh cells, and the interface develops high curvature (see Fig. 11(*h*)). This, in turn, results in strong numerical diffusion and a large mass accumulation. In order to improve mass conservation, one needs to either refine the mesh or use an adaptive projection level set formulation [16] in which there is local mesh refinement in regions of high curvature.

Bubble Rising in a Viscous Fluid. Modeling of a rising bubble in a viscous fluid is a popular benchmark problem for interface tracking methods [13,14,16]. Here, we simulate the case of an air bubble rising in a sugar-water solution, the problem studied experimentally by Bhaga and Weber [35]. In the experiment, the viscosity of the solution μ_L was varied by about an order of magnitude by changing the concentration of sugar, but the density ρ_L and surface tension σ of the liquid changed very little, with a maximum variation of 4%. However, the exact data for each test case were not reported. Consequently, in our work, we have set the solution density and surface tension to the average values measured in the experiment: $\rho_L = 1.35$ kg/m^3 and $\sigma = 0.078$ N/m. We consider three water solutions of different viscosities: $\mu_L = 2.73$, 1.28, and 0.54 kg/ms. The corresponding liquid-air density ratio is 1050, and the viscosity ratios are $1.6 \times 10^5, 7.5 \times 10^4$, and 3.2×10^4, respectively, for the three cases examined.

Initially, at $t = 0$, the bubble is approximated as a sphere of diameter $d_e = (6V/\pi)^{1/3}$, where V is the volume. In the experiment, the volume of the generated bubbles was 9.3 cm^3, so that $d_e = 2.61$ cm. The problem is assumed axially symmetric; therefore, we model only half of the bubble on a rectangular computational domain of size $2.5d_e \times 10d_e$ in cylindrical coordinates. The initial velocity field is set to zero everywhere. At the sides of the fluid domain, except the symmetry line at $r = 0$, far-field boundary conditions are employed (i.e., we assume that the pressure on the walls is $p = \rho_L g z$, where z is the vertical coordinate). The interfacial thickness parameter is set to $\varepsilon^* = 2h^*$.

For comparison purposes, we simulate the problem using both the level set fluid-fluid formulation and the standard CFX-4 interface-tracking method. We found that the use of the latter, in

Table 4 Convergence study of the FE-FV level set fluid-fluid method for the problem of a rising bubble in a viscous fluid for Eo=116

	Mo=848		Mo=41.1	
h^*	U_t(cm/s)	E_1^i(0.25s)	U_t(cm/s)	E_1^i(0.25s)
0.1	19.67	N/A	25.44	N/A
0.067	19.37	$7.72\cdot10^{-2}$	25.67	$6.39\cdot10^{-2}$
0.044	19.22	$4.41\cdot10^{-2}$	25.78	$2.92\cdot10^{-2}$

combination with the surface-sharpening algorithm, resulted in numerical instabilities. Consequently, the surface-sharpening algorithm is not used for these simulations.

To characterize the problem, we use the Eötvös number, Eo $=gd_e^2\rho_L/\sigma$, and the Morton number, Mo$=g\mu_L^4/(\rho_L\sigma^3)$. The Morton numbers for the three bubbles are 848, 41.1, and 1.31. Since the Eötvös number does not depend on viscosity, it is the same in all cases considered and equal to 116.

In the course of preliminary simulations, we found that the first two bubbles, with Mo=848 and 41.1, attain steady-state configurations quite rapidly, with terminal shape and constant rise velocity. In contrast, the third bubble, with Mo=1.31, does not reach steady state: it develops a slowly growing "skirt," and its rise velocity, after reaching a seemingly terminal value at approximately $t=0.2$ *s*, starts varying with time again.

Table 4 presents results of the convergence study undertaken for bubbles with Mo=848 and 41.1. Here, the error is estimated according to Eq. (15). We choose the value of the terminal velocity U_t as a target parameter. Due to limited computer resources available, convergence is studied by successively refining the mesh size using a ratio of 2/3 (rather than 1/2), with the smallest mesh size being $h^*=0.044$, where $h^*=2h/d_e$. As one can see, this mesh provides acceptable accuracy. The convergence rate is of the order of $O(h^{3/2})$ in the norm L_1^i. This conclusion agrees well with that of Sussman and Puckett [20], who modeled an axisymmetric, inviscid air bubble rising in water with the CLSVOF method.

We employ the CFX-4 standard interface-tracking method using the same problem formulation and mesh as those used for the level set simulations. The cross sections of the bubbles at different times, obtained using the two methods, are shown in Tables 5 and 6. The bubble shapes predicted using the CFX-4 standard method are visualized by locating the isosurface of $F_A=0.5$, where F_A is the volume fraction of air. As was mentioned before, the bubbles in the level set simulations for Mo=848 and 41.1 attain steady-state configurations within 0.25 s. The shapes of these bubbles are of the oblate ellipsoidal cap type; this result agrees well with the experimental data of Bhaga and Weber [35]. In contrast, with the CFX-4 standard interface-tracking method, the bubbles never reach steady state, but instead slowly transform into toroidal structures and eventually become completely diffused due to numerical diffusion.

The difference between the results obtained using the level set

Table 5 Columns 2–6 show cross sections of the bubble at different times, as computed using the FE-FV level set fluid-fluid method implemented into CFX-4. The last column shows the side view of the bubble observed in the experiment of Bhaga and Weber [35]. In all three cases, Eo=116.

Mo	t=0.05 s	t=0.10 s	t=0.15 s	t=0.20 s	t=0.25 s	Exp
848						
41.1						
1.31						

Table 6 Cross sections of the bubble at different times, as computed using the CFX-4 standard interface-tracking method without surface sharpening

Mo	t=0.05 s	t=0.10 s	t=0.15 s	t=0.20 s	t=0.25 s
848					
41.1					
1.31					

method and the CFX-4 standard interface-tracking method can also be clearly seen in Figs. 13 and 14. The first figure shows the bubble rise velocity (defined as the velocity of the center of mass) as a function of time. The second figure shows the bubble mass as a function of time (the mass of the bubble is that enclosed by the isosurface $F_A=0.5$ for the CFX-4 solution). Clearly, the use of the level set method results in good mass conservation. The CFX-4 standard method, however, is very diffusive, explaining why the bubbles never reach steady state, but instead become diffused over the computational domain and eventually disappear, as can be seen in Table 6. The excessive mass loss evident in Fig. 14(*b*) is associated with this disappearance.

Table 7 gives numerical and experimental values of the terminal

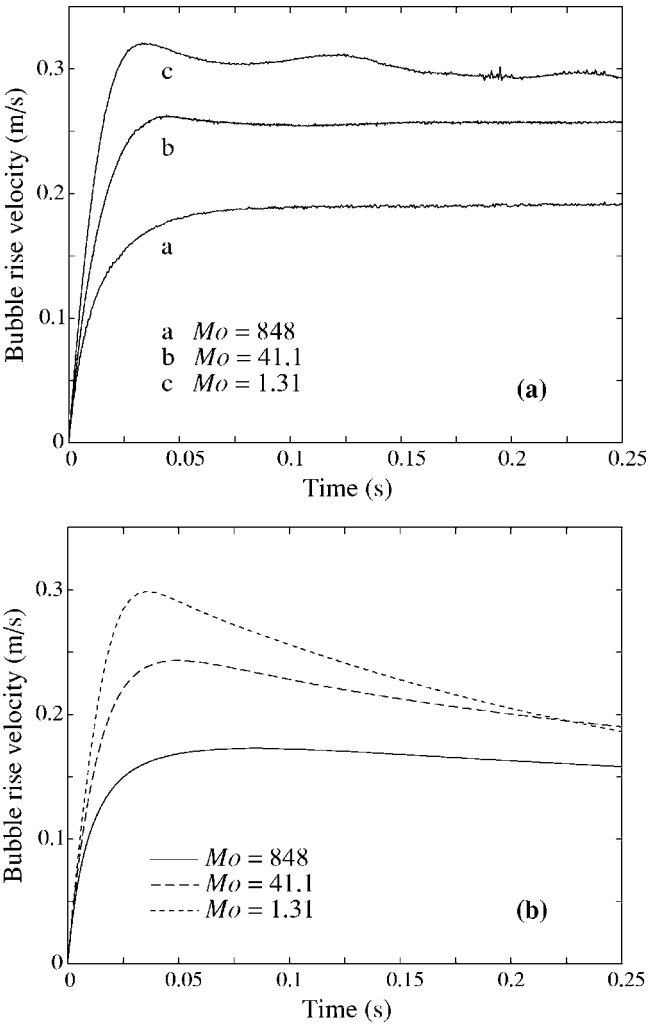

Fig. 13 Bubble rise velocity as a function of time: (*a*) level set solution and (*b*) standard CFX-4 model

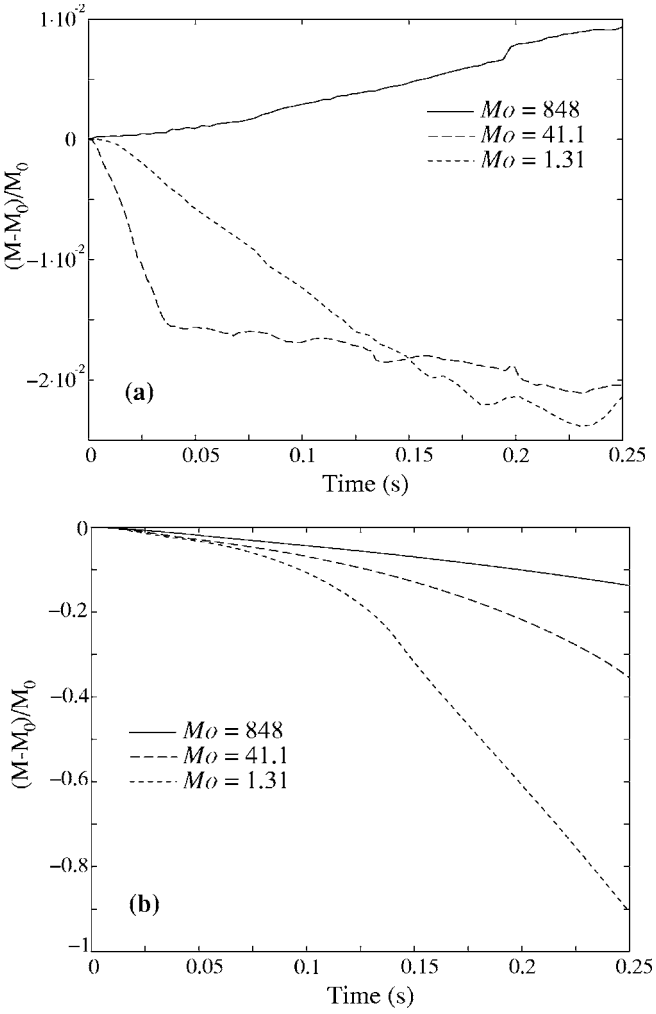

Fig. 14 Bubble mass as a function of time in the problem of a rising bubble: (*a*) level set solution and (*b*) standard CFX-4

rise velocities and the dimensionless height and width of the fully developed bubbles for Mo=848 and 41.1, as obtained using the level set method. The bubble height l_b is defined as the difference between the highest and lowest points on the bubble surface, and the width w_b as the diameter of the horizontal cross section of the bubble with largest area. Clearly, there is good agreement between the experimentally measured terminal rise velocities and numerical predictions: the difference is $<1\%$. The agreement between the dimensionless bubble heights and widths is also good, despite the relatively large experimental uncertainty in measuring the linear dimensions of the bubbles which was, $\sim 7\%$ according to Bhaga and Weber [35], .

The growing bubble skirt, predicted in the simulation for Mo =1.31, seems to be in contradiction with the experimental observations of Bhaga and Weber [35]. The problem of the development of unphysical skirts in two-dimensional and axisymmetrical simulations of bubbles rising in viscous fluids has been reported before by Sussman and Smereka [14] and Ginzburg and Wittum [36], who used the level set and VOF methods, respectively. We believe that the numerical artifact of skirt formation in the cited simulations, as well as in our simulation for bubble Mo=1.31, is a consequence of two possible causes. The first is the effect of the initial condition on the steady-state configuration of the bubble. Earlier, Koh and Leal [37] found experimentally that an air bubble in viscous castor oil could develop into a spherical shape, or develop an unstable skirt, depending on the initial shape of the bubble. Hence, it is possible that the skirt formation in our simulation for bubble Mo=1.31 is a result of the inappropriate approximation of the initial shape of the bubble, at $t=0$, as a sphere, and that this ultimately resulted in exciting one of the unstable modes. The second possible cause is the limitation of the axisymmetrical model, which cannot resolve capillary instabilities developing on the bubble surface. Tomiyama et al. [38] modeled the same bubble, with Mo=1.31, using a three-dimensional VOF model and did not predict any skirt formation. Consequently, in order to investigate this issue, it is necessary to conduct a numerical study of the sensitivity of a bubble to initial conditions using a three-dimensional level set model. This study will be pursued at a later date.

Table 7 Experimental (exp) and numerical (num) terminal rise velocities, and dimensionless heights and widths of the fully developed bubbles. The numerical data were obtained using the FE-FV level set method. The experimental data are taken from Figs. 3 and 5 of Bhaga and Weber [35].

Mo	Case	U_t(cm/s)	w_b/d_e	l_b/d_e
848	exp	19.14	1.14	0.71
	num	19.22	1.12	0.76
41.1	exp	26.02	1.25	0.65
	num	25.78	1.22	0.69

Computational Overhead Due to Level Set Modeling. As mentioned earlier, the inflexibility of FIDAP results in inefficient level set simulations: approximately 80% of the CPU time is spent on read-write operations. This results in a tenfold slowdown in code performance.

In contrast, the package CFX-4 allows inclusion of the level set model into the code in quite an efficient way. To evaluate the computational overhead of the level set model within the framework of CFX-4, we have separately calculated the CPU times involved in solving the level set (3) and (8) and the Navier-Stokes (1) equations. The most time-consuming operation in this case is the reinitialization procedure, which is performed once per fluid time step, whereas the solution of Eq. (3) is obtained very quickly because of its linear form. In the course of reinitialization, Eq. (8) is solved for $N_{\Delta\tau}$ time steps. The value of $N_{\Delta\tau}$ is set in advance, depending on the problem.

All CFX-4 simulations have been conducted using a workstation with a 833 MHz AlphaServer DS20 processor. Results are given in Table 8 in terms of the average CPU time per iteration $\mathrm{CPU}_{it}^{\mathrm{ave}}$ and the average number of iterations per time step N_{it}^{ave} for both the level set and Navier-Stokes iterative solvers. As can be seen, the computational overhead of the level set model is problem dependent. It should be emphasized that we have not attempted to optimize the performance of the level set iterative solver. In addition, the total CPU times will also depend on the convergence criteria chosen for the solvers. Consequently, the overall increase in CPU times given in Table 8 should be viewed only as order-of-magnitude estimates. In the case of the collapsing water cylinder problem, the computational overhead due to the level set modeling is quite high; this is a consequence of the formation of a long interface of complex shape in the later stages of the simulation. In the other two cases, the increase in CPU times resulting from the level set computation is reasonable.

Conclusions

We have presented a streamline-upwind–Petrov-Galerkin finite element level set method that may be implemented within the framework of commercial CFD codes (both FE and FV based) for solving problems involving incompressible, two-phase flows with moving interfaces. Two formulations have been considered: fluid-fluid and fluid-void, which differ in the way the interaction between the phases is treated.

Table 8 Comparison of CPU times spent on reinitialization of the level set field and the solution of the Navier-Stokes equations using the CFX-4 code. Test cases considered: 1, broken dam; 2, collapsing cylinder of water; and 3, bubble rising in a viscous fluid. The last column shows the overall increase in CPU time, as a multiple of the time needed to perform the CFX-4 calculation without the level set model.

	SUPG FE level set solver			CFX-4 Navier-Stokes solver		Overall increase in CPU time
Case	CPU_{it}^{ave} (s)	N_{it}^{ave}	$N_{\Delta\tau}$	CPU_{it}^{ave} (s)	N_{it}^{ave}	
1	5.4	1.0	5	1.2	17.8	2.3
2	9.3	1.6	5	0.7	22.5	5.7
3	6.9	1.4	10	1.7	34.3	2.6

The first level set formulation simulates the coupled motion of the two phases. Away from the interface, the fluid properties are set to be those of the appropriate constituent phases, whereas in the vicinity of the interface they are interpolated across the interface to ensure smooth transition from one phase to the other. We have implemented this formulation within the commercial code CFX-4, in which the fluid-flow equations are solved using a finite volume method. Therefore, the joint solution of the level set and fluid-flow equations is termed the FE-FV combination.

The second formulation is used for gas-liquid flows in which effects of the gaseous phase on the motion of the liquid phase are negligibly small. This formulation is implemented into the commercial code FIDAP, in which the fluid-flow equations are also solved using the SUPG FE method. In this case, the joint solution of the fluid-flow and level set equations is termed the FE-FE approach.

We have applied the SUPG FE level set method to several problems involving two-phase incompressible flows with density ratios of the order of 10^3 and viscosity ratios as high as 1.6×10^5. Both structured and unstructured grids have been used. Surface tension effects have also been considered. The numerical results obtained have been compared against available experimental data. We have demonstrated that the SUPG FE level set method provides robust convergence and accurate results. We have also shown that the SUPG FE level set method displays good mass conservation properties, provided the mesh is adequate for the problem.

The successful implementation of the level set method within the framework of the commercial CFD codes FIDAP and CFX-4, as demonstrated in the present paper, broadens the scope of applicability of these codes, since the method offers new opportunities for handling problems that cannot be solved to the same level of accuracy (or cannot be solved at all) using the codes' standard interface-tracking models. The range of problems for which the SUPG FE level set method can offer better robustness and accuracy includes those with strong surface tension effects and for which interface tracking is considered in the context of unstructured grids.

Acknowledgments

The authors are sincerely grateful to Dr. W. Maschek of the Institute for Nuclear and Energy Technologies, Karlsruhe, Germany, for his permission to use the experimental photographs of the collapsing water cylinder.

References

[1] Tryggvason, G., Bunner, B., Esmaeeli, A., Juric, D., Al-Rawahi, N., Tauber, W., Han, J., Nas, S., and Jan, Y.-J., 2001, "A Front-Tracking Method for the Computations of Multiphase Flow," J. Comput. Phys. **169**, pp. 708–759.

[2] Hou, T. Y., Lowengrub, J. S., and Shelley, M. J., 2001, "Boundary Integral Methods for Multicomponent Fluids and Multiphase Materials," J. Comput. Phys. **169**, pp. 302–323.

[3] Jacqmin, D., 1999, "Calculation of Two-Phase Navier-Stokes Flows Using Phase-Field Modeling," J. Comput. Phys. **155**, pp. 96–127.

[4] Jamet, D., Lebaigue, O., Coutris, N., and Delhaye, J. M., 2001, "The Second Gradient Method for the Direct Numerical Simulation of Liquid-Vapor Flows With Phase Change," J. Comput. Phys. **169**, pp. 624–651.

[5] Hirt, C. W., and Nichols, B. D., 1981, "Volume of Fluid Method (VOF) for the Dynamics of Free Boundaries," J. Comput. Phys. **39**, pp. 201–225.

[6] Brackbill, J. U., Kothe, D. B., and Zemach, C., 1992, "A Continuum Method for Modeling Surface Tension," J. Comput. Phys. **100**, pp. 335–354.

[7] Sethian, J. A., 1999, *Level Set Methods and Fast Marching Methods: Evolving Interfaces in Computational Geometry, Fluid Mechanics, Computer Vision, and Materials Science*, Cambridge University Press, Cambridge, England.

[8] Osher, S., and Fedkiw, R. P., 2001, "Level Set Methods: an Overview and Some Recent Results," J. Comput. Phys. **169**, pp. 463–502.

[9] CFX-4, 2000, AEA Technology, Harwell, Oxfordshire, OX11 0RA, UK.

[10] FIDAP 8.60, 2001, Fluid Dynamics Analysis Package, Fluent Inc., 10 Cavendish Court, Lebanon, NH, 03766, USA.

[11] Rider, W. J., and Kothe, D. B., 1998, "Reconstructing Volume Tracking," J. Comput. Phys. **141**, pp. 112–152.

[12] Barth, T. J., and Sethian, J. A., 1998, "Numerical Schemes for the Hamilton-Jacobi and Level Set Equations on Triangulated Domains," J. Comput. Phys. **145**, pp. 1–40.

[13] Sussman, M., Smereka, P., Osher, S., 1994, "A Level Set Approach for Computing Solutions to Incompressible Two-Phase Flow," J. Comput. Phys. **114**, pp. 146–159.

[14] Sussman, M., and Smereka, P., 1997, "Axisymmetric Free Boundary Problems," J. Fluid Mech. **341**, pp. 269–294.

[15] Sussman, M., and Fatemi, E., 1999, "An Efficient Interface-Preserving Level Set Redistancing Algorithm and its Application to Interfacial Incompressible Fluid Flow," SIAM J. Sci. Comput. (USA) **20**, pp. 1165–1191.

[16] Sussman, M., Almgren, A. S., Bell, J. B., Colella, P., Howell, L. H., and Welcome, M. L., 1999, "An Adaptive Level Set Approach for Incompressible Two-Phase Flow," J. Comput. Phys. **148**, pp. 81–124.

[17] Yu, J.-D., Sakai, S., and Sethian, J. A., 2003, "A Coupled Level Set Projection Method Applied to Ink Jet Simulation," Interfaces Free Boundaries **5**, pp. 459–482.

[18] Chang, Y. C., Hou, T. Y., Merriman, B., and Osher, S., 1996, "A Level Set Formulation of Eulerian Interface Capturing Methods for Incompressible Fluid Flows," J. Comput. Phys. **124**, pp. 449–464.

[19] Tornberg, A.-K., and Engquist, B., 2000, "A Finite Element Based Level-Set Method for Multiphase Flow Applications," Comput. Visual Sci. **3**, pp. 93–101.

[20] Sussman, M., and Puckett, E. G., 2000, "A Coupled Level Set and Volume-of-Fluid Method for Computing 3D and Axisymmetric Incompressible Two-Phase Flows," J. Comput. Phys. **162**, pp. 301–337.

[21] Mulder, W., Osher, S., and Sethian, J. A., 1992, "Computing Interface Motion in Compressible Gas Dynamics," J. Comput. Phys. **100**, pp. 209–228.

[22] Shepel, S. V., 2002, "Numerical Simulation of Filling and Solidification of Permanent Mold Castings," Ph.D. thesis, University of Notre Dame, Notre Dame, IN.

[23] Hetu, J.-F., and Ilinca, F., 1999, "A Finite Element Method for Casting Simulations," Numer. Heat Transfer, Part A **36**, pp. 657–679.

[24] Pillapakkam, S. B., and Singh, P., 2001, "A Level-Set Method for Computing Solutions to Viscoelastic Two-Phase Flow," J. Comput. Phys. **174**, pp. 552–578.

[25] Chessa, J., and Belytschko, T., 2003, "An Enriched Finite Element Method and Level Sets for Axisymmetric Two-Phase Flow with Surface Tension," Int. J. Numer. Methods Eng. **58**, pp. 2041–2064.

[26] Dussan, V. E. B., 1979, "On the Spreading of Liquids on Solid Surfaces: Static and Dynamic Contact Lines," Annu. Rev. Fluid Mech. **11**, pp. 371–400.

[27] Rhie, C. M., and Chow, W. L., 1983, "Numerical Study of the Turbulent Flow Past an Airfoil with Trailing Edge Separation," AIAA J. **21**, pp. 1527–1532.

[28] Van Doormaal, J. P., and Raithby, G. D., 1984, "Enhancements of the SIMPLE Method for Predicting Incompressible Fluid Flows," Numer. Heat Transfer, **7**, pp. 147–163.

[29] Adalsteinsson, D., and Sethian, J. A., 1999, "The Fast Construction of Extension Velocities in Level Set Methods," J. Comput. Phys. **148**, pp. 2–22.

[30] Sussman, M., 2003, "A Second Order Coupled Level Set and Volume-of-Fluid Method for Computing Growth and Collapse of Vapor Bubbles," J. Comput. Phys. **187**, pp. 110–136.

[31] Hughes, T. J. R., Franca, L. P., and Balestra, M., 1986, "A New Finite Element Formulation for Computational Fluid Dynamics: V. Circumventing the Babuska-Brezzi Condition: A Stable Petrov-Galerkin Formulation of the Stokes Flow Problem Accomodating Equal-Order Interpolations," Comput.

Methods Appl. Mech. Eng. **59**, pp. 85–99.
[32] Martin, J. C., and Moyce, W. J., 1952, "An Experimental Study of the Collapse of Liquid Columns on a Rigid Horizontal Plane," Philos. Trans. R. Soc. London **244**, pp. 312–324.
[33] Munz, C.-D., and Maschek, W., 1992, "Comparison of Results of Two-Phase Fluid Dynamics Codes and Sloshing Experiments," Technical Report No. KfK 5091, Kernforschungszentrum Karlsruhe Gmbh, Karlsruhe, Germany.
[34] Meier, M., 1999, "Numerical and Experimental Study of Large Steam-Air Bubbles Injected in a Water Pool," Ph.D. thesis No. 13091, Swiss Federal Institute of Technology Zurich, Zurich, Switzerland.
[35] Bhaga, D., and Weber, M. E., 1981, "Bubbles in Viscous Liquids: Shapes, Wakes, and Velocities," J. Fluid Mech. **105**, pp. 61–85.
[36] Ginzburg, I., and Wittum, G., 2001, "Two-Phase Flows on Interface Refined Grids Modeled With VOF, Staggered Finite Volumes, and Spline Interpolants," J. Comput. Phys. **166**, pp. 302–335.
[37] Koh, C. J., and Leal, L. G., 1990, "An Experimental Investigation on the Stability of Viscous Drops Translating Through a Quiescent Fluid," Phys. Fluids A **2**(12), pp. 2103–2109.
[38] Tomiyama, A., Sou, A., Zun, I., Sakaguchi, T., 1994, "Three-Dimensional Detailed Numerical Simulation of Bubbly Upflow in a Vertical Square Duct," *Proc. German-Japanese Symp. on Multi-Phase Flow*, Karlsruhe, Germany, U. Müller, T. Saito, and K. Rsut, eds., Kernforschungszentrum, pp. 487–497.

M. A. M. Al Khatib[1]
e-mail: alkhatibm@yahoo.com
HBCC, Department of Mathematical Sciences,
King Fahd University of Petroleum & Minerals,
P.O. Box 5087,
Dhahran, Saudi Arabia

S. D. R. Wilson
e-mail: simondrw@btinternet.com
10 Belfield Road,
Didsbury Manchester M20 6BH, UK

Slow Dripping of Yield-Stress Fluids

The dripping problem of a viscoplastic (yield-stress) liquid running slowly out of a narrow vertical tube is considered. The volume of the drops which break away is determined. A Lagrangian coordinate system is used to analyze the extension of the thread as it sags under its own weight, neglecting inertia and capillarity. The biviscosity model has been used to characterize viscoplastic fluids; the Newtonian and Bingham models can be recovered as limiting cases. The Bingham limit is of special interest.
[DOI: 10.1115/1.1949633]

Keywords: Bingham Model, Viscoplastic Fluids, Slow Dripping, Biviscosity Model

1 Introduction

Dripping and drop formation have practical applications ranging from separation processes in the chemical and petrochemical industries to more modern ones, such as ink-jet printing and microarraying [1–3]. Theoretical, experimental, and computational studies of the dripping problem have been presented by many authors see, for example, [4–9].

In the present work it is supposed that a liquid runs out of the open end of a narrow tube pointing vertically downward. Various flow regimes may be established, a continuous jet, for example, or a sequence of slowly growing pendant drops. Both these regimes have been extensively studied [10–12].

We are interested in determining droplet sizes of a viscous fluid in the situation where the flow rate is neither large nor small, but somewhere in between, so that it cannot form a jet. Instead, a drop forms and grows slowly into a short thread or column; this thread stretches under its own weight and snaps off. Then the upper part recoils fairly rapidly to form a new drop, and the process repeats so that a periodic dripping process will be seen. This was done for the Newtonian liquid by Wilson [7] The purpose of the present paper is to extend that work to the case of fluids exhibiting a yield stress (viscoplastic liquids).

For the rheological description of the fluid we shall use the so-called biviscosity model. This is a simple generalization of the well-known Bingham model in which the unyielded material is supposed to behave as a Newtonian liquid of "large" viscosity, and is one that avoids certain indeterminacies that stem from the assumption (in the Bingham model) of absolute rigidity. The model has been critically discussed by Barnes and Walters [13] who show that it accords with the real behavior at least as well as the Bingham model. It has the advantage of being relatively easy to handle, analytically. Typical materials described by this model are wet concrete, soft foods, greases, and gels.

To our knowledge this is the first use of models of this type in this problem. Note that the fluid has a yield stress but no memory, and an important theoretical interest is to locate and track the yield surface.

As in Wilson [7] a simple quasi-one-dimensional approach is used. The balance of forces is between gravity and longitudinal viscous stresses. Capillarity and inertia are neglected. The approximation will fail near the bottom of the thread and probably during the recoil process, but again the breakaway volume will not be much affected.

[1]Corresponding author.

Contributed by the Fluids Engineering Division for publication in the JOURNAL OF FLUIDS ENGINEERING. Manuscript received by the Fluids Engineering Division July 9, 2004; Final manuscript received April 3, 2005. Associate Editor: Dennis Siginer.

2 Analysis

Now we deal with our problem by analyzing the motion from the instant when a thread of liquid first emerges from the tube and extends downward, stretching somewhat under its own weight. We continue up to the time when the first drop falls away, then we estimate the size of the first drop, which is part of our interest. We then turn to the periodic dripping motion, which is established after a time.

We shall adopt the procedures and notations used by Wilson [7] for the Newtonian fluid, where a Lagrangian coordinate system is employed. We label the fluid particles by the time T at which they emerged from the tube. Thus if t is the present time, we have $0 \leqslant T \leqslant t$, with $T=0$ on the bottom end of the thread and $T=t$ on the fluid element, which is emerging at the present instant (see Fig. 1).

Let $X(T,t)$ be the distance below the orifice of a typical particle P, labeled by T, at time t, and let $A(T,t)$ be its cross-sectional area. We suppose that the volume flow rate Q is constant. Then considering two neighboring elements T and $T+dT$, the equation of conservation of volume reads

$$Q\,dT = -A\,dX$$

i.e.,

$$A\frac{\partial X}{\partial T} = -Q \tag{1}$$

Next we consider the force balance on the fluid between T and $T+dT$, denoting longitudinal stress by $S(T,t)$. (The sign convention here is that positive S corresponds to tension.) We find

$$(SA)_T - (SA)_{T+dT} - \rho g A\,dX = 0 \tag{2}$$

Thus,

$$\frac{\partial}{\partial T}(SA) = -\rho g A\frac{\partial X}{\partial T} = \rho g Q \tag{3}$$

which can be integrated to give

$$SA = \rho g Q T \tag{4}$$

because $S=0$ at $T=0$. Of course, this equation has a simple interpretation that the longitudinal force at P equals the weight of all the fluid below.

Capillarity was included in the equations of motion by Wilson [7], who showed that its importance is measured by the dimensionless parameter $\gamma(\mu\rho g Q)^{-1/2}$. We are supposing that this is very small. For example, with $\gamma = 5\times10^{-4}$ kg s^{-2}, $\mu = 10^5$ Pa s (see Fig. 3 in [13]), $\rho = 1\times10^3$ kg m^{-3} and $Q = 1\times10^{-4}$ m^3/s, we find $\gamma(\mu\rho g Q)^{-1/2} = 5\times10^{-6}$.

Now we select the biviscosity model to characterize viscoplastic fluids. This model assumes that the material behaves as a New-

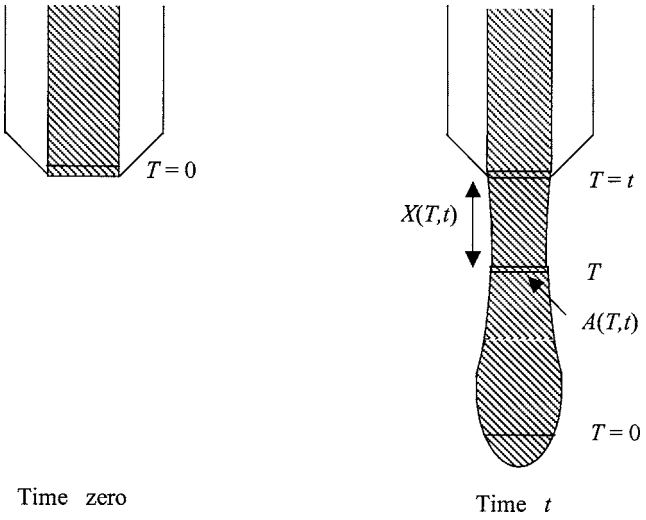

Fig. 1 Sketch indicating the coordinate system

tonian fluid with very large viscosity until the critical "yield stress" is exceeded. Above the yield stress, the material has a rapidly decreasing viscosity (see, for example, [14–16]). Thus,

$$\tau_{ij} = 2\eta_1 e_{ij}; \quad \frac{1}{2}\tau_{ij}\tau_{ij} < \tau_1^2$$

$$\tau_{ij} = 2\eta_2 e_{ij} + \frac{\tau_o}{(2e_{ij}e_{ij})^{1/2}} e_{ij}; \quad \frac{1}{2}\tau_{ij}\tau_{ij} > \tau_1^2 \tag{5}$$

where τ_{ij} is the deviatoric stress tensor, e_{ij} is the strain rate tensor, and τ_o and τ_1 are two distinguished stresses (see Fig. 2). The stresses are related by

$$\tau_o = \tau_1(1-\epsilon) \tag{6}$$

where ϵ is the dimensionless ratio η_2/η_1, and the Bingham model is approached in the limit $\epsilon \to 0$ ($\epsilon = 1$ gives the Newtonian case). Barnes and Walters [13], by using an accurate rheometer, give experimental evidence that shows some flow of viscoplastic liquids can occur at stresses less than the yield stress, and they found that these liquids demonstrate (approximately) Newtonian behavior in this region, with a very large viscosity. These results motivate the use of biviscosity model to characterize viscoplastic fluids.

We continue the theory for the biviscosity model. The longitudinal stress is given by

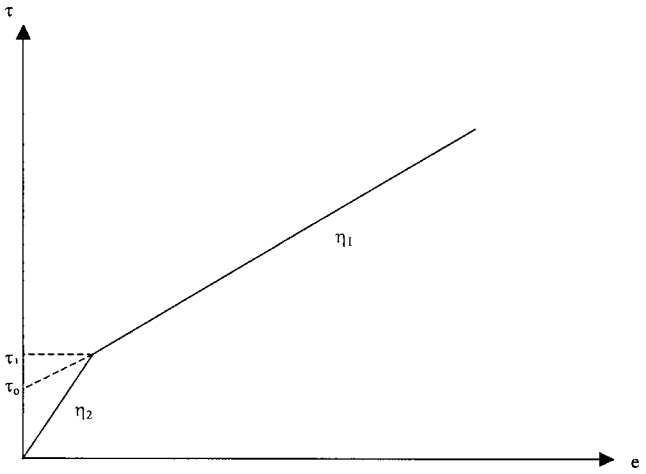

Fig. 2 Biviscosity model with τ as tress and ϵ as strain

$$S = 3\eta_1 a; \quad \frac{1}{2}\tau_{ij}\tau_{ij} < \tau_1^2$$

$$S = \left(\eta_2 + \frac{\tau_o}{\sqrt{3a}}\right)3a; \quad \frac{1}{2}\tau_{ij}\tau_{ij} > \tau_1^2 \tag{7}$$

where $a(t) = -\dot{A}/A$. (The strain rate for a fluid cylinder of length $L(t)$ is $\dot{L}/L$ which is the same as $-\dot{A}/A$.)

As the first part of the emerged liquid will be unyielded, that is, Newtonian with viscosity η_1, we combine Eq. (4) and (7) as follows:

$$3\eta_1 a = \frac{\rho g Q T}{A}$$

i.e.,

$$\frac{\partial A}{\partial t} = -\frac{\rho g Q T}{3\eta_1} \tag{8}$$

By integrating (8) we get

$$A = A_o - \frac{\rho g Q}{3\eta_1}(Tt - T^2) \tag{9}$$

where A_o is the tube cross-sectional area and the initial condition

$$A = A_o \text{ at } t = T \tag{10}$$

has been used. Equation (9) represents the cross-sectional area of the unyielded part of the thread.

Next we have to find the cross-sectional area of the yielded part of the thread. The yield criterion will be satisfied sooner or later on any fluid particle because A decreases and, thus, S increases (from (4)). But it is not clear which element yields first. This problem will be discussed later in this section. Using the yield criterion, $(1/2)\tau_{ij}\tau_{ij} = \tau_1^2$, and Eq. (5), we get

$$\eta_1 \sqrt{3a} = \tau_1 \tag{11}$$

Equations (8) and (11) may be combined to give

$$A = \frac{\rho g Q T}{\sqrt{3}\tau_1} \tag{12}$$

where A is the area of the fluid element T when it reaches the yield point. From (9) and (12), we get

$$\frac{\rho g Q T}{\sqrt{3}\tau_1} = A_o - \frac{\rho g Q}{3\eta_1}(Tt - T^2) \tag{13}$$

By scaling A with A_o and t and T with $(A_o\eta_2/\rho g Q)^{1/2}$, the dimensionless form of (12) and (13), respectively, is given by

$$A = kT \tag{14}$$

$$kT = 1 - \frac{\epsilon}{3}(Tt - T^2) \tag{15}$$

where $k = (1/\tau_1)(\rho g Q \eta_2/3A_o)^{1/2}$.

Summing this up, for the fluid element T (14) gives the area when it reaches the yield point and (15) gives the time t. And as $T \leqslant t$, then the diagram of (15) will be as shown in Fig. 3.

In Fig. 3, the curve of (15) divides the region, bounded by $T \leqslant t$ and $t \geqslant 0$, into two parts. The shaded part represents all the points (t,T) for which the fluid is unyielded, whereas the unshaded part represents all the points (t,T) for which the fluid is yielded.

We can understand this in the following way. The history of any particular fluid element T consists of a line parallel to the t axis, beginning on $T=t$ and proceeding to the right. Initially $A=1$ of course. The two curves in Fig. 3 intersect at $T=1/k$. For a fluid element for which $T<1/k$, which is on the sector OC, $A>kT$ and the fluid is below the yield point. As t increases, A decreases and

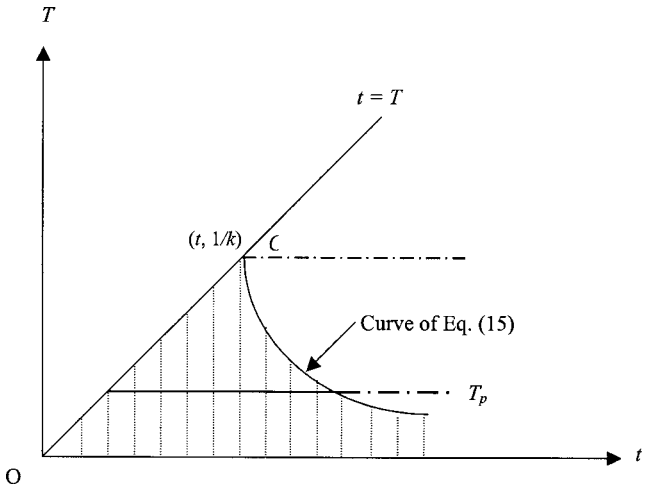

Fig. 3 Diagram of Eq. (15) with T_p a typical history of a fluid element.

the fluid element yields at the value of t corresponding to the curve (15). For elements where $T>1/k$, which is beyond C, the fluid emerges already yielded.

This implies that the area of the fluid element at the yield point is given by

$$A=1, \quad t=T \quad kT>1$$

$$A=kT, \quad t=T+\frac{3}{\epsilon T}(1-kT) \quad kT<1 \tag{16}$$

(see Fig. 3).

Now, we find the cross-sectional area of the yielded part of the thread; that is, when $(1/2)\tau_{ij}\tau_{ij}>\tau_1^2$. From (4) and (7), we get

$$\left(\eta_2+\frac{\tau_o}{\sqrt{3a}}\right)3a\,.\,A=\rho gQT$$

that is,

$$\dot{A}-\frac{\tau_o}{\sqrt{3}\,\eta_2}A=-\frac{\rho gQT}{3\eta_2} \tag{17}$$

The dimensionless form of (17) is given by

$$\dot{A}-lA=-\frac{1}{3}T \tag{18}$$

where $l=\tau_o(A_o/\rho gQ\eta_2)^{1/2}$. Note that $3lk=(1-\epsilon)$. Since (18) applies only after the yield point has been reached, the initial condition is not $A=1$ on $t=T$ in all cases but is given by (16). So we get

$$A=\left(1-\frac{T}{3l}\right)\exp[l(t-T)]+\frac{T}{3l}, \quad kT>1$$

$$A=\left(k-\frac{1}{3l}\right)T\exp\left[-l\left(T+\frac{3}{\epsilon T}(1-kT)-t\right)\right]+\frac{T}{3l}, \quad kT<1 \tag{19}$$

Now we want to discover which element shrinks to zero first (T_c) and the time at which this occurs (t_c). Of course, this will not happen in the unyielded part of the thread because the longitudinal stress $S(T,t)$ will exceed the yield stress τ_1 before the element snaps. This is clear from (7) and (11) ($\eta_1 3a>\eta_1\sqrt{3}a=\tau_1$). This means that the element that shrinks to zero first must belong to the yielded part of the thread where we have two cases.

When $kT>1$, from (19) we set $A=0$ and combine the resulting equation with its derivative with respect to T to get

$$T_c=U \tag{20}$$

and

$$t_c=U+\frac{1}{l}\ln\left(\frac{U}{U-3l}\right) \tag{21}$$

where $U=(3l+\sqrt{9l^2+12})/2$.

When $kT<1$, from (19) with similar steps as above we get

$$T_c=\sqrt{\frac{3}{\epsilon}} \tag{22}$$

and

$$t_c=\sqrt{\frac{3}{\epsilon}}+\sqrt{\frac{\epsilon}{3}}-\frac{3k}{\epsilon}+\frac{1}{l}\ln\left(\frac{1}{1-3kl}\right) \tag{23}$$

Now we have to decide which value of T_c is smaller, whether it is the value in (20) or that in (22). In fact, it depends on the values of ϵ and k. For many engineering materials of yield stress type, the value of ϵ is $<10^{-2}$. Thus, it appears that, in practice, the smaller value of T_c is given by (20).

3 Periodic Dripping

Now we consider periodic dripping. Suppose we set $t=0$ at the instant when a drop breaks away. At this instant, the fluid element just emerging is labeled $T=0$ and the fluid element at the bottom of the remaining thread is labeled $T=-T_o$, which is to be determined (see Fig. 4). We have to replace (4) by

$$SA=\rho gQ(T+T_o) \tag{24}$$

and then proceed almost exactly as above until we get

$$A=\left(1-\frac{T+T_o}{3l}\right)\exp[l(t-T)]+\frac{T+T_o}{3l}, \quad r>1$$

$$A=\left(r-\frac{1}{3l}\right)(T+T_o)\exp\left\{-l\left[T+\frac{3}{\epsilon}\left(\frac{1}{T+T_o}-k\right)-t\right]\right\}+\frac{T+T_o}{3l}, \quad r<1 \tag{25}$$

where $r=k(T+T_o)$.

Suppose t_s is the time at which the new drop breaks away and that it does so at the element T_s; then the volume left behind is t_s-T_s. If the dripping is periodic, then this volume must equal T_o, so that what is left behind each drop here will be the same as what was left behind the first drop. Hence,

$$t_s-T_s=T_o$$

or

$$t_s=T_s+T_o \tag{26}$$

Again we want to discover which element shrinks to zero first (T_s) and the time at which this occurs (t_s). In other words we have to find T_o. Once again we have two cases.

When $k(T+T_o)>1$, by using (25) and (26) we get, instead of (20) and (21),

$$T_s=U-\frac{1}{l}\ln\left(\frac{U}{U-3l}\right) \tag{27}$$

and

$$t_s=U \tag{28}$$

where

$$T_o=\frac{1}{l}\ln\left(\frac{U}{U-3l}\right) \tag{29}$$

When $k(T+T_o)<1$, by using (25) and (26) we get, instead of (22) and (23),

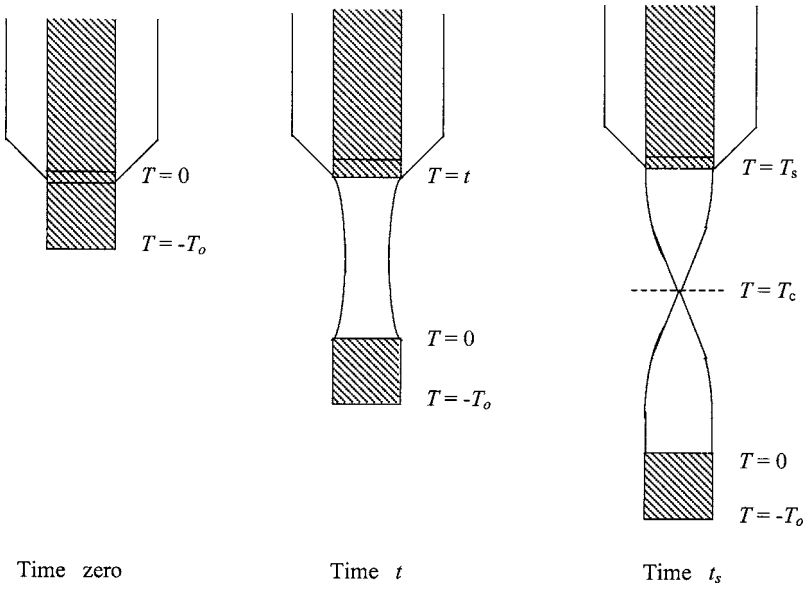

Fig. 4 Sketch indicating periodic dripping

$$T_s = \frac{3k}{\epsilon} - \frac{1}{l}\ln\left(\frac{1}{1-3kl}\right) \tag{30}$$

and

$$t_s = \sqrt{\frac{3}{\epsilon}} \tag{31}$$

where

$$T_o = \sqrt{\frac{3}{\epsilon}} - \frac{3k}{\epsilon} + \frac{1}{l}\ln\left(\frac{1}{1-3kl}\right) \tag{32}$$

Again because of the assumption $\epsilon < 10^{-2}$, the value of t_s in (28) is smaller than that in (31). This implies that the value of T_o is that which is given in (29), and the drips have volume $t_s = U = (3l + \sqrt{9l^2+12})/2$.

4 Concluding Remarks

1. The thread of a biviscosity fluid that runs out of the tube ruptures only in its yielded part.
2. The volume of the drops T_c and the period of the periodic dripping T_o of the biviscosity fluid depend on the values of ϵ and k. And if we take $\epsilon < 10^{-2}$, as the case of many engineering materials of yield stress, then

$$T_c = U = (3l + \sqrt{9l^2+12})/2$$

and

$$T_o = (1/l)\ln[U/(U-3l)]$$

T_c and T_o are given in dimensional form by

$$T_c = U = [3\tau_o(A_o/\rho g Q \eta_2)^{1/2} + \sqrt{(9\tau_o^2 A_o/\rho g Q \eta_2) + 12}]/2$$

and

$$T_o = (\rho g Q \eta_2/\tau_o^2 A_o)^{1/2}\ln\{U/[U - 3\tau_o(A_o/\rho g Q \eta_2)^{1/2}]\}$$

Acknowledgments

The authors are grateful to HBCC and King Fahd University of Petroleum & Minerals for their continuous help and support and to the referees for their useful comments.

References

[1] Rezanka, I., and Eschbach, R., 1996, *Recent Progress in Ink Jet Technologies*, IST Press, Springfield, VA.
[2] Pappen, R., 1998, *Procee. of IBC Int. Conf. on Massively Parallel DNA Analysis*, San Francisco.
[3] Heideger, W. J., and Wright, M. W., 1986, AIChE J. **32**, p. 1372.
[4] Ambravaneswaran, B., Phillips, S. D., and Basaran, O. A., 2000, "Theoretical Analysis of a Dripping Faucet," Phys. Rev. Lett., **85**, pp. 5332–3325.
[5] Wilkes, E. D., Phillips, S. D., and Basaran, O. A., 1999, "Computational and Experimental Analysis of Dynamics of Drop Formation," Phys. Fluids **11**, pp. 3577–3598.
[6] Chen, A. U., Notz, P. K., and Basaran, O. A., 2002, "Computational and Experimental Analysis of Pinch-off and Scaling," Phys. Rev. Lett. **88**, pp. 174501–174504.
[7] Wilson, S. D. R., 1999, "The Slow Dripping of a Viscous Fluid," J. Fluid Mech. **190**, pp. 561–570.
[8] Fuchikami, N., Ishioka, S. and Kiyono, K., 1999, "Simulation of a Dripping Faucet," J. Phys. Soc. Jpn. **68**, pp. 1185–1196.
[9] Coullet, P., Mahadevan, L. and Riera, C., 2000, "Return Map for the Chaotic Dripping Faucet," Prog. Theor. Phys. Suppl. **139**, pp. 507–516.
[10] Renardy, M., 1994, "Some Comments on the Surface-Tension Driven Break-up (or the Lack of it) of Viscoelasticets," J. Non-Newtonian Fluid Mech. **51**, pp. 97–107.
[11] Renardy, M., 1995, "A Numerical Study of the Asymptotic Evolution and Breakup of Newtonian and Viscoelastic Jets," J. Non-Newtonian Fluid Mech. **59**, pp. 267–282.
[12] Eggers, J., 1997, "Nonlinear dynamics and breakup of free-surface flows," Rev. Mod. Phys. **69**(3), pp. 865–929.
[13] Barnes, H. A., and Walters, K., 1985, "The Yield Stress Myth?" Rheol. Acta **24**(4), pp. 323–326.
[14] Beverly, C. R., and Tanner, R. I., 1992, "Numerical Analysis of Three Dimensional Bingham Plastic Flow," J. Non-Newtonian Fluid Mech. **42**, pp. 85–115.
[15] Wilson, S. D. R., 1993, "Squeezing flow of a Bingham material," J. Non-Newtonian Fluid Mech. **47**, pp. 211–219.
[16] Al Khatib, M. A. M., 2003, "The Stretching of a Viscoplastic Thread of Liquid," ASME J. Fluids Eng. **125**, pp. 946–951.

M. Coussirat
e-mail: coussirat@mf.upc.es
CDIF, Dept. Mec. de Fluïds,
Universidad Politècnica de Catalunya,
Av. Diagonal 647, 08028 Barcelona, Spain

J. van Beeck
von Kármán Institute for Fluid Dynamics,
Belgium

M. Mestres
Instituto de Ingeniería del Agua y Medio Ambiente,
Universidad Politècnica de Valencia, Spain

E. Egusguiza
CDIF, Dept. Mec. de Fluïds,
Universidad Politècnica de Catalunya,
Av. Diagonal 647, 08028 Barcelona, Spain

J.-M. Buchlin
von Kármán Institute for Fluid Dynamics,
Belgium

X. Escaler
CDIF, Dept. Mec. de Fluïds,
Universidad Politècnica de Catalunya,
Av. Diagonal 647, 08028 Barcelona, Spain

Computational Fluid Dynamics Modeling of Impinging Gas-Jet Systems: I. Assessment of Eddy Viscosity Models

Computational fluid dynamics plays an important role in engineering design. To gain insight into solving problems involving complex industrial flows, such as impinging gas-jet systems (IJS), an evaluation of several eddy viscosity models, applied to these IJS has been made. Good agreement with experimental mean values for the field velocities and Nusselt number was obtained, but velocity fluctuations and local values of Nusselt number along the wall disagree with the experiments in some cases. Experiments show a clear relation between the nozzle-to-plate distance and the Nusselt number at the stagnation point. Those trends were only reproduced by some of the numerical experiments. The conclusions of this study are useful in the field of heat transfer predictions in industrial IJS devices, and therefore for its design. [DOI: 10.1115/1.1949634]

Keywords: CFD, Eddy Viscosity, Heat Transfer, Impinging Jet, Numerical Modeling, RANS Turbulence Model, Velocity Field

1 Introduction

Heating or cooling of large surface products is often carried out in devices called impinging jets systems (IJS). These devices consist of a single round or slot nozzle (SRN and SSN, respectively), through which air or another fluid impinges, in a tilted or vertical direction, on a product surface (see Fig. 1). Frequently, the nozzles are arranged forming an array. Such impinging flow devices allow relatively high heat transfer rates.

Jet impingement is one of the oldest and most attractive techniques for convective process intensification where convective heating, cooling, or drying is applied. In order to achieve a suitable device design, both from an economic and a technical viewpoint, knowledge about the dependence of the heat and mass transfer rates on the external variables is required. The gas flow rate, the turbulence characteristics at the nozzle, the angle of impingement, the diameter (or slot width) of the nozzles, their spacing, and their distance to the product surface are the main variables, which can be chosen to identify the Nusselt or Stanton number for a given heat or mass transfer problem. It is essential that the effects of these important parameters are identified and understood, and to do so, both extensive experimental and computational fluid dynamics (CFD) tests have been carried out.

Because of the industrial applications of these devices, most of the experimental studies related to IJS deal with heat transfer phenomena along the wall. Experimental data about mean and fluctuating velocity fields are more difficult to find. Reviews of experimental fluid dynamic databases (e.g., [1,2] clearly point out the lack of suitable experimental data and show that, for a better understanding of the jet impingement heat transfer process, details of the turbulent flow and thermal fields are required. A very important parameter in order to quantify this process is the heat transfer coefficient. Experimental results of the local heat transfer coefficient h along the wall (including values at the stagnation point h_0) can be found for a SRN jet (e.g., [3,4], see Fig. 5) and for a SSN jet (e.g., [5], see Fig. 10).

These results showed several interesting phenomena such as higher levels of h for higher Re_0, the existence of a maximum in the variation of h_0 when the nozzle-to-plate distance H is changed, and several secondary peaks in the distribution of h along the wall. Moreover, in order to quantify the effects of the various parameters that influence the industrial design, numerical analysis is very useful because of the technological and economical difficulties in performing laboratory or field experiments.

Over the last years, CFD using Reynolds-averaged Navier-Stokes (**RANS**) equations, coupled with some kind of turbulence modeling, has become a standard industrial simulation tool for the design, analysis, performance determination, or investigation of engineering systems involving fluid flows. The spread in the use of CFD has been driven by the availability of in-house or commercial software and by the massive increase in available computer speed and memory capacity, leading to the reduction of simulation costs compared to physical prototypes and model experiments. The CFD model approach that the user must choose to obtain reliable results will depend on how much of the flow physics is wanted to recover. The CFD analysis on the basis of the RANS equations, with a suitable turbulence model, will most probably form the basis of most industrial engineering flow calculations for the next many years. Although modeling by large eddy simulations (LES), or direct numerical simulations (DNS) is becoming more affordable nowadays, it is still far from common in industrial applications. The RANS solutions will still be used for industrial design explorations; therefore, dealing with the uncertainty arising from the RANS equations with EVM schemes is a current problem. Several of these schemes have been evaluated to gain insight into EVM schemes and their application to a complex industrial flow, such as IJS for cooling metal plates. Modeling of IJS devices is a challenge for the actual commercial CFD packages because many of the particular flow characteristics that

Contributed by the Fluids Engineering Division for publication in the JOURNAL OF FLUIDS ENGINEERING. Manuscript received by the Fluids Engineering Division July 21, 2004; final manuscript received April 19, 2005. Associate Editor: Surya P Vanka

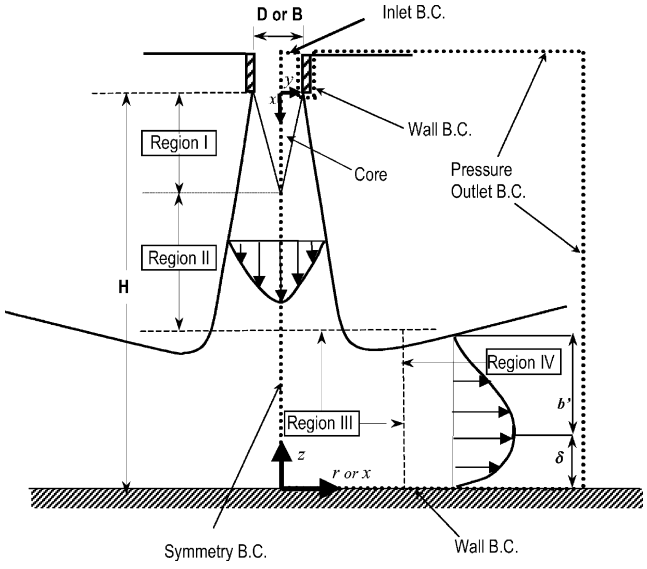

Fig. 1 Characterization of impinging jets for single round nozzle (SRN) jet or single slot nozzle (SSN) jet

generate strong exchanges of mass, momentum, and heat are not easy to capture (e.g., transition flow and turbulence development, a stagnation point flow with strong streamline curvature, wall jet and entrainment of surrounding low velocity flow, see [2] for details).

A revision of actual impinging jets numerical databases shows a broad range of modeled cases, usually focused on the prediction of heat transfer rates. The results reported by different numerical studies, including modeling at several Reynolds numbers (Re_0), and different nozzle-to-plate ratios (H/D for round jets, and H/B for slot jets), show big variations among them, and also disagreement with experimental results. However, no extensive turbulence modeling comparison was found for any of those cases. In most of those numerical databases (some of them are cited below), one or two turbulence models were compared, and the near-wall treatment was confined to the use of standard wall functions or damping functions. More in detail, only high and low Reynolds standard k-ε models were extensively checked (e.g., see [6–10]). For impinging jets, comparisons between a low Reynolds version of the standard k-ε with other types of EVM are scarce, but some studies can be found; for example, the comparative studies from Behnia et al. [11,12]. The last of the aforementioned works deals with a comparative exercise between the Standard k-ε model and the four-equation model from Durbin [13] (V2F model), but only SRN jet cases were examined. A one-equation turbulence model developed by Spalart and Allmaras [14] produces promising results in several cases of parallel flow, but applications of this model to IJS flow have not yet been used extensively. Concerning the second-order models (RSM), some modeling of this kind of flow has been made (e.g, [7,15]), and the obtained results showed that RSM only gave slightly better results than the EVM.

It is interesting to note that the experimental results also show that the inlet turbulence intensity level I plays an important role in the predictions of heat exchange along the wall. However, previous works [8,14,16] point out that the majority of RANS turbulence models appear to be insensitive to changes in I, although the V2F model has given some encouraging results for SRN cases [11,12]. More recently, a work from Shi et al. [15] showed numerical results for confined **SSN** jet cases, but for low Reynolds numbers (higher $Re \simeq 10,000$). In the majority of the cases, the flow is a transitional flow [17,18]. Results reported by Shi et al. show modest changes in Nu_0 when the inlet I level was changed between $2\% < I < 10\%$. On the other hand, changes in the turbulence length scale show a greater impact on Nu_0.

Summarizing, all the aforementioned details reveal that the flow in IJS is a very difficult test for EVM due to its characteristics. Industrial design of three-dimensional IJS devices remains a big challenge for the CFD tool. No clear conclusion about which model is best can be extracted from the available numerical experiments. Another difficulty is to ensure the level of uncertainty of the CFD results, because there are only detailed experimental databases under laboratory conditions. Experimental test cases oriented to industrial IJS cases are more difficult to find. More sophisticated numerical experiments, useful for EVM calibration, are available only for a few two-dimensional test cases, e.g., SSN cases, but at low Reynolds number (higher $Re \simeq 10,000$), modeled by LES (see, e.g., [19–21]). The work of Hoffman [19], uses $Re = 10,000$ and $H/B = 20$, the work from Voke and Gao [20] uses $Re = 6,500$ and $H/B = 7.22$, and the work of Cieszla et al. [21] uses $5800 < Re < 10,000$ and $8 < H/B < 12$. Results obtained by these researchers reinforce the idea that, in general, the LES studies deal with cases having low Reynolds number and, sometimes, high H/B ratios. On the other hand, no IJS cases modeled by means of the DNS strategy were found. Therefore, computational resources for LES or DNS for high Reynolds number are not actually available for industrial applications [16].

The main motivation of this work is to learn about the capabilities of RANS with EVM for turbulence in the CFD computations applied to the design of IJS cooling devices. The enlargement of the present numerical databases, and extending the number of turbulence models used and the test cases simulated in the aforementioned references, is another interesting result, which is ensured because it is not easy to find extensive test cases that compare the application of different turbulence models to the same IJS case, nor test cases with numerical experiments containing extensive sensitivity studies associated to parameters that strongly influence the flow behavior (e.g., H/D ratio, inlet turbulence parameters, or Re).

The following sections show the procedure developed for all the cases modeled, and the results obtained. Finally, conclusions concerning the possibilities of EVM in industrial IJS computations are given.

2 Classification of Applied Turbulence Models

A good knowledge of the influence of turbulence is of vital importance in heat transfer predictions for impinging jets cases. It is of paramount importance to know which turbulence model is the most adequate to compute mean and local values of heat transfer coefficients in the design of cooling and heating jet devices. The system of equations used is constituted by the Reynolds-averaged continuity, momentum, and energy equations. The Reynolds-averaging technique leads to transport equations for mean quantities (velocity u and passive scalar c)

$$\frac{\partial \rho}{\partial t} + \frac{\partial}{\partial x_j}(\rho\, u_j) = 0 \tag{1}$$

$$\frac{\partial u_i}{\partial t} + u_j \frac{\partial u_i}{\partial x_j} = -\frac{1}{\rho}\frac{\partial p}{\partial x_i} + \frac{\mu}{\rho}\frac{\partial^2 u_i}{\partial^2 x_j} - \frac{1}{\rho}\frac{\partial}{\partial x_j}(\rho\, \overline{u_i' u_j'}) + f_i \tag{2}$$

$$\frac{\partial c}{\partial t} + u_i \frac{\partial c}{\partial x_i} = \alpha \frac{\partial^2 c}{\partial x_i^2} - \frac{\partial}{\partial x_i}(\overline{u_i' c'}) + f_c \tag{3}$$

The influence of the turbulence is accounted for by using turbulence models that compute the averaged correlation of fluctuations $\overline{u_i' u_j'}$ by means of transport equations. More details and an extensive list of references with a complete description of these equations can be found in reference [2].

The general philosophy of introducing a higher number of transport equations for fluctuating quantities should imply a more realistic flow description, leading to a more general model. The research on this subject has led to the development of several

classes of eddy viscosity turbulence models for closing the RANS equations. Currently, this issue remains an open matter.

Often, the turbulence models are classified according to the number of differential transport equations for turbulent quantities that they solve. The following classification scheme was made taking into account only the models used in this work:

- ***One-equation model:*** Spalart-Allmaras model [14]. This model solves a differential transport equation for the turbulent viscosity. The turbulent variable modeled is the effective viscosity, $\nu_{eff}=\nu_T+\nu$.
- ***Two-equation models:*** The Standard k-ε model [22] and two variants of it (RNG k-ε [23] and realizable k-ε [24]). The standard k-ω model is also used [25,26]. These models solve two differential transport equations. For the k-ε family of models, the variables modeled are the turbulent kinetic energy k and its rate of dissipation ε. For the k-ω model, k and the specific dissipation rate ($\omega=\varepsilon/k$) are modeled.
- ***Four-equation model:*** V2F model [13]. This model may be thought of as a simplification of a full second-order closure model. It uses the $\overline{v'^2}$ component of the turbulent velocity instead of the turbulent kinetic energy $k^{1/2}$ as a velocity scale. It has four differential equations. Two of these equations are similar to the k-ε model transport equations, (k and ε equations). A third differential transport equation is included for the scale of the velocity component responsible for turbulent transport $\overline{v'^2}$, and an elliptic operator (the fourth equation) is considered to compute a term that is analogous to the pressure-strain correlations, denoted by f. This last equation introduces wall effects and, therefore, the use of wall or damping functions is not necessary.

The EVM is currently the most extended (usually, the unique) option for industrial turbulent flow modeling nowadays, but its strategy considers an isotropic eddy viscosity. The limitations of these eddy viscosity models stem largely from the turbulence being represented by its kinetic energy, which is a scalar, and from the eddy viscosity assumption [27]. The former does not correctly represent turbulence anisotropy. The latter assumes an instantaneous equilibrium between the Reynolds stress tensor and the mean rate of strain. This assumption forces the alignment of the mean axis of $\overline{u_i'u_j'}$ and the main rate of deformations $S_{ij}=\frac{1}{2}(\partial u_i/\partial x_j+\partial u_j/\partial x_i)$, which is correct in cases of pure stress, but not so in flows with mean vorticity. Walls are the main source of vorticity and turbulence, because in these regions, large gradients of velocity (and temperature) exist and the momentum transport is more vigorous [28].

Anisotropy exists in all real flows. In general, EVM are designed to represent shear stress anisotropy, but not normal stress anisotropy [27] because the kinetic energy is computed assuming that normal fluctuations are the same in all directions. To take into account the nonisotropic nature of turbulence in near-wall regions, a near-wall treatment is necessary. Several attempts were made to fix these problems, among which is the V2F model from Durbin [13,29–31]. This model tries to correct the EVM weakness by defining the eddy viscosity with a different time scale. Additionally, the wall blocking is considered in a deeper way (see more details in Refs. [13,27,29–31]).

2.1 Near-Wall Treatment. In IJS flows, the terms corresponding to shear stresses are not small, and the turbulent viscosity becomes anisotropic. To take into account the nonisotropic nature of turbulence in near-wall regions, the isotropic turbulence models have been refined in several forms using wall functions (WF), damping fuctions (DF), or a two-layer model (TLM). The TLM [32] replaces the inconsistent and improperly behaved ε equation in the near-wall layer, changing the length scale model [33]; therefore, this model is more adequate than DF or WF even though larger computational resources in terms of CPU time are necessary due to mesh requirements (sometimes finer meshes are necessary for a suitable convergence). The Spalart-Allmaras model implementation employed here uses either DF or WF, the k-ω model uses only DF, and the k-ε family (and RSM) uses either a TLM or WF. The V2F model has a more sophisticated near-wall modeling because the wall influence is accounted for by the model itself. The application of one of these strategies is defined by analyzing the y^+ values along the wall. The strategy used depends on the y^+ value obtained; therefore, it is necessary to perform a preliminary computation to know such values. Previous computations can be made with the Spalart-Allmaras model because the near-wall treatment changes automatically, depending on the values computed for y^+, and the suitable near-wall treatment can be defined afterwards.

Applications of the above models to several IJS configurations were performed, including a comparison of the local and mean Nusselt numbers against experimental data, and the mean numerical Nusselt number against empirical Nusselt correlations [34].

3 Numerical Results

The IJS flow is a complex flow for numerical modeling due to the aforementioned characteristics. Flow and heat and mass transfer show a complex behavior that is not easy to model by means of CFD codes. Some of these characteristics, such as the particular distribution of the heat transfer along the wall or the inlet flow turbulence influence on the heat transfer distribution, are detailed below. Experimental evidence [33,35] confirms that, in single impinging jet systems, there is a secondary peak in the Nusselt number profile along the wall for low H/D or H/B (SRN or SSN jet cases, respectively) ratios. Experiments for SSN jet cases [5] also show the influence of the prescribed inlet turbulence level on the Nusselt number at the stagnation point and on the Nusselt number profile along the wall. This physical evidence of the link between the Nu_0, the secondary Nusselt peak, and the I levels at the wall was numerically checked with all the aforementioned EVM models changing the nozzle-to-plate-ratio, the Reynolds number, or the inlet intensity level.

The first step was to select the suitable experimental databases for SRN [35] and SSN [5] jets cases to check the capabilities of the CFD tool under clearly defined conditions (geometry, boundary condition, uncertainty in the experimental measurements, etc.). The computations were made by simulating the IJS flow using the various EVM strategies. Previous CFD background in backward-facing step (BFS) flows was also accounted for, since the flow on a BFS can be thought of as a tilted impinging jet on a plate [2].

3.1 Modeling Procedure Followed. Studies of the behavior of the selected EVM were performed. The features checked were:

- *Two-dimensional (2D) SRN jet cases:* The accuracy of the flow field predictions by means of comparisons between the mean and fluctuating velocities from the CFD results and experimental data (and with some numerical results found in the literature). The "grid dependence" of the numerical results. The accuracy of the prediction of the local Nusselt number by means of comparison between the CFD simulations and experimental results. The influence of the nozzle-to-plate distance (H/D) on the Nusselt number at the stagnation point. The effect of the turbulent Prandtl number (Pr_t) on the local Nusselt number.
- *2D SSN jet cases:* The accuracy of the local Nusselt number predictions (Nusselt number profile along the wall, Nu, by comparing CFD simulations with different EVM and experimental data, including a detailed study of sensitivity to the inlet turbulence conditions. The influence of the nozzle-to-plate distance (H/B) on the Nusselt number at the stagnation point for two Reynolds numbers.

Table 1 Cases modeled, single round nozzle (SRN jet)

Case	Nozzle D (m)	Re_0 ($\times 10^4$)	H/D	Turbulence model					
				St k-ε	Rlz k-ε	RNG k-ε	S-A	V2F	RSM
1	0.0260	2.3	2	x	x	x	x	x	x
2	0.0260	7.0	2	x	x	x	x	x	x
3	0.1016	2.3	2	x	x	x	x	x	
4	0.1016	7.0	2	x	x	x	x	x	x
5	0.1016	2.3	6	x	x	x	x		
6	0.1016	7.0	6	x	x	x	x	x	x
7	0.1016	2.3	10	x	x		x		

For near-wall modeling in all the cases, damping functions or a two-layer modeling scheme were applied to some of the EVM used.

3.2 CFD Tool. Computations were carried out with a commercial computer code (FLUENT® v5.4.8 and v6.1.18). This solver has a finite-volume solution scheme for the mean momentum, energy, and turbulent transport equations. Incompressible flow was assumed; thus, the use of a segregated solver is adequate. The schemes selected to perform computations were second-order upwind, except for the diffusion terms, for which an implicit second-order central differences scheme was used. The SIMPLE method was selected to solve the pressure-velocity coupling. More details about all the above-mentioned numerical schemes and methods can be found in Refs. [36,37].

3.3 Single Round Nozzle (SRN) Jet Case. The selected database combines the results of the fluid flow from Cooper et al. [35], and the heat transfer measurements from Baughn et al. [3,4]. The experimental results are integrated in a unique set of data in the ERCOFTAC [38] database. The Cooper experiment was carried out to give "fluid dynamic data" to the Baughn experiments. Geometrical and flow parameters defined in the aforementioned experiments were used for CFD computations, see Table 1. The reported uncertainty in mean and root-mean-square fluctuating velocities was 2% and 4–6 %, respectively, and the uncertainty in Nusselt number was 2.4%.

The values of Re_0 defined in experiments ensure that the flow is fully turbulent [39,2]. In this case, some minor discrepancies remain between the Re_0 used in Ref. [35,3].

3.3.1 Numerical Test Setup. The set of turbulence models described earlier was applied to the numerical prediction of several cases of turbulent impinging jet from a SRN. For the k-ε family models, a TLM scheme was used to couple the near-wall zone with the buffer layer. Table 1 shows the main characteristics of the modeled cases, which differ in the values for Re_0, H/D, and D. Changes in Re_0 and H/D show their influence on the Nusselt number obtained (at the stagnation point Nu_0, and along the wall Nu). The experimental results from Cooper show values for the same Reynolds number, but for two nozzle diameters and, therefore, changes in the nozzle diameters D (for the same Re_0) allow one to determine the influence of inlet kinematic conditions on the Nusselt number along the wall (small differences were reported by Cooper). As was expected, no noticeable differences were found. Comparisons with the numerical databases of [7,11] were also made.

3.3.2 Domain Definition and Computational Mesh Characteristics. The SRN jet case was modeled, bearing in mind that the jet is unconfined and the problem can be handled as a 2D axisymmetric case. The outlet plane should be placed at a sufficiently large radial distance from the stagnation point so that the error arising from the application of zero-gradient or outlet-pressure conditions will not significantly affect the region of interest. Measurements were taken up to position $r/D=3$ and, therefore, a computational domain up to $r/D=10$ was taken for numerical modeling. The inlet boundary was defined at two nozzle diameters from the nozzle to prevent instabilities in the nozzle mouth zone (see Fig. 1) For this domain, a computational mesh and boundary conditions were defined.

3.3.3 Boundary Conditions. The inlet velocity condition was defined by means of prescribed profiles for velocity and turbulent quantities, depending on the turbulence model used. In order to obtain these profiles, a separate computation was made for a developed pipe flow with the same diameter as the inlet nozzle.

At the jet axis, a symmetry condition was defined. The values of the physical variables along the axis were determined from the corresponding values in the adjacent cell.

At the upper and lateral boundaries, a pressure outlet boundary condition was defined, requiring the specification of a static (gauge) pressure. All other flow quantities were extrapolated from the interior. The lateral outlet boundary was defined at a distance $r/D=10$ from the stagnation point. At this distance, the boundary edge is far from the zone were the secondary peak in the heat transfer coefficient appears ($\sim r/D=2.0$), guaranteeing that there is no numerical influences from the boundary.

At the walls, a no-slip boundary condition was defined. Shear stresses and heat transfer between the fluid and the wall were computed considering the details of the local flow field. In this case, a constant heat flux, computed according to experimental data, was prescribed. Usually, the CFD user cannot prescribe the shear stress values at the wall, since they are predicted internally by the CFD code. The properties of the flows adjacent to the wall/fluid boundary were used to compute these values, guaranteeing that they verify the no-slip wall conditions. An accurate representation of the flow in the near-wall regions is important for a successful prediction of wall-bounded turbulent flows. The near-wall treatment depends on the mesh size near the wall, and also on the turbulence model used. Estimations of y^+ allow one to define the adequate near-wall modeling [2,39]. The effect of the turbulent Prandtl number Pr_T on the local Nusselt number Nu was checked. The Pr_T varies with y^+ as both experimental and DNS numerical results show [40]. Experimental measuring is difficult at low y^+, but the results obtained show that the range of variation for air and water is $1.7 > Pr_T > 0.85$ for $5 < y^+ < 30$. The DNS numerical results were obtained to verify these experimental values due to the aforementioned experimental difficulties, but unfortunately, the obtained values are not the same. Obtained numerical values were around $Pr_T=1.0$ when $y^+ < 10$. Kays [40] obtained a formula that shows a reasonable representation of Pr_T data near the wall, but he also points out that a value of $Pr_T=0.85$ is acceptable. To check the influence on Nu_0 and local Nusselt number (Nu), numerical experiments were performed by Benhia et al. [11] for the same SRN cases as for this work. They used several constant values for Pr_T (0.73, 0.85, and 0.92) and the Kays expression to compute the Nu profile along the wall. Their results showed that there is not a strong influence of Pr_T on Nu. They also pointed

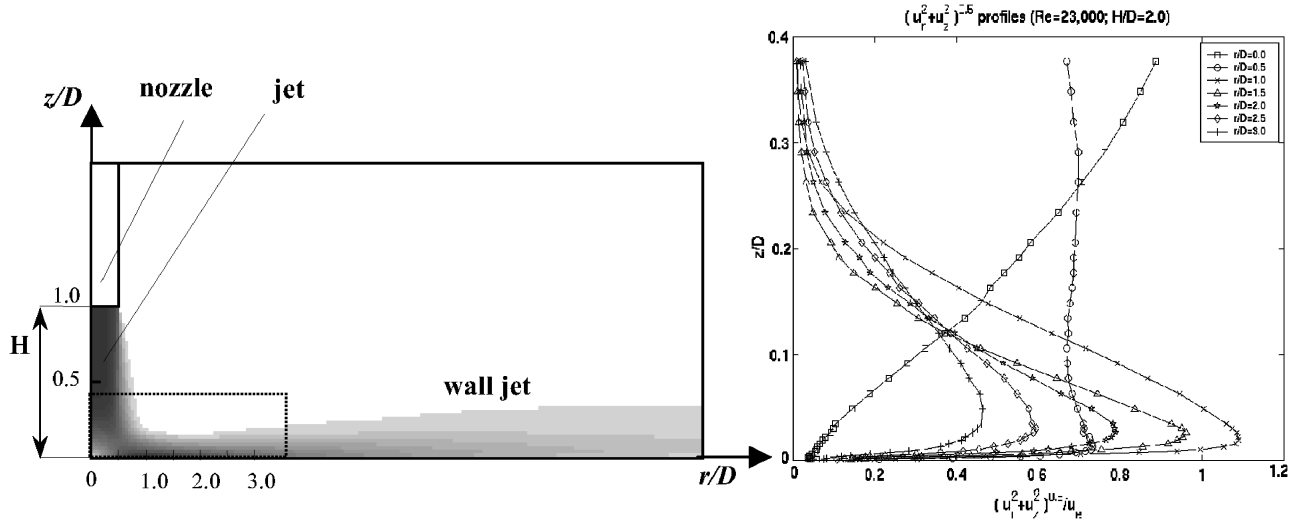

Fig. 2 Left: SRN jet numerical flow pattern indicating the domain of analysis (r/D from 0 to 3, $z/D \simeq 0.5$). Right: Experimental [35] mean velocity profiles at several positions along the bottom wall, in the domain described earlier (box on left). $Re_0 = 2.3 \times 10^4$, $H/D = 2.0$, $D = 0.1016$ m.

out that Durbin [30] obtained similar conclusions for boundary layer flows. On the other hand, Morris et al. [8] report some differences for Nu using FLUENT with a constant value for Pr_T (0.85) and several postprocessed results from FLUENT using expressions found in the literature for Pr_T, but the Reynolds numbers modeled were lower than in the work of Behnia et al. [11]. Therefore, some tests to check the influence of Pr_T on Nu were performed, varying Pr_T between 0.7 and 1.2. No noticeable changes in Nu were observed, in accordance with results reported by Benhia et al. [11]. Then, a constant value of 0.85 for the turbulent Prandtl number was defined for all cases.

3.3.4 Mesh Sensitivity Study. A mesh sensitivity study was carried out to guarantee the accuracy of the numerical results, analyzing the influence of the mesh and obtaining the adequate computational mesh, yielding credible numerical results. The mesh influence study was carried out by analyzing the variation of mean velocity profiles computed for several meshes in a set of preliminary computation cases. The meshes defined were classified in terms of their y^+ values. Previous studies [2] performed in backward-facing step flows allow one to ensure that, for boundary layer flows and wall jet flows ($25 \times 10^3 < Re_0 < 75 \times 10^3$), values of $y^+ < 3$ could guarantee the asymptoticity of the results. This condition is sufficient for meshes with homogeneous cell sizes, but it is known that for industrial problems, an important requirement is to define an affordable number of cells, being more critical in three-dimensional 3D problems. This means that large-size cell gradients appear, and under this condition, the abovementioned rule for asymptoticity could be violated. Therefore, it is necessary to be careful with the transition (size of the elements) from the boundary layer toward the inside of the domain, because oscillations can appear in the results. Bearing in mind the industrial 3D design, four hybrid triangular/quadrilateral nonstructured meshes were defined for case 1 (see Table 1), for which a very careful definition of the mesh from the boundary layer into the domain was made. The y^+ was computed for each mesh, and maximum values of 3, 0.3, 0.15, and 0.04 (mesh 01–5,000, mesh 02–7,500, mesh 03–34,000, and mesh 04–64,000 cells, respectively) were obtained. Comparison of velocity profiles and Nusselt number showed that asymptoticity is reached for meshes 03 and 04 for each turbulence model used. The Spalart-Allmaras model was more sensitive to mesh changes than the k-ε models used. Results of this analysis allow one to define suitable meshes for other cases.

3.3.5 Numerical Results. For this case, fluid flow and thermal field numerical results were obtained, i.e., the mean and fluctuating velocity profiles at several positions along the wall ($0 < r/D, 3.0$) (see Figs. 2–4), the Nusselt number at the wall stagnation point ($r/D = 0$) (see Fig. 5), and profiles of the Nusselt number along the wall (see Fig. 6).

3.3.6 Profiles of Mean Velocity in the Wall Jet Zone. For all the modeled cases shown in Table 1, profiles of mean and fluctuating velocities were obtained at several positions, r/D. Figure 3 presents the nondimensional mean and fluctuating (rms) velocity profiles for position $r/D = 1$, case 3. The comparison of numerical and experimental mean velocity profiles shows different quality fittings for the turbulence models used (Fig. 3, upper left). For the peak value, the V2F model shows the best fitting, whereas the worst fitting corresponds to the Standard k-ε. Similar results were obtained for other positions along the wall, from $r/D = 0$ to $r/D = 3.0$ in all the test cases from Table 1. The trend of the experimental wall jet velocity profiles is captured at all positions along the wall. A more detailed analysis of these results shows that the V2F model fits the velocity profiles better at positions where the wall jet is developing ($1 \leqslant r/D \leqslant 2$). The RNG k-ε and realizable k-ε models also show quite good results, although worse than the V2F model results. The Spalart-Allmaras model closely follows the realizable k-ε model.

To compare EVM and **RSM** performances, a modified Daly and Harlow [41] RSM was used in cases 3 and 4 (modifications are the slow pressure strain model from Rotta, 1970 rapid strain term model from Fu et al., 1987 and the wall reflection model from Launder and Shima 1981, full details of these models can be seen in Ref. [42]). Results obtained show that the peak value of the velocity profile is underpredicted by this model, and the model performance is similar to that of the standard k-ε model. Shi et al. [15] reported that the Nv_0 predicted by means of RSM shows discrepancies with experiments.

Observations of the development of profiles for the mean and fluctuating velocities, and from the wall boundary layer to the outer layer, were made for all cases from Table 1. For the mean velocity profile (Fig. 3 upper left), it is observed that, in the near-wall region ($z/D < 10^{-2}$) the standard k-ε, the **RNG** k-ε, the re-

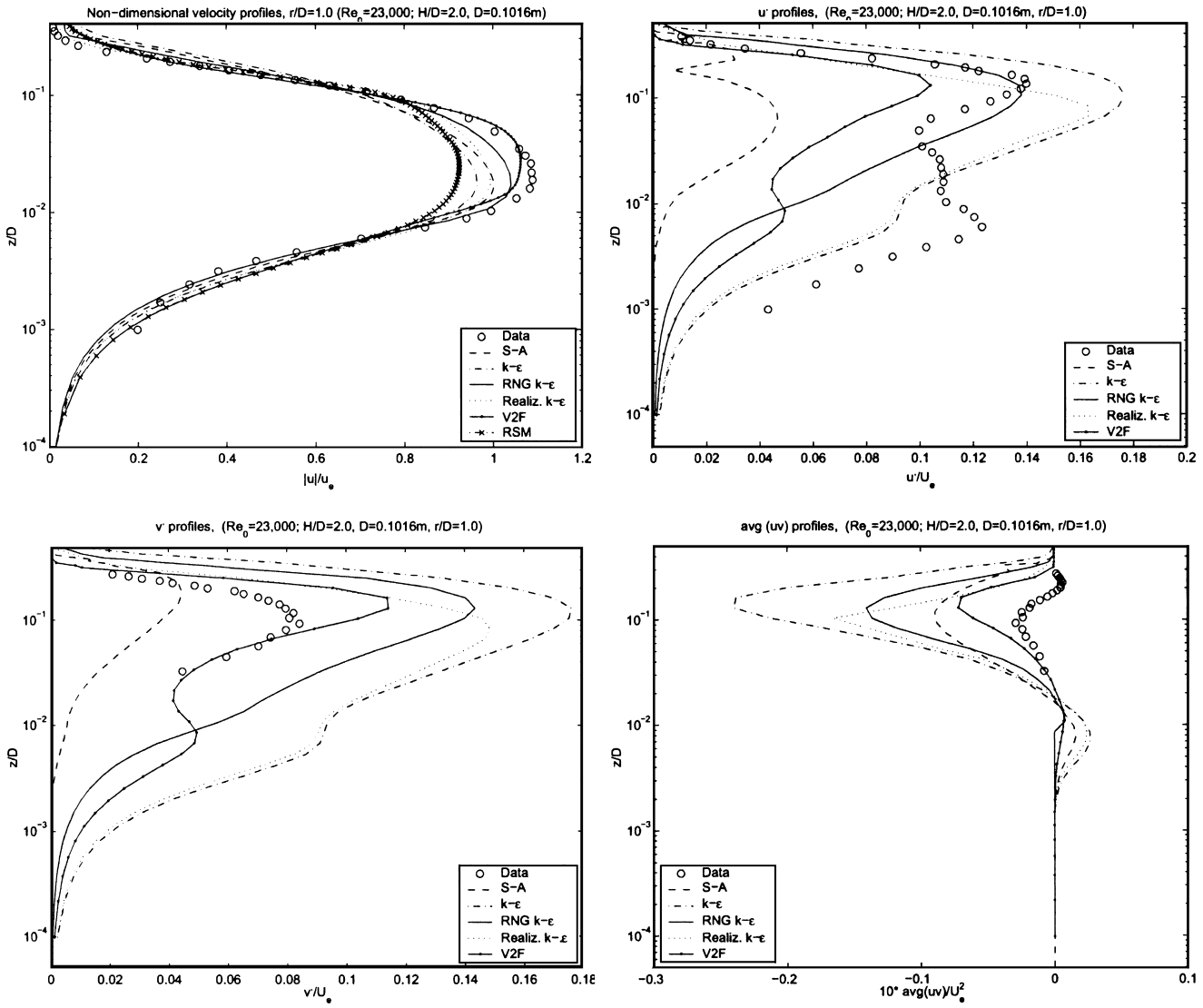

Fig. 3 Mean and fluctuating velocity profiles for SRN jet at position $r/D=1.0$, for $Re_0=2.3\times10^4$, $H/D=2.0$, $D=0.1016$ m. Upper left, mean velocities; upper right, u_{rms} fluctuations; lower right, v_{rms} fluctuations; lower right, $\overline{u_i'u_j'}$ fluctuations (average uv in figure). Experimental data from Cooper et al. [35].

alizable k-ε, and the RSM models showed similar results, which is to be expected because they are coupled with the same TLM scheme.

Above the near-wall region ($z/D>10^{-2}$), the scattering of the results begins. Near the stagnation point, the maximum value of the profiles is best predicted by the V2F model, followed by the RNG k-ε, the Spalart-Allmaras, the realizable k-ε, and the standard k-ε, respectively. For profiles far from the stagnation point, the performance of the **V2F** model is maintained and the Spalart-Allmaras, RNG k-ε, and realizable k-ε models improve their performance. The standard k-ε model showed a strong underprediction of velocities at $z/D=10^{-2}$, whereas for $z/D>10^{-1}$, these were overpredicted for all the profiles observed ($0\leqslant r/D\leqslant3.0$), irrespective of which Reynolds number was used. The poor performance of this model was expected because it does not correctly solve the development of the boundary layer (stagnation anomaly [27]). This anomaly is the reason for the turbulent kinetic energy level (k) overpredictions, leading to overpredicted values in the outer region and underpredicted velocity values in the wall region. Consequently, the computed wall jet is too thick, and the value of the peak velocity is too low. Clearly, this effect is stronger for the profiles computed closer to the stagnation point. This drawback can be alleviated by means of a TLM scheme. Compared with numerical databases, the two-layer scheme used here shows better behavior than the "Yap" correction [7] or damping functions [11,12]. On the other hand, the Spalart-Allmaras model predicts the near-wall velocity profile very well at all positions over the whole domain for all the cases modeled. The prediction capability of the maximum value is similar to (or better than) the other models, depending on the case or positions analyzed.

3.3.7 Profiles of fluctuating velocity in the wall jet zone. The nondimensional profiles for the fluctuating velocities u_{rms} and v_{rms} and the shear stress $\overline{u'v'}$ are shown in Fig. 3. The k-ε family models gave similar trends to those found in the experiments, but with a large scattering of u_{rms} and overpredictions of v_{rms} for $z/D>10^{-2}$. It can be seen that the overprediction of k obtained with the standard k-ε model leads to high values of the fluctuating quantities due to the stagnation point anomaly. Also, the lack of sensitivity of these models to the effects of streamline curvature should play an important role here. The trends are best followed by the V2F model and, although values for u_{rms} are underpredicted, the best fitting for v_{rms} and $\overline{u'v'}$ was obtained with this model. For u_{rms} and v_{rms}, the Spalart-Allmaras model could not be

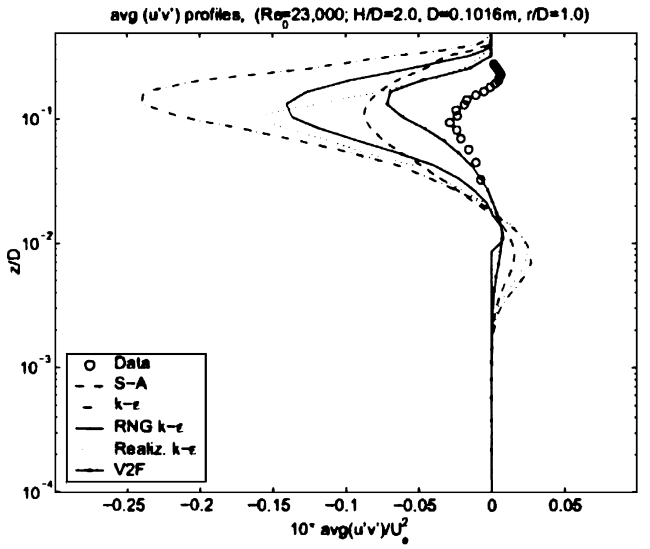

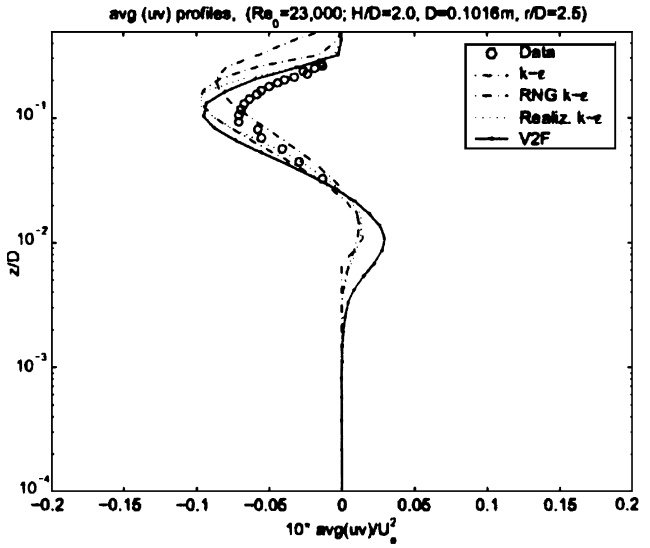

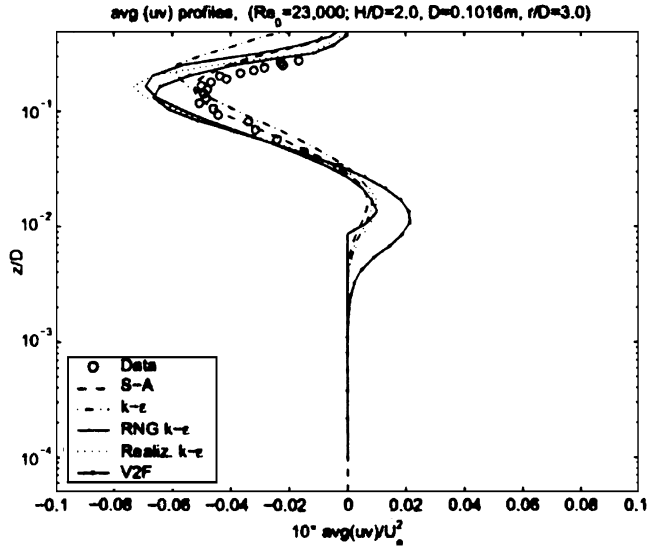

Fig. 4 Fluctuating $\overline{u'v'}$ velocity profiles for SRN jet for several r/D, with $Re_0=2.3\times10^4$, $H/D=2.0$, $D=0.1016$ m, (average uv in figure). Experimental data from Cooper et al. [35].

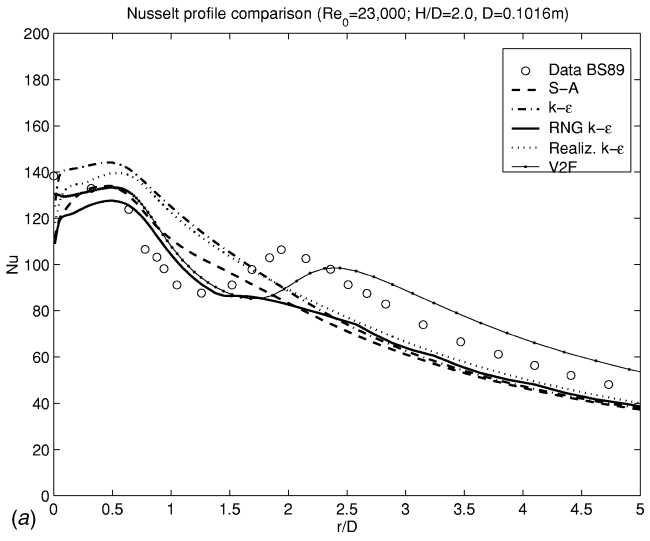

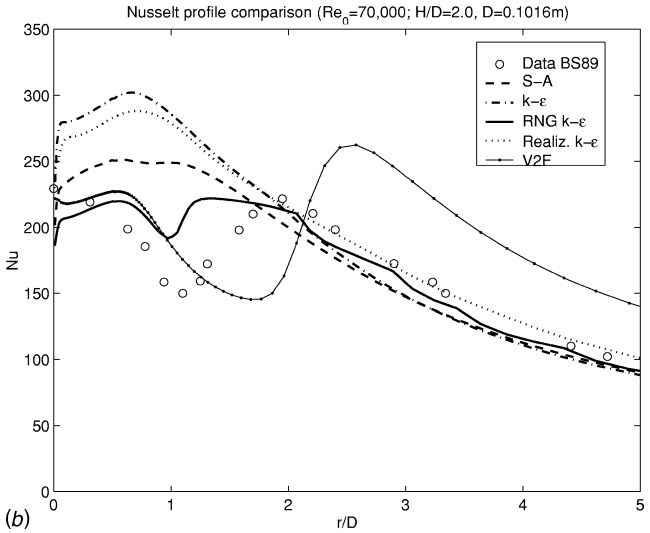

Fig. 5 Variation of the Nusselt number profile along the wall for SRN jet case, $H/D=2.0$, and $D=0.1016$ m. Left, $Re_0=2.3\times10^4$; right, $Re_0=7.0\times10^4$. Experimental data from Baughn and Shimizu [3].

compared in a straightforward way because it does not consider k in the computation of the fluctuating quantities, using the Boussinesq assumption. Therefore, the comparison was made using the ν_T definition from Spalart and Allmaras [14]. In zones closest to the stagnation point, the k-ε family models go from overprediction in the buffer layer zone to underprediction in the near-wall zone along the profile (not shown here). For the $v_{\rm rms}$ fluctuation component, the Spalart-Allmaras model shows a similar behavior to the V2F model, but the latter is closer to the experimental results. For the Reynolds shear stress $\overline{u'v'}$ and for low r/D ratios ($r/D\leqslant1.5$), the V2F model gave the best fittings, but for ratios $r/D>2.5$, the best fittings were achieved with the realizable k-ε. These results are strongly dependent on the Reynolds number Re_0.

Summarizing, for the fluctuating velocity components ($u_{\rm rms}$ and $v_{\rm rms}$), and the Reynolds shear stress $\overline{u'v'}$, there is a larger scattering of numerical values obtained for low r/D ratios. When the ratio r/D is increased, the agreement with experimental data is improved. This is so because the coefficients in the turbulence models used are mainly calibrated for parallel flows (e.g., see Fig. 4).

This large scattering of the fluctuating values for the checked models is reflected in slight differences in the predicted mean

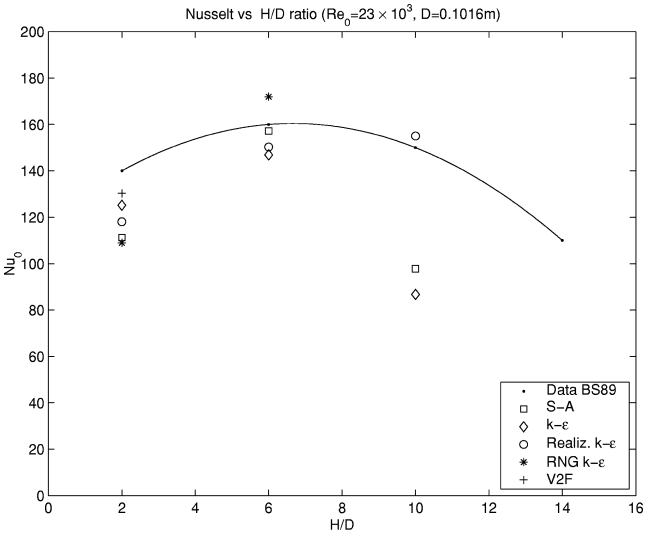

Fig. 6 Variation of the Nusselt number at the stagnation point (Nu_0) with the ratio H/D for $Re_0=2.3\times10^4$. Nozzle diameter $D=0.1016$ m. Experimental data from Baughn and Shimizu [3].

velocity field. This analysis confirms that the k-ε model produces an excessively rapid mixing, which is to be expected from the overprediction of fluctuating velocity levels shown in Fig. 3. Although the RNG k-ε and realizable k-ε include corrections for the stagnation anomaly in their formulations, disagreement between numerical and experimental results remain. On the other hand, they slightly improved the mean velocity predictions. The V2F and the Spalart-Allmaras models gave the best results. Probably, the inadequate modeling of curvature effects are responsible for this disagreement in the corrected k-ε models. Results for case 6 showed the same general behavior for all the turbulence models as when cases with a lower H/D ratio were modeled. Similar results for case 4 were also found. A general observation is that the EVM strategy was more successful for lower Re_0 and higher H/D ratios, even though for higher Re the turbulence structure is more isotropic. The behavior of the turbulence models will influence the heat transfer predictions because thermal and flow boundary layers are closely related, since flow data are used as input in the heat transfer computations. In all cases, the analogy between thermal and flow boundary layer is assumed.

3.3.8 Nusselt Number as a Function of the Distance From Stagnation Point (r/D). In Fig. 5, the evolution of the Nusselt number with r/D for the two modeled Reynolds numbers has been represented. Experimental data show, for cases 3 and 4, a secondary peak in the Nusselt number distribution. Concerning the numerical results for case 3 (low Re_0), in general, a good fitting has been obtained for all models. However, only the V2F model reproduces the secondary peak (Fig. 5, left), although its value is lower and its location is not well predicted. For case 4 (high Re_0), the general trend is not as good, especially near the stagnation point region (i.e., $r/D<2$, see Fig. 5, right). In case 4, both the V2F and the RNG k-ε models reproduce the peak, although the latter model yields a better prediction. The Spalart-Allmaras model only insinuates this secondary peak, but at a wrong position. When the nozzle-to-plate distance is increased to $H/D=6$ and the higher Reynolds number is considered (case 6), the global agreement is still reasonable for all models, except for the V2F model [39,2] (not shown here). This model predicts an anomalous peak in the place where the experimental data only insinuate the secondary peak. Similar results were pointed out by Ref. [11], who remarked that the RNG k-ε model does not improve the standard k-ε predictions. However, the cases modeled here show good predictions at the stagnation point and along the wall when the standard k-ε model is used. Again, it is possible to confirm that the TLM scheme improves the results compared to damping functions or the "Yap" correction shown in the above cited references.

3.3.9 Wall Stagnation Point Heat Transfer (at $r/D=0$). Simulations to determine the dependence of the heat transfer coefficient at the stagnation point (related to the Nusselt number Nu_0) on the H/D ratio have been carried out for cases 3, 5, and 6 (see Table 1). The computed values were compared with the experimental data from Ref. [3,4], grouped together in the ERCOFTAC database. Cases 3 and 5 are shown in Fig. 5. All models gave a reasonable prediction of Nu_0 values at the stagnation point for $Re_0=2.3\times10^3$ (Fig. 5, left). For $Re_0=7.0\times10^3$, there is a larger spreading in the numerical results (Fig. 5, right). In both cases, the Spalart-Allmaras and RNG k-ε models predict similar lower Nu_0 values, while the V2F model gives a better fitting. For the standard k-ε model, there is an improvement in the prediction compared to results presented in Ref. [7,11]. These improvements in Nu_0 prediction may be related to a better performance of the TLM scheme used here, compared to the damping functions used in the aforementioned references for near-wall modeling.

Moreover, the experimental data show variations of Nu_0 when the H/D ratio changes, with a maximum Nu_0 value in the interval $6<H/D<8$, where experimental and numerical results are presented (see Fig. 6). Three H/D ratios (2, 6, and 10) were modeled to investigate the possibility of capturing the experimental Nu_0 behavior when the H/D ratio is changed. This behavior might be attributed to the increase of turbulent kinetic energy k, related to the heat transfer phenomena, as the jet is moved away from the impingement surface, reaching a maximum value and then starting to decrease. The numerical values obtained follow the trend of the experimental data, and a maximum value of Nu_0 at $H/D\approx6$ is predicted with the k-ε and Spalart Allmaras models. The realizable k-ε model does not predict the maximum value in the correct position. The trends for the V2F and RNG k-ε models are not clear because the higher H/D ratios were not modeled with these EVM.

Regarding the Nusselt number distribution along the wall (local Nusselt number) Nu, Fig. 5 shows its evolution with r/D. Experimental data show, for cases 3 and 4, that a secondary peak in the Nu distribution along the wall appears.

Both cases share the same nozzle diameter. Numerical results for case 3 show that only the V2F model captures this peak, although its value is lower than in the experimental data, and its location is not well predicted. The RNG k-ε model only insinuates the peak in the same position as the experimental data (see Fig. 5, left). The fitting in the interval $0<r/D<1.5$ is quite good for the Spalart-Allmaras, RNG k-ε, and V2F models. All models, except the V2F model, underpredict Nu for $r/D>1.5$. At these distances, the V2F model gives a slight overprediction of Nu values. For case 4, both the V2F and RNG k-ε models capture the peak, but it is better predicted by the latter model (see Fig. 5, right). A large scattering of results in the interval $0<r/D<1.5$ for all models can also be observed. The Spalart-Allmaras, standard, and realizable k-ε models overpredict Nu in this interval. The predictions improve in the wall jet zone ($r/D\geq1.5$) for all models except the V2F model. When the H/D ratio is increased (case 6), the overall agreement is still reasonable for all the models used (not shown here), except for the V2F model, when $r/D>1.5$. The V2F model predicts an anomalous peak in the place where data only insinuate the secondary peak, and there is a strong overprediction of Nu in the interval $0<r/D<3$. There is no explanation for the behavior of this model in this situation. Numerical results from Ref. [11] also show this spurious peak, but at slightly different position ($r/D\simeq0.8$). Also, this reference explicitly states that there is no explanation for this peak, and it also points out that the RNG k-ε model does not improve the standard k-ε predictions. The cases modeled here show that the RNG k-ε model shows a better

Table 2 Cases modeled, single slot nozzle (SSN jet)

Case	Nozzle B (mm)	Re_0 ($\times 10^4$)	H/B	Turbulence model (inlet I_1=2.5%) St k-ε	Rlz k-ε	RNG k-ε	S-A	V2F
1	3.125	1.1	2	x	x	x	x	x
2	3.125	1.1	6	x	x	x	x	x
3	3.125	1.1	8	x	x	x	x	x
4	3.125	1.1	10	x	x	x	x	x
5	3.125	1.1	16	x	x	x	x	
6	3.125	2.2	2	x	x	x	x	x
7	3.125	2.2	6	x	x	x	x	x
8	3.125	2.2	8	x	x	x	x	x
9	3.125	2.2	10	x	x	x	x	x
10	3.125	2.2	16	x	x	x	x	

behavior than the standard k-ε.

Summarizing, for the SRN jet case, the average velocity predictions of the EVM, using either wall functions or a two-layer modeling approach, were in close agreement with experimental data. However, the near-wall turbulence predictions were poor for all the models tested in this exercise, especially near the point of jet impingement. This affected the heat transfer predictions along the impingement plate for $R/D<2.0$. The EVM used performed poorly because they assume a linear stress-strain relation and a turbulence length scale based on thin shear layer flow; conditions that do not exist near the impingement point of a jet. Despite the fact that the V2F model has improvements to account for these problems, its predictions showed only a slightly better behavior. Also, the present work shows differences (in terms of data fitting) between the hydrodynamic and heat transfer results found using the V2F and k-ε models, and the corresponding results from Refs. [12,11]. Nu_0 variations as a function of H/D are captured by the Spalart-Allmaras and k-ε models, but in general with underpredicted values. Concerning the secondary peak, it is best captured by the V2F model for low Re_0 cases. For high Re_0 cases, both the V2F and RNG k-ε models capture this peak. The Spalart-Allmaras model does not capture it.

3.4 Single Slot Nozzle (SSN) Jet Case. The second test case to be modeled is that of a single slot nozzle. The database used was from Gardon and Afkirat [5,33]. The experiments aimed at estimating the local and average heat transfer coefficients (h and $\bar{h}$) in a single, and in an array of slot jets (SSN and ASN, respectively). Temperature at the wall was measured with a 0.9 mm diameter copper-constantan termocouple. Sensitivity of the probe was 0.024 mV/(W/cm^2). In the experiments, the velocity field measurements were not performed for this case. The experimental setup consisted of jets of air impinging on a vertical, electrically heated plate, and it was possible to modify the nozzle-to-plate distance, now defined as H/B. Additionally, several nozzle widths (B) were used. This database has been used in several numerical benchmarks, (e.g., see, [6]).

3.4.1 Numerical Test Setup. Regarding the solver, an identical setup as for the SRN jet case was made. Several cases were modeled, consisting of a 3.175 mm width nozzle (B), with an H/B variation from 2 to 16, and for two Reynolds numbers ($Re_0=1.1\times10^4$ and $Re_0=2.2\times10^4$), ensuring a fully turbulent flow [2,39].

3.4.2 Domain Definition and Computational Mesh Characteristics. As for the SRN jet test case, the jet is also two-dimensional (but not axisymmetric) and unconfined. Therefore, the lateral and the top outlet conditions were defined in the same way as for the SRN jet test case. The lateral outlet was placed at a distance of $x/B=25$ from the stagnation point. At this distance, the boundary edge is far from the zone where the secondary peak appears (at about $x/B=7$), guaranteeing that there are no numerical boundary effects over the region in which the secondary peak is found. A prescribed value of velocity was defined in accordance with the Reynolds number used (computed using the slot width as the characteristic length). Turbulent parameters were defined by means of a prescribed value, both for the turbulence intensity level I and for the length scale (related to the size of the more energetic turbulence vortex). Concerning the symmetry boundary, since the shear stress is zero at this boundary, it can also be interpreted as a "slip" wall, like the one employed in viscous flow calculations. This condition implies a zero normal velocity, and zero normal gradients of all variables.

3.4.3 Mesh Sensitivity Study. To define a good computational mesh, the previous SRN modeling experience allows us to define the same strategy for this case. Therefore, a suitable mesh was obtained when y^+ was less than 3.

3.4.4 Numerical Results. The fluid dynamic field for this case has been computed, but emphasis has been put on modeling the thermal field. To check the capabilities of the turbulence models selected, two studies were made. The first one consisted of changing the H/B ratio while maintaining the turbulence inlet conditions at the same level (48 tests were modeled, see Table 2). The second one consisted of changing the I level while maintaining the H/B ratio, and these I changes were applied for other H/B values (36 tests were modeled, see Table 3). Both studies were carried out for two Re_0 values (1.1×10^4 and 2.2×10^4), and all the turbulence models applied in the SRN test case (except the RSM model) were used. Therefore, concerning the Spalart-Allmaras, RNG k-ε, and V2F models, Tables 2 and 3 are complementary.

3.4.5 Nusselt Number at the Stagnation Point (Nu_0). For the first study (changes in H/B ratio), Nu_0 was obtained and compared with experiments. Figure 7 (left) shows results for $Re_0=1.1\times10^4$. It can be seen that Nu_0 variations appear when H/B changes, such as in the SRN jet test case (see Fig. 6). There is a maximum Nu_0 value at $H/B\simeq10$ (for SRN jet, the maximum value is found between $H/D=6$ and $H/D=8$). Figure 7 (left) also shows that these Nu_0 values were overpredicted for low H/B ratios, unlike the SRN jet case (the Nu_0 was underpredicted for $H/D=2$). A similar behavior was observed in cases with $Re_0=2.2\times10^4$ (cases from 6 to 10, see Table 2 and Fig. 7, right). For $Re_0=1.1\times10^4$ (Fig. 7, left), the V2F model gave acceptable results for nozzle-to-plate ratios between $6<H/B<10$. The Spalart-Allmaras gave a trend similar to the experimental results over the same interval, but with the most underpredicted values. Results for the smallest H/B ratio showed strong Nu_0 overpredictions. Only the V2F model overpredicted Nu_0 at $H/B=16$, whereas the other models underpredicted the values. For $Re_0=2.2\times10^4$ (Fig. 7, right), similar trends appeared, but the RNG k-ε model gave the best trend in the $6<H/B<16$ range. Again, the V2F model overpredicted Nu_0 at $H/B=16$, but the realizable k-ε also overpredicted Nu_0.

Table 3 Cases modeled, single slot nozzle (SSN jet): I_0=0.2%, I_2=6.0% I_3=18.0%

				Sensitivity to the inlet I level								
				RNG k-ε			**S-A**			**V2F**		
Case	B (mm)	Re_0 ($\times 10^4$)	H/B	I_0	I_2 (%)	I_3	I_0	I_2 (%)	I_3	I_0	I_2 (%)	I_3
1	3.125	1.1	2	x	x	x	x	x	x	x	x	x
2	3.125	1.1	6	x	x	x	x	x	x	x	x	x
3	3.125	1.1	10	x	x	x	x	x	x	x	x	x
4	3.125	2.2	2	x	x	x	x	x	x	x	x	x
5	3.125	2.2	6	x	x	x	x	x	x	x	x	x
6	3.125	2.2	10	x	x	x	x	x	x	x	x	x

Summarizing, it can be observed that, depending on the combination of H/B and Re_0 selected, different models show the best agreement with experiments, and it is not possible to define an overall "best model" for all the modeled cases.

The goal of the second study (changes in the inlet turbulence parameters) was to reproduce the experimental influence of these changes on Nu_0. Figure 8 shows results for $Re_0=2.2\times10^4$. A similar behavior for $Re_0=1.1\times10^4$ was found (not shown here). This figure shows that the experimental behavior at the stagnation point again was not reproduced by any tested model because the higher Nu_0 appears for $H/B\simeq2$, whereas experimental data show the maximum Nu_0 at $H/B\simeq6$ (see Fig. 10). This numerical behavior was observed for all values of I. It is also interesting to note that the variation of Nu_0 when I is increased is only captured by the V2F model, but only for the $H/B=2$ and $H/B=10$ cases. For $H/B=6$, levels of Nu_0 predicted decrease when I rises. Numerical results reported by Shi et al. [15] showed variations of Nu_0 when the inlet turbulence parameters were changed. One difference between present results and the ones from Shi et al. [15], was the length scale defined. To check these differences, 16 more cases were run. Each case consists of defining an I level and changing only the length scale (from D_h to $0.07D_h$) at the inlet. The same procedure was repeated for different I values (see Table 4). Figure 9 depicts the results obtained, showing that the trend followed by the present standard k-ε modeling agrees with the results presented in Shi's work when the value of $0.07D_h$ was used as the length scale (i.e., Nu_0 rises when the I level rises), except for very low I values. When the length scale value was D_h, the results obtained show differences from those of Shi's work. The trends of Spalart-Allmaras are insensitive to this scale change. Also, for each I value, Nu_0 depends on the turbulence length scale used and the EVM used. The selection of a value of $0.07D_h$ implies the assumption that the size of the energetic vortex is very

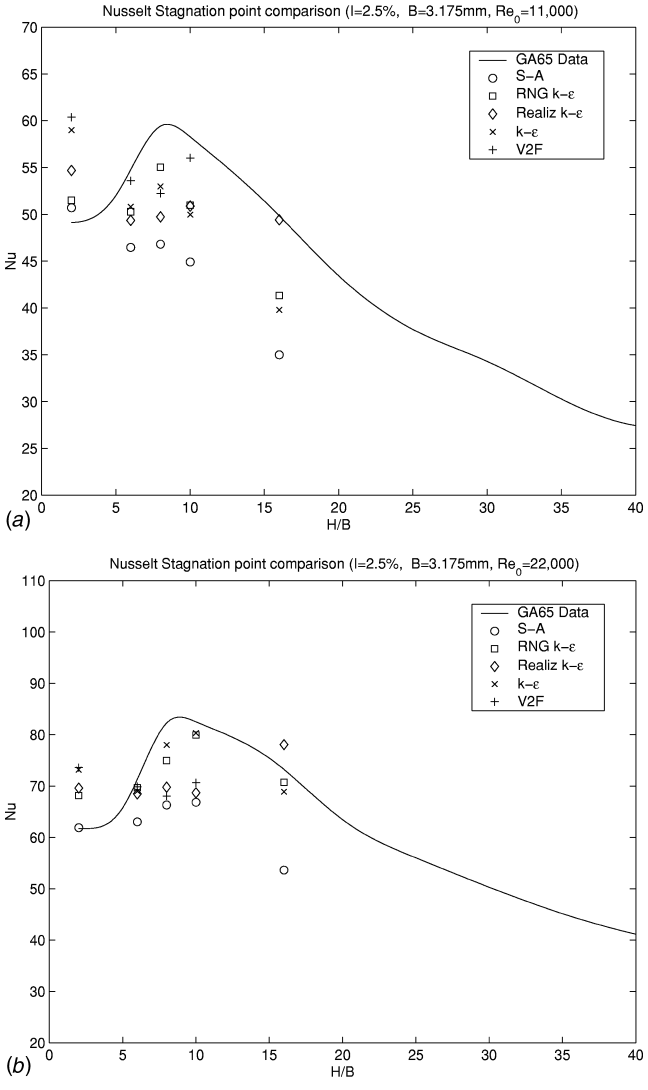

Fig. 7 Variation of the Nusselt number at the stagnation point (Nu_0) for changes in the ratio H/B (nozzle width B=3.175 mm). Left, $Re_0=1.1\times10^4$; right, $Re_0=2.2\times10^4$. Experimental data from Gardon and Afkirat [5].

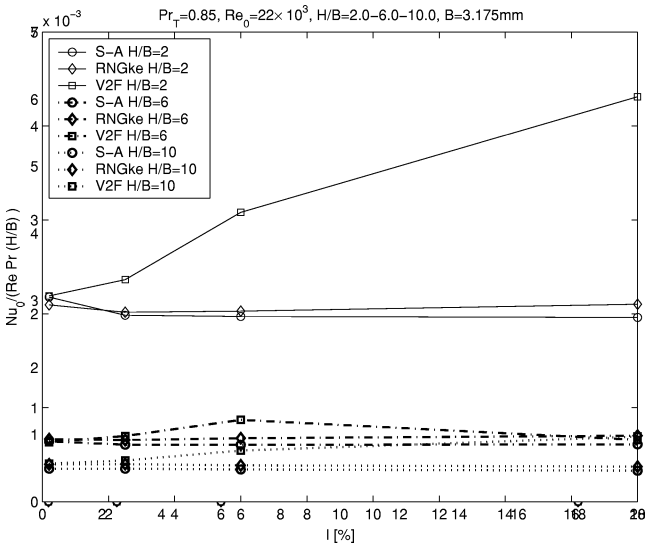

Fig. 8 Variation of the Nusselt number at the stagnation point Nu_0 with I for $Re_0=2.2\times10^4$, $Pr_T=0.85$. Nozzle width B =3.175 mm.

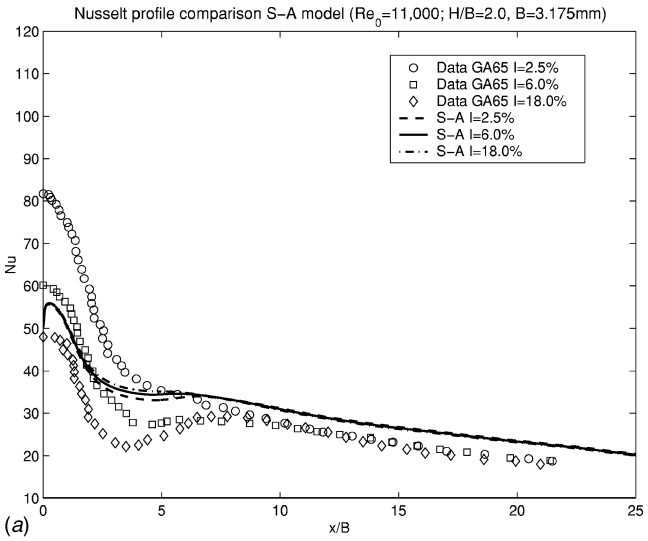

Fig. 10 Variation of the Nusselt number profile along the wall for inlet turbulence intensity (*I*) changes, SSN jet case $Re_0=1.1\times10^4$, $H/B=2.0$, $B=3.75$ mm. Left, Spalart-Allmaras model; right, V2F model. Experimental data from Gardon and Afkirat [5].

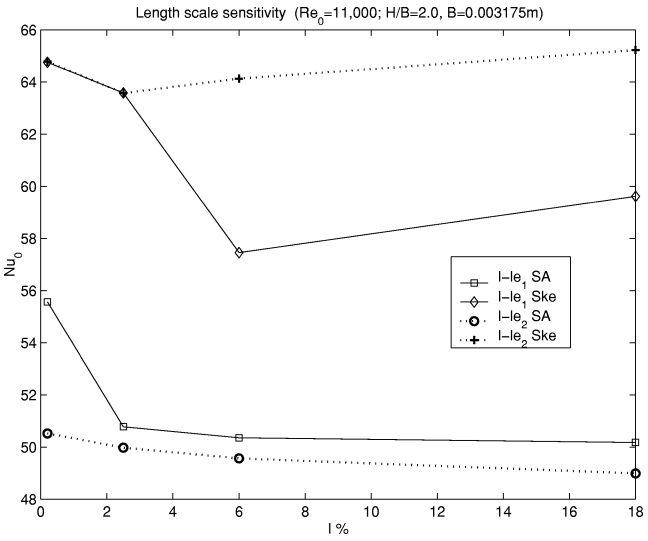

Fig. 9 Variation of the Nusselt number at the stagnation point Nu_0 with the length scale for $Re_0=1.1\times10^4$, Pr=0.85. Nozzle width $B=3.175$ mm. Length scale: $le_1=D_h$, $le_2=0.07Dh$.

small. This could be unrealistic for jet cases, because it is commonly assumed that values in the range $0.1<D_h<0.5$ are more realistic in these cases [28].

3.4.6 Nusselt Number Profiles Along the Wall. This study included a detailed analysis of the sensitivity of Nu profile along the wall to changes in the inlet turbulence level *I*. The study was performed for three H/B ratios (2, 6, and 10) and for two Reynolds numbers ($Re_0=1.1\times10^4$ and $Re_0=2.2\times10^4$). Only the Spalart-Allmaras, RNG k-ε and V2F models were checked in this study (54 tests, see Table 3).

Experiments [5] show that for low H/B ratios, the Nu profile along the wall presents a secondary peak at $x/B\simeq7$. A similar behavior was discussed for the SRN jet case, but that secondary peak appeared at $r/D\simeq4$. These experimental results also show that the peak is strongly influenced by the inlet turbulence level *I*. When the *I* level is increased, by adding a turbulent promoter at the inlet, the secondary peak of the Nu profile decreases and the Nu_0 value rises. These changes in the *I* level contribute to a better mixing at the stagnation point, increasing the heat exchange.

Numerical modeling was carried out to check the capability of the turbulence models to capture this phenomenon. Three inlet *I* values ($I_1=2.5\%$, $I_2=6.0\%$, and $I_3=18.0\%$) were defined for each of the aforementioned H/B ratios (see Table 3). Table 3, together with Table 2 (cases for $I=2.5\%$ and for the above-mentioned turbulence models), show the complete set of modeled tests for this sensitivity study. The secondary peak position and its maximum value were identified and compared to experimental data (see Fig. 10). This study started by modeling test 1 from Table 2 and test 1 from Table 3 (both cases are for $H/B=2$). Comparisons between the computed and experimental values for Nu along the wall for the aforementioned inlet *I* values were made. Figure 10 shows the results for the Spalart-Allmaras and V2F models. The RNG and realizable k-ε models gave similar results to the Spalart-Allmaras model (not shown here), qualitatively reproducing the experimental Nu profile trend, but only the Spalart-Allmaras model showed some slight sensitivity in the zone where the secondary peak is. The modeled secondary peak diminishes when the *I* rate rises, reproducing the experimental behavior (see Fig. 10, left). The re-

Table 4 Sensitivity to the length scale level changes: SSN jet, Re=11,000, $H/B=2$; $I_0=0.2\%$, $I_1=2.5$ $I_2=6.0\%$, $I_3=18.0\%$; S-A, Spalart-Allmaras; k-ε, Standard k-ε model

Case	Length scale	k-ε				S-A			
		I_0	I_1 (%)	I_2	I_3	I_0	I_1 (%)	I_2	I_3
1	$le_1=D_h$	x	x	x	x	x	x	x	x
2	$le_2=0.07D_h$	x	x	x	x	x	x	x	x

sults obtained for SSN are not similar to those obtained in the SRN jet test cases because the secondary peak is less clearly identified for all EVM models. In the SRN cases, some EVM capture this peak (Fig. 5).

Only the V2F model produced changes in the Nusselt number at the stagnation point when the inlet I was changed, but it did not show the secondary peak from the experimental profiles (see Fig. 10, right). From the previous results for the SRN jet case with the V2F model, it was expected to capture this feature, but the secondary peak was not captured. Therefore, the V2F model is sensitive to I variations, but only at the stagnation point, yielding only a qualitative agreement with the experimental values for this case. An additional characteristic of the V2F results is the presence of wiggles along the wall profile, which did not appear in the SRN case. The mesh and boundary conditions for the mean quantities were the same for all models. Similar features are found for other H/B ratios. The residual errors for all turbulence modeling cases were $\sim 10^{-4}$. The V2F model shows a lower convergence ratio than the other models, sometimes reaching a level of 10^{-3}. Therefore, a complementary convergence analysis was carried out in the V2F modeling case, to ensure similar convergence levels as for other turbulence models, by checking the variation of an integral (e.g., the drag force along the wall) and a local quantity (e.g., the velocity at a defined point). No oscillation in the integral and local quantities was observed at these levels of residual convergence. Another possibility was that these wiggles could be a consequence of an increased sensitivity to the mesh size in the transition from the boundary layer to the inside of the domain. To check this possibility, a test was performed with a reformulated mesh consisting of a similar size mesh, but with a smoother transition in the cell size between the boundary layer and the outer flow, and wiggles of less amplitude were obtained. This result shows that the V2F model is more sensitive to the definition of the smoothing level of the mesh.

Conclusions of the exercise for the SSN jet case are that similar problems as for the SRN case were found. The Nu_0 variations as a function of H/B are captured by the RNG and standard k-ε models, but with underpredicted values, except for the $H/B=2$ ratio. At this value, Nu_0 was overpredicted by all models. Concerning the secondary peak, the Spalart-Allmaras model suggests its existence, while all the k-ε models fail to capture it. Unlike in the SRN cases, the V2F model does not capture the secondary peak. Experimental evidence [33] shows that inlet turbulence conditions have a strong influence on the heat transfer at the wall. Numerical modeling changing the inlet turbulence conditions (I level and the turbulence length scale) showed the ability of all the tested models to predict the variations of Nu_0. All models, except the V2F model, were insensitive when only the I level was changed. The V2F results for Nu_0 showed sensitivity, but unfortunately, without a quantitative agreement. On the other hand, changes in D_h showed some improvements in predictions of Nu_0 trends for the standard k-ε model (only the Spalart-Allmaras and the standard k-ε were checked, see Fig. 9). The results obtained in the present work show some differences with the results from Shi et al. [15] when the I level is changed (the above-mentioned reference shows Nu_0 variations). But when the turbulence length scale is changed, variations in Nu_0 were detected, as the results from the aforementioned reference show.

4 Conclusions

A study of the capabilities of several turbulence models to capture physical characteristics of SRN and SSN jets was conducted. For all the cases modeled, both mean fluid dynamic and mean heat transfer features of the impinging jet are quite well captured, showing a reasonable agreement with the experimental databases used. A detailed analysis of fluctuating velocities was also made for the SRN jet case. Computations performed confirm that velocity fluctuations are not adequately predicted at the stagnation zone, and their values are strongly dependent on the turbulence model used. Predictions are better for zones far away from the impingement region. The performance of all models in predicting the Nusselt number at the stagnation point (Nu_0) shows a strong dependence on the nozzle-to-plate ratio for both the SRN and SSN jets test cases.

In general, comparisons presented in this work show that the checked EVM changed their performance when SRN or SSN nozzles were modeled. Cases studied show that the behavior of all the checked EVM was slightly better for the SRN cases. For both the SRN and SSN jets test cases, the "relative" performance among models varies from test to test, and it is not possible to give a clear and general recommendation about which model is best, in accordance with the broad discussion existing about this subject. This work does not close the problem, but permits one to gain some insight about it. In terms of CPU costs and accuracy, the Spalart-Allmaras model provides an interesting performance. The V2F needs more iterations to obtain slightly better results than the other models checked. The mesh sensitivity study shows that the Spalart-Allmaras model is more sensitive to mesh refinement, and the V2F model shows sensitivity to the mesh smoothing. The standard, realizable, and RNG k-ε models gave similar results to the Spalart-Allmaras model. The V2F model gave the best mean velocity fittings and acceptable heat transfer results, but only for the lower Re_0 numbers selected.

In summary, with the guidelines obtained in this work, it is possible to apply the commercial CFD tool to acquire a better knowledge of how this type of cooling devices behave, in order to improve its design, as was made in the second part of this work [43]. A careful usage of commercial CFD code is mandatory when studies concerning the variations of the nozzle-to-plate ratio are performed. Results obtained show that, depending on the EVM model used, the Nu_0 trends are reproduced with more or less quality. Accurate quantitative estimations of the Nu_0 variation are difficult to obtain. Concerning an appropriate modeling strategy, the Spalart-Allmaras could be a good starting point to compute more complex impinging jet flows because its performance is similar to that of the k-ε family models. Depending on which EVM is used (some of them showed more sensitivity), it will be very important to define suitable inlet turbulence scales to obtain realistic Nu_0 trends. The use of more than one turbulence model is highly recommended. Results reported using only one model may be considered completely insufficient.

Nomenclature

Variables and Parameters

B = nozzle width, m

D = nozzle diameter, m

H = nozzle-to-plate distance, m

h = heat transfer coefficient, $W/m^2\ K$

h_0 = heat transfer coefficient at the stagnation point, $W/m^2\ K$

I = intensity of turbulence (relative magnitude of the axial velocity u'_{rms} fluctuations, referred to as the local values of the time-averaged axial velocity, u_m), $\frac{u'_{rms}}{u_m}$, N-d

k = turbulence kinetic energy, m^2/s^2

k_f = flow thermal conductivity, W/(m K)

L_T = distance between nozzles, m

L = slot length, m

Nu_0 = Nusselt number at the stagnation point based on the nozzle's dimension $\frac{h_0 D(or\ 2B)}{k_f}$, N-d

Nu = local Nusselt number, hL/k, N-d

Pr = Prandtl number, $Pr=\nu c_{e_{ref}}/(k_f)$, N-d

Re_0 = critical Reynolds number based in the nozzle's dimension and exit velocity, $\frac{u_e D(or\ B)}{\nu}$, N-d

Re_s = critical Reynolds number based on the hydraulic diameter, N-d
T = temperature, °C, K
r = round nozzle radial direction coordinate, m
x = slot width direction coordinate, m
y = slot longitudinal axis direction coordinate, m
y^+ = nondimensional geometric-turbulence variable, $y^+ = u^* y/\nu$, N-d
z = jet axis direction coordinate, m

Greek symbols

ε = rate of dissipation of kinetic energy, m^2/s^3
μ = dynamic viscosity, kg/(ms)
ν = kinematic viscosity, m^2/s
μ_T = eddy dynamic viscosity, kg/(ms)
ν_T = eddy kinematic viscosity, m^2/s
ω = specific dissipation rate, $\omega = \varepsilon/k$, 1/s

Subscripts

0 = stagnation point
r = round (axisymmetrical) nozzle
s = nozzle slot
w = wall

Superscripts

$\bar{a}$ = time average value
a' = fluctuating quantity

Acronyms

ASN = array of slot nozzles
CFD = computational fluid dynamics
EVM = eddy viscosity models
IJS = impinging jet systems
MWF = modified wall functions
RANS = Reynolds averaged navier-stokes
RNG = renormalization group theory
RSM = Reynolds stress models
SRN = single round nozzle
SSN = single slot nozzle
SWF = standard wall functions
TLM = two-layer model
V2F = eddy viscosity model from Durbin [13]
WF = wall functions

References

[1] Jambunathan K., Lai E., Moss M., and Button B., 1992, "A Review of Heat Transfer Data for Single Circular Jet Impingement," Int. J. Heat Fluid Flow **13**, pp. 106–115.

[2] Núñez, M., Coussirat, 2003, "Theoretical/Numerical Study of Flows With Strong Streamline Curvature," Ph.D. Thesis, CDIF-Dpto. Mecánica Fluidos-ETSEIB Universidad Politécnica de Cataluña.

[3] Baughn, J., and Shimizu, S., 1989, "Heat Transfer Measurements From a Surface With Uniform Heat Flux and an Impinging Jet," ASME J. Heat Transfer **82**, pp. 1096–1098.

[4] Baughn, J., Hechanova, A., and Yan, X., 1991 "An Experimental Study of Entrainment Effects on the Heat Transfer From a Flat Surface to Heated Circular Impinging Jet," ASME J. Heat Transfer **113**, pp. 1023–1025.

[5] Gardon, R., and Afkirat, C., 1965, "The Role of Turbulence in Determining the Heat-Transfer Characteristics of Impinging Jets," Int. J. Heat Mass Transfer **8**(9), pp. 1261–1272.

[6] Polat, S., Huang, B., Mujumdar, A., and Douglas, J., 1989, "Numerical Flow and Heat Transfer Under Impinging Jets: A Review," Annu. Rev. Numer. Fluid Mech. Heat Transfer **2**, pp. 157–197.

[7] Craft, T., Graham, L., and Launder, B., 1993, "Impinging Jet Studies for Turbulence Model Assessment: II. An Examination of the Performance of Four Turbulence Models," Int. J. Heat Mass Transfer **36**(10), pp. 2685–2697.

[8] Morris, G., Garimella, S., and Amano, R., 1996, "Prediction of jet impingement heat transfer using a hybrid wall treatment with different turbulent Prandtl number functions," J. Heat Transfer **118**, pp. 562–569.

[9] Roy, S., 2000, "Numerical Investigation of the Blade Cooling Effect Generated by Multiple Jets Issuing at an Angle Into a Incompressible Horizontal Crossflow," Numer. Heat Transfer, Part A **38**, pp. 701–718.

[10] Patel, P., and Roy, S., 2001 "Study of Jet impingement Heat Transfer for Varying Flow Characteristics," *ASME Fluid Engineering Division Summer Meeting*, pp. 1–7.

[11] Behnia, P., Parneix, S., and Durbin, P., 1998, "Prediction of Heat Transfer in an Axisymmetric Turbulent Jet Impinging on the Flat Plate," Int. J. Heat Mass Transfer **41**(12), pp. 1845–1855.

[12] Behnia, P., Parneix, S., Shabany, Y., and Durbin, P., 1999, "Numerical Study of Turbulent Heat Transfer in Confined and Unconfined Impinging Jets," Int. J. Heat Fluid Flow **20**, pp. 1–9.

[13] Durbin, P., 1991, "Near-Wall Turbulence Closure Without Damping Functions," Theor. Comput. Fluid Dyn. **3**, pp. 1–13.

[14] Spalart, P., and Allmaras, S., 1992, "A One-Equation Turbulence Model for Aerodynamics Flow," AIAA Paper No. 92-0439, pp. 1-22.

[15] Shih, Y., Ray, M., and Mujemdar, S., 2002, "Computational Study of Impingement Heat Transfer Under a Turbulent Slot Jet," Ind. Eng. Chem. Res. **41**, pp. 4643–4651.

[16] Spalart, P., 2000, "Strategies for Turbulence Modelling and Simulations," Int. J. Heat Fluid Flow **21**, pp. 252–263.

[17] Popiel, C., and Trass, O., 1991, "Visualization of a Free and Impinging Round Jet," Exp. Therm. Fluid Sci. **4**, pp. 253–264.

[18] Gauntner, J., Livingood, J., and Hrycak, P., 1970, "Survey of Literature on Flow Characteristic of a Single Turbulent Jet Impinging on a Flat Plate," N.A.S.A. Technical Note TN D-5652, pp. 1–41.

[19] Hoffmann, G., 1996, "Engineering Applications of Large Eddy Simulation to Turbulent Free and Wall-Bounded Shear Layers," Ph.d. Thesis, Lehrstuhl für Fluidmechanik Technische Universität München.

[20] Voke, P., and Gao, S., 1998, "Numerical Study of Heat Transfer From a Impinging Jet," Int. J. Heat Mass Transfer **141**, pp. 671–680.

[21] Cziesla, T., Biswas, G., Chattopadhyay, H., and Mitra, N., 2001, "Large-Eddy Simulation of Flow and Heat Transfer in an Impinging Slot Jet," Int. J. Heat Fluid Flow, **22**, pp. 500–508.

[22] Launder, B., and Spalding, D., 1974, "The Numerical Computation of Turbulent Flows," Comput. Methods Appl. Mech. Eng. **3**, pp. 269–289

[23] Choudhury, D., Kim, S., and Flannery, W., 1993, "Calculation of Turbulent Separated Flows Using a Renormalization Group Based k-ε Turbulence Model," *ASME Fluids Engineering Conf.*, ASME Paper No. TN-044

[24] Shih, T., Liu, W., Shabir, A., Yang, Z., and Zhu, J., 1995, "A New k-ε Eddy Viscosity Model for High Reynolds Number Turbulence Flows," Comput. Fluids **24**(3), pp. 227–238.

[25] Wilcox, C., 1988, "Reassessment of the Scale Determining Equation for Advanced Turbulence Models," AIAA J. **26**(11), pp. 1299–1310.

[26] Wilcox, C., 1988, "Multiscale Model for Turbulent Flows," AIAA J. **26**(11), pp. 1311–1320.

[27] Durbin, P., and Petterson, R., 2001, *Statistical Theory and Modeling for Turbulent Flows*, 1st Edition, Wiley, New York.

[28] Tennekes, H., and Lumley, J., 1983, *A First Course in Turbulence*, 9th Edition, Massachusetts Institute of Technology, Cambridge, MA.

[29] Durbin, P., 1993 "A Reynolds-Stress Model for Near Wall Turbulence," J. Fluid Mech. **249**, pp. 465–498.

[30] Durbin, P., 1993, "Application of a Near-Wall Turbulence Model to Boundary Layers and Heat Transfer," Int. J. Heat Fluid Flow **14**(4), pp. 316–323.

[31] Durbin, P., 1995 "Separated Flow Computations With the k-ε-v^2 Model," AIAA J. **13**, pp. 659–664.

[32] Wolfshtein, M., 1969, "The Velocity and Temperature Distribution in One-Dimensional Flow With Turbulence Augmentation and Pressure Gradient," Int. J. Heat Mass Transfer, **12**, pp. 301–308.

[33] Gardon, R., and Afkirat, C., 1966, "Heat Transfer Characteristic of Impinging Two-Dimensional Air Jets," ASME J. Heat Transfer **88**, pp. 101–108.

[34] Martin, H., 1977, "Heat and Mass Transfer Between Impinging Gas Jets and Solid Surfaces," Adv. Heat Transfer **13**, pp. 1–60.

[35] Cooper, D., Jackson, B., and Liao, G., 1993, "Impinging Jet Studies for Turbulence Model Assessment: I. Flow-Field Experiments," Int. J. Heat Mass Transfer **36**(10), pp. 2675–2684.

[36] Hirsch, Ch., 1988, *Numerical Computation of Internal and External Flows*, Vol. 1 and 2, 1st Edition, Wiley, New York.

[37] Ferziger, J., and Perić, M., 1997, *Computational Methods for Fluid Dynamics*, 2nd Edition, Springer, New York.

[38] Turbulence European Research Community on Flow and ERCOFTAC Combustion, 1998, ERCOFTAC, on-line web database edition.

[39] Coussirat, M. G., 2001, "Numerical Study of Turbulence Models for Impinging Gas-Jet Systems," von Kármán Institute for Fluid Dynamics, EA Report No. VKI-PR 2001-05.

[40] Kays, W., 1994 "Turbulent Prandtl Number - Where Are We?" J. Heat Transfer **116**, pp. 284-295.

[41] Daly, B., and Harlow, F., 1970, "Transport Equations in Turbulence," Phys. Fluids **13**, pp. 2634-2649.

[42] Jaw, S., and Chen, J., 1998, "Present Status of Second Order Closure Turbulence Models: I. Overview," J. Eng. Mech., pp. 484-501.

[43] Coussirat M., van Beeck J., Mestres M., Equsguiza E., Buchlin J.-M., and Valeroe, C., 2005, J. Fluids Eng. (to be published).

M. Coussirat
e-mail: coussirat@mf.upc.es
CDIF, Dpto. Mec. de Fluids,
Universidad Politècnica de Catalunya,
Av. Diagonal 647,
08028 Barcelona, Spain

J. van Beeck
von Kármán Institute for Fluid Dynamics,
Belgium

M. Mestres
Instituto de Ingeniería del Agua y Medio Ambiente,
Universidad Politècnica de Valencia, Spain

E. Egusquiza
CDIF, Dpto. Mec. de Fluids,
Universidad Politècnica de Catalunya,
Av. Diagonal 647,
08028 Barcelona, Spain

J.-M. Buchlin
von Kármán Institute for Fluid Dynamics,
Belgium

C. Valero
CDIF, Dpto. Mec. de Fluids,
Universidad Politècnica de Catalunya,
Av. Diagonal 647,
08028 Barcelona, Spain

Computational Fluid Dynamics Modeling of Impinging Gas-Jet Systems: II. Application to an Industrial Cooling System Device

A numerical analysis of the flow behavior in industrial cooling systems based on arrays of impinging jets has been performed, using several eddy viscosity models to determine their modeling capabilities. For the cooling system studied, and in terms of mean Nusselt number values, the best agreement between experimental results and numerical predictions was obtained with the realizable k-ε model. On the other hand, numerical predictions of the local Nusselt number and its spatial variations along the wall are better adjusted to the experiments when using either the standard k-ε or the standard k-ω models. The results obtained also show that the predicted thermal field depends strongly on the combination of near-wall treatment and selected turbulence model. [DOI: 10.1115/1.1949635]

Keywords: Impinging Jets, Turbulence Model, Eddy Viscosity, Jet Array, Numerical Modeling, Heat Transfer

1 Introduction

Heating or cooling of large surface area products is often carried out in devices consisting of an array of round or slot nozzles (ARN or ASN, respectively), through which air or another fluid impinges, frequently vertically, over the product's surface (see Fig. 1). Occasionally, the target plate is in a translational motion. Such impinging flow devices allow relatively high heat transfer rates. In order to achieve a suitable device design, both from an economic and a technical viewpoint, knowledge about the dependence of the heat and mass transfer rates on the external variables is required. Both the gas flow rate and the geometry of the device are the main variables, which can be chosen or modified to solve a given heat or mass transfer problem. It is essential that the effects of these important parameters are identified and understood. The first part of this work [1] allows one to identify and to know them in a first approximation, because only single jet systems were studied.

Because of the industrial applications of these devices, the majority of experimental studies related to impinging jets deals with heat transfer phenomena. Experimental data on mean and fluctuating velocity fields are more difficult to find. A review of experimental fluid dynamic databases, presented in paper I [1], clearly points out this problem and suggests that a better understanding of the jet impingement heat transfer process, the details of the flow, the geometry, the mean fluid dynamics, and turbulence conditions are necessary.

Due to the technological and economical difficulties found when performing and comparing experiments, numerical studies of the problem appear to be a promising method for quantifying the effects of the various parameters that influence the industrial design. In the last decade, numerical methods have become increasingly important in the study of impinging gas-jet systems (IJS). However, turbulent impinging jets have complex features that generate strong exchanges of mass, momentum, and heat, which depend strongly on the flow regime, on the nozzle geometry, and on the wall-to-jet distance. IJS flows prove to be somewhat difficult to represent with most of the existing EVM, which were developed (and tested) more extensively for flows parallel to a wall. EVM assume a linear stress-strain relation and a turbulence length scale based on thin shear layer flow, conditions that do not exist near the impingement point of a jet. Most of the actual IJS numerical databases show a broad range of modeled cases, but only for a single nozzle. The majority of these works have used EVM, but some studies using Reynolds stress models (RSM) or large eddy simulations (LES) can also be found. Details of the above-mentioned single IJS jets cases were discussed in the first part of this work. However, one of the actual engineering interests is the prediction of the heat and mass transfer rates for arrays of jets interacting with plates in motion (see Figs. 1 and 4). Numerical results for IJS corresponding to such configurations are scarce. Works from Chen et al. [2] and Chattopadhyay et al. [3] present numerical results obtained by modeling an array of slot jets (infinite array) with the target plate in translational motion. The work from Chen et al. is for laminar flow, and the code used in this study was based on the simple algorithm and utilized the line-by-line method and the tri-diagonal matrix algorithm. The work from Chattopadhyay et al. is for low Reynolds numbers ($500 < \mathrm{Re} < 3,000$) using LES. Under the defined velocity condition defined by these Reynolds numbers, experimental evidences show that the flow is laminar or transitional, but not fully turbulent [4,5]. Industrial devices frequently have higher Reynolds

Contributed by the Fluids Engineering Division for publication in the JOURNAL OF FLUIDS ENGINEERING. Manuscript received by the Fluids Engineering Division July 21, 2004; final manuscript received April 19, 2005. Associate Editor: Surya P Vanka.

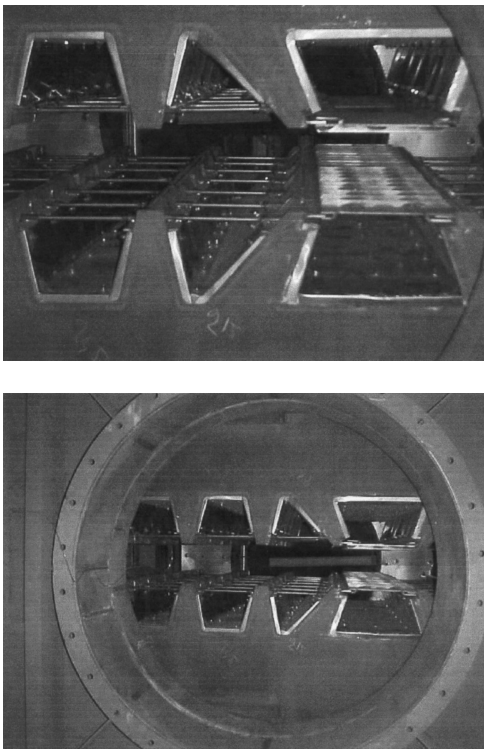

Fig. 1 Industrial impinging gas jet system for steel plate cooling

numbers. At the moment, the application of LES or DNS to arrays of IJS for high Reynolds numbers is not possible with existing computational resources [6].

The wall heat transfer is a local effect restricted to the near-wall zone. Industrial IJS show a strong geometrical complexity, and an accurate near-wall modeling leads to the definition of large computational meshes. In addition, large computational resources are necessary for an accurate modeling of the near-wall flow. A commonly used alternative to this strategy is to relax the mesh size and to use wall functions to solve the near-wall flow, although the introduction of wall functions implies the assumption of a more simple flow and, therefore, a loss of accuracy in the results, although it does allow the problem to become more affordable.

Summarizing, turbulent IJS provide a strikingly difficult test flow for turbulence models due to its characteristics. There are several detailed experimental and numerical databases, but only for single nozzle jets. Experimental industrially oriented test cases for arrays of jets are difficult to find. Also, numerical results for three-dimensional cases are scarce because the mesh size for a suitable near-wall treatment quickly becomes unaffordable in some cases due to the increase of the mesh size. EVM could become a useful tool for designing industrial IJS if the capabilities of the numerical models to reproduce this kind of flow are well known.

The main motivation of this work is to learn the behavior of EVM when applied to the design of industrial IJS cooling devices. The experience gained in the previous modeling of single jet cases already presented in the first part of this work was applied to carry out this task. Cases from experimental databases for ASN jets from Gardon and Afkirat [7] and Buchlin et al. [8] were modeled by means of Reynolds-averaged Navier-Stokes (RANS) strategy using the Boussinesq assumption and several EVM. The results obtained for single nozzle IJS in the first part of this work showed that credible results require simulations with more than one EVM. Also, these results showed that the Spalart-Allmaras model could be a good starting point to model more complex cases.

Therefore, the studies for ASN cases presented here will provide some guidelines and strategies to obtain a good heat transfer modeling. The present modeling work takes into account the optimization from the modeling strategy and the computational resources viewpoints.

2 Classification of Applied Turbulence Models

It is very important to know which turbulence model is the most adequate to compute mean and local values of heat transfer coefficients in the design of cooling/heating jet devices. The research directed to improve turbulence modeling has led to the development of several types of EVM. These models are based on transport equations for the turbulent variables (0, 1, 2, or more differential equations). The general philosophy assumes that the use of a larger number of transport equations implies a more realistic flow description, leading to a more general model. The turbulence models used in this work were based on a one-equation model from Spalart-Allmaras [9], three variants of a k-ε, a two-equation model (i.e., a standard k-ε model from Launder and Spalding [10]; the RNG k-ε from Choudhury et al. [11] and the realizable k-ε from Shi et al. [12]), the standard k-ω model from Wilcox [13,14], and the four-equation model V2F from Durbin [15]. The second-order models (Reynolds stress modeling, RSM) have a much closer connection to the physical phenomena in a turbulent flow; but for industrial CFD applications, the EVM approach is preferred over the RSM because the latter is more "expensive" in terms of CPU time and memory, and in some cases the RSM approach is very "stiff" for solving complex flows, and convergence problems arise. In spite of that, a comparison with a modified Daly and Harlow [16] RSM was also made. RSM's modifications were the slow pressure strain model from Rotta, the rapid strain term model from Fu et al., and the wall reflection model from Launder and Shima. See more details of the aforementioned models in Ref. [17].

2.1 Near-Wall Treatment. Anisotropy exists in all real flows. In general, EVM are designed to represent shear stress anisotropy, but not normal stress anisotropy [18] because the kinetic energy is computed assuming that normal fluctuations are the same in all directions. To take into account the nonisotropic nature of turbulence in near-wall regions, different strategies were followed, depending on the test cases. More details of the near-wall modeling strategies used will be given in the next sections.

Applications of the above models to several ASN impinging jet configurations were performed, including a comparison of the local and mean Nusselt numbers against experimental data, and the mean numerical Nusselt number against empirical Nusselt correlations [19].

3 Modeling Procedure and Numerical Results

Computations were carried out with a commercial computer code (FLUENT® v5.4.8 and v6.1.18). This solver has a finite-volume solution scheme for the mean momentum, energy, and turbulent transport equations. Incompressible flow was assumed; thus, the use of a segregated solver is adequate. The schemes selected to perform computations were second-order upwind implicit; except for the diffusion terms, where an implicit second-order central difference scheme was used. The SIMPLE method was selected to solve the pressure-velocity coupling. Details on all numerical schemes and methods mentioned above can be found in Refs. [20–23].

For the ASN cases, a comparison of the local Nusselt number against experimental data has been done. This study also includes a comparison of the mean numerical Nusselt number against empirical Nusselt correlations from Martin [19]. Experience gained in previous modeling of SRN and SSN jet cases was very useful in defining characteristic parameters of the simulations and to check the sensitivity of the results to changes in the mesh or boundary conditions. For SRN cases, databases from Cooper et al.

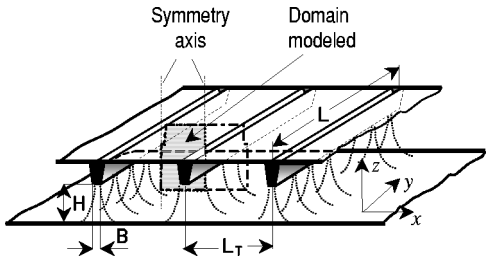

Fig. 2 Characterization and nomenclature of ASN jets for the numerical modeling of the Gardon and Afkirat [7] experiment: *B*, nozzle width; *H*, nozzle-to-plate distance; L_T, distance between nozzles; and *L*, nozzle span

[24] and Baughn et al. [25,26], both integrated in a unique set of data in the ERCOFTAC database [27], were used. For SSN cases, the databases used were from Gardon and Afkirat [7,28]. More details and results of these previous SRN and SSN jet cases modeled can be seen in the first part of this work.

3.1 Experimental Test Setups. The present work deals with ASN jet systems. The databases used were from Gardon and Afkirat [7] and Buchlin et al. [8].

Gardon and Afkirat's experiment has only results of the heat transfer coefficient along the wall. The experimental test cases consist of two ASN jets setups, containing two and three slot jets, respectively. The fluid is air, impinging on an electrically heated plate (see Fig. 2). The plate was made of aluminium (high thermal conductivity) in order to suppress lateral differences of temperature within it. Its temperature level was controlled at a fixed level, low enough for heat losses by radiation to be negligible. Steady-state convective heat transfer was obtained between the isothermal hot surface and the jet of cooling air from the slot nozzle. The local heat transfer rates were measured with a heat-flow transducer mounted on the hot plate and flush with its surface, without disturbing the isothermal characteristic of the heat transfer surface. The probe consisted of a 0.9 mm dia copper-constantan thermocouple, with a sensitivity of 0.024 mV/(W/cm^2). A motor-driven device allowed the hot plate to move. In this manner, a plot of the local rate of heat transfer versus the position of the test area relative to the jets could automatically be recorded. The nozzle width used was $B=3.175$ mm, and provision was made for varying the nozzle-to-plate spacing ($4.0<H/B<40.0$), the air flow rate, the plate temperature (which was usually maintained 2 °C above the ambient air temperature), and the incoming velocity at the jet nozzle.

The Buchlin et al. [8] experiment also presents results only for the heat transfer coefficient along the strip in a small-scale model (see Fig. 3). This setup is a 2:3 scale model of an industrial IJS (see Fig. 1). There are no velocity field measurements.

In the industrial IJS, the strip moves with a constant velocity, increasing the complexity of the numerical study. The exhausting jet velocity often reaches 75 m/s, but the Mach number is 0.2 (air) and, therefore, the compressibility effects are still negligible. The scale model also fulfills the incompressibility condition in order to extend the laboratory correlations to the industrial situation. The scale-model facility allows the investigation of the cooling rate when the jet Reynolds number Re_s, based on the hydraulic slot diameter, $S=2B=22$ mm, varies between 60,000 and 100,000. The slot arrangement consists of a set of perpendicular and sloped slot nozzles, which can be adjusted in order to investigate the effect of parameters such as the nozzle spacing L_T ($6 \leqslant L_T/S \leqslant 18$), the length of the nozzle E ($5 \leqslant E/S \leqslant 15$), the nozzle-to-plate distance H ($3 \leqslant H/S \leqslant 10$), and the impingement angle β (60 deg $\leqslant \beta \leqslant$ 90 deg; $\beta=90$ deg corresponds to a perpendicular jet (see Fig. 4). The flat plate in the scale model (the strip in the industrial IJS device) is a constant heat-flux surface 1.7 m long and 0.27 m wide, designed to provide a uniform heat flux. The plate temperature field was measured with an infrared scanner consisting of a HgCdTe detector, sensitive in the 8–12 μm wavelength range and cooled by liquid nitrogen [8]. The geometrical resolution obtained on the skin was less than 1 mm and the aforementioned spectral sensitivity is equal to a resolution of 0.08 °C at 30 °C (see details in Ref. [29]).

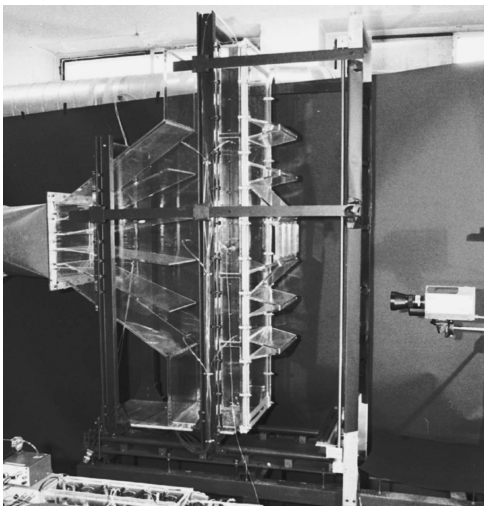

Fig. 3 VKI test setup for ASN jets. The setup consists of a 2:3 scale model of the cooling moving strip unit of Fig. 1. Temperature field was measured by means of an infrared IR scanner (from Ref. [8]).

Because of its geometrical configuration and boundary conditions, this case can be considered as a full three-dimensional case, but the comparison between the numerical simulations and experiments are quantified along the strip centerline.

3.2 Gardon and Afkirat [7] Case. The numerical prediction of two ASN jet cases (see Table 1, and for notation, see Fig. 2) was made. The problem was defined as steady, and the aforementioned set of turbulence models was applied. The main goal of this test is to check the behavior of the turbulence models already used in cases of SRN and SSN jet cases (see the first part of this work), and to assess the predictions of interaction between jets. Comparison against the Gardon and Afkirat experimental database was

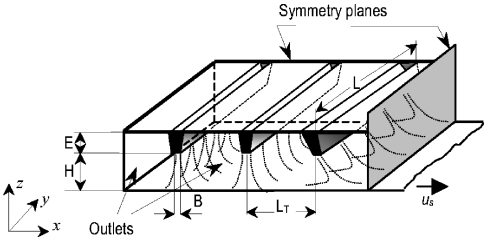

Fig. 4 Characterization and nomenclature of ASN jets for the Buchlin et al. [8] experiment: *B*, nozzle width; *H*, nozzle-to-plate distance; L_T, distance between nozzles; *E*, nozzle height; *L*, nozzle span; and u_s, velocity of the strip

Table 1 Modeled cases, array of slot nozzle jets (ASN); Gardon and Afkirat [7] case

Case	Pipe width (m)	Re ($\times 10^3$)	H/B	L_T (m)	Nozzles
1	0.003175	5.5	4	0.1016	2
2	0.003175	5.5	4	0.0508	3

made, together with a comparison of the mean values of the heat transfer coefficient against values given by empirical and widely used relations extracted from Martin [19]. The experimental Reynolds number was $Re_s=5500$; at this Reynolds number, it is not clear that the flow is fully turbulent [5], so strong influences due to the transition regime are expected. It is necessary to emphasize that the transition problem is not well modeled by all the EVM used here. Additionally, influences of transition cannot be computed, although it is very usual to use EVM to model transitional flow assuming the flow as fully turbulent (e.g., see Ref. [30]). Concerning the geometry, two symmetry axes were defined, the first one at the center of one nozzle and the other at half the distance between jets, in both cases (see Fig. 2). Despite that the end effects could influence the performance of the array, careful consideration of the problem reveals that periodic domain can be employed [2]. To check the differences between modeling an infinite array of jets and the experimental cases, some comparisons were made. The comparisons made were focused on the Nusselt number distribution along the wall, between the two jets. Results obtained did not show appreciable differences between the two cases (real and infinite arrays) in agreement with Ref. [2]. The difference between the two- and three-nozzle cases, from the numerical viewpoint, is the distance between jets.

3.2.1 Domain Definition, Mesh Characteristics, and Boundary Conditions. Conditions similar to those for SRN and SSN jet cases were defined (see the first part of this work). Also, the guidelines obtained in the previous cases to define a suitable mesh were used here. Again, mesh independence was obtained when y^+ was smaller than 3.

The boundary conditions were the following: At the inlet boundary, an inlet velocity condition was defined by means of a prescribed mean velocity value. It was possible to do this due to the nozzle configuration (i.e., there is a nondeveloped flow at the nozzle). Turbulence quantities were computed from a defined value of the turbulence intensity at the inlet ($I=2.5\%$), using empirical expressions that depend on the turbulence model used [23,31,32]. At the axis boundary, a symmetry condition was defined. A similar symmetry condition was also defined at the lateral boundary, at which the two jets merge—at a distance of $x/B=L_T/2$ in both cases (two and three nozzles). At the upper boundary, a pressure outlet boundary condition was defined through the specification of a static (gauge) pressure. All other flow quantities were extrapolated from the interior. At the wall boundaries, the no-slip boundary condition was enforced. Shear stresses and heat transfer between the fluid and the wall were computed considering the flow details in the local flow field. In this case, a constant heat flow was prescribed, according to experimental data. To predict the wall shear stress in the fluid for the enforcement of no-slip wall conditions, the properties of the flow adjacent to the wall were used. An accurate representation of the flow in the near-wall regions is important for a successful prediction of wall-bounded turbulent flows. The near-wall treatment depends on the type of turbulence model used.

3.2.2 Near-Wall Modeling. The knowledge of y^+ values along the heated plate will allow us to define the suitable near-wall treatment [i.e., the use of wall functions (WF), damping functions (DF), or a two-layer modeling (TLM)]. Therefore, it is necessary to perform a preliminary computation to estimate this value. This was done by means of the Spalart-Allmaras model, following the guidelines given in the first part of this work. Its implementation in the computational code used allows the selection of the suitable near-wall modeling automatically because the y^+ are computed internally and the near-wall treatment is activated in accordance with the y^+ value. Values of y^+ are stored in a file for inspection. Checking the y^+ values along the bottom wall allows us to decide which near-wall treatment is more suitable for the k-ε family models.

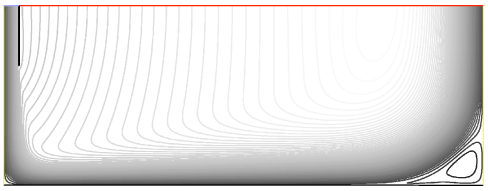

Fig. 5 Streamlines obtained with the standard $k-\varepsilon$ for Re $=(5.5)\times10^3$, $H/B=4.0$, $B=3.175$ mm, two nozzles, Gardon and Afkirat [7] case. The nozzle is at the left, and the symmetry edge is at the right.

After checking the y^+ value, and depending on which EVM is used, different near-wall strategies were defined. For the Spalart-Allmaras and the standard k-ω models, ad hoc damping functions were used [9,13], whereas for the k-ε family models, the TLM scheme was used [17,33]. The V2F model has a specific near-wall treatment (see Refs. [34] and [35] for details). A brief description of these models can also be found in Coussirat [5,31].

3.2.3 Convergence Criteria. The first required criteria for convergence was to diminish the normalized residuals by four orders of magnitude in all quantities, but sometimes this criteria was not successfully fulfilled. To guarantee that the results reached a steady state, complementary controls over the mean quantities (such as drag coefficient or temperature at the wall) and a local quantity (e.g., the velocity at a defined point) were performed. This control consisted of checking that the analyzed quantity did not change its value over 1000 iterations. Differences between flow rates at the inlet and at the outlet were also computed to check the fulfillment of the "global" continuity condition.

3.2.4 Obtained Results. For the Gardon and Afkirat setup, results of the flow and thermal fields were obtained. With regard to thermal quantities, profiles of the Nusselt number along the wall and the wall heat transfer coefficient h_0 at the stagnation point ($x/B=0$) were computed for the two cases (two and three nozzles).

3.2.5 Flow Field. The computed flow field for $Re=5.5\times10^3$, $H/B=4$, and two nozzles is shown in Fig. 5. The features of the mean flow in this region are captured by the computations, showing the stagnation point, the shear layer, the entrainment zones, and the zone where the jets merge. A careful comparative study of the hydrodynamic field was not performed because experimental hydrodynamic data for this case was not available in the Gardon and Afkirat database. A similar flow pattern was observed in the three-nozzles case (not shown here).

3.2.6 Nusselt Number Profiles Along the Wall. Results of the Nu distribution along the wall are depicted in Fig. 6 for the two- and three-nozzles arrays (top and bottom, respectively). These results show a reasonable agreement between numerical and experimental values. For the Spalart-Allmaras and k-ε family models, the results have similar predictions both in the two-nozzles array and in the three-nozzles array cases. On the other hand, the standard k-ω and V2F models showed strong differences; the V2F gave unrealistic results at the beginning of the jet interaction zone ($x/B=14.0$ for the two nozzles and $x/B=5.0$ for the three nozzles), whereas the standard k-ω gave strongly overpredicted values at the stagnation point in both cases. In the three-jets case, all the models showed some oscillations at the jet interaction zone. To check the influence of the imposed symmetry condition, in spite of the evident physical symmetry of the problem (see Fig. 2), a modeling of the complete domain was carried out, showing the same oscillations (not shown here). Therefore, the symmetry condition does not affect the results.

More in detail, for the two-jet array case (Fig. 6, top), the realizable k-ε model gave a very good fitting of the Nu trend and only

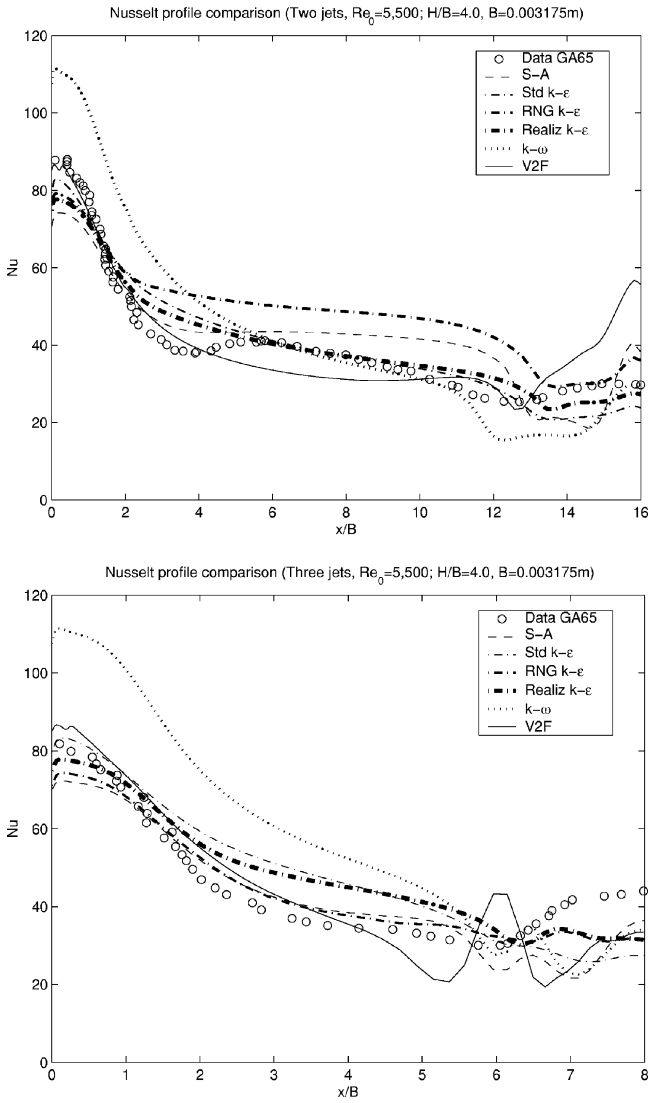

Fig. 6 Variation of Nusselt number with *x* distance: Re=(5.5) $\times 10^3$, $H/B=4.0$, $B=3.175$ mm, Gardon and Afkirat [7] case. Top, two nozzles; bottom, three nozzles.

failed in the Nu_0 value prediction. This model underpredicted the values in a similar way to the Spalart-Allmaras and other k-ε family models (around 10%). The V2F model gave an accurate Nu_0 value, and the standard k-ω model strongly overpredicted the value of the Nu_0 (around 18%). At the zone where the jets meet together ($x/B=16$), the V2F model strongly overpredicted the local Nusselt number (almost a 100% discrepancy). Here, the other models computed a more accurate value. For the three-jets array (Fig. 6, bottom), the V2F model showed good behavior, except in the jet interaction zone, as in the two-jet array case. This model slightly overpredicted the value of Nu_0 (around 3%). The standard k-ε model gave a good prediction of Nu_0, while all the other models underpredicted the Nu_0 value (maximum underprediction is around 10%). The standard k-ω model again overpredicted Nu_0, as in the two-jet case (around 40%). The Nusselt number profile along the wall was predicted in a similar way by all models, except the standard k-ω model, which overpredicted values along the wall up to $x/B=6$. At the zone where the jets meet together ($x/B=8$), all the models gave similar predictions of the local Nusselt number value. The behavior of all the models was worse in the zone where the jets merge, because they all presented oscillation in their predictions. The V2F model showed the worst behavior in this zone.

3.2.7 Mean Nusselt Number. An integration of the area under the experimental and numerical curves was performed to obtain the mean Nusselt number $\overline{Nu}$ and the mean heat transfer $\bar{h}$.

Table 2 gives computed values of $\overline{Nu}$ and $\bar{h}$ for all the turbulence models used in cases 1 (two nozzles) and 2 (three nozzles). A comparison of the values of $\overline{Nu}$ and $\bar{h}$ against the empirical correlations to compute $\overline{Nu}$ and $\bar{h}$ from Martin [19] was also carried out, assuming a constant value of $k_f=2.52\ 10^{-2}$ W/(mK). Quite good predictions of these values were obtained with all the EVM used, except the RNG k-ε model (see Table 2). Taking the experimental value as a reference, the worst value is for the RNG k-ε model, with a 23.5% overprediction for the two-jet array case. All the other models overpredicted by about 2.5%. For the three-jet array, the largest discrepancy was obtained with the standard k-ω model, which gave a 23% overprediction. The realizable k-ε model and the Spalart-Allmaras model underpredicted the heat transfer coefficient, but by 8.3% and 3.6%, respectively. Martin's correlation gives an overprediction of 25% for the three-jet case.

Summarizing, the computed flow field pattern for Re=5.5 $\times 10^3$ and $H/B=4$ is quite similar for both the two- and three-nozzle arrays. The main features of the flow are captured by the computations. The trend of the Nusselt number along the wall was followed by all the models, but unrealistic oscillations appear near the zone where the jets merge. Predictions of the mean heat transfer coefficient $\bar{h}$ are acceptable for the three-nozzle array; but surprisingly, the RNG k-ε model gave overpredictions in the two-nozzles case, despite the good behavior shown in the previously modeled SRN and SSN cases (see the first part of this work). For the three-nozzle case, the mean Nusselt number prediction given by the RGN k-ε model is better than that obtained for the two-nozzle case. Concerning the Nu_0, only the standard k-ω model

Table 2 Mean Nusselt $\overline{Nu}$ and heat transfer coefficient $\bar{h}$ computed for the two- and the three-jets array cases: $Re_0=5.5\times10^3$, $B=3.175$ mm; Gardon and Afkirat [7] case

	Two jets		Three jets	
Case	Nusselt, $\overline{Nu}$	$\bar{h}$ [W/(m^2 K)]	Nusselt, $\overline{Nu}$	$\bar{h}$ [W/(m^2 K)]
Martin correlation	38.999	148.500	55.550	211.640
Gardon and Afkirat data	39.078	148.908	44.212	168.495
Spalart-Allmaras model	41.834	159.430	42.595	162.330
Standard k-ε model	40.100	152.800	48.000	182.900
RNG k-ε model	48.260	183.920	44.198	168.437
Realizable k-ε model	40.305	153.602	47.978	182.846
Standard k-ω model	42.600	162.500	57.800	220.400
V2F model	40.270	153.471	43.874	167.205

gave a strong overprediction of this value in both cases, probably due to a local excess of the estimated kinetic energy. Compared with the standard k-ε model, the standard k-ω model predicts a 30% higher level of k at the stagnation point. Discrepancies between experiments and numerical results are probably due to the use in all these EVM of a linear stress-strain relation and a turbulence length scale based on thin shear layer flow, conditions which do not exist near the impingement point of a jet.

3.3 Buchlin et al. [8] Case. The background obtained in the simulations of the previous cases is applied to the modeling of the full three-dimensional small-scale model from Buchlin et al. [8] experiment (see Fig. 4). The problem was defined as a steady and fully turbulent flow. The Spalart-Allmaras model, standard, RNG, and realizable k-ε models, and the standard k-ω model, were used. Besides checking the behavior of these turbulence models, another goal of this test is to check the hardware capabilities, because the CPU and memory requirements will grow considerably. After performing some tests, the impossibility of using a TLM scheme in this case was confirmed due to the lack of computational resources, because of the large increase in the mesh size (more than 600,000 cells).

3.3.1 Domain Definition, Mesh Characteristics, and Boundary Conditions. Several hybrid and nonstructured three-dimensional meshes were defined. A boundary layer mesh was defined at the bottom, where the strip is located, by means of the distance between the plate and the first node (d_n), and a certain increasing factor (Δ). A test of grid independence was made by varying d_n and Δ, and comparing the Nusselt number distribution along the plate. No noticeable variation was observed when the mesh had about 250,000 cells with $d_n=0.1$ mm and $\Delta=1.1$. Some details of the mesh, which is only suitable for the use of wall functions, can be seen in Fig. 7.

Similar considerations, as in previous cases, were made. Therefore, the boundary conditions are the following: inlet, symmetry, pressure outlet, and wall (no-slip).

At the inlet faces, an inlet velocity condition was defined by means of a prescribed value for the mean velocity, computed from the experimental Re. Three inlets were defined, corresponding to the jet nozzles (one marked in blue, Fig. 7, left). Turbulence quantities were computed by means of a defined value of the turbulence intensity at the inlets, as in the previous ASN cases.

Accounting for the geometry of the real device (Fig. 1) and the model (Fig. 3), several symmetry planes were defined (marked in yellow in Fig. 7). At these planes, symmetry conditions were defined in the same way as in the previous two-dimensional cases.

At the lateral outlet, placed opposite the symmetry plane (marked in red, Fig. 7), an outlet pressure boundary condition was defined, requiring the specification of a static (gauge) pressure. Its value was set to zero, implying that the relative pressure was equal to the atmospheric pressure. In this boundary, all other mean flow quantities were extrapolated from the interior. The levels of turbulence parameters were estimated in the same way as in the previous ASN cases.

At the wall boundaries (top and bottom), a no-slip boundary condition was imposed, as in previous cases (marked in black, Fig. 7). Shear stresses (both walls) and heat transfer (bottom wall) between the fluid and the wall were computed, considering the flow details in the local flow field. The bottom wall is divided into two parts; in one, the width of which is the same as the lateral length of the jets (y direction, see Fig. 4), a constant heat flow was prescribed, according to experimental data. In the other part of the wall, a zero heat flow was prescribed.

3.3.2 Near-Wall Modeling. The near-wall treatment depends on the type of turbulence model used. A similar study was made as in the previous ASN cases for the y^+ variation along the wall. It allowed us to know if the mesh was suitable for the use of wall functions or other near-wall treatments. This computation also allows us to obtain a preliminary set of results for the flow velocity and the heat transfer fields.

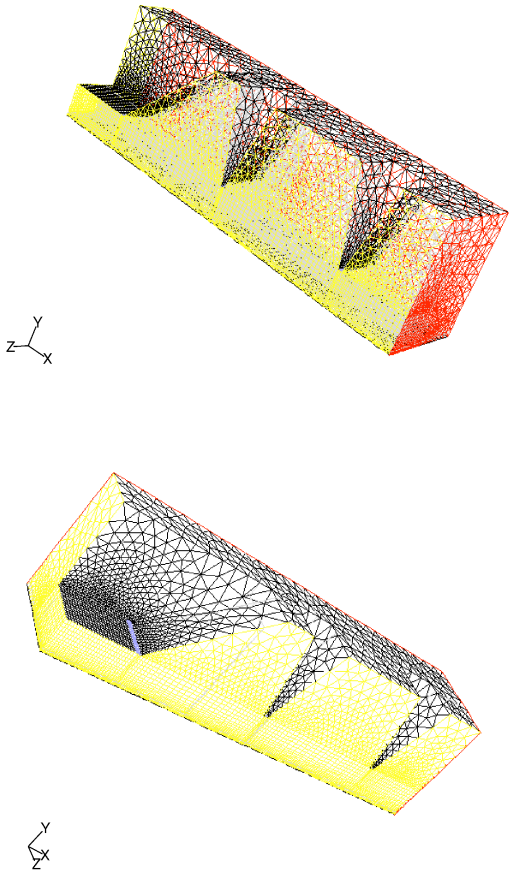

Fig. 7 Generated three-dimensional mesh, Buchlin et al. [8] case

The computed values of y^+ vary between 2, in the impingement zones, and maximum values of about 120 along the wall. Therefore, in many places, the use of wall function is not suitable because y^+ has low values ($<$20–30). Due to this variation in the y^+ values, it is not possible to use WF or a TLM scheme in all of the domain. Use of a TLM scheme implies a refinement of the mesh, but it is not easy because the necessary cell size reduction leads to a large increase of the number of cells in the mesh. Many times, the use of the refined mesh is not possible due to the lack of computational resources. A selective refining of the mesh should allow one to obtain a mesh that fulfills the "y^+ requirements," but it is often not possible because many "trial-and-error cycles," implying modeling to obtain y^+ values, are necessary. To use wall functions implies the coarsening of the mesh. After performing some tests, successful coarsening was not possible because many zones reach values greater than the upper boundary value of y^+ for a suitable use of wall functions. Therefore, it was assumed that the unique possibility of near-wall treatment was by means of wall functions for the k-ε model family, and zones with values of $y^+=2$ were "assumed" (i.e., wall functions have been applied). Both standard wall functions, SWF, and modified wall functions, MWF (i.e., nonequilibrium wall function sensitized to account for mild adverse pressure gradients), were used in computations with the standard, realizable, and RNG k-ε models. For the Spalart-Allmaras model and the standard k-ω model, damping functions were used.

3.3.3 Convergence Criteria. The same guidelines as for the previous Gardon and Afkirat modeling cases were followed. In

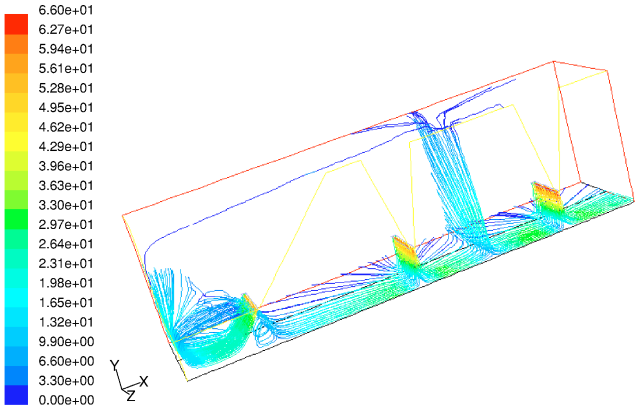

Fig. 8 Numerical pathlines obtained with the standard $k-\varepsilon$ model for the Buchlin et al. [8] case

general, to decrease the normalized residuals in all quantities by four orders of magnitude was very hard. Therefore, the aforementioned complementary convergence controls become more important.

3.3.4 Obtained Results. For this setup, results of flow and thermal fields were obtained. With regard to thermal quantities, profiles of the Nusselt number along the bottom wall were computed. A comparative study of the hydrodynamic field was not performed because experimental hydrodynamic data for this case was not available.

3.3.5 General Flow Field View. A general view of the pathlines obtained for this case is shown in Fig. 8. The three stagnation points can easily be seen. A strong recirculation is observed near the wall in the tilted jet zone. In the other nozzles, there is also some recirculating flow near the wall. There is a strong decrease of the velocity along the wall when the flow travels toward the lateral outlet, as the pathlines show. The interaction between jets can also be observed, as in the previous two-dimensional cases modeled. In the near-wall zone, the strong flow toward the lateral outlet has an important role in the heat transfer. Here, the flow is fully three dimensional.

The computed flow field for $\mathrm{Re}=6.0\times10^5$, $H/D_H=4.55$, and $L_T/D_H=14.5$ ($D_H\simeq S=2B$ for long slots), the stagnation zones, and the zones where the jets meet together are also shown in Fig. 9(top). In Fig. 9(bottom) the turbulent viscosity μ_T distribution can be observed.

Concerning the mixing in the near-wall region, a similar behavior as for the presented two-dimensional cases was found. Higher values of μ_T indicate a strong mixing in the zone where the jets merge.

3.3.6 Nusselt Number Profiles Along the Wall. A comparison between the experimental data and the obtained numerical results is presented in Fig. 10.

It can be observed that the fittings are different, depending on the turbulence model used. The minimum Nusselt values (at $x/D_H\simeq15$ and at $x/D_H\simeq35$) were underpredicted by all models. A reason for this disagreement between numerical results and experiments could be the aforementioned lack of accuracy due to the intrinsic formulation of the EVM. Another possible reason for this behavior could be that all the tested EVM turbulence models are only suitable for flows without strong streamline curvature, but the use of a RSM model that captures the streamline curvature in its formulation does not improve the predictions. Therefore, it is possible to think that streamline curvature is not an important effect in three-dimensional cases. The strong interaction between jets is not well predicted, and the wall functions are not suitable at these positions (y^+ is less than 20 at these places). The realizable

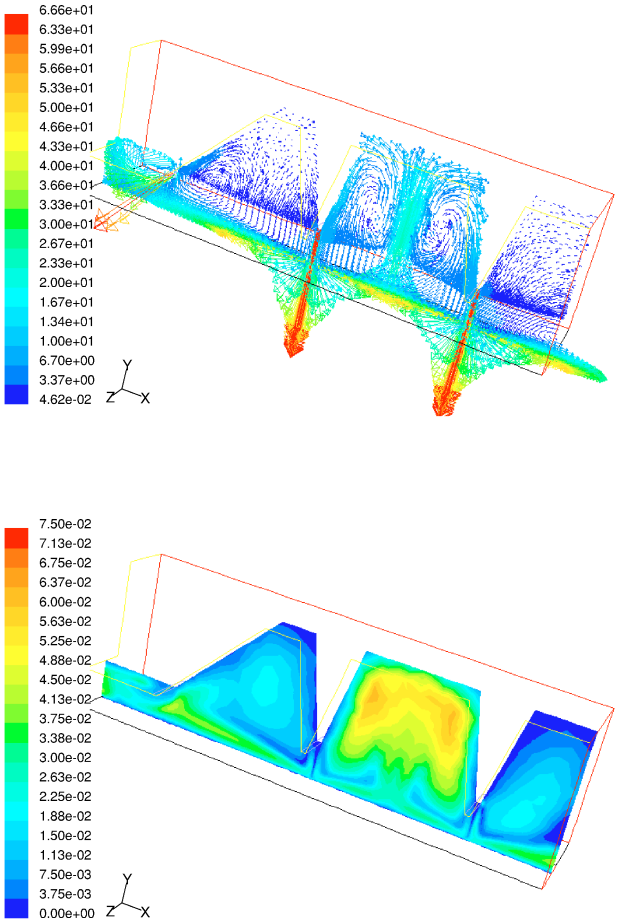

Fig. 9 Numerical results for standard $k-\varepsilon$ model, Buchlin et al. [8] case. Top, velocity vectors; bottom, μ_T contours

k-ε model showed the best agreement with the experimental data. The values at the stagnation point for the nontilted nozzles (at $x/D_H\simeq25$ and at $x/D_H\simeq45$) were well predicted by the standard k-ε model. The predicted positions of the maximum heat transfer showed a slight displacement with respect to the experimental

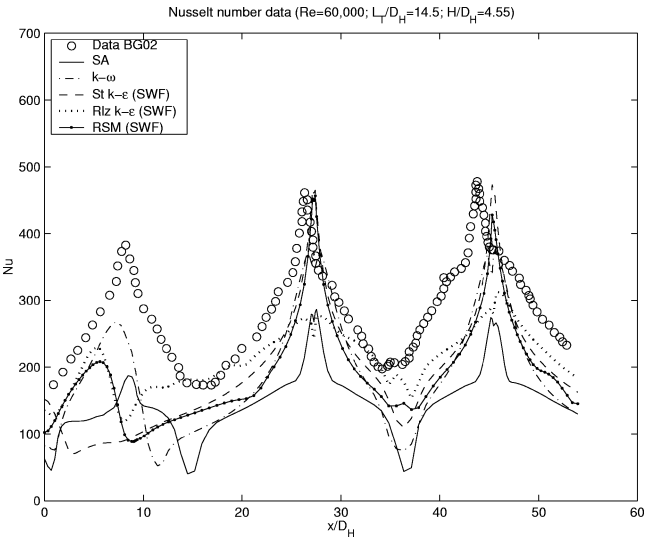

Fig. 10 Comparison between turbulence models used, Buchlin et al. [8] case

values. The performance of this model worsens closer to the tilted nozzle ($0<x/D_H<15$), and it did not predict the peak at this position. The standard k-ω and the Spalart-Allmaras models underpredicted these maxima, and they also showed a little drop in the variation of the Nusselt number near the stagnation point. It is necessary to remark that at these positions, y^+ was less than 20. Therefore, it seems that the inadequate use of wall functions did not significantly affect the obtained results at the stagnation point, because the predictions at these points were better than predictions at other points where y^+ was greater than 20. The k-ω model follows the local trend of the Nusselt number along the wall better than any other model, improving the behavior observed in the previous two-dimensional array cases presented (see Fig. 6). For the tilted nozzle, the standard k-ω showed underpredicted values for the Nusselt number, but followed its trend; the Spalart-Allmaras model showed a similar level of Nusselt number underpredictions, and the realizable k-ε model showed some unexpected drops at the stagnation points. In this zone, the results from the latter model showed some wiggles. The RNG k-ε model predictions of maximum values of the Nusselt number showed strong drops at the positions of maximum heat transfer, implying that very low eddy viscosity values are predicted at these positions. To understand the near-wall behavior of this model, the near-wall parameters were checked. The analysis of the y^+ profile along the wall obtained with all the turbulence models showed similar drops, as in the Nusselt number profiles along the wall computed with the RNG k-ε model (not shown here). These minimum values of y^+ revealed that there are low strain deformation rates computed at these positions. Only the RNG k-ε model showed coupling between y^+, eddy viscosity ν_T, and Nusselt number results, showing this strange behavior.

Two reasons could explain this behavior. The first one may be noticed by comparing the standard k-ε and the RNG k-ε models in detail. The only difference between them is the ε equation, since the equation for the turbulent kinetic energy k is the same. The ε equation for the RNG k-ε model includes a term that is a function of the mean strain and a time scale for turbulent deformation rate with respect to the mean deformations (see Ref. [31] for more details). This term affects the ν_T computation for rapidly strained flows, diminishing its value and, therefore, the RNG k-ε model yields a lower turbulent viscosity than the standard k-ε model. Rapidly strained three-dimensional flows could strongly affect the ν_T computations when the RNG k-ε model is used.

The second reason is the possible influence of wall functions in the predictions of the kinetic energy dissipation ε in this case. Thus, the use of wall functions could affect the RNG k-ε performance. To gain insight about this behavior, a study of the influence of wall functions was made, because the study of the influence of ε variations was not possible due to the lack of experimental flow field data. For this study, both SWF and MWF were used in computations with the standard, realizable, and RNG k-ε models. Small differences in the results can be observed for each model, but only the results of RNG k-ε model showed the drops, as seen in Fig. 11. The last result was expected because the impinging jet flow is pressure driven (i.e., there are no adverse pressure gradients along the wall). The use of other near-wall modeling strategies could give some insight on the lack of realistic numerical predictions. The use of a TLM in this case was not possible due to the lack of computational resources but, for this computational mesh, the use of damping functions is possible. This near-wall treatment is used by the Spalart-Allmaras and the standard k-ω models. The obtained results showed the same y^+ behavior, but there are no realistic drops in the Nusselt number prediction for these two last models (see Fig. 10). Therefore, it is possible to conclude that the use of wall functions combined with the RNG k-ε model, in this case, strongly affects the near-wall predictions of the kinetic energy dissipation ε.

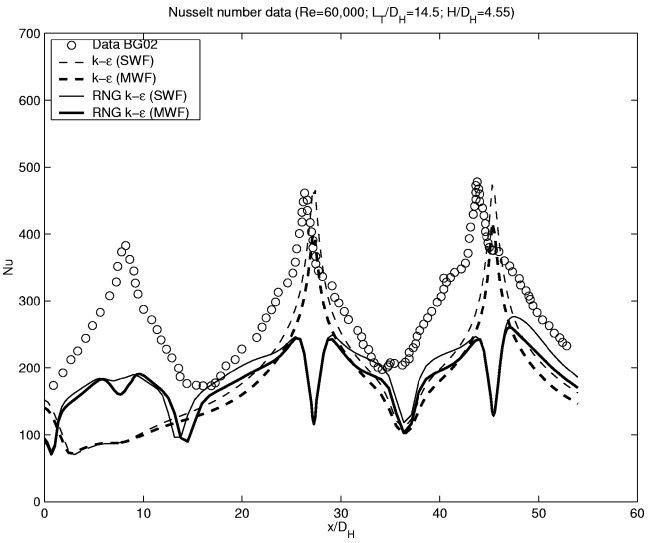

Fig. 11 Comparison between near-wall strategies used, Buchlin et al. [8] case

3.4 Mean Nusselt Number. It is also very important to evaluate the mean value of the Nusselt number because it is a strategic design parameter in an impinging gas-jet system cooling device. The importance of a good prediction of the averaged Nusselt number is justifiable under industrial work conditions, in which the plate to be cooled is in motion as the arrays of jets blow air over it. Comparison between turbulence model results for the mean value of the Nusselt number reveals that the realizable k-ε model shows the most accurate value (23% lower) compared to the experimental data. The Martin correlation [19], however, shows a 13% overprediction of this value (see Table 3).

4 Conclusions

A complete study of the capabilities of several eddy viscosity turbulence models implemented in a commercial code to capture physical characteristics of flows with strong streamline curvature was conducted. It has been proven that the compared turbulence models do not capture the influence of the turbulence over the mean flow with good accuracy in complex three-dimensional cases.

The first general conclusion of this work is that, nowadays, one of the challenges in using CFD codes is to adequately choose between the several physical and numerical models available. The comparisons presented in this work have proved that the basic numerical techniques (commonly, the default options in a CFD code) could deliver the expected performance in terms of "industrial accuracy," at least when both the computational grid and the

Table 3 Mean Nusselt $\overline{\mathrm{Nu}}$ and heat transfer coefficient $\bar{h}$ computed for the three-dimensional array cases: $\mathrm{Re}_0=6.0\times10^5$, $H/S=4.55$, and $L_T/S=14.5$; Buchlin et al. [8] case

Case	Nusselt, $\overline{\mathrm{Nu}}$	$\bar{h}$ [W/(m^2 K)]
Martin correlation	246.74	465.63
Experiment from Buchlin et al. [7]	312.00	514.80
Spalart-Allmaras model	146.05	240.98
Standard k-ε model, (SWF)	192.23	317.18
Standard k-ε model, (MWF)	174.76	288.36
RNG k-ε model, (SWF)	194.37	320.70
Realizable k-ε model, (MWF)	212.02	349.83
Standard k-ω model	198.87	313.29
Reynolds stress modeling RSM, (SWF)	190.90	314.99

boundary conditions are carefully defined. The selection of the most adequate turbulence model is crucial for the success of the simulations and to surpass the industrial accuracy level in the mean values computed ($\leqslant 10\%$). In the three-dimensional case modeled, unfortunately, this level is not reached and the impossibility to define a better computational mesh could be the reason for disagreement between numerical and experimental results.

Concerning the two-dimensional ASN test configuration, results obtained for the local Nusselt number show a reasonable agreement with experimental data. Local Nusselt number computations also allow one to compute an average Nusselt number $\overline{\mathrm{Nu}}$ (by profile integration) and a mean heat transfer coefficient $\bar{h}$, which are key parameters in industrial design. Comparisons of the obtained numerical mean Nusselt number against experimental correlations from Martin [19] were carried out. Good agreement between numerical and experimental "mean" values of heat transfer was found for all modeled cases. For the modeled three-jet system, the performance of all the models improves compared to the two-jet array case.

For three-dimensional cases, the agreement of the local Nusselt number is not good. The turbulence models used show strong difficulties in capturing the three-dimensional effects of turbulence. In spite of that, the positions where the peaks of Nu appear are quite well predicted by the Spalart-Allmaras, standard k-ε, and k-ω models, The realizable k-ε and RSM models show some disagreements in the predictions for the tilted nozzle peak. The standard k-ε and RSM models predict the maximum values for the perpendicular jets very well, but their performance worsens for the tilted jet in the three-dimensional case checked. The guidelines obtained here allow one to apply the CFD tool to better investigate the behavior of this kind of cooling device in order to improve its design, but in a qualitative way. The wall functions do not show a good behavior in the three-dimensional case when they are coupled with the RNG k-ε model. This model is more sensitive to the wall condition when it is not "well posed" (i.e., using wall functions when y^+ does not remain in the interval $20 \leqslant y^+ \leqslant 120$). Finally, for heat transfer prediction in jet systems, it is more important to choose a suitable near-wall treatment than to select a more sophisticated turbulence model (i.e., V2F or RSM models), because the results that EVM provide are of similar quality, showing that the streamline curvature could possibly not be a very relevant phenomena in three-dimensional impinging jet flows.

Nomenclature

Variables and Parameters

B = nozzle width, m
D = nozzle diameter, m
H = nozzle-to-plate distance, m
h = heat transfer coefficient, $\mathrm{W/m^2\,K}$
h_0 = heat transfer coefficient at the stagnation point, $\mathrm{W/m^2\,K}$
I = intensity of turbulence (relative magnitude of the axial velocity u'_{rms} fluctuations, referring to the local values of the time-averaged axial velocity, u_m), u'_{rms}/u_m, N-d
k = turbulence kinetic energy, $\mathrm{m^2/s^2}$
k_f = flow thermal conductivity, W/(m K)
L_T = distance between nozzles, m
L = slot length, m
Nu_0 = Nusselt number at the stagnation point based on the nozzle's dimension $h_0 D(\text{or } 2B)/k_f$, N-d[1]
Nu = local Nusselt number, hL/k N-d
Pr = Prandtl number, $\mathrm{Pr}=\nu c_{e_{ref}}/(k_f)$, N-d
Re_0 = critical Reynolds number based on the nozzle's dimension and exit velocity, $u_e D(or\ B)/\nu$, N-d
Re_s = critical Reynolds number based on the hydraulic diameter, N-d
T = temperature, °C, K
r = round nozzle radial direction coordinate, m
x = slot width direction coordinate, m
y = longitudinal axis slot direction coordinate, m
y^+ = nondimensional geometric-turbulence variable, $y^+=u^* y/\nu$, N-d
z = jet axis direction coordinate, m

Greek Symbols

ε = rate of dissipation of kinetic energy $\mathrm{m^2/s^3}$
μ = dynamic viscosity, kg/(ms)
ν = kinematic viscosity, $\mathrm{m^2/s}$
μ_T = eddy dynamic viscosity, kg/(ms)
ν_r = eddy kinematic viscosity, $\mathrm{m^2/s}$
ω = specific dissipation rate, $\omega=\varepsilon/k$ 1/s

Subscripts

0 = stagnation point
r = round (axisymmetrical) nozzle
s = slot nozzle
w = wall

Superscripts

$\bar{a}$ = time-averaged value
a' = fluctuating quantity

Acronyms

ARN = array of round nozzles
ASN = array of slot nozzles
CFD = computational fluid dynamics
EVM = eddy viscosity models
IJS = impinging jet systems
MWF = modified wall functions
RANS = Reynolds-averaged Navier-Stokes
RNG = renormalization group theory
RSM = Reynolds stress models
SRN = single round nozzle
SSN = single slot nozzle
SWF = standard wall functions
TLM = two layer model
V2F = eddy viscosity model from Durbin [15]
WF = wall functions

[1]N-d = nondimensional variable

References

[1] Coussirat, M., van Beeck, M., Mestres, M., Egusquiza, E., Buchlin, J.-M., and Escaler, X., 2005, "Computational Fluid Dynamics Modeling of Impinging Gas-Jet Systems: I. Assessment of Eddy Viscosity Models," ASME J. Fluids Eng., **127**(4), pp. –.

[2] Chen, J., Wang, T., and Zumbrunnen, A., 1994, "Numerical Analysis of Convective Heat Transfer From a Moving Plate Cooled by an Array of Submerged Planar Jets," Numer. Heat Transfer, Part A, **26**, pp. 141–160.

[3] Chattopadhyay, H., Biswas, G., and Mitra, K., 2002, "Heat Transfer From a Moving Surface Due to Impinging Slot Jets," J. Heat Transfer, **124**, pp. 433–440.

[4] Gauntner, J., Livingood, J., and Hrycak, P. 1970, "Survey of Literature on Flow Characteristic of a Single Turbulent Jet Impinging on a Flat Plate," N.A.S.A. Technical Note TN D-5652, pp. 1–41.

[5] Coussirat, M. G., 2001, "Numerical Study of Turbulence Models for Impinging Gas-Jet Systems," von Kármán Institute for Fluid Dynamics, EA Report VKI-PR 2001-05.

[6] Spalart, P., 2000, "Strategies for Turbulence Modelling and Simulations." Int. J. Heat Fluid Flow, **21**, pp. 252–263.

[7] Gardon, R., and Afkirat, C., 1966, "Heat Transfer Characteristic of Impinging Two-Dimensional Air Jets," ASME J. Heat Transfer, **88**, pp. 101–108.

[8] Buchlin, J., Gouriet, J., Planquart, P., van Beeck, J., and Renard, M., 2002, "Experimental and Numerical Study of Convective Heat Transfer in Array of Slot Jets," *ASME Flows in Manufacturing Processes*, ASME, New York, pp. 1–7.

[9] Spalart, P., and Allmaras, S., 1992, "A One-Equation Turbulence Model for Aerodynamics Flow," AIAA Paper No. 92-0439, pp. 1–22.

[10] Launder, B., and Spalding, D., 1974, "The Numerical Computation of Turbulent Flows," Comput. Methods Appl. Mech. Eng., **3**, pp. 269–289.
[11] Choudhury, D., Kim, S., and Flannery, W., 1993, "Calculation of Turbulent Separated Flows Using a Renormalization Group Based $k-\varepsilon$ Turbulence Model," *ASME Fluids Engineering Conf.*, TN-044.
[12] Shih, T., Liu, W., Shabir, A., Yang, Z., and Zhu, J., 1995, "A New $k-\varepsilon$ Eddy Viscosity Model for High Reynolds Number Turbulence Flows," Comput. Fluids, **24**(3), pp. 227–238.
[13] Wilcox, C., 1988, "Reassessment of the Scale Determining Equation for Advanced Turbulence Models," AIAA J. **26**(1), pp. 1299–1310.
[14] Wilcox, C., 1988, "Multiscale Model for Turbulent Flows," AIAA J., **26**(11), pp. 1311–1320.
[15] Durbin, P., 1991, "Near-Wall Turbulence Closure Without Damping Functions," Theor. Comput. Fluid Dyn., **3**, pp. 1–13.
[16] Daly, B., and Harlow, F., 1970, "Transport Equations in Turbulence," Phys. Fluids, **13**, pp. 2634–2649.
[17] Jaw, S., and Chen, J., 1998, "Present Status of Second Order Closure Turbulence Models: I. Overview," J. Eng. Mech., **124**(5), pp. 486–501.
[18] Durbin, P., and Petterson, R., 2001, *Statistical Theory and Modeling for Turbulent Flows*, 1st Edition, Wiley, New York.
[19] Martin, H., 1977, "Heat and Mass Transfer Between Impinging Gas Jets and Solid Surfaces," Adv. Heat Transfer, **13**, pp. 1–60.
[20] Patankar, D., 1980, *Numerical Heat Transfer and Fluid Flow*, 1st Edition, Hemisphere, New York.
[21] Hirsch, Ch., 1988, *Numerical Computation of Internal and External Flows, Vols. 1 and 2*, 1st Edition, Wiley, New York.
[22] Ferziger, J., and Perić, M., 1997, *Computational Methods for Fluid Dynamics*, 2nd Edition, Springer, New York.
[23] Fluent Inc., 2000, *Fluent v5.3 On-Line Handbook*, Fluent Inc., France (on-line web edition).
[24] Cooper, D., Jackson, B., and Liao, G., 1993, "Impinging Jet Studies for Turbulence Model Assessment: I. Flow-Field Experiments," Int. J. Heat Mass Transfer, **36** (10), pp. 2675–2684.
[25] Baughn, J., and Shimizu, S., 1989, "Heat Transfer Measurements From a Surface With Uniform Heat Flux and an Impinging Jet," ASME J. Heat Transfer, **82**, pp. 1096–1098.
[26] Baughn, J., Hechanova, A., and Yan, X, 1991, "An Experimental Study of Entrainment Effects on the Heat Transfer From a Flat Surface to Heated Circular Impinging Jet," ASME J. Heat Transfer, **113**, pp. 1023–1025.
[27] Turbulence European Research Community on Flow and ERCOFTAC Combustion, 1998, Classic ERCOFTAC Database at University of Surrey, http://cfd.me.umist.ac.uk/ercoftac/, ERCOFTAC, on-line web database edition.
[28] Gardon, R., and Afkirat, C., 1965, "The Role of Turbulence in Determining the Heat-Transfer Characteristics of Impinging Jets," Int. J. Heat Mass Transfer, **8** (9), pp. 1261–1272.
[29] Wisniewski, T., Rebow, M., and Blogowska, K., 1998, "Infrared and Liquid Crystal Thermography in Natural Convection," *Proc. of 8th Int. Symp. on Flow Visualization*, Sorrento, G. M. Carlomagno and I. Grant, eds., CD ROM Proceedings, 212.1–212.8.
[30] Polat, S., Huang, B., Mujumdar, A., and Douglas, J., 1989, "Numerical Flow and Heat Transfer Under Impinging Jets: A Review," Annu. Rev. Numer. Fluid Mech. Heat Transfer, **2**, pp. 157–197.
[31] Coussirat Núñez, M., 2003, "Theoretical/Numerical Study of Flows With Strong Streamline Curvature," Ph.d. thesis, CDIF-Dpto. Mecánica Fluidos-ETSEIB Universidad Politécnica de Cataluña, 2003.
[32] Coussirat, M., van Beeck, J., Egusquiza, E., Buchlin, J., and Mestres, M., 2003, 'Turbulence Models Applied to Impinging Jets Systems," *Proc. of VII Int. Conf. on Advances in Turbulence*, STC-1481 European Union Project Neuro-Network for Turbulence Mixing.
[33] Wolfshtein, M., 1969, "The Velocity and Temperature Distribution in One-Dimensional Flow With Turbulence Augmentation and Pressure Gradient," Int. J. Heat Mass Transfer, **12**, pp. 301–308.
[34] Durbin, P., 1993, "A Reynolds-Stress Model for Near Wall Turbulence," J. Fluid Mech., **249**, pp. 465–498.
[35] Wizman, V., Laurence, D., Kanniche, M., Durbin, P., and Demuren, A., 1996, "Modeling Near-Wall Effects in Second-Moment Closures by Elliptic Relaxation," Int. J. Heat Fluid Flow, **17**, pp. 255–266.

Numerical Simulation of Vortex Cavitation in a Three-Dimensional Submerged Transitional Jet

Tao Xing[1]
Zhenyin Li[2]
Steven H. Frankel[3]

School of Mechanical Engineering, Purdue University, West Lafayette, IN 47907

Vortex cavitation in a submerged transitional jet is studied with unsteady three-dimensional direct numerical simulations. A locally homogeneous cavitation model that accounts for non-linear bubble dynamics and bubble/bubble interactions within spherical bubble clusters is employed. The velocity, vorticity, and pressure fields are compared for both cavitating and noncavitating jets. It is found that cavitation occurs in the cores of the primary vortical structures, distorting and breaking up the vortex ring into several sections. The velocity and transverse vorticity in the cavitating regions are intensified due to vapor formation, while the streamwise vorticity is weakened. An analysis of the vorticity transport equation reveals the influence of cavitation on the relative importance of the vortex stretching, baroclinic torque, and dilatation terms. Statistical analysis shows that cavitation suppresses jet growth and decreases velocity fluctuations within the vaporous regions of the jet. [DOI: 10.1115/1.1976742]

1 Introduction

Cavitation is a dynamic process involving the growth and collapse of gas cavities in liquids. The bubbles usually form and grow in regions of low pressure and then subsequently collapse when they are convected to regions of high pressure. If the bubble collapse occurs near a solid wall, asymmetries can result in the generation of extremely high pressure jets, which can cause considerable material damage or erosion. This problem is particularly important in hydraulic applications involving fluid machinery. Additionally, the alternating growth and collapse of bubbles associated with cavitation can result in high-frequency pressure fluctuations, the generation of excessive noise, and vibration. The ability to understand and predict cavitation flow physics is important in fluid engineering.

It is well known that there is a strong link between cavitation inception and turbulent flow structures [1]. Evidence for this link exists in both wall-bounded flows, as well as free-shear flows [2]. Billard et al. [3] presented further experimental evidence for this effect where they used a vortex (turbulence) generator upstream of a venturi to produce preturbulence and observed a delay in cavitation inception and a reduction in noise. This behavior was attributed to the generation of small-amplitude, high-frequency pressure fluctuations affecting bubble behavior, in particular the morphology of the cavities. In another study, Baur and Ngeter [4] studied the three-dimensional features of cavitation structures in a turbulent shear layer. They considered a channel flow with a rectangular sill mounted upstream on the bottom wall of the channel. This produced separated flow and a turbulent shear layer downstream in a similar manner to the turbulence generator used by Billard et al. [3]. The shear layer produced a region of high turbulence and horseshoe-shaped cavitation tubes that they associated with the bursting process in wall-bounded channel flows.

For a given flow, the location of cavitation inception can be specified in different ways. In wall-bounded flows, such as Billard's studies on venturi, minimum pressure occurs at or close to a solid surface, according to the maximum-modulus theorem. However, the most common exception to this rule is in vortex cavitation, where the unsteady effects and/or viscous effects associated with vortex shedding or turbulence cause deviation from the maximum-modulus theorem [5].

In vortex cavitation, often associated with separated flows, cavitation occurs in the cores of eddies formed in the shear layer emanating from the separation point [2]. This is due to these being regions of minimum pressure. Hence, flow separation and transition to turbulence can have a considerable effect on cavitation. Even without flow separation, intense pressure fluctuations due to turbulence can influence the position of cavitation. In both cases, the temporal pressure fluctuations dictate the cavitation process.

Gopalan et al. [6] found that the location and degree of cavitation was dependent on the nature of the vortical structures produced in a submerged water jet. If the jet was deliberately tripped, cavitation occurred in the cores of the vortex rings which formed downstream ($x/D=2$) of the nozzle. If the jet was not tripped, cavitation occurred in the cores of comparatively strong streamwise vortex tubes just downstream ($x/D=0.55$) of the nozzle. As observed by Arndt [7], tripping the boundary layer of the jet apparently suppresses the secondary vortex cavitation. This mechanism of cavitation control is very similar to the one studied by Billard et al. [3]. Sridhar and Katz et al. [8] have also shown that the presence of a few microscopic bubbles at very low void fraction can significantly affect the vortex dynamics within a water jet.

Recent PIV (particle imaging velocimetry) measurements in a cavitating turbulent shear layer reported by Iyer and Ceccio [9] did not show a significant effect of cavitation on the vortical structure of the jet but did show an increase in streamwise velocity fluctuations and a decrease in the maximum cross-stream fluctuations and Reynolds stresses due to cavitation. They speculated that the presence of cavitation in the cores of the streamwise vortices decreased the coupling between the streamwise and cross-stream velocity fluctuations.

The effects of cavitation on vortex dynamics in a two-dimensional submerged planar laminar forced jet were studied

[1]Ph.D., currently Postdoctoral Researcher at The University of Iowa
[2]Doctoral student
[3]Professor, Member ASME, corresponding author, E-mail: frankel@ecn.purdue.edu

Contributed by the Fluids Engineering Division for publication in the JOURNAL OF FLUIDS ENGINEERING. Manuscript received by the Fluids Engineering Division May 2, 2003; final manuscript received April 7, 2005. Associate Editor: Steven Ceccio.

numerically by Xing and Frankel [10]. A locally homogeneous cavitation model that accounts for nonlinear bubble dynamics and bubble/bubble interactions within spherical bubble clusters was employed [11]. The effects of varying key flow and cavitation model parameters on flow-cavitation interactions were investigated. The parameters varied included the cavitation number (effectively the vapor pressure), the bubble number density, the bubble-cluster radius, and the Reynolds number (limited by the two-dimensional assumption). The results showed cavitation occurring in the cores of primary vortical structures when the local pressure fell below the vapor pressure. Low levels of void fraction caused significant vortex distortion, with the details depending upon the model parameters. For higher Reynolds numbers and small values of bubble cluster radius, cavitation inhibited vortex pairing and resulted in vortex splitting and intensification. All of these observations were in good qualitative agreement with previous experimental and numerical studies. The vorticity transport equation was used to examine the mechanisms behind the effects of cavitation on vortex structures and it was found that both cavitation-induced dilatation and baroclinic torque terms played a role in vorticity generation. More details can be found in the recent paper by Xing and Frankel [10]. Three-dimensional simulations are required to simulate more complex cavitating flows.

In the recent review article by Arndt [7], in reference to several of the above studies, as well as others, it is stated that, "There is also mounting evidence that vortex cavitation is a dominant factor in the inception process in a broad range of turbulent flows." He also states that, "while a vortex model for cavitation in jets does not exist, the mechanism of inception appears to be related to the process of vortex pairing." Finally, he states that, "a new and important issue is that cavitation is not only induced in vortical structures but is also a mechanism for vorticity (turbulence) generation." Our previous two-dimensional results [10] seem to bear this out but more work is needed before the ramifications of this become apparent.

The objective of the present study is to conduct unsteady three-dimensional direct numerical simulations of a round transitional jet and examine the effect of vapor formation due to cavitation on the vortical structure of the jet. Our simulations predict cavitation occurring in the core of the primary azimuthal vortical structures. The presence of low levels of vapor suppressed jet growth and decreased velocity fluctuations in the vicinity of and downstream of the cavitation regions of the jet. The rest of the paper presents the mathematical model, some details of the numerical methods, a problem description, results, and finally some conclusions.

2 Mathematical Model

Cavitating flows feature both incompressible and compressible flow behaviors due to the presence of pure liquid in noncavitating region and mixed liquid and vapor in the cavitating regions. This makes the modeling and numerical methods challenging, especially when a pure compressible formulation is applied. Kubota [11] avoids this problem by using the homogeneous incompressible formulation with variable density. This model was employed in this study for its significant improvement in the following three ways: nonlinear interaction between viscous flow and cavitation bubbles, consideration of the effects of bubble nuclei on cavitation inception and development, and ability to express unsteady characteristics of vortex cavitation. However, it should also be noted that surface tension, thermal, and viscous effects have been neglected in the model and the constant bubble number density per unit volume has restricted this model to be only valid for low void fraction flows.

The form of the Navier-Stokes equations, the local homogeneous model (LHM) equation, and the definition of the fluid properties, such as mixture density and viscosity, are identical to those applied in Kubota's study [11] and were presented more recently in Ref. [10]. The key equations are repeated here for completeness.

The following form of the Navier-Stokes equations was considered in this study:

$$\frac{\partial \rho}{\partial t} + \nabla \cdot (\rho \mathbf{V}) = 0, \tag{1}$$

$$\frac{\partial (\rho \mathbf{V})}{\partial t} + \nabla \cdot (\rho \mathbf{V}\mathbf{V}) = -\nabla p + 2\nabla \cdot (\mu \mathbf{S}) - \frac{2}{3}\nabla (\mu \nabla \cdot \mathbf{V}), \tag{2}$$

where $\mathbf{S}$ is the strain-rate tensor. The density of the liquid-vapor bubble mixture is defined as

$$\rho = (1 - f_v)\rho_\ell, \tag{3}$$

where ρ_ℓ is the liquid density (the vapor density is assumed to be negligible compared to the liquid density) and f_v, the local void fraction, is defined as

$$f_v = n\frac{4}{3}\pi R^3 \tag{4}$$

with $0 < f_v < 1$, n is the bubble number density, and R is the bubble radius. The mixture viscosity is evaluated using

$$\mu = (1 - f_v)\mu_\ell + f_v \mu_v, \tag{5}$$

where μ_ℓ is the liquid viscosity and μ_v is the vapor viscosity, and both are assumed constant.

The bubble number density is assumed constant in both space and time, which limits the accuracy of the model for large void fractions by neglecting bubble coalescence and splitting. The Rayleigh equation governs the dynamic behavior of a single bubble in a quiescent medium [5]. Because grid resolution in most numerical simulations is insufficient to resolve individual bubbles, Kubota et al. modified the Rayleigh equation to account for interactions between bubbles (of the same radius, R), which may occur at scales below the grid scale. The final equation, referred to as the local homogeneous model (LHM) equation is given as:

$$(1 + 2\pi(\Delta r)^2 nR)R\frac{D^2R}{Dt^2} + \left(\frac{3}{2} + 4\pi(\Delta r)^2 nR\right)\left(\frac{DR}{Dt}\right)^2 + 2\pi(\Delta r)^2 \frac{Dn}{Dt}R^2\frac{DR}{Dt} = \frac{p_v - p}{\rho_\ell}, \tag{6}$$

where D/Dt is the material derivative, Δr is the bubble cluster radius (distance over which bubbles may interact with each other in a given cluster), and p_v is the vapor pressure of the liquid for a given temperature. Notice as the bubble cluster radius goes to zero, the Rayleigh equation for a single bubble is recovered and bubble-bubble interactions are no longer included in the equation. Recently, Delale et al. [12] have revised Kubota's model and have addressed two important effects related to bubble/bubble interactions and viscous damping. In Kubota's original model, the bubble cluster radius is chosen to be the grid size. In Delale et al., they related the bubble cluster radius to the radius of the bubbles within the cluster itself (which is assumed the same for all bubbles within the cluster, but may grow or decay depending upon the local pressure) as follows:

$$\Delta r = \Lambda R, \tag{7}$$

where $\Lambda = \text{constant} \gg 1$ (if $\Lambda = 1$ then the classical Rayleigh equation is recovered). This model assumes that local number of bubbles within a cluster is proportional to the local volume of a bubble, and hence the local void fraction.

To couple the LHM equation for the bubble radius to the Navier-Stokes equations, Kubota et al. derived a quasi-Poisson equation for the pressure which is given below (for more details see Ref. [11])

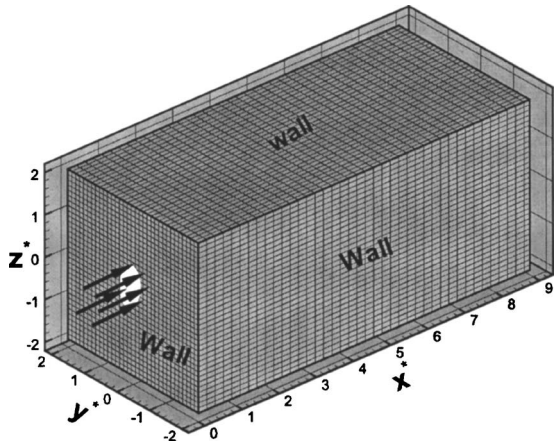

Fig. 1 Computational domain showing boundary surfaces and inflow plane

$$\nabla^2 p + \Theta(p) = \Phi\left(\rho\mathbf{V}, \mathbf{V}, \frac{\partial R}{\partial t}, R\right) + \Omega(\rho\mathbf{V}, \mathbf{V}) \tag{8}$$

with

$$\Theta(p) = \rho_L 4n\pi R^2 \frac{p_v - p}{(1 + 2\pi(\Delta r)^2 nR)R\rho_L} \tag{9}$$

and

$$\Phi\left(\rho\mathbf{V}, \mathbf{V}, \frac{\partial R}{\partial t}, R\right) = -\rho_L 4n\pi R\left\{R\Psi\left(\rho\mathbf{V}, \mathbf{V}, \frac{\partial R}{\partial t}, R\right) + 2\left(\frac{\partial R}{\partial t}\right)^2\right\} \tag{10}$$

with

$$\Psi\left(\rho\mathbf{V}, \mathbf{V}, \frac{\partial R}{\partial t}, R\right) = \frac{\partial^2 R}{\partial t^2} - \Pi(p) \tag{11}$$

and

$$\Pi(p) = \frac{p_v - p}{(1 + 2\pi(\Delta r)^2 nR)R\rho_L} \tag{12}$$

Maximum and minimum void fractions were specified to avoid pure liquid and vapor states with $\Theta = \Phi = 0$ and the bubble radius fixed. In the present implementation, a hyperbolic tangent function was used to ensure a smooth variation between these two extreme states. All quantities and equations were nondimensionalized by the liquid density and viscosity, the jet nozzle diameter, D, jet inlet velocity, U_0, and dynamic pressure, $\rho_\ell U_0^2$. In the results, all non-dimensional quantities will be indicated by an asterisk, e.g., t^*, x^*, u^*, etc..

The numerical methods employed in this study were modified from our previous work [10] with the main difference here being related to how the quasi-Poisson equation for the pressure is solved in three dimensions. The details are described in the next section.

3 Numerical Methods

A well known difficulty in obtaining time-accurate solutions for an incompressible flow is the lack of a time derivative term in the continuity equation. Therefore, satisfying mass conservation is a key issue in solving the incompressible Navier-Stokes equations and a variety of different approaches have been pursued to address this issue. These approaches include the pressure-correction technique based on the SIMPLE algorithm, as well as approaches which directly solve a Poisson equation for the pressure via iterative methods. Many previous studies have employed a staggered grid where velocity and pressure nodes are not collocated. This avoids the grid-scale (odd-even) oscillations in the pressure field associated with pressure-velocity decoupling often encountered when using non-staggered grids. This is a popular method, especially when combined with the SIMPLE algorithm, because of its strongly elliptic nature which does not allow energy accumulation at the grid-scale wave number preventing grid-scale pressure oscillations. However, there are difficulties in discretizing non-linear terms on non-uniform staggered grids and the amount of programming and computational cost are more than with a non-staggered grid.

Table 1 Description of the flow and cavitation parameters for the simulation cases

Case	σ	p_v	Δr	n	Re	R_0
1	1.80	0.10	1.0	10^6	1500	1.33×10^{-3}
2	0.60	0.70	1.0	10^6	1500	1.33×10^{-3}
3	0.50	0.75	1.0	10^6	1500	1.33×10^{-3}

The approach taken here employs a non-staggered grid and solves the pressure Poisson equation using a compact fourth-order accurate scheme which tends to suppress the spatial odd-even decoupling of the pressure-velocity fields [13].

3.1 Fourth-Order Pressure-Correction Approach. Through the use of the fractional-step method formalism (first-order accurate in time [14]), Dormy [13] developed a new pressure correction approach. Dormy derived this new scheme for totally incom-

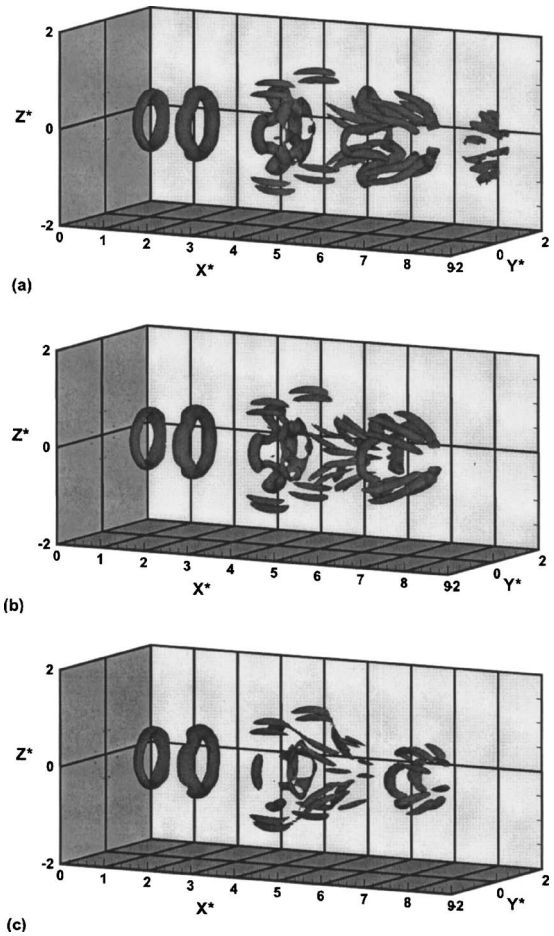

Fig. 2 Instantaneous isosurface of *Q*-criterion magnitude at $t^*=22$. The isolevel shown is 3.2. (*a*) $\sigma=1.8$, (*b*) $\sigma=0.6$, (*c*) $\sigma=0.5$.

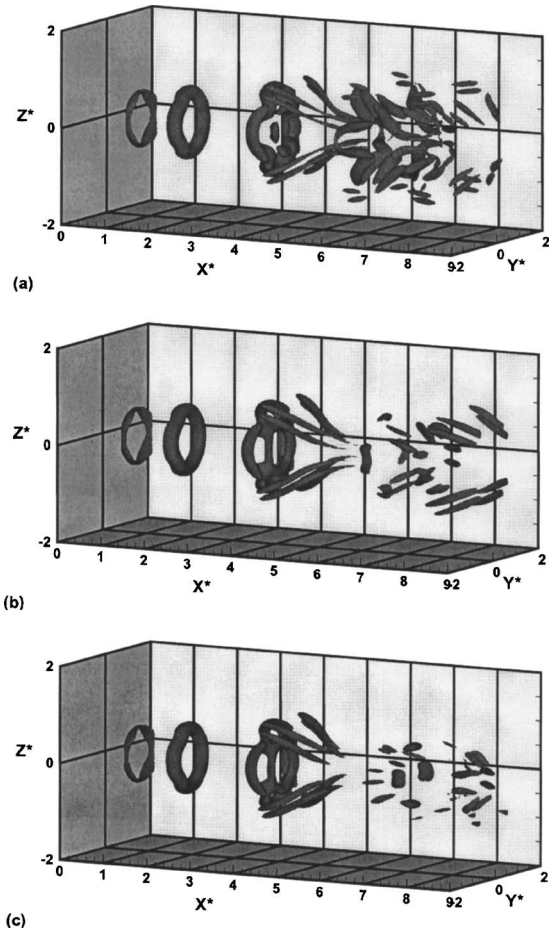

Fig. 3 Instantaneous isosurface of *Q*-criterion magnitude at $t^*=26$. The isolevel shown is 3.2. (*a*) $\sigma=1.8$, (*b*) $\sigma=0.6$, (*c*) $\sigma=0.5$.

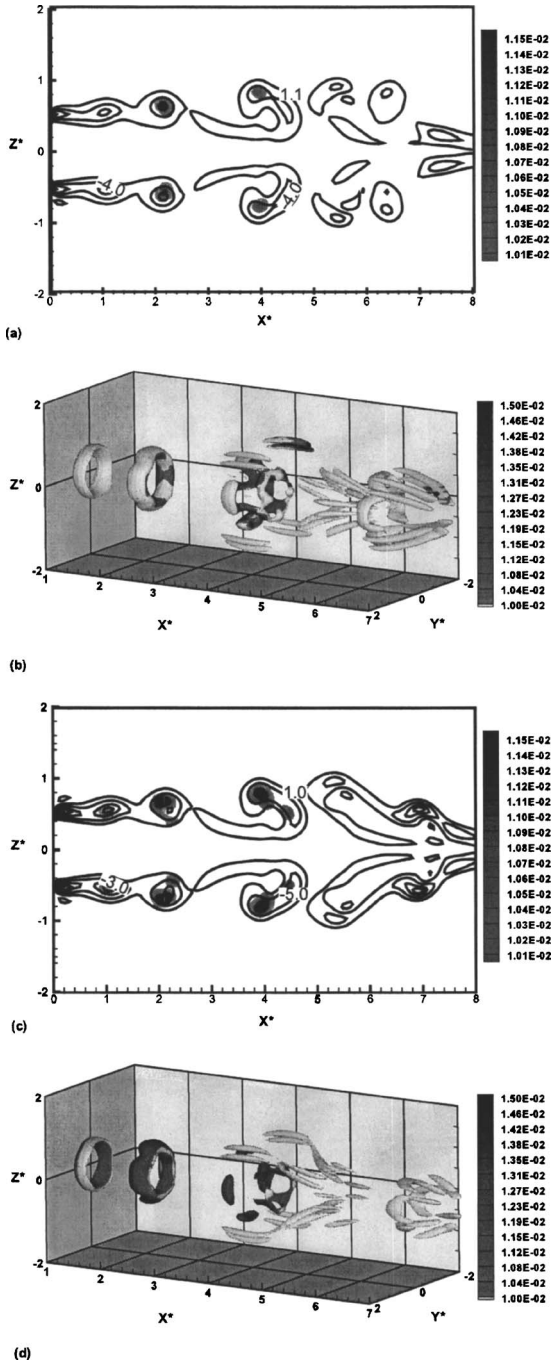

Fig. 4 Void fraction and vorticity plots at $t^*=22$. The isolevel shown is 3.2. (*a*) Contour plot showing void fraction (flood) and out-of-plane vorticity ($\sigma=0.6$). (*b*) *Q*-criterion isosurface colored by the contour of void fraction ($\sigma=0.6$). (*c*) Contour plot showing void fraction (flood) and out-of-plane vorticity ($\sigma=0.5$). (*d*) *Q*-criterion isosurface colored by the contour of void fraction ($\sigma=0.5$).

pressible flows. Here we attempt to apply Dormy's methodology for the quasi-Poisson equation featured in the cavitation model of Kubota et al. [11]. Additional terms including the density and its time derivative are associated with cavitation effects, such as bubble growth and collapse, on the pressure field. By dropping these terms, the governing equations revert back to the form for a totally incompressible flow.

Consider a velocity field $(\rho\mathbf{V})^*$ which does not satisfy the continuity equation (for instance, obtained by time advancing the Navier-Stokes equations without including the pressure gradient). The objective is to project this onto a divergence-free field by subtracting the gradient of a pressure-like variable ϕ such that

$$\rho\mathbf{V} = (\rho\mathbf{V})^* - \nabla_h\phi, \tag{13}$$

where V is the velocity field which satisfies the continuity equation. Taking the divergence of this equation yields

$$\Delta_{2h}\phi = \nabla_h \cdot (\rho\mathbf{V})^*, \tag{14}$$

where Δ_{2h} is a second-order centered approximation of the Laplacian skipping the neighboring points. The sparse nature of this operator leads to pressure oscillations. The remedy proposed by Dormy is to introduce a fourth-order "compact equivalent" to the conservative discrete pressure equation.

The original non-compact formulation of the three-dimensional Poisson equation can be written as

$$\frac{\partial^2\phi}{\partial x^2} + \frac{h_x^2}{3}\frac{\partial^4\phi}{\partial x^4} + \mathcal{O}(h_x^4) + \frac{\partial^2\phi}{\partial y^2} + \frac{h_y^2}{3}\frac{\partial^4\phi}{\partial y^4} + \mathcal{O}(h_y^4) + \frac{\partial^2\phi}{\partial z^2} + \frac{h_z^2}{3}\frac{\partial^4\phi}{dz^4} + \mathcal{O}(h_z^4) = \nabla_h \cdot (\rho\mathbf{V})^* + \frac{\partial\rho}{\partial t}. \tag{15}$$

To solve this equation with fourth-order accuracy, Dormy proposed two-step approach that allows fourth-order accuracy at twice the computational cost of the second-order interpolated

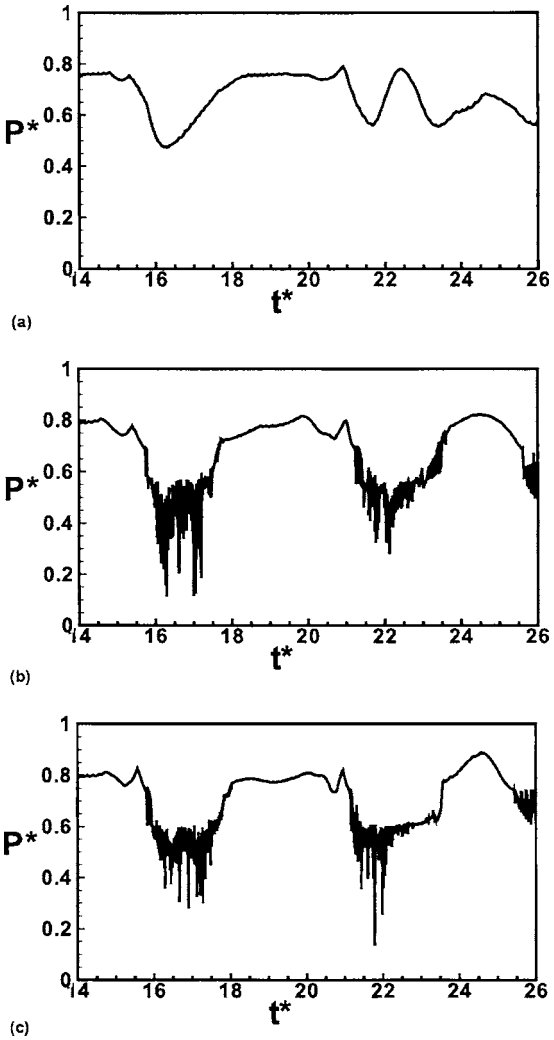

Fig. 5 Instantaneous minimum pressure within domain versus time. (*a*) $\sigma=1.8$, $p_v=0.10$, (*b*) $\sigma=0.6$, $p_v=0.70$, (*c*) $\sigma=0.5$, $p_v=0.75$

scheme. The above equation can be approximated with four-order accuracy using a two-step method. The first step is a second-order approximation to the second-order truncation terms written as:

$$\Delta_h \psi = \left(h_x^2 \frac{\partial^4}{\partial x^4} + h_y^2 \frac{\partial^4}{\partial y^4} + h_z^2 \frac{\partial^4}{\partial z^4} \right) \left[\nabla_h \cdot (\rho \mathbf{V})^* + \frac{\partial \rho}{\partial t} \right]. \quad (16)$$

The fourth-order central differences scheme was applied to calculate the right hand side of the above equation as shown here for some function of f

$$f_{xxxx_i} = \frac{f_{i-2} - 4f_{i-1} + 6f_i - 4f_{i+1} + f_{i+2}}{\Delta x^2}. \quad (17)$$

At the boundaries, a third-order extrapolation was used

$$f_{xxxx_i} = \frac{6f_{i+1} + f_{i-1} - 4f_{i+2} + f_{i+3} - 4f_i}{\Delta x^2}, \quad (18)$$

$$f_{xxxx_i} = \frac{6f_{i-1} + f_{i+1} - 4f_{i-2} + f_{i-3} - 4f_i}{\Delta x^2}. \quad (19)$$

The second step uses ψ as a correction term

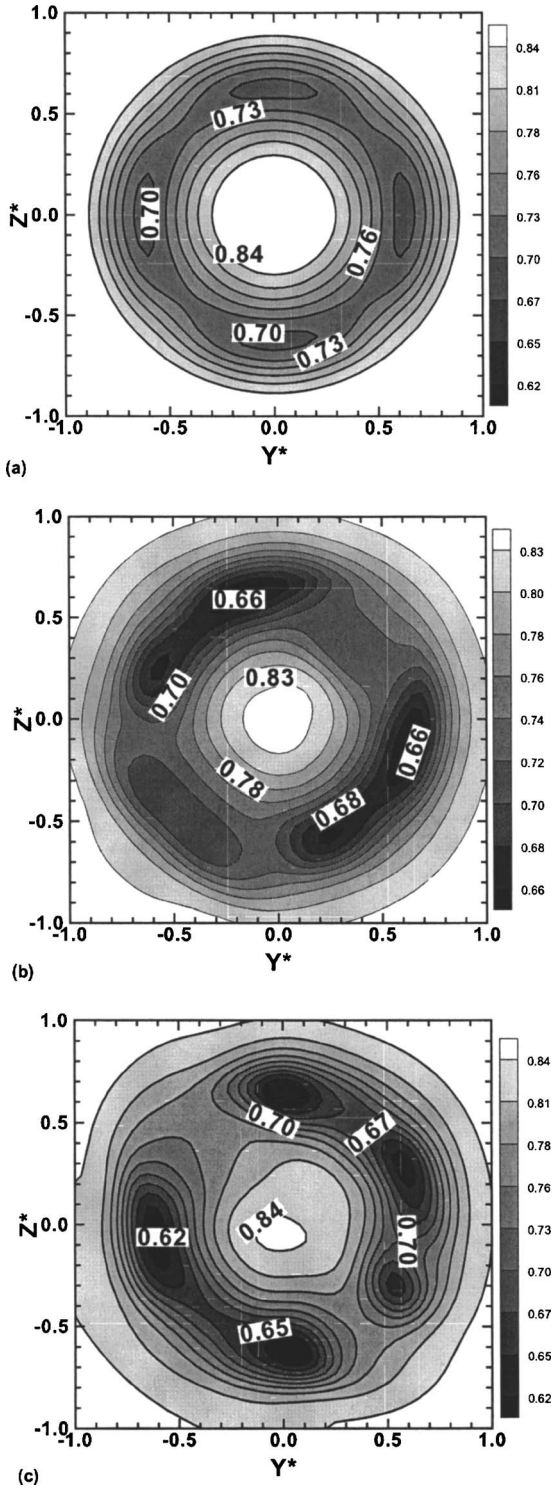

Fig. 6 Axial slices showing instantaneous contour plot of pressure at $x^*=2.0$ and $t^*=22$. (*a*) $\sigma=1.8$, (*b*) $\sigma=0.6$, (*c*) $\sigma=0.5$.

$$\Delta_h \phi = \left[\nabla_h \cdot (\rho \mathbf{V})^* + \frac{\partial \rho}{\partial t} \right] - \frac{1}{4}\psi. \quad (20)$$

Hence, the pressure was solved to fourth-order accuracy and the computational cost is exactly twice the cost of the second-order scheme as each of the steps requires the resolution of a seven-point compact Laplace operator [13]. Point successive over-relaxation was applied together with Dormy's method to solve the

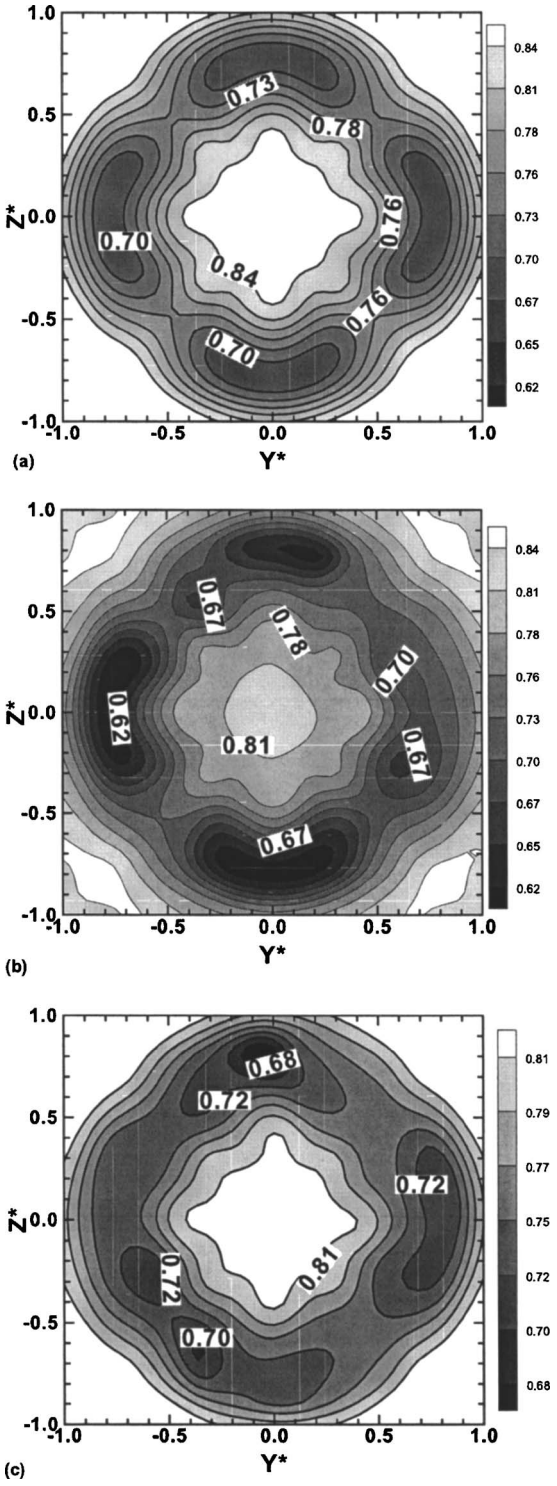

Fig. 7 Axial slices showing instantaneous contour plot of pressure at $x^*=4.0$ and $t^*=22$. (*a*) $\sigma=1.8$, (*b*) $\sigma=0.6$, (*c*) $\sigma=0.5$.

three-dimensional Poisson equation. The convergence criterion selected was

$$\max(|\Delta P|) < 1 \,.\, D - 5, \tag{21}$$

where ΔP is the residual of pressure in the iterations. A stricter criterion was tried and no significant differences between the results were observed. It was also found that if the time step was sufficiently small, the Poisson equation converged quickly at each time step.

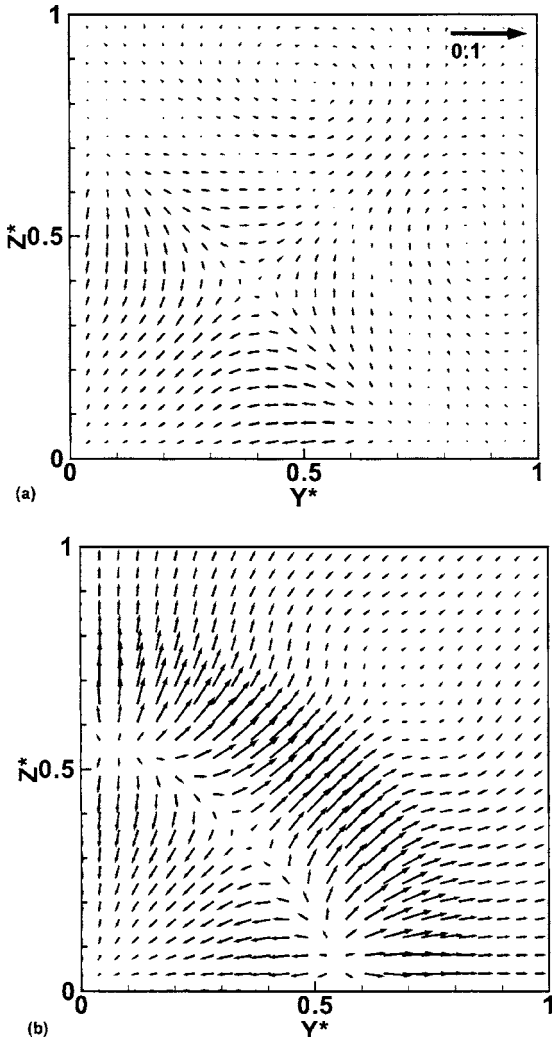

Fig. 8 Instantaneous velocity vector at stream cross-section $x^*=2.0$ at $t^*=22$. The vector was subtracted by the vector of $\sigma=1.8$. (*a*) $\sigma=0.6$, (*b*) $\sigma=0.5$.

3.2 Discretization Schemes. Spatial derivatives appearing on the right hand side of the quasi-Poisson equation were discretized with a fourth-order central difference scheme, whereas all other spatial derivatives were discretized using a second-order central difference scheme. Time discretization was based on a simple Euler explicit forward difference with a conservative CFL number of 0.08 enforced to adequately resolve short time scales associated with small-scale vortical structures and bubble growth and collapse. A second-order accurate scheme based on Heun's method was also considered to allow a larger time step. A comparison between the Euler and Heun methods showed similar results at the same time. For simplicity the Euler time-stepping method was used for the simulations in this study.

4 Problem Description

Three-dimensional direct numerical simulations of a submerged, round water jet exhausting into a water-filled chamber were conducted. A rectangular box computational domain was chosen to represent the chamber. Top hat velocity profiles were specified at the inlet with nondimensional momentum thickness of 0.3. A small amplitude sinusoidal disturbance was added to this base profile with the Strouhal number corresponding to the primary frequency chosen as 0.223 and the secondary frequency chosen as half this value. The jet Reynolds number was based on the nozzle diameter of the jet. The cavitation number was defined here

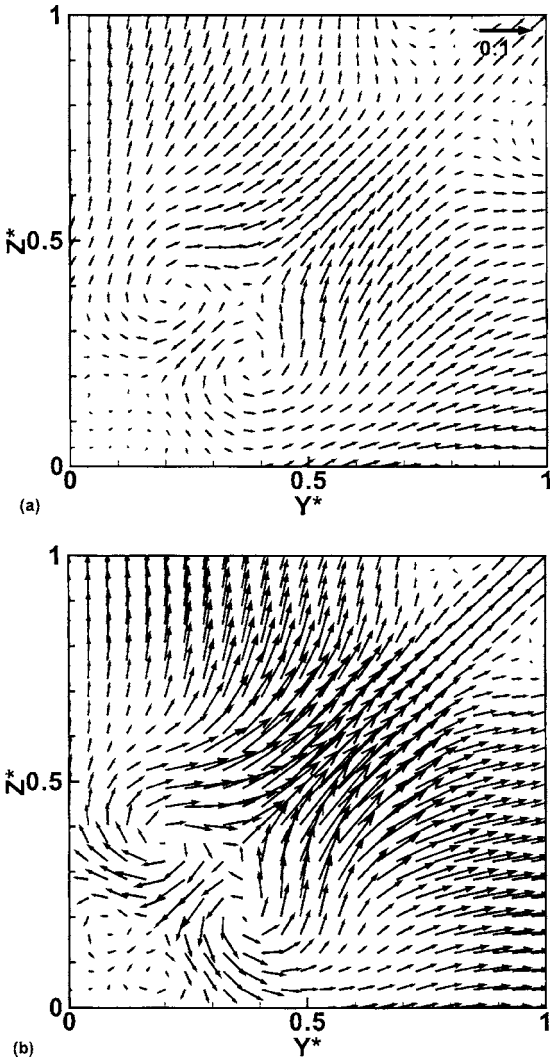

Fig. 9 Instantaneous velocity vector at stream cross-section $x^*=4.0$ at $t^*=22$. The vector was subtracted by the vector of $\sigma=1.8$. (*a*) $\sigma=0.6$, (*b*) $\sigma=0.5$.

in terms of dimensional quantities as $\sigma=(p_\infty-p_v)/0.5\rho_\ell U_0^2$, where p_∞ is the chamber pressure. The cavitation number was varied by changing the vapor pressure. The Reynolds number was defined as $\rho_\ell h U_0/\mu_\ell$ and serves to determine the liquid viscosity. The ratio of the vapor to liquid viscosity was 0.00912 following Kubota et al.

A sketch of the computational domain is given in Fig. 1. The computational domain extended from $-2\leqslant y^*\leqslant 2$ in the spanwise direction, $-2\leqslant z^*\leqslant 2$ in the transverse direction, and $0\leqslant x^*\leqslant 8.9$ in the streamwise direction. The domain was discretized using a uniform Cartesian mesh with $120\times 100\times 100$ points. The use of a uniform mesh avoids problems related to transforming the quasi-Poisson equation, involving computer memory and numerical accuracy, when using a non-uniform mesh.

No-slip velocity boundary conditions were enforced on the sides of the box, and the inflow plane except for the nozzle opening. Fourth-order extrapolation was used for the pressure on the walls and outflow boundary

$$p_{i\max,j}=(104p_{i\max-1,j}-114p_{i\max-2,j}+56p_{i\max-3,j}-11p_{i\max-4,j})/35. \tag{22}$$

The convective boundary condition was used for velocity at the outflow boundary

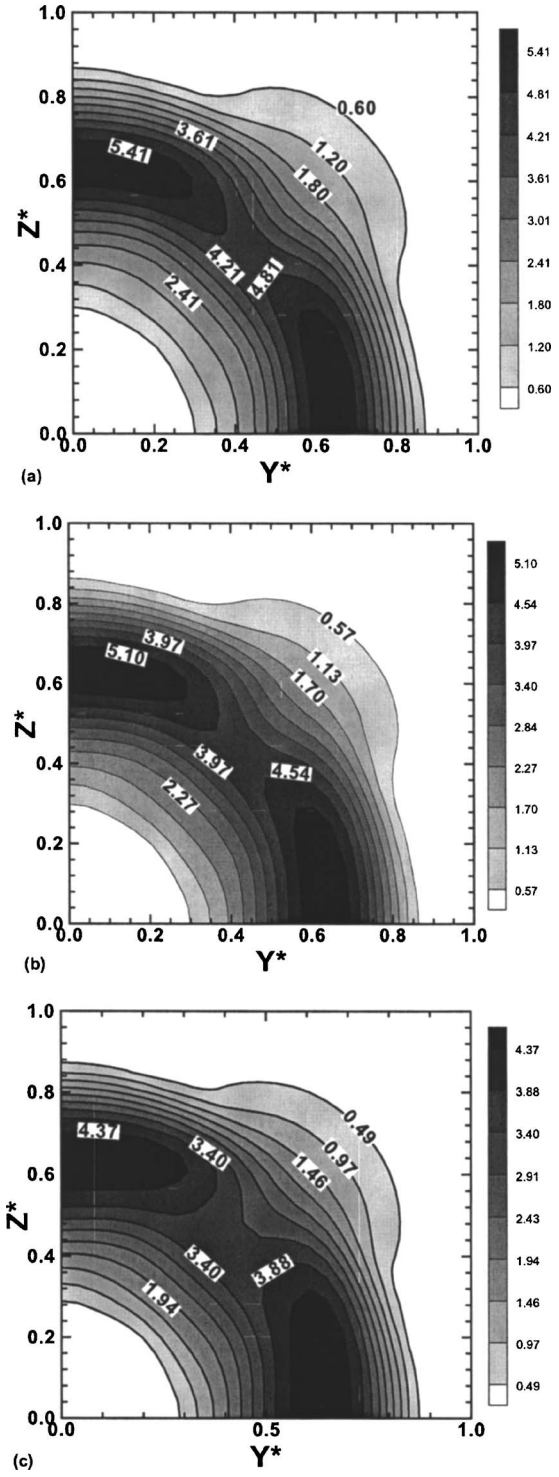

Fig. 10 Axial slices showing instantaneous contour plot of streamwise vorticity at $x^*=2.0$ and $t^*=22$. (*a*) $\sigma=1.8$, (*b*) $\sigma=0.6$, (*c*) $\sigma=0.5$.

$$\frac{\partial \mathbf{V}}{\partial t}+u_0\frac{\partial \mathbf{V}}{\partial x}=0. \tag{23}$$

For all cases the Reynolds number based on the jet diameter, inlet velocity, and liquid viscosity was fixed at 1500. The effects of the bubble number density (fixed at 10^6) and bubble-cluster radius (fixed at 1.0) have already been studied in the two-dimensional submerged laminar jet simulations [10] and are not studied further here. The only parameter related to the cavitation

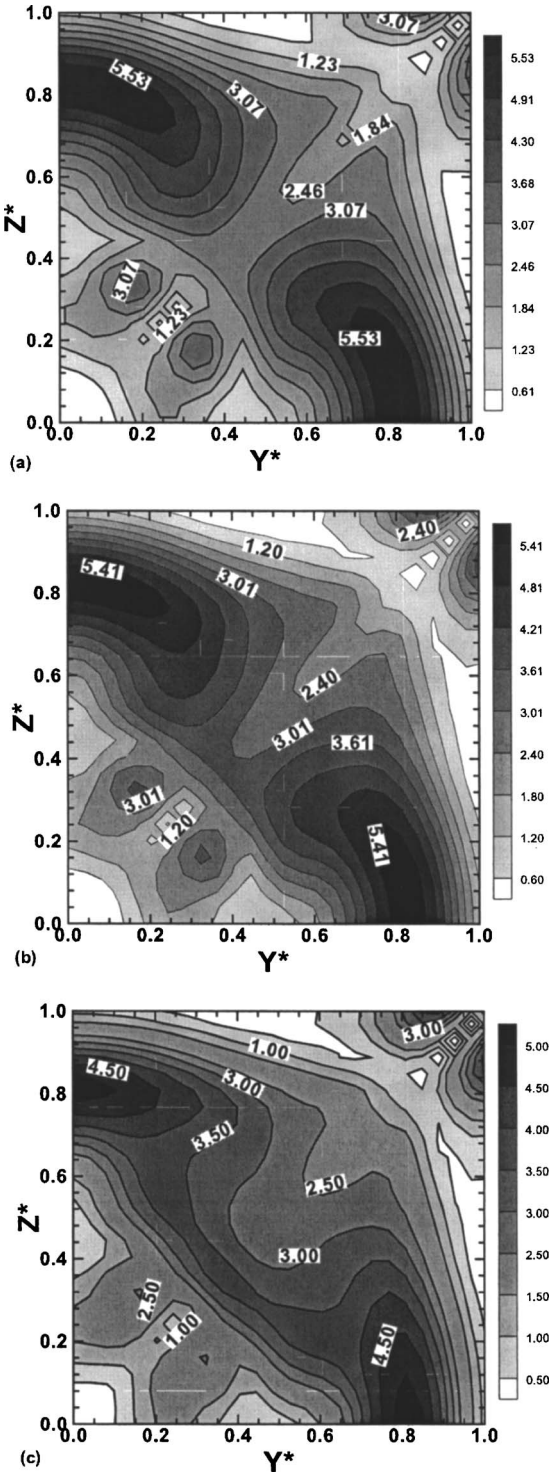

Fig. 11 Axial slices showing instantaneous contour plot of streamwise vorticity at $x^*=4.0$ and $t^*=22$. (*a*) $\sigma=1.8$, (*b*) $\sigma=0.6$, (*c*) $\sigma=0.5$.

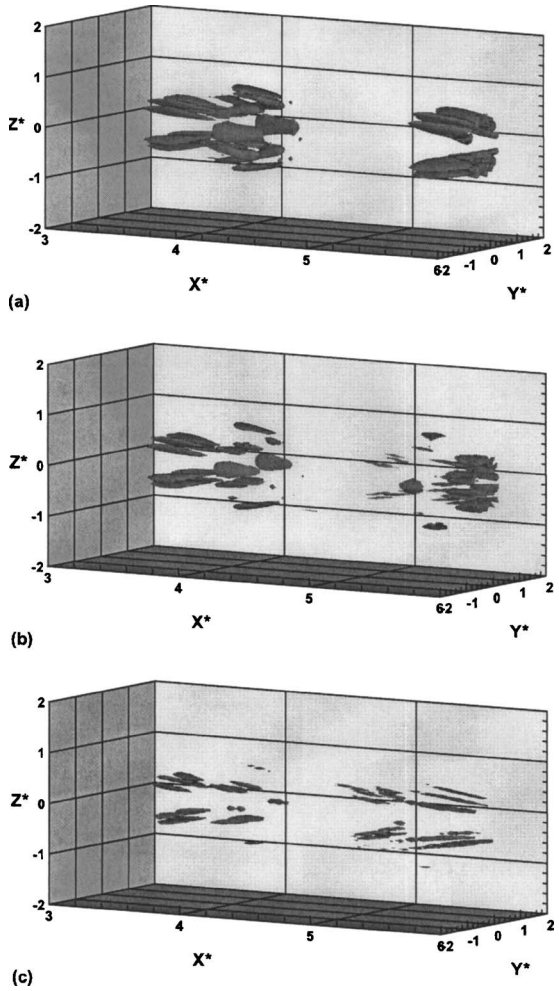

Fig. 12 Isosurface showing magnitude of vortex stretching term at $t^*=22$. The isolevel shown is 3.7. (*a*) $\sigma=1.8$, (*b*) $\sigma=0.6$, (*c*) $\sigma=0.5$.

model varied here is the cavitation number σ (or equivalently the vapor pressure, p_v). Three values of the cavitation number will be used to consider jets under non-cavitating ($\sigma=1.8$, $p_v=0.1$) and cavitating conditions ($\sigma=0.6$, $p_v=0.7$ and $\sigma=0.5$, $p_v=0.75$). All cases are summarized in Table 1 and were tested on IBM RISC/6000 SP POWER3+ thin nodes with 375 MHz CPU and 4 GB memory.

The results to be presented in the next section were checked for grid independence through comparisons of flow statistics obtained on both the current mesh and with approximately twice the number of grid points and differences of less than 2% were observed. Hence, the simulations presented next can be considered grid independent.

5 Results and Discussion

The effects of cavitation on the instantaneous jet vortical structure can be observed in Figs. 2 and 3, where pairs of isosurfaces of the magnitude of Q, defined as [15]

$$Q=\frac{1}{2}(\Omega_{ij}\Omega_{ij}-S_{ij}S_{ij}), \tag{24}$$

where $\Omega_{ij}=(u_{i,j}-u_{j,i})/2$ and $S_{ij}=(u_{i,j}+u_{j,i})/2$ are the antisymmetric and symmetric components of $\nabla\mathbf{u}$, are plotted for all three cases.

General features of the round jet transition process, from nominally laminar conditions near the nozzle exit, through the vortex roll-up and pairing process, formation of streamwise vortex tubes, and eventual breakdown into small-scale structures, are shared by all cases. Careful examination of the plots reveals distortion of the primary vortex ring structures located at approximately $x^*=2$ and $x^*=4$, with a weakening of the streamwise vortex tube structures downstream of these locations for the $\sigma=0.6$ and $\sigma=0.5$ cases as compared to the $\sigma=1.8$ case. These modifications to the jet vortex structure can be attributed to vapor formation in these regions due

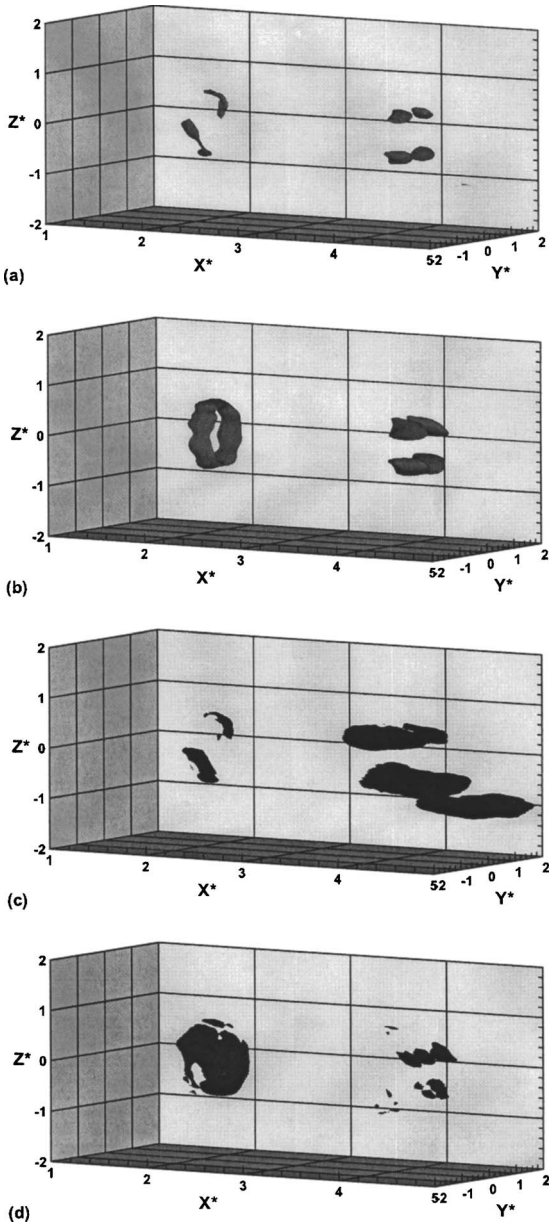

Fig. 13 Isosurface showing magnitude of the dilatation term in (*a*) and (*b*) and the baroclinic torque term in (*c*) and (*d*) at $t^*=22$. The isolevel shown is 1.5 for the dilatation term and 0.005 for the baroclinic torque term. (*a*) $\sigma=0.6$, (*b*) $\sigma=0.5$, (*c*) $\sigma=0.6$, (*d*) $\sigma=0.5$.

to cavitation inception, as evidenced by superimposing instantaneous void fraction and vorticity as shown in Fig. 4. The formation of vapor in the cores of the primary vortex rings is clearly visible in Figs. 4(*a*) and 4(*b*). Evidence of vapor formation downstream of the primary vortex rings, in the vicinity of streamwise vortex tubes, can be seen in Fig. 4(*c*), but not in Fig. 4(*d*) at the simulation time shown.

Further evidence of cavitation inception and the unsteady bubble dynamics that result can be seen in Fig. 5, which plots a time history of the minimum pressure within the computational domain. This figure clearly shows that the local fluid pressure drops below the specified vapor pressure for the two cavitating cases, $p_v=0.7$ and 0.75, at several times during the time span shown, including the times corresponding to the instantaneous results shown previously. The high-frequency fluctuations for the minimum pressure are only observed in the two cavitating cases—

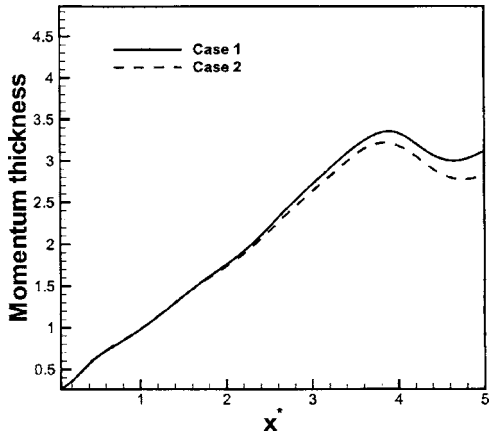

Fig. 14 Momentum thickness versus axial distance

not in the noncavitating case. This is caused by the alternative growth and decay of bubbles inside the cavitating regions within very short periods and is similar to observations in our previous two-dimensional cavitating jet study [10]. Also, the periodic shedding of vortex rings caused the jet to behave in an alternating cavitating and noncavitating mode. The increase of cavitation number delays the inception of cavitation and also reduces the duration time for the jet to be cavitating.

In order to quantify the effect of cavitation on vortex dynamics, instantaneous contour plots of pressure at $x^*=2$ (Fig. 6) and $x^*=4$ (Fig. 7) are shown at $t^*=22$. For the noncavitating case, the pressure field is nearly uniform in the core of the vortex ring. In contrast, there are several regions where the pressure has dropped below the vapor pressure for the two cavitating cases. The formation of vapor tends to break the vortex ring into several sections in the azimuthal direction. Evidence for local flow acceleration in the cavitating cases can be seen by comparing instantaneous velocity vector plots at $t^*=22$ in Figs. 8 and 9. This local flow acceleration can be explained by the continuity equation [Eq. (1)]. When vapor forms within the center of a vortex, the local density decreases with respect to time. As a result, the spatial derivatives of velocity become positive based on conservation of mass law. For the same cavitation number, further downstream, greater acceleration can be observed. For the same axial location, the smaller the cavitation number the greater the flow acceleration. This is because a smaller cavitation number corresponds to greater vapor pressure, thus larger zones within the vortex will cavitate and the derivative of fluid density with respect to time inside those zones becomes larger.

Local distortion and intensification of vortical structures due to vaporous cavitation can be seen in instantaneous contour plots of streamwise vorticity in Figs. 10 and 11. The vorticity of a fluid particle can be altered by vortex stretching, dilatation, baroclinic torque, and viscous diffusion, according to the vorticity transport equation in a three-dimensional, variable density flow,

$$\frac{D\omega}{Dt}=(\omega\cdot\nabla)\mathbf{V}-\omega(\nabla\cdot\mathbf{V})+\frac{\nabla\rho\times\nabla p}{\rho^2}+\frac{1}{\mathrm{Re}}(\nabla^2\omega). \quad (25)$$

The magnitude of the vortex stretching term has increased by close to a factor of 4 due to cavitation as seen in Fig. 12. The dilatation and baroclinic torque terms are identically zero in the non-cavitating jet, but are nonzero in the vapor-containing regions of the cavitating jet as seen in Fig. 13. The baroclinic torque term is over two orders of magnitude smaller than the dilatation term, consistent with our previous two-dimensional cavitating jet simulations. However, the maximum values of dilatation and baroclinic torque terms in the current simulation are two orders of magnitude larger than in the two-dimensional cavitating jet simulations. The increase of baroclinic torque terms can be explained by consider-

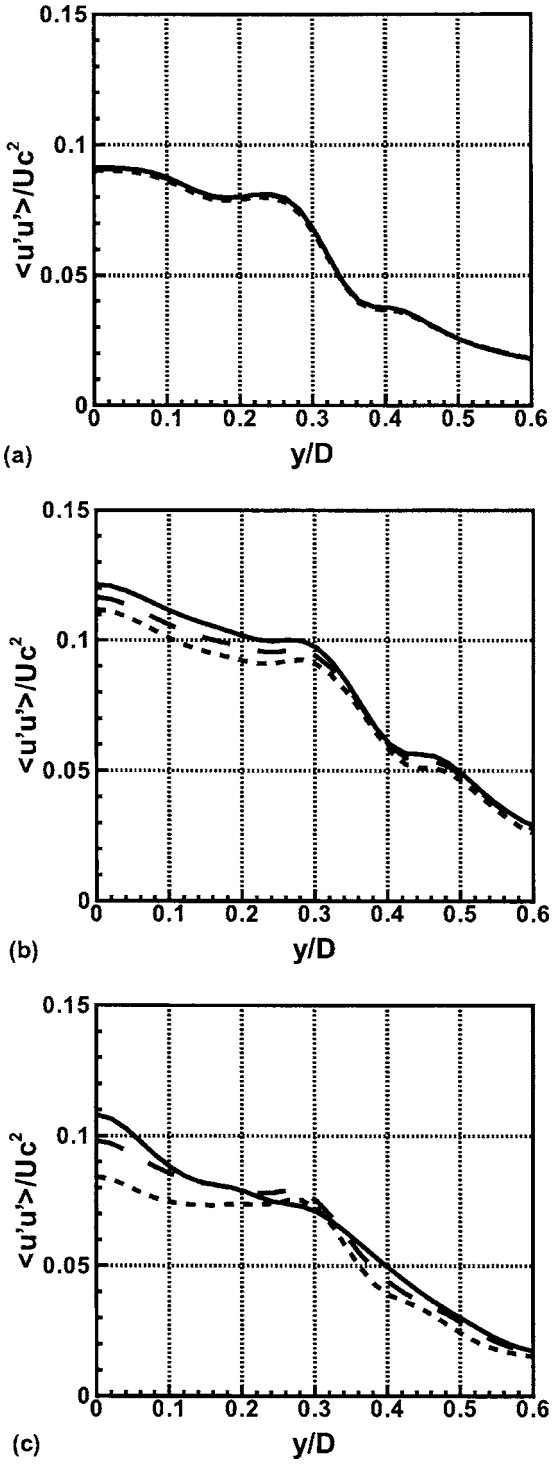

Fig. 15 Profiles of Reynolds stress component $\langle u'u' \rangle / U_c^2$ at axial stations for all cases. Solid line is $\sigma=1.8$, long dashed line is $\sigma=0.6$ and short dashed line is $\sigma=0.5$. (*a*) $x^*=2.0$, (*b*) $x^*=4.0$, (*c*) $x^*=6.0$.

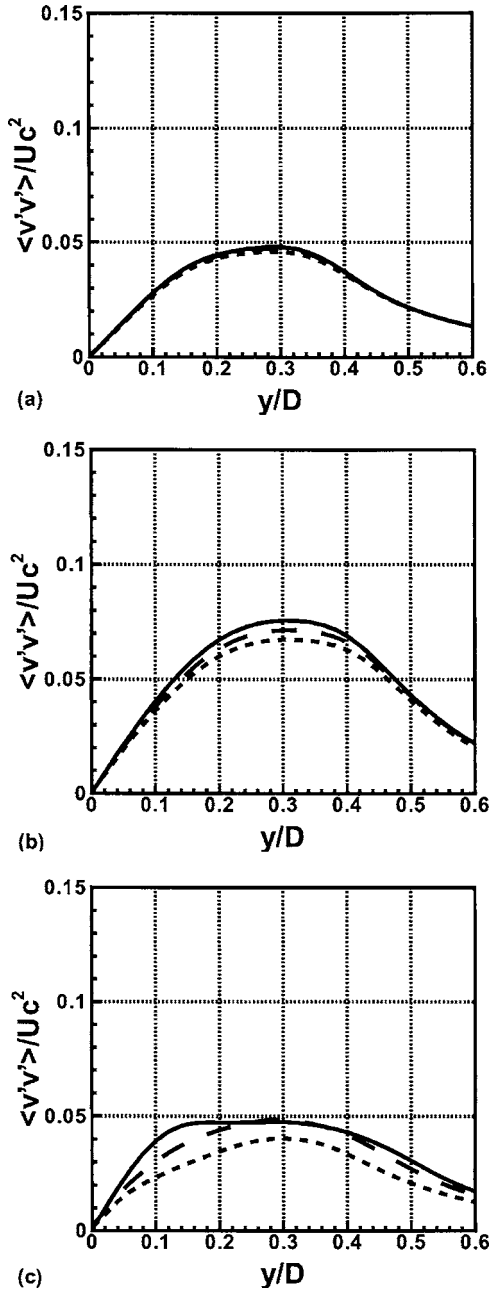

Fig. 16 Profiles of Reynolds stress component $\langle v'v' \rangle / U_c^2$ at axial stations for all cases. Solid line is $\sigma=1.8$, long dashed line is $\sigma=0.6$ and short dashed line is $\sigma=0.5$. (*a*) $x^*=2.0$, (*b*) $x^*=4.0$, (*c*) $x^*=6.0$.

ing the current void fraction is ≈25 times larger than in the two-dimensional simulations. This will increase the local pressure and density gradient. The increase of the dilatation term suggests local vorticity has been intensified by bubbles in the cavitating regions.

Instantaneous data from eight flowthrough times (defined as $x^*/\langle U_0 \rangle$) were averaged to obtain mean and rms velocity and Reynolds stress profiles. The axial variation of the jet momentum thickness, shown in Fig. 14, indicates that cavitation suppressed jet growth. Radial profiles of streamwise, cross-stream, and shear components of the Reynolds stress tensor at axial stations corresponding to the main cavitation regions and just downstream of these regions are shown in Figs. 15–17, respectively. These plots suggest that cavitation suppressed velocity fluctuations downstream of the cavitation regions, consistent with the suppressed jet growth and weaker streamwise vortices noted earlier. The suppression of cross-stream and shear Reynolds stress components due to cavitation is consistent with the recent PIV (particle imaging velocimetry) measurements of Iyer and Ceccio [9] for a cavitating shear layer and it is greatest for the case with the lowest cavitation number. They observed an increase in streamwise velocity fluctuations near the outer edge of the shear layer, and a decrease near the shear layer center. The location of maximum

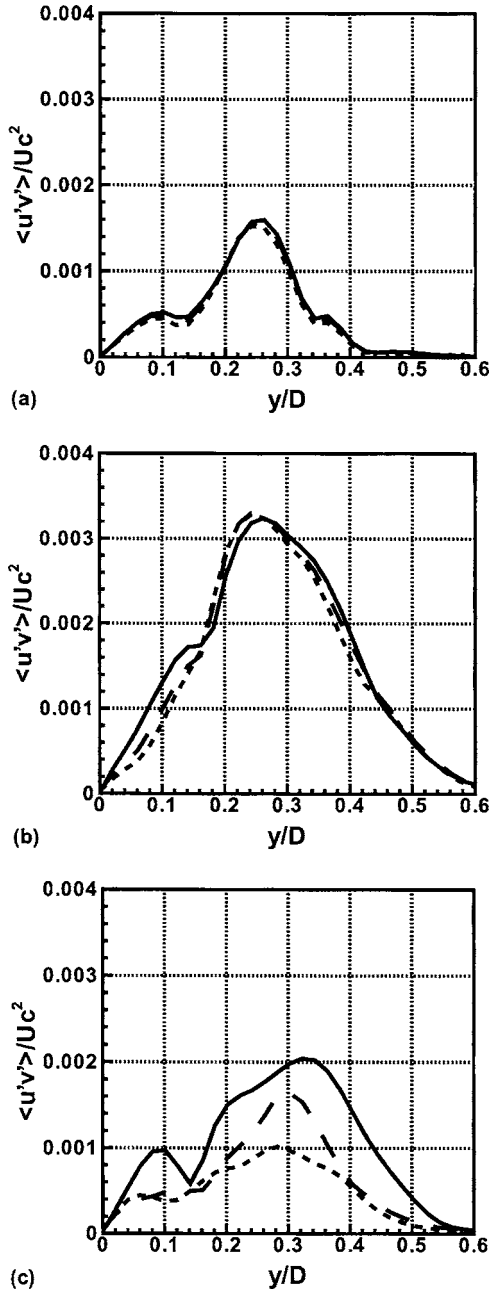

Fig. 17 Profiles of Reynolds stress component $\langle u'v' \rangle / U_c^2$ at axial stations for all cases. Solid line is $\sigma = 1.8$, long dashed line is $\sigma = 0.6$ and short dashed line is $\sigma = 0.5$. (*a*) $x^* = 2.0$, (*b*) $x^* = 4.0$, (*c*) $x^* = 6.0$.

velocity fluctuations is not at the center of the shear layer, also consistent with Iyer and Ceccio [9]. Further downstream the influence of cavitation on the Reynolds stresses becomes more significant, especially for the case with the lowest cavitation number.

6 Conclusions and Future Work

Numerical simulations of low Reynolds number, transitional submerged round jets reveal that cavitation occurs within the cores of the primary vortex rings formed just downstream of the nozzle exit when the local fluid pressure drops below the vapor pressure. Cavitation tends to distort and breakup the vortex rings and also weakens the secondary streamwise vortex tubes. Evidence for local flow acceleration and intensification of spanwise vorticity at the expense of streamwise vorticity due to cavitation is observed. Analysis of various terms in the vorticity transport equation reveals a decrease in the magnitude of the vortex stretching term and the presence of non-zero dilatation and baroclinic torque terms in the main cavitation regions. Statistical analysis of the flow field demonstrates that cavitation tends to suppress jet growth and reduce Reynolds stresses. These effects are in qualitative agreement with previous experimental studies of cavitating shear flows and bubble-flow interactions. Future efforts should focus on extending the cavitation model to apply to larger void fraction flows by relaxing the constant bubble number density assumption, accounting for bubble size distributions, and considering thermal nonequilibrium effects. Finally, inclusion of a subgridscale turbulence model to facilitate large eddy simulations of cavitating flows would allow higher Reynolds number and more complex geometries, and hence scaling effects, to be considered.

Acknowledgments

The authors would like to gratefully acknowledge Caterpillar Inc., Peoria, IL, and the Indiana 21st Century Research and Technology Fund for support of this research.

Nomenclature

D = nozzle diameter
f_v = void fraction
n = bubble number density
p = pressure
p_∞ = chamber pressure
R = bubble radius
Re = Reynolds number
S = strain rate tensor
t = time
U_0 = maximum velocity at inlet
$\mathbf{V}$ = velocity vector
U_c = centerline velocity
u_0 = convective velocity at outlet
(x, y, z) = Cartesian coordinate system
μ = molecular viscosity
ω = vorticity
ρ = density
Δr = bubble cluster radius
σ = cavitation number
∇ = gradient operator
Λ = constant

Subscripts

ℓ = liquid
v = vapor

Superscripts

* = on-dimensional quantity

References

[1] Rood, E. P., 1991, "Review—Mechanisms of Cavitation Inception," J. Fluids Eng., **113**, pp. 163–175.
[2] Arndt, R. E. A., 1981, "Cavitation in Fluid Machinery and Hydraulic Structures," Annu. Rev. Fluid Mech., **13**, pp. 273–328.
[3] Billard, J.-Y., Galivel, P., and Fruman, D. H., 1993, "Effect of Preturbulence on the Cavitating Bubble Inception, Noise and Morphology in A Venturi," ASME FED, **176**, pp. 31–38.
[4] Baur, T., and Ngeter, J. K., 1998, "Measurements in the Shear-Layer Behind a Surface-Mounted Obstacle for the Determination of Coherent Structures," *Ninth Int. Symp. on Applications of Laser Techniques to Fluid Mechanics*, Lisbon, Portugal, pp. 1–7.
[5] Brennen, C. E., 1995, *Cavitation and Bubble Dynamics*, Oxford University Press, Oxford, Chap. 2.
[6] Gopalan, S., Katz, J., and Knio, O., 1999, "The Flow Structure in the Near Field of Jets and Its Effects on Cavitation Inception," J. Fluid Mech., **398**, pp. 1–43.
[7] Arndt, R. E. A., 2002, "Cavitation in Vortical Flows," Annu. Rev. Fluid Mech.,

34, pp. 143–175.
[8] Sridhar, G., and Katz, J., 1999, "Effect of Entrained Bubbles on the Structure of Vortex Rings," J. Fluid Mech., **397**, pp. 171–202.
[9] Iyer, C. O., and Ceccio, S. L., 2002, "The Influence of Developed Cavitation on the Flow of a Turbulent Shear Layer," Phys. Fluids, **14**(10), pp. 3414–3431.
[10] Xing, T., and Frankel, S. H., 2002, "Effect of Cavitation on Vortex Dynamics in a Submerged Laminar Jet," AIAA J., **40**(11), pp. 2266–2276.
[11] Kubota, A., Kato, H., and Yamaguchi, H., 1992, "A New Modeling of Cavitating Flows: A Numerical Study of Unsteady Cavitation on a Hydrofoil Section," J. Fluid Mech., **240**, pp. 59–96.
[12] Delale, C. F., Schnerr, G. H., and Sauer, J., 2001, "Quasi-One-Dimensional Steady-State Cavitating Nozzle Flows," J. Fluid Mech., **427**, pp. 167–204.
[13] Dormy, E., 1999, "An Accurate Compact Treatment of Pressure for Colocated Variables," J. Comput. Phys., **151**, pp. 676–683.
[14] Perot, J. B., 1993, "An Analysis of the Fractional Step Method," J. Comput. Phys., **108**, pp. 51–58.
[15] Hunt, J. C. R., Wray, A. A., and Moin, P., 1988, "Eddies, Stream, and Convergence Zones in Turbulent Flows," Report CTR-S88, Center For Turbulence Research.

Effect of Wall Roughness on the Dynamics of Unsteady Cavitation

Olivier Coutier-Delgosha[1]
e-mail: olivier.coutier@lille.ensam.fr

Jean-François Devillers[2]
e-mail: devilJF@aol.com

Mireille Leriche
e-mail: leriche@ensta.fr

Thierry Pichon
e-mail: pichon@ensta.fr

ENSTA - UER de Mécanique Chemin de la Hunière,
91761 Palaiseau Cedex, France

The present paper is devoted to the experimental study of unsteady cavitation on the suction side of a two-dimensional foil section positioned in a cavitation tunnel with a small incidence angle. When the pressure is decreased in the tunnel, a sheet of cavitation characterized by large amplitude fluctuations is obtained on the foil. The present study focuses on the effects of the foil wall roughness on the cavity unsteady behavior. Four different sizes d of irregularities have been tested, from the smooth surface to a 400 μm *grain size. The characteristic frequency of the flow unsteadiness is investigated by analyzing the data measured by a pressure transducer mounted flush on one vertical wall of the test section, whereas the mean cavity length is obtained by visual measurements on the foil side. Several types of cloud cavitation are identified in the case of the smooth surface. The effect of roughness is a significant decrease of the cavity length and a large increase of the oscillation frequency. It results in Strouhal numbers higher than the classical values obtained for partial cavity fluctuations. Moreover, the cavitation cycle is disorganized by the increase of the roughness, as it can be detected by the fast fourier transform analysis of the pressure signal. The general effect is a reduction of the pressure fluctuation intensity.* [DOI: 10.1115/1.1949637]

1 Introduction

Rocket-engine turbopumps are generally equipped with an inducer stage that operates in cavitating conditions because of the low pressure of the fluid at the inlet of the pumps. Cavitation mainly consists in vaporized areas on the suction side of the blades, usually denoted sheets of cavitation (Fig. 1). Additional low-pressure areas, such as the tips of the blades and the gap between the rotor and the stator, also exhibit cavitation. Two major types of instability due to cavitation have been detected in inducers. The first one consists in nonsymmetrical flow arrangements (one little sheet of cavitation and three large ones, for example, in the case of a four-blade inducer) that rotate with a speed different from that of the pump, as explained, for example, by de Bernardi et al. [1]. The second one is based on large amplitude fluctuations of the sheets of cavitations on the blades, which result in significant pressure fluctuations at the outlet of the inducer. These fluctuations may deteriorate the operation of the other stages of the turbopump, so they must be avoided or at least controlled.

The second category of instability has been extensively investigated in cavitation tunnels by analyzing the flow around two-dimensional foil sections [2–5] or Venturi-type sections [6–9]. In both configurations, the sheet cavity on the foil suction side or the Venturi throat is characterized by cyclic oscillations, whose frequency mainly depends on the cavity length. According to these previous studies, the periodic fluctuations of the cavity are driven by a reentrant jet that regularly flows from its downstream end up to the foil leading edge, close to the wall. This reverse flow thus periodically cuts the cavity interface in its upstream part, which results in the detachment of the rear part. The resulting cloud of vapor is then convected downstream until it encounters an adverse pressure gradient and collapses. Other mechanisms, such as the destabilization of the cavity interface combined with the reentrant jet, have also been proposed by Lush and Peters [7] to explain the self-sustained oscillations. The role of shock waves due to the collapse of the cloud of vapor is also investigated by Song and Qin [10] on the basis of numerical simulations.

To control the self-oscillating behavior by stopping the reentrant jet is the basic idea that was proposed by Kawanami et al. [2]. These authors experimented with the use of obstacles characterized by a significant height (2 mm) to prevent cloud cavitation. The objective was reached even with a little length of the obstacle in the spanwise direction, which confirms that the flow unsteadiness is mainly triggered by the reentrant jet. Similar results were obtained by Pham et al. [3] with the same type of obstacle: a modification of the cloud-shedding phenomenon was observed, associated with a large reduction of the reverse flow momentum. Recently, Stutz [11] analyzed the effects of using striated or rough bottoms instead of a polished one in a Venturi-type section. No noticeable influence of these parameters on the two-phase flow structure was detected. However, the irregularities on the surface were, in this case, much smaller than the characteristic size of the obstacle used by Kawanami et al. [2].

The present paper focuses on the experimental investigation of the effects of the roughness of the foil surface on the dynamics of the cavitating flow. Experiments are conducted in the ENSTA cavitation tunnel where various cavitation conditions can be obtained: pressure can be lowered down to 150 mbar and the flow velocity can be increased up to 10 m/s. Although the shape of the foil section is very simple (Fig. 2), its sharp leading and trailing edges and small angle of attack make it representative for the flow over the blades of a rocket-engine turbopump inducer. This is the main advantage of using a foil section, instead of a Venturi-type section.

When the pressure is decreased in the cavitation tunnel, sheet cavitation appears on the foil suction side. Its behavior is rather steady at small incidence, with only small-scale fluctuations in its rear part, whereas periodical self-oscillations of large amplitude involving vapor cloud shedding are obtained when the angle of attack is increased. Figure 3 presents side views of the flow corresponding to the successive steps of the cycle for an angle of attack $\alpha=3$ deg, an inlet velocity $V_{ref}=6$ m/s and a cavitation number $\sigma=1$. The limit between stable and unstable configurations is usually contained in the range 2–3 deg. The foil suction side is equipped with interchangeable plates characterized by different roughness. This device enables one to investigate the effect

[1]Now at ENSAM Lille / LML Laboratory, 8 bld Louis XIV, 59046 Lille cedex, France

[2]Now Scientific Consultant, 4 rue Mirabeau, 91120 Palaiseau, France

Contributed by the Fluids Engineering Division for publication in the JOURNAL OF FLUIDS ENGINEERING. Manuscript received by the Fluids Engineering Division April 13, 2004; Final manuscript reveived March 27, 2005. Associate Editor: Yoshinoba Tsujimoto.

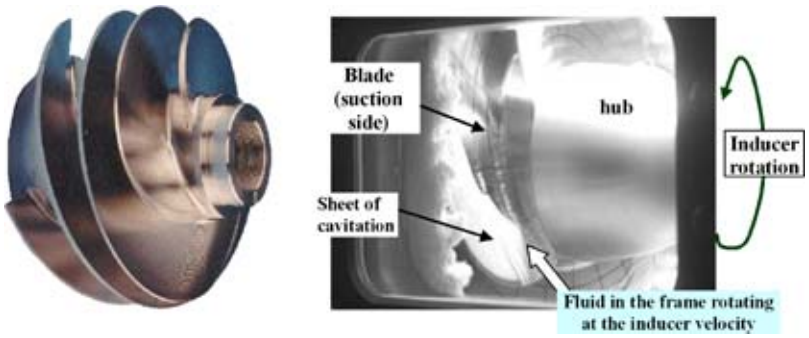

Fig. 1 (*a*) **Geometry of a rocket-engine turbopump inducer,** (*b*) **cavitating flow**

of the roughness on the cavity dynamics in order to determine whether irregularities of the surface modify the progression of the reentrant jet or not.

Section 2 is devoted to the presentation of the experimental setup and estimation of the measurement uncertainties. Results obtained with the smooth surface are presented in Sec. 3, and Sec. 4 focuses on the effects of roughness.

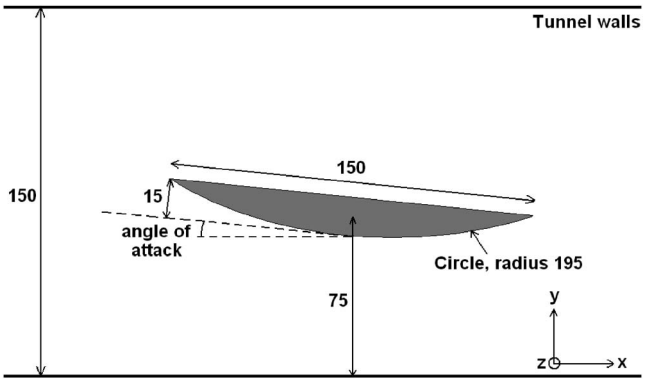

Fig. 2 Foil geometry

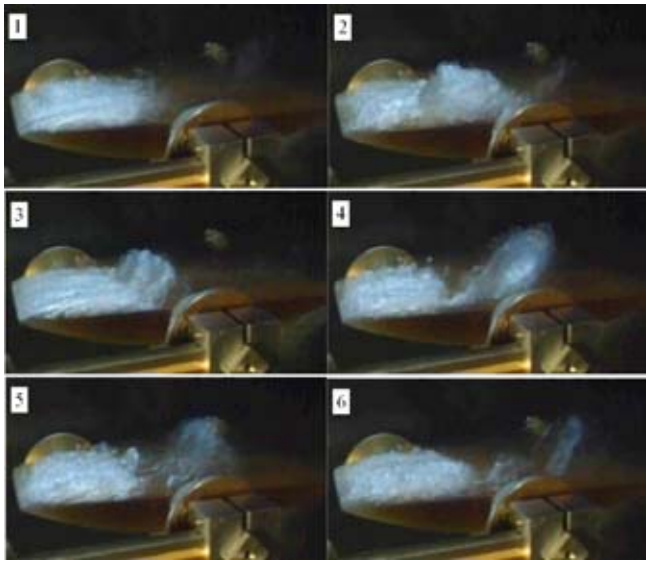

Fig. 3 Vapor cloud shedding on the foil suction side (Incidence 3 deg, V_{ref}=6 m/s, σ=1)

2 Experimental Setup

The considered geometry is a two-dimensional foil of 150 mm chord and 80 mm span. Its cross section is composed of a flat upper surface and a convex lower surface of 195 mm radius, as illustrated by Fig. 2. Experiments were performed in the ENSTA cavitation tunnel whose test section is 150 mm height, 80 mm width, and 640 mm length. The foil was located at midheight, with a small angle of attack, so a cavitation sheet appears on the upper face, when the pressure is decreased in the tunnel. Compared to the Venturi configuration, studied previously by Stutz and Reboud [8,9], the cavitation behavior is modified by the possible interaction between the foil pressure and suction sides.

The upper wall of the foil section is equipped with interchangeable plates characterized by various roughnesses. Preliminary tests have been performed with abrasive paper sized on the foil, but cavitation systematically resulted in its destruction. In the present case about 55% of the foil surface is covered by the plates, which are screwed, as indicated in Fig. 4. Four plates with various

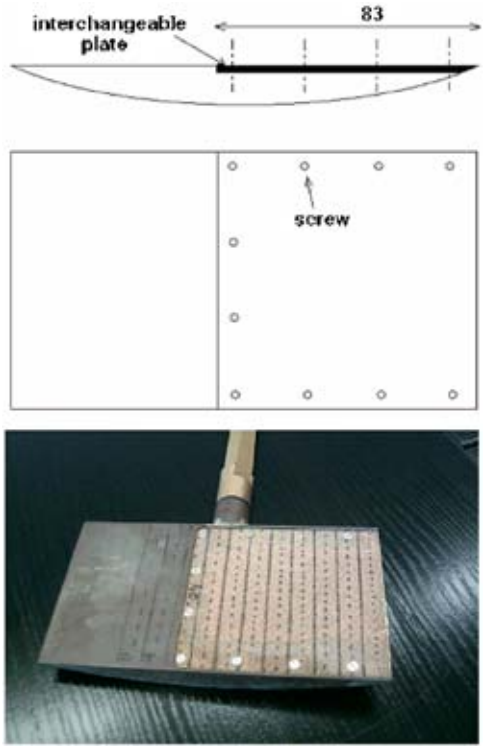

Fig. 4 (*a*) **Scheme of the adaptable foil section, and** (*b*) **view of the foil**

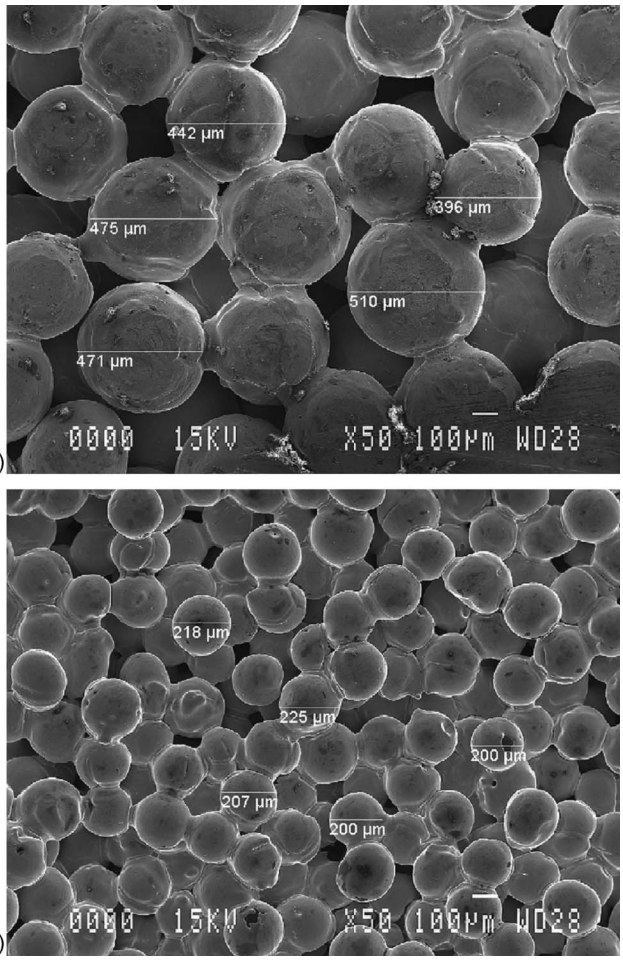

Fig. 5 Detail of the roasted metal (microscope, magnitude 50) (*a*) Mean grain size 400 μm, and (*b*) mean grain size 200 μm

roughnesses and a fifth one, perfectly smooth, are available. Roughness is obtained by metal roasting based on the compression of microscopic brass balls close to the melting conditions. Roughness can thus be defined in the present experiments by the mean diameter d of the balls, like the grain size in the Nikuradse's sand roughness [12]. The detail of the protrusions, obtained by a microscope with magnitude $\times 50$, can be seen in Fig. 5. Four ball diameters are considered, namely, $d=100$, 200, 300, and 400 μm. They are denoted hereafter "Roughness 100, 200, 300, 400." These values result from a preliminary study based on the work of Schlichting, who indicates a condition to obtain a completely rough regime characterized by protrusions larger than the laminar viscous sublayer. This condition is given by a minimum Reynolds number $\mathrm{Re}=V_{\mathrm{ref}}\times d/\nu=100$, where ν denotes the kinematic viscosity of the fluid. In the experiments $V_{\mathrm{ref}}=6$ m/s and $\nu=10^{-6}$ m^2/s so the minimal size of the balls should be ~ 16 μm.

Another foil composed of a single piece with a smooth upper face is also used to check that the fixation of the plates has a negligible influence on the behavior of the cavity. The reference pressure P_{ref} is measured with a JPB model TB 142 absolute pressure sensor connected to two pressure taps located, respectively, at the bottom and at the top of the test section inlet. These two taps enable one to take into account the effect of a possible velocity gradient in the height of the cavitation tunnel. The reference velocity V_{ref} is derived from the mass flow rate Q and the size of the cross section of the test section inlet. Q is controlled by a propeller flow meter. These flow conditions are regulated with 3% and 1% precision respectively, for P_{ref} and V_{ref}, which leads to a 5% uncertainty on the cavitation number $\sigma=(P_{\mathrm{ref}}-P_{\mathrm{vap}})/(\frac{1}{2}\rho V_{\mathrm{ref}}^2)$, where P_{vap} denotes the vapor pressure and ρ the water density.

The unsteady behavior of cavitation is characterized by measurements of the fluctuating pressure with a PCB model M106B50 piezoelectric pressure transducer whose resonant frequency is 40 kHz and sensibility is 0.07 mV/Pa. The transducer is mounted flush on one of the vertical walls of the test section, 30 mm upstream the foil leading edge. The pressure data are processed by a HP 35665 spectrum analyzer whose frequency full span and default resolution are, respectively, 102.4 kHz and 400 lines. No filtering is applied to the pressure signal. To obtain the frequency f of the cavity self-oscillation, Fourier transforms are performed from 1024 sample data and then averaged over 40 tests.

The length L_{cav} of the sheets of cavitation is estimated visually using signs painted on the foil surface each 5 mm. In this work, L_{cav} denotes the maximum length of the leading edge cavity, i.e., the part that remains attached to the foil, without considering the wake downstream. To estimate the uncertainty concerning this measurement, another method is applied in the case of the smooth foil surface. For each flow condition, 60 side views and top views of the sheet cavity are recorded with a standard B&W CCD camera operating at 25 fps. The mean shape and thus the mean length L_{cav} of the vaporized area are obtained by averaging the gray levels on these 60 random pictures and then applying a filter to the resulting picture (see Fig. 6). The results obtained by the three methods are compared in Fig. 7 in the configuration $\alpha=6$ deg for σ varying between 1.6 and 1. A reliable agreement is obtained for small cavities, whereas the uncertainty is significantly increased for large sheet cavities, mainly because of their large amplitude fluctuations. On the basis of this result, the precision of the direct measurements is finally estimated to be 8%.

The setup presented here was exploited during two sets of measurements achieved with different experimental procedures:

- For set 1, the flow was investigated by successively using the smooth foil, and three plates with, respectively, a smooth surface, $d=200$ μm, and $d=400$ μm. A large range of cavitation numbers was tested, from $\sigma=1.8$ down to $\sigma=0.7$. The angle of attack was varied between 0 and 6 deg by steps of 1 deg, and the reference velocity V_{ref} was equal to 6 m/s.
- For set 2, the cavitation number was $\sigma=1.3$ and $V_{\mathrm{ref}}=6$ m/s. Four plates have been tested (the smooth one, and $d=100$, 200, and 400 μm) with an angle of attack ranging from $\alpha=0$ to 5 deg by steps of 0.25 deg.

3 Results With the Smooth Wall

In this section, the results obtained in the case of the smooth foil section (without the setup for the interchangeable plates) are presented. They were obtained in conditions similar to the ones reported previously by Pham et al. [3]. However, the present experiments indicate that the unsteady behavior of the cavitation sheet is characterized by three different types of oscillations, which depend both on the cavity length and the cavitation number σ.

Six values of the cavitation number are investigated from $\sigma=1.8$ down to $\sigma=0.7$. The reference velocity V_{ref} is kept equal to 6 m/s. For each flow condition, the angle of attack is varied from $\alpha=0$ deg up to $\alpha=0$ deg by steps of 1 deg (measurement set 1). Sheet cavitation on the foil suction side appears for a very low incidence usually close to 1 deg. No significant unsteadiness can be detected on the pressure signal for angles lower than 2 deg: only high-frequency perturbations (between 200 and 500 Hz) are obtained. This is because of small-scale fluctuations in the rear part of the cavity, as previously reported by De Lange et al. [13] and Pham et al. [3]. When the angle of incidence is increased over 2 deg, large fluctuations of the cavity length are observed, while

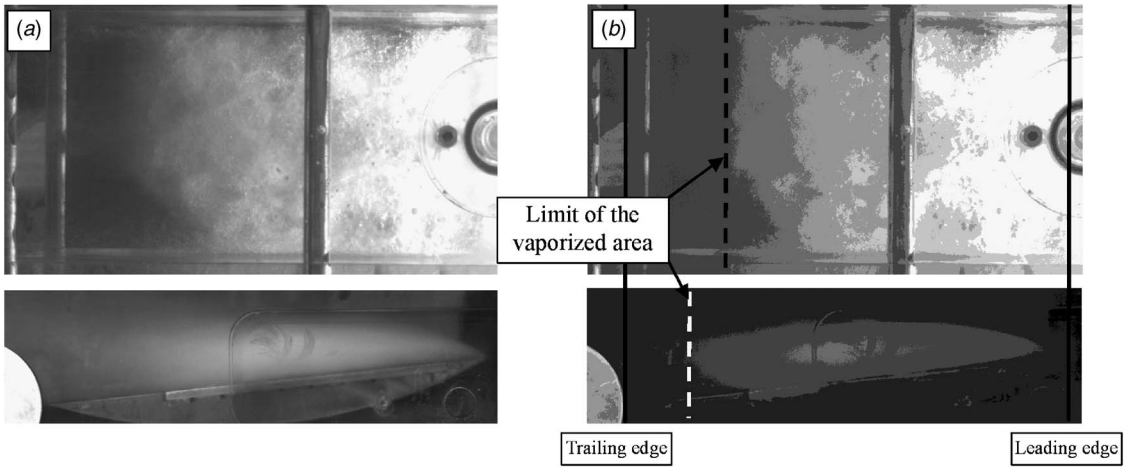

Fig. 6 Estimation of the cavity length from top and side views of the cavity (α=6 deg, σ=1) (*a*) initial pictures, (*b*) postprocessing to visualize the limit of the cavity

the spectra of the fluctuating pressure signal exhibit one or several sharp dominant peaks. The corresponding frequencies decrease when the cavity length is increased, i.e., when the angle of attack is augmented. This behavior is systematically obtained for all cavitation numbers.

We focus hereafter on the conditions that lead to a pronounced flow unsteadiness characterized by large-scale fluctuations involving periodical vapor cloud shedding (2 deg$<\alpha<$6 deg). Such behavior is usually referred to as cloud cavitation in previous studies [3,8,9]. Figure 8 presents the evolution of the cavity length according to the cavitation number σ and the incidence α. The values are plotted as a function of the parameter σ/α, derived from the one ($\sigma/2\alpha$) proposed by Acosta [14] in his linearized theory of partial cavitation on flat-plate hydrofoils. Le et al. [15] have more recently correlated the cavity length L_{cav} with the parameter σ/α, in the case of hydrofoils similar to the present one. This result is confirmed by the present experiments, since the cavity lengths measured in all flow conditions are very close to a unique chart, which suggests that they only depend on σ/α. The data scattering may be mainly due to the 8% measurement uncertainty on L_{cav}. Note also that the foil angle of attack is known with a 1% precision and σ with a 5% precision (see Sec. 2), so the uncertainty on σ/α is about 6%. The chart represented by the solid line is a polynomial approximation of the experimental points, and its equation is

$$\frac{L_{cav}}{L_{ref}} = \frac{A}{\left(\frac{\sigma}{\alpha}\right)^n} \tag{1}$$

with $A\approx 100$ and $n\approx 2$.

The dynamics of the sheet of cavitation is investigated in Fig. 9 by plotting the Strouhal number Str=$f\times L_{cav}/V_{ref}$ as a function of σ/α. The frequency f is the one corresponding to the dominant peak on the spectrum of the pressure signal. Actually, several peaks are often obtained with different magnitudes. In such cases only the dominant peak with the highest amplitude is considered. The only exception concerns the very large cavities (L_{cav}/L_{ref} $>75\%$), since in these cases the spectra suddenly exhibit a supplementary peak of much higher amplitude than all others. This is due to a new type of instability in the flow; therefore, in these configurations this peak and the dominant one of lower amplitude are both regarded.

Several different behaviors can be distinguished:

i. For σ lower than 1.3, a single sharp dominant peak of large magnitude is usually obtained, leading to a Strouhal number very close to a value of 0.25, which is the most classical one for cloud cavitation [3,8]. The Strouhal num-

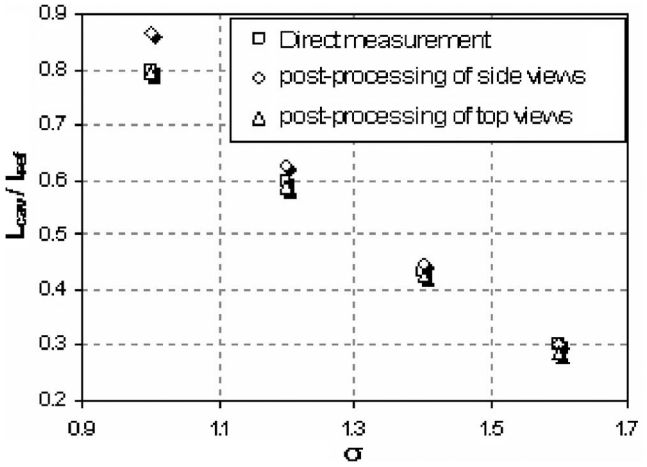

Fig. 7 Comparison of the cavity lengths obtained (i) by direct measurements, (ii) by postprocessing of side and top views of the cavity

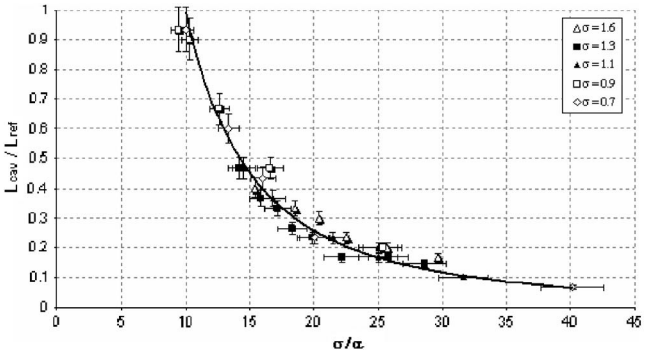

Fig. 8 Evolution of the maximum attached cavity length for several flow conditions and angles of attack varying from 2–6 deg (measurement set 1)

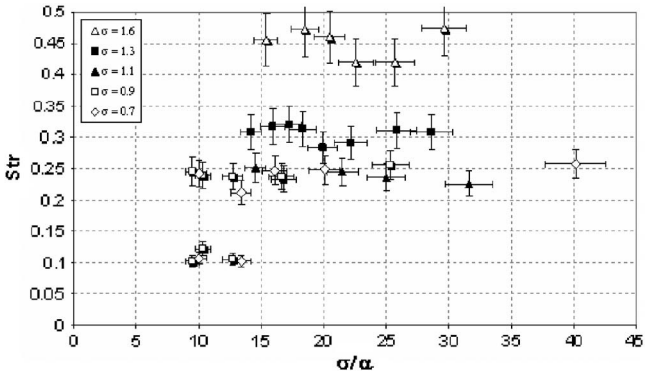

Fig. 9 Strouhal number associated with the cavity self-oscillation (measurement set 1)

ber is almost constant in this configuration, and no influence of the cavitation number σ is detected.

ii. For σ higher than 1.3 (only $\sigma=1.3$ and $\sigma=1.6$ are represented here), the Strouhal number progressively increases, while the magnitude of the dominant peak decreases significantly and the number of secondary peaks of comparable amplitude increases. Visually, in this situation the flow remains clearly unsteady, whereas the large-scale fluctuations seem to be weaker. However, the value of the Strouhal number is still almost constant for a given value of σ ($St\approx 0.3$ for $\sigma=1.3$ and $St\approx 0.45$ for $\sigma=1.6$). The diminution of the dominant peak magnitude suggests that only a part of the cavity is affected by the vapor shedding. This would explain the acceleration of the cavitation cycle. Strouhal numbers based on the size of the unstable rear part of the cavity instead of its maximum length may result in recovering the value $St=0.25$.

iii. In the case of very large sheets of cavitation (mainly at low cavitation number $\sigma\leqslant 0.9$ and high angle of attack $\alpha\geqslant 4$ deg), a new dominant peak of great intensity is obtained in the spectra, while the standard peak corresponding to $St=0.25$ is still present. This new peak is associated with a lower frequency that leads to a Strouhal number close to 0.10/0.12. It characterizes a trailing-edge instability due to the interaction between the foil suction and pressure sides. It has been shown recently by numerical simulations [16] that such an interaction governs the whole cavitation cycle by periodically imposing a low-pressure level at the foil trailing edge. As a result, the adverse pressure gradient in the rear part of the cavitation sheet is too weak to enable the progression of the reentrant jet under the cavity toward the leading edge. This progression, which is responsible for the cavity break-off, is only possible when the trailing-edge interaction periodically decreases. So the entire cavitation cycle adopts the frequency of the trailing-edge instability. This phenomenon is usually intermittent when the cavity length is about 80%, which explains that two peaks corresponding, respectively, to $St\approx 0.25$ and $St\approx 0.11$ appear on the spectra, whereas it is almost permanent when the cavity length is still increased.

The low Strouhal number reported in iii is similar to the normalized frequency $f\times L_{ref}/V_{ref}\approx 0.1$ obtained theoretically by Watanabe et al. [17] in the case of very large sheets of cavitation. Actually, these authors distinguish the "partial cavity oscillations," corresponding to cloud cavitation with $L_{cav}/L_{ref}<75\%$, from "transitional cavity oscillations," occurring for sheets of cavitation larger than 75% of the chord and characterized by a lower Strouhal number. These expressions will be used hereafter in the present work to differentiate the two behaviors.

4 Effects of Roughness

Both measurement sets 1 and 2 are analyzed in this section in order to investigate the effect of the surface roughness on the cavity dynamics. The first step consists of checking the influence of the irregularities due to the fixation of the plate on the foil. So the smooth plate is first used, and the characteristics of the sheet cavitation are compared to the results presented in the previous section. Figure 10 shows the evolution of the cavity length according to the parameter σ/α for three values of σ (0.9, 1.1, and 1.3). The polynomial approximation obtained in the case of the other foil is also reported in dashed line. All these results belong to the measurement set 1. No significant discrepancy is observed, apart from a slight general increase of the lengths, which is systematically smaller than the uncertainty on their measurement.

It is then checked in Fig. 11 that the surface roughness does not induce any supplementary effect of the cavitation number on the cavity length: its evolution is drawn according to σ/α in the case $d=400$ μm. Results corresponding to $\sigma=0.9$, 1.1, and 1.3 are reported. All the points almost form a single curve whose approximation is indicated in solid line, so the cavity length depends only on σ/α, as in the previous case of the smooth surface.

Figure 12 presents the evolution of the cavity length as a function of the angle of attack α, with four different plates. Although

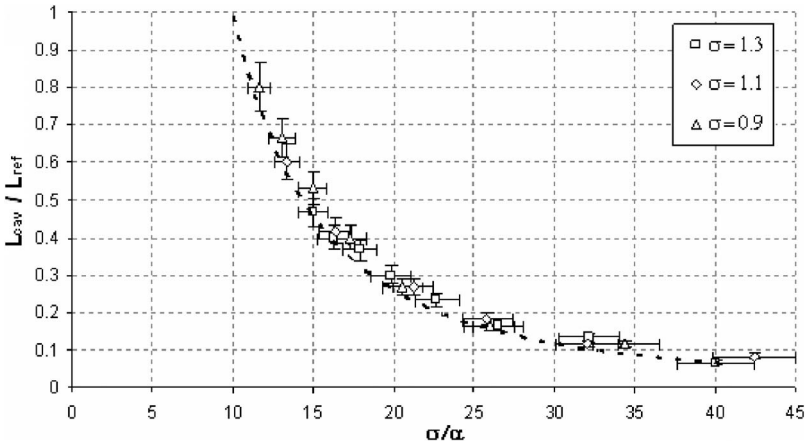

Fig. 10 Evolution of the maximum attached cavity length on the foil equipped with the smooth plate (measurement set 1). The dashed line corresponds to the approximation curve plotted previously on Fig. 8.

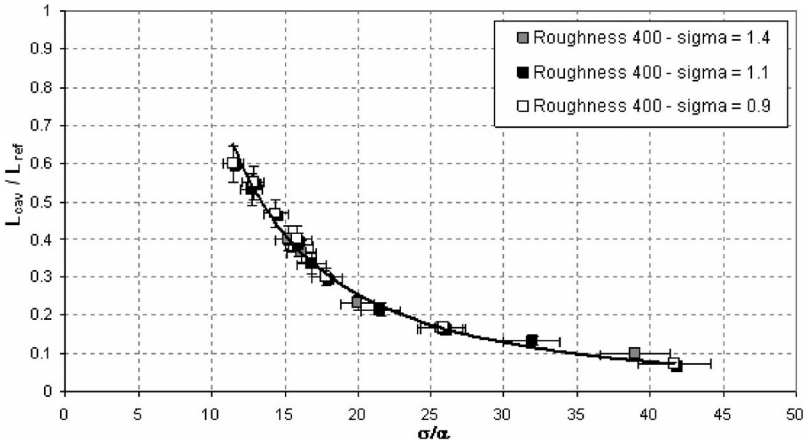

Fig. 11 Cavity lengths for roughness 400 and three values of σ (measurement set 1)

the present results focus on a single value of $\sigma=0.8$ (measurement set 2), similar conclusions have been obtained for higher values of σ. It can be observed that the size of the cavity only slightly depends on the roughness when $\alpha<2.5$ deg, i.e., when only small-scale fluctuations affect the sheet of cavitation. However, as soon as large amplitude oscillations start, significant discrepancies are obtained: L_{cav} is much lower with roughness 200 and 400 than with the smooth plate. The difference is about 40–50 % for 2.5 deg $<\alpha<4$ deg. This gap is partially reduced for $\alpha>4$ deg, and it equals only 25% for $\alpha=5$ deg. The case of roughness 100 gives intermediate values of L_{cav}. Two conclusions can be derived from this evolution: (i) roughness affects significantly the cavity length only in conditions of cloud cavitation and (ii) the effect of roughness does not linearly depend on the size of the protrusions; a noticeable modification of the cavity length is obtained by increasing d from 0 to 200 μm, but it seems that increasing d over 200 μm does not lead to any substantial evolution.

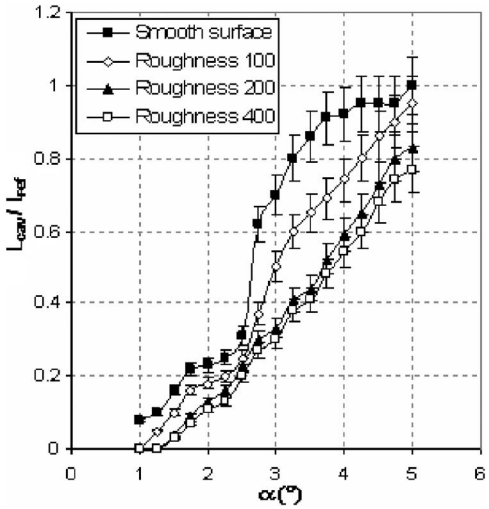

Fig. 12 Evolution of the cavity length with the incidence for $\sigma=0.8$ and three different plates of various roughnesses (measurement set #2)

When the sheet cavitation becomes longer than the plates, the cavity continues to increase in the case of roughness 400, whereas it almost stabilizes on the smooth plate. However, the discrepancy between roughness 400 and 100 remains approximately constant. Thus, these results do not indicate clearly if the end of the roughness at 55% of the foil plays a major role or not.

The analysis of the Strouhal numbers obtained for $\sigma=0.9$ and 1.3 (Figs. 13 and 14, respectively) shows a major effect of roughness on the cavity dynamic. Note that the first flow condition was characterized previously by a constant Strouhal number St ≈ 0.25, whereas the second one, and higher values of σ, resulted in a progressive increase from St ≈ 0.25 up to St ≈ 0.45 for $\sigma=1.6$. Both roughnesses 200 and 400 clearly lead here to a notable augmentation of these values: St is about 0.35–0.45 for $\sigma=0.9$,

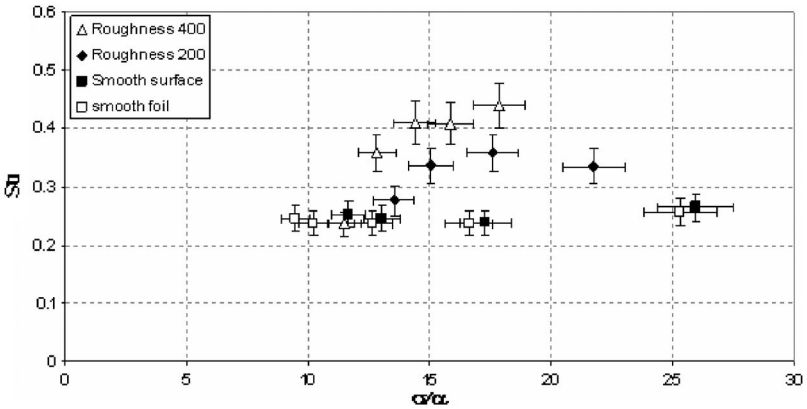

Fig. 13 Strouhal numbers for various roughness and $\sigma=0.9$ (measurement set 1)

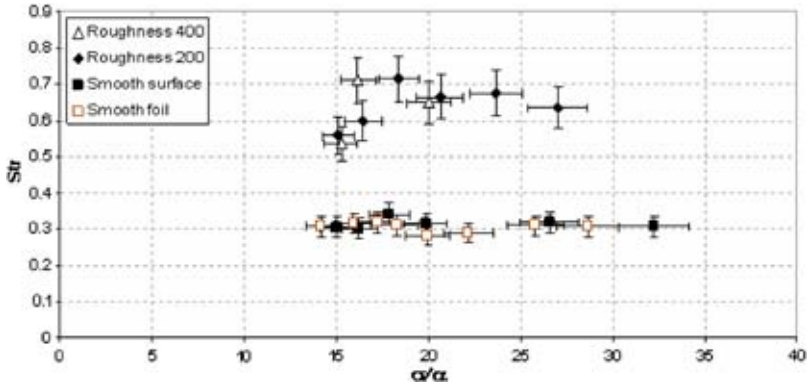

Fig. 14 Strouhal numbers for various roughness and $\sigma=1.3$ (measurement set 1)

and 0.55–0.75 for $\sigma=1.3$. Although the data are scattered into these ranges, this discrepancy with the previous results cannot be attributed to the experimental uncertainties (see Figs. 13 and 14). It indicates that the protrusions make the shedding frequency much increase. This result must be associated with the visual observations, which display a notable modification of the aspect of the cavity. Its downstream end is not so clearly limited as before, and the noise resulting from the self-oscillations seems to be significantly weaker. This trend is confirmed by the spectra of the fluctuating pressure signal; the sharp dominant peaks have been replaced by dominant frequencies distributed in broad ranges of a few tens of hertz width and characterized by much lower magnitudes (see Fig. 15). As a matter of fact, these magnitudes are divided by a factor comprised between three and five when d is increased from 0 to 400 μm. This modification, which can be interpreted as a reduction of both intensity and regularity of the cavitation cycle, suggests that the shedding process is strongly perturbed by roughness. This may be due to a premature decrease of the reentrant jet momentum because of the additional stress induced by the protrusions. As a result, only a small part of the cavity is detached from the foil. Such small vapor shedding (close to the one observed at low incidence) is usually characterized by a high and fluctuating frequency, which explains both the high Strouhal numbers and the modification of the pressure signal spectra. The general effect that may be interesting for spatial applications is a large reduction of the pressure fluctuations in the tunnel.

Figure 16 presents for $\sigma=0.8$, the Strouhal number evolution according to the angle of attack. Three values of roughness and the smooth plate are considered (measurement set 2). This figure confirms that St strongly increases when roughness is augmented. However, this effect is only present for $\alpha>2.5$ deg (beginning of the unsteadiness) and $\alpha<4$ deg (cavity smaller than the plates). For a higher incidence, a constant value close to 0.25–0.3 is recovered in all cases. It indicates that the surface roughness in the downstream end of the cavity is the dominant parameter that governs the modification of the cavitation cycle. For a sheet cavity longer than 60% of the chord, the smooth surface in the rear part enables a correct initial progression of the reverse jet and then no modification of the oscillations is obtained. It suggests that the reentrant jet is affected by roughness only in the cavity closure area. This may be due to an increase of its thickness during its progression toward the leading edge, which makes it less sensitive to the friction caused by the protrusions. The configuration of transitional cavity oscillations with roughness, which is not reported in Fig. 16, also leads to nonmodified Strouhal numbers close to 0.11. This is not surprising, since such cavities are much longer than the rough plates.

Other information given by Fig. 16 concerns the inception of cloud cavitation. The angle of attack α at which it occurs progressively increases when roughness is augmented (1.75 deg for the

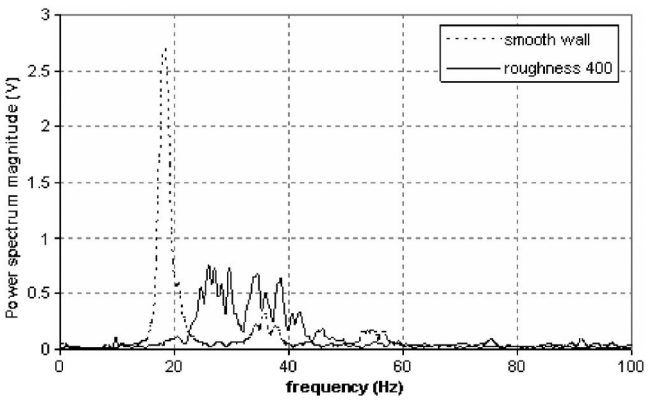

Fig. 15 Spectra of pressure signal fluctuations at incidence 5 deg and $\sigma=1$ with (*a*) a smooth surface ($L_{cav}/L_{ref}=0.7$) and (b) roughness 400 ($L_{cav}/L_{ref}=0.55$)

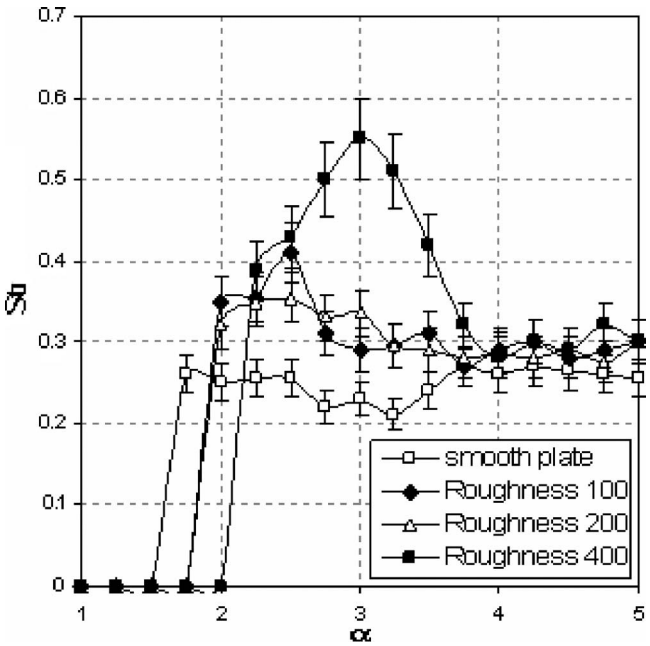

Fig. 16 Strouhal numbers for various roughness and $\sigma=0.8$ (measurement set 2)

smooth plate, 2.25 deg for roughness 400). Below this limit, only high-frequency fluctuations with no dominant peak on the spectra are obtained. This is a supplementary indication of the destabilization of the cavitation cycle in the case of a rough wall: periodical oscillations require a minimum angle of attack slightly higher than in the case of the smooth wall. This is consistent with the diminution of the reentrant jet momentum due to friction discussed previously.

5 Conclusion

The effect of the surface roughness on the dynamics of sheet cavitation on a two-dimensional foil section was investigated in this paper. We have focused mainly on cloud cavitation conditions, characterized by large amplitude oscillations involving periodical vapor cloud shedding. Acquisitions are based on cavity-length measurements and analysis of the spectra given by the fluctuating pressure signal in the cavitation tunnel. A careful analysis of several sets of measurements was performed in order to identify (i) the different unsteady behaviors in the case of a smooth foil and (ii) the modification of these behaviors due to roughness.

Concerning the first point, it has been found that cavitation numbers σ lower than 1.3 systematically lead to Strouhal numbers close to 0.25; thus far, the sheet of cavitation remains smaller than about 80% of the chord. In the case of larger cavities, a new frequency due to the interaction between the foil pressure and suction sides is obtained, which gives Strouhal numbers ranging from 0.1 to 0.12. The first configuration corresponds to partial cavity oscillations, while the second one is similar to transitional cavity oscillations, according to the theoretical work of Watanabe et al. [17]. Cavitation numbers higher than 1.3 lead to a progressive increase of the Strouhal numbers. In all cases the cavity length only depends on the parameter σ/α.

Concerning the second point, it has been noticed that roughness induces a significant diminution of the cavity length, associated with a clear increase of the Strouhal numbers. This second effect has been observed mainly for a self-oscillating cavity whose length is smaller than the one of the rough plates, which indicates that roughness in the downstream end of the sheet cavity plays a major role in the arrangement of the cavitation cycle. The general effect of roughness is a disorganization of the periodical shedding, characterized by much lower pressure fluctuations than previously. It has been suggested that the protrusions, which are here much larger than the viscous sublayer width, cause an increase of the friction experienced by the reentrant jet. The premature decrease of the reentrant jet momentum would thus be responsible for the modification of the cavity dynamics.

Acknowledgeents

This work was performed with the contribution of successive teams of students from ENSTA (Ecole Nationale Supérieure de Techniques Avancées) and l'Ecole Navale (French Naval academic school). They are all associated with this study. The measurement set 1 corresponds to the data obtained by T. Federici and R. Meireles [18] during their second year research project, while the measurement set 2 was obtained by L. Bouchentouf [19] during his Master's project.

Nomenclature

d = mean size of the protrusions on the rough plates, m
f = frequency of the cavity oscillations, Hz
$L\text{ref}$ = chord length of the foil, m
L_{cay} = maximum length of the attached cavity, m
P_{ref} = reference pressure at the inlet of the test section, Pa
P_{vap} = vapor pressure, Pa
Q = mass flow rate in the tunnel, m^3/s
Re = Reynolds number $L_{\text{ref}} \times V_{\text{ref}}/v$
St = Strouhal number $f \times L_{\text{cav}}/V\text{ref}$
V_{ref} = reference velocity based on the mass flow rate, m s^{-1}
α = foil angle of attack
v = kinematic viscosity, m^2/s
ρ = density, kg m^{-3}
σ = cavitation number

References

[1] de Bernardi, J., Joussellin, F., and Von Kaenel, A., 1993, "Experimental Analysis of Instabilities Related to Cavitation in Turbopump Inducer", *Proc. of 1st Int. Symp. on Pump Noise and Vibrations, Paris, France*, pp. 91–99.

[2] Kawanami Y., Kato H., Yamaguchi H., Tayaga Y., and Tanimura M., 1997, "Mechanism and Control of Cloud Cavitation," ASME J. Fluids Eng., **119**, pp. 788–794.

[3] Pham, T. M., Larrarte, F., and Fruman, D. H., 1999, "Investigation of Unstable Sheet Cavitation and Cloud Cavitation Mechanisms," ASME J. Fluids Eng., **121**, pp. 289–296.

[4] Laberteaux, K. R., and Ceccio, S. L., 2001, "Partial Cavity Flows, Part 1. Cavities Forming on Models Without Spanwise Variation," J. Fluid Mech. vol **431**, pp. 1–41.

[5] Leroux, J-B., Astolfi, J-A., and Billard, Y., 2004, "An Experimental Study of Unsteady Partial Cavitation," ASME J. Fluids Eng. **126**, 94–101.

[6] Furness, R. A., and Hutton, S. P., 1975, "Experimental and Theoretical Studies of Two-Dimensional Fixed-Type Cavities," ASME J. Fluids Eng. **97**, pp. 515–522.

[7] Lush, P. A., and Peters, P. I., 1982, "Visualization of the Cavitating Flow in a Venturi Type Duct Using High-Speed Cine Photography", *Proc. of International Association of Hydraulic Engineering and Research Conference on Operating Problems of Pump Stations and Power Plants*, Amsterdam, Netherlands, **5**, pp. 1–13.

[8] Stutz, B., and Reboud, J-L., 1997, "Experiments on Unsteady Cavitation," Exp. Fluids **22**, pp. 191–198.

[9] Stutz, B., and Rebound, J-L., 2000, "Measurements Within Unsteady Cavitation," Exp. Fluids, **29**, pp. 545–552.

[10] Song, C. C. S., and Qin, Q., 2001, "Numerical Simulation of Unsteady Cavitating Flow," *Proc. of 4th Int. Symp. on Cavitation*, California Institute of Technology, Pasadena, http://cav2001.library.caltech.edu/

[11] Stutz, B., 2003, "Influence of Roughness on the Two Phase Flow Structure of Sheet Cavitation," ASME J. Fluids Eng., **125**, pp. 652–659.

[12] Schlichting, H., 1979, *Boundary layer theory*, McGraw-Hill Series in Mechanical Engineering, Seventh Edition.

[13] De Lange, D. F., Bruin, G. J., and Van Winjngaarden, L., 1994, "On the Mechanism of Cloud Cavitation-Experiment and Modeling," *Proc. of 2 Int. Symp. on Cavitation*, Tokyo, Japan, H. Kato, ed., pp. 45–49.

[14] Acosta, A., J., 1955, "A Note on Partial Cavitation of Flat Plate Hydrofolis," California Institute of Technology, Report N° E-19.9.

[15] Le, Q., Franc, J. P., and Michel, J. M., 1993, "Partial Cavities: Pressure Pulse Distribution Around Cavity", ASME J. Fluids Eng. **115**, pp. 249–254.

[16] Coutier-Delgosha, O., Devillers, J-F., Pichon, T., Vabre, A., Woo, R. and Legoupil, S., "Internal Structure and Dynamics of Sheet Cavitation," Phys. Fluids (submitted).

[17] Watanabe, S., Tsujimoto, Y., and Furukawa, A., 2001, "Theoretical Analysis of Transitional and Partial Cavity Instabilities," ASME J. Fluids Eng. **123**, pp. 692–697.

[18] Federici, T., and Meireles, R., 2003, "Cavitation sur profil portant," unpublished.

[19] Bouchentouf, L., 2003, "Influence de la rugosité sur le développement des poches de cavitation sur les hydrofoils," Master report, Ecole centrale de Nantes.

Numerical Investigation of Multistage Viscous Micropump Configurations

M. Abdelgawad

I. Hassan[1]
e-mail: Hassan@me.concordia.ca

N. Esmail

P. Phutthavong

Department of Mechanical and Industrial Engineering, Concordia University, Montreal, QC, Canada, H3G 1M8

The viscous micropump consists of a cylinder placed eccentrically inside a microchannel, where the rotor axis is perpendicular to the channel axis. When the cylinder rotates, a net force is transferred to the fluid because of the unequal shear stresses on the upper and lower surfaces of the rotor. Consequently, this causes the surrounding fluid in the channel to displace toward the microchannel outlet. The simplicity of the viscous micropump renders it ideal for micropumping; however, previous studies have shown that its performance is still less than what is required for various applications. The performance of the viscous micropump, in terms of flow rate and pressure capabilities, may be enhanced by implementing more than one rotor into the configuration either horizontally or vertically oriented relative to each other. This is analogous to connecting multiple pumps in parallel or in series. The present study will numerically investigate the performance of various configurations of the viscous micropumps with multiple rotors, namely, the dual-horizontal rotor, triple-horizontal rotor, symmetrical dual-vertical rotor, and eight-shaped dual-vertical rotor. The development of drag-and-lift forces with time, as well as the viscous resisting torque on the cylinders were studied. In addition, the corresponding drag, lift, and moment coefficients were calculated. The flow pattern and pressure distribution on the cylinders' surfaces are also included in the study. Results show that the symmetrical dual-vertical rotor configuration yields the best efficiency and generates the highest flow rate. The steady-state performance of the single-stage micropump was compared to the available experimental and numerical data and found to be in very good agreement. This work provides a foundation for future research on the subject of fluid phenomena in viscous micropumps. [DOI: 10.1115/1.1949639]

Keywords: Multiple Rotor, Viscous Micropump, CFD Simulation, MEMS

1 Introduction

Micropumps are among the most promising microelectromechanical systems (MEMS) and are ready to be implemented into many industrial applications. Micropumps operate on principles far different from those applied to conventional-sized micropumps. Because of the microscopic dimensions of the pump and its large surface-to-volume ratio, viscous forces dominate over centrifugal and viscous forces [1]. Positive displacement micropumps are most common, however, they require check valves at the inlet and outlet, thus complicating their design [1]. Stemme and Stemme [2] suggested replacing the check valves with a nozzle at the inlet and a diffuser at the outlet; however, the idea was not practical since very specific operating conditions were required in order for the pump to operate correctly. Electrohydrodynamic pumps were also proposed, where an electric field passes through the working fluid, which is a dielectric fluid. As a result, the induced charges within the fluid cause the fluid to displace, thus generating flow [3]. On the other hand, electrokinetic pumps use the moving electric field to displace ions of the electric double layer, rather than the charges in a dielectric fluid, in order to generate flow [4]. Lastly, sequential generation of thermal bubbles was also proposed, where one bubble is generated by the means of a microelectric heater to serve as a check valve, and is followed by another bubble, which is generated by another heater and growing in the opposite direction of the first bubble. As a result, fluid is pumped in the desired direction, and the process is repeated once again [5].

The viscous micropump, first introduced by Sen et al. [1], incorporates both applicability at the microscale and simplicity in design. The viscous micropump is simply a cylinder placed eccentrically inside a channel with its axis perpendicular to the channel axis. When the cylinder rotates, a net force is transferred to the fluid due to the unequal shear rates on the upper and lower surfaces of the cylinder, thus forcing the fluid to displace. Its operation depends mainly on viscous forces, and it can operate in any situation where viscous forces are dominant. This situation would exist for either low-viscosity liquids in micropassages, due to the high surface-to-volume ratio characteristic of MEMS, or for highly viscous liquids, such as heavy polymers, in macroducts. Sen et al. [1] performed an experiment to test the pump performance. The study focused on the effect of the channel height, rotor eccentricity, and angular velocity on the pump performance and on the fluid bulk velocity in the duct.

In a later study, the same research team performed a numerical simulation of the viscous micropump solving Navier-Stokes equations for the case of the cylindrical rotor [6]. Critical values for optimum performance were calculated. The highest bulk velocity was achieved when the spacing between the plates is around one and one-half times the cylinder diameter for a fixed eccentricity or at the maximum eccentricity for a fixed plate spacing. The load-flow rate curve for the pump was also plotted, with part of the curve in the negative part of the flow-rate axis. This showed that the flow would change direction if the load were increased beyond the pump's capability. The maximum efficiency of the pump was determined to be ~2.5% for the optimum plate spacing. However, it was observed that the viscous dissipation might cause a mea-

[1]Author to whom correspondence should be addressed.

Contributed by the Fluids Engineering Division for publication in the JOURNAL OF FLUIDS ENGINEERING. Manuscript received by the Fluids of Engineering Division on January 6, 2004; Final manuscript received March 10, 2005, Associate Editor: Kenneth Brauer.

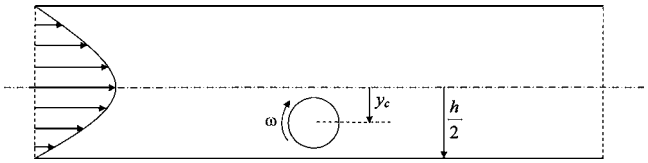

Fig. 1 Schematic of the micropump geometry for the single rotor [9]

surable temperature rise since viscous forces are the driving forces. In order to check the effect of viscous dissipation on pump performance, the same team performed a second numerical simulation [7]. In this study, they solved the continuity equation, the momentum equation with temperature-dependent viscosity, and the energy equation with viscous dissipation terms retained, all coupled together. It was determined that viscous dissipation would not cause a measurable rise in the bulk temperature of the fluid in MEMS applications, yet it may cause a significant rise in the fluid temperature combined with steep temperature gradients near the rotor where the shear stresses are maximum. Decourtye et al. [8] introduced the effects of the sidewalls of the channel in their study. As expected, the pump performance decreased in terms of bulk velocity, yet pumping action existed even for channel widths less than the rotor diameter. It was observed that the sidewall effect reduces the channel height corresponding to maximum bulk velocity and also increases the back pressure at which backflow occurs.

The transient performance of a single-rotor viscous micropump was investigated by Abdelgawad et al. [9]. The effect of the microchannel height, rotor eccentricity, Reynolds number, and pump load on the transient performance of the single-rotor viscous micropump was studied in detail. The rotor eccentricity was determined to be the parameter that affected the transient performance of the micropump most significantly. The steady-state performance was compared to the available experimental data and found to be in very good agreement.

The present study is an extension of the work conducted by Abdelgawad et al. [9] and is aimed at studying the transient and steady-state performance of multistage viscous micropumps where more than one rotor is used in order to enhance the performance. The addition of rotors is expected to improve the performance of the single-rotor viscous micropump because these rotors are essentially being placed in series or parallel inside the microchannel thus increasing the pressure rise or flow rate, respectively. More over, in some cases, the use of more than one rotor is expected to increase the pumping efficiency because of the interaction between the flow fields around all rotors which helps reduce the shear stress and, hence, the resisting torque on the rotors. Four configurations of rotors were studied in detail: the dual-horizontal rotor, triple-horizontal rotor, symmetrical dual-vertical rotor, and finally the eight-shaped dual-vertical rotor. Parameters such as average velocity, drag and moment coefficients, and efficiency will be calculated. Results obtained in [9] will be used for comparison purposes in order to determine the effect multiple rotors have on the performance of the viscous micropump. The single-rotor case used for comparison purposes was that of best pumping effect, namely, $S=1.5$, $\epsilon=0.95$, and $\mathrm{Re}=1$.

2 Problem Geometry

2.1 Problem Configuration. The present study is a numerical investigation of multiple rotors inside a microchannel. The problem configuration for a single rotor is shown in Fig. 1, and the geometric parameters used are identical to those defined by Abdelgawad et al. [9]. The main geometrical parameters in the study will be the channel height (S), defined as

$$S=\frac{h}{d} \tag{1}$$

and the rotor eccentricity ϵ, which indicates the rotor position inside the channel, defined as

$$\epsilon=\frac{y_c}{\frac{h}{2}-\frac{d}{2}} \tag{2}$$

Based on this definition, $\epsilon=0$ corresponds to the rotor being centered on the channel axis and $\epsilon=1$ corresponds to the rotor touching the lower wall. The rotor is forced to rotate with an angular velocity ω. In this problem, the Reynolds number will be based on the rotor velocity at its surface $U=\omega d/2$ since the average velocity in the channel $\bar{u}=(1/h)\int_0^h u\,dy$ is an output of the solution. Therefore, the Reynolds number will be defined as

$$\mathrm{Re}=\frac{Ud}{v}=\frac{\omega d^2}{2v} \tag{3}$$

The pressure is specified on the inlet and outlet of the channel, where a higher pressure is specified at the outlet. The nondimensional pressure rise is defined as

$$\Delta P^*=\frac{P_{\mathrm{out}}-P_{\mathrm{in}}}{\frac{\rho v^2}{d^2}}, \tag{4}$$

where P_{out} is the pressure on the channel outlet and P_{in} is the pressure on the channel inlet, ρ is the fluid density, and v is the fluid kinematic viscosity. The scale used to nondimensionalize the time in the simulation was chosen to be the time taken by the rotor to finish one complete revolution

$$t^*=\frac{t}{\frac{2\pi}{\omega}}=\frac{t\omega}{2\pi} \tag{5}$$

According to this definition, the nondimensional time is simply the number of revolutions of the rotor. This provides an easier tracking of the changes in the flow field over time regardless of the rotor angular velocity. The drag and moment coefficients are defined as

$$C_D=\frac{F_D}{\frac{1}{2}\rho U^2 d} \tag{6}$$

and

$$C_M=\frac{M}{\frac{1}{2}\rho U^2 d^2} \tag{7}$$

where U is the cylinder surface velocity defined before.

2.2 Mathematical Modeling and Boundary Conditions. The two-dimensional 2D Navier-Stokes equations will be solved for the specified geometry where all the dimensions will be normalized by the rotor diameter d.

The continuity equation is

$$\nabla\cdot\vec{V}=0 \tag{8}$$

and the momentum equation is

$$\rho\left[\frac{\partial\vec{V}}{\partial t}+\left(\vec{V}\cdot\vec{\nabla}\right)\vec{V}\right]=\rho\vec{\alpha}-\vec{\nabla}P+\mu\nabla^2\vec{V} \tag{9}$$

where α represents the body forces per unit mass. Based on the above-mentioned method for nondimensionalizing and assuming that the flow is incompressible with neglected body forces, the momentum equation becomes

$$\frac{\rho\omega^2 d}{4}\left[\frac{1}{\pi}\frac{\partial\vec{V}^*}{\partial t^*}+\left(\vec{V}^*\cdot\vec{\nabla}\right)\vec{V}^*\right]=\frac{\mu\omega}{2d}\vec{V}^*-\frac{\mu^2}{\rho d^3}\vec{\nabla}P^* \tag{10}$$

which, in nondimensional terms, become

$$\frac{1}{\pi}\frac{\partial\vec{V}^*}{\partial t^*}+\left(\vec{V}^*\cdot\nabla\right)\vec{V}^*=\frac{1}{\mathrm{Re}}\nabla^2\vec{V}^*-\frac{1}{\mathrm{Re}^2}\nabla P^* \tag{11}$$

The main independent parameters in the solution will be the channel height S, the rotor eccentricity ϵ, Reynolds number Re, and the pressure load ΔP^*. When additional rotors are added, new geometrical independent parameters will arise and their effect will be studied. These new parameters will be mentioned and defined in the corresponding sections. The flow will be assumed laminar, incompressible, and unsteady, and the fluid itself is considered Newtonian with constant properties. No-slip, no-penetration boundary conditions are assumed on the microchannel walls, and the fluid velocity is zero on the upper and lower walls and equal to the rotor surface velocity on the rotor boundary. The pressure is specified on the inlet and outlet of the microchannel. Pressure will be always assumed to be zero gage pressure at the inlet, and its value at the exit will be varied to simulate different loads. The location of the inlet and outlet were chosen to be eight diameters upstream and downstream of the microchannel vertical centerline, respectively. This distance was found to be large enough to achieve uniform flow at the inlet and outlet without being affected by the rotors existence. The fluid will be assumed to be initially at rest ($\vec{V}=0$) and the motion will start by rotating the cylinder clockwise with an angular velocity ω.

3 Numerical Modeling

The CFD package FLUENT 6.0 is used to numerically solve the Navier-Stokes equations. This CFD package uses the finite volume method and supports unstructured grids. It enables the use of different discretization schemes and solution algorithms, together with various types of boundary conditions. As part of the same package, a preprocessor, GAMBIT, is used to generate the required grid for the solver. An unstructured grid with triangular elements is used. The cylinder surface was divided into 100 equally spaced elements. The upper and lower walls were divided into 200 nonuniformly spaced elements using the bell-shaped meshing scheme with a ratio $R=0.4$. The grid was finer in regions near the center and adjacent to the cylinder and coarser in regions far upstream and downstream. The bell-shaped scheme meshes the edge so that the node distribution follows a normal distribution curve centered at the geometric center of the edge. The ratio R specifies whether the nodes will be denser at the center of the edge or at its ends and also specifies the intensity of this distribution. In addition to this meshing method, which refines the grid in the cylinder region, grid adaptation by the solver itself was performed in the gap between the cylinder and the lower wall for cases of high eccentricities, where this gap size is very small. The PISO-SIMPLE algorithm, where PISO stands for pressure-implicit with splitting of operators, was used for the pressure-velocity coupling. It is nearly the same as the SIMPLE algorithm, presented in [10], except that it takes into account two additional corrections. The first one is the neighbor correction. This correction incorporates more iterations into the pressure correction equation in order to satisfy the continuity and momentum equations more precisely. Thus, the PISO algorithm requires more time per iteration, but at the same time reduces the total number of iterations. Therefore, the total time is much less, rendering it more suitable for transient applications. The second correction is the skewness correction, which simply enables the solver to deal with highly skewed meshes and reduce the total number of iterations required for the convergence of such meshes.

Two different discretization schemes were used for the time and momentum equations. A power-law scheme was used for the two momentum equations, whereas a second-order discretization scheme was used for the time derivatives. Under relaxation was used during the solution with the underrelaxation factors varying between 0.3 and 1 to ensure convergence. Multigrid methods were also used in order to reduce convergence time. The use of multigrids helps reduce the low-frequency error components when the equations are iterated on a coarser mesh. By default, a V-cycle multigrid is chosen for the pressure correction equation, whereas a flexible cycle was chosen for momentum equations. In the V-cycle, one iteration is first performed on the finest grid to reduce the high-frequency components of the error and then the solution is restricted to the coarser grid. After a certain number of iterations on the coarser grid, the solution is interpolated to the finer grid where it is reiterated. For the flexible cycle, the use of coarse grid corrections is called only in the cases where the convergence rate on the current grid is slow.

Different meshes were used to determine the optimum grid size and to ensure grid-independent solutions. Grid-independent solution was assured by observing three parameters. The first parameter is the distribution of the x-velocity component on a vertical plane just one diameter from the cylinder axis, which will indicate whether the grid is fine enough in the neighborhood of the cylinder where the largest shear stresses exist. The second parameter is the change of the drag coefficient of the cylinder with time, which tests the coupling between the grid size and the time step chosen. The convergence of the drag coefficient over the grid size was achieved on the third mesh used. The trend of the drag coefficient variation with time on all the meshes used was the same, where differences only occurred between the coefficient values themselves. This was also the case for the x-velocity distribution. The third parameter is the average velocity of the flow at the outlet of the microchannel, which will give a good indication of the effect of the grid size in the entire microchannel domain. As a convergence criterion in the present work, the solver iterated the equations until the scaled residuals are less than 10^{-5} or until it stabilized at a constant value, which is still small enough to ensure convergence. This value varied approximately from 10^{-5} to 3×10^{-4}, based on the parameters for each specific case. The time step used for simulating the transient behavior of the flow needed to be small enough to pick the physical changes over time inside the flow field, as well as to ensure stability. Different time steps were tested at the beginning in order to determine the optimum time step to be used. Obviously, the optimum time step size varies from one case to another, since the Reynolds number (i.e., the cylinder angular velocity) is different in the various cases. The optimum time step should be the one that, when coupled with the cylinder angular velocity, corresponds to small changes in the cylinder angular displacement so that any changes in the flow field that result from this angular displacement may be monitored. The change of the average velocity inside the microchannel with time was used as a criterion to determine the optimum step size. The results for $\Delta t=0.0001$, 0.001, and 0.01 s (corresponding to $\Delta t^*=32\times10^{-6}$, 32×10^{-5}, 32×10^{-4}, respectively) were nearly the same, whereas for $\Delta t=0.1$ s (corresponding to $\Delta t^*=32\times10^{-3}$), instability and large fluctuations in the average velocity occur. The time step chosen for nearly all cases studied was 0.001 s ($\Delta t^*=32\times10^{-5}$), which was small enough to recognize all the changes in the flow field over time, and, in addition, was large enough to achieve reasonable computation time.

4 Results and Discussion

In this section, the steady-state and transient performance of the dual-horizontal, triple-horizontal, symmetrical dual-vertical, and the eight-shaped rotors were compared to those of the single-rotor viscous micropump. Steady-state cases for the single-rotor viscous micropump were first simulated by Abdelgawad et al. [9], and the results were compared to existing experimental results obtained by Sen et al. [1] and numerical results obtained from Sharatchandra et al. [6]. The effect of the microchannel height on the flow rate was studied both experimentally and numerically in [1] and [6]. For comparison purposes, 11 cases were simulated with chan-

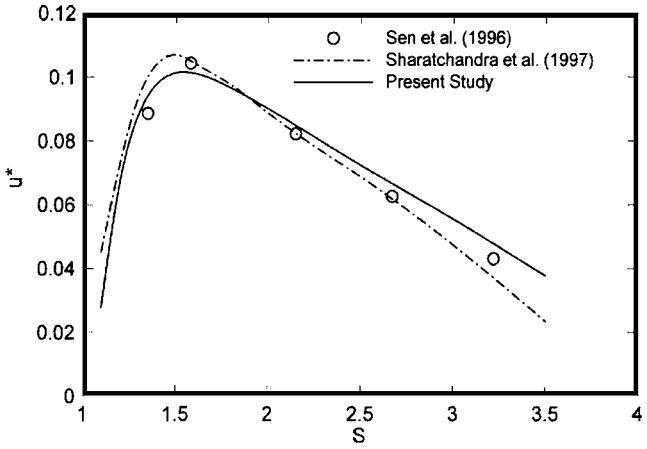

Fig. 2 Comparison of average velocity versus channel height for the single rotor (Re=0.5, ΔP^*=0.5 and ϵ=0.9) [9]

nel heights ranging from S=1.1 to 3.5 with an eccentricity ϵ =0.9. In all cases studied, the Reynolds number was kept constant at Re=0.5 and the pressure load was held constant at ΔP^*=0.5. Figure 2 shows that the results are in very good agreement with both the computational and experimental results of the previous group [1,6]. The rotor eccentricity in the microchannel is the main parameter that initiates the driving force in the microchannel. Sharatchandra et al. [6] studied the effect of the rotor eccentricity on the fluid average velocity in the channel and observed that the average velocity increases nearly linearly with the eccentricity. Figure 3 generated by Abdelgawad et al. [9] compares the results calculated by Sharatchandra et al. [6] to those calculated in the present study. Both show the linear variation of the average velocity with the rotor eccentricity.

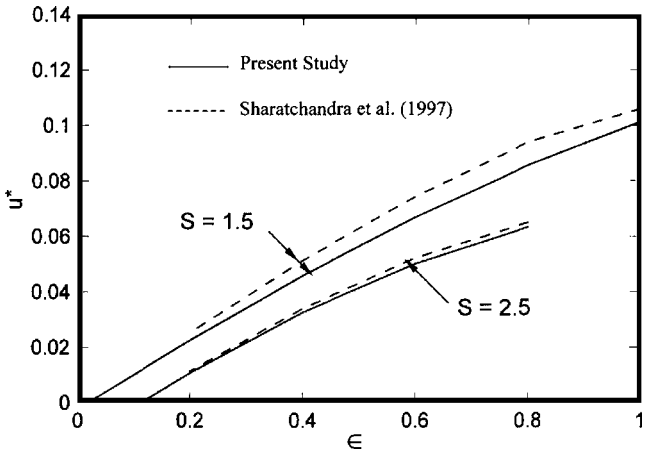

Fig. 3 Comparison of average velocity versus eccentricity at ΔP^*=1 and Re=1 for the single rotor [9]

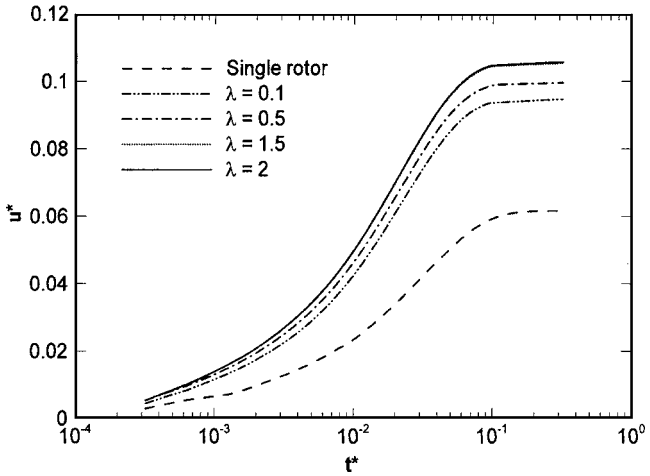

Fig. 5 Comparison of the variation of velocity with time for the dual-horizontal rotor for different rotor spacing with that for the single rotor (S=1.5, ϵ=0.95, ΔP^*=10, and Re=1)

4.1 Dual- and Triple-Horizontal Rotors. The mesh used to study the dual-horizontal rotor is shown in Fig. 4. The effect of the horizontal distance between the two cylinders L was studied, where it was varied between $0.1d$ and $2d$. The parameter λ was used and is defined as

$$\lambda = \frac{L}{d} \tag{12}$$

Figure 5 presents the variation of velocity with time for different rotor spacing. As expected, the flow rate for the dual rotor yields higher flow rates than that for the single rotor at the same back pressure. At all values of λ the average velocity inside the channel increases gradually until it reaches its steady-state value. The flow field inside the micropump reaches steady state within one rotor revolution in the single-rotor case and at all values of λ in the dual-rotor case. It can be observed that the flow rate increases with increasing λ until the value of λ=1.5 after which, the flow rate remains constant. At smaller values of λ, the two flow fields around both rotors interact together, thus the pumping action resulting from each rotor is not maximum. Although at λ≥1.5 these flow fields become independent of each other and each rotor produces its maximum pumping effect. As shown in Fig. 5, the flow rate for λ=2.0 is 1.72 times that generated in the single-rotor micropump *at the specified conditions* (ΔP^*=10). The effect of increasing λ on the flow field is shown in Fig. 6. For small values of λ, two big vortices and a small one exist in the flow field. The two big vortices are located upstream of the upstream cylinder and downstream of the downstream cylinder. The small vortex exists between the two cylinders on the upper wall. This vortex increases in size with increasing λ until it becomes two big vortices encircled together inside a bigger vortex at λ=2.

When the development of the flow field with time is examined

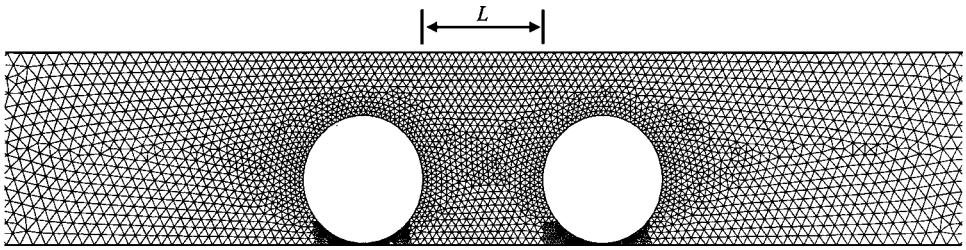

Fig. 4 Mesh used for the dual-horizontal-rotor viscous micropump

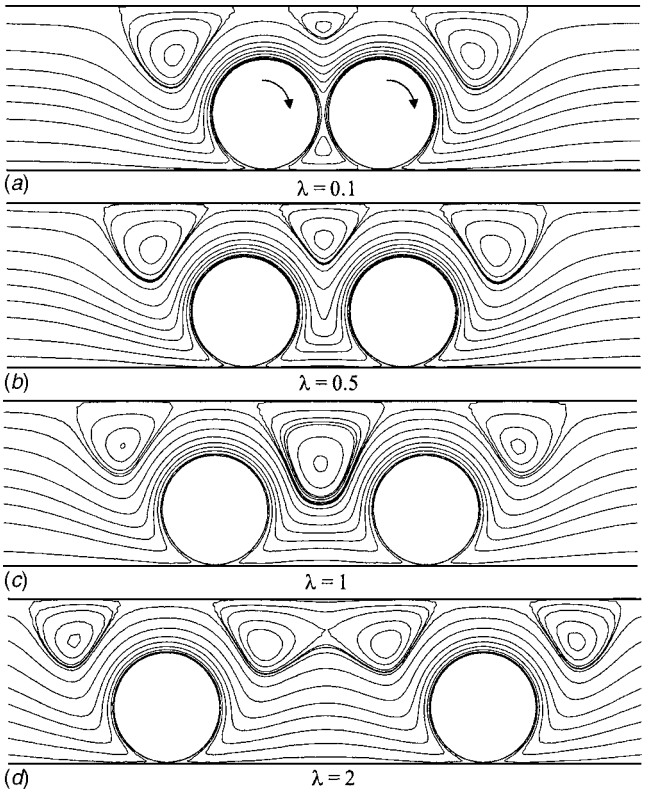

Fig. 6 Streamlines for different rotor spacing of the dual-horizontal rotor (S=1.5, ϵ=0.95, ΔP^*=10, and Re=1)

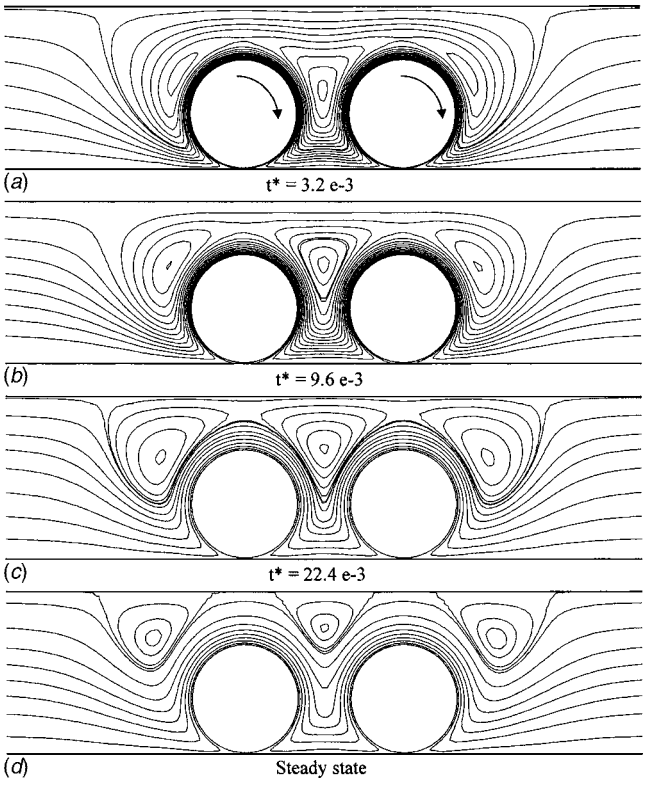

Fig. 7 Streamlines at different times at λ=0.5 for the dual-horizontal rotor (S=1.5, ϵ=0.95, ΔP^*=10, and Re=1)

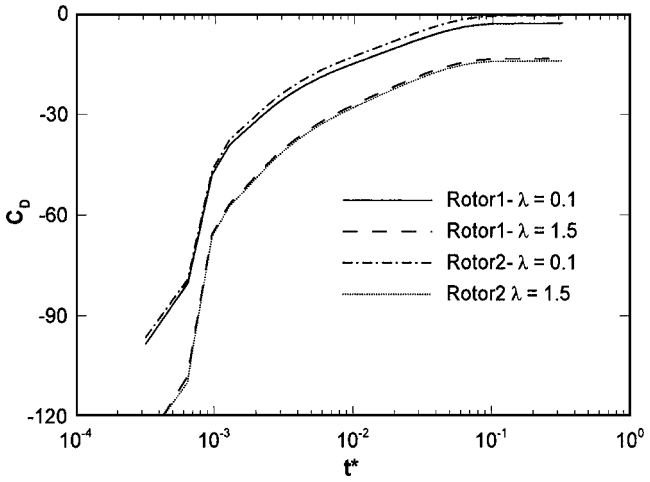

Fig. 8 Variation of the drag coefficient with time on rotors 1 and 2 for different rotor spacing of the dual-horizontal rotor (S=1.5, ϵ=0.95, ΔP^*=10, and Re=1)

(Fig. 7), it can be seen that all the vortices start very close to the cylinder's surface, as in the case of the single-rotor micropump. With time, all the vortices move away from the cylinders until they rest on the channel upper wall.

Figure 8 presents the variation of the drag coefficient with time in the dual-horizontal configuration for each of the rotors. The upstream rotor is designated as rotor 1 and the downstream rotor as rotor 2. The drag coefficient on both rotors is negative (i.e, to the left) as expected starting with a large value and decreases with time until it reaches its steady-state value. This behavior is a result of the high-rotor eccentricity, which means a very small gap between the rotors and the lower channel wall. This small gap makes the lower wall obstruct the vertical component of the fluid velocity forming a semi-stagnation zone, which increases the pressure on the downstream lower surface of both rotors resulting in a high drag coefficient. With time, and because of this high pressure, the fluid velocity is developed and is directed away from the wall, causing the pressure to be reduced and, consequently, the drag coefficient decreases.

The contribution of viscous forces to the drag coefficient is considerably less than that of the pressure forces. Figure 9 compares the value of the viscous drag to that of the pressure drag for the case of the single-rotor viscous micropump, which was studied in detail by the authors in [9]. Moreover, it should be noted that viscous forces on the upper and lower surfaces of the rotor are opposite in direction, so that they nearly cancel out in cases of low eccentricities. In cases of high eccentricities, such as the one in Fig. 8, the viscous stresses on the lower surface are higher than

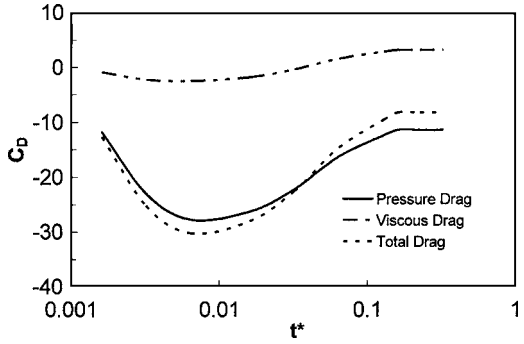

Fig. 9 Viscous, pressure, and total drag coefficients for ϵ =0.4 in the single-rotor viscous micropump. (S=1.5, ΔP^*=0, and Re=1)

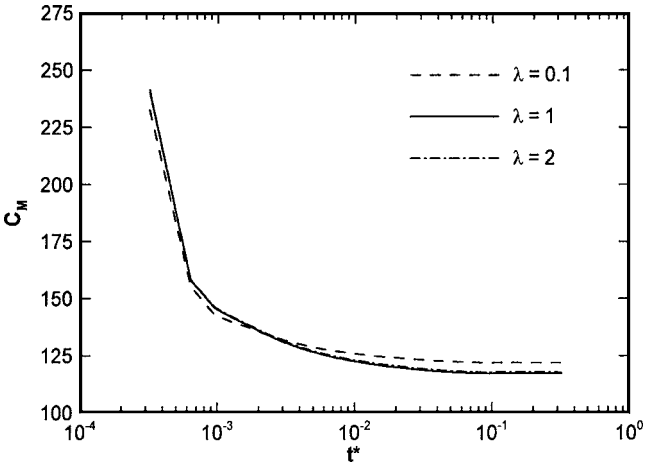

Fig. 10 Total moment coefficient at different rotor spacing of the dual-horizontal rotor (S=1.5, ϵ=0.95, ΔP^*=10, and Re=1)

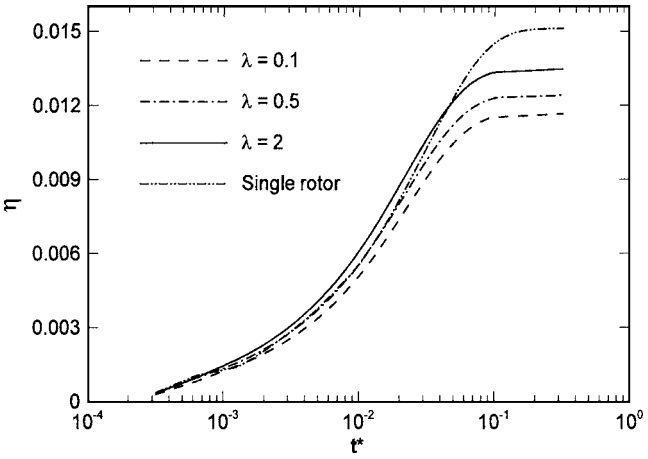

Fig. 11 Comparison of the efficiency at different rotor spacing of the dual-horizontal rotor

that on the upper surface, thus the net viscous drag will be positive (i.e., to the right). Yet it will still be lower than the pressure drag, and the total drag coefficient will remain negative.

As expected, the drag coefficient curves are nearly identical at high values of λ since the flow fields are uncoupled. For smaller values of λ, slight discrepancies occur as the flow reaches steady state, where rotor 1 is subjected to higher drag than rotor 2. The drag coefficient increases on both rotors as λ is increased. This is because of the separation of the pressure fields around each rotor from each other when the rotors are farther apart. When the rotors are very close to each other, the high-pressure zone downstream of the first rotor is very close to the low-pressure zone upstream of the second rotor and so the pressure in the space between the rotors attains a moderate value. This makes the pressure drag force on each rotor less than the case when the two rotors are far from each other, with each one having a high-pressure zone on its downstream side and a low-pressure zone on its upstream side.

The moment coefficient for rotors 1 and 2 were added to yield the total moment coefficient. Its variation with time for different values of λ is shown in Fig. 10. This total moment coefficient, together with the Reynolds number, specifies the energy input to the micropump. At the beginning the moment coefficient is very high because of the very high-velocity gradients, and shear stresses, consequently, on rotors surfaces. With time, the velocity of the fluid layers adjacent to the rotors increases and the velocity gradient and shear stresses on the rotors' surfaces are reduced, causing the moment coefficient to decrease. When the effect of λ is studied, it is found that the total moment coefficient is higher at smaller values of λ because of the increase in the shear stress on the parts of cylinder surfaces facing each other. The cylinder surface velocities are moving in opposite directions in the region between the two rotors, thus increasing the velocity gradient and, hence, the shear stress on the surfaces flanking this middle region. Hence, the resisting torque and the overall moment coefficient will increase when λ is small.

The efficiency of the viscous micropump is defined as

$$\eta = \frac{\text{flow energy rise}}{\text{input mechanical energy}}$$

which, when mathematically formulated, gives the following relation:

$$\eta = \frac{\dfrac{m\Delta P}{\rho}}{M\omega} = \frac{\Delta P^* u^* S}{C_M \mathrm{Re}^2} \tag{13}$$

Based on the aforementioned information, the efficiency will be higher for higher values of λ since there will be less resisting torque, as shown in Fig. 11. However, the single rotor still has a higher efficiency since for the dual-horizontal rotor, the resisting torque is higher than that of the single rotor.

The triple-horizontal-rotor viscous micropump is the same as the dual-rotor micropump except that three rotors are used (Fig. 12). The parameter λ is defined as before in Eq. (12), and its value is the same in between adjacent rotors. The behavior for the triple-horizontal rotor is similar to that of the dual-horizontal rotor. At steady state, vortices exist adjacent to the upper wall in regions between rotors (Fig. 12), as well as in the most upstream and most downstream portions of the microchannel. As λ is increased, the flow fields once again become uncoupled, and therefore the flow rate increases and the resisting torque decreases, thus increasing the efficiency. Figure 13 shows the average velocity against the back pressure for the single-, dual-, and triple-rotor viscous micropumps. The maximum allowable pressure load for the triple-horizontal configuration is three times that for the single rotor, as expected for a series arrangement of three rotors.

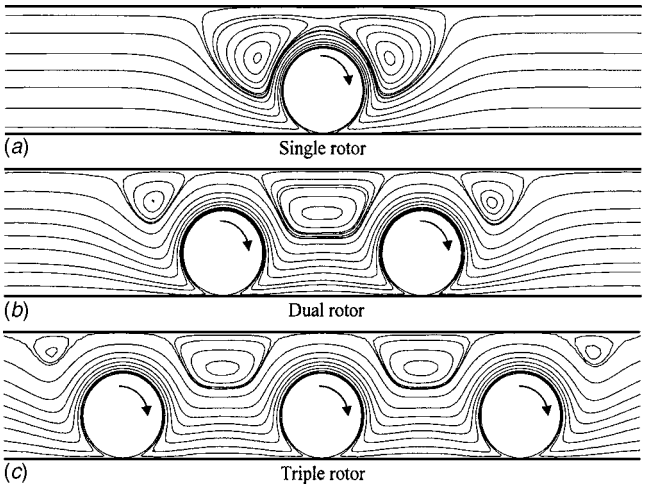

Fig. 12 Flow field around rotors in the single-rotor, dual-horizontal-rotor, and triple-horizontal-rotor viscous micropump

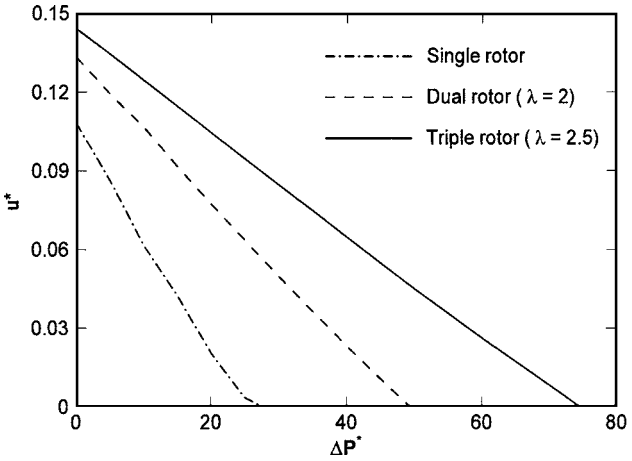

Fig. 13 Average velocity versus pressure load for the single, dual-horizontal and triple-horizontal rotors (S=1.5, ϵ=0.95, and Re=1)

4.2 Symmetrical and Eight-Shaped Dual-Vertical Rotor. The symmetrical dual rotor is a configuration in which the rotors work in parallel, as two rotors are placed above each other with each rotor close to one of the channel walls. In the symmetrical dual-rotor viscous micropump, no new geometrical parameters were introduced. The eccentricity ϵ is still the only parameter that identifies the position of each cylinder inside the channel. Yet, it has to be mentioned that in the symmetrical dual rotor configuration, the eccentricity of each cylinder is calculated separate from the other one and, based on the value of (S), equals half the actual channel height. This configuration is expected to be very efficient since one of its characteristics is the reduction of the shear stress, and hence the resisting torque, on both rotors.

Figure 14 shows the variation of the flow pattern with time for the symmetrical dual-vertical rotor. The flow pattern is symmetrical about the centerline of the channel, where the flow pattern of a single rotor is mirrored about the line of symmetry. The main advantage of the dual-symmetrical-rotor configuration of the viscous micropump is that it permits a higher velocities at the centerline of the channel compared to a zero velocity restriction on the upper wall if the upper half of the micropump did not exist. This directly increases the flow rate pumped for the same shear level (i.e, the same rotor speed). Moreover, permitting the velocity to be maximum at the centerline reduces the velocity gradient and viscous shear stress on the rotor's inward surfaces, which reduces the required torque and increases the pumping efficiency. Another consequence of the fluid velocity being highest at the centerline is the reduction in the size of the upstream and downstream vortices above each rotor, as shown in Fig. 14(c).

Figure 15 compares the variation of the average velocity at the outlet with time for the single rotor and the symmetrical dual-vertical rotor at two different eccentricities for $\Delta P^*=10$. The symmetrical dual-vertical rotor is capable of overcoming the back pressure, and therefore the velocity remains positive until steady state is attained. It must be noted that for the same average velocity, the symmetrical dual-vertical rotor will deliver a higher flow rate than the single-rotor viscous micropump because the channel height is doubled for the first one. For the symmetrical dual-vertical-rotor micropump, higher eccentricities still yield higher average velocities, as is the case for the single-rotor micropump [9].

In the eight-shaped dual-vertical-rotor micropump, two cylinders rotating clockwise were placed together, one on top of the other, to form the shape of number eight. This eight-shaped rotor was placed near the lower wall. This configuration was not expected to improve the performance of the viscous micropump, yet it was investigated to expand the knowledge of the viscous micropump, as well as for comparison purposes. Figure 16 shows the streamlines for this configuration at channel heights S=2.5 and S=3. It is clear that at S=3, the pump is unable to sustain a net flow against a pressure of $\Delta P^*=10$, which is not relatively high, thus a back flow occurs and the flow passes from right to left in the passage between the upper wall and the big vortex around the two cylinders. In such a geometrical configuration, it is expected to have a higher resisting torque on the lower rotor because of its position between the lower wall and the upper rotor. This position helps increase the velocity gradient and consequently, the shear stress on its lower and upper surfaces.

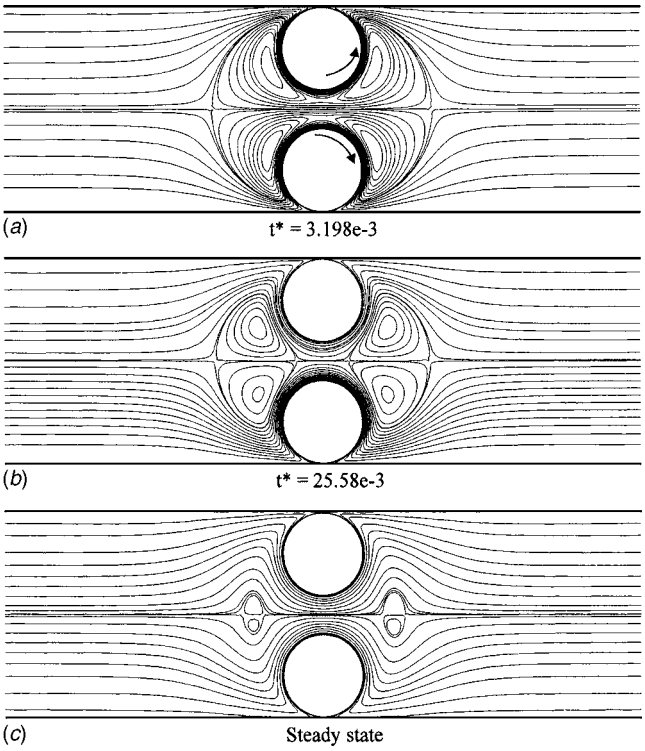

Fig. 14 Variation of the streamlines for the symmetrical dual-vertical-rotor viscous micropump with time (S=2.5, ϵ=0.95, ΔP^*=10, and Re=1)

Figure 17 compares the shear stress distribution on the upper and lower rotors of the eight-shaped rotor to the shear stress on

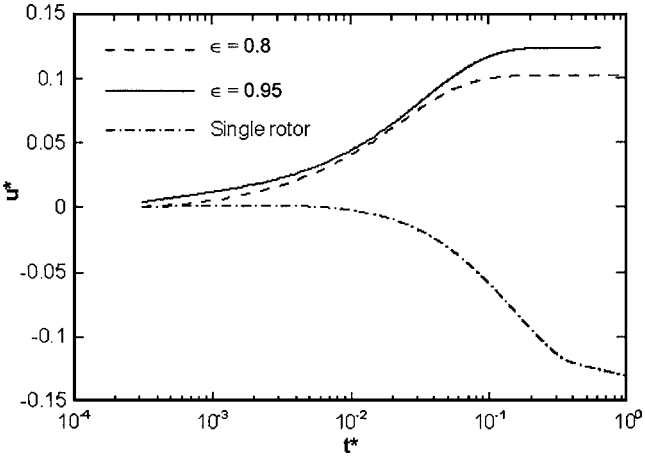

Fig. 15 Comparison of the variation of the average velocity with time for the symmetrical dual-vertical rotor with that for the single rotor (S=2.5, ϵ=0.95, and Re=1)

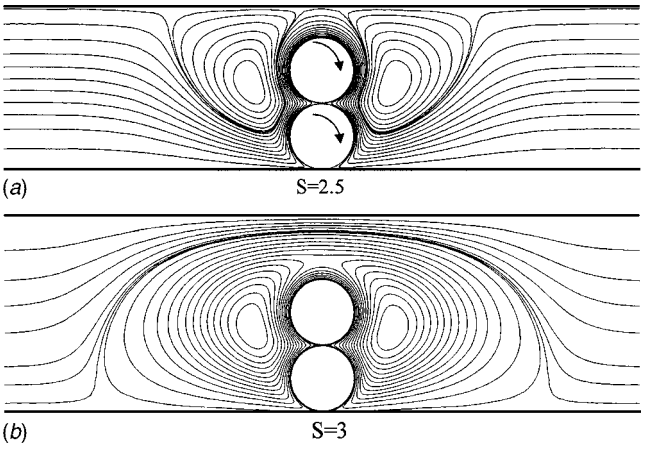

Fig. 16 Streamlines in the eight-shaped dual-vertical-rotor micropump for different S (ϵ=0.95, ΔP^*=10, and Re=1)

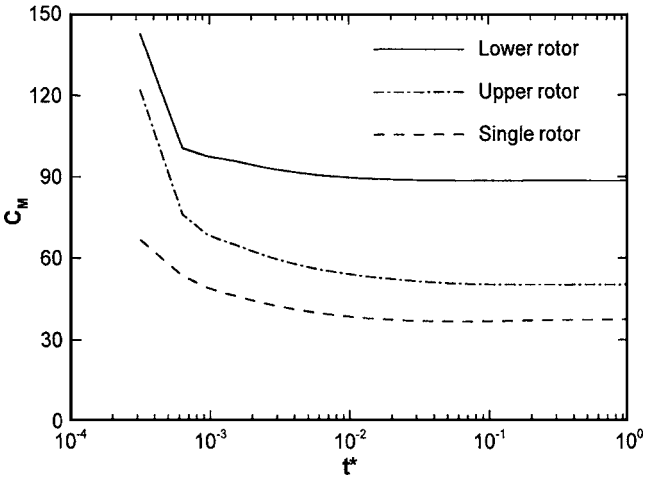

Fig. 18 Moment coefficient on lower and upper rotors compared to the single rotor (S=2.5, ϵ=0.95, ΔP^*=10, Re=1)

the single rotor. It is very clear from the figure that the shear stress is higher on the lower rotor than on the upper rotor and both are higher than the shear stress on the single rotor. It should be noted that the eccentricity is based on half the channel height and, therefore, the eccentricity based on the entire channel height is greater than 0.95. This accounts, partially, for the higher values of shear stress for the eight-shaped rotor. The increase in the shear stress on the lower rotor will certainly increase its moment coefficient more than it is on the upper rotor. This is confirmed by Fig. 18, which compares the moment coefficient on both rotors to that of the single rotor.

In order to determine which configuration for the multistage viscous micropump yields the best performance, the variation of the volumetric flow rate with the pressure load (Fig. 19), as well as the variation of the efficiency with time (Fig. 20) for all configurations were plotted. In Fig. 19, it was observed that the performance of the eight-shaped rotor is almost identical to that of a single rotor. The triple-horizontal rotor can withstand the highest-pressure load; however, the volumetric flow rate is not very high with values similar to that generated by the single rotor. The best compromise is the symmetrical dual-vertical rotor because it yields the highest flow rate and is also able to accommodate higher-pressure loads. Figure 20 gives final confirmation that the symmetrical dual-viscous rotor is superior to all others. The efficiency is much higher than any of the other configurations, with the eight-shaped dual-vertical rotor yielding the worst performance of them all. The second-best configuration is the dual-horizontal rotor, which is capable of withstanding higher pressure loads than that for the symmetrical dual-vertical rotor.

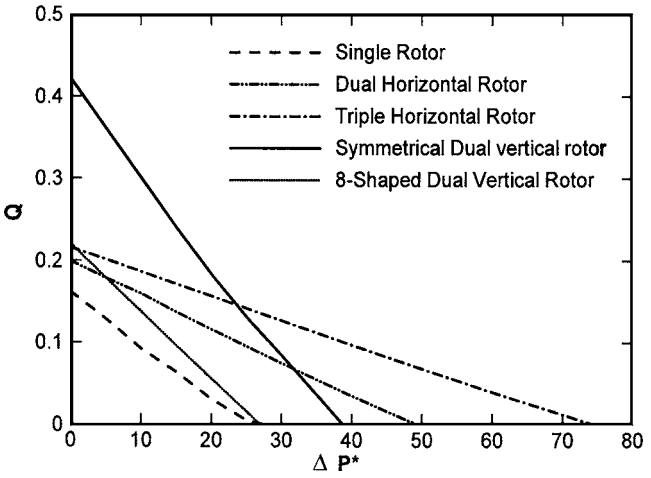

Fig. 19 Comparison of the Q-P curves of all the multistage viscous micropumps to the single-rotor viscous micropump

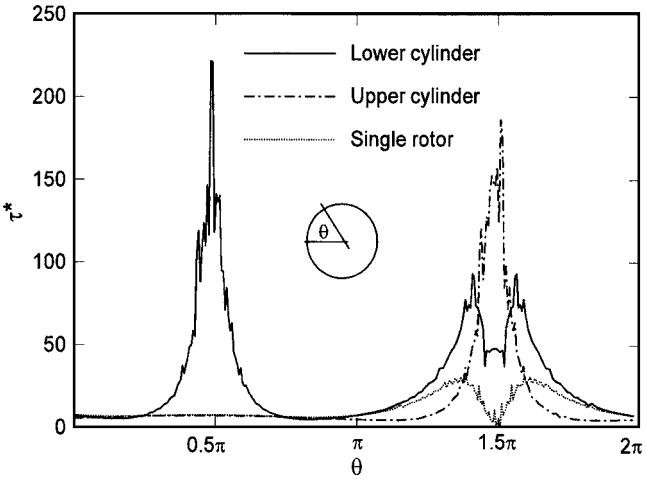

Fig. 17 Comparison of the shear stress distribution on lower and upper rotors of the eight-shaped rotor with that on the single rotor (S=2.5, ϵ=0.95, ΔP^*=10, and Re=1)

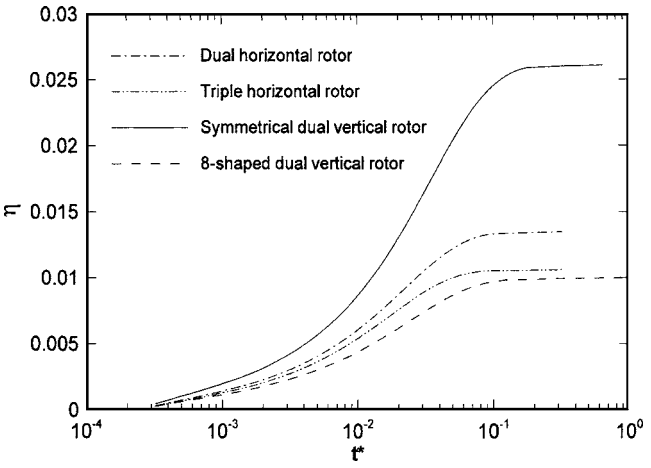

Fig. 20 Comparison of the efficiency for all the multistage viscous micropumps tested

5 Conclusions and Future Directions

Multirotor micropumps have been proven to provide flow rates and back pressures that are higher than single-rotor micropumps. They simulate the use of more than one pump, either in series or in parallel, depending on how they are placed relative to each other inside the micropump. A new geometrical parameter λ arises in the case of dual- and triple-horizontal-rotor micropumps, to account for the horizontal distance between rotors. Both the efficiency and the flow rate increase when λ increases because of the reduction in the interaction between the rotors. However, after a certain distance, the flow fields become uncoupled, there is little interaction between them, and λ has no effect on the pump performance. The dual- and triple-horizontal rotors were able to withstand higher-pressure loads than the single rotor, since the rotors are essentially placed in series.

The symmetrical dual-vertical rotor arranges two rotors in parallel. Two single-rotor flow patterns are mirrored about the centerline of the channel; thus, there is little interaction of the flow fields. The flow rate is highest of all configurations studied and able to overcome high back pressure when the single rotor could not. The efficiency is highest in this configuration because of the reduction in the shear stress and the viscous torque on both rotors.

The eight-shaped dual-vertical rotor was studied merely to further the knowledge of viscous micropumps and was not expected to improve the performance of the viscous micropump in any way. This configuration yields higher shear stress on the rotor surfaces, when compared to that on the single rotor. Consequently, there is higher viscous resistance, which hinders the performance of the micropump.

In terms of performance, the symmetrical dual-vertical-rotor micropump achieved the best efficiency and highest flow rate, while the triple-horizontal rotor achieved the highest back pressure with efficiency less than that of the single rotor. The eight-shaped dual-vertical rotor viscous micropump has the lowest efficiency with a ΔP^*–Q curve very close to that of the single-rotor micropump. In conclusion, the performance and efficiency of the viscous micropump have been increased through changing the pump geometry. This confirms the fact that there is still more to learn about it and opens the door for more research efforts to further enhance this performance and efficiency. The simplicity of the viscous micropump design and its size flexibility provides great potential for this device in commercial applications and is thus worthy of further study in the future.

Nomenclature

C_D = cylinder drag coefficient
C_M = cylinder moment coefficient
d = diagonal length of rotor, m
F_D = drag force on cylinder, N/m
h = channel height, m
L = distance between adjacent rotors, m
M = moment on cylinder, N m/m
$\dot{m}$ = mass flow rate, kg/s
P_{in} = inlet pressure, Pa
P_{out} = outlet pressure, Pa
P^* = nondimensional pressure
ΔP = channel pressure rise, Pa
ΔP^* = nondimensional pressure rise
Q = nondimensional volume flow rate
Re = Reynolds number
R = computations residuals
S = nondimensional channel height
t = time, s
t^* = nondimensional time
Δt = time-step size, s
$\bar{u}$ = average velocity inside microchannel, m/s
u^* = nondimensional average velocity
U = cylinder surface velocity, m/s
$\vec{V}$ = fluid velocity vector, m/s
y_c = distance from channel axis to cylinder center, m

Greek Letters

α = body forces per unit mass, m/s^2
ϵ = rotor eccentricity
λ = nondimensional distance between adjacent rotors
μ = fluid dynamic viscosity, Pa s
υ = fluid kinematic viscosity, m^2/s
θ = angle sweep over surface, rad
ρ = fluid density, kg/m^3
τ = fluid shear stress, Pa
τ^* = nondimensional fluid shear stress
ω = rotor angular velocity

References

[1] Sen, M., Wajerski, D., and Gad-el-Hak, M., 1996, "A Novel Pump for MEMS Applications," ASME J. Fluids Eng. **118**, pp. 624–627.
[2] Stemme, E., and Stemme, G., 1993, "Valveless Diffuser/Nozzle-Based Fluid Pump," Sens. Actuators, A **39**(2), pp. 159–167.
[3] Bart, S. F., Tavrow, L. S., Mehregany, M., and Lang, J. H., 1990, "Microfabricated Electrohydrodynamic Pumps," Sens. Actuators, A **21**(1–3), pp. 193–197.
[4] Harrison, D. J., Manz, A., and Glavina, P. G., 1991, "Electroosmotic Pumping Within a Chemical Sensor System Integrated on Silicon," *Proc. of Int. Conf. on Solid-State Sensors and Actuators Transducers*, pp. 792–795.
[5] Kim, C. J., 2000, "Microfluidics Using the Surface Tension Force in Microscale," *Microfluidic Devices and Systems III, Proc. SPIE*, **4177**, pp. 49–55.
[6] Sharatchandra, M. C., Sen, M., and Gad-el-Hak, M., 1997, "Navier-Stokes Simulation of a Novel Viscous Pump," ASME J. Fluids Eng., **119**, pp. 372–382.
[7] Sharatchandra, M. C., Sen, M., and Gad-el-Hak, M., 1998, "Thermal Aspects of a Novel Viscous Pump," ASME J. Heat Transfer **120**, pp. 99–107.
[8] Decourtye, D., Sen, M., and Gad-el-Hak, M., 1998, "Analysis of Viscous Micropumps and Microturbines," Int. J. Comput. Fluid Dyn. **10**, pp. 13–25.
[9] Abdelgawad, M., Hassan, I., and Esmail, N., 2004, "Transient Behavior of the Viscous Micropump," Microscale Thermophys. Eng. **8**(4), pp. 361–381.
[10] Patankar, Suhas V., 1980, *Numerical Heat Transfer and Fluid Flow*, Taylor and Francis, New York.

Unsteady Hydrodynamic Forces due to Rotor-Stator Interaction on a Diffuser Pump With Identical Number of Vanes on the Impeller and Diffuser

M. Zhang
Graduate Student
Department of Mechanical Engineering, Kyushu Institute of Technology, 1-1 Sensui-cho, Tobata, Kitakyushu, 804-8550 Japan

H. Tsukamoto
Professor
Department of Biological Functions and Engineering, Graduate School of Life Science and Systems Engineering, Kyushu Institute of Technology, 2-4, Hibikino, Wakamatsu, Kitakyushu, 808-0196 Japan

Experimental and computational study was developed for unsteady hydrodynamic forces on a diffuser pump impeller excited by the interaction between the impeller and the vaned diffuser with the same number of vanes as impeller. Unsteady flow calculations are made using commercially available CFD software, CFX-TASCflow, as well as the two-dimensional vortex method. Calculated pressure and fluid forces on the impeller show good agreement with measured ones. It has been demonstrated that the fluid forces on the impeller with the same number of vanes as the vaned diffuser are smaller compared with other combinations of vane numbers. However, the pressure fluctuations are found to be greater than other cases. [DOI: 10.1115/1.1949640]

Introduction

In a diffuser pump, the centrifugal impeller interferes with its successive diffuser vanes and produces pressure fluctuations downstream of the impeller. This phenomenon is the so-called rotor-stator interaction. Big hydrodynamic forces will be caused by the pressure fluctuations, which are the main factors that will generate noise and violent vibration of the main shaft.

Hydrodynamic radial forces on a centrifugal pump impeller have been extensively studied and reported. Guelich et al. [1] reviewed, in some detail, the design parameters that affect radial force. A further summary of the applicable open literature can be found in de Ojeda and Flack [2]. Stepnoff [3] suggested that the radial force was a function of the discharge pressure, impeller tip diameter, impeller tip width, and a constant. Agostinelli et al. [4] completed an experimental investigation to understand the effects of specific speed and pump housing geometry on radial force.

The mechanism of the rotor-stator interaction in the diffuser pump has also been extensively studied. Qin and Tsukamoto [5,6] and Qin [7] calculated an unsteady flow caused by impeller-diffuser interaction in a diffuser pump with a singularity method. Following their works, Shi and Tsukamoto [8] calculated the pressure fluctuations downstream of the diffuser pump impeller using two-dimensional (2D) and three-dimensional (3D) unsteady RANS code with standard k-ε turbulence models. Wang and Tsukamoto [10] used an advanced vortex method to calculate the impeller-diffuser interaction, in which the changing operating points of pump were taken into account. All of these works contributed to the understanding of rotor-stator interaction in pumps, however, little work was reported on the cases in which the rotor and the stator vanes number have common factors, especially when the number of vanes on the impeller and diffuser is identical. Traditionally, the case in which the rotor and the stator have the same vane numbers is thought to be unacceptable for actual engineering since it will cause great interaction forces.

The objective of this paper is to apply an experimental method and a commercially available computational fluid dynamics (CFD) code, CFX-TASCflow, as well as a two-dimensional vortex method to the hydrodynamic radial forces and the pressure fluctuation in a diffuser pump, which has a six-bladed impeller and a six-bladed diffuser. The calculated results were compared with the experimental data. These comparisons will enhance our understanding of the mechanism of rotor-stator interaction and the resulting hydrodynamic radial forces.

Test Facility and Method

The arrangement of the test rig and instrumentation system is illustrated schematically in Fig. 1. In order to avoid cavitation, water is supplied to the suction port from a large reservoir with a water level of 1 m above the pump center through a short inlet pipe. The water discharged from the pump returns to the reservoir via two symmetrically arranged discharge pipes.

A single-stage diffuser type centrifugal pump is used for the experiment, and its principal specifications are summarized in Table 1. The test impeller is installed at the center of a vaned or vaneless diffuser and a circular casing with two parallel discharge pipes. In order to measure the influence of various combinations of impeller and diffuser vane numbers, the diffuser vanes are designed to be removable.

The test pump is driven by a two-pole 7.5 kW induction motor. The rotational speed of the pump can be adjusted by controlling the line voltage of the transistor inverter to the motor. The rotational speed of the pump shaft is detected by the pulse signals (60 pulses per revolution), which are fed to a frequency analog converter for recording. The flow rate in each discharge line is adjusted to be equal by flow control valves, and the turbine flow meters installed in the discharge lines are used to measure the flow rate. The repetition precision of the flow meters is ±1.22%. The experimental error on flow rate measurements was estimated to be ±2.1%.

The unsteady hydrodynamic forces acting on the impeller were measured by strain gages on the rotating shaft of the pump, as can be seen in Fig. 2. At the same time, the displacements of the main shaft ($\varepsilon_x, \varepsilon_y$) were measured by gap sensors set on the casing wall. The repetition precision of the strain gages is ±1.05%. The relation between load cell outputs and fluid forces was obtained dynamically by adding a fixed weight to a rotating dummy disk. Neglecting small cross-interaction, the impeller forces were evaluated using $F_x = a_x E_x + b_x$ and $F_y = a_y E_y + b_y$. The experimental error

Contributed by the Fluids Engineering Division for publication in the JOURNAL OF FLUIDS ENGINEERING. Manuscript received by the Fluids Engineering Division August 20, 2003; Final manuscript received March 26, 2005. Associate Editor: Jinkook Lee.

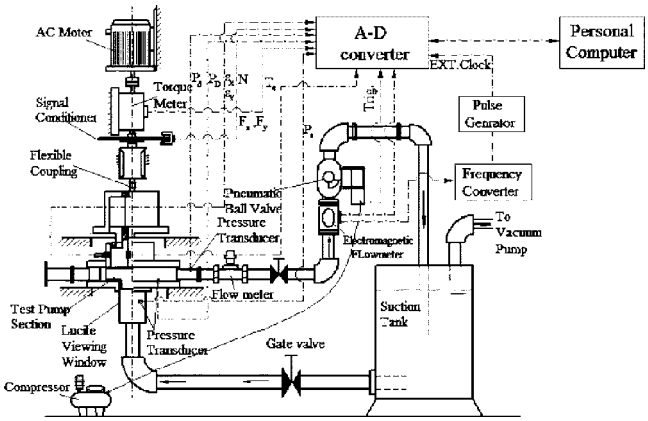

Fig. 1 Schematic view of test rig and instrumentation system

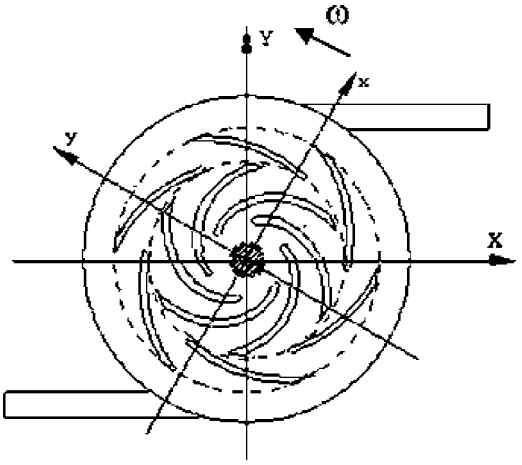

Fig. 3 Schematics of reference coordinate systems for test diffuser pump

on fluid force measurements was estimated to be ±1.7%. Figure 3 shows the relative positions of the reference coordinate systems. The signals were led to the slip ring and then recorded in a computer data file after A-D (analog to digital) conversion. In order to investigate the effect of the natural frequency of the main shaft system, two different material impellers were used in the experiment; one is made of steel and the other is synthetic resin. Because of the different materials, these two types of impellers have different natural frequencies; 396 and 947 Hz for the resin and the steel, respectively. The comparison of the hydrodynamic forces on both impellers showed that the natural frequency of the main shaft system has little effect on the experimental data, since the dominant frequencies of the hydrodynamic forces caused by rotor-stator interaction were the same for both impellers.

Unsteady pressures were measured downstream of the test pump impeller with a vaned diffuser as well as a vaneless one. Figure 4 illustrates the unsteady pressure measurement stations on the shroud-casing side of the diffuser in the test pump. The coordinates of the pressure taps were formed by the cross of five radial grid lines and three streamwise grid lines in a blade-to-blade passage as shown in Fig. 4. Because of the limited space in the measuring sections, the pressure taps for tangential traverse pressure were located only at one radial location in each passage of the diffuser so that the upstream pressure taps could not affect the downstream ones. As a result of the numerical calculations by CFX-TASCflow software, it was found that the circumferential distribution of the flow in the circular casing has little effect on the pressure distribution in the diffuser passages; and thus, the blade-to-blade distributions of unsteady pressure were identified by a phase shift of the measured data. Moreover, two pressure taps were set on both the suction and discharge lines for measurement of the pressure fluctuations in the pipe line. During the tests, unsteady pressures were sampled in 50 circulations of the impeller, and then ensemble averaged to compare with the calculation results. The experimental error on the unsteady pressure measurements was estimated to be ±2.3%.

Semi-conductor-type pressure transducers were used to measure the unsteady pressures. The repetition precision of the transducers is ±0.5%. Silicon oil was filled in the lead tube between the pressure tap and the transducers to construct a pressure measurement system with a higher natural frequency. The viscosity of the silicon oil was adjusted to keep the balance of gain and phase

Table 1 Specifications of test pump

Rating:		
Flow rate	Q_r	0.1449 m^3/min
Total head	H_r	4.91 m
Rotational speed	N	1750 min^{-1}
Specific speed	N_s	202 (m^3/min, m, min^{-1})
Impeller:		
Outlet diameter	D_2	130 mm
Outer passage width	b_2	6.4 mm
Discharge angle	β_2	22.5 deg
Number of vanes	Z_i	6
Diffuser:		
Inlet radius	R_3	67 mm
Passage width	b_3	10 mm
Outlet radius	R_4	90 mm
Number of vanes	Z_d	0, 5, 6

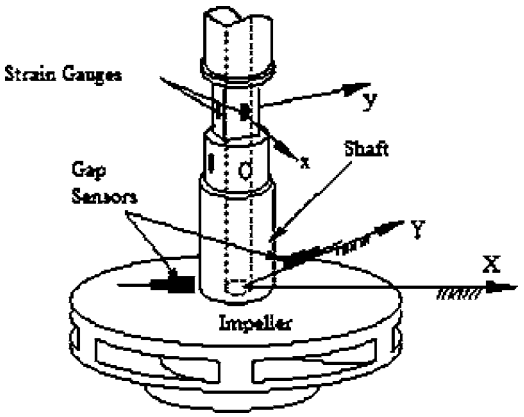

Fig. 2 Schematics of fluid force measurement system

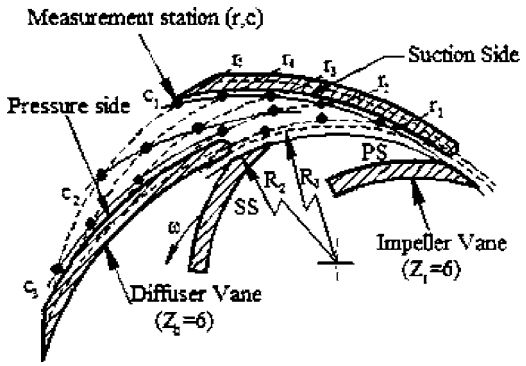

Fig. 4 Locations of pressure taps in vaned diffuser

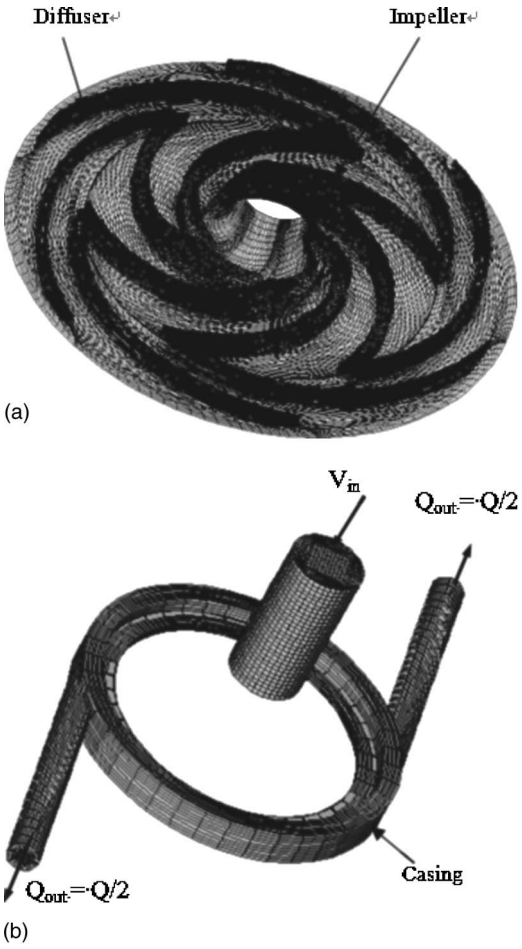

Fig. 5 Computational domain and grids: (*a*) Impeller and diffuser; (*b*) casing and pipe systems

delay. In the experiments, the natural frequency of the measurement system is 2348.9 Hz, the damping ratio is 0.728, and the viscosity of the oil is 276 St. As a result, the gain showed the flat frequency characteristics, and the unsteady pressures could be measured by the current measurement system. The signals were recorded in a computer data file after A-D conversion. The recorded data were transformed to the pressure coefficient Cp and then were ensemble averaged.

Numerical Calculations

In order to deepen the understanding of the experimental results, the CFX-TASCflow software [9] and a 2D vortex method [10] are employed for this study.

Numerical Analysis by CFX-TASCflow software. The validation of this code can be found, for example, in the work of Flathers and Baché [11] and Flathers et al. [12], and Gu et al. [13]. The code solves the Reynolds-averaged Navier-Stokes equations in primitive variable form. The effects of turbulence were modeled using the standard k-ε turbulent model, in which the following parameters were used, referring to a comprehensive assessment by Lakshminarayana [14] on the computation of turbomachinery flows using the k-ε turbulence model

$$c_\mu = 0.09, \quad c_{\varepsilon 1} = 1.44, \quad c_{\varepsilon 2} = 1.92, \quad \sigma_k = 1.0,$$

$$\sigma_\varepsilon = 1.3, \quad \text{and } \mathrm{Pr}_t = 0.9$$

To make the simulation time economical, a wall function is used to resolve the near-wall flows. The simulation is believed to be converged when the nondimensionalized maximum residuals are reduced to 1.0×10^{-4}.

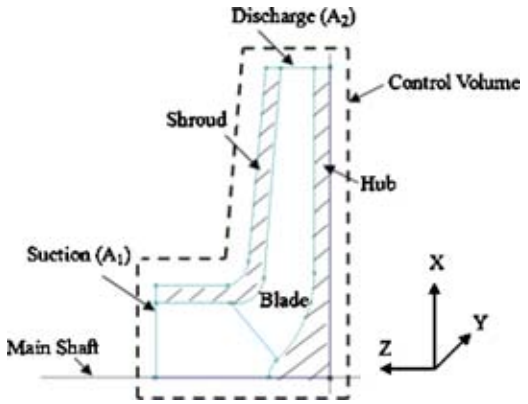

Fig. 6 Schematics of coordinate system and control volume for fluid force calculation

The code allows for connecting simple blocks into a multiblock assembly. A convenient feature of TASCflow is that the grids are not required to match at the connecting interface. This makes it easy to connect casing grids at the critical surface, where one side is of the smaller area and the other side of the larger one. Whereas a self-coded program was used to generate the casing grid, the commercial impeller grid generator, TURBOgrid [15], is employed to generate the impeller grid. The total grid size is about 300,000; about 160,000 for impeller, 100,000 for diffuser, and 40,000 for the casing and pipe lines. The same wall function was used for all the runs, and the y^+ of the first grid point on the wall is in the range of logarithmic sublayer of the boundary layer.

In this calculation, as shown in Fig. 5, there are two distinct components: rotating impeller, and stationary casing and vaned diffuser. A mixing grid interface between these two components is defined as the "transient rotor-stator interface," using the TASCflow grid attachment facility. All the flow passages were calculated simultaneously.

The inflow boundary condition was assigned at the entrance of the inlet pipe as velocity. Inlet turbulence quantities are expressed in terms of the turbulence intensity T_u and the energy-containing eddy length scale L_ε, where $K_{\text{inlet}}=3/2(T_u|\vec{V}|)^2$, $\varepsilon_{\text{inlet}}=k_{\text{inlet}}^{3/2}/L_\varepsilon$, and $|\vec{V}|$ is the local magnitude of the inlet velocity. Here, T_u and L_ε were set as 0.03. Variations in these parameters showed little effect on the pressure distribution in the diffuser and the fluctuation in the hydrodynamic forces. Mass flow rate was imposed on the exit of the discharge pipe. It is assumed that the flow is approximately fully developed at the outlet, and thus zero gradients of k and ε are specified at the outlet. The CFD study ran at the same conditions as the experiment.

The momentum law was used in the coordinate system shown in Fig. 6 to predict the radial forces in both the CFD and the vortex method simulation. In a stationary frame, applying the momentum law [16] to the control volume formed by the dashed line in Fig. 6, and then omitting the terms with small effects, gives

$$F_X + \iint_{A_2} \cos(\theta+\omega t)p(r_2,\theta)dA + \rho\frac{\partial}{\partial t}\int_V dQV_x - \left(\iint_{A_2} V_X\rho V_r dA - \iint_{A_1} V_X\rho V_r dA\right) = 0$$

$$F_Y + \iint_{A_2} \sin(\theta + \omega t) p(r_2, \theta) dA + \rho \frac{\partial}{\partial t} \int_V dQ V_Y - \left(\iint_{A_2} V_Y \rho V_r dA - \iint_{A_1} V_Y \rho V_r dA \right) = 0 \quad (1)$$

Here, A_1 and A_2 denote the suction and discharge cross-sectional areas of the impeller, respectively, and Vr denotes the radial velocity of a certain point in the impeller. The second term represents the pressure forces due to P_2, and the forces caused by P_1 were omitted because the suction cross section is perpendicular to the main shaft and, thus, the resultant forces have no effect on radial forces. The third term represents the force caused by the rate of change in the fluid momentum in the impeller, and the last two are the momentum flux across the impeller. The calculated forces were compared with ones calculated by the direct integration of the force acting on the entire surface of the impeller (hub, shroud, and blades). The difference between the momentum law and the direct integration method was tested to be small [17]. The fluid forces have to be compared within the same coordinate system, or the phase and the dominant frequency of the fluid forces may be different. As shown in Fig. 3, the radial forces (F_X, F_Y) calculated in the stationary frame are transformed to the rotating frame (F_x, F_y) to compare with the experimental results by

$$F_x + jF_y = (F_X + jF_Y)e^{j\omega t} \quad (2)$$

Convergence Judgment and Numerical Error Control. All the computations were performed on a VT-Alpha 600AXP computer (600 MHz Alpha processor, 1 GB RAM). The time step, which is related to rotational speed and angular displacement of the impeller between two successive computations, was set to 0.95×10^{-dt} (360 steps per revolution). The combination of mesh density and time step was chosen such that the maximum cell Courant number (defined as $C = |V| \Delta t / \Delta x$, where V is the estimated local velocity, and Δx is the corresponding local mesh dimension) was <50, although CFX-TASCflow's implicit AMG (algebraic multigrid coupled) solver does not have this requirement. The modified transient Rhie-Chow pressure velocity coupling algorithm [9] was used for the unsteady simulation. At each time step in the transient simulation, the solver performs several coefficient iterations, either to a specified maximum iteration number 10 or to the predefined residual tolerance 0.0001. In the simulation, the maximum number of iterations (10 per time step) was not reached because the residual target level was achieved first. Within each time step, iterations between three and five were found sufficient to limit the solution error in the coefficient loop to 0.0001. The two to four revolutions of the impeller are necessary to get the convergence to a periodic unsteady solution. The final numerical results for the comparisons with experimental data were extracted from the sixth revolution of the impeller, after checking the convergence of calculated values. In order to determine the sensitivity of numerical results to the magnitude of the time step and the grid size, the magnitude and the fluctuation of the fluid forces were selected on the numerical accuracy basis. Figure 7(*a*) shows the comparison of calculated fluid force fluctuations for 360 and 540 time steps per revolution. It can be seen that the magnitude of the time step has no significant effect on the fluid force fluctuation. The sensitivity of the model to grid size was also checked by performing the calculations on two grid systems; one with 293,437 cells and the other with 370,523 cells, as shown in Fig. 7(*b*). The numerical results showed that accurate computations are expected from 360 time steps per revolution and 293,437 grids in the present unsteady calculation. Furthermore, various spatial difference schemes, such as, the first-order UD (upwind differencing), the second-order high resolution (modified linear profile + physical advection correction) were tested at the mesh density of 293,437 cells. The differences in the results were negligible. The numerical tests based on two-grid systems and different convective flux formulations indicated that the well-known numerical diffusion (a form of numerical truncation error) and numerical dispersion (a kind of numerical instability) diminished to a maximum extent. Moreover, the influences of boundary locations and boundary specifications were reduced to their respective minimums. Therefore, for the present calculations, the numerical deviations from the experimental data can be attributed to physical modeling errors: (i) difference between CFD pump modeling and real pump modeling, (ii) pump geometry deviation, and (iii) turbulence models.

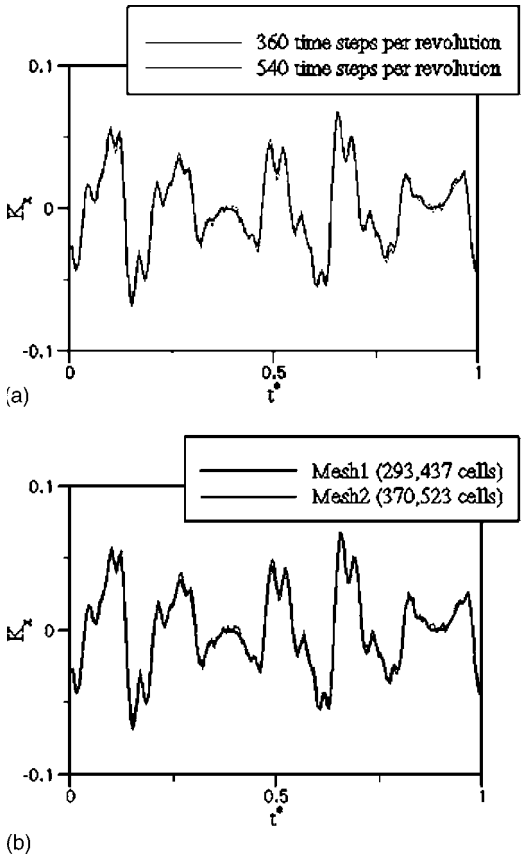

Fig. 7 (*a*) Effect of time step on dynamic fluid forces for rated condition and (*b*) effect of grid density on dynamic fluid forces for rated condition

Numerical Analysis by Vortex Method. The hydrodynamic forces and the unsteady pressure fluctuations were also calculated by the vortex method of Wang and Tsukamoto [10]. The vortex method is one of high-accuracy methods in CFD, as explained by Wang and Tsukamoto [10]: (i) The vortex method is grid-free, and thus there is no error due to mesh discretization; (ii) The vortices in the flow field are simulated directly in the Lagrangian method, and thus there is no error due to turbulence models application in the complicated unsteady flow; (iii) The variables (e.g., vorticity, velocity, and pressure) are obtained directly, without an iteration process at every time step, thus there is no error due to convergence truncation. However, the CPU time for 3D vortex methods was too huge to be applied in high Reynolds flows in engineering, until now. The unsteady flow in the test diffuser pump was investigated by calculating the 2D flow field around the impeller and diffuser vanes [18]. The relative movement of the impeller and the diffuser was taken into account. The velocity for a given location in the flow field was calculated directly by the well-known Biot-Savart law. The boundary element method was used to obtain the unsteady pressure according to the calculated velocity and vorticity time to time. Moreover, for a more realistic prediction of the

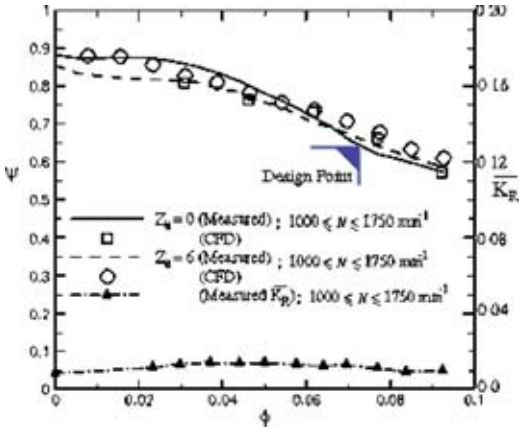

Fig. 8 Steady characteristic curves of test pump; experimental uncertainty in $\phi = \pm 2.1\%$, in $\Psi = \pm 2.3\%$, in $\overline{K_R} = \pm 2.5\%$

pressure fluctuations and the unsteady fluid forces, the instantaneous pump operation is calculated by considering the change in the pump operating point [18]. The unsteady hydrodynamic forces were calculated by the same method as in CFD calculations. For all the cases with a larger flow rate ratio than 0.70, the results calculated by the vortex method agree well with the experimental data. Therefore, the present vortex method is suitable for the calculation of unsteady hydrodynamic forces.

Results and Discussion

Seady Performance and Steady Fluid Forces. Figure 8 shows characteristic curves of the test pump with the vaned (Z_d=6) and vaneless (Z_d=0) diffuser! The steady fluid forces on the impeller are also presented for the vaned diffuser (Z_d=6) in this figure. The steady characteristics of the test pump and the steady fluid forces on the impeller were tested for various rotational speeds, and those were found to be independent on rotational speed for 1000–1750 rpm. The steady fluid forces do not equal zero, due to the displacement of the pump shaft. The steady fluid forces are very small, and almost constant for a wide flow range. The measured total head rise across the pump is also compared with the one calculated by CFD in this figure. Good agreement can be found between the measured and calculated total head rise.

Hydrodynamic Radial Forces. Figures 9(*a*) and 9(*b*) show the effects of flow rate and rotational speed on the unsteady fluid forces on the impeller for Z_d=Z_i=6, respectively. Figure 9(*a*) indicates the time histories of the unsteady fluid forces for three different rotational speeds (N=1200, 1500, and 1750 rpm). Figure 9(*b*) presents the time histories of the unsteady fluid forces for three different flow rates (85, 100, and 119 %) of the rated flow rate. In this paper, only *x* components are presented because of the similar wave forms of both the *x* and *y* components. The effects of flow rate and rotational speed on unsteady fluid forces were small, as can be seen in these figures. Experiments are also carried out for Z_d=0, 2, 3, and 7. Table 2 lists the standard deviation of the unsteady fluid forces K_x. As can be seen in Table 2, the unsteady fluid forces for Z_d=0,2,3, and 6 are much smaller than for Z_d=5 and 7. The results will be presented only for three representative cases, Z_d=0, 5, and 6 among the cases of Z_d=0, 2, 3, 5, 6, and 7, in this paper. The impeller for Z_d=2 and 3 also caused smaller forces by the same mechanism as the case of Z_d=6; and the case of Z_d=7 caused larger forces by the mechanism similar to the case of Z_d=5.

Figure 10 indicates the time histories of the measured and calculated unsteady hydrodynamic forces during two revolutions of the test impeller. The experimental data are phase averaged for 55 revolutions of the impeller, while the results calculated by CFD

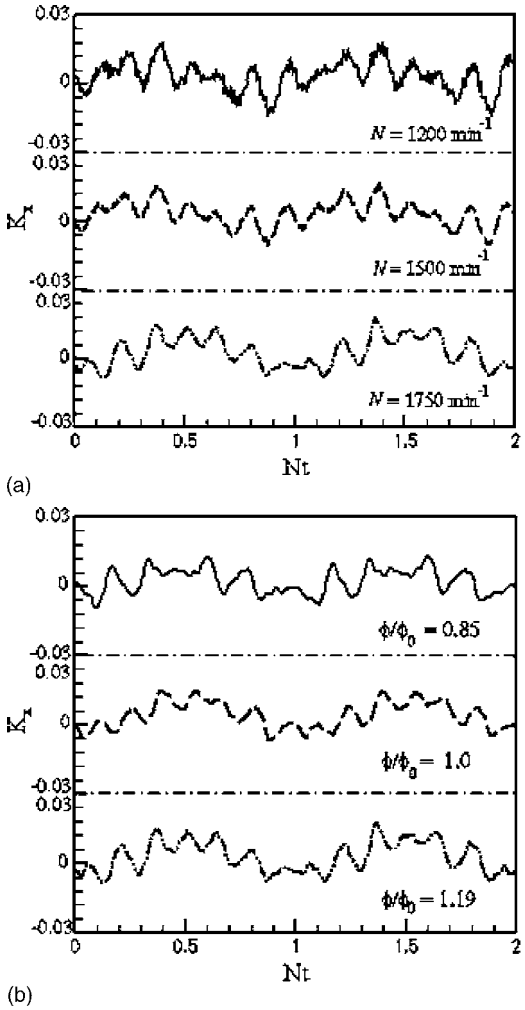

Fig. 9 Time histories of dynamic fluid forces; Z_d=6; experimental uncertainty in $K_x = \pm 1.7\%$: (*a*) Effect of rotational speed, ϕ/ϕ_0=1.0; (*b*) effect of flow rate, N=1750 min^{-1}

and the vortex method are not phase averaged, but instantaneous. The wave form of unsteady hydrodynamic forces calculated by the vortex method and CFD shows good agreement with the experimental data. In the vortex method, new vortices are induced near the solid boundary and shed into the flow field at every time step, thereby forming the vortex pattern. The interactions between these new vortices and existing ones result in an energy transfer cascade between the vortices and the pressure fluctuating in the higher frequency. The lack of higher frequency in the pressure predicted by RANS code shows that the RANS method has some limitation in unsteady flow applications. The higher frequencies in forces calculated by the vortex method may be attributed to the effect of the vortex shedding patterns.

As shown in Fig. 10, the unsteady hydrodynamic forces for Z_d=6 are much smaller than those for Z_d=5, and show trends similar to that for Z_d=0 without interaction between the impeller and diffuser vanes. The small hydrodynamic forces for Z_d=6 are due to the circumferentially symmetric arrangement of the vanes.

Table 2 Standard Deviations of K_x for various diffuser vanes' number

Diffuser blade number	0	2	3	5	6	7
Standard deviation	0.0044	0.0059	0.0062	0.035	0.0058	0.020

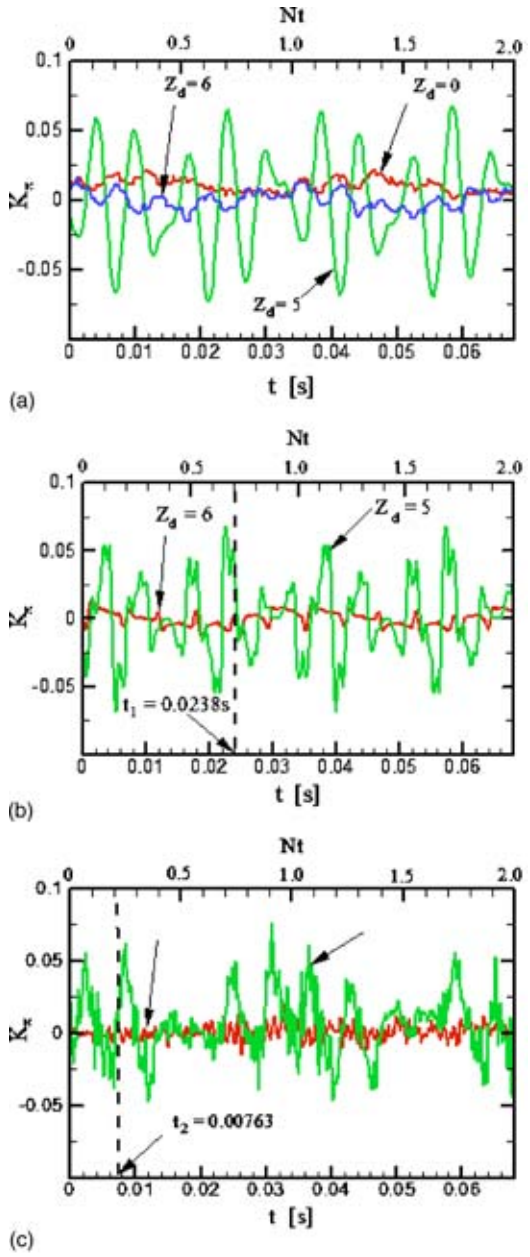

Fig. 10 Time histories of dynamic fluid forces for various diffuser vane numbers (N=1750 min^{-1}, ϕ/ϕ_0=1.0), experimental uncertainty in K_x=±1.7%: (*a*) Measured, (*b*) CFD predicted, and (*c*) calculated by vortex method

The fluid forces are the results of the integration of the pressures due to the interaction between the impeller blades and the diffuser vanes. The interaction occurs simultaneously between each impeller blade and diffuser vane for Z_d=6. The same amplitude of the pressure fluctuations results in smaller amplitudes of fluid forces for Z_d=6.

Figures 11(*a*) and 11(*b*) show the CFD predicted velocity vectors in the blade-to-blade plane at the midspan for Z_d=6 and Z_d=5 in the test-pump stage at the instant t_1=0.0238 s shown in Fig. 10(*b*). The color shows the magnitude of the relative speed. As can be seen in these figures, the low-speed regions of each flow passage for the diffuser with five blades are much more asymmetric than that for the one with six blades. As shown in an auxiliary graph, which shows the circumferential distributions of radial and tangential velocities (V_n, V_t), more circumferential symmetry can be found in the diffuser with six blades than the one with five blades. Figures 12(*a*) and 12(*b*) show the vortex pattern calculated by the 2D vortex method for Z_d=6 and Z_d=5 in the test-pump stage at the instant t_2=0.00763 s shown in Fig. 10(*c*). The red and blue colored dots in Figs. 10(*a*) and 10(*b*) show the rotating direction of vortices; that is, the red and blue colored dots represent the counter clockwise and clockwise directions, respectively. Velocity vectors in the blade-to-blade plane are also presented in Figs. 12(*a*) and 12(*b*). Two ellipses have been added to indicate the asymmetric flow structure for the case of the diffuser with five blades, while this kind of asymmetric flow structure cannot be found for the case of the diffuser with six blades. These figures show more circumferentially symmetric flow patterns and vorticity structures for Z_d=6 than for Z_d=5. A circumferentially symmetric flow field leads to small hydrodynamic forces. Hydrodynamic forces caused by the impeller-diffuser interaction are smaller for Z_d=6=Z_i, compared to the one for Z_d=5.

Unsteady Pressure in Vaned Diffuser Passage. Figure 13(*a*) indicates the time history of the unsteady part of the instantaneous pressure coefficient on the suction-side pressure tap (r_1,c_1) near the diffuser vane leading edge (see Fig. 4). The wave forms of unsteady pressure calculated by CFD and the vortex method show good agreement with the measured one. The magnitude of the pressure fluctuations predicted by the vortex method, however, is the biggest because of the 2D flow assumption in the calculation. The power spectral density function shown in Fig. 13(*b*) demonstrates that the pressure fluctuates with the impeller-blade passing frequency NZ_i and its higher harmonics. Good agreement can be seen between the measured frequency components and those calculated by the vortex method and CFD.

Figure 14 shows the comparisons of the pressure fluctuations for Z_d=6 and Z_d=5 on the pressure taps (r_1,c_1),(r_2,c_1), and (r_3,c_1) predicted by CFD. As shown in Fig. 14, the fluctuations of the unsteady pressure decay much more slowly for Z_d=6 than for Z_d=5, with increasing radius. Comparing the magnitudes of the unsteady pressure, it can be found that the magnitude of the pressure fluctuations for Z_d=6 are much bigger than those for Z_d=5; and the higher-frequency components are larger for Z_d=6 than those for Z_d=5. The local pressure fluctuation is larger when the vane numbers on the impeller and diffuser are identical, and should not be neglected in actual engineering design. The interaction between every impeller blade and diffuser vane occurs simultaneously for the diffuser with six blades. The pressure fluctuations have the same amplitude and phase in this case, and thus the circumferential pressure gradient is stronger than for nonidentical numbers of impeller and diffuser vanes. Therefore, the diffusion of pressure may be weaker in the downstream direction because of a stronger circumferential pressure gradient.

Figures 15(*a*) and 15(*b*) show the CFD-predicted and measured instantaneous pressure at the pump inlet for Z_d=6 and Z_d=5. The effect of the length of the suction pipe is also calculated using two different pipe lengths, 150 and 250 mm. The pressure fluctuations for Z_d=6 are found to be much larger than that for Z_d=5. The suction pipe length has little effect on the pressure fluctuation at the pump inlet. As can be seen in this figure, the unsteady pressure has much larger magnitude for Z_d=6 than for Z_d=5.

Figure 16 shows the CFD-predicted pressure fluctuation in the pump discharge. As shown in this figure, the pressure fluctuation has a larger magnitude for Z_d=6 than for Z_d=5, and the pressure fluctuations in the pump discharge have almost the same magnitude as that in the pump inlet.

Figure 17 shows the power spectrum density of the measured unsteady pressure at the pump inlet and discharge. As shown in this figure, the dominant frequency of the unsteady pressure at the pump inlet is NZ_i, whereas the higher harmonies are also dominant at the pump discharge in addition to the NZ_i component. The unsteady fluctuations are very weak for the other combinations of the numbers of impeller and diffuser vanes. Therefore, it can be concluded that the larger fluctuation of the inlet and discharge

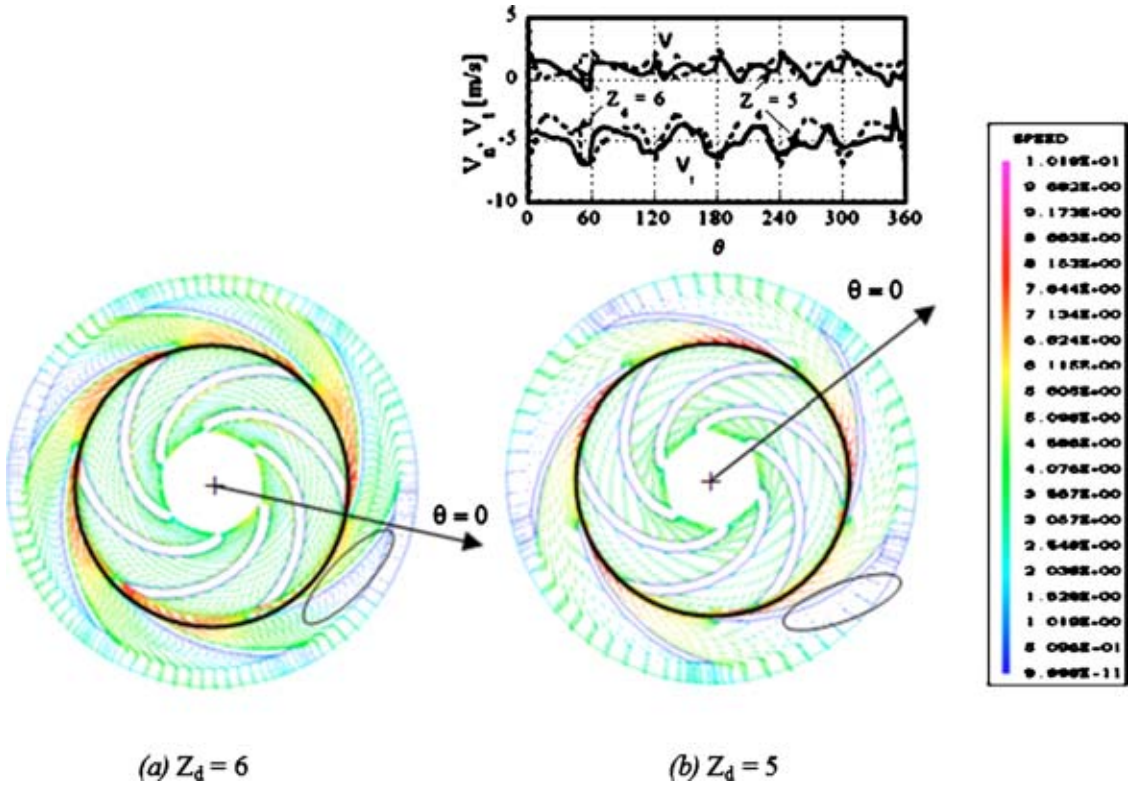

(a) $Z_d = 6$ (b) $Z_d = 5$

Fig. 11 Velocity diagram calculated by TACSflow (at $t=t_1$ in Fig. 10(*b*): (*a*) $Z_d=6$ and (*b*) $Z_d=5$

unsteady pressures is not due to the resonance of the pipe system, but is caused by the strong potential interaction, which decays more slowly.

Conclusions

A theoretical and experimental investigation was performed for unsteady hydrodynamic force on the impeller due to the rotor-stator interaction in a diffuser pump when the numbers of vanes on the rotor and stator are identical. The fluctuations of pressure and hydrodynamic forces were computed using the commercially available CFD software, CFX-TASCflow, and the 2D vortex method.

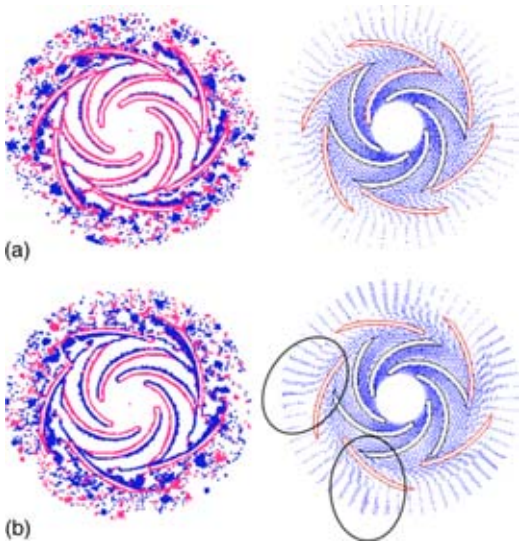

Fig. 12 Vorticity distribution and velocity vectors calculated by vortex method (at $t=t_2$ in Fig. 10(*c*)): (*a*) $Z_d=6$ and (*b*) $Z_d=5$

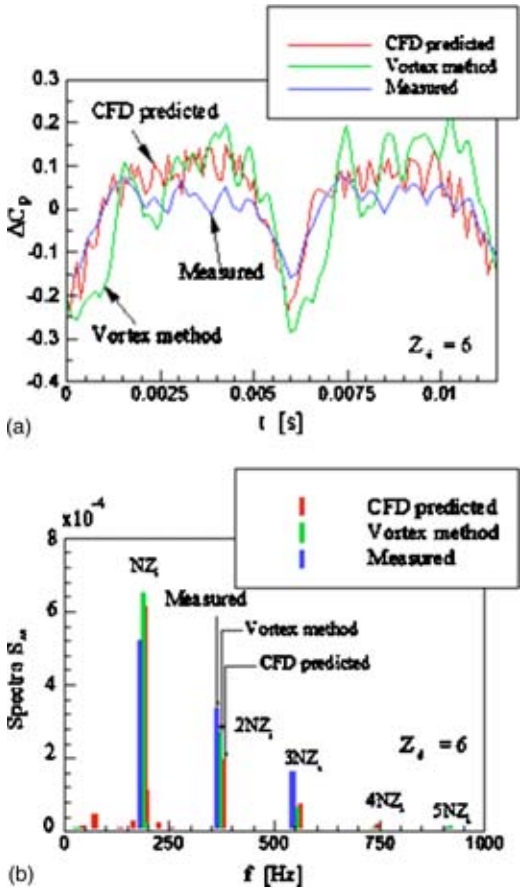

Fig. 13 Pressure fluctuation at station (r_1, c_1), $\phi/\phi_0=1.0$, experimental uncertainty in $f=\pm3.1\%$, in $S_{xx}=\pm5.5\%$, (*a*) time histories of ΔC_p and (*b*) power spectrum

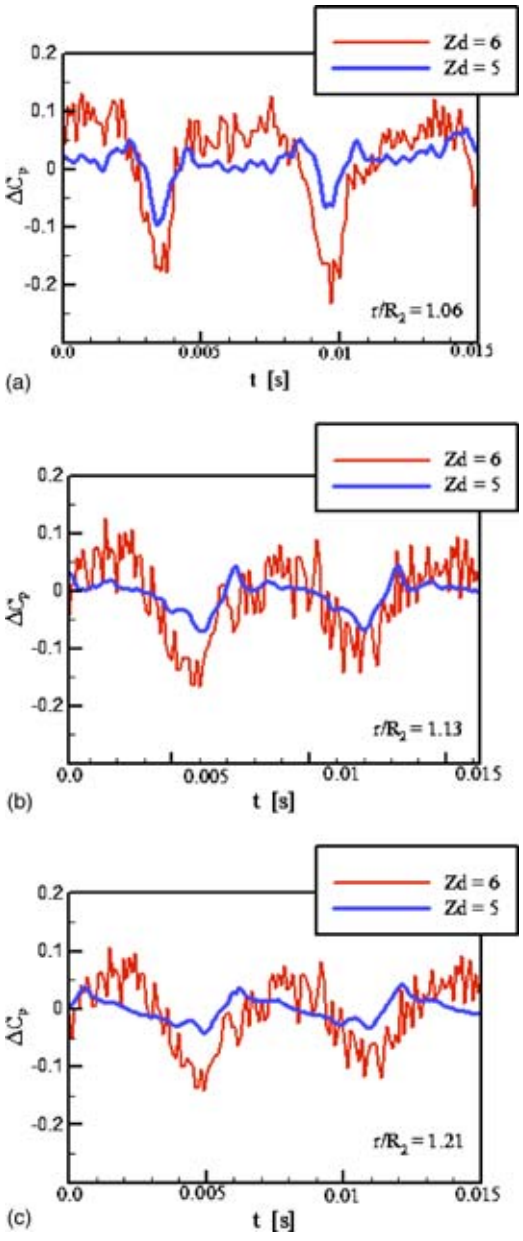

Fig. 14 Calculated pressure fluctuation in vaned diffuser passage ϕ/ϕ_0=1.0: (*a*) Station (r_1, c_1), (*b*) station (r_2, c_1), and (*c*) station (r_3, c_1)

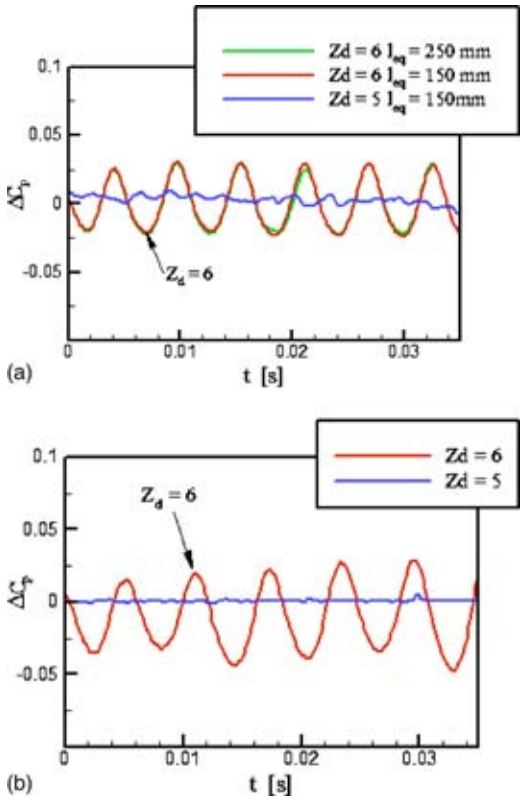

Fig. 15 Pressure fluctuations at pump inlet, ϕ/ϕ_0=1.0: (*a*) CFD predicted and (*b*) measured

The calculated results were compared with the measured one, and it was found that the pressure fluctuations in the diffuser passage and the hydrodynamic forces acting on the impeller can be predicted by the current 3D CFX-TASCflow software, and the present 2D vortex method. As a result of the present study for the case when the number of the impeller vanes equals to that of the diffuser, the following conclusions are derived, compared with the case with the number of impeller vanes different from that of the diffuser:

1. Hydrodynamic forces acting on the diffuser pump impeller are smaller for the circumferentially symmetric arrangement of vanes.
2. Local pressure fluctuations in the diffuser passages downstream of the impeller have larger magnitude, and the decay of the pressure fluctuations downstream is slow. Moreover, the pressure includes the higher harmonics of blade passing frequency.

The combination of impeller and diffuser with identical vane numbers can be employed because of its smaller unsteady forces, although the pressure fluctuations are bigger compared to other combination cases.

Acknowledgments

The work in this paper is a portion of the cooperative research with Ebara Research Co., Ltd. This support is gratefully acknowledged. The authors would like to acknowledge the efforts of T. Ito and T. Hatamoto in establishing the test rig and experimental procedure. The authors appreciate the dedicated assistance in the experimental work by T. Hatamoto, K. Ozaki, S. Akiyama, S. Kaneko, and T. Hiraoka.

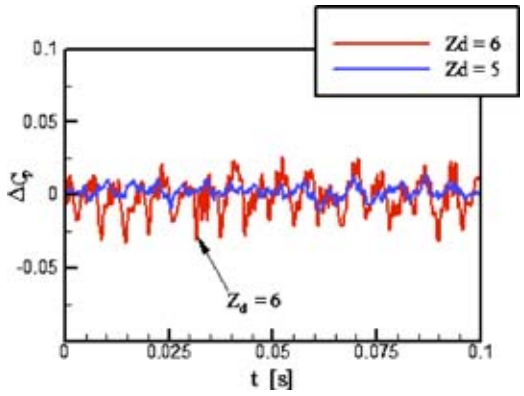

Fig. 16 Calculated pressure fluctuation at pump discharge

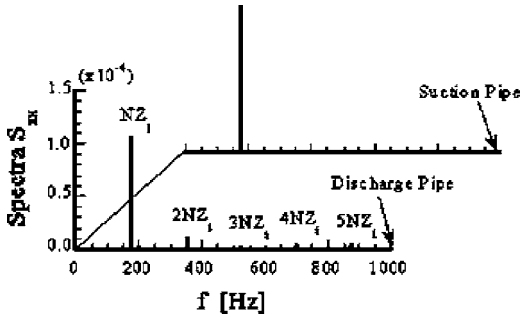

Fig. 17 Power spectra of measured pressure fluctuation at pump suction and discharge pipe; experimental uncertainty in $f = \pm 2.3\%$, in $S_{xx} = \pm 4.1\%$

Nomenclature

A = area
BEP = best efficiency point
b_2 = impeller discharge width
C_p = pressure coefficient $=(p-\rho g H_s)/(\rho u_2^2/2)$
F_x, F_y = hydrodynamic force in x and y directions
F_R = hydrodynamic force in radial direction
f = frequency
H = total hydraulic head rise across pump
K_x, K_y = normalized hydrodynamic force components, $K_{x,y}=F_{x,y}/(\rho u_2^2 \pi D_2 b_2/2)$
K_R = normalized radial hydrodynamic force
N = rotational speed
Nt = number of impeller revolutions
PS = pressure side
Ps = total pressure at pump suction port
p = static pressure
Q = flow rate
R_2 = radius in pump geometry
SS = suction side
S_{xx} = power spectrum density
t = time
t^* = nondimensional time $=t/T_i$
u_2 = peripheral speed of impeller $=R_2\omega$
$\bar{V}$ = absolute velocity
X, Y = stationary coordinates $(R=\sqrt{X^2+Y^2})$
x, y = rotating coordinates
Z = number of vanes
ΔC_p = nondimensional unsteady pressure $=C_p-\overline{C_p}$
$\varepsilon_X, \varepsilon_Y$ = displacements of the main shaft in X and Y direction
ϕ = flow coefficient, $Q/2\pi R_2 b_2 u_2$
η = pump efficiency
ρ = density
σ = standard deviation
τ_d = shaft power coefficient
ω = impeller angular velocity $=2\pi N$
Ψ = total head rise coefficient $=2gH/u_2^2$

Subscripts

d = diffuser
i = impeller
X, Y = component in X and Y direction
0 = rated condition

Superscript

- = time averaged

References

[1] Guelich, J., Jud, W., and Hughes, S. F., 1986, "Review of Parameters Influencing Hydraulic Forces on Centrifugal Impellers," Fluid Machinery Committee of the Power Industries Division of the Institution of Mechanical Engineers, London, England, pp. 1–16.

[2] de Ojeda, W., and Flack, R. D., 1992, "Experimental Pressures and Momentum Forces on the Impeller of Single and Double Volute Centrifugal Pumps," ROMAC Report No. 338, University of Virginia, Charlottesville.

[3] Stepanoff, A. J., 1957, *Centrifugal and Axial Flow Pumps—Theory, Design and Application*, 2nd Edition, Wiley, New York.

[4] Agostinelli, A., Nobles, D., and Mockridge, C. R., 1960, "An Experimental Investigation of Radial Thrust in Centrifugal Pumps," ASME J. Eng. Power **82** (2), pp. 120–126.

[5] Qin. W., and Tsukamoto, H., 1997, "Theoretical Study of Pressure Fluctuations Downstream of a Diffuser Pump Impeller-Part I: Fundamental Analysis on Rotor-Stator Interaction," ASME J. Fluids Eng. **119**, pp. 647–652.

[6] Qin. W., and Tsukamoto, H., 1997, "Theoretical Study of Pressure Fluctuations Downstream of a Diffuser Pump Impeller - Part 2: Effects of Volute, Flow Rate and Radial Gap," ASME J. Fluids Eng. **119**, pp. 653–658.

[7] Qin, W., 1996, "Pressure Fluctuations Downstream of Impeller Due to Rotor-Staotr Interaction in a Diffuser Pump," Ph.D. thesis, Kyushu Institute of Technology (in Japanese).

[8] Shi, F., and Tsukamoto, H., 2001, "Numerical Study of Pressure Fluctuations Caused by Impeller-Diffuser Interaction in a Diffuser Pump Stage," ASME J. Fluids Eng., **123**, pp. 466–474.

[9] *CFX-TASCflow, Version 2.10, Primer Manual*, AEA Technology Engineering Ltd., Harwell, UK,

[10] Wang, H., and Tsukamoto, H., 2001, "Fundamental Analysis on Rotor-Stator Interaction in a Diffuser Pump by Vortex Method," ASME J. Fluids Eng. **123**(4), pp. 737–747.

[11] Flathers, M. B., and Baché, G. E., 1999, "Aerodynamically Induced Radial Forces in a Centrifugal Gas Compressor: Part 2—Computational Investigation," ASME J. Eng. Gas Turbines Power **121**, pp. 725–734.

[12] Flathers, M. B., Baché, G. E., and Rainsberger, R., 1994, "An Experimental and Computational Investigation of Flow in a Radial Inlet of an Industrial Pipeline Centrifugal Compressor," 39th ASME Turbo Expo, The Hague, The Netherlands, ASME, New York, ASME Paper No. 94-GT-134.

[13] Gu, F. H, Engeda, A., Cave, M., and Liberti, J-L. D., 2001, "A Numerical Investigation on the Volute/Diffuser Interaction Due to the Axial Distortion at the Impeller Exit," ASME J. Fluids Eng. **123**, pp. 475–483.

[14] Lakshminarayana, B., 1991, "An Assessment of Computational Fluid Dynamics Techniques in the Analysis and Design of Turbomachinery," ASME J. Fluids Eng. **113**, pp. 315–352.

[15] *CFX-Turbogrid, Version 1.5, Primer Manual*, AEA Technology Engineering Ltd., Harwell, UK.

[16] Vavra, M. H., 1960, *Aero-Thermodynamics and Flow in Turbomachines*, Wiley, New York.

[17] Sun, J. and Tsukamoto, H., 2001, "Off-Design Performance Prediction for Diffuser Pumps," , **215**, pp. 191–201.

[18] Zhang, M., Wang, H., and Tsukamoto, H., 2002, "Numerical Analysis of Unsteady Hydrodynamic Forces on a Diffuser Pump Impeller Due to Rotor-Stator Interaction," *Proc. of FEDSM 02, 14–18 July, Montreal, ASME, New York*, ASME Paper No. FEDSM2002-31181.

Performance and Development of a Miniature Rotary Shaft Pump

Danny Blanchard

Phil Ligrani[1]
e-mail: ligrani@mech.utah.edu

Bruce Gale

Department of Mechanical Engineering, University of Utah, 50 South Central Campus Drive, Rm. 2110, Salt Lake City, UT 84112

The development and performance of a novel miniature pump called the rotary shaft pump (RSP) is described. The impeller is made by boring a 1.168 mm hole in one end of a 2.38 mm dia shaft and cutting slots in the side of the shaft at the bottom of the bored hole such that the metal between the slots defines the impeller blades. The impeller blades and slots are 0.38 mm tall. Several impeller designs are tested over a range of operating conditions. Pump performance characteristics, including pressure rise, hydraulic efficiency, slip factor, and flow rate, are presented for several different pump configurations, with maximum flow rate and pressure rise of 64.9 ml/min and 2.1 kPa, respectively, when the working fluid is water. Potential applications include transport of biomedical fluids, drug delivery, total analysis systems, and electronics cooling.
[DOI: 10.1115/1.1949641]

Introduction

The area of microfluidics is developing with many new sensors, separation devices, drug delivery systems, and other small-scale and microscale fluidic devices. For many of these devices there is a need to circulate or move fluid through macro and microscale channels. A variety of micropumps are available to meet this need, generally to fulfill specific applications [1]. These include membrane pumps [2–8] (both without check valves [2–5] and with check valves [6–8]), electrohydrodynamic (EHD) pumps [9–11], electrokinetic (EK) pumps [12,13], rotary pumps [14–18], peristaltic pumps [4,19–21], ultrasonic pumps [22,23], and several other types of pumps [24–27]. Other small-scale pumps have been developed for uses as blood pumps in ventricular assist devices [28–30]. Nonmechanical pumps, such as the electrohydrodynamic and electrokinetic pumps, do not have moving parts, which increases reliability. However, such devices are generally limited by low flow-rate and pressure-rise capabilities, the applications of the pump, the working fluids that can be pumped, and high supply voltage requirements [1]. Mechanical pumps, such as rotary, peristaltic, and membrane pumps, have a wide variety of possible working fluids and applications. However, such mechanical micropumps (such as rotary micropumps) are believed to be feasible only when they are greater than a certain size [1].

One motivation of the present effort is to demonstrate the operation and feasibility of a millimeter-scale pump, which imposes fluid motion and pressure rise by means of viscous and inertial forces. The behavior and performance of macroscale centrifugal pumps are well established and well known. However, the dynamics, performance, and efficiency of centrifugal pumps change as the size of the pump is altered. For example, secondary flows, and the losses associated with them, become more important as macroscale impeller passage size decreases. As size decreases further, surface (viscous) forces become more significant [31] and can dominate the performance of the pump. However, this does not appear to prevent the operation of the centrifugal micro- and minipumps developed by Ahn and Allen [17] and Hainan et al. [14]. The micropump by Ahn and Allen [17] is a radial-inflow–radial-outflow design and is powered by an integrated magnetic micromotor with a 12 pole, 500 μm dia stator that also acts as the impeller. The advantage of this pump is the integrated magnetic motor, which also serves as a completely sealed pumping chamber with no leaks. This pump reaches a maximum flow rate of 24 μl/min, with a maximum theoretical pressure rise of 100 Pa. The mini-pump by Hainan et al. [14] is a centrifugal pump with an axial inflow and a radial outflow configuration. This pump is created using precision machining techniques and measures 6 mm $\times$ 12 mm. This axial-inflow–radial-outflow pump produces a maximum flow rate of 100 ml/min, with a maximum pressure rise of 10 kPa. One disadvantage of this micropump is the potential leakage at the shaft-pump housing interface, which creates losses and reductions in performance. Even though some flow conditions are provided, extensive performance data for these pumps are not provided, nor are any details given regarding efforts to optimize the pump and impeller designs.

The present paper presents a novel rotary pump (shown schematically in Fig. 1), which has a 2.38 mm dia impeller and relatively high hydraulic efficiency at low flow rates. The design modifications [32], relative to other small-scale centrifugal devices, include the impeller integrated into the body of the shaft, instead of on the top of the shaft. This design is unique and novel because of its simplicity, which allows it to be easily manufactured at low cost, and because all problems of tip blade clearance and flow leakage around the blade tips are not present. Pump performance is characterized since the pressure rise, flow rate, and the hydraulic efficiency are given for a wide range of impeller speeds and impeller configurations. Tested impeller designs include radial two-, four-, and six-blade; backward-curved four-blade; and forward-curved four-blade arrangements. The fluid flow for each impeller design is throttled using outlet tubing inner diameters of 0.254, 0.508, and 1.397 mm of the same length, or by placing a valve at the end of the 1.397 mm outlet tubing. The present pump, or a variation of it, is useful for a variety of microbiological and biomedical analysis systems, electronics cooling, and drug delivery devices. For example, a larger-scale version of this pump has potential use as a blood pump for a ventricular assist device.

Pump Configuration and Geometry

One important dimension of many centrifugal pumps is the gap distance between the tips of the blades and the pump housing. As the gap increases, there is more leakage across blades and the overall hydraulic efficiency of the pump decreases. If the gap is too small or zero, then the blades can be damaged by contacting the pump housing. On a macroscale, this "gap problem" is generally insignificant, but on a microscale, or a millimeter-scale, the gap between the tips of the blades and the pump housing can be about the same as the height of the impeller blades.

The design of the rotary shaft pump (RSP) eliminates this "gap problem." The RSP impeller is constructed by boring a hole in the

[1]Author to whom correspondence should be addressed.

Contributed by the Fluids Engineering Division for publication in the JOURNAL OF FLUIDS ENGINEERING. Manuscript received by the Fluids Engineering Division April 21, 2004; final manuscript received April 15, 2005. Associate Editor: Akira Goto.

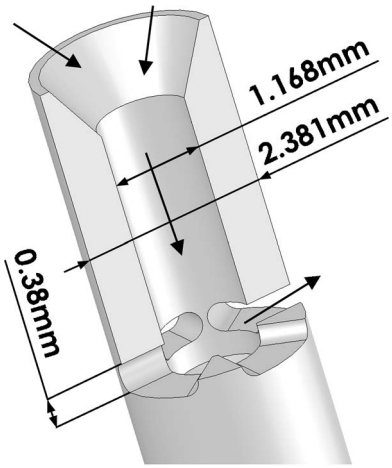

Fig. 1 Cutaway view of the rotary shaft pump (RSP) impeller. Shown is the radial four-blade impeller. Arrows indicate flow direction.

end of a shaft and then cutting slots in the side of the shaft at the bottom of the bored hole as shown in Fig. 1, which presents a cutaway view of the RSP impeller. Thus, the metal between the slots acts as the blades of the impeller, and the slots form passages between the bored interior and outer shaft surface. The gap at the tip of the blades is zero because the tips of the blades also connect to the shaft.

The rotating shaft is mounted using bearings located above and below the exit plenum, which are mounted in the pump housing. The volute and an outlet channel are then located in the region between the upper and lower bearings and pump housing, as seen in Fig. 2. The water reservoir is connected to the pump housing by a plastic tube with an inner diameter of 4.5 mm and length of 381 mm. This plastic tube is press fit into the inlet channel as shown in Fig. 2. There is a continuous channel, from the inlet tubing, through the pump housing and top of the upper bearing, to the inlet of the RSP. Inside the channel through the upper bearing, the fluid flow transitions from a nonrotating bearing wall to the inside of a rotating shaft. The bearing forms a seal for the spinning shaft of the RSP, which reduces the leakage from the impeller outlet to the shaft inlet of the RSP. The sidewalls of the volute and part of the outlet channel are formed by a piece of machined brass shim stock that is 416 μm tall. This volute and outlet channel is aligned with the slot ports of the shaft. With this construction, when the shaft spins, centrifugal forces from the spinning impeller shaft forces fluid flow through the shaft inlet, through the interior of the shaft, through the slots, out through the slot ports, into the volute,

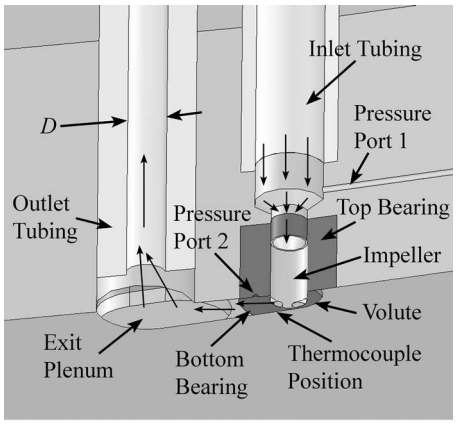

Fig. 2 Cutaway view of the RSP assembly

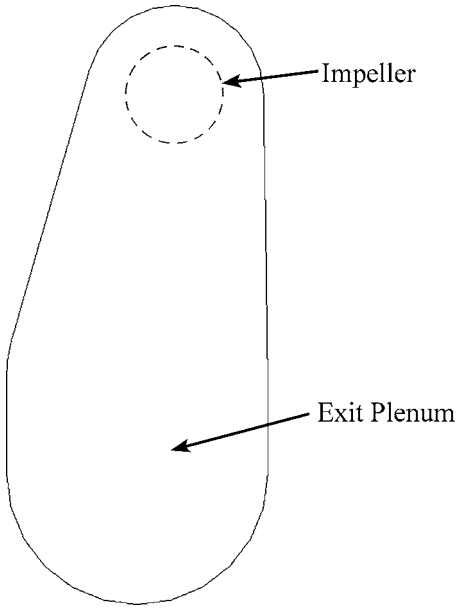

Fig. 3 Open volute configuration

and then into and through the outlet channel, as shown by the arrows in Figs. 1 and 2. The volute design employed for the present investigation, to minimize the effects of surface forces, is called the open volute design. The open volute design is characterized by a large "open" channel from the impeller to the exit plenum, as shown in Fig. 3.

One of the purposes of a volute is to efficiently direct fluid toward the outlet channel. The volute designs employed in macroscale pumps, where fluid motion is induced by inertial forces, are different from the design employed here. This design difference is because flow from the impeller exit and within the volute is significantly influenced by both inertial forces and surface forces. The present open volute design increases the width and maximizes the hydraulic diameter thereby decreasing the average fluid velocity and velocity gradients, which also reduces viscous losses.

Pump Component Fabrication

There are five main fabricated components of the rotary shaft pump assembly: (i) the impeller, (ii) top housing, (iii) bottom housing, (iv) bearings, and (v) volute.

Fabrication of the impeller is realized using precision machining techniques. A lathe is used to obtain the desired outside diameter of the shaft and to bore the hole in the end of the shaft. The cone shape at the inlet of the shaft is made using a center drill. Slots are then cut into the side of the shaft using a milling machine and an indexing tool. The impeller is made from 304 stainless steel. Five impeller designs are constructed for testing: radial two-, four-, and six-blade; backward-curved four-blade; and forward-curved four-blade. The blades are evenly spaced around the circumference of the shaft. The blades on the impellers are 0.38 mm tall (the slots are 0.38 mm tall). The geometry of the backward-curved four-blade impeller is shown in Fig. 4. The geometry of the other impellers is shown in Fig. 5. The backward-curved four-blade impeller has β_1 and β_2 angles of 80 and 85 deg, respectively. The forward-curved four-blade impeller has β_1 and β_2 angles of 144 and 114 deg, respectively.

The top housing is made from acrylic to allow the flow passing into and through the pump to be visualized. The top housing has an inlet channel and outlet channel, as seen in Fig. 2, and also has two pressure ports. The first pressure port is connected to the inlet channel passage, as seen in Fig. 2, and is just above the upper bearing at the inlet to the top of the rotary shaft pump. The second

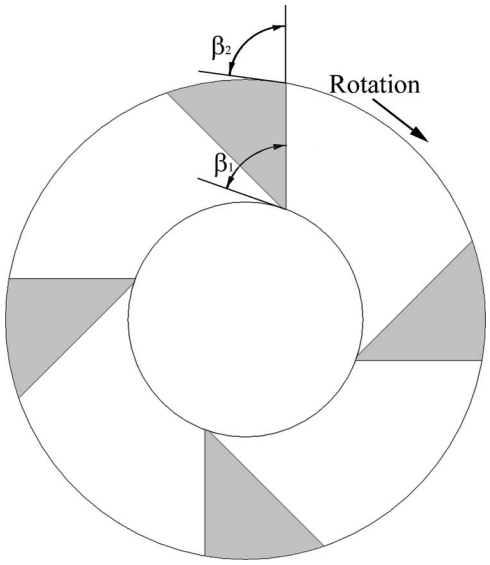

Fig. 4 Impeller blade configuration and angles. Impeller shown is the backward-curved four-blade impeller.

pressure port is connected to part of the volute and comes through the upper bearing into the volute region about 2 mm from the outer surface of the shaft. The diameter of the pressure ports at the fluid channel interface is ~0.4 mm. Each of these then expands to 3.1 mm. The ends of clear plastic tubes are press fit into the 3.1 mm dia holes, and the opposite ends of the tubes are connected to opposite sides of the differential pressure transducer (which is described later). Thus, the pressure transducer measures the differential pressure between the two pressure ports. The bottom housing is made from aluminum and contains the lower bearing. The bottom housing also has a recess that forms the exit plenum. The expansion of the fluid channel as it enters the exit plenum slows the fluid and minimizes losses as the fluid turns to the outlet channel.

The bearings are made from Torlon, a strong self-lubricating plastic. The upper and lower bearings are press fit into the top and bottom housing, respectively. Torlon is used because it has a low coefficient of friction and can be easily machined. The outer diameter of the bearings is 6.35 mm, and the inner diameter is 2.38 mm. The locations of these bearings are shown in Fig. 2.

The volute is machined from brass shim stock using a computer numerically controlled (CNC) milling machine and is positioned and designed as seen in Figs. 2 and 3. Each piece of brass shim stock is 104 μm thick. Thus the height of the volute can be changed by stacking pieces of brass shim stock. For all the present tests, a height of 0.416 mm is used because it is just larger than the height of the slots located in the shaft.

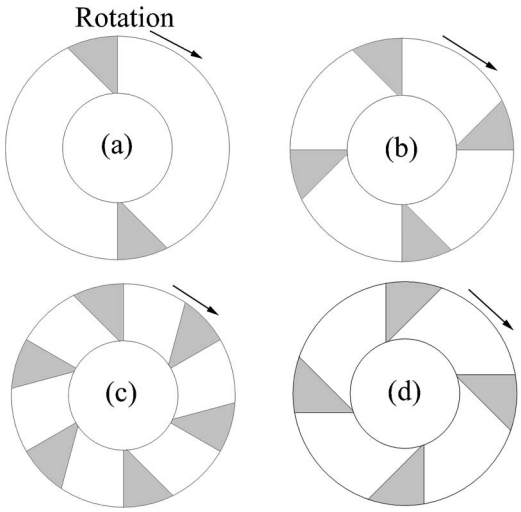

Fig. 5 Impeller blade configurations for the (*a*) radial two-blade, (*b*) radial four-blade, (*c*) radial six-blade, and (*d*) forward-curved four-blade impellers

Pump Performance

Parameters that characterize pump performance include head pressure rise, volumetric flow rate, overall slip factor magnitude, and hydraulic efficiency. The Euler equation relates pumping head to impeller geometry, speed of the impeller, and the flow rate of the fluid [33]. For the impeller configuration shown in Fig. 4, this equation is given by

$$H_{th} = \frac{1}{g}(U_2 C_{u2} - U_1 C_{u1}) \tag{1}$$

With the present impeller arrangement, shown in Figs. 1 and 2, the rotating hollow interior of the RSP transfers momentum to the passing fluid through viscous forces. This "preswirl" can be significant on a millimeter- or micrometer-scale, especially when the ratio of the hollow interior length to diameter is large and the circumferential wall velocity is greater than the average axial fluid velocity. The preswirl may aid the overall pumping process by reducing the sudden acceleration of the fluid at the inner blade tip, which may reduce the flow separation near the leading edge of the impeller blade. Tangential components of absolute velocity are also induced at the inlets of the slots that make up the pump impeller. The spatially averaged magnitude of this tangential fluid motion can be characterized using αU_1. The contribution to theoretical head is then contained in the last term of Eq. (1), which can then be expressed using $U_1 C_{u1} = \alpha U_1^2$. This imposed inlet swirl then reduces the work required by the impeller blades, for a particular magnitude of induced overall pressure rise for the pump.

In general, even though some local swirling motions may be induced near the slot inlets, the overall effects of the inlet swirl on the present pump configuration are believed to be relatively small, and so they are neglected to give $\alpha \approx 0$ and $C_{u1} = 0$. The Euler equation, with no inlet preswirl, or no prerotation of the fluid at the inlet of the impeller, is then employed to analyze the present experimental data. The corresponding form of this theoretical head equation is given by

$$H_{th} = \frac{1}{g}(U_2 C_{u2}) \tag{2}$$

Fluid slip is present when the actual tangential component of absolute velocity of the flow at the impeller exit C_{u2} deviates from the ideal value ($C_{u2,i}$) given by the outlet blade angle β_2 [34] as given by

$$C_{u2,i} = U_2 - \frac{\cot(\beta_2) Q}{\pi D_2 h} \tag{3}$$

Slip thus occurs when the flow through the pump deviates from the exact contours of the impeller blades [34]. In the present study, a slip velocity and a slip factor are employed that are defined using equations of the form [35]

$$v_{\theta s} = C_{u2,i} - C_{u2} \tag{4}$$

and

$$\sigma = 1 - \frac{v_{\theta s}}{U_2} \tag{5}$$

Substituting Eqs. (3)–(5) into Eq. (2) then gives an equation for the theoretical pumping head [35], which can be written as

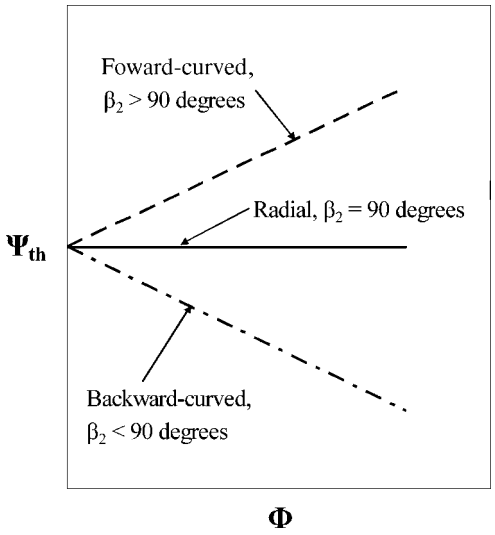

Fig. 6 Idealized trends of nondimensional pump head and nondimensional flow rate for different impeller designs

$$H_{th} = \sigma \frac{U_2^2}{g} - \frac{U_2 \cot(\beta_2) Q}{\pi D_2 h g} \tag{6}$$

The slip factor thus provides a means to relate volumetric flow rate (Q) to Euler or theoretical head H_{th}. Although the actual pumping head H_{act} is given by subtracting the flow losses from H_{th}, the actual $Q-H_{\text{act}}$ characteristics are often well represented by $Q-H_{th}$ characteristics, especially when the flow losses are relatively small. With radial impeller designs, $\beta_2 = 90$ deg and the second term in Eq. (6) is zero. For the corresponding impeller configuration shown in Fig. 5 (with constant rotational speed), the nondimensional theoretical head (Ψ_{th}) is constant as the flow rate increases and represented by the horizontal line in Fig. 6. With forward-curved impeller designs, $\beta_2 > 90$ deg, and constant speed, Fig. 6 shows that nondimensional theoretical head increases as the flow rate increases. Backward-curved impeller designs have $\beta_2 < 90$ deg, and the nondimensional theoretical head decreases as flow rate increases for constant impeller rotational speed, which is also illustrated in Fig. 6. Here, the flow rate and head are normalized using the equations given by

$$\Phi = \frac{4Q}{\pi D_2^2 U_2} \tag{7}$$

and

$$\Psi = \frac{Hg}{U_2^2} \tag{8}$$

Note that Ψ can be given either in terms of H_{th} or H_{act}, which leads to Ψ_{th} and Ψ_{act} respectively.

In the present investigation, the slip factor correlation proposed by Wiesner [36] is used to determine σ magnitudes in the RSP impellers. This correlation is given by

$$\sigma = 1 - \frac{\sqrt{\sin \beta_2}}{n^{0.7}} \tag{9}$$

Slip-factor correlations proposed by Stodola [37], Stanitz [38] and Paeng and Chung [39] are not employed because the values produced from these correlations are unrealistic and unreasonable for the RSP impellers tested.

The actual measured head H_{act}, measured between the pump inlet and outlet (described earlier), is generally less than the theoretical head given by Eq. (6) since H_{th} represents the work imposed onto the fluid around the circumference of the pump impeller. The actual measured head (H_{act}) is based on the fluid density, gravitational constant, and the pressure measurements made at pressure ports 1 and 2 (shown in Fig. 2), and is given by

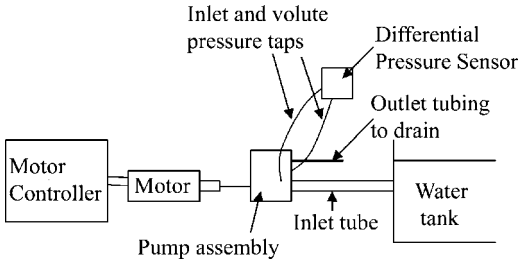

Fig. 7 Experimental testing apparatus. Differential pressure sensor measures pressure rise across the pump. Motor controller has an output signal for shaft speed and motor current.

$$H_{\text{act}} = \Delta P / \rho g \tag{10}$$

Hydraulic efficiency accounts for the flow losses in the volute between the circumference of the pump impeller and locations at the pump inlet and outlet. As such, hydraulic efficiency relates H_{th} and H_{act} and is determined using

$$H_{\text{act}} = H_{th} \eta_H \tag{11}$$

With the slip factor, the hydraulic efficiency is then a useful parameter for characterizing the performance of the different impeller designs, volute arrangements, and pump configurations. The Wiesner [36] slip-factor correlation is widely used for macroscale centrifugal impellers and also provides viable representations of physical behavior for micro and miniscale pumps. The Wiesner slip correlation is employed for analysis of the miniscale pumps of the present study because most other slip-factor correlations [37–39] give values that are physically implausible.

Experimental Apparatus and Procedures

The rotary shaft pump is powered by an externally mounted Maxon EC32 number 118891, brushless DC motor that is 32 mm in diameter, with an 80 W power rating. The maximum speed is 25,000 rpm, with a stall torque of 0.35 N-m. The maximum testing speed is limited by the maximum speed of the optical encoder (16,000 rpm) attached to the motor shaft. The motor has a torque constant of 7.45 mN-m A^{-1} and a voltage constant of 1281 rpm V^{-1}. The brushless motor is controlled by an Advanced Motion Controls power amplifier (Model #BE12A6). The power amplifier has a DC supply voltage of 40 V, a peak current of 12 A, and continuous current rating of 6 A. A negative feedback controller is employed to maintain constant speed for any variation in torque. The speed is controlled by adjusting a 15-turn potentiometer. The speed range is 100–15,300 rpm. The motor controller determines the rotational speed from the signal from an optical encoder attached to the motor shaft. This apparatus produces a voltage signal that is proportional to speed and one that is proportional to motor current. These voltages are measured using a Keithley 131 Digital Multimeter.

The test setup is shown in Fig. 7 and includes a water reservoir, which is large enough that the water-level change during operation is negligible. The outlet channel is connected to the outlet tubing. All outlet tubing is a constant length of 89 mm. The inside diameters of the outlet tubing are changed to throttle the outflow of the rotary shaft pump. The outlet tubing inside diameters (D) are 0.254, 0.508, 1.397, and 4.5 mm. The outflow of the RSP is also throttled using a valve at the exit of the 1.397 mm outlet tubing. The pump housing is mounted to the base of a linear slide. The brushless motor and coupling shaft are mounted to the shuttle of the linear slide. The coupling shaft is used to connect the impeller shaft with the motor shaft. The coupling shaft is made from aluminum and is secured by ball bearings at each end. The rotary

shaft pump impeller shaft is connected to the coupling shaft. The position of the shuttle, along with the motor and impeller shaft, are adjusted and secured using 4-40 positioning bolts. There is one positioning bolt at each of the two ends of the shuttle, such that one positioning bolt is used to adjust the position and the other is used to immobilize the shuttle. A microscope is used to aid the positioning of the impeller shaft by means of the positioning bolts. The microscope is an Infinevar Continually-Focusable Microscope (CFM) (0-330X magnification), manufactured by Infinity Photo-Optical Co., with a Hitachi HV-C20U-S4 video camera connected to a Sony Tinitron PVM-14N5U high-resolution monitor.

The pressure ports in the pump housing, shown in Fig. 2, are connected to a DP-15 differential Validyne pressure sensor through two tubes. The pressure-sensor diaphragm used in this transducer has a full range of 0–3.5 kPa. The range of pressure measurements during testing is 0–2.1 kPa. The output signal from the pressure sensor is processed using a Celesco Model No. CD10D Carrier Demodulator, which produces a voltage output that is proportional to pressure. The voltage is measured by a Keithley 131 Digital Multimeter.

A type-T thermocouple made by Omega Engineering Inc. (Part No. TT-T-36-SLE) is used in several experiments to determine the temperature rise through the impeller. Figure 2 shows that the thermocouple is positioned next to the sidewall of the volute, about 2 mm from the outer surface of the shaft. The signal from the thermocouple is measured by an HP 3497A data acquisition control unit that electronically compensates for a reference voltage level at 0 °C. Temperature measurements indicate that the water temperature increases 1–2 °C while traveling through the impeller for rotational speeds of 1000–15,300 rpm. Because of the small range in temperature rise, the condition of constant fluid properties is a good assumption for the water employed as the working fluid.

Pump assembly starts by connecting the impeller shaft to the coupling shaft on the motor. The bottom housing is then mounted to a plate on the face of the linear slider, and the position of the slots is adjusted so that the bottom of the slots is flush with the top surface of the bottom housing. The volute is positioned and secured in place. The top housing is secured and tightened to minimize leakage. The inlet and outlet tubes are then connected to the top housing. After assembly and positioning of the impeller shaft and housing, all the air is bled from the system using a syringe attached to the end of the inlet tubing. This includes the inlet channel, outlet channel, and tubing to and from the pressure sensors. After these steps are completed, testing is comprised of the following procedures: (i) The system is flushed to ensure there are no air bubbles or trapped particulates in the pumping chamber; (ii) the pump motor is activated and adjusted to produce the desired speed; (iii) the pump then continues to operate at constant speed until steady state is reached, which usually requires 20–30 s, and (iv) the timer is started, and water from the outlet tubing is collected. Output signals related to shaft rotational speed, motor current, pressure rise, and volumetric flow rate are then collected. The volumetric flow rate is determined by dividing the amount of water collected by the collection time. The motor torque is determined by multiplying the motor current obtained from the motor controller by the torque constant of the motor. All data are recorded, and then entered and processed using a Dell Latitude laptop computer with a 1.15 GHz Pentium III processor, 256 MB RAM, with a Microsoft Windows XP Professional operating system, and Microsoft Excel XP software.

Experimental Uncertainty Analysis

A first-order uncertainty analysis is performed using constant-odds combination method, based on a 95% confidence level as described by Moffat [40]. Table 1 presents uncertainties associated with experimental data. The uncertainty is greatest at low rotational speed, and pressures, due to the small signal to uncertainty ratios. The uncertainty decreases significantly as the rotational speed and pressure increase.

Table 1 Uncertainties associated with experimental data

Variable	Percent uncertainty at 2640 rpm	Percent uncertainty at 7920 rpm	Percent uncertainty at 15,300 rpm
H_{th}	5	2.5	2
H_{act}	15	3	1
η_H	15	3	2
Q	2	2	2
T	10	5	2

Results and Discussion

The experimental results are presented in three sections. The first section discusses head and flow-rate variations for the radial two-, four-, and six-blade; backward-curved four-blade; and forward-curved four-blade impeller configurations for a constant rotational speed. The second section discusses the performance characteristics of the radial six-blade and the backward-curved four-blade impellers over a range of rotational speeds. Here, each impeller design is tested using outlet tubing diameters of 0.254, 0.508, 1.397, and 4.5 mm of the same length or by partially closing a valve located at the exit of the outlet tubing with a 1.397 mm i.d. The third section discusses the slip factor and hydraulic efficiency of all the rotary shaft pump (RSP) impellers.

Trends for Different Impeller Designs. The variations of idealized nondimensional head with nondimensional volumetric flow rate for macroscale pumps with different impeller blade configurations are shown in Fig. 6. Figure 8 shows actual nondimensional head with nondimensional flow rate for different RSP impeller designs, all for an impeller rotational speed of 10,710 rpm. To obtain the data presented in Fig. 8, the flow is throttled in the rotary shaft pump experiments by changing the inside diameter of the outlet tubing, or by partially closing a valve located at the exit of the outlet tubing with a 1.397 mm inner diameter. All outlet tubing is a constant length of 89 mm. The flow circuit determines the head requirements for a given flow rate through the tubing and pump and can be determined using the Darcy friction factor and

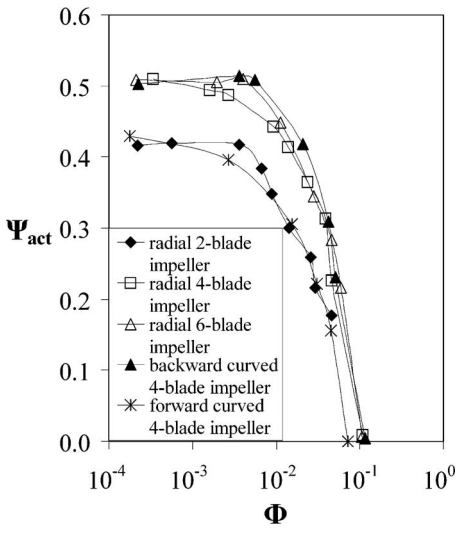

Fig. 8 Variation of nondimensional pumping head with nondimensional volumetric data for different impeller designs, where each data set is obtained at a constant impeller rotational rate of 10,710 rpm

minor loss correlations for expansions and contractions [33]. By decreasing the outlet tubing diameter, with constant length, the flow resistance out of the pump is changed, which changes the pressure rise and flow rate for a constant rotational speed. This arrangement is thus used to provide information on the performance of the rotary shaft pump over a range of rotational speeds, flow rates, and pressure rises.

For each impeller configuration (operating at constant impeller rotational speed), Fig. 8 shows that increasing the exit tube diameter, or more fully opening the exit valve, gives a higher volumetric flow rate through the pump, which, for the impellers tested, gives lower magnitudes of nondimensional head for flow rates greater than 5 ml/min. Qualitative trends of Fig. 8 data for each impeller configuration (at constant impeller rotational speed) are similar for $Q>5$ ml/min, or $\Phi>0.014$. Here, different data sets have similar slopes, sometimes with different ranges of pump head. At lower volumetric flow rates, data sets for different impeller configurations sometimes show completely different slopes, as well as different quantitative trends. Overall, data trends shown in Fig. 8 are similar to ones also observed at impeller rotational speeds of 1530 and 15,300 rpm.

Pumping head magnitudes produced by the impeller generally decrease as the flow rate is increased (as outlet tubing diameter increases) for a constant rotational speed. For the backward-curved four-blade impeller, one contributor for the head reduction at higher flow rates is the reduction in Euler work due to the increasing relative velocity at the exit of the impeller. For the forward-curved four-blade impeller, the Euler work should increase with increased flow rate, and therefour the lower head generation at higher flow rates suggests much higher flow losses compared to the backward-curved impeller. Note that for a volumetric flow rate of $Q=10$ ml/min$=1.66\times10^{-7}$ m^3/s, the average fluid velocity in the 1.168 mm bored hole of the RSP impeller is 0.156 m/s. The head reduction at higher flow rates is also associated with a decrease of hydraulic efficiency, which is related to overall impeller behavior, and to increased hydrodynamic losses as flow rate increases. This is discussed further later in the paper.

Performance Characteristics of Pumps with Backward-Curved Four-Blade and Radial Six-Blade Impellers. Figures 9(*a*) and 9(*b*) show the non-dimensional variation of actual head with flow rate for the radial six-blade impeller and for the backward curved four-blade impeller, respectively, for different rotational speeds. The flow rate for each rotational speed is varied by using outlet tubing with inner diameters of 0.254, 0.508, 1.397, and 4.5 mm of the same length or by partially closing a valve located at the exit of the outlet tubing with a 1.397 mm I.D. As the rotational speed is increased, the dimensional head and flow rate also increase for each configuration. Note that the nondimensional Φ-Ψ_{act} data curves for the different impeller speeds tested are similar.

From Figs. 9(*a*) and 9(*b*), the maximum nondimensional flow rate obtained for both impeller configurations is about $\Phi=0.127$, or $Q=64.9$ ml/min at a rotational speed of 15,300 rpm. This maximum flow rate is obtained with an outlet tubing inner diameter of 4.5 mm. The maximum nondimensional head obtained at a rotational speed of 15,300 rpm is about $\Psi_{act}=0.577$, or $H_{act}=2.1$ kPa for both impeller configurations. Note that greater pressure rises and greater flow rates are present at higher rotational speeds.

The data given in Fig. 9 are given for the backward curved four-blade impeller and the radial six-blade impeller because these produce the highest pressure rise at a particular flow rate and also have the highest hydraulic efficiency at a particular volumetric flow rate. Of the pumps tested, the best millimeter-scale pump has backward-curved blades, and 4–6 impeller blades.

Figures 10 and 11 show the dimensional actual head and flow rate as they depend on rotational speed for the radial six-blade impeller and for the backward curved four-blade impeller, respectively. The data shown in Figs. 10 and 11 are obtained using rotational speeds from 1530 to 15,300 rpm and outlet tubing inner diameters of 0.0254, 0.508, and 1.397 mm of the same length. From the data presented, it is apparent that the flow rate can be changed easily by adjusting the rotational speed of the impeller and by changing outlet tubing diameter and length.

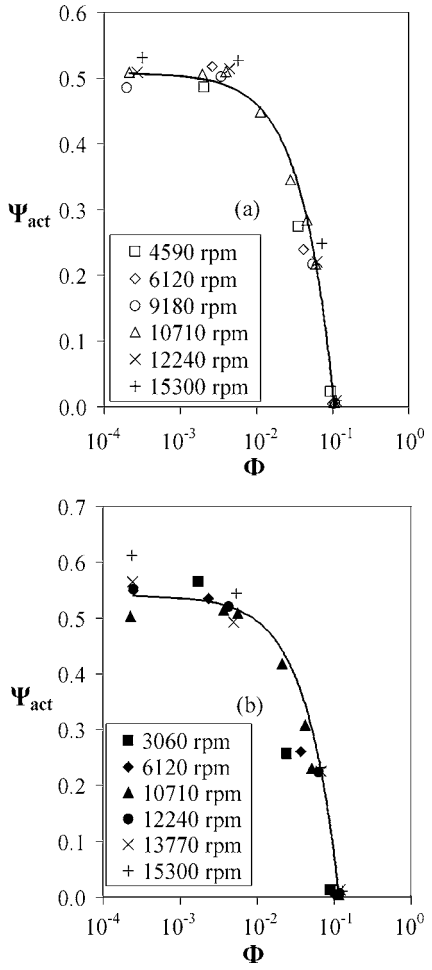

Fig. 9 Nondimensional pressure-rise and flow-rate data for the (*a*) radial six-blade and (b) backward-curved four-blade impellers for different rotational speeds. Flow rate is varied by using outlet tubing of different inner diameter from 0.254 to 4.5 mm, or by partially closing a valve on the end of the 1.397 mm outlet tubing.

Hydraulic Efficiency and Slip Factor for All Impeller Configurations. Figure 12 shows hydraulic efficiency and nondimensional flow-rate variations for all the tested impellers. The data shown in Fig. 12 is a combination of all experimental data taken at rotational speeds between 1530 and 15,300 rpm and with the different outlet tubing diameters. Note that all hydraulic efficiency values are determined without accounting for any inlet swirl. Table 2 shows the slip factor magnitudes for the different impeller configurations. Note that the slip factor correlation from Eq. (9) gives values that are independent of flow rate and rotational speed. In Fig. 12, overall, the hydraulic efficiency decreases as flow rate increases. This is tied to impeller performance at higher flow rates. Note that greater viscous stresses are also present at higher flow rates because of larger velocity gradients. The maximum value of hydraulic efficiency is 0.87, which is obtained with the backward-curved four-blade impeller at a flow rate of $Q=0.12$ ml/min, or $\Phi=2.35\times10^{-4}$. The average magnitude of η_H decreases by 57% for the backward-curved four-blade impeller

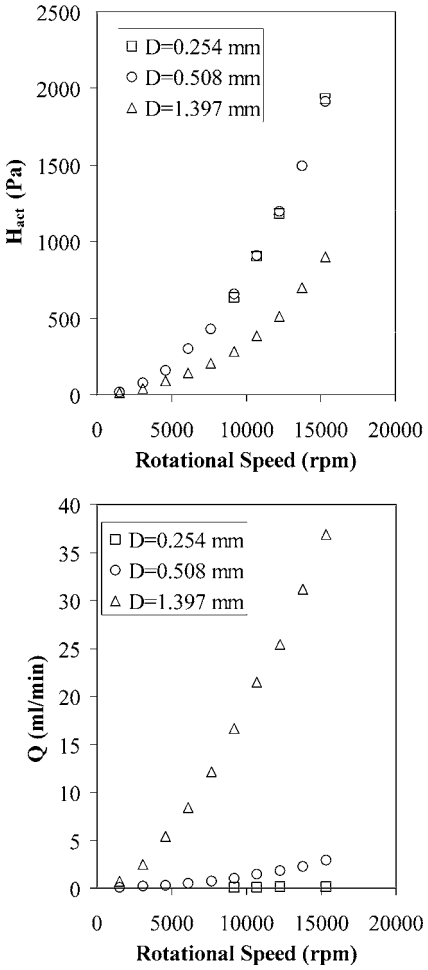

Fig. 10 Pressure-rise and flow-rate data for different rotational speeds for the radial six-blade impeller. Data are taken with impeller rotational speeds from 1530 to 15,300 rpm.

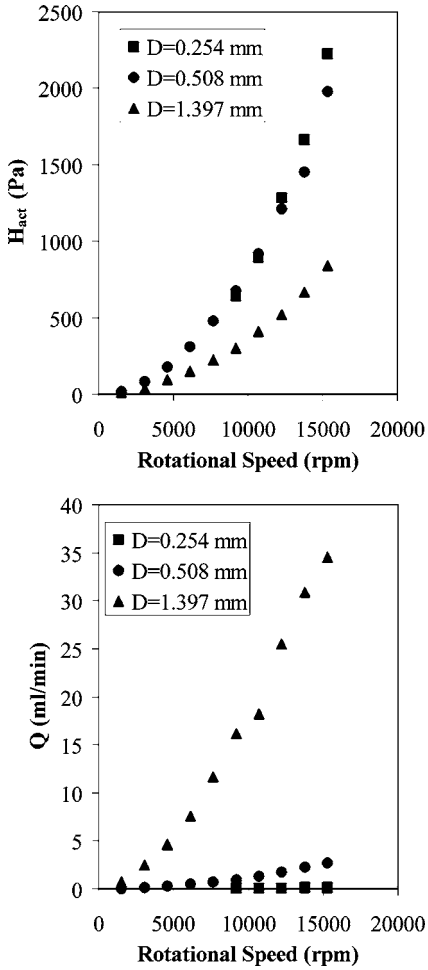

Fig. 11 Pressure-rise and flow-rate data for different rotational speeds for the backward-curved four-blade impeller. Data are taken with impeller rotational speeds from 1530 to 15,300 rpm.

as the flow rate increases to $Q=34.5$ ml/min or $\Phi=0.068$. There is also a difference of 22% in the average magnitude of η_H between the backward-curved and forward-curved four-blade impellers at flow rates of <5 ml/min. This implies that both the impeller design and flow rate are significant, but the flow rate has a more significant effect on the performance of the rotary shaft pump. Also, note that the motor torque increases from 2.7 to 4.5 mN-m as the rotational speed increases from 1530 to 15,300 rpm for the backward-curved four-blade impeller. Similar changes of motor torque are observed for all impeller blades tested for the same rotational speeds.

The most efficient impeller configurations are the radial six-blade and backward-curved four-blade impellers. The impeller configurations with the lowest hydraulic efficiency are the radial two-blade and forward-curved four-blade impellers.

Summary and Conclusions

A novel millimeter-scale rotary micropump called the rotary shaft pump (RSP) is developed, characterized, and tested. The top and bottom of the impeller blades of this device are integral parts of the rotary shaft, which serves as the inlet duct passage to the impeller. This arrangement increases reliability with well-supported impeller blades and reduces risk of blade damage due to contacting the top pump housing. The device is mechanically robust and easy to manufacture. The hollow interior of the RSP transfers momentum to the passing fluid, which may aid the pumping process by inducing circumferential momentum at the inlets of the impeller blades.

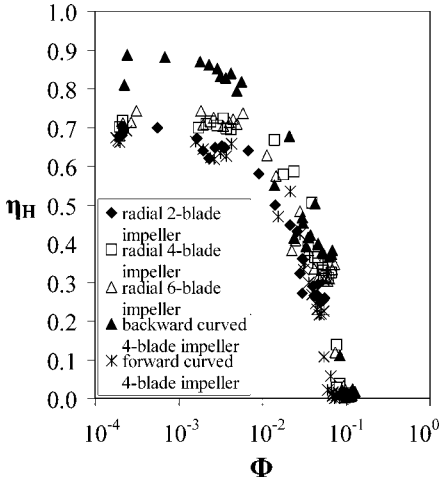

Fig. 12 Hydraulic efficiency for the different impeller configurations as dependent nondimensional volumetric flow rate. Data are taken with impeller rotational speeds from 1530 to 15,300 rpm.

Table 2 Slip factors obtained from Eqs. (5) and (9) for various impellers

Impeller configuration	Slip factor (σ)
Radial 2-blade impeller	0.384
Radial 4-blade impeller	0.621
Radial 6-blade impeller	0.715
Backward-curved 4-blade impeller	0.622
Forward-curved 4-blade impeller	0.638

The tested pump impeller is 2.38 mm in diameter, the height of the impeller blades is 380 μm, and the impeller speed varies from 1530 to 15,300 rpm. The bored hole in the impeller shaft is 1.168 mm in diameter, as seen in Fig. 1. Similar pressure versus flow rate slope characteristics for all impeller designs, and the differences relative to macroscale arrangements, provide evidence that the trends of these data are influenced by viscous forces, as well as by the impeller design (backward-curved, forward-curved, radial blades). Centrifugal-inertial forces also play an important role, since greater centrifugal forces are obtained at higher impeller rotational speeds, which generally increase pumping head magnitudes. By keeping the rotational speed constant and changing the flow rate by varying the outlet tube diameter and outlet valve, the pumping head is shown to decrease with increased flow rate. Such behavior is associated with overall impeller behavior and with increased hydrodynamic losses as flow rate increases.

The hydraulic efficiency changes by as much as 22% between different impeller configurations (i.e., the radial two-blade and backward curved four-blade impeller designs) for the same flow rate. The hydraulic efficiency for all impeller configurations decreases significantly for flow rates of >5 ml/min, or for $\Phi > 0.014$, due to the increased hydrodynamic losses. The highest hydraulic efficiency of 0.87 is produced by the backward-curved four-blade impeller with a rotational speed of 15,300 rpm and a flow rate of 0.12 ml/min, or a Φ value of 2.35×10^{-4}.

The performance of the RSP shows that pressure rise and flow rate increase for a constant outlet tubing diameter as rotational speed increases. The present millimeter-scale RSP produces flow rates up to 64.9 ml/min. Figure 13 shows the maximum flow rate for the RSP relative to the flow rate of several other different micropumps [2–13,17–27]. The typical size is defined as the membrane diameter, or the pumping chamber width. The flow rate of the RSP is larger than many other micropumps of similar size, as seen in Fig. 13, which generally reach flow rates only up to about 16 ml/min. Figure 14 shows the pressure and flow rate of the backward-curved four-blade impeller at different rotational speeds relative to the maximum flow rate and maximum pressure

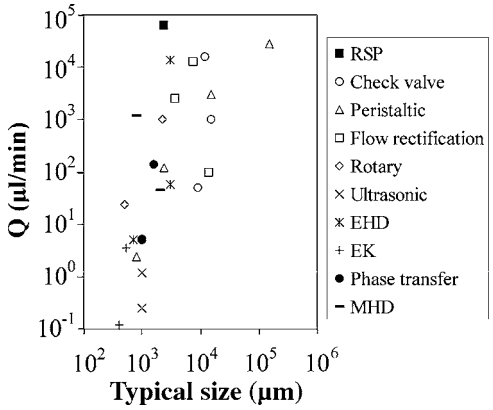

Fig. 13 Flow rate and typical size for various micropumps. Typical size is defined by the impeller diameter, diaphragm diameter, or pumping channel width [2–13,17–27].

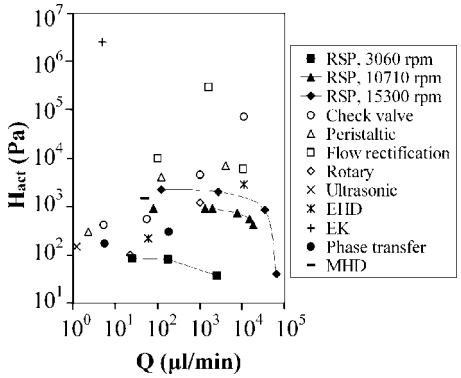

Fig. 14 Pressure-rise and flow-rate data for various micropumps. For all points other than the RSP, the data corresponds to the maximum flow rate and maximum pressure. The data shown for the RSP is for the backward-curved four-blade impeller [2–9,11,13,17–20,23–26].

rise of other micropumps [2–9,11,13,17–20,23–26]. Larger-scale versions of the rotary shaft pump may be ideal for applications in blood pumping, and ventricle assist devices [28–30], chemical analysis systems, drug delivery, and electronics cooling. Smaller-scale versions are ideally suited for chemical analysis systems, μ-TAS, and drug delivery.

Acknowledgment

Work presented in this paper was supported by the National Science Foundation (NSF) through the IGERT Program, Grant Number DGE 9987616.

Nomenclature

C_{ul} = tangential component of the absolute fluid velocity at the impeller blade inlet
C_{u2} = tangential component of the absolute fluid velocity at the impeller blade outlet
$C_{u2,i}$ = ideal value of tangential component of the absolute fluid velocity at the impeller blade inlet
D = inner diameter of tubing
D_2 = outer diameter of impeller
g = gravitational constant
h = height of blades
H = pumping head
H_{th} = theoretical head or Euler head
H_{act} = actual measured head between pump inlet and outlet
n = number of impeller blades
ΔP = pressure rise across pump measured between pump inlet and outlet
Q = volumetric flow rate
T = motor torque
U_1 = blade speed at the impeller inlet
U_2 = blade speed at the impeller outlet
$v_{\theta s}$ = slip velocity

Greek Symbols

α = impeller inlet swirl factor
β = blade angle
β_1 = inlet blade angle measured relative to the tangential direction
β_2 = outlet blade angle measured relative to the tangential direction
η_H = hydraulic efficiency
ρ = density
σ = slip factor

Φ = nondimensional volumetric flow rate, $\Phi = 4Q/\pi D_2^2 U_2$

Ψ = nondimensional pump head, $\Psi = Hg/U_2^2$

Ψ_{act} = nondimensional actual measured pump head between pump and inlet and outlet

Ψ_{th} = non-dimensional theoretical pump head or Euler head

References

[1] Nhuyen, N.-T., and Wereley, S. T., 2002, *Fundamentals and Applications of Microfluidics*, Artech House, Norwood, pp. 292–337.

[2] Olsson, A., Steeme, G., and Steeme, E., 1995, "A Valve-Less Planar Fluid Pump With Two Pump Chambers," Sens. Actuators, A **47**(2), pp. 549–556.

[3] Tsia, J. H., and Lin, L., 2002, "A thermal Bubble Actuated Micro Nozzle-Diffuser Pump," J. Microelectromech. Syst. **11**(6), pp. 665–668.

[4] Nguyen, N. T., and Huang, X. Y., 2001, "Miniature Valveless Pumps Based on Printed Circuit Board Technique," Sens. Actuators, A **88**(2), pp. 104–111.

[5] Benard, W. L., Kahn, H., Heuer A. H., and Huff, M. S., 1998, "Thin Film Shape-Memory Alloy Actuated Micropumps," J. Microelectromech. Syst. **7**(2), pp. 245–251.

[6] Meng, E., Wang, X.-Q., Jak, H., and Tai, Y.-C., 2000 "A Check-Valved Silicone Diaphragm Pump," *Proc of MEMS '00, 13th Int. Workshop Micro ElectroMechanical Systems*, Japan, Jan. 23–27, IEEE, New York, pp. 23–27.

[7] Gass, V., Van der Schoot, G. H., Jeanneret, S., and DeRooij, N. F., 1994, "Integrated Flow-Regulated Silicon Micropump," Sens. Actuators, A, **43**, pp. 335–338.

[8] Saggere, L., Hagood, N. W., Roberts, D. C., Li, H. Q., Steyn, J. L., Turner, K., Carretero, J. A., Yaglioglu, O., Su, Y. H., Mlcak, R., Spearing, S. M., Breuer, K. S., and Schmidt, M. A., 2000, "Design, Fabrication, and Testing of a Piezoelectrically Driven High Flow Rate Micro-Pump," *Proc. of 12th IEEE Int. Symp. on Applications of Ferroelectrics*, July-Aug, IEEE, New York, Vol. 1, pp. 297–300.

[9] Richter, A., Plettner, A., Hofmann, K. A., and Sandmaier, H., 1991, "A Micromachined Electrohydrodynamic (EHD) Pump," Sens. Actuators, A **29**, pp. 159–168.

[10] Fuhr, G., Hagedorn, R., Muller, T., Benecke, W., and Wagner, B., 1992, "Microfabricated Electrohydrodynamic (EHD) Pumps for Liquids of Higher Conductivity," J. Microelectromech. Syst. **1**(3), pp. 141–146.

[11] Ahn, S. H., and Kim, Y. K., 1998, "Fabrication and Experiment of a Planar Micro Ion Drag Pump," Sens. Actuators, A **70**, pp. 1–5.

[12] Furuya, A., Shimokawa, F., Matsuura, T., and Sawada, R., 1996, "Fabrication of Fluorinated Polyimide Microgrids Using Magnetically Controlled Reactive Ion Etching (MC_RIE) and Their Applications to a Ion Drag Integrated Micropump," J. Micromech. Microeng. **6**, pp. 310–319.

[13] Zeng, S., Chen, C. H., Mikkelsen, J. C., and Santiago, J. G., 2000, "Fabrication and Characterization of Electrokinetic Micro Pumps," 7th Intersociety Conf. on Thermal and Thermomechanical Phenomena in Electronic Systems, CPMT/IEEE, Las Vegas, 2, pp. 31–36.

[14] Hainan, C., Ahaoying, Z., Yong, L., Xiongying, Y., and Yihua, Y., 1997, "A Novel Centrifugal Miniature Pump and Its Medical Application," *Proc. of the 1997 Int. Symp. on Micromechatronics and Human Science*, Oct., IEEE, New York, pp. 115–117.

[15] Kilani, M., Galambos, P., Haik, Y., and Chen, C. J., 2003, "Design and Analysis of a Surface Micromachined Spiral-Channel Viscous Pump," ASME J. Fluids Eng. **125**(2), pp. 339–344.

[16] Sen, M., Wajerski, D., and Gad-el-Hak, M., 1996, "A Novel Pump for MEMS Applications," ASME J. Fluids Eng. **118**(3), pp. 624–627.

[17] Ahn, C. H., and Allen, M. G., 1995, "Fluid Micropumps Based on Rotary Magnetic Actuators," *Proc. of MEMS 1995*, Jan.–Feb., IEEE, New York, pp. 408–418.

[18] Dopper, J., Clemens, M., Ehrfeld, W., Jung, S., Kamper, K.-P., and Lehr, H., 1997, "Micro Gear Pumps for Dosing of Viscous Fluids," J. Micromech. Microeng. **7**(2), pp. 230–232.

[19] Mizoguchi, H., Ando, M., Mizuno, T., Takagi, T., and Nakajima, N., 1992, "Design and Fabrication of Light Driven Micropump," *Proc. of MEMS '92, 5th IEEE Int. Workshop MEMS*, Germany, Jan. 25–28, IEEE, New York, pp. 31–36.

[20] Grosjean, C., and Tai, Y. C., 1999, "A Thermopneumatic Peristaltic Micropump," *Proc. of Transducer '99, 10th Int. Conf. on Solid State Sensors and Actuators*, Japan, June 7–10, IEEE, New York, pp. 1776–1779.

[21] Cabuz, C., Herb, W. R., Cabuz, E. I., and Lu, S. T., 2001, "The Dual Diaphragm Pump," *Proc. of MEMS '01, 14th IEEE Int. Workshop MEMS*, Switzerland, Jan. 21–25 IEEE, New York, pp. 519–522.

[22] Luginbuhl, Ph., Collins, S. D., Racine, G. A., Gretillat, M. A., de Rooij, N. F., Brooks, K. G., and Setter, N., 1997, Flexural-Plate-Wave Actuators Based on PZT Thin Films," *Proc. of MEMS '97*, Jan, 1997, IEEE, New York, pp. 327–332.

[23] Miyazaki, S., Kawai, T., and Araragi, M., 1991, "A Piezoelectric Pump Driven by a Flexural Progressive Wave," *Proc. of MEMS'91, 4th Int. Workshop MEMS*, Japan, Jan. 30–Feb. 4, IEEE, New York, pp. 283–288.

[24] Takagi, H., Maeda, R., Ozaki, K., Parameswaran, M., and Mehta, M., 1994, "Phase Transformation Type Micropump," *Proc. of Int. Symp. on Micro Machine and Human Sciences*, Japan, Oct., IEEE, New York, pp. 199–202.

[25] Geng, X., Yuan, H., Oguz, H. N., and Prosperetti, A., 2001, "Bubble-Based Micropump for Electrically Conducting Liquids," J. Micromech. Microeng. **11**, pp. 270–276.

[26] Hatch, A., Kamholz, A. E., Holman, G., Yager, P., and Bohringer, K. F., 2001, "A Ferrofluidic Magnetic Micropump," J. Microelectromech. Syst. **10**(2), pp. 215–221.

[27] Huang, L., Wang, W., Murphy, M. C., Lian, K., and Ling, Z. G., 2000, "LIGA Fabrication and Test of a DDC Type Magnetohydrodynamic (MHD) Micropump," Microsc. Res. Tech. **6**, pp. 235–240.

[28] Shen, J. X., Tseng, K. J., Vilathgamuwa, D. M., and Chan, W. K., 2000, "A Novel Compact PMSM with Magnetic Bearing for Artificial Heart Application," IEEE Trans. Ind. Appl. **36**(4), pp. 1061–1068.

[29] Wan, S. and Tseng, K. J., 2001, "Novel Bearingless Centrifugal Blood Pump," *Proc. of 4th Int. Conf. on Power Electronics and Drive Systems*, Denpasar, IEEE, New York, Vol. 2, pp. 743–748.

[30] Nishimura, K., Park, C.-H., Akamatsu, T., Yamada, T., and Ban, T., 1996, "Development of a Magnetically Suspended Centrifugal Pump as a Cardiac Assist Device for Long-Term Application," ASAIO J. **42**(1), pp. 68–71.

[31] Karniadakis, G. E., Beskok, A., 2002, *Micro Flows, Fundamentals and Simulation*, Springer, New York, pp. 1–31.

[32] Blanchard, D., Ligrani, P., and Gale, B., 2004, "Rotary Centrifugal and Viscous Micropumps", US Patent Office, Application No. PCT\US2004\028890, International Publication No. WO2005/024230 A2 March 17, 2005 (pending).

[33] Fox, R. W., and McDonald, A. T., 1998, *Introduction to Fluid Mechanics*, 5th Edition, Wiley, New York, pp. 493–522.

[34] Gorla R. S. R. and Khan, A. A., 2003, *Turbomachinery, Design and Theory*, Marcel Dekker, New York, pp. 47–90.

[35] Brennan, C. E., 1995, *Hydrodynamics of Pumps*, Oxford University Press, Cary, NC.

[36] Wiesner, F. J., 1967, "A Review of Slip Factors for Centrifugal Impellers," ASME J. Eng. Power **89**, pp. 558–572.

[37] Stodola, A., 1927, *Steam and Gas Turbines*, McGraw-Hill, New York, Vols I and II.

[38] Stanitz, J. D., 2001, "Some Theoretical Aerodynamic Investigations of Impellers in Radial and Mixed Flow Centrifugal Comressors," ASME J. Appl. Mech., **74**(4), pp. 473–497.

[39] Paeng, K. S., and Chung, M. K., 2001, "A New Slip Factor for Centrifugal Impellers," Proc. Inst. Mech. Eng., Part A **215**(5), pp. 645–649.

[40] Moffat, R J, 1982, "Contributions to the Theory of Single-Sample Uncertainty Analysis," ASME J. Fluids Eng. **104**, pp. 250–260.

Experimental Investigation of Cavity-Induced Acoustic Oscillations in Confined Supersonic Flow

B. Umesh Chandra[1]
e-mail: Umesh.Bhayaraju@dlr.de

S. R. Chakravarthy

Department of Aerospace Engineering,
Indian Institute of Technology - Madras,
Chennai - 600 036, India

The focus of the present work is the acoustic oscillations exhibited by confined supersonic flow past a rectangular cavity of varying length-to-depth (L/D) ratio, with a view to identify optimal dimensions for application in scramjet combustors. Experiments were conducted to study the acoustic oscillations induced by supersonic flow at a Mach number of 1.5 past a rectangular cavity of variable dimensions mounted on one wall of a rectangular duct. The effect of L/D ratio of the cavity on the dominant acoustic modes registered on the wall of the duct opposite to the cavity is investigated. The range of L/D ratio varied is 0.25–6.25. The dominant acoustic modes and the amplitudes are observed to be quite sensitive to L/D ratio in the above range. Shifts in the dominant acoustic modes are observed predominantly for $L/D \approx 0.94$ and $L/D \approx 1.5$. The variation of the Strouhal number with L/D ratio indicates a transition in the modal content in the $0.94 < L/D < 1.5$ range. Further shifts in the dominant frequencies are observed in the $1.5 < L/D < 5.0$ range. Peak amplitudes occur at L/D ratios of around 0.75 and 2.25, with over twice the magnitude at the former than at the latter condition. Time-averaged schlieren visualization indicates the presence of quasi-steady shocks at about 0.75 the length of the cavity for $L/D \leqslant 1$ as opposed to being nearly at the trailing edge for higher L/D ratio. Instantaneous phase-locked schlieren images show the quasi-steady shocks are due to the movement of vortices and compression waves along the length of the cavity. It is also observed that the number of vortices in the shear layer roll up along the length of the cavity increases corresponding to the mode shifts for cavities with $L/D > 1$. Such distinct streamwise oscillations are also observed for cavities with $L/D < 1$, when the length is appreciable. The presence of higher modes in the acoustic oscillations is correlated with shocks produced at the lip of the cavity at a different frequency than the compression waves inside the cavity. [DOI: 10.1115/1.1949642]

Keywords: Cavity-Induced Oscillations, Supersonic Flow, Mode Shifts, Shear Layer Instability, L/D Ratio

Introduction

Supersonic flow past cavities is receiving a lot of attention in recent times in the context of the potential for enhancement of fuel-air mixing and flame-holding in supersonic combustion ramjets [1–4]. Of particular interest is the unsteadiness in the flow field and the consequent emission of acoustic oscillations that could enhance the fuel-air mixing process. The focus of the present study is the choice of dimensions of a rectangular cavity that would produce acoustic oscillations at large amplitude levels for this purpose, in a confined supersonic flow. To this end, the length-to-depth (L/D) ratio of the cavity has to be nearly continuously varied on either side of unity. Furthermore, the phenomena occurring within the cavity has to be understood clearly in conjunction with their effect on the flow field outside the cavity, as the L/D ratio transitions across unity, by means of instantaneous time-resolved flow visualization within and outside the cavity.

Several studies have been reported in the past on flow past cavities in the context of the unsteady loading in weapons bays and wheel wells on aircraft wing surfaces. While these studies focus on flow past cavities as an external flow problem as opposed to the internal flow that is of present interest, the flow phenomena in the vicinity of the cavity are of great relevance here. The pressure oscillations induced due to flow past a cavity falls in the general class of problems relating to coherent oscillations of shear layers impinging on a surface, broadly termed as "impinging shear layer instability" [5]. Rockwell and Naudauscher [6] have presented a review on the nature of the oscillations induced by flow past cavities. Of importance to the present work is their classification of fluid dynamic and fluid-resonant mechanisms of cavity oscillations, both of which could coexist under certain geometrical conditions, such as when the L/D ratio of the cavity is not too much greater than unity. Rossiter [7] has made a distinction between these cavities based on the predominance between random and periodic components of the observed oscillations in the subsonic-to-transonic regime. He has given an empirical formula for the prediction of the different modes as a function of the flow Mach number. Heller et al. [8] have noted, based on whether the fluid-resonant type of cavity oscillations are transverse or longitudinal in nature, that the L/D ratio of the cavity dimensions could be less than unity (deep cavities) for the establishment of transverse waves and greater than unity (shallow cavities) for longitudinal waves. This is in contrast to Rossiter's terminology, wherein cavities with $L/D < 4$ are termed deep. They have also modified the Rossiter's formula recognizing the disparity in the speeds of

[1]Present Address: DLR- German Aerospace Centre, Institute of Propulsion Technology, Linder Höhe, 51147, Cologne, Germany.

Contributed by the Fluids Engineering Division for publication in the JOURNAL OF FLUIDS ENGINEERING. Manuscript received by the Fluids of Engineering Division on August 26, 2003; Final manuscript received March 28, 2005. Associate Editor: Hamid Johari.

sound in the free stream and within the cavity. However, neither formula contains an explicit dependence on the depth of the cavity.

Hankey and Shang [9] have schematically shown the time-resolved events relating to the oscillation of the oblique shock system in the supersonic flow field outside the cavity and its association with the compression waves propagating back and forth along the length of shallow cavities. Zhang and Edwards [10,11] and Zhang [12] have reported experimental and computational works in the free-stream Mach number range of 1.5–2.5 for cavities with $L/D \geq 1$, including tandem cavity configurations. They have showed that amplitude of oscillations attains a peak value for an optimum L/D value of around 2.0. The shear layer dynamics at the lip of the cavity and the pressure oscillations inside and in the outer vicinity of the cavity were elucidated by means of spark-schlieren or interferometric images, and computed vorticity distribution.

Several investigators have worked in the low subsonic Mach number range of the free stream, with some of them spanning a wide range of L/D ratios from geometrically deep cavities to shallow ones [13–15]. One of the primary interests of these studies is to study the effect of the nature of the boundary layer of free-stream flow approaching the cavity leading edge, beside that of the free-stream Mach number in the low range. Some notable theoretical works that have attempted to predict the dominant frequencies include that of Plumblee et al. [16], Covert [17], Bilanin and Covert [18], and Tam [19]. Recently, Arunajatesan and Sinha [20] have reported a hybrid computational approach combining large-eddy simulation and the Reynolds-averaged Navier-Stokes equations to predict the amplitudes of oscillations excited by flow past cavities. Anavaradham et al. [21] have presented experimental and computational results for flow past cavities and shown good comparison between predicted and measured dominant frequencies in the transition regime of the cavity flow as the L/D ratio changes from shallow to square to deep, for a given Mach number. Shieh and Morris [22] have computationally investigated the difference between two- and three-dimensional cavities, and have confirmed earlier observations obtained at low flow speeds that a wakelike behavior is exhibited in two-dimensional cavities, whereas oscillations in a three-dimensional cavity are similar to shear-layer oscillations.

In spite of a large of number of works relating to flow past cavities, a few issues are yet to be addressed clearly. First, the transition between the behavior of shallow and deep cavities does not appear to be clearly demarcated as indicated by Rossiter [7] or Heller et al. [8]. In particular, there are very few works that have focused on supersonic flow past cavities with $L/D \leq 1$. Cavities that are apparently deep (i.e., with $L/D < 1$) could still exhibit longitudinal oscillations of a fluid dynamic nature as opposed to those of an acoustic nature near the cavity lip, if their length is appreciably larger than the length scale of vortex roll-up. Furthermore, it is likely that deep cavities would produce much higher amplitudes of oscillations than shallow ones [6], but this has not been investigated under supersonic free-stream conditions thus far. Second, although several works indicate the prevalence of different dominant modes of the cavity oscillations, the shifts between the dominant modes and the conditions under which they occur have not received much attention. The dynamics of the shear layer at the lip of the cavity and the pressure oscillations within and the shock oscillations outside the cavity in association with the mode shifts are also not clearly understood. Instantaneous visualization of the flow field is needed to understand the effect of the L/D ratio of the cavities on the shifts in the dominant modes and the different cavity flow regimes. This has been investigated by means of phase-locked instantaneous schlieren visualization in the present work. Third, the nature and amplitude of oscillations sensed in the outer flow field, particularly at the wall opposite the cavity in the duct confining the outer flow, and its sensitivity to the L/D ratio of the cavity is of interest in the present study. This is important in the context of the propulsion applications mentioned earlier, wherein the oscillations are considered conducive to enhance the mixing of fuel and air in the combustor. The confinement of the outer supersonic flow could cause reflection of shocks originating from the leading edge of the cavity, and the reflected shocks could, in turn, interfere with the shear layer at the cavity lip and its dynamics, depending on the height of the outer flow duct and the length of the cavity, which could affect the nature of the oscillations sensed at the opposite wall.

Table 1 Cavity dimensions tested in the study

S. No.	Length L (mm)	Depth D (mm)	L/D
1	10	10–40	0.25–1.00
2	15	10–40	0.38–1.50
3	20	10–40	0.50–2.00
4	25	8–34	0.74–3.13
5	30	9–38	0.79–3.33
6	35	8–70	0.50–4.38
7	40	8–92	0.44–5.00
8	50	8–78	0.64–6.25

The present work intends to address some of these issues, at least partially. The dimensions of the cavity are closely varied in order to resolve the mode shifts that occur during transition between transverse and longitudinal oscillations, as the cavity geometry changes from deep to shallow. A significant limitation in the scope of the present work is that it is performed at a single Mach number of the free-stream flow. The effect of the nature of the boundary layer approaching the cavity is also not investigated in the present work, although the conditions are maintained such that the boundary layer characteristics are unaltered throughout the study. Even though the cavity runs all along the width of the test section in the present work, the cross-sectional dimensions of the test section are comparable to the length and depth of the cavity, thus the flow field is expected to be three-dimensional, as confirmed by the shear-layer-like oscillations observed here, similar to that reported by Shieh and Morris [22].

Experimental Details

The experimental test facility has provision to supply compressed air at a maximum stagnation pressure of 10 bar from three reservoirs with a combined capacity of 36 m^3. The stagnation pressure of the flow is maintained at 3.6 bar absolute, and the stagnation temperature is the ambient temperature in the present experiments. The air outlet from the reservoir is connected to a settling chamber with a circular-to-rectangular transition duct. A nozzle is attached to the rectangular end of the transition duct. The top and bottom surfaces of the nozzle are converging and diverging, and the side surfaces are parallel to each other. The area ratio of the nozzle is designed to yield a flow Mach number of 1.5. This is verified by means of a Pitot survey across the flow cross section at the nozzle exit to be within a Mach number band of ±0.01. The divergent portion of the C-D nozzle is expanded to a rectangular cross section of 40 mm height and 30 mm width, which is the same as the test-section cross section. The length of the test section is 180 mm. Rectangular cavities of different dimensions are located along the bottom wall of the test section, 30 mm downstream of the nozzle exit, by a suitable combination of movable and fixed blocks. The cavity dimensions tested in the present study are summarized in Table 1. The length is varied in steps of 5 or 10 mm, but the depth is varied more closely, in steps of 1 or 2 mm, at a given length. The width of the cavity (W=30 mm) spans the entire test section. Figure 1 shows the schematic of the C-D nozzle and the test section. The boundary layer is taken to grow from the nozzle throat, and the Reynolds number of the boundary layer approaching the cavity leading edge is calculated

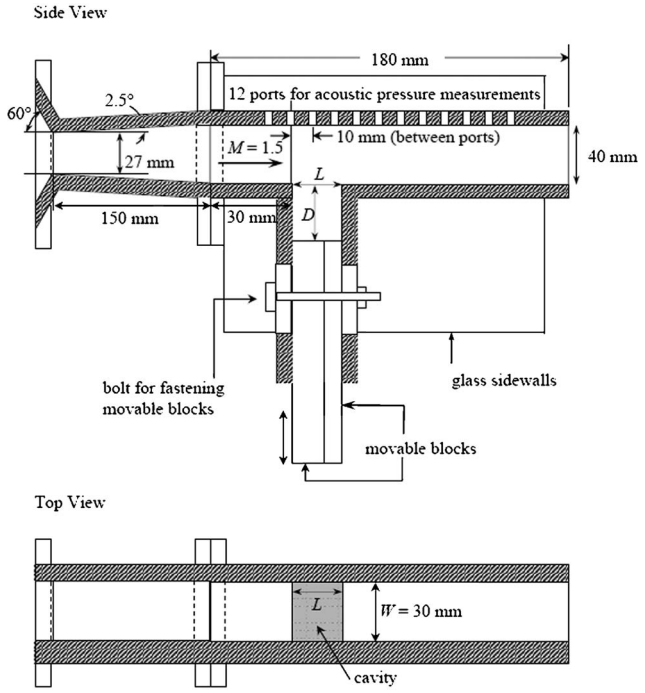

Fig. 1 Schematic of the test section

to be 2.052×10^6. The boundary layer thickness at that location is estimated to be 4 mm, based on the assumption of the 1/7 power law for the streamwise velocity distribution, which has been successfully adopted in computationally predicting the acoustic results of the present study for one length of the cavity in the companion work of Anavardham et al. [21].

The test section is made using Plexiglas walls at the top and bottom surfaces and optically clean glass as sidewalls, for the purpose of acoustic characterization of the cavities and flow visualization. On the top wall of the test section, 12 transducer ports are provided to perform acoustic pressure measurements. The first port at the top wall is located 20 mm downstream of the nozzle exit and is 10 mm upstream of the leading edge of the cavity. The distance between the transducer ports is 10 mm. The measurements are performed on the wall opposite to the cavity, to examine the acoustic field radiated by the cavity into the test section, from the standpoint of the scramjet propulsion applications. Measurements are also performed in a few cases at the leading edge and the bottom walls of the cavity.

Piezoelectric pressure transducers (PCB Piezotronics make, Model No. 112A22, with a sensitivity of 100 mV/psi) are used to perform the acoustic pressure measurements. The signal from the transducer is conditioned using a signal conditioner and fed to a computer through a 12-bit analog-to-digital (A/D) data acquisition board, which can sense signals up to a maximum peak-to-peak voltage level of 5 V. Therefore, the maximum uncertainty in the measurement of the acoustic pressure amplitude is 6 Pa. Since the dominant frequency to be measured is estimated as in the 4–25 kHz range, the sampling frequency is set at 100 kHz. The number of samples taken is 32,768 ($=2^7$). Fast Fourier transform (FFT) is performed on the stored signal with a frequency resolution of 3 Hz. The output of the FFT is used to determine the amplitude of the dominant frequency and its amplitude. The power spectra have been averaged by combining four 3 Hz bins to make the spectra less noisy and obtain consistent data. All the experimental test runs are repeated three times. The variations in the dominant frequencies during the repeated tests are within 20 Hz in the 4–25 kHz range, and those in the amplitudes of the dominant frequencies are $<5\%$ under identical experimental run conditions.

Time-averaged and instantaneous schlieren visualization is performed in the vicinity of the cavity. The field of view in the time-averaged images is larger than in the instantaneous ones. For the time-averaged schlieren, a 150 W halogen lamp is used as a constant point light source. A Pentax SLR film camera with an exposure time of 1 s is used to obtain the time-averaged images. For the instantaneous imaging, a strobe light that gives a spark for about 9 ns duration is used as the source of illumination. The instantaneous images are acquired with a high-speed digital CCD camera (HiSIS 2000 model manufactured by KSV Instruments, Finland) at a framing rate of 2250 frames per second.

When oscillations of discrete frequencies at appreciable amplitudes are observed, the instantaneous schlieren images are phase locked with respect to the acoustic oscillations, in the following manner. A pulse is obtained from the strobe light at every instant when the spark is emitted. These pulses are acquired along with the pressure transducer signal by the A/D data acquisition system, which also simultaneously triggers the image acquisition by the high-speed camera. The time instant in the acoustic cycle when an image is obtained is inferred by comparing the acoustic data with the pulses from the strobe light.

Results and Discussion

Acoustic Pressure Measurements. Strong oscillations are observed mainly between the fifth and tenth ports on the wall opposite to the cavity at a distance of 30–80 mm downstream of the cavity leading edge, depending on the length and depth of the cavity. The maximum amplitudes of the dominant frequencies are observed at the seventh and eighth ports, 50–60 mm downstream of the cavity leading edge, for most of the cavities tested. These locations fall just downstream of the Mach wedge originating from the cavity leading edge and intersecting the opposite wall. Higher modes are also present at the ports where the dominant frequency is observed.

Discrete dominant frequencies with quite high amplitudes are generally observed for most cavity dimensions, but a broadband spectrum of relatively low amplitudes is observed in some cases, such as when the L/D ratio is either large (>5) or for $\sim 0.94 < L/D < 1.5$. Typical spectra for the different cases are shown in Fig. 2. These spectra are recorded at the seventh port, at a distance of 50 mm downstream of the cavity leading on the opposite wall. Despite the low amplitudes, a few discrete dominant frequencies are identifiable in these cases, as opposed to the broadband noise in the 50–100 Pa range (128–134 dB) measured for the flow without any cavity. The low amplitudes at the dominant frequencies for cavities with $L/D > 5$ is due to diminishing of the fluid dynamic feedback mechanism at the free-stream Mach number of 1.5 considered here. It can be seen from the flow visualization images shown later that at this Mach number, the length scale of the vortex roll-up at the leading edge of the cavity is quite small, so that appreciable fluid dynamic feedback does not occur beyond $L/D > 5$. The range of $0.94 < L/D < 1.5$ is considered in greater detail later.

It is important to know whether any difference exists in the frequency excited within the cavity and that measured at the wall of the test section opposite to the cavity. Simultaneous acoustic pressure measurements were performed inside of the cavity on the leading edge wall and at the top wall of the test section. Figure 3 shows the spectra corresponding to the two signals. It can be observed that the same dominant frequencies exist at both the locations. It is also observed that, in most of the cases, the amplitudes inside the cavity are more than those at the opposite wall. The dominant frequencies are the same due to the source of the disturbance being the same, that is, the shear layer oscillations.

The variation of the dominant frequency as a function of depth at constant length of the cavity is shown in Fig. 4. The measurements are performed at the eighth port at a distance of 60 mm downstream of the cavity leading edge on the opposite wall in these experiments. It can be seen that the dominant frequencies

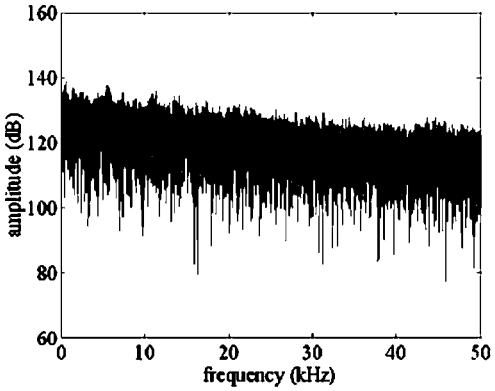

(a) $L = 50$ mm, $D = 47$ mm ($L/D = 1.06$)

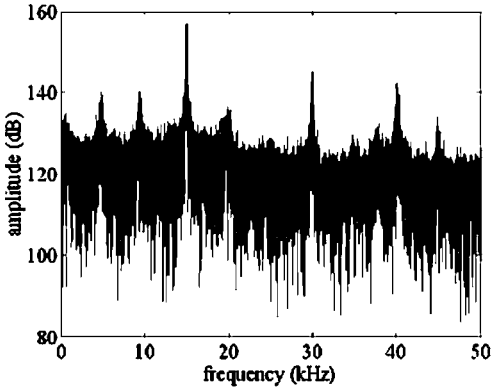

(b) $L = 25$ mm, $D = 14$ mm ($L/D = 1.79$)

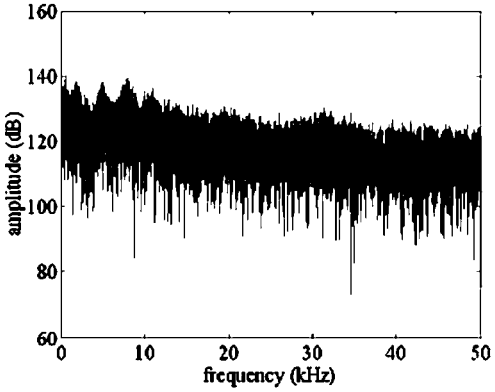

(c) $L = 50$ mm, $D = 7$ mm ($L/D = 7.14$)

Fig. 2 Typical spectra of acoustic oscillations for different cavity dimensions

are higher for smaller lengths. Jumps in the dominant frequencies are observed at different depths for the different lengths of the cavity tested. To highlight this, the variation in frequency with depth for one set of cavities with 40 mm length is shown in Fig. 5 for clarity. The amplitude at the dominant frequency is also plotted alongside as a function of depth in Fig. 5.

No single dominant frequency with significant amplitude is observed up to a depth of 8 mm for the length of 40 mm ($L/D > 5$). It is observed in Fig. 5 that the dominant frequency jumps abruptly at depths of 12, 26, and 40 mm. Note that the depth of 40 mm corresponds to a geometrically square cavity at the length being considered. The amplitudes continue to be low as the depth

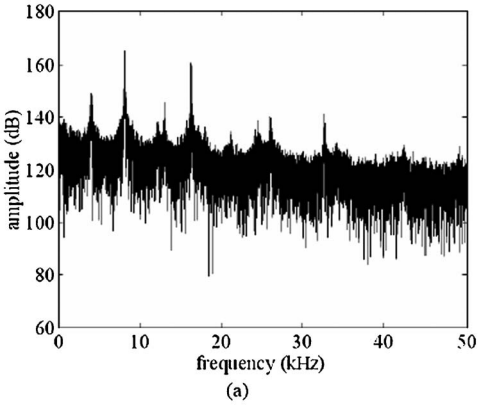

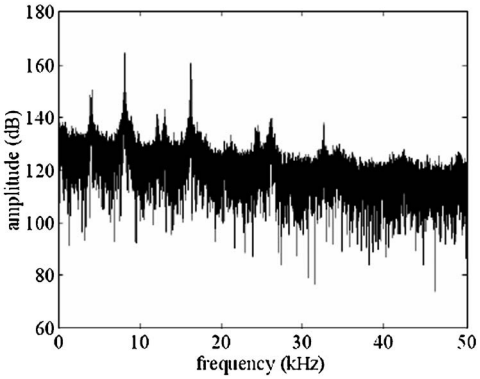

Fig. 3 Spectra of acoustic signals measured (*a*) in the cavity and (*b*) at the wall of the test section opposite the cavity, for a cavity with L=30 mm and D=15 mm(L/D=2.0)

is increased above 8 mm ($L/D < 5$), although a dominant frequency can be identified. The amplitude rises significantly for $L/D < 3.33$ coinciding with the jump in the dominant frequency at 12 mm depth. The depth of 26 mm at this length forms a geometrically shallow cavity ($L/D = 1.54$). The jump in frequencies for $L/D > 1$ is observed for all the cavity lengths tested, as the depth is varied. In the ranges of depth in between the abrupt jumps, the dominant frequency slightly decreases with increase in depth. The amplitude variation attains a maximum in the middle of these ranges and drops to low values at the depths corresponding to the jumps in the dominant frequency. As the amplitude corresponding to the dominant frequency decreases within the range of depth between the jumps, the next dominant frequency to which the jump occurs increases in amplitude simultaneously. Be-

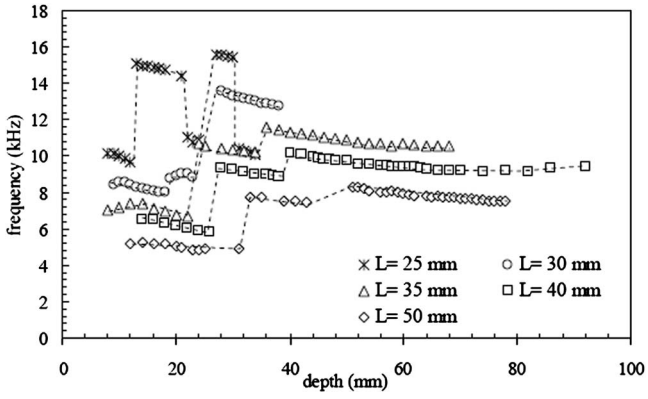

Fig. 4 Effect of cavity depth on dominant frequency for various lengths

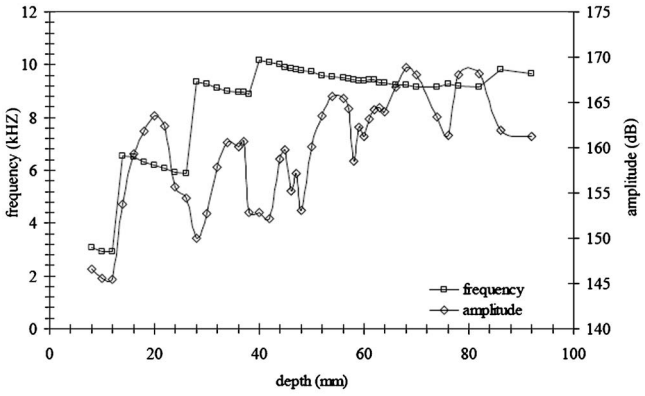

Fig. 5 Effect of cavity depth on frequency and amplitude for cavities with $L=40$ mm

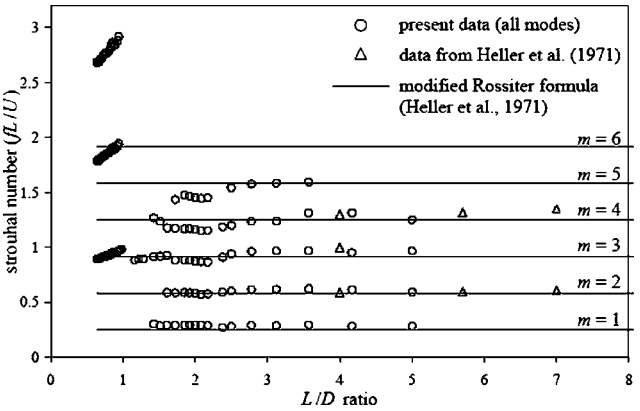

Fig. 7 Effect of the cavity L/D ratio on the Strouhal number based on the cavity length and the various discrete frequencies excited for cavities of 50 mm length. Data from Heller et al. [7] taken for $L/D=4.0$, 5.7, and 7.0 at free-stream Mach number 1.5.

yond the jump in the dominant frequency at a depth of 40 mm ($L/D=1$), there are no further jumps over a large range of depth, signaling a transition in the nature of oscillations between shallow and deep cavities.

The variation in the Strouhal number based on both the length and the depth of the cavity is examined as a function of the L/D ratio of the cavity in Fig. 6. The observed dominant acoustic frequency and the average inlet free stream velocity are used in determining the Strouhal number. It can be seen that all the data for different lengths of the cavity fall on a single set of curves when plotted in this manner. Jumps are observed in the Strouhal number based on both the length and depth of the cavity at L/D ratios of around 0.94 and 1.5. Further, the Strouhal number exhibits multiple values and jumps from one value to the other for $L/D<1$, but most of the data fall on to an approximately constant Strouhal number for $L/D>1.5$–2. The constant value is around 0.45–0.5 when the Strouhal number is based on the cavity length, whereas it is around 0.2 when based on the depth. It is well known that a constant value of the Strouhal number is associated with fluid dynamic oscillations, such as vortex shedding in a recirculation zone. It is evident from the above results that geometrically shallow cavities with $L/D>1.5$–2 exhibit oscillations that are fluid dynamic in nature, accompanied by the shifts in the dominant frequencies observed for these cavities in Figs. 4 and 5. On the other hand, the trends in the Strouhal numbers based on the cavity length and depth with L/D ratio indicate that a nearly constant frequency is excited in the case of geometrically deep cavities ($L/D<1$), dictated by considerations of transverse natural acoustic modes of the cavity along its depth. This is observed in Figs. 4 and 5, as the depth increases beyond the length of the cavity. The multiple values and jumps in the Strouhal numbers in Fig. 6 for the deep cavities indicates that a single dominant acoustic mode is prevalent in the deep cavities without undergoing any jumps as the depth is varied, but the mode could be different for different lengths of the cavity (Fig. 4).

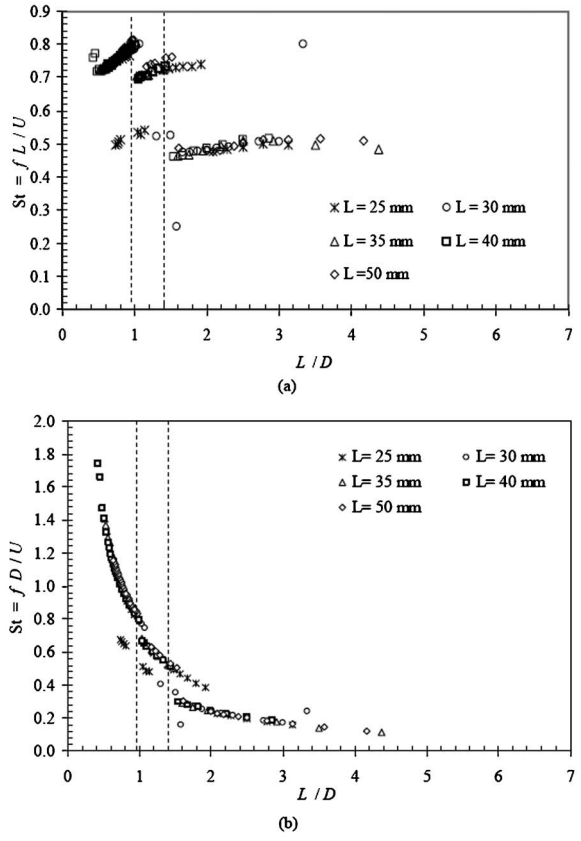

Fig. 6 Effect of L/D ratio on Strouhal number based on (*a*) length and (*b*) depth of the cavity

The data presented in Fig. 6 is extended by considering other prevalent modes besides the dominant modes. The Strouhal number based on the cavity length and the frequencies of the different modes is plotted versus the L/D ratio of the cavity in Fig. 7. The data in Fig. 7 is restricted to a cavity length of 50 mm for the sake of clarity. The modes are counted from the lowest frequency excited. The Rossiter's formula modified by Heller et al. [8] is also calculated for $M=1.5$ and plotted in Fig. 7. Note that both the original Rossiter's formula as well as the modified one used here do not contain any explicit dependence on the L/D ratio of the cavity. Hence, the calculated Rossiter modes are parallel to the abscissa in Fig. 7. Furthermore, the data obtained by Heller et al. [8] for $M=1.5$ at three L/D ratios, all greater than unity, are also plotted in Fig. 7 for comparison. It can be seen that the data obtained in the present work over a wide range of L/D ratio compares very well with the calculated Rossiter modes and the data of Heller et al. [8] obtained at $M=1.5$. The comparison is mainly valid for shallow cavities where data from Heller et al. [8] are available, and for which, Rossiter [7] derived the phenomenological formula, later modified by Heller et al. [8]. For deep cavities, only three modes are seen to be excited as opposed to as many as nine modes distinctly observed in the case of the shallow cavities. The third mode is the most dominant with the deep cavities, but with the shallow ones, it is the second. However, the third and fourth modes are also relatively significant in the latter case.

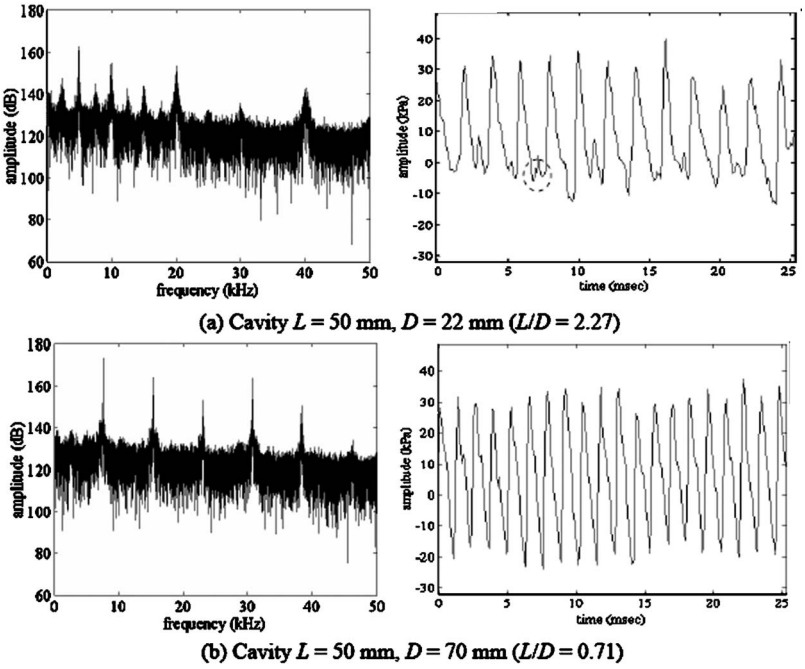

Fig. 8 Real-time acoustic signals along with their respective acoustic spectra for typical shallow and deep cavities

The multiple modes and the jump in the dominant mode from one to the other are due to the dynamics of vortex shedding, splitting, pairing, or merging, and to its interaction with the pressure waves along the length of the cavity, particularly, when the cavity is shallow. Such dynamics is also observed in the case of deep cavities with large lengths, as will be discussed in the next subsection, but they are not dominant when compared to the fluid-resonant mechanism noted earlier.

The difference in the prevalence of a large number of modes for shallow cavities versus fewer modes for deep cavities can be further discerned by looking at the time-series acoustic pressure signals and their corresponding spectra for two cases in Fig. 8, both with a cavity of 50 mm length, but one with a depth of 22 mm (shallow, $L/D=2.27$) and another with a depth of 70 mm (deep, $L/D=0.71$). In the former case, all the modes of the cavity get excited, with one among them being considerably dominant. Some harmonic content, marked by a circle in the time series data in Fig. 8, is observed for the shallow cavity. The higher harmonics are excited by a shock originating at the lip of the cavity and propagating at twice the dominant frequency and along the Mach wedge, as observed from the instantaneous flow visualization discussed in the next subsection. In the latter case, the modes excited are fewer, although they are integral multiples of the dominant mode. The corresponding pressure signal versus time is smoother when compared to that for the shallow cavity. In general, this kind of a transition in the nature of the signal and its harmonic content is observed at the points of frequency jumps, and the signals remain similar until the next frequency jump.

The effect of L/D ratio on the acoustic amplitudes at the dominant frequencies is shown in Fig. 9 both in decibel and kilopascal scales, taking into account all the conditions tested in the present study. As the L/D ratio increases, the amplitude reaches a maximum value in the ranges of 0.5–0.8 and 2.0–2.4. Zhang and Edwards [10] have reported maximum amplitudes for cavity $L/D \sim 2.0$ for a few L/D ratios greater than unity but at three Mach numbers. But it can be seen from Fig. 9 that a maximum observed around L/D ratio of 0.5–0.8 (i.e., deep cavities) is quite higher than that observed with $L/D \sim 2.0$–2.4 (i.e., shallow cavities). In the $0.94 < L/D < 1.5$ range corresponding to the frequency shifts referred to earlier, the amplitudes registered are very low. This range corresponds to a coexistence of transverse and longitudinal modes as shown by Zhang [12], both of which do not register any significant amplitude levels. However, it is important to note that the amplitudes are sensitive particularly to the length of the cavity: larger cavity length excites greater amplitudes in general, even on a decibel scale. Furthermore, this trend is observed even in the

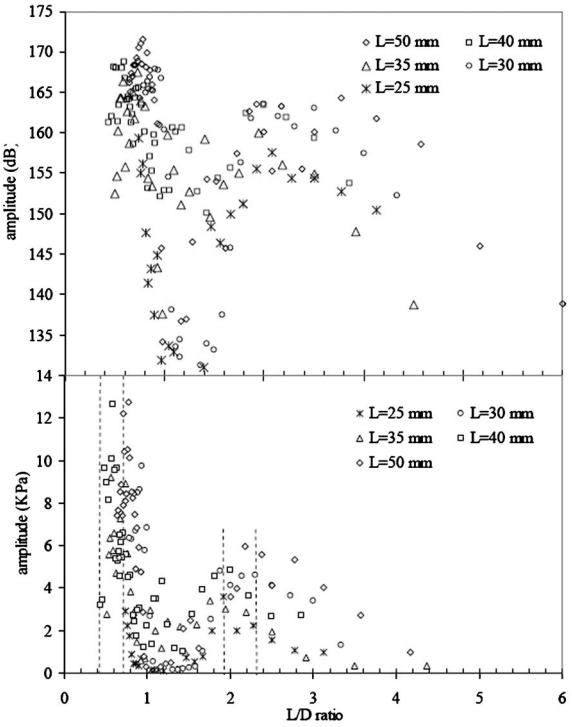

Fig. 9 Effect of L/D ratio on acoustic amplitude at the dominant frequency

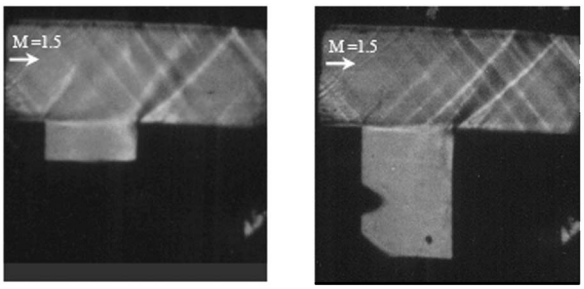

(a) $D = 16$ mm (b) $D = 54$ mm

Fig. 10 Time-averaged schlieren images for a cavity of 40 mm length and different depths

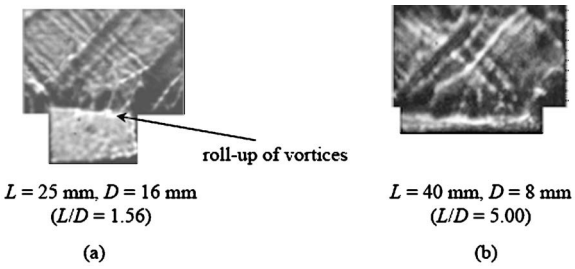

Fig. 11 Instantaneous schlieren images of flow over cavities that do not excite discrete oscillations

case of square cavities. It can be seen from the instantaneous flow visualization images that larger lengths allow for distinct roll up of the shear layer separating from the cavity leading edge and shedding of those vortices along the lip of the cavity, even when the cavities are deep and excite predominantly transverse oscillations.

Flow Visualization. Time-averaged color schlieren imaging was performed to visualize the mean flow field in the vicinity of the cavity. The shock structures for a typical cavity length of 40 mm are shown in Fig. 10 (gray-scale images) for two depths of the cavity. A shock originating from the leading edge of the cavity is clearly visible. The shear layer is also visible at the lip of the cavity for all dimensions, which grows in thickness from the cavity leading edge to the trailing edge. A strong double-shock structure and an expansion fan originating at the trailing edge of the cavity can also be observed. For the shallow cavity with $D = 16$ mm, a region of high density gradient is observed at the corner of the bottom wall and the trailing edge wall in Fig. 10(a). This has been observed more clearly in instantaneous visualization experiments, which are discussed next. This is due to the movement of the vortical structures along the trailing edge and along the bottom wall, following the circulation present at the trailing edge, as described by Zhang [12]. For the deep cavity with $D=54$ mm, the mean density gradients are quite low inside the cavity. In general, this indicates that the mean static pressure variations inside the cavity are not steep, except near the trailing edge, (in Fig. 10(b)). In addition, relatively strong shocks are seen originating at about 3/4 along the length of the cavity from the leading edge for the deep cavity. This is in contrast to the double-shock structure observed in the case of the shallow cavity. These shocks are due to the unsteady nature of the shear layer, as can be seen in the instantaneous visualization presented next. This indicates that the shear layer roll up is of a length scale that is shorter than the length of the cavity considered, even in the case of the deep cavity. For both types of cavities, the reflection of any shocks on the top wall of the test section does not cause shock incidence within the length of the cavity, for the dimensions considered and the test Mach number.

Instantaneous flow visualization is performed to study the unsteady nature of the flow past cavities. As mentioned in the earlier sections, the cavity oscillations are weak when the $L/D > 5$ or for $0.94 < L/D < 1.5$. As can be seen in Fig. 11(a) for the specific case of a cavity with $L=25$ mm and $D=16$ mm($L/D=1.56$) around the above L/D range, the roll up of vortices is confined to a narrow region along the lip of the cavity, but there is not much activity visible inside the cavity and, correspondingly, in the main flow. This indicates a lack of coupling between the shear-layer oscillations and the excitation of the discrete frequencies by the cavity. For the cavity with $L=40$ mm and $D=8$ mm($L/D=5$), shown in Fig. 11(b), it can be seen that the shear layer at the lip of the cavity grows and reaches very close to the bottom wall appreciably ahead of the cavity trailing edge. A movement of large-scale vortical structures in the shear layer is observed, but the shear-layer thickness is comparable to the depth of the cavity itself in this case, leading to a situation approaching that of a closed cavity wherein the shear layer separated at the cavity leading edge attaches to the bottom wall of the cavity rather than at the trailing edge. A shock originating from the shear layer due to the presence of the large-scale structures is also seen at around a third of the length from the leading edge. But, this shock does not appear to be related to propagation of any compression waves inside the cavity [9].

As opposed to the above, cavities that excite discrete oscillations exhibit distinct structures, such as a λ shock due to vortex roll up, weak shock waves associated with the unsteady shear layer, and compression waves traveling back and forth along the length of the cavity. Three cases of cavities with 40 mm length, and depths of 15, 27, and 70 mm are considered here, and their instantaneous schlieren images are phase locked with respect to the dominant frequency (the second mode in this case) to examine the shear layer dynamics. The first two depths correspond to shallow cavities, which are on either side of a jump in the dominant acoustic frequency observed in Fig. 5; the third depth yields a deep cavity. In the case of the cavity with the 15 mm depth, the large-scale structures in the shear layer impinge on the trailing edge, as can be seen in Figs. 12(a) and 12(b). These produce compression waves, which travel in the upstream direction. But the compression wave seen in Fig. 12(b) is not a single wave; rather it is a set of multiple curvilinear waves produced as a result of the interaction with the vortices convecting at the cavity lip and the wall at the bottom of the cavity. These waves impinge on the shear layer at the leading edge of the cavity and alter its characteristic response. This is one of the possible mechanisms of excitation of multiple dominant frequencies in the case of shallow cavities. In Figs. 12(c)–12(f), a λ shock in the free stream is observed to arise from the compression waves propagating inside the cavity. Since these compression waves propagate toward the upstream direction at the speed of sound, the multiple prongs of the λ shock are progressively inclined to form such a structure in association with the compression waves.

Instantaneous schlieren images for a cavity in the transition regime with $L/D=1.48$ are presented in Fig. 13. The images could not be phase-locked in this case because the dominant frequency is not sufficiently strong relative to the other modes. It is important to note the prevalence of two quasi-steady shock waves along the length of the cavity, associated with the shear layer roll up in this case, as opposed to a single system of λ shocks in the external flow distinctly associated with strong compression waves inside the cavity in the previous case. The shear layer is also thinner than in the previous case. This correlates with the jump in the dominant frequency between the two cases, wherein the length scale of the vortex is decreased and the number of vortices along the length of the cavity is correspondingly increased at any instant [21].

For the case of the deep cavity, the phase-locked images are shown in Fig. 14. As in the case of the shallow cavity, compression waves originate from the cavity trailing edge as a vortex

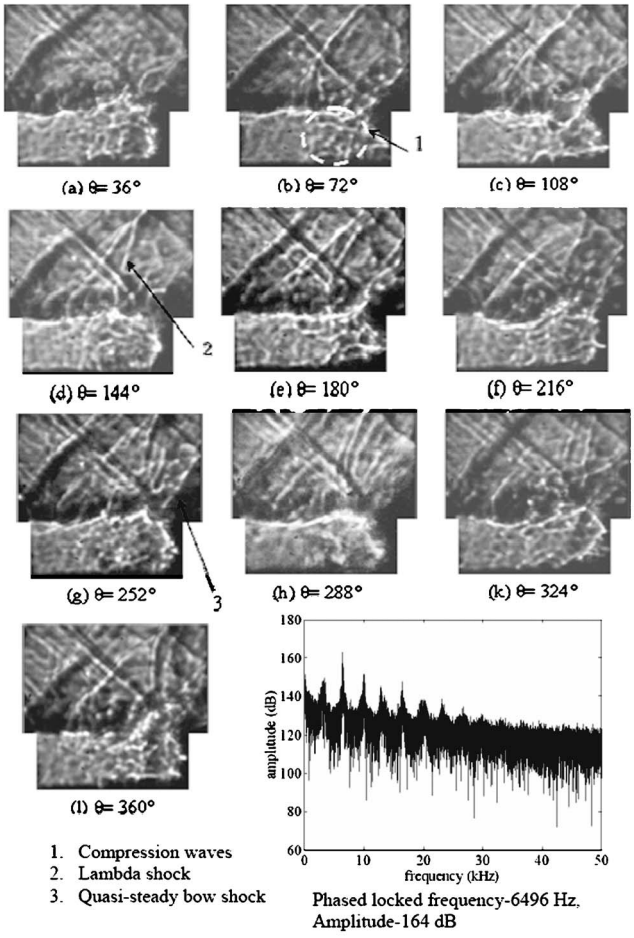

Fig. 12 Phase-locked images and corresponding acoustic spectrum for a cavity with L=40 mm and D=15 mm(L/D =2.67)

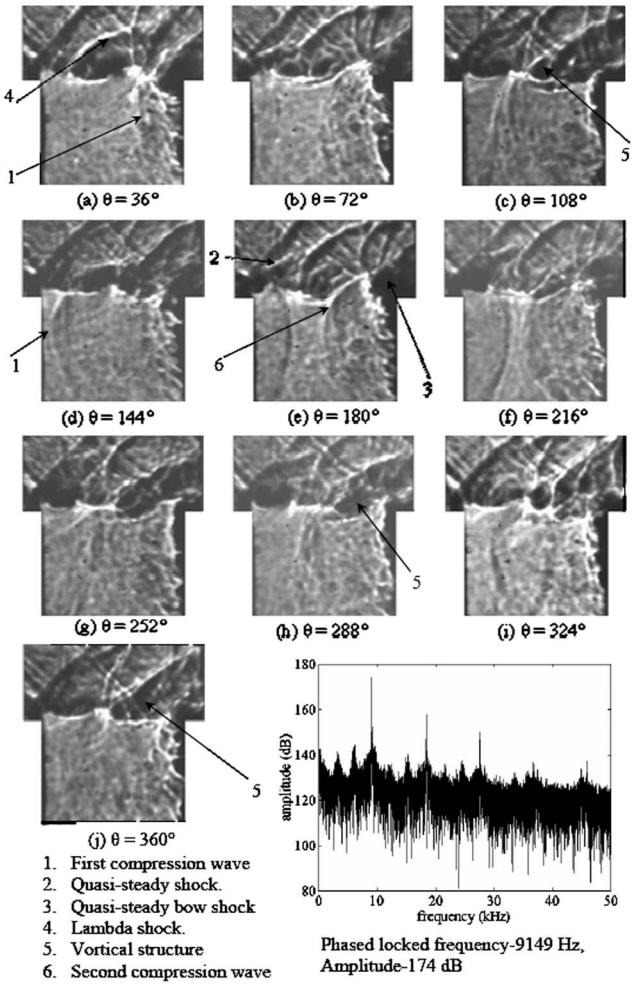

Fig. 14 Phase-locked images and the corresponding acoustic spectrum for a cavity with L=40 mm and D=70 mm(L/D =0.57)

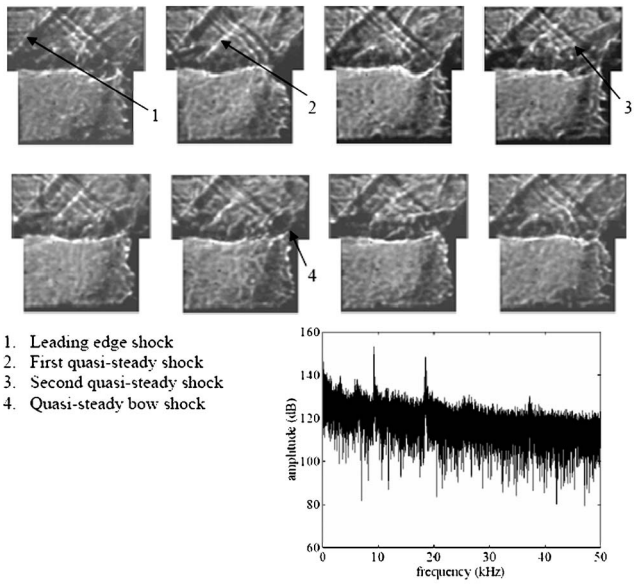

Fig. 13 Instantaneous images at different time instants and corresponding acoustic spectrum for a cavity with L=40 mm and D=27 mm(L/D=1.48)

impinges there (Fig. 14(*a*)) and propagates upstream (Figs. 14(*b*) and 14(*c*)). The vortex is observed to move along the rear wall of the cavity subsequently. Successive compression waves are generated and reflected at the cavity leading edge (Figs. 14(*d*) and 14*e*)). They intersect each other (Fig. 14(*f*)) and momentarily merge (Figs. 14(*g*) and 14*h*)), but subsequently emerge and continue to propagate in their respective directions, probably with reduced strength (Fig. 14(*i*)), and are completely dampened before they reach the walls of the cavity. The cycle is repeated, as seen in Fig. 14(*j*). The λ shock observed in the free stream is formed twice in a cycle, once at the beginning, and again at about 180 deg phase angle. Unlike in the case of the shallow cavity discussed first, the λ shock is formed because of the intersection of two shocks, one attached to compression wave and another emerging due to rollup of the shear layer from the leading edge of the cavity. The shear layer is thicker than in the case of the shallow cavity, and the number of vortices at any instant, correspondingly fewer.

The above description shows that, given sufficient length, significant longitudinal oscillations occur even when the cavity is geometrically deep and the excited acoustic oscillations exhibit transverse modes. This is because the length of the cavity is larger than the lengthscale of vortex rollup in the shear layer at the cavity lip, as indicated by the time-averaged schlieren images.

This shows that the oscillatory behavior of the shear layer cannot be strictly classified as that of shallow or deep cavities solely based on the L/D ratio.

Conclusions

The cavity-induced acoustic oscillations are studied for a free-stream Mach number of 1.5. There exists frequency jumps at L/D ratios of 0.94 and 1.5 of the cavity. The jumps occur when there is change from longitudinal oscillations for shallow cavities with $L/D > 1.5$ to transverse oscillations for deep cavities with $L/D < 0.94$. The amplitudes reach peak values at L/D ratios of around 2.0 and 0.5, respectively. The Strouhal number based on the cavity depth decreases in a hyperbolic fashion from 1.8 to 0.2, asymptotically. The variation in the Strouhal number based on the cavity length shows that for shallow cavities it is constant for increasing L/D ratio, implying that the frequency decreases with length. The time-averaged flow visualization shows the details of the shock structure formed due to the unstable shear layer along the length of the cavity. The instantaneous visualization offers insight into the mechanism of quasi-steady shock formation due to the shear layer rollup and propagation of compression waves inside the cavity for different L/D ratios. The observed mode shifts are explained due to such interaction between the shocks, the shear layer, and compression waves.

Acknowledgment

This work was supported by the Aerodynamics Panel of the Aeronautical Research and Development Board, Ministry of Defence, Government of India.

References

[1] Yu, K. H., and Schadow, K. C., 1994, "Cavity-Actuated Supersonic Mixing and Combustion Control," Combust. Flame **99**, pp. 295–301.
[2] Ben-Yakar, A., and Hanson, R. K., 2001, "Cavity Flame-Holders for Ignition and Flame Stabilization in Scramjets: An Overview," J. Propul. Power **17**(4), pp. 869–877.
[3] Seiner, J. M., Dash, S. M., and Kenzakowski, D. C., 2001, "Historical Survey on Enhanced Mixing in Scramjets," J. Propul. Power. **17**(6), pp. 1273–1286.
[4] Gruber, M. R., Baurle, R. A., Mathur, T., and Hsu, K. -Y., 2001, "Fundamental Studies of Cavity-based Flameholder Concepts for Supersonic Combustors," J. Propul. Power. **17**(1), pp. 146–153.
[5] Rockwell, D., 1983, "Oscillations of Impinging Shear Layers," AIAA J. **21**(5), pp. 645–663.
[6] Rockwell, D., and Naudascher, E., 1978, "Review- Self-Sustaining Oscillations of Flow Past Cavities," ASME J. Fluids Eng. **100**(6), pp. 152–165.
[7] Rossiter, J. E., 1966, "Wind-Tunnel Experiments on the Flow Over Rectangular Cavities at Subsonic and Transonic Speeds," RAE Tech. Report 64037, R & M No. 3438.
[8] Heller, H. H., Holmes, D. G., and Covert, E. E., 1971, "Flow-Induced Pressure Oscillations in Shallow Cavities," J. Sound Vib. **18**(4), pp. 545–553.
[9] Hankey, W. L., and Shang, J. S., 1980, "Analyses of Pressure Oscillations in an Open Cavity," AIAA J. **18**, pp. 892–898.
[10] Zhang, X., and Edwards, J. A., 1990, "An Investigation of Supersonic Oscillatory Cavity Flows Driven by Thick Shear Layers," Aeronaut. J., **94**(940), pp. 355–364.
[11] Zhang, X., and Edwards, J. A., 1992, "Experimental Investigation of Supersonic Flow Over Two Cavities in Tandem," AIAA J. **30**(5), pp. 1182–1189.
[12] Zhang, X., 1995, "Compressible Cavity Flow Oscillation Due to Shear Layer Instabilities and Pressure Feedback," AIAA J. **33**(8), pp. 1404–1411.
[13] East, L. F., 1966, "Aero-Dynamically Induced Resonance in Rectangular Cavities," J. Sound Vib.., **3**(3), pp. 277-287.
[14] Tam, C. K. W., and Block, P. J. W., 1978, "On the Tones and Pressure Oscillations Induced by Flow Over Rectangular Cavities," J. Fluid Mech.. **89**(2), pp. 373–399.
[15] Sarohia, V., 1977, "Experimental Investigation of Oscillations in Flows Over Shallow Cavities," AIAA J. **15**(7), pp. 984–991.
[16] Plumblee, H. E., Gibson, J. S., and Lassiter, L. W., 1962, "A Theoretical and Experimental Investigation of the Acoustic Response of Cavities in an Aerodynamic Flow," WADD-TR- 61–75.
[17] Covert, E. E., 1970, "An Approximate Calculation of the Onset Velocity of Cavity Oscillations," AIAA J. **18**(12), pp. 2189–2194.
[18] Bilanin, A. J., and Covert, E. E., 1973, "Estimation of Possible Excitation Frequencies for Shallow Rectangular Cavities," AIAA J. **11**(3), pp. 347–351.
[19] Tam, C. K. W., 1976, "The Acoustic Modes of a Two-Dimensional Rectangular Cavity," J. Sound Vib.. **49**, pp. 353–364.
[20] Arunajatesan, S., and Sinha, N., 2001, "Unified Unsteady RANS-LES Simulations of Cavity Flowfields," AIAA Paper No. 2001-0516.
[21] Anavardham, T. K. G., Chandra, U. B., Babu, V., Chakravarthy, S. R., and Paneerselvam, S., 2004, "Experimental and Numerical Investigation of Confined Unsteady Supersonic Flow Over Cavities," Aeronaut. J., **108**(1081), pp. 135–144.
[22] Shieh, C. M., and Morris, P. J., 2001, "Comparison of Two- and Three-Dimensional Turbulent Cavity Flows," AIAA Paper No. 2001-0511.

Can F. Delale
e-mail: delale@gursey.gov.tr
Faculty of Aeronautics and Astronautics,
Istanbul Technical University,
34469 Maslak, Istanbul, and
Tübitak Feza Gürsey Institute,
P.O. Box 6,
81220 Çengelköy, Istanbul, Turkey

Kohei Okita
e-mail: okita@fel.t.u-tokyo.ac.jp

Yoichiro Matsumoto
e-mail: mats@mech.t.u-tokyo.ac.jp

Department of Mechanical Engineering,
The University of Tokyo,
7-3-1 Hongo, Bunkyo,
Tokyo 113-8656, Japan

Steady-State Cavitating Nozzle Flows With Nucleation

Quasi-one-dimensional steady-state cavitating nozzle flows with homogeneous bubble nucleation and nonlinear bubble dynamics are considered using a continuum bubbly liquid flow model. The onset of cavitation is modeled using an improved version of the classical theory of homogeneous nucleation, and the nonlinear dynamics of cavitating bubbles is described by the classical Rayleigh-Plesset equation. Using a polytropic law for the partial gas pressure within the bubble and accounting for the classical damping mechanisms, in a crude manner, by an effective viscosity, stable steady-state solutions with stationary shock waves as well as unstable flashing flow solutions were obtained, similar to the homogeneous bubbly flow solutions given by Wang and Brennen [J. Fluids Eng., ***120****, 166–170, 1998] and by Delale, Schnerr, and Sauer [J. Fluid Mech.,* ***427****, 167–204, 2001]. In particular, reductions in the maximum bubble radius and bubble collapse periods are observed for stable nucleating nozzle flows as compared to the nonnucleating stable solution of Wang and Brennen under similar conditions.*
[DOI: 10.1115/1.1949643]

1 Introduction

Recent investigations of steady-state cavitating nozzle flows of homogeneous bubbly mixtures using spherical bubble dynamics with a polytropic law for the partial gas pressure have shown flow instabilities that correspond to nonphysical solutions (e.g., see Wang and Brennen [1] and Delale et al. [2]). The existence of such instabilities has suggested the need for improvements and modifications in the original model equations, especially by introducing the damping mechanisms left out in the description of bubble dynamics. By taking thermal damping into account in a model similar to that given by Prosperetti [3], Delale [4] has shown that the steady-state instabilities encountered in homogeneous bubbly cavitating nozzle flows can disappear to some extent. A recent numerical investigation by Preston et al. [5] shows the possibility that the instabilities in steady-state nozzle flow solutions of homogeneous bubbly mixtures may correspond to bubbly shock waves found in the diverging section of the nozzle and propagated downstream.

The aim of this investigation is to construct and test a cavitating flow model with nucleation. Although bubble formation in most cavitating flows occurs by heterogeneous nucleation, we here use homogeneous nucleation theory due to a lack of a heterogeneous theory with reasonable nucleation rates. For this reason the model equations for quasi-one-dimensional cavitating nozzle flows with spherical bubble dynamics are modified to take into account the effect of bubble nucleation. An improved version of the classical nucleation rate equation for homogeneous bubble nucleation by Delale et al. [6] is applied to determine the onset of cavitation using a parametric investigation, which treats some of the unknown quantities, such as the initial partial gas pressure of the bubble and the initial bubble radius at the onset of cavitation, as parameters. The nonlinear bubble dynamics is described by the classical Rayleigh-Plesset equation. Using a polytropic law for the partial gas pressure and lumping all damping mechanisms together, in a crude manner, in the form of viscous dissipation, quasi-statically stable solutions with or without bubbly shock waves as well as unstable solutions are obtained, similar to the ones obtained by Wang and Brennen [1] in nonnucleating nozzle flows of bubbly liquids. Reductions in the maximum bubble radius and in the collapse periods of bubbles are observed in the nucleating bubbly flow of this investigation as compared to that of Wang and Brennen in nonnucleating bubbly flows.

2 Cavitating Flow Model With Nucleation

In this section we incorporate homogeneous bubble nucleation into the flow equations and introduce a cavitating flow model based on the two-phase homogeneous flow description. In particular, for the reasons we clarify in Sec. 3, we use an improved version of the classical theory of homogeneous bubble nucleation, although most cavitating flows would demand the use of heterogeneous bubble nucleation. We neglect the effects of bubble-bubble interactions and bubble coalescence, which are significant when bubbles grow to relatively large sizes. Bubble fission, which can lead to significant energy dissipation during violent collapses [7,8], is also neglected. The classical damping mechanisms (viscosity, thermal damping, and acoustic radiation) are taken into account, somewhat in a crude manner, by an effective viscosity. A more realistic model, in addition to these effects, would require the use of two fluid equations, one for the gaseous and the other for the liquid phase, together with the interface interactions between the phases. In our opinion, this can be considered separately when a successful cavitation model, based on homogeneous two-phase flow and that accounts for all relevant effects of bubble nucleation and bubble dynamics, is constructed and tested against bubbly cavitating flow simulations in different geometries. In what follows we consider a quasi-one-dimensional cavitating nozzle flow model under the above-stated assumptions. The equations of motion, in this case, can be written as

$$A'\frac{\partial \rho'}{\partial t'} + \frac{\partial}{\partial x'}(\rho' u' A') = 0 \tag{1}$$

$$\frac{\partial n'}{\partial t'} + \frac{1}{A'}\frac{\partial}{\partial x'}(n' u' A') = J' \tag{2}$$

$$\rho'\frac{du'}{dt'} = -\frac{\partial p'}{\partial x'} \tag{3}$$

where p', ρ', u', and n' are, respectively, the mixture pressure, mixture density, mixture flow speed, and number density of bubbles (per unit volume of the mixture), and where t' is the time,

Contributed by the Fluids Engineering Division for publication in the JOURNAL OF FLUIDS ENGINEERING. Manuscript received by the Fluids Engineering Division May 11, 2004; final manuscript received April 2, 2005. Associate Editor: Georghes Chahine.

x' is the nozzle axial coordinate, A' is the cross-sectional area of the nozzle, and $d/dt' = \partial/\partial t' + u' \partial/\partial x'$ is the material or total derivative. The mixture density ρ' is related to the liquid density ρ'_L at some reference pressure p'_0 by

$$\rho' = \rho'_L(1+\rho_c)(1-\beta) \tag{4}$$

where β is the void fraction and where $\rho_c \ll 1$ is introduced to take into account the compressibility of the liquid. For Tait's equation of state of the liquid, it assumes the form

$$1+\rho_c = \left(\frac{p+B'/p'_0}{1+B'/p'_0}\right)^{1/m} \tag{5}$$

where $p \equiv p'/p'_0$ is the normalized pressure and B' and m are constants ($B'=3010$ atm and $m=7.15$ for water). If we further assume that the bubbles are spherical and monodispersed with radius R', the void fraction β is related to the bubble number density n' by the relation

$$\beta = \tfrac{4}{3}\pi R'^3 n' \tag{6}$$

Assuming that the gas phase is sufficiently dilute, the nonlinear bubble dynamics can be described by the classical Rayleigh-Plesset equation as

$$R'\frac{d^2R'}{dt'^2} + \frac{3}{2}\left(\frac{dR'}{dt'}\right)^2 = \frac{p'_B - p'}{\rho'_L} - \frac{4\nu'_L}{R'}\left(\frac{dR'}{dt'}\right) - \frac{2S'}{\rho'_L R'} \tag{7}$$

where S' is the surface tension, ν'_L is the kinematic viscosity of the liquid, and p'_B is the total pressure of the bubble, assumed to be uniform within the bubble and taken as the sum of the partial vapor pressure p'_v and partial gas pressure p'_g as

$$p'_B = p'_v + p'_g \tag{8}$$

Equations (1)–(8) yield a complete system of model equations for quasi-one-dimensional cavitating nozzle flows, which should be supplemented by appropriate initial and boundary conditions (nozzle inlet and exit conditions), provided that the local nucleation rate J' and the partial gas pressure p'_g can be evaluated by some reliable means. Such an evaluation of activated cavitation nuclei by an improved version of the classical theory of homogeneous bubble nucleation will be considered, in detail, in Sec. 3. A polytropic law for the partial gas pressure will be used here solely for comparison with the results of Wang and Brennen [1], despite the fact that thermal conduction and gas diffusion through the bubble should be accurately taken into account. The above governing equations can be simplified if we consider the algebraic relations (4) and (6). It follows from Eqs. (2) and (6) that

$$\frac{d\beta}{dt'} + \beta\left[\frac{\partial u'}{\partial x'} + u'\left(\frac{1}{A'}\frac{dA'}{dx'}\right) - \frac{3}{R'}\frac{dR'}{dt'}\right] = \frac{4}{3}\pi R'^3 J' \tag{9}$$

On the other hand, the continuity equation (1) and Eq. (4) yield

$$\frac{d\beta}{dt'} - (1-\beta)\left[\frac{\partial u'}{\partial x'} + u'\left(\frac{1}{A'}\frac{dA'}{dx'}\right) + \frac{1}{\rho'_L c'^2_L(1+\rho_c)}\frac{dp'}{dt'}\right] = 0 \tag{10}$$

where c'_L is the speed of sound in the liquid given by

$$c'^2_L = \frac{1}{\rho'_L}\frac{dp'}{d\rho_c} \tag{11}$$

It then follows from Eqs. (9) and (10) that

$$\frac{(1-\beta)}{\rho'_L c'^2_L(1+\rho_c)}\frac{dp'}{dt'} + \frac{\partial u'}{\partial x'} + u'\left(\frac{1}{A'}\frac{dA'}{dx'}\right) - \frac{3\beta}{R'}\frac{dR'}{dt'} - \frac{4}{3}\pi R'^3 J' = 0 \tag{12}$$

The momentum equation (3) together with the Rayleigh-Plesset equation (7) and Eqs. (10) and (12) constitute the model equations for quasi-one-dimensional nozzle flows. Introducing the normalization

$$u = \frac{u'}{U'_i}, \quad p = \frac{p'}{\rho'_L U'^2_i}, \quad \rho = \frac{\rho'}{\rho'_L}, \quad R = \frac{R'}{R'_i}, \quad J = \frac{H'^4_i J'}{U'_i}$$

$$p_B = \frac{p'_B}{\rho'_L U'^2_i}, \quad p_v = \frac{p'_v}{\rho'_L U'^2_i}, \quad p_g = \frac{p'_g}{\rho'_L U'^2_i}$$

$$x = \frac{x'}{H'_i}, \quad t = \frac{t'U'_i}{H'_i}, \quad A = \frac{A'}{A'_i}, \quad \text{and} \quad \ell = \frac{R'_i}{H'_i} \tag{13}$$

where U'_i is the inlet flow speed, H'_i is the inlet nozzle height, A'_i is the inlet cross-sectional area of the nozzle, and R'_i is either the inlet bubble radius (for nonnucleating bubbly flows) or the critical bubble radius at the onset of cavitation (for nucleating flows), the reduced system of normalized equations for quasi-one-dimensional cavitating nozzle flows with nucleation assume the form

$$\frac{d\beta}{dt} - (1-\beta)\left[\frac{\partial u}{\partial x} + u\left(\frac{1}{A}\frac{dA}{dx}\right) + \frac{M^2}{(1+\rho_c)}\frac{dp}{dt}\right] = 0 \tag{14}$$

$$\frac{M^2(1-\beta)}{(1+\rho_c)}\frac{dp}{dt} + \frac{\partial u}{\partial x} + u\left(\frac{1}{A}\frac{dA}{dx}\right) - \frac{3\beta}{R}\frac{dR}{dt} - \frac{4}{3}\pi\ell^3 R^3 J = 0 \tag{15}$$

$$(1+\rho_c)(1-\beta)\frac{du}{dt} = -\frac{\partial p}{\partial x} \tag{16}$$

and

$$R\frac{d^2R}{dt^2} + \frac{3}{2}\left(\frac{dR}{dt}\right)^2 = \frac{1}{\ell^2}\left[p_B - p - \frac{4}{(\mathrm{Re})R}\left(\frac{dR}{dt}\right) - \frac{2}{(\mathrm{We})R}\right] \tag{17}$$

where $d/dt = \partial/\partial t + u\partial/\partial x$ is the normalized material derivative and the flow Mach number M, the flow Reynolds number Re and the Weber number We are defined by

$$M = \frac{U'_i}{c'_L}, \quad \mathrm{Re} = \frac{H'_i U'_i}{\nu'_L}, \quad \text{and} \quad \mathrm{We} = \frac{\rho'_L R'_i U'^2_i}{S'} \tag{18}$$

Equations (14)–(17) with appropriate initial values and nozzle inlet and exit conditions constitute the model equations for quasi-one-dimensional cavitating nozzle flows provided that they are supplemented by expressions for the normalized total pressure p_B and normalized nucleation rate J.

3 Homogeneous Bubble Nucleation and Onset of Cavitation

In this section we consider homogeneous bubble nucleation in pure liquid and its extension to gas-liquid solutions, in particular, to the problem of cavitation inception. Homogeneous bubble nucleation has been investigated for years both experimentally and theoretically (e.g., see [9], and references therein). Although nonclassical methods, such as the density functional method [10] and molecular dynamics simulations [11], can yield a better understanding of the phenomenon, they seem to be of limited practical use in bubbly cavitating flows. Despite its simplicity, the classical theory fails to quantitatively predict the tensile strengths of liquids at relatively low temperatures and provides very low steady-state nucleation rates [10–12]. In a recent paper, Delale et al. [6] have corrected for the critical radius and for the expression of steady-state nucleation rate of the classical theory by constructing a phenomenological nucleation barrier suitable for direct comparison with the results of experiments. Their results show that the critical radius r'_c beyond which a spherical bubble can grow is given by

$$r_c' = \frac{2S'}{(p_v' - p_L')_{\exp}} \tag{19}$$

where p_v' is the vapor pressure inside the bubble, p_L' denotes the pressure of the surrounding liquid, and S' is the surface tension. The subscript "exp" denotes the value of superheat achieved in experiments rather than the value that would be attained in a reversible process. The steady-state nucleation rate J' is then given by

$$J' = Z_v \left(\frac{2S' \rho_L'^2}{\pi m_1'^3} \right)^{1/2} \exp\left[- \frac{4\pi r_c'^2 S'}{3k_B T_L'} (1 - 2\alpha) \right] \tag{20}$$

where m_1' denotes the mass of a single molecule of the vapor, T_L' is the liquid temperature, Z_v denotes the compressibility factor of the saturated vapor at the liquid temperature T_L', k_B is Boltzmann's constant, and $\alpha (0 \leqslant \alpha < 1/2)$ is a correction factor, which, in general, is both substance and temperature dependent and accounts for the difference between the superheat threshold (or tensile strength) achieved in experiments and that would occur in a reversible process. In particular, $\alpha = 0$ yields the well-known classical expression for the steady-state nucleation rate. Delale et al. [6] show that the predicted superheat temperatures are in excellent agreement with those measured in boiling experiments at various liquid pressures for a variety of substances. They also achieve reasonable nucleation rates by using $\alpha = 1/3$ for reduced superheat temperatures of >0.85 in homogeneous boiling experiments for most of the substances investigated, with the exception of water. For the homogeneous boiling of water, Delale et al. reach nucleation rates comparable to those of experiments for $\alpha = 7/16$, a value that is close to the limiting value $1/2$.

In contrast to the explosive boiling experiments discussed above, where bubble formation occurs by homogeneous nucleation, bubble formation in cavitation, in most cases, occurs by heterogeneous nucleation. In this case attached voids, developed in crevices of solid particles (Harvey nuclei) contained in the liquid or on hydrophobic surfaces, act as *cavitation nuclei* [13,14]. These voids, unfortunately, depend on numerous parameters related to the solid surface and to the composition and temperature of the liquid, as well as to the dynamical operating conditions of the system. Most of these parameters demand the detailed topography of the solid surfaces and are therefore statistical in nature. Consequently, the classical theory of heterogeneous nucleation requires substantial modifications to account for the parameters mentioned above before it can be applied to the problem of bubble formation in cavitation. The improved classical theory of homogeneous nucleation [6] can, nevertheless, be applied to predict reasonable critical sizes and nucleation rates in cavitation, compared to those reached in numerical simulations and experiments, provided that it is extended to account for the effect of dissolved gas in the liquid. Various investigations [15–17] show that for weak gas-liquid solutions, Eq. (19) for the critical radius can be extended as

$$r_c' = \frac{2S'}{p_v' + p_g' - p_L'} = \frac{2S'}{p_v' + c'H' - p_L'} \tag{21}$$

to account for the dissolved gas effect where p_L' is the liquid pressure and p_v' and p_g' are, respectively, the partial pressure of the vapor and that of the gas inside the bubble of critical size. In Eq. (21), we have also utilized Henry's law $p_g' = H'c'$, where c' denotes the concentration of dissolved gas in the liquid and H' is Henry's constant.

We now consider the cavitation onset point with local liquid pressure p_i' defined as that point where sufficient nucleation sites are activated for measurable nucleation rates. The bubble radius R_i' at the onset of cavitation (the critical radius at the onset of cavitation) now follows from Eq. (21) as

$$R_i' = \frac{2S'}{(p_v' - p_i')(1 + \delta)} \tag{22}$$

where

$$\delta = \frac{c'H'}{(p_v' - p_i')} \tag{23}$$

It should be mentioned that, with the contaminant gas, it is, in fact, possible to have the cavitation onset point at $p_i' > p_v'$ (e.g., see [18]). In this case $\delta < -1$ since $R_i' > 0$. The steady-state nucleation rate following the onset of cavitation point along path lines can now be evaluated by Eqs. (20), (21), and (23) as

$$J' = Z_v \left(\frac{2S' \rho_L'^2}{\pi m_1'^3} \right)^{1/2} \exp\left\{ - \frac{16\pi S'^3 (1 - 2\alpha)}{3k_B T_L' [p_v' - p_L' + \delta(p_v' - p_i')]^2} \right\} \tag{24}$$

with $0 \leqslant \alpha < 1/2$ and with local the critical radius given by

$$r_c' = \frac{2S'}{p_v' - p_L' + \delta(p_v' - p_i')} \tag{25}$$

4 Quasi-One-Dimensional Steady-State Cavitating Nozzle Flows With Nucleation

In this section we restrict the cavitating flow model with nucleation discussed in Sec. 2 to quasi-one-dimensional steady-state cavitating flow model in order to compare the flow field in nucleating flows to that of nonnucleating bubbly flows, discussed, in detail, by Wang and Brennen [1] and Delale et al. [2]. To do so, we further neglect the compressibility of the liquid by taking the limit $M \to 0$ and $\rho_c \to 0$. The normalized quasi-one-dimensional equations (14)–(17) then reduce to

$$(1 - \beta) uA = 1 - \beta_i \tag{26}$$

$$\frac{du}{dx} + u\left(\frac{1}{A} \frac{dA}{dx} \right) - \frac{3\beta u}{R} \frac{dR}{dx} - \frac{4}{3} \pi \ell^3 R^3 J = 0 \tag{27}$$

$$(1 - \beta) u \frac{du}{dx} = - \frac{dp}{dx} \tag{28}$$

and

$$R\left(u^2 \frac{d^2R}{dx^2} + u \frac{du}{dx} \frac{dR}{dx} \right) + \frac{3}{2} u^2 \left(\frac{dR}{dx} \right)^2 = \frac{1}{\ell^2} \left[p_B - p - \frac{4u}{(\mathrm{Re})R} \left(\frac{dR}{dx} \right) - \frac{2}{(\mathrm{We})R} \right] \tag{29}$$

where β_i denotes the inlet void fraction (for pure liquid flow at the inlet $\beta_i = 0$). In Eq. (27), the normalized nucleation rate J can be written as

$$J = J_0 \exp[-Gb] \tag{30}$$

where J_0 is the normalized preexponential factor given by

$$J_0 = \frac{H_i'^4}{U_i'} Z_v \left(\frac{2S' \rho_L'^2}{\pi m_1'^3} \right)^{1/2} \tag{31}$$

and where Gb denotes the normalized Gibbs activation energy, defined by

$$Gb = \frac{16\pi S'^3 (1 - 2\alpha)}{3k_B T_L' [p_i' - p' + 2S'/R_i']^2}. \tag{32}$$

In arriving at Eq. (32), we have eliminated δ between Eqs. (22) and (24). It is also worthwhile to note that the total normalized bubble pressure p_B in the Rayleigh-Plesset equation (29), until now, has been left quite arbitrary in our formulation and, therefore, needs detailed consideration. It is well known that the bubble pressure p_B significantly affects bubble dynamics (e.g., see

[3,19,20]) and requires simultaneous consideration of the energy and transport equations within the bubble and in the surrounding liquid. For cavitating bubbly flows the coupling of these equations with the flow equations makes the solution formidable. Therefore, approximations need to be introduced. A simple model for cavitating flows that discusses the thermal conduction within the bubble has been proposed by Delale [4] following the work of Prosperetti [3]. Here, we will restrict our calculations only to the polytropic expansion and compression of the gas within the bubble solely to be able to compare our results of steady-state cavitating nozzle flows with nucleation to those of bubbly cavitating flows, obtained by Wang and Brennen [1] and by Delale et al. [2]. Consequently, we assume that the gas within the bubble obeys the polytropic law and write

$$p_B = p_v + p_g = p_v + \frac{p_{gi}}{R^{3k}} \tag{33}$$

where k is the polytropic index and p_{gi} denotes the normalized partial gas pressure at the inlet for bubbly cavitating flows and the normalized partial gas pressure at the onset of cavitation for cavitating flows with nucleation.

By eliminating β between Eqs. (26)–(28), we obtain

$$\frac{uA-(1-\beta_i)}{R^3} = \beta_i + \frac{4}{3}\pi\ell^3 \int_{x_i}^{x} J(\xi)A(\xi)d\xi \tag{34}$$

and

$$\frac{du}{dx} + \frac{A}{(1-\beta_i)}\frac{dp}{dx} = 0 \tag{35}$$

where we have defined the normalized axial coordinate x_i to denote the location at the onset of cavitation. It then follows that $J \approx 0$ whenever $x < x_i$. In particular, for nonnucleating bubbly cavitating flows, Eqs. (26) and (34) yield

$$\frac{\beta}{(1-\beta)R^3} = \frac{\beta_i}{(1-\beta_i)} = \text{const} \tag{36}$$

as required in the formulation of quasi-one-dimensional bubbly nozzle flows (e.g., see, [1,2,21]). On the other hand, for the flow of pure liquid with cavitation onset at $x=x_i$, Eq. (34) takes the form

$$uA = 1 + \tfrac{4}{3}\pi\ell^3 R^3 \int_{x_i}^{x} J(\xi)A(\xi)d\xi \tag{37}$$

We now define

$$\mathcal{F}_1(p,R,x) = u = \frac{(1-\beta_i)}{A} + \left[\beta_i + \frac{4}{3}\pi\ell^3\int_{x_i}^{x} J(\xi)A(\xi)d\xi\right]\frac{R^3}{A} \tag{38}$$

the p dependence of the functional $\mathcal{F}_1$ arising from the p dependence of the normalized nucleation rate J. It then follows by direct differentiation that

$$\mathcal{F}_2\left(p,R,\frac{dR}{dx},x\right) = \frac{du}{dx} = -\frac{(1-\beta_i)}{A^2}\frac{dA}{dx} + \frac{4}{3}\pi\ell^3 R^3 J + \left[\beta_i + \frac{4}{3}\pi\ell^3\int_{x_i}^{x} J(\xi)A(\xi)d\xi\right] \times \frac{R^3}{A}\left(\frac{3}{R}\frac{dR}{dx} - \frac{1}{A}\frac{dA}{dx}\right) \tag{39}$$

The integro-differential system of equations characterizing quasi-one-dimensional cavitating nozzle flows with nucleation can now be written as

$$\frac{dR}{dx} = \phi, \tag{40}$$

$$\frac{dp}{dx} = -\frac{(1-\beta_i)}{A}\mathcal{F}_2(p,R,\phi,x) \tag{41}$$

and

$$\frac{d\phi}{dx} = \left\{-\mathcal{F}_1(p,R,x)\mathcal{F}_2(p,R,\phi,x)R\phi - \tfrac{3}{2}[\mathcal{F}_1(p,R,x)]^2\phi^2 + \frac{1}{\ell^2}\left[p_v + \frac{p_{gi}}{R^{3k}} - p - \frac{4}{(\mathrm{Re})R}\mathcal{F}_1(p,R,x)\phi - \frac{2}{(\mathrm{We})R}\right]\right\} \Big/ \{R[\mathcal{F}_1(p,R,x)]^2\} \tag{42}$$

where $\mathcal{F}_1(R,x)$ and $\mathcal{F}_2(R,dR/dx,x)$ are given by Eqs. (38) and (39), respectively. For a given fluid, the above system of equations contains the parameters α, R_i', H_i' (or ℓ), β_i (only for bubbly flows at inlet), the surface tension S' and the nozzle inlet velocity U_i' (or the Weber number We and the Reynolds number Re), and the polytropic index k. The system of equations (40)–(42) are then solved for the pressure p and the bubble radius R subject to nozzle inlet-exit conditions. The flow speed u follows by Eq. (38).

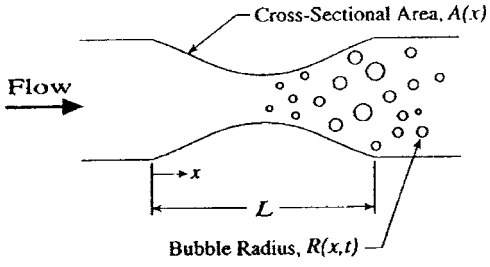

Fig. 1 Geometric configuration of the nozzle employed by Wang and Brennen [1] (in our normalization $L=5$)

5 Results and Discussion

We now consider the flow of water, possibly containing dissolved air and particles (Harvey nuclei), which can act as bubble nucleation sites, through a converging-diverging nozzle at 20 °C (with $\rho_L' = 1000\ \mathrm{kg/m^3}$, $\mu_L' = 1\times10^{-3}\ \mathrm{Ns/m^2}$, $S' = 0.074\ \mathrm{N/m}$, $p_v' = 0.0234$ bar). For reasons of comparison with the steady-state bubbly cavitating nozzle flow solution of Wang and Brennen [1], we employ their geometric nozzle configuration as shown in Fig. 1. With appropriate scaling so that the throat is located at $x=2.5$, we can write the normalized area of Wang and Brennen as

$$A(x) = \left\{1 + 0.5\left[1 - \cos\left(\frac{2\pi x}{5}\right)\right]\right\}^{-1/2} \quad \text{for } 0 \leqslant x \leqslant 5 \tag{43}$$

and is equal to unity elsewhere, corresponding to $\ell = 1.4\times10^{-3}$. The correction factor α for the Gibbs activation energy, the critical radius R_i' at the onset of cavitation and δ, defined by Eq. (23), are chosen as parameters in the model since there are uncertainties in determining these quantities. As for the nozzle inlet conditions, the inlet void fraction is set equal to zero ($\beta_i = 0$) implying liquid flow without bubbles at the inlet. The inlet flow speed and inlet cavitation number are set, respectively, at $U_i' = 10\ \mathrm{m/s}$ and $\sigma_i = 0.8$ so that cavitation inception can take place. For reasons of comparison, the same effective viscosity of Wang and Brennen (30 times that of water replacing the Reynolds number given by Eq. (18) by an effective Reynolds number) is used to account, *in an ad hoc manner*, for the classical damping mechanisms. The

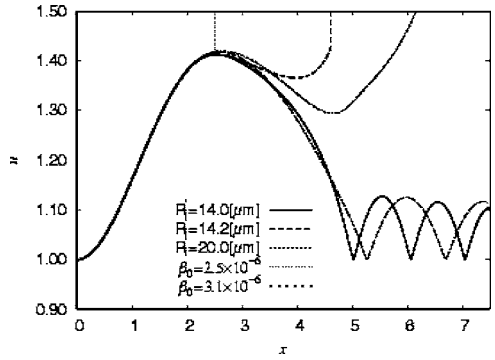

Fig. 2 Distributions of the flow speed u along the axis of the nozzle in Fig. 1 under the flow conditions with flow speed U_i' =10 m/s, inlet cavitation number σ_i=0.8, and nucleation rate parameters α=0.499 999 9927 and δ=0.5 for the values of the critical bubble radius R_i'=14.0, 14.2, and 20.0 μm at the onset of cavitation in nucleating bubbly flows of the present investigation and for the values of the void fractions $\beta_i=2.5\times10^{-6}$ and $\beta_i=3.1\times10^{-6}$ in the nonnucleating bubbly flow of Wang and Brennen [1] (stable nucleating and nonnucleating cavitating flow solutions with a downstream ringing structure are shown, respectively, for R_i'=14.0 μm and for $\beta_i=2.5\times10^{-6}$)

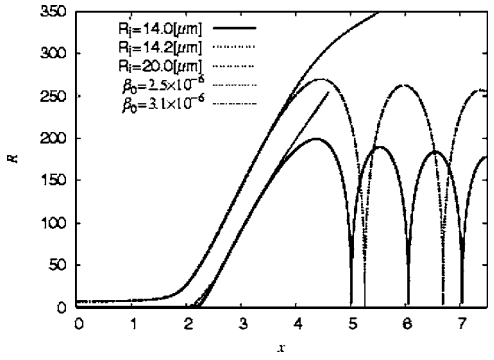

Fig. 4 Distributions of the normalized radius R along the axis of the nozzle in Fig. 1 under the flow conditions and nucleation rate parameters stated in Fig. 2 for the values of the critical bubble radius R_i'=14.0, 14.2, and 20.0 μm at the onset of cavitation in nucleating bubbly flows of the present investigation and for the values of the void fractions $\beta_i=2.5\times10^{-6}$ and $\beta_i=3.1\times10^{-6}$ in the nonnucleating bubbly flow of Wang and Brennen [1] (stable nucleating and nonnucleating cavitating flow solutions with a downstream ringing structure are shown, respectively, for R_i'=14.0 μm and for $\beta_i=2.5\times10^{-6}$)

correction factor α for the normalized Gibbs activation energy in Eq. (32) for the cavitation of water was varied critically close to the limiting value 0.5 (within ten decimal places) in order to obtain reasonable nucleation rates that have been reported by many previous investigators [10–12]. The onset of nucleation was determined by varying the critical bubble size R_i' between 9 and 20 μm for δ=0.5 and δ=1.0.

The integrodifferential system of equations (40)–(42) was solved under the above specific conditions using a fourth-order Runge-Kutta method with adaptive step size. Stable steady-state flow solutions, including those with bubbly shock waves, as well as unstable flow solutions were obtained. The results of the present investigation for nucleating bubbly flows are plotted in Figs. 2–6 against those of Wang and Brennen [1] for nonnucleating bubbly flows under similar conditions to identify the effect of nucleation on the flow field. The distributions for the normalized flow speed u, the pressure coefficient C_p (defined as $C_p=(p'-p_0')/(0.5\rho_L'U_i'^2)$ with p_0' denoting the liquid pressure at the inlet of the nozzle), the normalized radius R (normalized with respect to the critical radius R_i' at the onset of cavitation), and the void fraction β as a function of the normalized axial coordinate x for each case are shown in Figs. 2–5, whereas the variation of the nucleation rate along the nozzle axis is shown in Fig. 6. The nucleating flow results are computed for δ=0.5 and α =0.499 999 9927 with the initial critical radius R_i' varied between 14 and 20 μm and the nonnucleating bubbly flow results of Wang and Brennen [1] are computed for the initial void fractions β_i $=2.5\times10^{-6}$ and $\beta_i=3.1\times10^{-6}$. The stable solutions for nucleating (R_i'=14.0 μm) and non-nucleating ($\beta_i=2.5\times10^{-6}$) bubbly flows look qualitatively similar, but there are quantitative differences arising from the effects of nucleation. In the nucleation zone, defined as the zone where significant nucleation rates are obtained with a maximum at the throat (in our case, approximately the interval $2<x<3$), the newly nucleated bubbles reach the corresponding growth rates of the growing bubbles of nonnucleating bubbly flows over a very short distance, but the

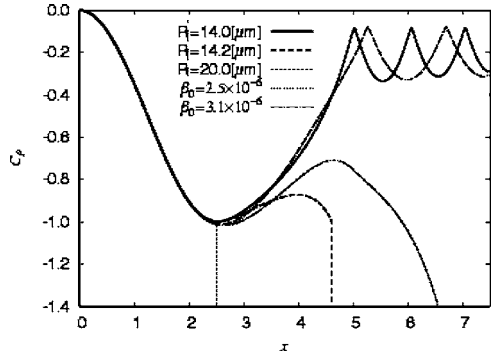

Fig. 3 Distributions of the pressure coefficient C_p along the axis of the nozzle in Fig. 1 under the flow conditions and nucleation rate parameters stated in Fig. 2 for the values of the critical bubble radius R_i'=14.0, 14.2, and 20.0 μm at the onset of cavitation in nucleating bubbly flows of the present investigation and for the values of the void fractions $\beta_i=2.5\times10^{-6}$ and $\beta_i=3.1\times10^{-6}$ in the nonnucleating bubbly flow of Wang and Brennen [1] (stable nucleating and nonnucleating cavitating flow solutions with a downstream ringing structure are shown, respectively, for R_i'=14.0 μm and for $\beta_i=2.5\times10^{-6}$)

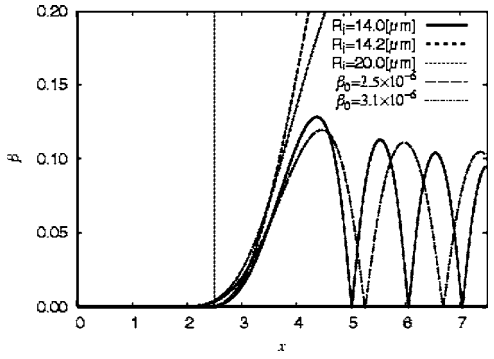

Fig. 5 Distributions of the void fraction β along the axis of the nozzle in Fig. 1 under the flow conditions and nucleation rate parameters stated in Fig. 2 for the values of the critical bubble radius R_i'=14.0, 14.2, and 20.0 μm at the onset of cavitation in nucleating bubbly flows of the present investigation and for the values of the void fractions $\beta_i=2.5\times10^{-6}$ and $\beta_i=3.1\times10^{-6}$ in the nonnucleating bubbly flow of Wang and Brennen [1] (stable nucleating and nonnucleating cavitating flow solutions with a downstream ringing structure are shown, respectively, for R_i' =14.0 μm and for $\beta_i=2.5\times10^{-6}$)

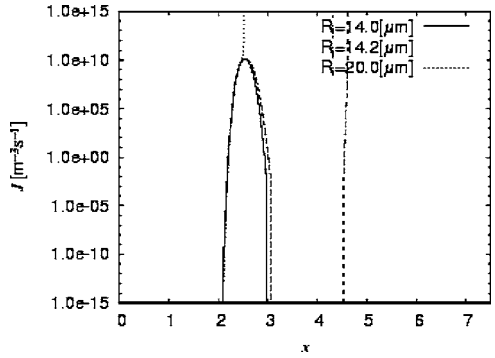

Fig. 6 Distributions of the nucleation rate J' along the axis of the nozzle in Fig. 1 under the flow conditions and nucleation rate parameters stated in Fig. 2 for the values of the critical bubble radius $R_i'=14.0$, 14.2, and 20.0 μm at the onset of cavitation in nucleating bubbly flows of the present investigation (a stable cavitating flow solution is shown for $R_i'=14.0$ μm)

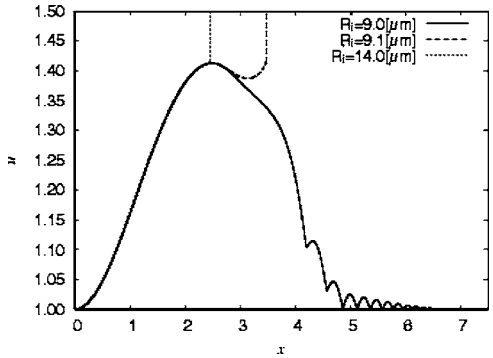

Fig. 7 Distributions of the flow speed u along the axis of the nozzle in Fig. 1 under the flow conditions with flow speed $U_i'=10$ m/s, inlet cavitation number $\sigma_i=0.8$, and nucleation rate parameters $\alpha=0.499\,999\,9930$ and $\delta=1.0$ for the values of the critical bubble radius $R_i'=9.0$, 9.1, and 14.0 μm at the onset of cavitation in nucleating bubbly flows of the present investigation (a stable cavitating flow solution with a stationary bubbly shock wave is shown for $R_i'=9.0$ μm)

bubbles are still not large enough, both in size and in population, to alter the incompressible flow field significantly (Fig. 4). Consequently, the flow field remains almost incompressible in most of the nucleation zone in nucleating flows, whereas, over the same region, the bubbles grow to sizes that alter the incompressible flow field, though not significantly, in nonnucleating bubbly flows (Figs. 2, 3, and 5). In this zone the nucleation rate peaks at a value of $J'_{\max}=10^{10}$ m^{-3}s^{-1} (Fig. 6). Downstream of the nucleation zone ($x>3$), where nucleation has completely vanished, both nucleating and nonnucleating bubbly flows seem to exhibit the same rate of growth until the maximum radius is reached around $x=4.5$ (Fig. 4, it should be mentioned that the normalization of the radius for both cases is made with respect to the critical size R_i' at cavitation onset). This leads to a higher maximum radius for the nonnucleating bubbly flows of Wang and Brennen [1]. The distributions for the flow speed and pressure coefficient, in both cases, show only slight deviations from each other, the deviations arising mainly from the differences in the nucleation zone (Figs. 2 and 3). On the other hand, the corresponding distributions of the void fraction β in these regions show significant deviations when compared to each other, with a higher maximum in the case of nucleating flows. This implies a higher number density for the case of nucleating flow as compared to the nonnucleating bubbly flow case of Wang and Brennen. Now, because of their lower maximum bubble radii, the collapse of bubbles in nucleating flows proceeds over a shorter distance than that of nonnucleating bubbly flows, with a distance lag in between. This distance lag continues also for the ringing structure downstream of the nozzle in the constant area region ($x>5$) although the amplitude of oscillations are almost the same (Figs. 2–5). The net effect of nucleation seems to be the reduction of the maximum bubble radius in nucleating bubbly flows, resulting in a shorter collapse period, as compared with nonnucleating bubbly flows under similar conditions. For the same values of the parameters and under the same flow conditions, a bifurcation to a "quasi-statically unstable flow" occurs around $R_i'=14.2$ μm for nucleating flows and around $\beta_i=3.0\times10^{-6}$ for the nonnucleating bubbly flows of Wang and Brennen [1] (Figs. 2–6). For nucleating flows, the nucleation rate first reaches a peak and then diminishes, with almost no difference compared to the "quasi-statically stable" case. However, the normalized radius R and the void fraction β continue to grow. Consequently, the pressure cannot recover. It suddenly falls down resulting in a second nucleation zone, where the nucleation rate now grows without limit and the computation for the normalized radius R breaks down around $x=4.5$. As R_i' is further increased in nucleating flows (Figs. 2–6 for $R_i'=20$ μm), the nucleation rate grows exponentially and without limit after onset, causing instabilities to occur near the throat.

Finally, it seems that a cavitating nozzle flow solution with a bubbly shock wave in the diverging section of the nozzle is also possible under the flow conditions stated in Fig. 7 for the values of the parameters $\delta=1.0$ and $\alpha=0.499\,999\,9930$ when the initial bubble radius R_i' exceeds 8 μm (unfortunately, for this case a nonnucleating bubbly flow solution of similar nature is not available for the nozzle of Wang and Brennen [1] for comparison). Figures 7–11 show the results of cavitating nozzle flows with a stationary bubbly shock wave in the divergent section of the nozzle for $R_i'=9$ μm. The solutions for the normalized flow speed u, the pressure coefficient C_p, the normalized radius R, and the void fraction β are shown in Figs. 7–10. The normalized radius relaxes toward unity after a few rebounds, and the pressure recovers toward the inlet pressure within a thin zone with some pressure loss due to dissipation. The nucleation rate now peaks at a value of $J'_{\max}=10^{11}$ m^{-3}s^{-1} (Fig. 11). Under the same conditions and the same fixed values of the parameters δ and α, if the initial radius is further increased, a bifurcation to a quasi-statically unstable solution with a sudden pressure drop in the divergent section of the nozzle occurs. Consequently, a second nucleation zone,

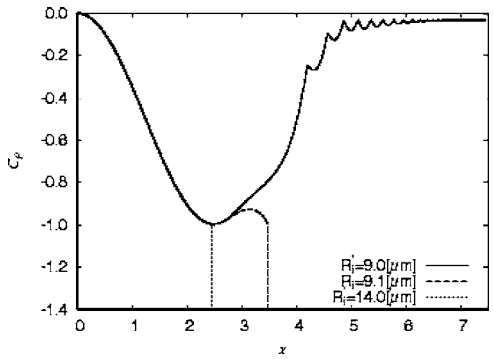

Fig. 8 Distributions of the pressure coefficient C_p along the axis of the nozzle in Fig. 1 under the flow conditions and nucleation rate parameters stated in Fig. 7 for the values of the critical bubble radius $R_i'=9.0$, 9.1, and 14.0 μm at the onset of cavitation in nucleating bubbly flows of the present investigation (a stable cavitating flow solution with a stationary bubbly shock wave is shown for $R_i'=9.0$ μm)

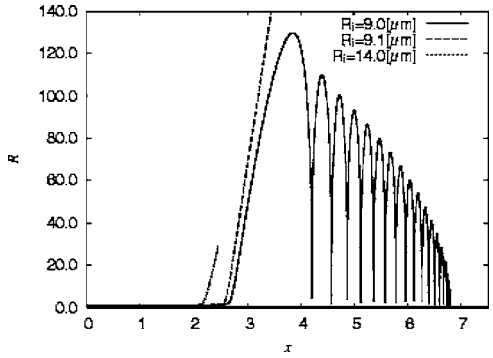

Fig. 9 Distributions of the normalized radius R along the axis of the nozzle in Fig. 1 under the flow conditions and nucleation rate parameters stated in Fig. 7 for the values of the critical bubble radius $R_i'=9.0$, 9.1, and 14.0 μm at the onset of cavitation in nucleating bubbly flows of the present investigation (a stable cavitating flow solution with a stationary bubbly shock wave is shown for $R_i'=9.0$ μm)

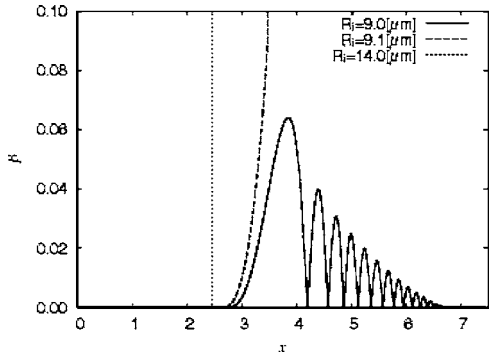

Fig. 10 Distributions of the void fraction β along the axis of the nozzle in Fig. 1 under the flow conditions and nucleation rate parameters stated in Fig. 7 for the values of the critical bubble radius $R_i'=9.0$, 9.1, and 14.0 μm at the onset of cavitation in nucleating bubbly flows of the present investigation (a stable cavitating flow solution with a stationary bubbly shock wave is shown for $R_i'=9.0$ μm)

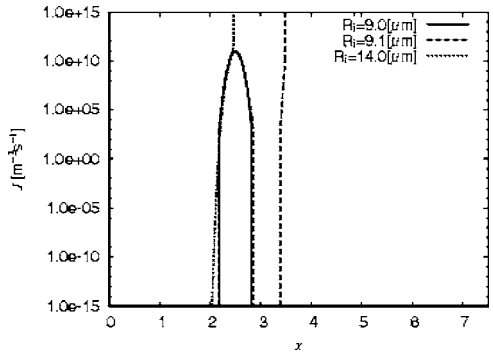

Fig. 11 Distributions of the nucleation rate J' along the axis of the nozzle in Fig. 1 under the flow conditions and nucleation rate parameters stated in Fig. 7 for the values of the critical bubble radius $R_i'=9.0$, 9.1, and 14.0 μm at the onset of cavitation in nucleating bubbly flows of the present investigation (a stable cavitating flow solution with a stationary bubbly shock wave is shown for $R_i'=9.0$ μm)

now growing without limit, occurs resulting in an unstable solution. Increasing the initial radius at the onset of nucleation even further results in the location of the instability moving toward the throat as shown in Figs. 7–11 for $R_i'=14.0$ μm. In this case the instability occurs very close to the throat, where the pressure falls down and the flow speed increases almost discontinuously, the nucleation rate now growing exponentially and without limit. The computation for the radius breaks down at a finite growth rate in this case.

This investigation has demonstrated the effect of homogeneous bubble nucleation in cavitating nozzle flows as compared to nonnucleating bubbly flows. Although the flow field in the diverging part of the nozzle looks qualitatively similar in both cases, there are quantitative differences. Lower maximum bubble radii and shorter collapse distances are observed in stable nucleating bubbly cavitating flows as compared to the nonnucleating bubbly flow investigation of Wang and Brennen [1]. Both solutions show bifurcations to unstable "flashing" flows, which are nonphysical. Recent investigations have shown that these unstable solutions can either be stabilized by thermal damping [4] or they correspond to unsteady flows with bubbly shocks propagating downstream in the divergent section of the nozzle [5].

6 Conclusions

Quasi-one-dimensional steady-state cavitating nozzle flows with homogeneous nucleation are considered (despite the fact that bubbles are formed by heterogeneous nucleation in most cavitating flows). For this reason the onset of cavitation is modelled by using an improved version of the classical nucleation theory and by treating the unknown quantities, such as the initial partial gas pressure and initial bubble radius at the onset of cavitation, as parameters. Therefore, a parametric investigation of the onset of cavitation in quasi-one-dimensional cavitating nozzle flows is carried out. The nonlinear dynamics of cavitating bubbles is described by the classical Rayleigh-Plesset equation where a polytropic law for the partial gas pressure is employed by taking into account the effect of damping mechanisms, in a rather crude manner, in the form of viscous dissipation using an effective viscosity for a direct comparison with the results obtained by Wang and Brennen [1] for homogeneous bubbly flows. The results of this investigation show similar qualitative characteristics with those of steady-state nonnucleating bubbly flows of Wang and Brennen [1]. Namely, stable steady-state cavitating nozzle flow solutions as well as a quasi-statically unstable flow solutions are obtained. In particular, a nucleation zone (where the flow is almost incompressible and the nucleation rate shows a maximum at the nozzle throat) followed by a bubble growth zone, where the effects of compressibility are observed, in the divergent section of the nozzle can be distinguished for the stable steady-state solutions of nucleating bubbly flows. Compared to the steady-state nonnucleating nozzle flow solution of Wang and Brennen [1] under similar conditions, a reduction in the maximum bubble radius followed by a somewhat shorter collapse distance are observed for the nucleating bubbly flow solution of this investigation. Moreover, when the parameters entering the nucleation rate equation are properly chosen, stable steady-state cavitating nozzle flow solutions with stationary bubbly shock waves in the diverging section of the nozzle seem also possible. We should finally mention that the instabilities obtained for quasi-one-dimensional steady-state nozzle flows with nucleation in this investigation can be stabilized by taking into account thermal damping (e.g., [4]) and/or flow unsteadiness (see [5]). These and other effects (liquid compressibility, bubble fission, etc.) not considered here are left for future investigations.

Acknowledgments

This work is supported, in part, by the Research Foundation (BAP) of Istanbul Technical University under Project No. 1874. C. F. Delale would also like to thank the Intelligent Modeling

Laboratory of the University of Tokyo for the Visiting Fellowship in the summer of 2002.

Nomenclature

A' = cross-sectional area of the nozzle
C_p = pressure coefficient
G_b = Gibbs activation function
H' = Henry's constant
H_i' = inlet height of nozzle
J' = nucleation rate
M = flow Mach number
R' = bubble radius
R_i' = critical bubble radius at the onset of cavitation
Re = flow Reynolds number
S' = surface tension coefficient
T_L' = liquid temperature
U_i' = inlet flow speed
Z_v = compressibility of vapor
c' = concentration of dissolved gas in liquid
c_L' = speed of sound in liquid
k = polytropic exponent
k_B = Boltzmann's constant
ℓ = micro to macro scale
m_1' = mass of a single vapor molecule
n' = number density of bubbles
p = mixture pressure
p_B' = total bubble pressure
p_g' = partial gas pressure
p_i' = liquid pressure at the onset of cavitation
p_0' = liquid pressure at the inlet of the nozzle
p_v' = partial vapor pressure
t' = time coordinate
u' = flow speed
x' = nozzle axial coordinate

Greek

α = correction factor for nucleation work
β = void fraction
δ = gas parameter at the onset of cavitation
μ_L' = liquid dynamic viscosity
ν_L' = kinematic viscosity of liquid
ρ_c = nondimensional measure of liquid compressibility
ρ' = mixture density
ρ_L' = liquid density
σ_i = inlet cavitation number

Subscripts

g = gas
i = nozzle inlet or cavitation onset value
L = liquid phase
v = vapor phase

Superscripts

$'$ = signifies a dimensional quantity (otherwise dimensionless)

References

[1] Wang, Y. C., and Brennen, C. E., 1998, "One-Dimensional Bubbly Cavitating Flows Through a Converging-Diverging Nozzle," ASME J. Fluids Eng., **120**, pp. 166–170.
[2] Delale, C. F., Schnerr, G. H., and Sauer, J., 2001, "Quasi-One-Dimensional Steady-State Cavitating Nozzle Flows," J. Fluid Mech., **427**, pp. 167–204.
[3] Prosperetti, A., 1991, "The Thermal Behavior of Oscillating Gas Bubbles," J. Fluid Mech., **222**, pp. 587–616.
[4] Delale, C. F., 2002, "Thermal Damping in Cavitating Nozzle flows," ASME J. Fluids Eng., **124**, pp. 969–976.
[5] Preston, A. T., Colonius, T., and Brennen, C. E., 2002, "A Numerical Investigation of Unsteady Bubbly Cavitating Nozzle Flows," Phys. Fluids, **14**, pp. 300–311.
[6] Delale, C. F., Hruby J., and Marsik, F., 2003, "Homogeneous Bubble Nucleation in Liquids: The Classical Theory Revisited," J. Chem. Phys., **118**, pp. 792–906.
[7] Brennen, C. E., 2002, "Fission of Collapsing Cavitation Bubbles," J. Fluid Mech., **472**, 153–166.
[8] Delale, C. F., and Tunç, M., 2004, "A Bubble Fission Model for Collapsing Cavitation Bubbles," Phys. Fluids, **16**, pp. 4200–4203.
[9] Blander, M., and Katz, J., 1975, "Bubble Nucleation in Liquids," AIChE J., **21**, pp. 833–848.
[10] Oxtoby, D. W., and Evans, R., 1988, "Nonclassical Nucleation Theory for the Gas-Liquid Transition," J. Chem. Phys.. **89**, pp. 7521–7530.
[11] Kinjo, T., and Matsumoto, M., 1998, "Cavitation Processes and Negative Pressure," Fluid Phase Equilib., **144**, pp. 343–350.
[12] Lienhard, J. H., and Karimi, A. 1981, "Homogeneous Nucleation and the Spinodal Line," ASME J. Heat Transfer, **103**, pp. 61–64.
[13] Mørch, K. A., 2000, "Cavitation Nuclei and Bubble Formation: A Dynamic Liquid-Solid Interface Problem," ASME J. Fluids Eng., **122**, pp. 494–498.
[14] Marschall, H. B., Mørch, K. A., Keller, A. P., and Kjeldsen, M., 2003, "Cavitation Inception by Almost Spherical Solid Particles in Water," Phys. Fluids, **15**, pp. 545–553.
[15] Forest, T. W., and Ward, C. A., 1977, "Effect of a Dissolved Gas on the Homogeneous Nucleation Pressure of a Liquid." J. Chem. Phys., **66**, pp. 2322–2330.
[16] Ward, C. A. Balakrishnan, A., and Hooper, F. C., 1970, "On the Thermodynamics of Nucleation in Weak Gas-Liquid Solutions," ASME J. Basic Eng., **92**, pp. 695–704.
[17] Mori, Y., Hijikita, K., and Nagatani, T., 1977, "Fundamental Study of Bubble Dissolution in Liquid," Int. J. Heat Mass Transfer, **20**, pp. 41-50.
[18] Brennen, C. E., 1995, *Cavitation and Bubble Dynamics*, Oxford University Press, Oxford.
[19] Nigmatulin, R. I., Khabeev, N. S., and Nagiev, F. B., 1981, "Dynamics, Heat and Mass Transfer of Vapour-Gas Bubbles in a Liquid," Int. J. Heat Mass Transfer, **24**, pp. 1033–1044.
[20] Matsumoto, Y., and Takemura, F., 1994, "Influence of Internal Phenomena on Gas Bubble Motion: Effects of Thermal Diffusion, Phase Change on the Gas-Liquid Interface and Mass Diffusion Between Vapor and Non-Condensable Gas in the Collapsing Phase," JSME Int. J., Ser. B, **37** (2), pp. 288–296.
[21] van Wijngaarden, L., 1972, "One-Dimensional Flow of Liquids Containing Small Gas Bubbles," Annu. Rev. Fluid Mech., **4**, pp. 369–396.

Steady and Dynamic Models of Fuel and Air Flow in Carburetors for Small Engines

Diego A. Arias
e-mail: daarias@wisc.edu

Timothy A. Shedd[1]
e-mail: shedd@engr.wisc.edu

Multiphase Flow Visualization and Analysis Laboratory, Department of Mechanical Engineering, University of Wisconsin-Madison
Madison, 53706

This work presents the mathematical model of a complex flow network containing short metering orifices, compressible flow, and two-phase flow in small diameter pipes. It has been developed to study the steady and dynamic flows in a carburetor for small engines. It extends the previously published models by incorporating a detailed review of two-phase flow pressure drop, the effect of the fuel well on the control of air-bleed flow, and dynamic flow. The homogeneous two-phase flow model, which is commonly used in previous models, was compared to an empirical correlation derived from experiments in small pipes and found to be in poor agreement. In order to assess dynamic flow conditions, the model was extended by solving instantaneous one-dimensional Navier-Stokes equations in single-phase pipes. This strategy proved successful in explaining the mixture enrichment seen under pulsating flow conditions. The model was also used to derive a sensitivity analysis of geometries and physical properties of air and fuel.
[DOI: 10.1115/1.1949644]

Introduction

At the time of this publication, over 35 million small engines are sold every year in the United States and their emissions comprise a significant percentage of total pollutants in the U.S. and worldwide. As demonstrated by the automotive industry, significant reductions in emissions are technologically possible, particularly with the use of electronic fuel injection. However, due primarily to cost constraints, small-engine manufacturers rely on small, inexpensive carburetors to generate the fuel mixture for their engines. Thus, a better understanding of carburetor performance and modeling could lead to better fuel-mixture control and lower emissions from small engines.

More than a century of carburetor development has produced a device with a very complex set of internal passages designed to deliver to the engine the correct air-fuel mixture according to speed and load. This is achieved through several complex processes: flows through short lengths (non-fully developed flow) and complex geometries; flows that transition from laminar to turbulent; highly transient flow; two-phase flow of various forms (bubbles, sprays, and thin liquid films); and flows with changing fuel and air properties due to rapid changes in temperature and pressure.

Figure 1 shows the main systems of a simplified carburetor typically used in small engines. The acceleration of the airflow across the venturi creates a low pressure at the venturi throat. This low pressure drives the fuel flow from a constant-level reservoir to the venturi throat. In its path, fuel travels through a main fuel orifice, whose function is to restrict its flow, and the emulsion tube, where it can mix with air coming from an air-bleed system. Fuel flow may also go to a fuel well that surrounds the emulsion tube where it may cover or expose the holes in the emulsion tube according to varying pressures in the emulsion tube and well. When air flows through the air-bleed system, it passes through an air-bleed orifice at the entrance of the venturi, then through a series of small passages, and ends up at the top of the fuel well. When the holes in the emulsion tube are exposed, air is driven into the emulsion tube and mixes with fuel, creating a two-phase mixture of lower mean density than the fuel. This mixture of fuel and air arrive at the venturi throat, where the fuel may take the form of droplets, vapor, or a thin film on the wall. All these processes take place during each cycle of the engine, starting from zero air flow and peaking during the intake stroke.

The complexity of the problem and the lack of a complete model of the processes taking place in it have led manufacturers to develop carburetors based on a trial-and-error procedure. The design equations from internal combustion engine books (e.g., [1]) provide little practical design guidance, and modeling attempts (e.g., [2–4]) were necessarily based on several simplifying assumptions due to the limits of computational capabilities at the times that they were implemented. Those assumptions restricted the application of the models and extension to practical designs.

The present work describes the mathematical model of a complex dynamic multiphase flow network. Although it was derived for the characterization of processes inside a carburetor for small engines, it demonstrates the feasibility of capturing experimentally validated phenomena using a one-dimensional (1D) dynamic model of multiphase flow networks. It requires the use of appropriate two-phase flow correlations and the modeling of transient behavior through 1D instantaneous Navier-Stokes equations. For the specific case of carburetors, this model captures phenomena reported in the literature, such as enrichment of the air-fuel mixture due to the action of the air-bleed system and the pulsating venturi flow, which were not captured by the previous models found in the literature. The model also allows for the development of sensitivity analyses under steady or dynamic conditions, the implementation of secondary flow systems, such as idle or enrichment systems, and the implementation of the complete carburetor model in other computer codes for the prediction of engine performance.

Review of Previous Carburetor Models

The carburetor was the object of much research until emission regulations and fuel economy became major concerns in the 1970s, encouraging automotive engine designers to implement electronic fuel injection. A review of the published work on the metering problem in carburetors can be separated into studies on airflow, passages for fuel flow, the effect of air and fuel properties, and the treatment of two-phase flow in the emulsion tube.

[1]Author to whom correspondence should be addressed.

Contributed by the Fluids Engineering Division for publication in the JOURNAL OF FLUIDS ENGINEERING. Manuscript received by the Fluids Engineering Division June 21, 2004; Final manuscript received March 22, 2005. Associate Editor: Georges Chahine.

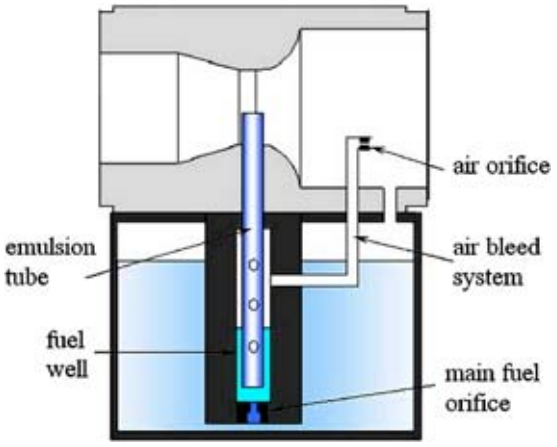

Fig. 1 Main systems in carburetor for small engines

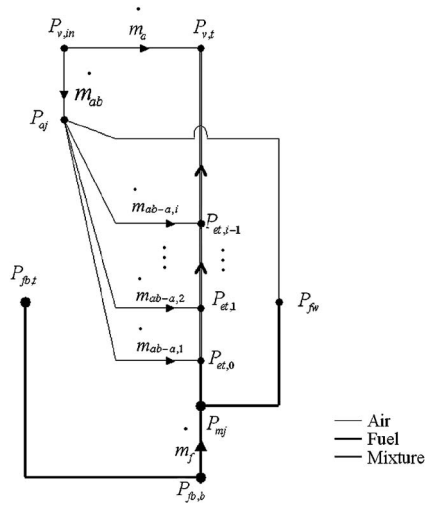

Fig. 2 Schematic of carburetor as flow network

Airflow. The airflow through the carburetor and intake system has been widely modeled with instantaneous Navier-Stokes equations and solved through the method of characteristics [5] and finite differences [6]. Both of these methods can predict, with high accuracy, the pressure and velocity fields for motored engines (i.e., assuming only airflow and no interaction with the fuel flow in the intake system). Simplifications (such as assuming ideal gas behavior, one-dimensional flow, quasi-steady boundary conditions, and that heat transfer, friction, and discharge coefficients are valid for both unsteady and steady flow [1]) are the basis of the implementation of these models in commercial engine prediction software [7].

Interaction of airflow with liquid flow in a venturi has been simulated for carburetors [8] and for venturi scrubbers [9], where the effect of liquid flow can be described as an increase in pressure drop for the same airflow, as reported by Lenz [10].

The largest restriction on the intake system is the throttle plate. Experimental works to characterize it were performed by Harrington and Bolt [2], Woods and Goh [11], and Ehara et al. [12]. Harrington determined that the flow through the throttle plate can be modeled as a compressible converging nozzle once the throat area is calculated. The effect of ambient conditions on carburetor performance was studied by Bolt and Boerma [13] and Brereton et al. [14].

Fuel Flow. One of the most comprehensive models of air and fuel metering in carburetors was developed by Harrington and Bolt [2]. The model consisted of a flow network under steady-state conditions; the equations used included the pressure losses on the network branches, and the unknowns were the mass flows in the network branches and static pressures at the network nodes. Experimental discharge coefficients for restriction elements were required and the air-fuel flow in the emulsion tube was modeled using the homogenous two-phase flow model. As the carburetor modeled was to be used in an eight-cylinder engine, steady flow was a convenient assumption that allowed prediction over a wide range of engine speeds. Similar models were developed by Asano et al. [15], Shinoda et al. [16], and Furuyama [17]. All these models were based on finding specific empirical discharge coefficients and solving for fuel flows and pressure drops under steady-state boundary conditions.

Szczecinsky and Rychter [3] and Sendyka and Filipczyk [4] extended the use of this model by assuming quasi-steady-state solutions for a varying pressure in the venturi. The results showed instantaneous and integrated air fuel ratios that were much leaner than those seen in real engines. Experiments have shown that the pulsating nature of airflow produces a mixture enrichment, as reported by Moss [18]. In addition, Bolt et al. [19] studied the effect of fuel properties on the amounts of fuel delivered by the carburetor by looking at the change in the discharge coefficient of restriction elements.

Two Phase Flow in Small Passages. The mixed airflow and fuel flow in the carburetor passages has been greatly simplified in previous models due to the complexity of the processes of two-phase flow. The models cited above assumed the homogeneous model for the two-phase flow as described by Wallis [20]. Visualization experiments conducted by Oya [21] suggested that very different two-phase flow regimes may occur in carburetor passages, greatly differing from a homogeneous case.

Two-phase flow regimes are important since they are needed to understand the most appropriate pressure drop model for the characteristics of the flow. Two-phase flow pressure drop correlations have been developed for long pipes and with diameters much larger than those typically found in carburetors. Oya [22] recognized this lack of appropriate models and developed empirical pressure drop correlations for small pipes. Measurements of the amounts of air flow through airbleed systems was performed by Hosho [23], but only for average values over an entire engine cycle. The reported results consisted of volumetric fractions where airflow was around four times the fuel flow.

Steady-State Model

General Equations. The general approach used here to create and solve a carburetor model is to solve for airflow first, which then sets the boundary conditions for the fuel flow network. A schematic of the flow network is shown in Fig. 2.

Venturi. The air mass flow rate $\dot{m}_a$ through the carburetor venturi can be modeled using the equations for a compressible nozzle given by

$$\dot{m}_a = C_{D,t} A_t \Phi \sqrt{2\rho_{a0}(P_{v,0} - P_{v,t})} \tag{1}$$

where $C_{D,t}$ is the discharge coefficient based on the throat area A_t, ρ_{a0} is the density of air at atmospheric conditions, $P_{v,0}$ is the total pressure at the inlet of the venturi, and $P_{v,t}$ is the static pressure at the throat [1]. Φ accounts for the compressible effects

$$\Phi = \left(\frac{[\gamma/(\gamma-1)][(P_{v,0}/P_{v,t})^{2/\gamma} - (P_{v,0}/P_{v,t})^{(\gamma+1)/\gamma}]}{1 - P_{v,0}/P_{v,t}} \right)^{1/2} \tag{2}$$

where γ is the isentropic coefficient of air.

Fuel Bowl. Assuming that the fuel level in the fuel bowl is kept constant, the pressure at the bottom of the fuel bowl $P_{fb,b}$ is given by

$$P_{fb,b} = P_{fb,t} + \rho_f g h_{fb} \tag{3}$$

where $P_{fb,t}$ is the pressure over the fuel level (which depends on the configuration of the carburetor), ρ_f is the fuel density, g is the gravitational acceleration constant, and h_{fb} is the fuel level.

Main Fuel Orifice. Fuel flow $\dot{m}_f$ through a calibrated orifice can be modeled by

$$\dot{m}_f = C_{D,mj} A_{mj} \sqrt{2\rho_f (P_{fb,b} - P_{mj})} \tag{4}$$

where $C_{D,mj}$ is the discharge coefficient based on the orifice area A_{mj}, and P_{mj} is the pressure after the orifice. The discharge coefficient is obtained experimentally (e.g., see [2,16]).

Single-Phase Flow in Emulsion Tube. Only fuel flows through the lower section of the emulsion tube. The single-phase flow in this section of the emulsion tube can be modeled using momentum conservation in a circular pipe, taking into account pressure losses due to friction and sudden expansions [24]. It is modeled as

$$\frac{P_{mj}}{\rho_f} + \frac{v_{mj}^2}{2} = \frac{P_{et,0}}{\rho_f} + g L_{et,0} + \frac{v_{et,0}^2}{2}\left(1 + f\frac{L_{et,0}}{D_{et}}\right) + k_m \frac{v_{mj}^2}{2} \tag{5}$$

where v_{mj} is the velocity in the main fuel orifice, $P_{et,0}$ is the pressure at the end of the single-phase part of the fuel tube, $L_{et,0}$ is the length of this tube, D_{et} its diameter, f is the Darcy friction factor, and k_m is the pressure loss coefficient for sudden expansion.

Fuel Well Surrounding the Emulsion Tube. The main function of the fuel well under steady-state conditions is to control the covering or exposure of the emulsion tube holes in order to allow air to bleed through this system. The fuel level h_{fw} in the well can be found from

$$\frac{P_{mj}}{\rho f} + \frac{v_{mj}^2}{2} = \frac{P_{fw}}{\rho f} + g h_{fw} \tag{6}$$

where P_{fw} is the pressure on top of the fuel well level.

Emulsion Tube Holes. The emulsion tube has several levels of holes. These holes are drilled in sets of 2 or 4. They divide the emulsion tube into sections along the flow direction where different amounts of air travel with the fuel flow. When a level of holes in the emulsion tube is exposed, air can enter the emulsion tube if the pressure of the air in the fuel well is higher than the static pressure inside the emulsion tube. The airflow $\dot{m}_{a-ab,i}$ through the ith level of emulsion tube holes is given by

$$\dot{m}_{a-ab,i} = C_{D-ab,i} A_{ab,i} \sqrt{2\rho_a \left[P_{fw} - \left(P_{et,i} - \frac{4\sigma}{D_{ab,i}} \right) \right]} \tag{7}$$

where $C_{D-ab,i}$ is the discharge coefficient for the emulsion tube hole based on the area $A_{ab,i}$, $D_{ab,i}$ is the diameter of the hole, and σ is the surface tension of the fuel. The airflow in each segment of the emulsion tube is found through mass balance equations,

$$\dot{m}_{a-ab,i} = \dot{m}_{a-et,i} + \dot{m}_{et-a,i-1} \tag{8}$$

where the mass flow through the segment i of the emulsion tube, $\dot{m}_{a-ab,i}$, is equal to the mass flow through the previous segment and the air drawn through the air-bleed hole. Finally, the total airflow through the air-bleed system is the sum of the air through all the levels of air-bleed holes,

$$\dot{m}_{a-ab} = \sum_{i=1}^{\text{levels}} \dot{m}_{a-ab,i} \tag{9}$$

Two-Phase Flow in Emulsion Tube. The pressure drop $\Delta P_{2\Phi}$ in the ith segment of the emulsion tube can be described as

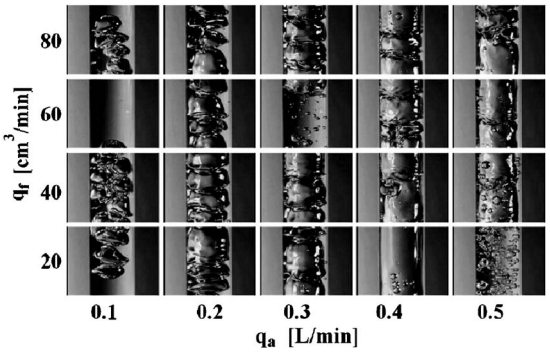

Fig. 3 Two-phase flow regimes in a small pipe

$$P_{et,i-1} - P_{et,i} = \Delta P_{2\Phi}(\dot{m}_f, \dot{m}_{a-et,i}) \tag{10}$$

where $P_{et,i-1}$ is the pressure at the beginning of this segment, $P_{et,i}$ the pressure at the end of the segment. A detailed description of this function will be given below.

Air Orifice. Airflow through the air-bleed system is restricted by an orifice located at the inlet of the venturi. Very little air flows through this system, so it can be described by the equation of incompressible nozzle

$$\dot{m}_{a-ab} = C_{D,aj} A_{aj} \sqrt{2\rho_a (P_{v,in} - P_{aj})} \tag{11}$$

where $C_{D,aj}$ is the discharge coefficient based on the orifice area A_{aj} and P_{aj} is the pressure after the orifice.

Air Path. The flow through the air-bleed system can be modeled as incompressible viscous pipe flow with friction losses and expansion losses

$$\frac{P_{aj}}{\rho_a} + \frac{v_{aj}^2}{2} = \frac{P_{fw}}{\rho_a} + \frac{v_{ap}^2}{2}\left(1 + f\frac{L_{ap}}{D_{ap}} + \sum k_{m,ap}\right) + k_m \frac{v_{aj}^2}{2} \tag{12}$$

where v_{ap} is the mean velocity in the air-bleed system whose length and diameter are L_{ap} and D_{ap}, and $k_{m,ap}$ is the pressure loss coefficient for bends and expansions in the system.

Details of Two-Phase Pressure Drop. Characterizing the pressure drop in the emulsion tube where a two-phase flow of air and fuel is created requires the determination of the effect of density change and friction losses. The homogeneous model was previously used by Harrington [25], Szczecinsky [3], Shinoda et al. [16], and Furuyama [17]. These models assume that the airflow and fuel flow create a mixture of homogeneous properties, so a mean density and viscosity are adequate to characterize the flow. Figure 3 shows a sample of different two-phase flow configurations that can be seen in a small pipe of similar dimensions to those found in carburetors, as a function of airflow and fuel flow (q_a and q_f, respectively). These visualization experiments, similar to those of Oya [21], indicate that the actual flows feature different two-phase flow regimes with bubbles of different sizes, depending on the combination of fuel flow and airflow: at low airflow, the bubbles are of small size and lenticular in shape; at higher airflow bubbles grow and stretch, becoming churn flow. The impact of fuel flow is less apparent, since the bubble sizes and structure do not change so much with fuel flow.

In order to assess the effect of two-phase flow in the emulsion tube, the pressure drop due to friction and to mixture-density change in a short pipe (10 cm long, 0.6 cm dia) were calculated with the homogeneous model as a function of volumetric fuel flow and airflow, as shown in Fig. 4. It can be noted that friction losses are two orders of magnitude smaller than the density term.

These predictions were compared to the actual pressure drops obtained in an experimental setup as depicted in Fig. 5. Fuel was pumped into a clear vertical pipe of 0.6 cm in diameter. The liquid

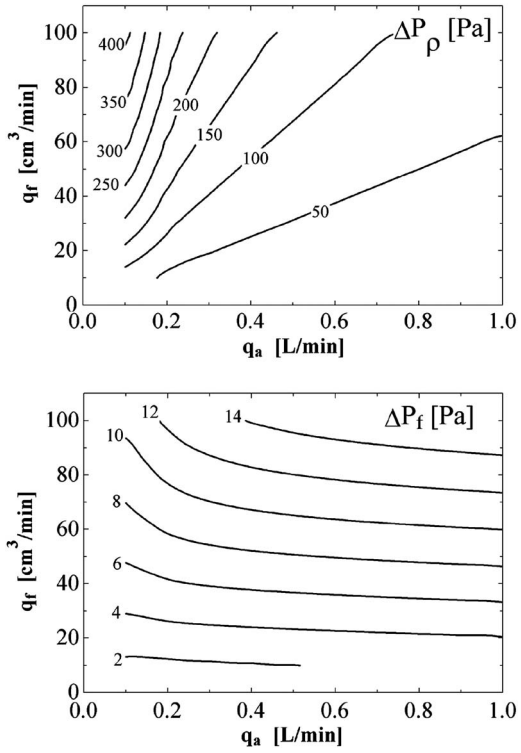

Fig. 4 Lines of constant gravitational and frictional pressure change for a short pipe, using the homogeneous model plotted versus airflow and fuel flow

used was mineral spirits, which has similar density and viscosity to gasoline, but lower volatility. House air was brought into the clear pipe through a mixer, which was designed as a manifold that mimicked the lateral holes in the emulsion tube. The test section was placed five pipe diameters above the mixer. An electronic pressure transducer was used to measure the pressure difference between pressure taps located 10 cm apart.

Figure 6 shows the contours that approximate the experimental results. When compared to the predictions by the homogeneous model (Fig. 4), it can be noted that they disagree in magnitudes and trends. For a range of airflow from 0 to ≈0.15 L/min, the pressure drop is a function of airflow only, which resembles the visualization experiments where the features of the two-phase flow, such as bubble sizes, change with airflow and not with fuel flow. This trend changes with higher airflow, where an increase in

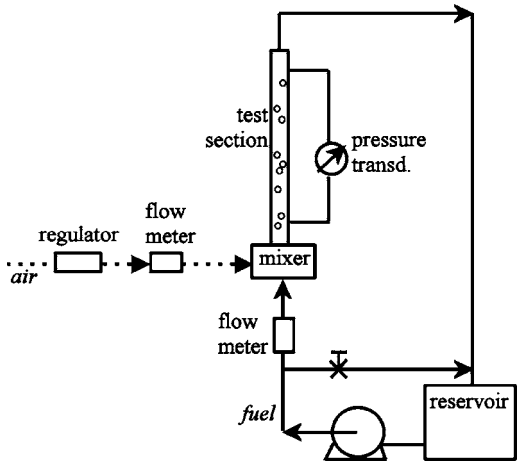

Fig. 5 Experimental setup for emulsion tube measurements

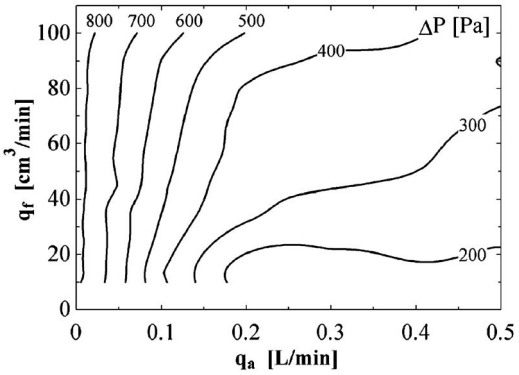

Fig. 6 Pressure contours derived from experiments for two-hole emulsion tube

fuel flow increases the pressure drop.

An empirical correlation was fitted to the data through a second-order linear regression that gave an agreement of $R^2 = 0.92$. The correlation is shown in Eq. (13), and its comparison with the experimental values is shown in Fig. 7

$$\frac{dP}{dL} = 5.66(10^3) + 3.70(10^6)\dot{m}_f + 1.51(10^9)\dot{m}_f^2 - 1.34(10^9)\dot{m}_a + 8.31(10^13)\dot{m}_a^2 \quad (13)$$

The pressure drop in the two-phase part of the emulsion tube (Eq. (10)) relates to this correlation by

$$\Delta P_{2\Phi}(\dot{m}_f, \dot{m}_{a-et,i}) = \frac{dP}{dL} L_{et,i} \quad (14)$$

Implementation in EES and Experimental Validation. The model was implemented in the Engineering Equation Solver (EES) [26], with configurations for one, two, or three levels of holes in the emulsion tube. Figure 8 shows the prediction of fuel flow as function of airflow through the venturi in the configuration of one level of emulsion tube holes for a range of inlet air velocity from 5 to 30 m/s. Figure 9 shows the fuel level in the fuel well. Several features can be found in these plots:

- There is a minimum air velocity required to overcome the hydrostatic pressure difference between the fuel bowl and the venturi throat.
- When an emulsion hole is exposed, it produces a sudden jump in fuel flow as the pressure drop in the upper segment of the emulsion tube is decreased by the two-phase flow. Such an effect was reported by Shinoda et al. [16]. The

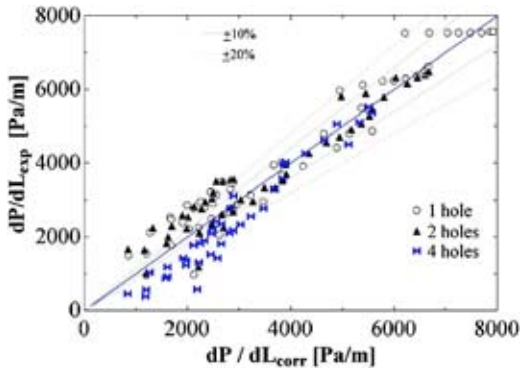

Fig. 7 Comparison of predicted and correlated data using the empirical correlation derived from data in this study

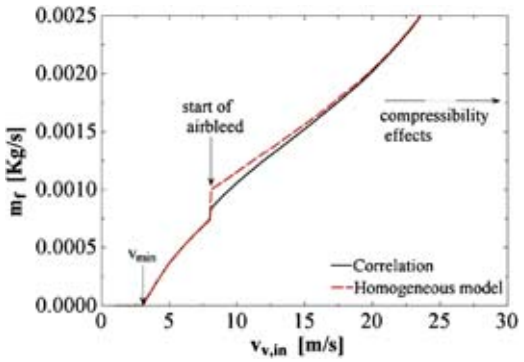

Fig. 8 Fuel flow versus airflow

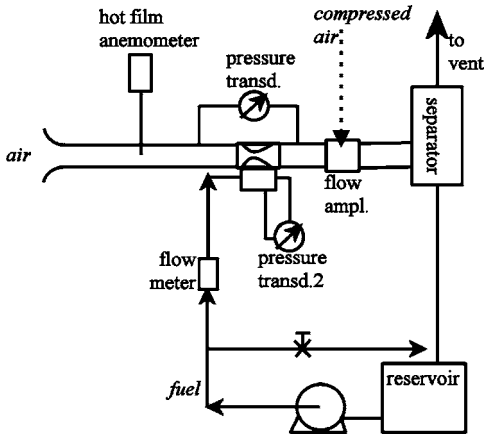

Fig. 11 Fuel height in fuel well versus airflow

difference between the two-phase flow models (homogeneous model and empirical correlation) is indicated by a smaller jump in fuel flow and a smoother transition in fuel level predicted by the empirical two-phase pressure drop correlation compared to the predictions from the homogeneous model.

- There is a wide range of air velocities where fuel flow increases linearly with airflow in the venturi.
- At higher airflows, compressibility effects start to be noticeable as a similar increase in pressure drop in the venturi draws less air mass due to its compressibility.

Implementation of the model with three levels of emulsion holes allows it to predict the flow through each of the emulsion hole levels and the effect on the fuel flow, as shown in Fig. 10, where the same features described above can be found.

The steady-state model was validated experimentally by measuring the fuel flow and airflow in a commercial carburetor (Nikki). Figure 11 shows the experimental setup. House air was used to create a low-pressure zone by means of a flow amplifier. This low pressure drove air from the laboratory conditions to pass through a commercial carburetor. The emulsion tube in the carburetor was a brass tube of 0.5 cm in diameter and 4 cm in length, with three levels of holes. A pump was used to supply mineral spirits to the float valve of the carburetor at approximately the same pressure that would be generated by an elevated fuel tank. The appropriate specification of the boundary conditions of the flow network required measurements of the inlet air velocity, the pressure at the inlet of the venturi, the pressure difference between the inlet and the outlet of the carburetor, and the fuel level inside the fuel bowl. Once the airflow was set, the system was allowed to reach a steady-state condition (e.g., constant fuel flow). At this moment, the measurements of the fuel flow were registered.

Figure 12 shows the comparison between the experiments and the prediction from the steady-state model. In this figure, the solid line represents the prediction of the model, and the circles the experimental results. The uncertainty propagation of the predicted fuel flow, based on the measurements of the boundary conditions, is shown as gray lines. The uncertainty of the measurements is ± 2 cm^3/min. These results indicate that the model is successful at capturing all the metering elements and the pressure drop in the emulsion tube. It is interesting to note that the model captured the sudden jump after the air-bleed system starts to work and the fuel flow at higher velocities when the two-phase mixture is formed in the emulsion tube. This indicates that although the correlation for two-phase flow was derived for a limited geometry, it scaled well for a smaller pipe. Future work will deal with the derivation of a more general correlation that takes into account a larger range of sizes of small diameter pipes.

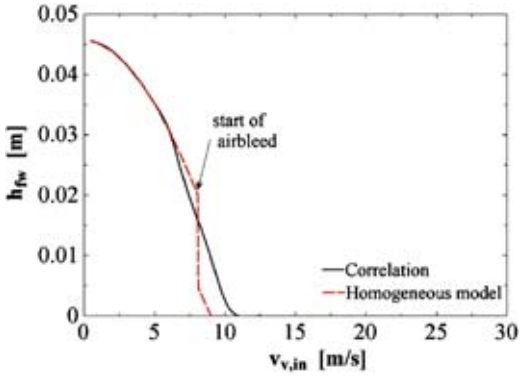

Fig. 9 Experimental setup for carburetor fuel flow and airflow

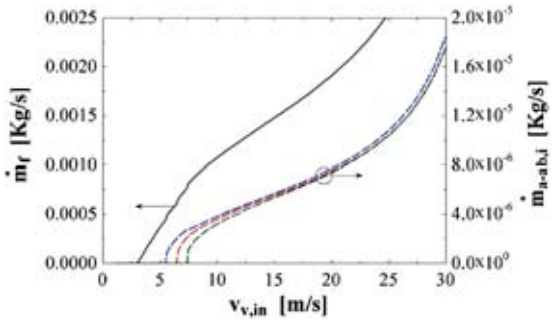

Fig. 10 Experimental validation of carburetor model under steady-state flow

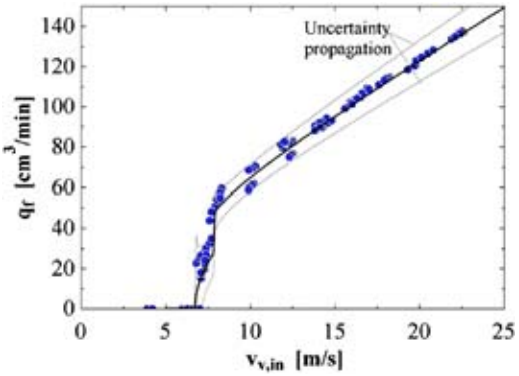

Fig. 12 Airflow in emulsion tube versus venturi airflow, for an emulsion tube with three levels of holes

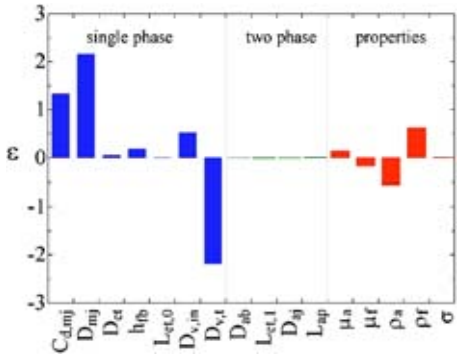

Fig. 13 Relative sensitivity analysis of fuel flow for different geometric and physical parameters

Sensitivity Analysis. The steady-state model can be used to study the effect of individual parameters (geometry and fuel properties) on the fuel flow by calculating the relative sensitivity ε_i defined as

$$\varepsilon_i = \frac{\partial \dot{m}_f}{\partial k_i} \frac{k_i}{\dot{m}_f} \tag{15}$$

where k_i is the parameter of interest [27]. For an air velocity of 15 m/s, ε_i was calculated for the parameters shown in Fig. 13. It is apparent that the discharge coefficient C_d of the main fuel orifice and the diameters of the main fuel orifice and venturi throat are the factors that cause the greatest impact on fuel flow. The negative value of the relative sensitivity of the venturi throat diameter indicates that an increase in diameter would reduce the fuel flow, since the pressure at the throat would be higher. The low sensitivity of parameters that affect the two-phase flow indicate that these elements are more important under transient conditions (e.g., engine operation conditions) than under steady-state conditions.

Quasi-Steady-State Approximation. The steady-state model may be extended to a dynamic one by assuming a quasi-steady-state approximation, as was done in the previous models [2–4,16,17]. Assuming a pressure in the inlet of the venturi that changes with time, "instantaneous" quasi-steady-state equations can be solved. Figure 14 shows an idealized sinusoidal pressure change with time and the air velocity at the inlet of the venturi. It shows fuel flow and airflow through the air-bleed system, which correspond to these changes in pressure. It can be noted that both airflow and fuel flow closely follow the pressure variation. In these plots, the horizontal axis is an angle θ, since the nature of the quasi-steady model makes the solution independent from the frequency of the pressure change.

The drawbacks of the quasi-steady-state model are that inertial effects are not seen, and an integrated air-fuel ratio remains constant independent of the frequency of the pressure change.

Unsteady Model.

Equations for Unsteady Flow. In order to extend the time response characteristics of the model, differential equations were derived for pipe flow and the fuel well. The mass balance for instantaneous one-dimensional Navier-Stokes equations for fuel flow in the single-phase part of the emulsion tube is given by

$$\frac{\partial \rho}{\partial t} + \rho \frac{\partial u}{\partial x} = 0 \tag{16}$$

For incompressible flow, it reduces to

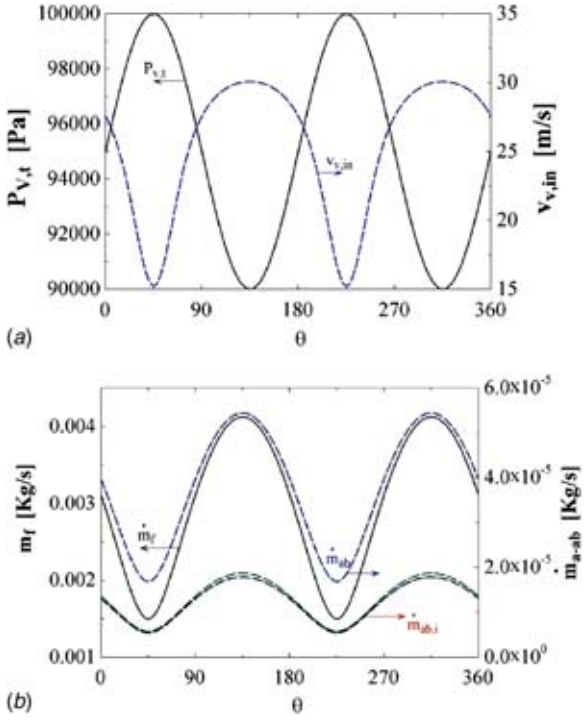

Fig. 14 Quasi-steady-state model; (a) Idealized pressure at venturi throat and air velocity at venturi inlet and (b) Instantaneous fuel flow and airflow

$$\rho \frac{\partial u}{\partial x} = 0 \tag{17}$$

Using this result, the momentum conservation equation can be simplified to

$$\frac{\partial u}{\partial t} + \frac{1}{\rho}\frac{\partial P}{\partial x} + \frac{4\tau_w}{\rho D} + g = 0 \tag{18}$$

where τ_w is the shear stress on the wall and D is the tube diameter. By using the Darcy friction factor f, defined as $f = 8\tau_w/(\rho u^2)$, Eq. (18) may be written as

$$\frac{\partial u}{\partial t} + \frac{1}{\rho}\frac{\partial P}{\partial x} + f\frac{1}{D}\frac{u^2}{2} + g = 0 \tag{19}$$

An approximation of this equation applied to the single-phase part of the emulsion tube can be written as

$$\frac{\partial u_{et,0}}{\partial t} + \frac{1}{\rho_f}\frac{P_{mj} - P_{et,0}}{L_{et,0}} + f\frac{1}{D_{et}}\frac{u_{et,0}^2}{2} + g = 0 \tag{20}$$

This differential equation replaces the algebraic equation (5) for pressure drop in the single-phase-flow segment of the emulsion tube. Equation (20) requires the term $\partial u_{et,0}/\partial t$ to be integrated in order to yield the instantaneous velocity $u_{et,0}$. A similar equation could be written for the air system, but it was not done considering that the inertia of the fuel is three orders of magnitude larger than the inertia of air.

Implementation in EES. The implementation of the unsteady model consisted of solving an initial-value problem for a differential equation with simultaneous nonlinear equations over time. The model was implemented in EES. Fuel flow is shown in Fig. 15 and the fuel level in the fuel well in Fig. 16, for hypothetical sinusoidal pressure changes at 900, 1800, and 3600 rpm. In these plots, the horizontal axis is time instead of angle, as in Fig. 14.

Some important differences between the quasi-steady model and unsteady model include the following:

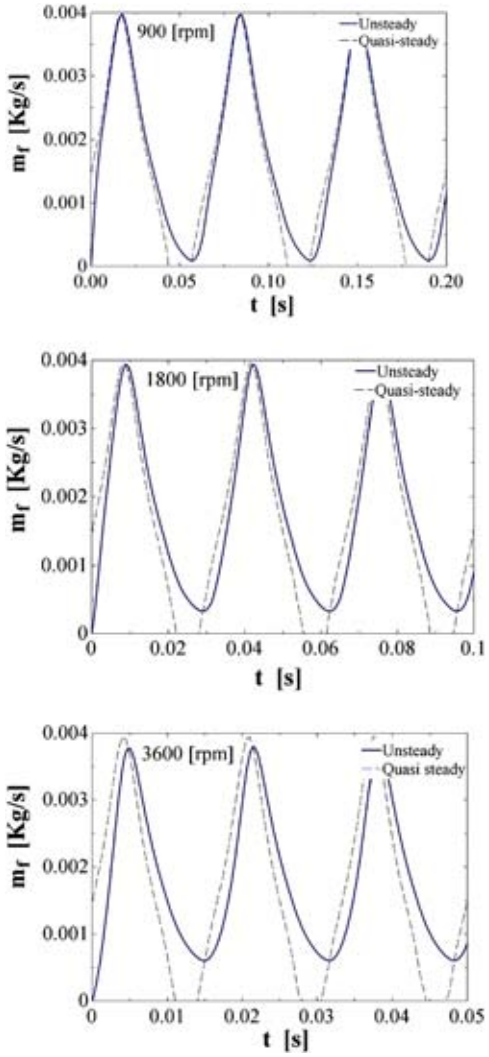

Fig. 15 Instantaneous fuel flow for changing venturi pressure at 900, 1800, and 3600 rpm

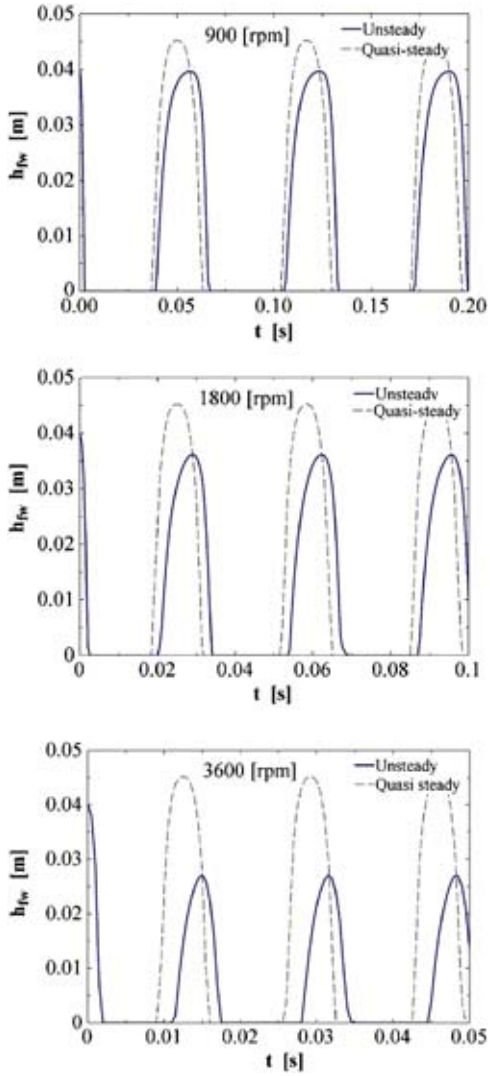

Fig. 16 Instantaneous fuel level in fuel well for changing venturi pressure at 900, 1800, and 3600 rpm

- There is a delay between pressure changes and fuel flow, which is more noticeable with increasing frequency.
- For the quasi-steady-state model, there are some periods of time where pressure drop in the venturi is not enough to drive fuel flow. This effect is eliminated with the unsteady model, since fuel has enough inertia to keep flowing even at very low quantities. With increasing frequency, the inertia overcomes these periods, so more fuel is drawn at the low-pressure difference periods of the venturi.
- The periods of time of low pressure drop in the venturi are also apparent in the fuel level in the fuel well, where the peak level increases to initial values for the quasi-steady model but decreases with increasing engine speed in the dynamic model.
- The peak in fuel flow is decreased, also due to the same inertial effect.

As expected, at lower frequencies (900 rpm) the unsteady model predictions approach those of the steady-state model since the inertial terms play a less important role when the pressure conditions change slowly.

Finally, the integrated air-fuel ratio was calculated and are shown in Fig. 17. A notable fuel-enrichment effect with increasing frequency is apparent, with the air-fuel ratio going from an average of 12.3 to 11.5. This enrichment due to pulsating flow compared to steady flow was reported by Moss [18].

Conclusions

The major contribution of the present work is the detailed implementation of the equations involved in dynamic fuel flow for a complex flow network that represents a carburetor for small engines. Special detail was put into the correct modeling of two-phase flow in the emulsion tube based on the comparison of the homogeneous model and an empirical correlation for small pipes in carburetors. Although the development of a correlation for small pipes was based on a limited geometry, the experimental results of the steady-state model showed that it was appropriate for the characterization of the emulsion tube inside a real carburetor. Future work will establish a more general description of the pressure drop in a larger range of pipe diameters and lengths.

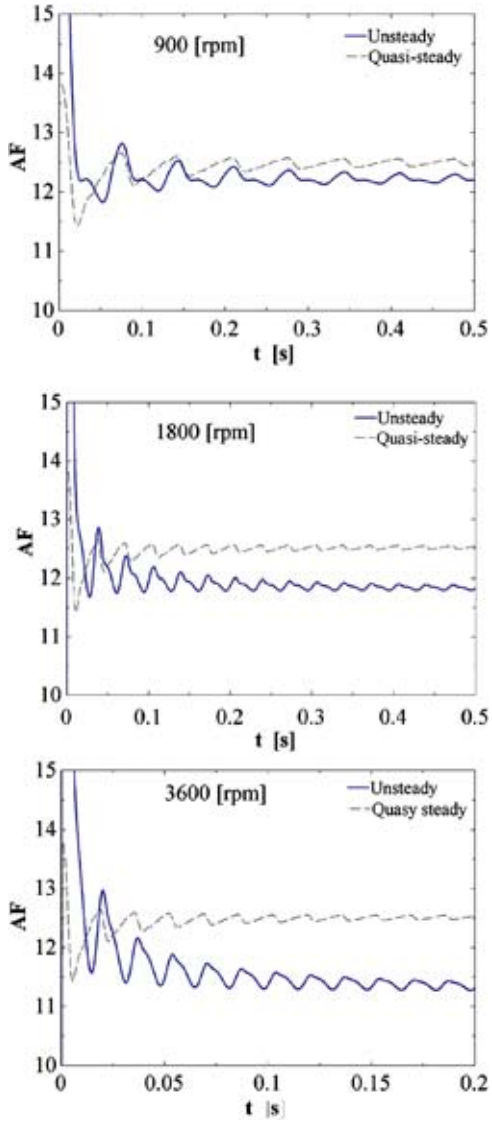

Fig. 17 Air-fuel ratio for changing venturi pressure at 900, 1800, and 3600 rpm

The implementation of partial differential equations to model unsteady flow in single-phase pipes expands the previous models, now allowing the model to take into account inertial terms that were shown to fuel enrich the delivered mixture.

Extensions of this work will consist of performing the sensitivity analysis on the unsteady model, using measurements from real engines to verify the dynamic model and coupling the model with engine-performance prediction software.

Acknowledgment

The present project was funded by the Wisconsin Small Engine Consortium. The authors would like to thank Katie Lieg and Jeremy Granquist for their collaboration in the development of this project.

Nomenclature

A = cross-sectional area, m^2
C_D = discharge coefficient
D = diameter, m
f = friction factor
g = gravitational constant, m/s^2
h = height, m
k = parameter for sensitivity analysis
k_m = pressure loss coefficient
L = pipe length, m
$\dot{m}$ = mass flow rate, kg/s
P = pressure, N/m^2
v = average velocity, m/s

Greek Symbols

ε = relative sensitivity
γ = isentropic coefficient
μ = dynamic viscosity, $N\,s/m^2$
Φ = compressibility factor
ρ = density, kg/m^3
σ = surface tension, N/m

Subscripts

a = air
ab = air bleed
aj = air orifice
ap = air passages
et = emulsion tube
f = fuel
fb = fuel reservoir
fw = fuel well
i = element of a series
in = venturi inlet
mj = main fuel orifice
t = venturi throat
v = venturi
0 = total inlet conditions

References

[1] Heywood, J., 1988, *Internal Combustion Engine Fundamentals*, McGraw-Hill, New York.
[2] Harrington, D. L., and Bolt, J. A., 1970, "Analysis and Digital Simulation of Carburetor Metering." SAE (700082).
[3] Szczecinsky, J., and Rychter, T., 1991, "Theoretical Analysis of Mixture Stoichiometry in Engine Carburetor," SAE Paper No. 910078.
[4] Sendyka, B., and Filipczyk, J., 1995. "Simulation of the Characteristic of a Carburettor of an Internal Combustion Engine," SAE (950987).
[5] Benson, R. S., Baruah, P. C., and Sierens, R., 1974, "Steady and Non-Steady Flow in a Simple Carburettor," Proc. Inst. Mech. Eng. **188**(53), pp. 537–548.
[6] Bajema, D. L., and Gatecliff, G. L., 1978, "Prediction and Measurement of Fluid Flow in Single Cylinder Engine Carburetors," SAE (780285).
[7] Gamma Technologies, 2001, *GT-Power: User's Manual and Tutorial*, Gamma Technologies, Westmond.
[8] Wu, B., Feng Y., and Liu, J., 1997, "Numerical simulation of gas-liquid two-phase flow in motorcycle carburetor," *Proc. of International Symp. on Multiphase Flow*, ISMF.
[9] Van Werven, M., Van Maanen H. R. E., Ooms G., and Azzopardi, B. J., 2003, "Modeling Wet-Gas Annular/Dispersed Flow Through a Venturi," AIChE J. **49**(6), pp. 1383–1391.
[10] Lenz, H. D., 1990, *Mixture Formation in Spark-Ignition Engines*, Springer-Verlag, Berlin.
[11] Woods, W. A., and Goh, G. K., 1979, "Compressible Flow Through a Butterfly Throttle Valve in a Pipe," Proc. Inst. Mech. Eng. **193**, pp. 237–244.
[12] Ehara, M., Kinabara Y., Shinoda, K., Meguro, T., and Ishihara, T., 1980, "A Study of Carburetor Design," SAE (805142).
[13] Bolt, J. A., and Boerma, M., 1966, "The Influence of Inlet Air Conditions on Carburetor Metering," SAE (660119).
[14] Brereton, G. J., De Araujo, A., and Bertrand, E., 1996, "Effects of Ambient Conditions on the Emissions of a Small Carbureted Four-Stroke Engine," SAE (961739).
[15] Asano, Y., Chuma, T., Haga, H., and Mochida, T., 1968, "Effects of Air-Bleed Systems on Carburetor Performance," Bull. JSME **11**(46), pp. 691–698.
[16] Shinoda, K., Koide, H., and Yii, A., 1971, "Analysis and Experiments on Carburetor Metering at the Transition Region to the Main System," SAE (710206).
[17] Furuyama, M., 1981, "Fuel Supply Characteristics in the Transition Region of Fixed-Venturi Type Carburetor," Bull. JSME **24**(191), pp. 842–848.
[18] Moss, P. J., 1980, "Pulsation Enrichment in Carburettors," Automot. Eng.

5(4), pp. 53–56.
[19] Bolt, J. A., Derezinski, S. J., and Harrington, D. L., 1971, "Influence of Fuel Properties on Metering in Carburetors," SAE (710207).
[20] Wallis, G. B., 1969, *One-Dimensional Two-Phase Flow*, McGraw-Hill, New York.
[21] Oya, T., 1971, "Upward Liquid Flow in Small Tube Into Which Air Streams (1st Report, Experimental Apparatus and Flow Patterns)," Bull. JSME, **14** (78), pp. 1320-1329.
[22] Oya, T., 1971, "Upward Liquid Flow in Small Tube Into Which Air Streams (2nd Report, Empirical Correlation)," Bull. JSME **14**(78), pp. 1330–1339.
[23] Hosho, Y., 1967, "Flow Quantities of Air Introduced Through Air Bleeds Into Carburetors and Pulsation Fuel Jet phenomena," Hitachi Rev. **16**(4), pp. 173–178.
[24] White, F. M., 1999, *Fluid Mechanics*, 4th Edition, McGraw-HIll, New York.
[25] Harrington, D. L., 1968, Analysis and digital simulation of carburetor metering. Ph.D. thesis, University of Michigan.
[26] Klein, S. A., 1992–2004 "Engineering Equation Solver ees," *F-Chart Software*.
[27] Warnatz, J., Mass, U., and Dibble, R. W., 1999, *Combustion*, 2nd Edition, Springer, New York.

Sébastien Poncet
e-mail: poncet@irphe.univ-mrs.fr

Roland Schiestel

Marie-Pierre Chauve

I.R.P.H.E., UMR 6594, CNRS-Université Aix-Marseille I & II, Technopôle Château-Gombert,
49 rue F. Joliot-Curie,
13384 Marseille Cédex 13, France

Centrifugal Flow in a Rotor-Stator Cavity

The present work considers the turbulent flow inside an annular rotor-stator cavity with and without centrifugal throughflow. Extensive measurements performed using a two-component laser-Doppler anemometer technique, and pressure transducers are compared to numerical predictions based on one-point statistical modeling using a low-Reynolds-number second-order full-stress transport closure. A study of the flow control parameters is performed, and, for the first time, a better insight into the transition from Batchelor to Stewartson types of flow is gained from this study. The advanced second-order model is confirmed to be the adequate level of closure to describe such complex flows. [DOI: 10.1115/1.1949645]

1 Introduction

The study of the flow in a rotor-stator cavity has significant relevance to many configurations encountered in turbomachinery. There have been many fundamental experimental and theoretical works [1–3] of the flow in a closed rotor-stator system. Nevertheless, when a centrifugal throughflow is added, relatively few works have been published. Daily et al. [4] measured the average velocity profiles and put forward the importance of the outflow on the development of the Ekman layer and on the values of the entrainment coefficient of the fluid. Firouzian et al. [5] performed velocity and pressure measurements for a wide range of flow rates and rotational speeds. They tested also the effect of inlet geometry on the flow between two disks enclosed by a peripheral shroud. Numerically, Chew [6] was the first to study the flow inside a rotor-stator cavity with centrifugal throughflow using a low-Reynolds-number k-ϵ model. Chew and Vaughan [7] studied this type of flow with and without imposed throughflow with a model based on a mixing length hypothesis inside the whole cavity. Their results were quite comparable to the experimental data of Daily and Nece [1] and Daily et al. [4] apart from a relaminarization area close to the rotating axis. The model of Iacovides and Theofanopoulos [8] used an algebraic modeling of the Reynolds stress tensor in the fully developed turbulence area and mixing length hypothesis near the wall. It provided good results in the case of a rotor-stator flow with and without throughflow, but some discrepancies remain on the Ekman layer thickness and the rotation rate in the central area. Iacovides and Toumpanakis [9] tested four turbulence models and showed, especially, that the Reynolds stress model was an appropriate level of closure to describe rotor-stator flows in a closed cavity. Schiestel et al. [10] have used both a low-Reynolds-number k-ϵ model near the walls and an algebraic stress model (ASM) in the core of the flow. Second-order information was found to be necessary in turbulence closure to get a sufficient degree of universality in predicting rapidly rotating flows. Later Elena and Schiestel [11] also proposed some numerical calculations of rotating flows based on a zonal approach. They have also used a new modeling of the Reynolds stress tensors derived from the Launder and Tselepidakis [12] one. It provides a better prediction than the simpler model of Hanjalic and Launder [13]. But there also, the authors emphasize the too high laminarization of the flow in comparison to the expected results. Iacovides et al. [14] tested two low-Reynolds-number models: a classical k-ϵ model and a modified Reynolds stress (RSM) model, which takes into account the effect of the rotation. More recently, Poncet et al. [15] compared pressure and velocities measurements to numerical predictions based on an improved version of the Reynolds stress modeling of Elena and Schiestel [16]. All the comparisons were in excellent agreement for the mean and turbulent fields. The RSM model is then, indeed, the adequate level of closure compared to the classical k-ϵ model to describe the turbulent flow with or without an imposed in- or outflow.

The present study puts forward a numerical approach, which is a valuable tool to predict the mean flow structure and the turbulent intensities in a rotor-stator system with outward throughflow. If the experimental approach and the DNS are both important routes for detailed investigations, then building an experimental rig remains very expensive and the DNS are limited at present time to small rotation rates (Reynolds number not higher than 4×10^5 [17] in practice). Then, the present RSM turbulence model still appears as a valuable tool for extending the range of geometrical and physical parameters under consideration and useful for industrial design. The predictions are found here in excellent agreement with the velocity and pressure measurements.

2 Experimental Setup

2.1 Apparatus. The cavity sketched in Fig. 1 is composed of a fixed disk (the stator) and a smooth rotating disk (the rotor). A fixed shroud encloses the cavity. The rotor and the central hub attached to it rotate at the uniform angular velocity Ω.

The mean flow is mainly governed by three control parameters: the aspect ratio G, the Reynolds number Re based on the outer radius of the rotor, and the flow-rate coefficient C_w [2], defined as follows:

$$G=\frac{h}{R_2}\quad \mathrm{Re}=\frac{\Omega R_2^2}{\nu}\quad C_w=\frac{Q}{\nu R_2}$$

where ν is the kinematic viscosity of water, $R_1=38$ mm and $R_2=250$ mm, respectively, the inner and outer radii of the rotating disk, $d=55$ mm and $R_3=253$ mm the central opening and the outer radius of the cavity, and Q the imposed throughflow. The height of the cavity h can vary between 0 and 12 mm. The radial gap $e=R_3-R_2$ is fixed to 3 mm.

A pump allows one to impose a variable throughflow Q. The rotation of the disk is produced by a 5.5 kW electric servomotor. The accuracy on the measurement of the angular velocity and on the flux is better than 1%. In order to avoid cavitation effects, the cavity is maintained at rest at a pressure of 2 bar using a tank-buffer. The temperature is also maintained constant (23 °C) using a heat exchanger, which allows one to remove the heat produced by friction in order to keep constant the density and the kinematic viscosity of water.

Contributed by the Fluids Engineering Division for publication in the JOURNAL OF FLUIDS ENGINEERING. Manuscript received by the Fluids Engineering Division November 17, 2004; Final manuscript received March 30, 2005. Associate Editor: Yoshinobu Tsujimoto.

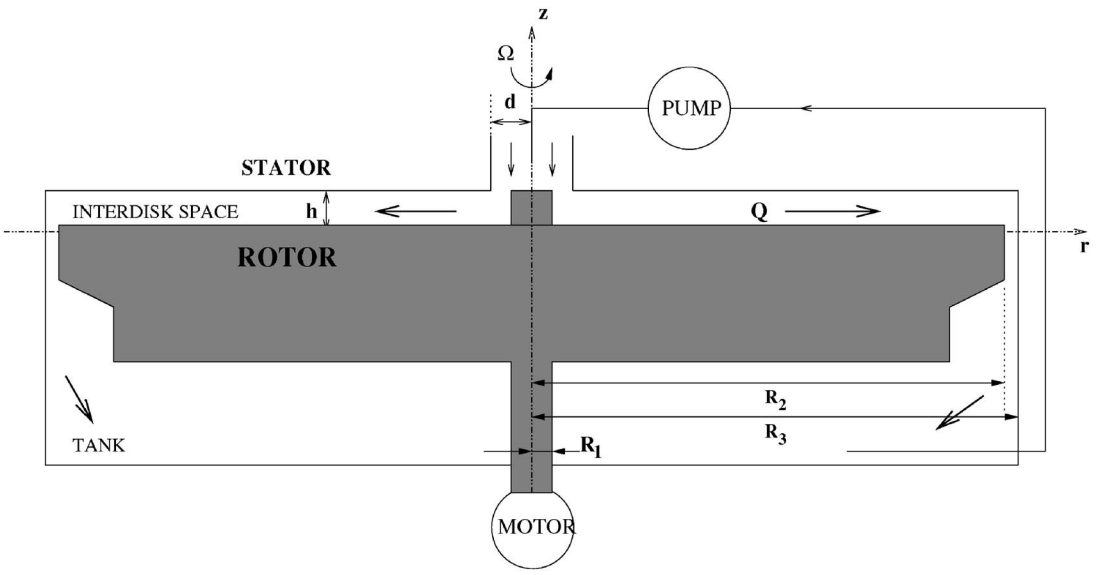

Fig. 1 Experimental setup and notations

2.2 Experimental Measurement Techniques. The measurements are performed by means of a two-component laser-Doppler anemometer (LDA) and also by pressure transducers. The LDA technique is used to measure, from above the fixed disk, the mean radial $\overline{V_r}$ and tangential $\overline{V_\theta}$ velocities as well as the associated Reynolds stress tensor components $R_{11}^*=\overline{v_r'^2}/(\Omega r)^2$, $R_{12}^*=\overline{v_r'v_\theta'}/(\Omega r)^2$, $R_{22}^*=\overline{v_\theta'^2}/(\Omega r)^2$ in a vertical plane (r,z) at a given azimuthal angle (v_r' and v_θ' are the fluctuating parts of the radial and tangential velocity components and r is the radial location). This method is based on the accurate measurement of the Doppler shift of laser light scattered by small particles (Optimage PIV Seeding Powder, 30 μm) carried along with the fluid. About 5000 validated data are necessary to obtain the statistical convergence of the measurements. Its main defect is due to the size of the probe volume (0.8 mm in the axial direction), which is large compared to the boundary layer thicknesses and for small values of the interdisk space h. Its main qualities are its non intrusive nature and its robustness. A three-dimensional 3D traverse system enables the LDA to move in the three directions with accuracy (0.01 mm).

Pressure is measured by six piezoresistive transducers, which are highly accurate (0.05% in the range 10–40 °C) and combine both pressure sensors and temperature electronic compensations. Nevertheless, according to the experimental conditions, the accuracy on the pressure is about 5%. They are fixed on the stator at the following radial locations 0.093, 0.11, 0.14, 0.17, 0.2, and 0.23 m disposed along two rows. Previous pressure measurements by embedded pressure gages [18] showed that the pressure on the rotor and the one on the stator at the same radius are, in fact, identical within 2.5% accuracy. This is a direct consequence of the Taylor-Proudman theorem, which forbids axial gradients in rapidly rotating flows.

3 Statistical Modeling

3.1 Differential Reynolds Stress Model. The flow studied here presents several complexities (high rotation rate, imposed through-flow, wall effects, transitional zones), which are a severe test for turbulence modeling methods. Our approach is based on one-point statistical modeling using a low-Reynolds-number second-order full stress transport closure derived from the Launder and Tselepidakis [12] model and sensitized to rotation effects [16]. This approach allows for a detailed description of near-wall turbulence and is free from any eddy viscosity hypothesis. The general equation for the Reynolds stress tensor R_{ij} can be written

$$\frac{dR_{ij}}{dt} = P_{ij} + D_{ij} + \Phi_{ij} - \epsilon_{ij} + T_{ij}, \tag{1}$$

where P_{ij}, D_{ij}, Φ_{ij}, ϵ_{ij}, and T_{ij}, respectively, denote the production, diffusion, pressure-strain correlation, dissipation, and extra terms. The diffusion term D_{ij} is split into two parts: a turbulent diffusion D_{ij}^T, which is interpreted as the diffusion due to both velocity and pressure fluctuations [19], and a viscous diffusion D_{ij}^ν, which cannot be neglected in the low-Reynolds-number region. In a classical way, the pressure-strain correlation term Φ_{ij} can be decomposed as follows:

$$\Phi_{ij} = \Phi_{ij}^{(1)} + \Phi_{ij}^{(2)} + \Phi_{ij}^{(w)} \tag{2}$$

$\Phi_{ij}^{(1)}$ is interpreted as a slow nonlinear return to isotropy and modeled as a quadratic development in the stress anisotropy tensor, with coefficients sensitized to the invariants of anisotropy. This term is damped near the wall. The linear rapid part $\Phi_{ij}^{(2)}$ includes cubic terms. A wall correction $\Phi_{ij}^{(w)}$ is applied to the linear part, which is modeled using the Gibson and Launder hypothesis [20] with a strongly reduced numerical coefficient. However, the widely adopted length scale $k^{3/2}\varepsilon^{-1}$ is replaced by the length scale of the fluctuations normal to the wall. The viscous dissipation tensor has been modeled in order to conform with the wall limits obtained from Taylor series expansions of the fluctuating velocities [21]. The extra term T_{ij} accounts for implicit effects of the rotation on the turbulence field. Indeed, high-speed rotation produces indirect effects on the turbulence field that are not modeled in usual closures, even in second-order closures. These effects modify the structure of the turbulence eddies in a complex manner that can be evidenced in two-point statistics [22]. A practical extension for one-point closures, to approximate the effects, has been developed in [23]. It consists of additional terms in the stress transport equations that act only when the flow is subjected to strong rotation. More precisely, the pressure-strain correlation is sensitized to the Reynolds and Cambon structure tensor, and a spectral jamming term is added that enhances bidimensionality. The effect of blocking of the spectral transfer is also included. These terms are fully explained and detailed analytically in [23].

3.2 Numerical Method. The computational procedure is based on a finite-volume method using staggered grids for mean

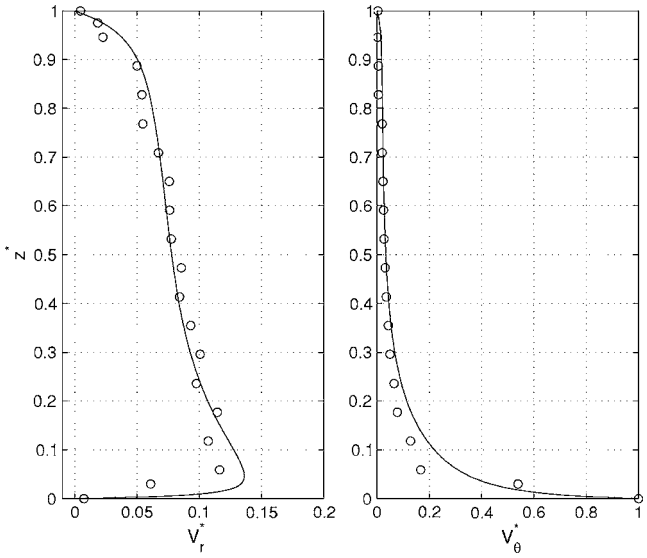

Fig. 2 Mean velocity profiles for Re=10^6, G=0.036, C_w=5929 at r^*=0.56: (-) the RSM model and (○) the experimental data

velocity components with axisymmetry hypothesis in the mean. A 140×80 mesh in the (r,z) frame proved to be sufficient in most cases ($\mathrm{Re}\leqslant1.038\times10^6$) considered in the present work to get grid-independent solutions. It has been verified that the numerical solution is, indeed, accurate within 1.5% (maximum error for velocity and stress components) compared to the solution obtained on a mesh using twice the number of nodes. Nevertheless, a more refined mesh 200×100 is necessary for the cases with Re=4.15×10^6. About 20,000 iterations (10 hr) on the NEC SX-5 (IDRIS, Orsay, France) are necessary to obtain the numerical convergence of the calculation. In order to overcome stability problems, several stabilizing techniques are introduced in the numerical procedure, such as those proposed by Huang and Leschziner [24]. Also, the stress component equations are solved using matrix block tridiagonal solution to enhance stability using nonstaggered grids.

3.3 Boundary Conditions. At the wall, all the variables are set to zero except for the tangential velocity V_θ, which is set to Ωr on rotating walls and zero on stationary walls. At the inlet and outlet areas, it is supposed that V_θ varies linearly from zero on the stationary wall up to Ωr on the rotating wall. When a throughflow is enforced, a parabolic profile is then imposed for the axial velocity V_z at the cavity inlet, with a given low level of turbulence intensity. In the outflow section, the pressure is fixed, whereas the derivatives for all the other independent quantities are set to zero if the fluid leaves the cavity, and fixed external values are imposed if the fluid reenters the cavity.

4 Results and Discussion

4.1 Model Performances. In order to show the detailed performances of the RSM model, a typical particular case has been considered: Re=10^6, G=0.036, C_w=5929 at the dimensionless radial location $r^*=r/R_2$=0.56 and the mean and turbulent fields have been studied. Figures 2 and 3 show, respectively, the dimensionless mean radial $V_\theta^*=\overline{V_\theta}/(\Omega r)$ and tangential $V_r^*=\overline{V_r}/(\Omega r)$ velocity profiles and the associated Reynolds stress tensors along the axial direction $z^*=z/h$. The model predictions are in very good agreement with the experimental data. Considering the narrow gap between the disks, the probe integration leads to underestimated velocities and stresses (Figs. 2 and 3) very near the wall. Previous works [16,15] have shown that this level of closure is the most appropriate to describe rotating flows with or without throughflow (centripetal or centrifugal), while the classical k-ϵ model, which is blind to any rotation effect, presents serious deficiencies. So, the second-order model can now be confidently used to carry parametric studies even for high values of the flow rate, as in the present case.

4.2 Pressure Distributions. We performed pressure measurements by means of six pressure transducers located on the stator along two rows because of geometrical constraints. We choose to take as a reference the pressure measured at the outer radial position r^*=0.92 and define the following pressure coefficient: $C_p^*(r^*)=P^*(r^*)-P^*(0.92)$. The dimensionless pressure P^* is given by: $P^*=2P/(\rho\Omega^2R_2^2)$, where ρ is the density of water and P the

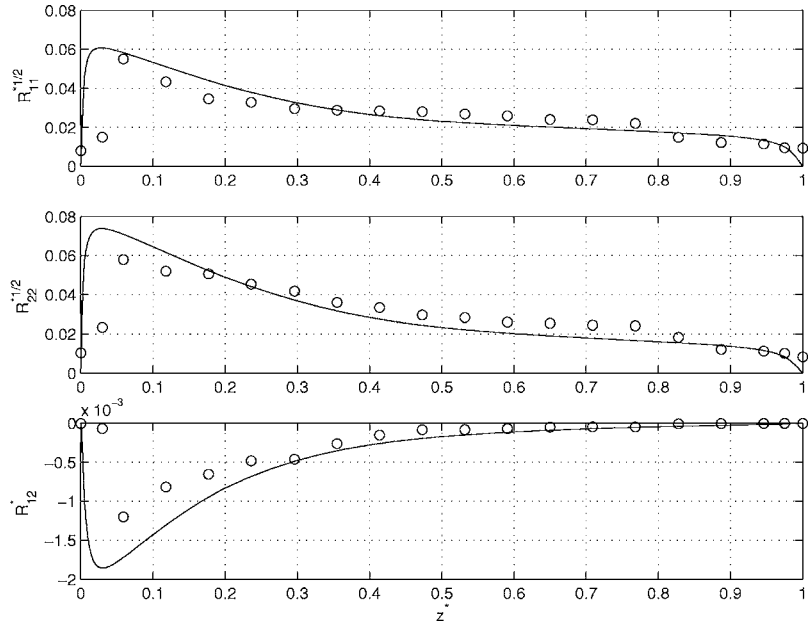

Fig. 3 Axial profiles of the Reynolds stress tensors for Re=10^6, G=0.036, C_w=5929 at r^*=0.56: (-) the RSM model and (○) the experimental data

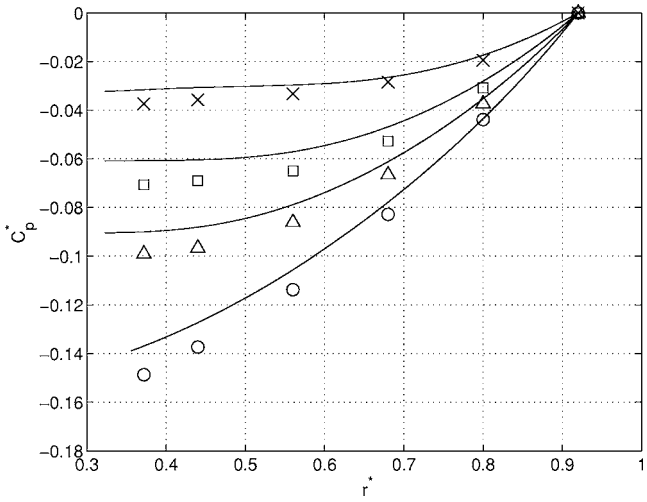

Fig. 4 Radial pressure distribution for Re=4.15×10⁶ and *G*=0.036: (-) the RSM model and the experimental data for (×) C_w=10317, (□) C_w=5159, (△) C_w=2579, (○) C_w=0

pressure. In Figs. 4 and 5, the pressure coefficient is plotted versus the dimensionless radial position for $\mathrm{Re}=4.15\times10^6$ and two values of the aspect ratio. As expected, the pressure decreases toward the center of the cavity; C_p^* is then always negative. At a given radius and for this Reynolds number, it can be observed that C_p^* decreases for increasing values of the flow rate, which is contrary to the case with a centripetal throughflow [25]. Note that, in the cases of weaker Reynolds numbers, the pressure coefficient is very close to zero.

The RSM model predicts very well the radial pressure gradient for both aspect ratios compared to the experimental data, considering that C_p^* is a very sensitive check to test numerical calculations and that the maximum error between the experimental data and the numerical predictions is not higher than 1 mbar, which is within expected experimental accuracy. Nevertheless, the numerical results seem to depend on the interdisk space, whereas it is not the case experimentally. Viscous terms at the wall are probably involved.

4.3 Mean Velocity Profiles. The aim of this section is to describe the transition between a Batchelor-type flow with two

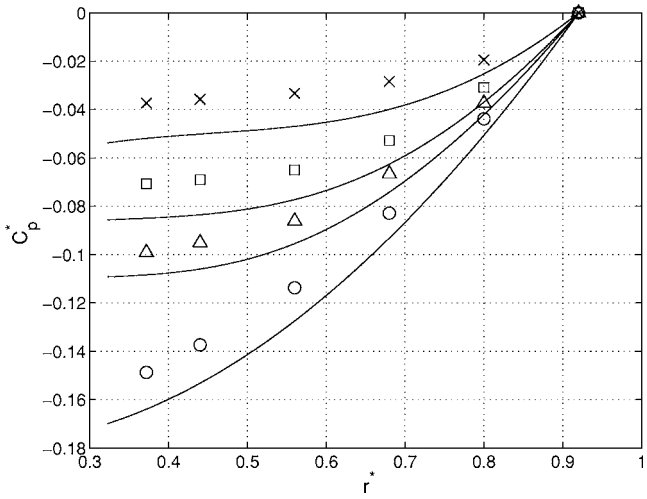

Fig. 5 Radial pressure distribution for Re=4.15×10⁶ and *G*=0.012: (-) the RSM model and the experimental data for (×) C_w=10317, (□) C_w=5159, (△) C_w=2579, (○) C_w=0

boundary layers separated by a central rotating core and a Stewartson-type flow with only one boundary layer on the rotor according to the flow control parameters: the Reynolds number, flow rate, and aspect ratio. The radial locations considered in Figs. 6–9 are chosen in order to show more clearly this transition.

4.3.1 Effect of the Reynolds Number. For a given centrifugal flow rate C_w=5159 and at a given radial position r^*=0.68, Fig. 6 shows the transition between a Stewartson- and Batchelor-type flow for increasing values of the Reynolds number. Until $\mathrm{Re}=1.038\times10^6$, there is only one boundary layer on the rotating disk. Apart from the rotor boundary layer, the tangential velocity is close to zero. The radial velocity is maximum in this layer and always positive. That denotes a Stewartson-type flow. For greater Reynolds numbers, the flow is of Batchelor type, with two boundary layers: a centripetal boundary layer on the stator (Bödewadt layer) and a centrifugal one on the rotor (Ekman layer) separated by a central rotating core. Note that, for these three Reynolds numbers, there is an excellent agreement between the experimental data and numerical results.

4.3.2 Effect of the Flow Rate. When a weak centrifugal throughflow is imposed (Fig. 7(*b*)), the flow keeps the same characteristics as in a closed cavity (Fig. 7(*a*)): two boundary layers and a central rotating core, that is known as a Batchelor-type flow. Note that the Batchelor-type profile can appear only if the Bödewadt layer is centripetal. The tangential velocity decreases, but we still observe these two boundary layers. By increasing the flow rate, the central core disappears. The profiles for the tangential velocity are then Stewartson profiles (Fig. 7(*d*)), it means that the tangential velocity is zero apart from the Ekman layer. The radial velocity is then always positive. The limit case between Batchelor and Stewartson profiles is presented in Fig. 7(*c*).

4.3.3 Effect of the Aspect Ratio. Figures 8 and 9 display the velocity profiles corresponding to the case $\mathrm{Re}=1.038\times10^6$, C_w =5159 for two aspect ratios and at three radial positions, and Fig. 10 brings out the corresponding streamlines.

Depending on the radial location (Figs. 8 and 9), the flow belongs to the Batchelor- or Stewartson-type flow. For $r^*\leqslant0.68$, the flow is a Stewartson-type flow with only one boundary layer on the rotor. The core disappeared, and the radial velocity (which is always positive) becomes significant compared to the tangential velocity; the flow is then fully centrifugal. For $r^*\geqslant0.68$, the flow switches to Batchelor type with two separated boundary layers. The central core reappears, and the Bödewadt layer becomes centripetal.

Figure 9 brings out the main defect of the LDA technique, too. When the interdisk space is small (h=3 mm), as compared to the probe volume in the axial direction (0.8 mm), the measurements failed indeed. The integration of the mean radial velocity profile (Fig. 9(*a*)) calculated by the model is in agreement with the imposed centrifugal throughflow rate, whereas it is not the case for the experimental data. For G=0.012(h=3 mm), the experimental values underestimate the radial and tangential velocities because these are integrated values on a too big probe volume compared to the interdisk space. It was also difficult sometimes to measure very close to the walls for this aspect ratio.

According to Figs. 9(*a*) and 10(*b*), the flow is centrifugal in the whole cavity for G=0.012. The mean radial velocity profile for r^*=0.44 gets closer to a Poiseuille-like profile.

4.4 Mean K-Curve. The predictions of the RSM model have been validated against experimental data measured using the two-component LDA. Poncet et al. [25] have shown, analytically, that the entrainment coefficient K of the rotating fluid (the ratio between the tangential velocity in the middle of the interdisk space and that of the disk at the same radius) can be correlated, in the case of a centripetal throughflow, to a flow rate coefficient $Cq_r=Q(\Omega r^2/\nu)^{1/5}/(2\pi r^3\Omega)>0$. In figure 11, several points deduced

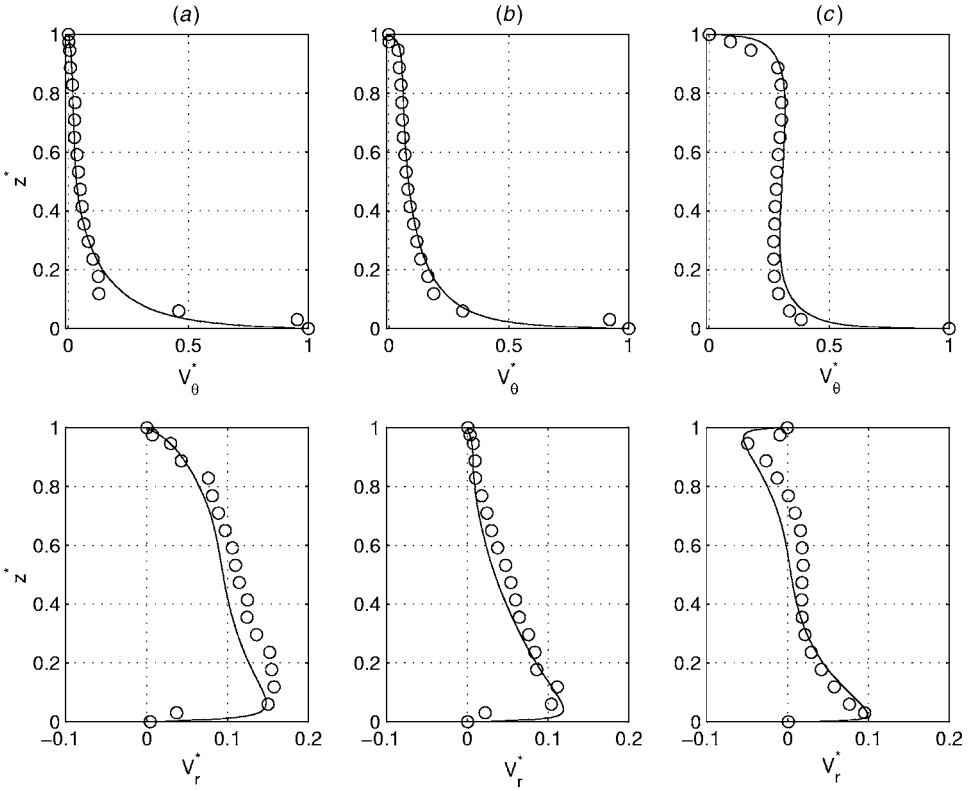

Fig. 6 Mean velocity profiles for C_w=5159, G=0.036 at r^*=0.68: (-) the RSM model and (○) the experimental data for (*a*) Re=5.189×10^5, (*b*) Re=1.038×10^6, and (*c*) Re=4.15×10^6

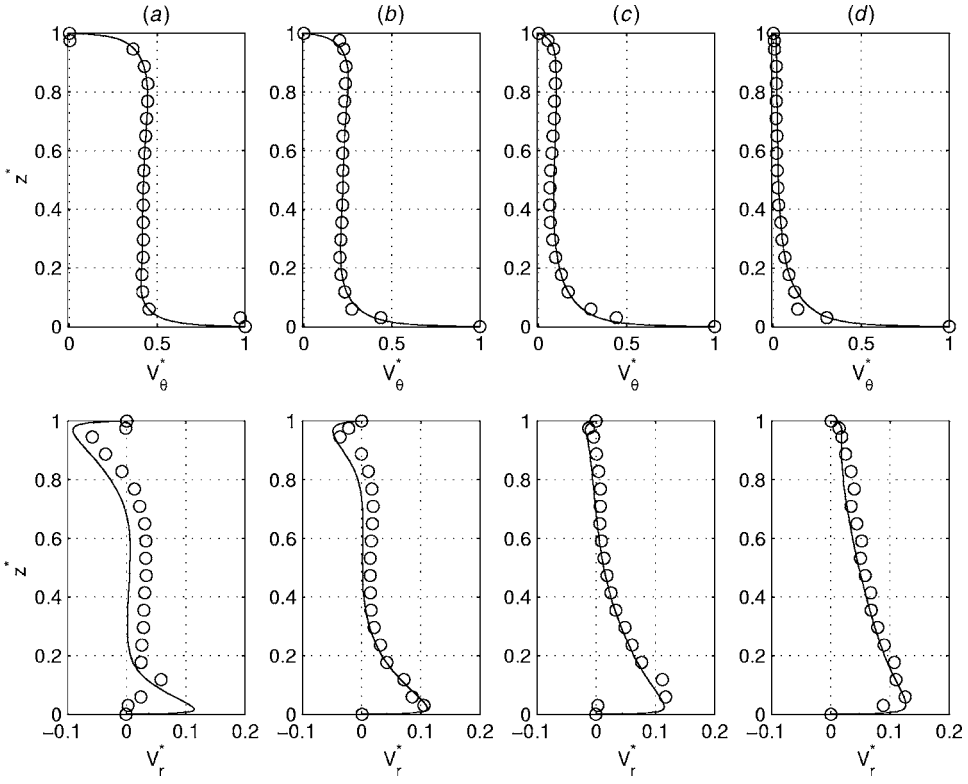

Fig. 7 Mean velocity profiles for Re=4.15×10^6, G=0.036 at r^*=0.44: (-) the RSM model and (○) the experimental data for (*a*) C_w=0, (*b*) C_w=2579, (*c*) C_w=5159, and (*d*) C_w=10317

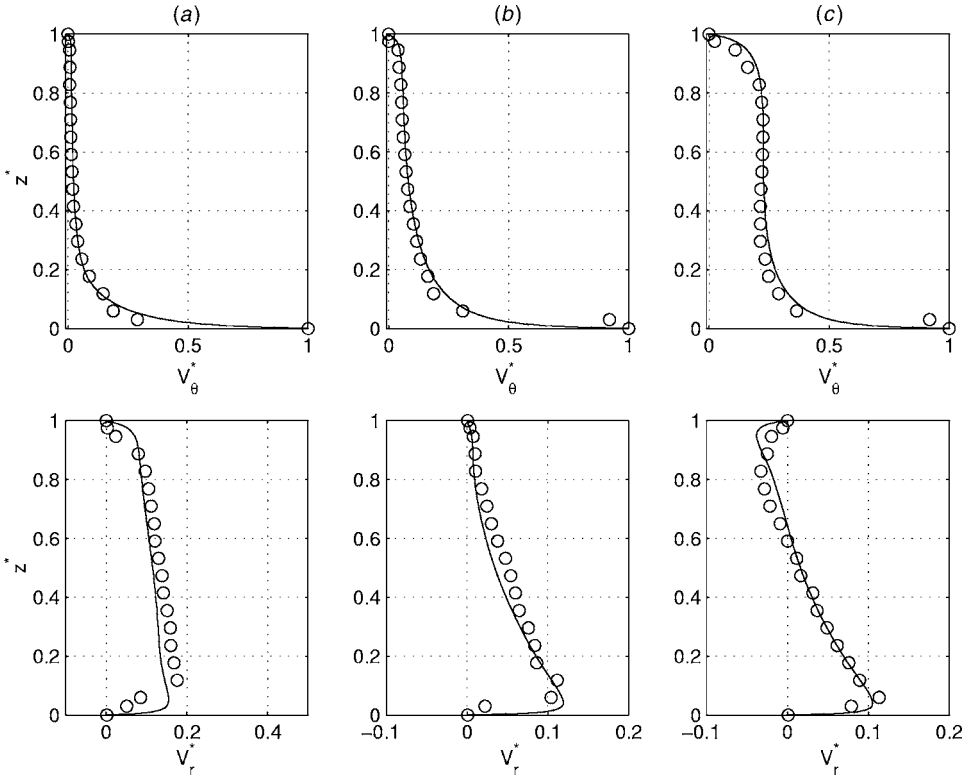

Fig. 8 Mean velocity profiles for $G=0.036$, $\mathrm{Re}=1.038\times10^6$, $C_w=5159$ at (*a*) $r^*=0.44$, (*b*) $r^*=0.68$, and (*c*) $r^*=0.92$: (-) the RSM model and (○) the experimental data

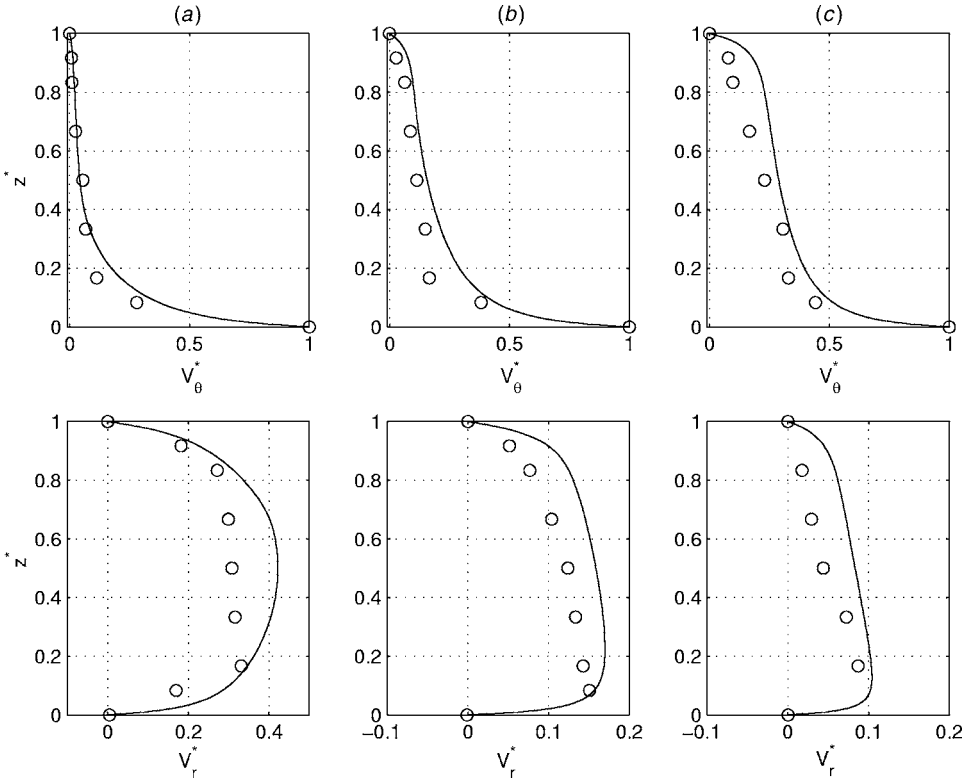

Fig. 9 Mean velocity profiles for $G=0.012$, $\mathrm{Re}=1.038\times10^6$, $C_w=5159$ at (*a*) $r^*=0.44$, (*b*) $r^*=0.68$, and (*c*) $r^*=0.92$: (-) the RSM model and (○) the experimental data

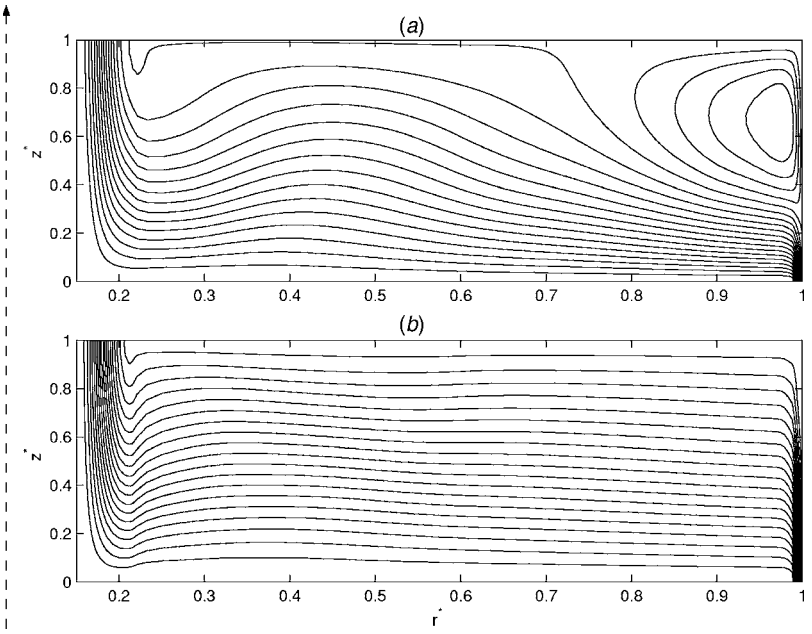

Fig. 10 Effect of the aspect ratio on the streamline patterns (RSM), 20 regularly spaced intervals for Re=1.038×10^6, C_w=5159: (*a*) G=0.036, $0 \leq \Psi/(\Omega R_2^2) \leq 0.0297$ and (*b*) G=0.012, $0 \leq \Psi/(\Omega R_2^2) \leq 0.0686$

from the modeling results are plotted in a log-log representation against the experimental data in the case of centrifugal throughflows. We note that, for a Batchelor-type flow, K follows the analytical law determined by Poncet et al. [25] with $-Cq_r$ (contrary to them, we consider here $Cq_r > 0$ in the case of centrifugal throughflows)

$$K = 2 \times (-5.9 \times Cq_r + 0.63)^{5/7} - 1 \tag{3}$$

For a Stewartson-type flow, K decreases exponentianally with increasing values of Cq_r following the equation:

$$K = 0.032 + 0.32 \times e^{-Cq_r/0.028} \tag{4}$$

Between these two types of flow, there is a transition zone. The results are in good agreement, which means that the model predicts quite well the mean turbulent flow for both Batchelor and Stewartson types of flow.

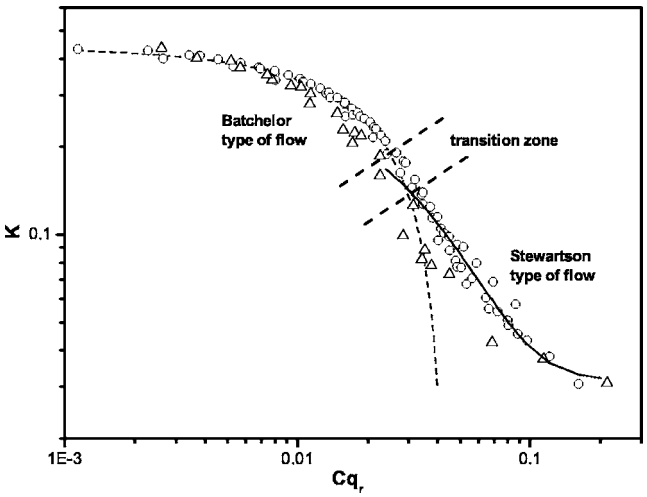

Fig. 11 Mean K-curve: (△) the RSM model, (○) the experimental data, (--) $K=2\times(-5.9\times Cq_r+0.63)^{5/7}-1$ and (-) $K=0.032+0.32\times e^{-Cq_r/0.028}$

5 Conclusion

Turbulence modeling and measurements of the turbulent flow in a rotor-stator cavity is a great challenge even more when a centrifugal throughflow is imposed. In the present work, we have compared second-order model predictions with new experimental data for three values of the Reynolds number, two aspect ratios of the cavity, and four flow rates. For weak throughflows, the flow still keeps the characteristics of a closed cavity. In the case of a strong centrifugal throughflow, we showed that the flow reverts to Stewartson-type flow with only one boundary layer on the rotating disk. For the first time, the transition from Batchelor to Stewartson profiles has been characterized according to the flow control parameters and to the radial location. The RSM model, which is a second-moment closure, proved to give a great improvement compared to known results using simpler models. Because good agreement with the measurements has been found in all the various cases under consideration, it is confirmed that the RSM model offers an adequate level of closure to describe the mean and the turbulent fields in such type of flows.

Acknowledgment

Numerical computations were carried out on the NEC SX-5 (IDRIS, Orsay, France). The experimental approach was supported by SNECMA Moteurs, Large Liquid Propulsion (Vernon, France). They are here gratefully acknowledged.

References

[1] Daily, J. W., and Nece, R. E., 1960, "Chamber Dimension Effects on Induced Flow and Frictional Resistance of Enclosed Rotating Disks," ASME J. Basic Eng. **82**, pp. 217–232.

[2] Owen, J. M., and Rogers, R. H., 1989, *Flow and Heat Transfer in Rotating-Disc Systems - Vol.1: Rotor-Stator Systems*, W. D., Morris ed., Wiley, New-York.

[3] Itoh, M., Yamada, Y., Imao, S., and Gonda, M., 1990, Experiments on Turbulent Flow Due to an Enclosed Rotating Disk, *Proc. Int. Symp. on Engineering Turbulence Modeling and Experiments*, W. Rodi and E. N. Galic, eds., Elsevier, New York, pp. 659–668.

[4] Daily, J. W., Ernst, W. D., and Asbedian, V. V. 1964, Enclosed Rotating Disks With Superposed Throughflow, Technical Report 64, M.I.T, Department of Civil Engineering.

[5] Firouzian, M., Owen, J. M., Pincombe, J. R., and Rogers, R. H., 1986, "Flow

and Heat Transfer in a Rotating Cylindrical Cavity With a Radial Inflow of Fluid, Part 2: Velocity, Pressure and Heat Transfer Measurements, Int. J. Heat Fluid Flow **7**(1) pp. 21–27.
[6] Chew, J. W., 1984, Prediction of Flow in Rotating Disc Systems Using the k-ϵ Model, *Gas Turbine Conf.*, ASME paper No. 84-GT-229, Amsterdam.
[7] Chew, J. W., and Vaughan, C. M., 1988, Numerical Predictions of Flow Induced by an Enclosed Rotating Disk, ASME paper No. 88-GT-127, Amsterdam. 33rd Gas Turbine and Aeroengine Congress.
[8] Iacovides, H., and Theofanopoulos, L. P., 1991, "Turbulence modeling of axisymmetric flow inside rotating cavities," Int. J. Heat Fluid Flow **12**(1), pp. 2–11,
[9] Iacovides, H., and Toumpanakis, P., 1993, Turbulence Modelling of Flow in Axisymmetric Rotor-Stator Systems, *5th Int. Symp. on Refined Flow Modelling and Turbulence Measurements*, Presses de l'Ecole Nationale des Ponts et Chaussées, Paris.
[10] Schiestel, R., Elena, L., and Rezoug, T., 1993, "Numerical Modeling of Turbulent Flow and Heat Transfer in Rotating Cavities," Numer. Heat Transfer, Part A **24**(1), pp. 45–65.
[11] Elena, L., and Schiestel, R., 1995, "Turbulence Modeling of Confined Flow in Rotating Disk Systems," AIAA J. **33**(5), pp. 812–821.
[12] Launder, B. E., and Tselepidakis, D. P., 1994, "Application of a new second-moment closure to turbulent channel flow rotating in orthogonal mode," Int. J. Heat Fluid Flow **15**(1), pp. 2–10,
[13] Hanjalic, K., and Launder, B. E., 1976, "Contribution Towards a Reynolds-Stress Closure for Low-Reynolds Number Turbulence," J. Fluid Mech. **74**(4), pp. 593–610.
[14] Iacovides, H., Nikas, K. S., and Te, M. A. F., Braak, 1996, "Turbulent Flow Computations in Rotating Cavities Using Low-Reynolds-Number Models." *Int. Gas Turbine and Aeroengine Congress and Exhibition*, ASME Paper No. 96-GT-159, Birmingham, UK.
[15] Poncet, S., Schiestel, R., and Chauve, M.-P., 2005, "Turbulence Modelling and Measurements in a Rotor-Stator System With Throughflow," *ERCOFTAC Int. Symp. on Engineering Turbulence Modelling and Measurements*, Sardinia, Italy.
[16] Elena, L., and Schiestel, R.., 1996, "Turbulence Modeling of Rotating Confined Flows," Int. J. Heat Fluid Flow **17**, pp. 283–289.
[17] Lygren, M., and Andersson, H. I., 2001, "Turbulent Flow Between a Rotating and a Stationary Disk," J. Fluid Mech. **426**, pp. 297–326.
[18] Gassiat, R. M., 2000, Etude expérimentale d'écoulements centripètes avec prérotation d'un fluide confiné entre un disque tournant et un carter fixe, Ph.D. thesis, Université de la Méditerranée Aix-Marseille II.
[19] Daly, B. J., and Harlow, F. H., 1970, "Transport Equation for Turbulence," Phys. Fluids **13**(11), pp. 2634–2649.
[20] Gibson, M., and Launder, B. E., 1978, "Ground Effects on Pressure Fluctuations in the Atmospheric Boundary Layer," J. Fluid Mech. **86**(3), pp. 491–511.
[21] Launder, B. E., and Reynolds, W. C., 1983, "Asymptotic Near-Wall Stress Dissipation Rates in a Turbulent Flow," Phys. Fluids **26**(5), pp. 1157–1158.
[22] Cambon, C., and Jacquin, L., 1989, "Spectral Approach to Non-Isotropic Turbulence Subjected to Rotation," J. Fluid Mech. **202**, pp. 295–317.
[23] Schiestel, R., and Elena, L., 1997, "Modeling of Anisotropic Turbulence in Rapid Rotation," Aerosp. Sci. Technol. **7**, pp. 441–451.
[24] Huang, P. G., and Leschziner, M. A., 1985, "Stabilization of Recirculating Flow Computations Performed With Second Moments Closures and Third Order Discretization," *Vth Int. Symp. on Turbulent Shear Flow*, Cornell University, Ithaca, NY.
[25] Poncet, S., Chauve, M.-P., and Le Gal, P., 2005, "Turbulent Rotating Disk Flow With Inward Throughflow," J. Fluid Mech. **522**, pp. 253–262.

Limitations of Richardson Extrapolation and Some Possible Remedies

Ismail Celik[1]
Jun Li
Gusheng Hu
Christian Shaffer

Mechanical and Aerospace Engineering Department,
West Virginia University,
Morgantown, WV 26506-6106

The origin of oscillatory convergence in finite difference methods is investigated. Fairly simple implicit schemes are used to solve the steady one-dimensional convection-diffusion equation with variable coefficients, and possible scenarios are shown that exhibit the oscillatory convergence. Also, a manufactured solution to difference equations is formulated that exhibits desired oscillatory behavior in grid convergence, with a varying formal order of accuracy. This model-error equation is used to statistically assess the performance of several methods of extrapolation. Alternative extrapolation schemes, such as the deferred extrapolation to limit technique, to calculate the coefficients in the Taylor series expansion of the error function are also considered. A new method is proposed that is based on the extrapolation of approximate error, and is shown to be a viable alternative to other methods. This paper elucidates the problem of oscillatory convergence, and brings a new perspective to the problem of estimating discretization error by optimizing the information from a minimum number of calculations. [DOI: 10.1115/1.1949646]

1 Introduction

Richardson extrapolation [1,2] is a commonly used method for quantifying the discretization errors in CFD (computational fluid dynamics) applications in fluids engineering and heat transfer problems. In the asymptotic range (i.e., for sufficiently small mesh size h), it is postulated (see Eq. (3.1))

$$\phi - \phi_h = ah^p \tag{1.1}$$

where p is the apparent order of the numerical scheme used, ϕ is the extrapolated solution, and ϕ_h is the numerical solution with mesh size h; a is a coefficient independent of h, but may change in space or time.

Richardson extrapolation uses calculations on multiple sets of grids (see also Sec. 5) to calculate the extrapolated value of a dependent variable to zero grid size, either using the theoretical order of the scheme (on at least two grid levels) or via the apparent or observed order that is calculated as part of the unknowns; in the latter case, at least three sets of calculations are needed on significantly different grid levels. The pros and cons of this method have been the topic of many recent publications [3–10]. In spite of it being a very useful tool for quantifying discretization errors in CFD, there still remain major problems that need to be addressed to advance the level of confidence that could be placed in this method.

This paper addresses the problem of oscillatory convergence. Several questions concerning the oscillatory convergence are (i) Does oscillatory convergence occur? (ii) What happens in the asymptotic range? Asymptotic range means the leading error term dominates in the Taylor expansion of the error function. (iii) Is Richardson extrapolation applicable to oscillatory converging cases? (iv) How can one best make use of results from an oscillatory converging computation?

Answers to the above questions are sought in the following order. First, some examples of oscillatory convergence are presented. Then, the existence of oscillatory is convergence exhibited by constructing (manufacturing) schemes whose discretization errors are forced to satisfy an oscillatory function when applied to a simple convection-diffusion equation. Several modeled equations are given to provide a large number of oscillatory samples. Different, viable methods are evaluated statistically, based on their performance in predicting the exact solution in the limit as h $\rightarrow 0$ using the sample data.

2 Examples of Oscillatory Convergence

We start by giving some examples of oscillatory convergence, one from the solution of simple linear PDE

$$(u\phi)_x = (\Gamma\phi_x)_x + \lambda\phi \tag{2.1}$$

and another from the solution of coupled nonlinear PDEs, namely, Navier-Stokes equations for a fairly complex problem utilizing a readily available commercial code. Here, $()_x$ denotes differentiation with respect to x.

As shown in the Appendix, one example is given by solving a simple steady one-dimensional convection-diffusion equation. The solutions (ϕ) at $x=0.5$ with different grid sizes h are shown in Fig. 1. Oscillatory convergence is seen to occur. The amplitudes of the error change less and less when h approaches zero. In the asymptotic range, as $h \rightarrow 0$ there seems to be at least three terms of the same order of magnitude no matter how small the h value is. More examples are given in the Appendix, where it is shown that oscillatory convergence may also occur with nonmixed schemes, i.e., central differencing.

Another example of oscillatory convergence can be observed in Fig. 2. The solutions were calculated using the FLUENT computational fluid dynamics (CFD) package for two-dimensional turbulent flow past a backward-facing step based on three sets of grids [11]. The expansion ratio is 9/8. The origin (0,0) is located at the lower corner of the step. U is the streamwise velocity, $\Delta U = U - U_{\text{med}}$, where U_{med} is the value calculated on the medium grid. The reference velocity U_{ref} is the maximum streamwise velocity at the inlet. If monotonic convergence happens, the solution with the medium grid should always be in between the solutions given by the coarse grid and the fine grid. However, this is not the case at several points between $y/H=1.5$ and $y/H=3$, where H is the step height.

[1]Please send all communications to the first author at Ismail.Celik@mail.wvu.edu

Contributed by the Fluids Engineering Division for Publication in the JOURNAL OF FLUIDS ENGINEERING. Manuscript received by the Fluids Engineering Division August 27, 2004; Final manuscript received: April 27, 2005; Review conducted by: Subrata Roy.

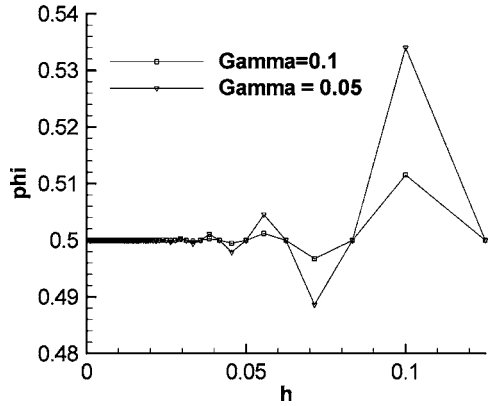

Fig. 1 An example of oscillatory convergence. First-order upwinding scheme applied to the convection term and second-order central differencing applied to the diffusion term with $u=\cos(4\pi x)$; Γ is the diffusion coefficient. (see Appendix)

3 Existence of Oscillatory Convergence

It has been argued [12,13] that oscillatory convergence cannot occur in the asymptotic range. At first glance, this argument seems reasonable in that as $h\to 0$ the leading term in the Taylor series expansion (3.1) dominates

$$\phi(h)=\phi(0)+a_1h+a_2h^2+a_3h^3+\cdots \tag{3.1}$$

where

$$a_k=\frac{1}{k!}\left(\frac{\partial^{(k)}\phi}{\partial h^k}\right)_{h=0} \qquad \mathrm{k}=1,2,3\ldots \tag{3.2}$$

hence, the error $E(h)$ can be expressed as

$$E(h)=\phi(h)-\phi(0)=a_ph^p \tag{3.3}$$

For $p\geqslant 0$, (3.3) shows that E is a monotonic function of h in the asymptotic range. This argument is flawed in the sense that it inherently assumes that the derivatives of $\phi(h)$ and, thus, a_k (3.2) are small as $h\to 0$. This is not necessarily so and it depends on the particular scheme. In fact, for upwind methods, and for mixed methods (i.e., different schemes being activated at different grid levels or in different flow regions), these derivatives are discontinuous. For a consistent scheme (stable and convergent), Eq. (3.3) is not a necessary condition—but a desirable condition.

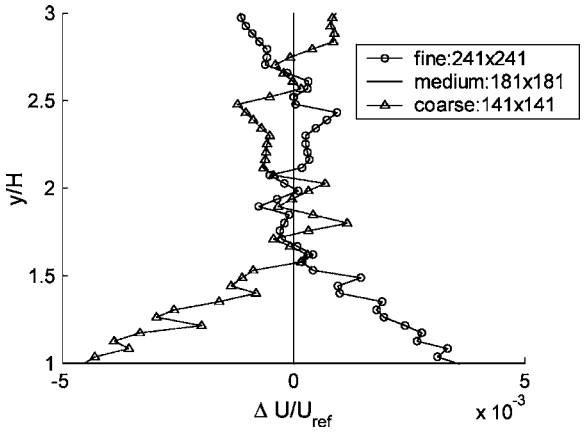

Fig. 2 Normalized streamwise velocity difference based on the medium grid at $x/H=1$ in a 2D turbulent flow over a backward-facing step (using FLUENT and Spalart-Allmaras turbulence model [11])

We can actually construct numerical schemes that force the discretization error to satisfy an oscillatory function. This idea follows a similar line of thinking to manufacture solutions for PDE. Here, we not only manufacture the solution but also derive the corresponding finite difference (FD) scheme. To do this, we use, as an example, a steady convection-diffusion equation with a source term

$$u\phi_x=\phi_{xx}-\lambda\phi \tag{3.4}$$

with boundary conditions $\phi(0)=0$ and $\phi(1)=1$.

Here, ϕ is the exact solution to (3.4), u is the convection velocity, and λ is a constant. The numerical solution $\tilde{\phi}$ with a finite difference scheme on a three-point stencil satisfies a general formula

$$-a_i\tilde{\phi}_{i-1}+b_i\tilde{\phi}_i-c_i\tilde{\phi}_{i+1}=0 \tag{3.5}$$

where a_i, b_i, and c_i are the coefficients of the discretized equation. They must satisfy

$$b_i=a_i+c_i+\lambda \tag{3.6}$$

in order that $\phi=$const is a solution when $\lambda=0$. We further assume that the scheme satisfies an additional condition

$$a_i=c_i+\frac{u_i}{h} \tag{3.7}$$

Let the discretization error E_i satisfy

$$E_i\equiv\tilde{\phi}_i-\phi_i=g_if \tag{3.8}$$

Assume

$$g_i=\beta(i-1)(nx-i) \tag{3.9}$$

$$f=h^p\cos(kh) \tag{3.10}$$

so that the error will be zero at the boundaries and oscillate inside of the domain. nx in (3.9) is the total grid number in the x direction. β is the coefficient that determines the amplitude of the oscillation. Based on the above assumptions, the solution $\tilde{\phi}_i$ is

$$\tilde{\phi}_i=\phi_i+g_ih^p\cos(kh) \tag{3.11}$$

Substituting $\tilde{\phi}$ into Eq. (3.5), we have

$$-a_i(\phi_{i-1}+g_{i-1}f)+b_i(\phi_i+g_if)-c_i(\phi_{i+1}+g_{i+1}f)=0 \tag{3.12}$$

Substituting (3.6) and (3.7) into Eq. (3.12), we obtain the solution

$$b_i=\frac{C-Au_i/h}{A+B} \tag{3.13}$$

where $A=(\phi_i-\phi_{i-1})+(g_i-g_{i-1})f$, $B=(\phi_i-\phi_{i+1})+(g_i-g_{i+1})f$ and $C=-\lambda(\phi_i+g_if)$. a_i and c_i can be solved for by substituting (3.13) back into (3.6) and (3.5). All these coefficients form a new scheme that one may not be familiar with. However, it ensures that the discretization errors oscillate when we refine the grids. In Fig. 3, it is shown that the manufactured scheme from (3.13), (3.6), and (3.7) do indeed result in the oscillatory solutions ϕ_n and exhibit oscillatory convergence as we designed in Eq. (3.8).

4 Modeled Equations for Oscillatory Convergence

Richardson extrapolation is based on the assumption that the first term of the Taylor expansion of the discretization error is dominant. As explained above, when oscillatory convergence occurs, this assumption may not be true, which makes the oscillatory convergence an unresolved problem. In an effort to statistically identify a good method from various possible methods to solve this problem, we need first to have a statistically significant number of oscillatory solution samples. To get these samples, we pro-

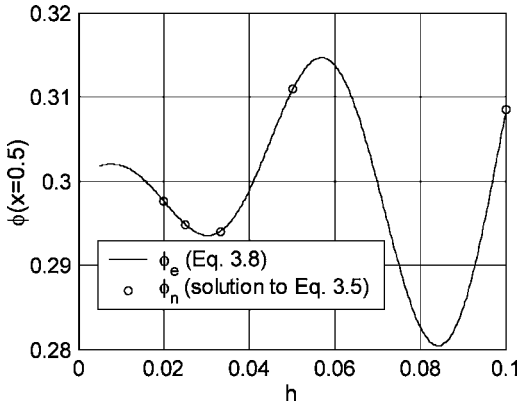

Fig. 3 Designed solutions ϕ_e to Eq. (3.8) and numerical solutions ϕ_n to Eq. (3.5) with the manufactured scheme

pose to use the following oscillatory model equations, which may represent the oscillatory convergence behavior of the solutions to a finite difference equation as shown in Sec. 2 and 3. These models include

$$\phi(h) = \phi_0 + a\cos(2\pi kh)h^p \quad (p \geqslant 1) \tag{4.1}$$

$$\phi(h) = \phi_0 + a(1 - e^{-bh})\cos(2\pi kh)h^p \quad (p \geqslant 0) \tag{4.2}$$

$$\phi(h) = \phi_0 + a\log(1+h)\cos(2\pi kh)h^p \quad (p \geqslant 0) \tag{4.3}$$

These equations can represent the error behavior of any scheme of first order or higher. a, k, and p (or $p+1$) correspond to the maximum error amplitude, the oscillation frequency, and the order of the scheme, respectively. Figure 4 depicts the oscillatory behavior of Eq. (4.1) for various values of k and p. It should be noted here that k, in general, can be a function of h, which means that the oscillation period could be a function of h. However, in the present study, k will be treated as an additional independent parameter. Let the refinement factor be a constant α such that

$$h_i = \alpha^{(i-1)}h_1 \tag{4.4}$$

with $i=1,2,3$ for three sets of grids and $i=1,2,3,4$ for four sets of grids. In the present analysis, α has been assigned the value of $\{0.5, 0.6, 0.7, 0.8, 0.9\}$, which represent the usual ranges in which the grid refinements are done. Without loss of generality, we can normalize h_1 to be 1 (i.e., $h \leftarrow h/h_{\max}$). By changing a, k, and p as listed in Table 1, we have ensembled 270 samples from oscillatory convergence and 270 samples for monotonic convergence. In what follows, we use these samples to assess the performance of various extrapolation methods.

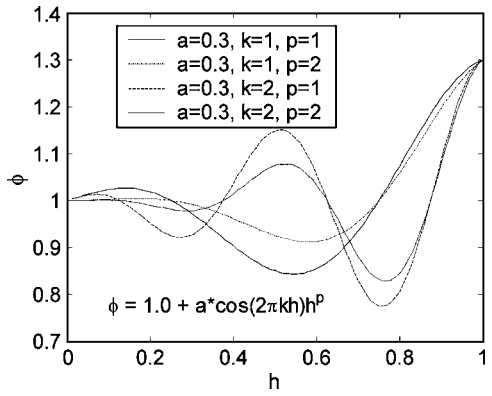

Fig. 4 An example of the behavior of oscillatory model Eq. (4.1)

Table 1 Parameter assignments in Eqs. (4.1)–(4.3)

a	0.2, 0.4, 0.6
k	0.5, 1 (for oscillatory); 0.01, 0.02 (for monotonic)
p	1, 2, 3
b	1
ϕ_0	1.0

5 Methods of Extrapolation for Oscillatory Convergence

In this section, we present the statistical results with four different methods that have the potential to solve the extrapolation problem in oscillatory convergence. These methods include (i) the polynomial method, (ii) the power law method, (iii) the cubic spline method, and (iv) the newly proposed approximate error spline method.

i. Polynomial method. This method uses the first few terms in Eq (3.1) to approximate $\phi(0)$. For instance, assuming the method is first order, we can use the first three terms if we have three sets of grids. That is,

$$\phi(h) = \phi(0) + a_1 h + a_2 h^2 \tag{5.1}$$

If we have four sets of grids, then we can use

$$\phi(h) = \phi(0) + a_1 h + a_2 h^2 + a_3 h^3 \tag{5.2}$$

If the discretization scheme has an order of two or higher, this method means essentially a curve fit to the actual error function. For a fourth-order method, one has to keep at least four terms, i.e., five sets of calculations are needed.

The extrapolation to the limit approach [14,15] is recommended to solve the equations formed by the polynomial method. This approach uses the following formula to calculate the extrapolated solution $\phi^{(3)}(h)$ for three sets of grids and $\phi^{(4)}(h)$ for four sets of grids:

$$\phi^{(m)}(h) = \frac{\phi^{(m-1)}(\alpha h) - \alpha^m \phi^{(m-1)}(h)}{1 - \alpha^m} \quad \mathrm{m} = 1,2,\ldots \tag{5.3}$$

It is easy to tabulate the sequential steps of the calculation procedure and to add more points later.

ii. Power law method. We use the power law method proposed by Celik and Karatekin [7] for three sets of grids. The idea follows:

$$\phi(0) - \phi(h_1) = ch_1^p \tag{5.4}$$

$$\phi(0) - \phi(h_2) = \mathrm{sign}\left(\frac{\varepsilon_{32}}{\varepsilon_{21}}\right)ch_2^p \tag{5.5}$$

$$\phi(0) - \phi(h_3) = ch_3^p \tag{5.6}$$

where $\varepsilon_{32}/\varepsilon_{32} = [\phi(h_3) - \phi(h_2)]/(\phi(h_2) - \phi(h_1))$, the sign of which is positive for monotonic convergence and negative for oscillatory convergence. There are three unknows, $\phi(0)$, c, and p. We can implement the same iterative method to solve (5.4)–(5.6) as done by Celik and Karatekin [7].

For four sets of grids, we can apply

$$\phi(h_i) - \phi(0) = a_1 h_i^p + a_2 h_i^{p+1} \quad i = 1,2,3,4 \tag{5.7}$$

Oscillatory convergence is facilitated if a_1 and a_2 are of opposite sign. It should be noted that for some cases there is no solution to Eq. (5.7). Those cases will be counted as unsuccessful outcomes.

iii. Cubic spline method. The well-known natural cubic splines curve fitting technique is used to create the cubic splines between three points or four points. $\phi(0)$ can be found by extrapolating the curve for the interval closest to $h=0$.

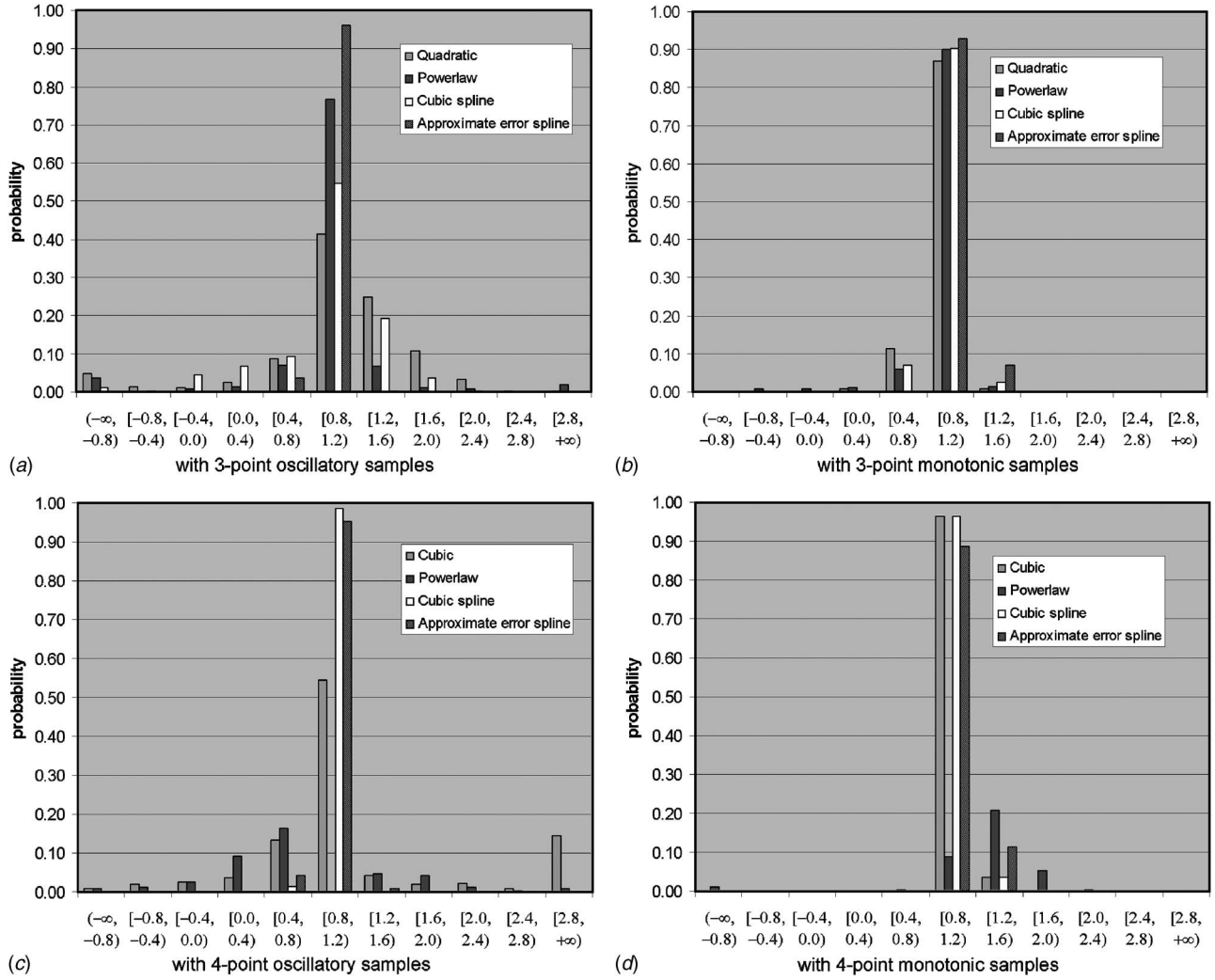

Fig. 5 Probability of $\phi(0)$ at different intervals, predicted with different methods

iv. Approximate error spline methods. Still using Taylor series expansion as in Eq. (3.1) for $\phi(h)$ and substituting αh for h, we have

$$\phi(\alpha h) = \phi(0) + a_1 \alpha h + a_2 (\alpha h)^2 + a_3 (\alpha h)^3 + \cdots \tag{5.8}$$

The true error E_t is given by

$$E_t(\alpha, h) \equiv \phi(\alpha h) - \phi(0) = \sum_{k=1}^{\infty} a_k \alpha^k h^k \tag{5.9}$$

and the approximate error E_a

$$E_a(\alpha, h) \equiv \phi(\alpha h) - \phi(h) \tag{5.10}$$

which presents the difference of the subsequent results with the fine grid and the coarse grid. Subtracting (3.1) from (5.8) gives

$$E_a(\alpha, h) = \sum_{k=1}^{\infty} a_k (\alpha^k - 1) h^k \tag{5.11}$$

Dividing (5.9) by (5.11) and moving $E_a(\alpha, h)$ to the right-hand side yields

Table 2 Probability and norm with different methods for oscillatory and monotonic samples

			Polynomial	Powerlaw	Cubic spline	Approximate error spline
3 points	Oscillatory	Probability in [0.8, 1.2)	41%	77%	55%	96%
		Norm	15.3	25.2	8.10	1.38
	Monotonic	Probability in [0.8, 1.2)	87%	90%	90%	93%
		Norm	2.62	3.55	2.01	1.69
4 points	Oscillatory	Probability in [0.8, 1.2)	54%	0%	99%	95%
		Norm	37.2	112	0.85	1.48
	Monotonic	Probability in [0.8, 1.2)	96%	9%	96%	89%
		Norm	1.43	353	1.27	2.20

Table 3 Probability and norm of extrapolation calculated with the three points out of four points, excluding the coarsest one

		Polynomial	Powerlaw	Cubic spline	Approximate error spline
Oscillatory	Probability in [0.8, 1.2)	67%	88%	73%	99%
	Norm	7.50	8.77	5.98	0.94
Monotonic	Probability in [0.8, 1.2)	95%	94%	96%	92%
	Norm	1.44	5.01	1.36	1.81

$$E_t(\alpha,h)=\frac{1}{1-\dfrac{\sum a_k h^k}{\sum a_k \alpha^k h^k}}E_a(\alpha,h) \tag{5.12}$$

letting

$$\frac{\sum a_k h^k}{\sum a_k \alpha^k h^k}=b_0+b_1 h+b_2 h^2 \tag{5.13}$$

and expanding the left-hand side of the above equation and comparing it with the right-hand side gives

$$b_0=\frac{1}{\alpha}\quad b_1=\left(\frac{1-\alpha}{\alpha}\right)\frac{a_2}{a_1}$$

$$b_2=\left(\frac{1-\alpha^2}{\alpha}\right)\frac{a_3}{a_1}-(1-\alpha)\left(\frac{a_2}{a_1}\right)^2 \tag{5.14}$$

Now Eq. (5.12) can be rewritten as

$$E_t(\alpha,h)=\frac{1}{1-(b_0+b_1 h+b_2 h^2)}E_a(\alpha,h) \tag{5.15}$$

In order to calculate b_0, b_1, and b_2, we need to calculate a_1, a_2, and a_3 first. It is seen from Eq. (5.11) that

$$a_k=\frac{E_a^{(k)}(\alpha,0)}{k\,!\,(\alpha^k-1)}\quad k=1,2,3 \tag{5.16}$$

$E^{(k)}$ is the kth derivative of E. Assuming that we have three sets of grids and the solutions as $[h_1,\phi(h_1)]$, $[h_2,\phi(h_2)]$, and $[h_3,\phi(h_3)]$ with $h_3=\alpha h_2=\alpha^2 h_1$, and noting that $E_a(\alpha,0)\equiv 0$ leads to three points as $[h_1,E_a(\alpha,h_1)]$, $[h_2,E_a(\alpha,h_2)]$, and $[0,E_a(\alpha,0)]$, which involves the approximate error instead of the numerical solution $\tilde{\phi}$ itself. Using the information on E_a, we can interpolate with cubic splines with the endslopes given by $E_a'(\alpha,0)\cong 0$ and $E_a'(\alpha,h_1)\cong[E_a(\alpha,h_1)-E_a(\alpha,h_2)]/(h_1-h_2)$. These endslopes are acceptable at $h=0$ for any scheme with order larger than 1. For the first-order methods, in general, the slope at $h=0$ is not zero. We could still obtain excellent results using the zero slope assumption for the first-order methods, as we demonstrate in the assessment part of this paper. Once we have $E_a^{(k)}(\alpha,0)$, we can calculate a_k from Eq. (5.16). As one might note, b_1 is singular at $h=0$ if $E_a'(\alpha,0)=0$. In order to avoid this singularity, $E_a'(\alpha,\varepsilon)$ can be used to represent $E_a'(\alpha,0)$ by using finite differencing at $h=\varepsilon$, where ε is a small value. Having obtained b_0, b_1, and b_2, we can calculate $\phi(0)$ from Eq. (5.15), together with the definition (5.9) and (5.10).

6 Assessment of Methods

Two parameters are used to evaluate the performance of these methods. One is the case percentage out of 270 samples for which the calculated $\phi(0)$ is in the region of $\phi_0\pm\mu$; with $\mu=0.2$, this represents the confidence level for the interval of ±20% error. Another is the L^2 norm of the true error. Here, the L^2 norm is defined by $L^2=(\Sigma_{\text{cases}}[\phi_0-\phi(0)]^2)^{1/2}$.

Figure 5 shows the probability distribution of the predicted $\phi(0)$ at different intervals with different methods. The probability for $\phi(0)\in[0.8,1.2]$ and the L^2 norm are listed in Table 2. For monotonically converging cases, all methods perform well, with the approximate error spline (AES) method being the best. With three-point oscillatory samples, the approximate error spline method is overwhelmingly superior to the others, and the power law method ranks second best. However, with four-point oscillatory samples, the power law method performs the worst because there are no solutions for 59% of the samples. The cubic spline method and the AES method both perform very well. With three-point monotonic samples, all methods perform well, but the power law method is not applicable for four-point monotonic samples since it's not solvable for 63% of the samples.

However, we can use three solutions on the finer meshes to predict $\phi(0)$ when four solutions are available [13]. For instance, if $[h_1,\phi(h_1)]$, $[h_2,\phi(h_2)]$, $[h_3,\phi(h_3)]$, and $[h_4,\phi(h_4)]$ are available and h_1 is the coarsest grid size, we may use the last three points to calculate $\phi(0)$, and the first three points to confirm the estimation. The results following this thought are shown in Table 3. It should be first noted that the extrapolation based on the coarse three points is the same as shown in the three-point rows of Table 2. It is seen that the extrapolations with the fine three points are better than the ones with the coarse three points. Improvements are also observed in the polynomial, power law, and AES methods when we compare them to the extrapolations with all four points. Out of the four sets of grids, four triplets can be used. The first three and the last three are used separately, and it was found that the last three triplets gave slightly better results than the first three, as should be expected. The other triplets, namely, (1,3,4) and (1,2,4), can be used to confirm the analysis based on the other triplets. This is not done here because the AES method is formulated only for a constant grid refinement ratio. The surprisingly good performance of the AES method can be attributed to the use of the extra information that both E_a and E_t tend to zero as h goes to zero.

7 Conclusions

The origin of oscillatory convergence in finite difference (FD) or finite volume (FV) solutions is investigated. It has been shown that this behavior may occur not only when mixed order methods are used, but also when the coefficients of the FD equations exhibit highly oscillatory behavior. A usual source for such variations could be the oscillatory velocity field that occurs in recirculation regions near separation and reattachment points. By way of manufactured solution to FD equations and constructing a corresponding finite difference scheme, it is shown that there exist infinitely many finite difference methods that will exhibit oscillatory convergence, even in the asymptotic range. This information is then used to construct model error equations that are used to ensemble a large number of cases with oscillatory convergence. These samples are then used to assess the performance of various extrapolation methods for both monotonic and oscillatory cases. The results show that for three-grid calculations, the newly proposed approximate error spline (AES) method performs overwhelmingly superior to the others, the commonly used power law method ranking second best.

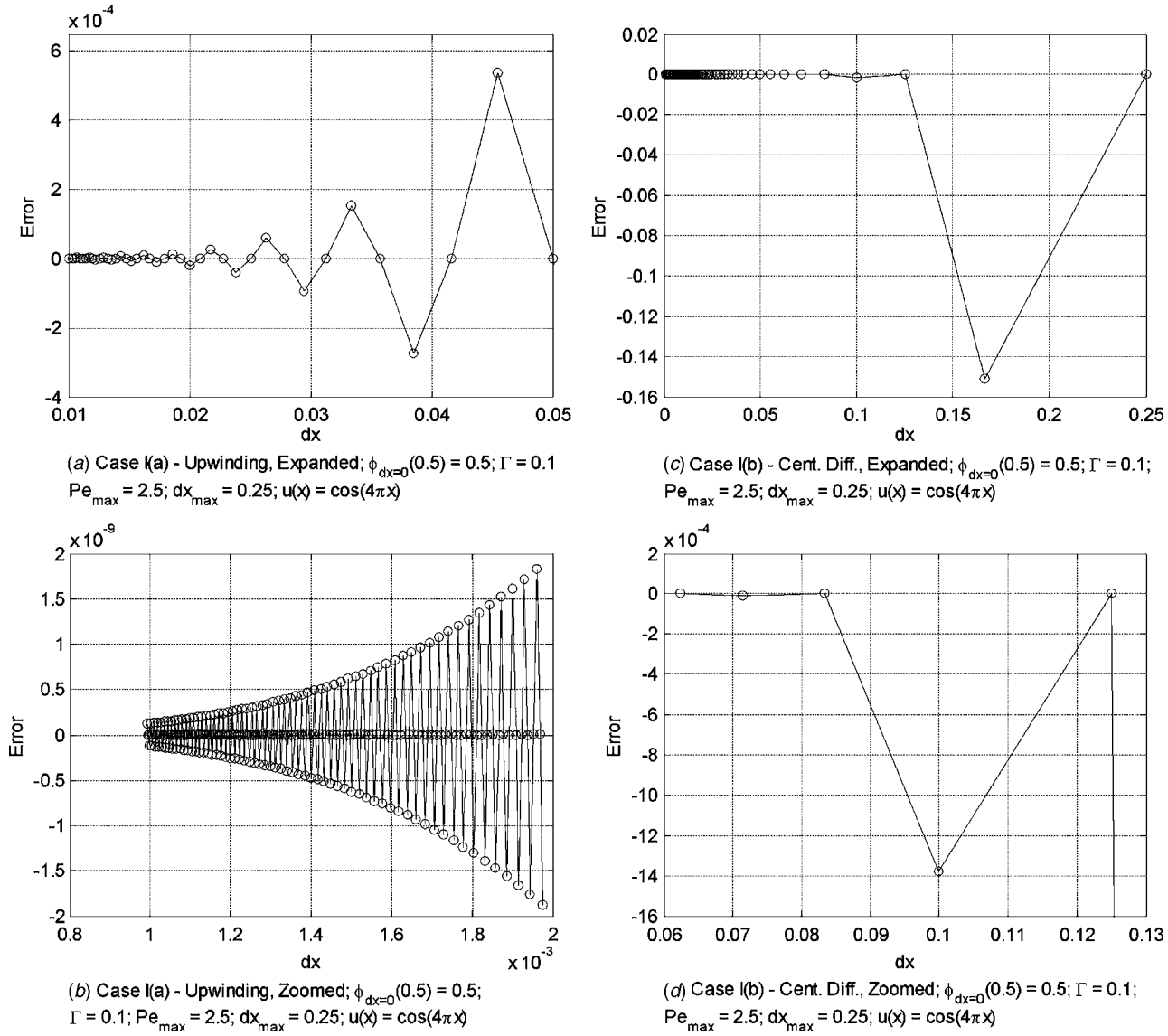

Fig. 6 Error plots showing cases I(a) and I(b) in both expanded and zoomed form

We recommend that four sets of calculations be performed; the last three should be used for extrapolation and the other triplets should be used for confirmation of analysis. When this is done, the best method is the approximate error spline method, and the next best is the power law method for oscillatory convergent cases. For monotonic convergence, all methods perform well.

Nomenclature

a_i, b_i, c_i = coefficients of the discretized equation
a,b,c,a_p,a_k = coefficients
A,B,C = intermediate variables
E_a = approximate error
E_t = true error
f = function of h
g = function of x
h = grid size
p = exponent
Pe = Peclet number
u = convection coefficient
U = velocity component
α = refinement factor
λ = factor
ϕ = variable to be solved
ϕ_n = numerical solution with mesh size h
Γ = diffusion coefficient
Ψ = function of x
ε_{21} = $\phi(h_2)-\phi(h_1)$
ε_{32} = $\phi(h_3)-\phi(h_2)$
ε = a small value
μ = confidence level

APPENDIX: GRID CONVERGENCE TRENDS FOR SOME FINITE DIFFERENCE SCHEMES

In applications of CFD, it is not unusual to observe oscillatory convergence in field variables, such as velocity [11,7]. It is suspected that this behavior is usually a consequence of the use of mixed-order methods such as first-order upwinding mixed with second-order upwinding, or first-order upwinding with central differencing, etc. Here, we investigate the grid convergence behavior of several schemes applied to the steady linear convection diffusion equation with variable velocities $u(x)$ and diffusivity $\Gamma(x)$. The model equations we use are

Conservative form:

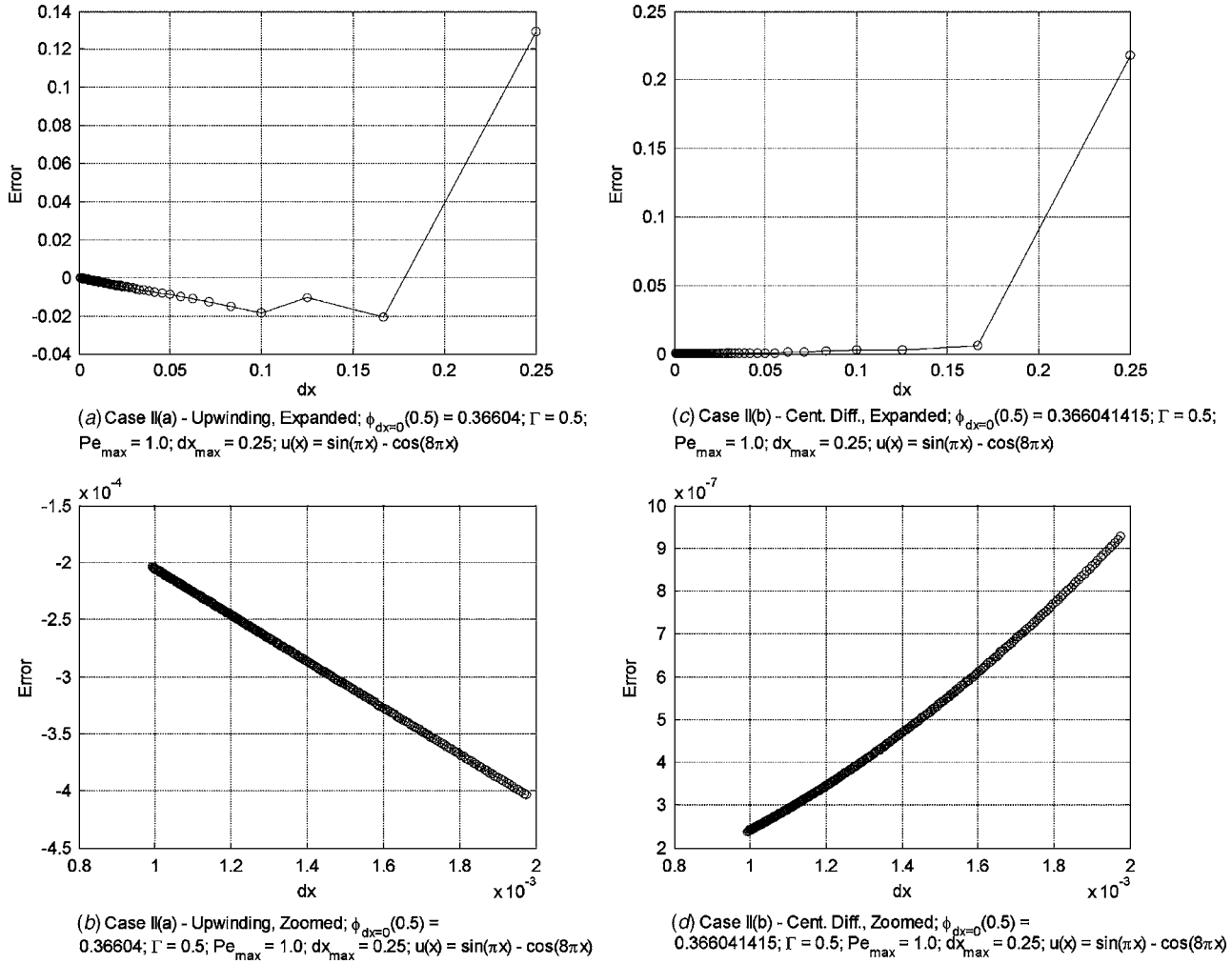

Fig. 7 Error plots showing cases II(a) and II(b) in both expanded and zoomed form; the lower plots show convergence behavior for very small *dx* values

$$\frac{\partial(u\phi)}{\partial x} = \frac{\partial}{\partial x}\left[\Gamma\frac{\partial\phi}{\partial x}\right] + \lambda\phi \tag{A1a}$$

Nonconservative form:

$$u\frac{\partial\phi}{\partial x} = \Gamma\frac{\partial^2\phi}{\partial x^2} + \lambda\phi \tag{A1b}$$

In this study, three different functions were utilized for the fluid velocity given by

$$u(x) = \cos(4\pi x) \tag{A2a}$$

$$u(x) = \sin(\pi x) - \cos(8\pi x) \tag{A2b}$$

$$u(x) = \sin(2\pi x) - \cos(4\pi x) \tag{A2c}$$

In all cases, the boundary conditions used were $\phi(0)=0$ and $\phi(1)=1$. Three different schemes were used in solving this equation: a first-order upwinding scheme, a second-order central differencing scheme, and a hybrid scheme that combined these two schemes based on the cell Peclet number defined as

$$\mathrm{Pe} = \frac{udx}{\Gamma} \tag{A3}$$

When the Peclet number was less than two, the hybrid scheme used the central differencing scheme, and when the Peclet number was greater than two, the hybrid scheme used the upwinding scheme.

In order to avoid using upwinding for the convective term, an alternative semianalytical formulation was also used. In this it was assumed that

$$\phi(x) = f(x)\psi(x) \tag{A4}$$

Substituting (A4) into (A1*a*), with Γ being constant, yields

$$[pf - 2f']\psi' = f\psi'' + [f'' - (pf)']\psi \tag{A5}$$

where $p=u(x)/\Gamma$. Equating the bracketed term on the left-hand side to zero eliminates the first derivative

$$pf - 2f' = 0 \tag{A6}$$

and solving (A6) gives

$$f(x) = e^{(1/2)\int p(x)dx} \tag{A7}$$

Substituting (A7) and its respective derivatives along with (A6) into (A5), after some simplification, we obtain

$$\psi'' = \tfrac{1}{2}\left[p' - \tfrac{1}{2}p^2\right]\psi \tag{A8}$$

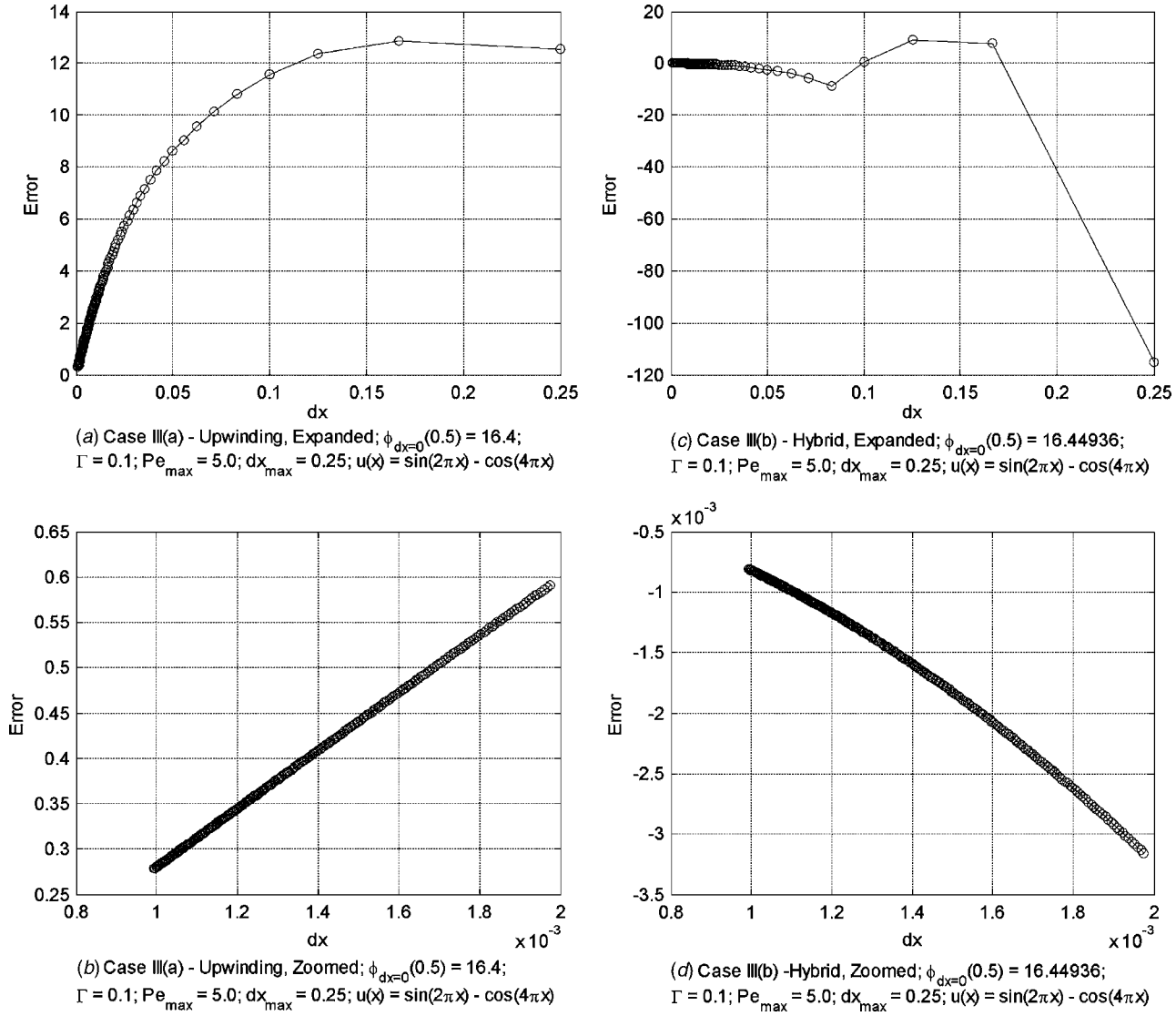

Fig. 8 Error plots showing cases III(a) and III(b) in both expanded and zoomed form; the lower plots show convergence behavior for very small *dx* values

The boundary conditions for (A8) can be derived using relation (A4). Without loss of generality, we can select $f(0)=1.0$ and $f(1.0)=1.0$, hence

$$\psi(0) = 0 \tag{A9a}$$

$$\psi(1) = 1 \tag{A9b}$$

If Eq. (A7) is analytically integrable, this approach avoids the necessity to use upwinding for the convection terms. Equation (A8) can be solved using central differencing for all Peclet numbers.

Exact Solution Verification

As another way of confirming the results from the central differencing and upwinding schemes, the Euler-Cauchy equation was put into the same form as the convection diffusion equation (A1*b*)

$$(x-2)^2\phi'' + 5(x-2)\phi' + 3\phi = 0 \tag{A10a}$$

$$u(x)\phi' = \Gamma(x)\phi'' + 3\phi \tag{A10b}$$

where $u(x)=-5(x-2)$, $\Gamma(x)=(x-2)^2$, and $\lambda=3$ as per Eq. (A1*b*). The analytical solution to this equation was found to be

$$\phi(x) = C_1(x-2)^{-3} + C_2(x-2)^{-1} \tag{A11a}$$

and after applying the boundary conditions $\phi(0)=0$ and $\phi(1)=1$ and solving for constants C_1 and C_2, Eq. (A11*a*) became

$$\phi(x) = \frac{-4}{3(x-2)^3} + \frac{1}{3(x-2)} \tag{A11b}$$

Equation (A11*b*) then gave an analytical solution with which to verify the results from the numerical procedure.

In a final attempt to verify the results of the numerical solutions, a manufactured solution for the steady convection diffusion Eq. (A1*a*) was found. With no source term and additional $f(x)$ terms, Eq. (A1*a*) becomes

$$\frac{\partial(u\phi)}{\partial x} = \frac{\partial}{\partial x}\left[\Gamma\frac{\partial\phi}{\partial x}\right] + f(x) \tag{A12}$$

Assuming a convenient solution $\phi(x)$, a velocity function $u(x)$, and a diffusivity $\Gamma(x), f(x)$ can be determined from

$$f(x) = u\frac{\partial\phi}{\partial x} + \phi\frac{\partial u}{\partial x} - \Gamma\frac{\partial^2\phi}{\partial x^2} - \frac{\partial\phi}{\partial x}\frac{\partial\Gamma}{\partial x} \tag{A13}$$

Next, a two-parameter solution can be assumed

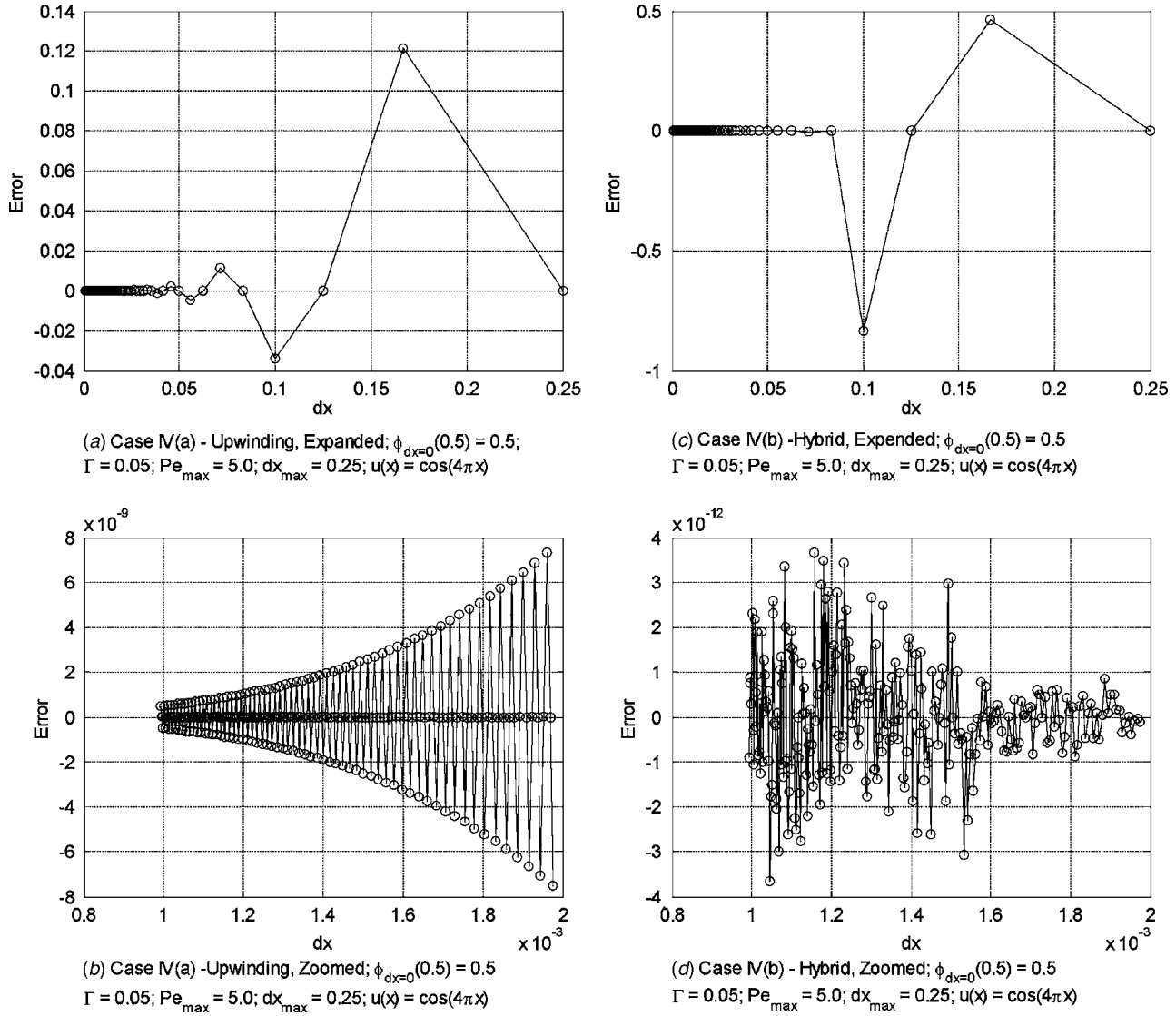

Fig. 9 Error plots showing cases IV(a) and IV(b) in both expanded and zoomed form; the lower plots show convergence behavior for very small dx values

$$\phi(x) = \phi_0 + bx + \tfrac{1}{2}\{\tanh[a(x - x_0)] - c\} \qquad \text{(A14}a\text{)}$$

for $0 \leqslant x \leqslant 1$, with

$$c = \tanh(-ax_0) \qquad \text{(A14}b\text{)}$$

$$b = \phi(1) - \phi(0) - \frac{1}{2}\{\tanh[a(1 - x_0)] - c\} \qquad \text{(A14}c\text{)}$$

where the derivatives of (A14a) are given by

$$\frac{\partial \phi}{\partial x} = b + \frac{a}{2}\{1 - \tanh^2[a(x - x_0)]\} \qquad \text{(A15)}$$

and

$$\frac{\partial^2 \phi}{\partial x^2} = -a^2[\{\tanh[a(x - x_0)]\}][1 - \tanh^2[a(x - x_0)]\}] \qquad \text{(A16)}$$

After calculating $\frac{\partial \phi}{\partial x}, \frac{\partial^2 \phi}{\partial x^2}, u, \frac{\partial u}{\partial x}, \Gamma$, and $\frac{\partial \Gamma}{\partial x}, f(x)$ can be determined from Eq. (A13). A much simpler solution is given by

$$\phi(x) = c(1 - e^{-x}) \qquad \text{(A17)}$$

where $c = (1 - e^{-1})^{-1}$. Letting

$$\Gamma = 0 \qquad \text{(A18)}$$

and

$$u(x) = x(1 - x) \qquad \text{(A19)}$$

it can be deduced from Eq. (A13) that

$$f(x) = \frac{\partial (u\phi)}{\partial x} = x(1 - x)ce^{-x} + c(1 - e^{-x})(1 - 2x) \qquad \text{(A20)}$$

Substituting Eqs. (A18)–(A20) into Eq. (A12), a numerical result is obtained. This result is then compared with the analytical solution given by equation (A17).

Results

A summary of all the cases used is listed in Table 4. This table includes the case number, scheme, velocity function ($u(x)$), diffusivity constant (Γ), and extrapolated solution for each case. Table 4 also shows L^2 error norms for each case with respect to the semianalytical solution for that case. The L^2 error norms show that the numeric solutions seem to be good. These cases will be referred to by their respective case numbers.

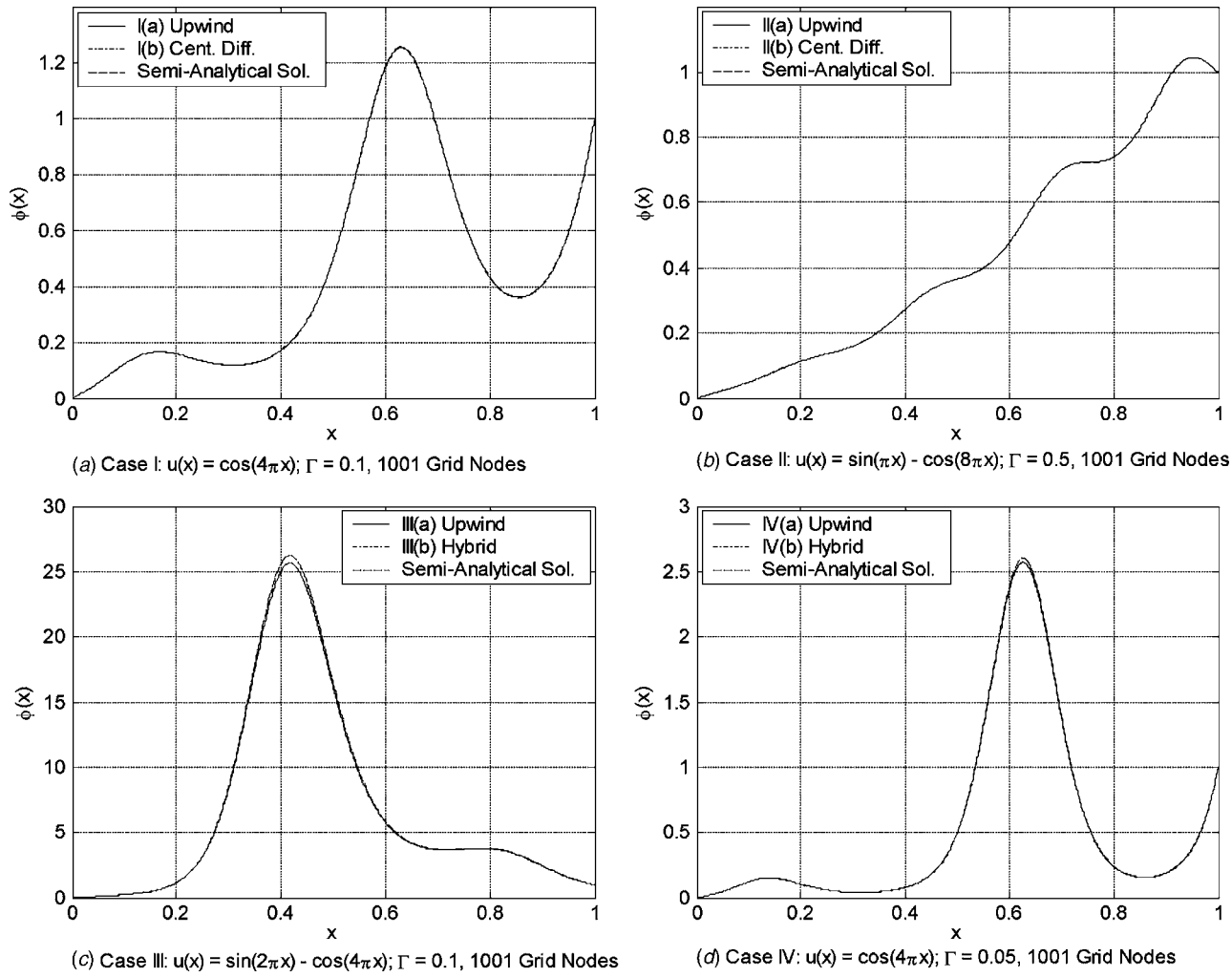

Fig. 10 Solutions for cases I—IV using upwinding and central differencing schemes, as well as the semi-analytical solution

Figures 6–9 show the error using the upwinding, central differencing, and hybrid schemes calculated at $x=0.5$ versus the grid spacing dx. The error is calculated from

$$E_h = \phi_{\text{ext}} - \phi_h(0.5)$$

where $\phi_h(0.5)$ is the solution from the scheme for the respective grid spacing of $h=dx$, and ϕ_{ext} is the extrapolated solution. The extrapolated solutions were found by taking the grid spacing to an appropriately small value and extrapolating with the same trend to $dx=0$. The error bounds for the extrapolated solutions were taken as the difference between the extrapolated solution and the solution at the finest grid spacing used.

Figure 6 shows the error versus the grid spacing for cases I(a) (upwinding) and I(b) (central differencing). Figures 6(*a*) and 6(*b*) show that the convergence with the upwind scheme was oscillatory, even as the grid spacing became very small. In these two plots, the error oscillated cyclically above and below zero as the grid spacing approached zero. Figures 6(*c*) and 6(*d*) show the convergence pattern with the central differencing scheme. With this scheme, the convergence behavior was also oscillatory, but the error oscillated only below zero rather than above and below the zero. Figure 6(*d*) illustrates the fact that even though the central differencing scheme converges very quickly, it still has small oscillations as the grid spacing becomes smaller.

Table 4 Case summary

Case	Scheme	u(x)	Γ	Extrapolated solution at $x=0.5$	L^2 error norm
I(a)	Upwind	$\cos(4\pi x)$	0.1	$0.5+/-0.25\times10^{-10}$	0.9375412
I(b)	Central	$\cos(4\pi x)$	0.1	$0.5+/-0.8\times10^{-11}$	0.0101842
II(a)	Upwind	$\sin(\pi x)-\cos(8\pi x)$	0.5	$0.36604+/-7\times10^{-5}$	0.1139626
II(b)	Central	$\sin(\pi x)-\cos(8\pi x)$	0.5	$0.366041415+/-3\times10^{-8}$	0.0009532
III(a)	Upwind	$\sin(2\pi x)-\cos(4\pi x)$	0.1	$16.4+/-0.12$	122.4437985
III(b)	Hybrid	$\sin(2\pi x)-\cos(4\pi x)$	0.1	$16.44936+/-1\times10^{-4}$	1.1804976
IV(a)	Upwind	$\cos(4\pi x)$	0.05	$0.5+/-1.0\times10^{-10}$	4.8115126
IV(b)	Hybrid	$\cos(4\pi x)$	0.05	$0.5+/-1.0\times10^{-11}$	0.1255890

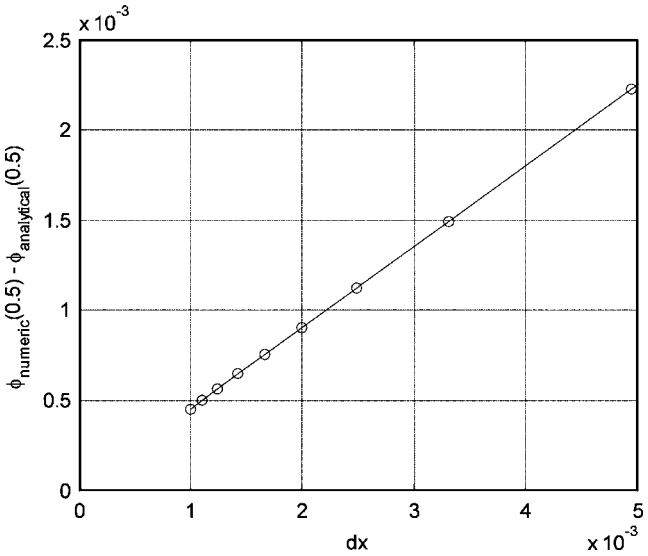

Fig. 11 Difference between analytical and numerical solutions at $x=0.5$ for equation (A10*b*)

Figure 7 gives the error versus the grid spacing for cases II(a) and II(b). Figures 7(*a*) and 7(*b*) illustrate the convergence pattern using an upwind scheme, while Figures 7(*c*) and 7(*d*) show the convergence using the central differencing scheme. It is evident that in both cases as the grid spacing became increasingly small, the solution monotonically approached the extrapolated solution given in Table 4.

For cases III(a) and III(b), Fig. 8 shows the error versus the grid spacing. The convergence pattern using an upwinding scheme is illustrated in Figs. 8(*a*) and 8(*b*), while Figs. 8(*c*) and 8(*d*) show the convergence using the hybrid scheme. Much like the results from cases II(a) and II(b) illustrated in Fig. 7 and 8 shows that once again as the grid spacing became small, the solution monotonically approached the extrapolated solution.

Figure 9 illustrates the convergence behavior of cases IV(a) and IV(b). Figure 9(*c*) shows that the hybrid scheme convergence behavior was oscillatory. The erratic behavior shown by the results of Figure 9(*d*) can probably be attributed to the accumulation of small round-off errors.

The numerical solutions obtained from the different approaches described above were compared to each other in order to assess the accuracy and the consistency of the solutions obtained. Figure 10 shows the plots of the solutions using the upwinding, central differencing (or hybrid), and semi-analytical solutions for cases I–IV. It is evident from these plots that the solutions from the central differencing (or hybrid) and semianalytical methods were very similar in all four cases. However, Figs. 10(*c*) and 10(*d*) show that the solutions from the upwind method were slightly different from those from the other two methods for cases III and IV.

Finally, the Euler-Cauchy Eq. (A10*b*) was solved using the upwinding scheme in order to verify the code. The analytical solution given in Eq. (A11*b*) and the numerical solution were very similar. Figure 11 shows the plot of the exact error, i.e., the difference in the two solutions at $x=0.5$ for different values of grid spacing dx. It is evident from the figure that the difference between the two solutions was, at most, on the order of 10^{-3}.

References

[1] Richardson, L. F., 1910, "The Approximate Arithmetical Solution by Finite Differences of Physical Problems Involving Differential Equations, With an Application to the Stresses In a Masonry Dam," Philos. Trans. R. Soc. London, Ser. A **210**, pp. 307–357.

[2] Richardson, L. F., and Gaunt, J. A., 1927, "The Deferred Approach to the Limit," Philos. Trans. R. Soc. London, Ser. A **226**, pp. 299–361.

[3] Celik, I., Chen, C. J., Roache, P. J., and Scheurer, G., eds., 1993, "Quantification of Uncertainty in Computational Fluid Dynamics," *ASME Fluids Engineering Div. Summer Meeting*, 158, Washington, DC, June 20-24.

[4] Roache, P. J., 1993, "A Method for Uniform Reporting of Grid Refinement Studies," *Proc. of Symp. on Quantification of Uncertainty in Computational Fluid Dynamics*, ASME, New York, I. Celik et al., eds., *ASME Fluids Engineering Div. Summer Meeting*, 158, Washington DC, June 20-24, pp. 109–120.

[5] Roache, P. J., 1998, *Verification and Validation in Computational Science and Engineering*, Hermosa Publishers, Albuquerque.

[6] Celik, I., and Zhang, W. M, 1993, "Application of Richardson Extrapolation to Some Simple Turbulent Flow Calculations," *Proc. of Symp. on Quantification of Uncertainty in Computational Fluid Dynamics*, ASME, New York, I. Celik et al., eds., *ASME Fluids Engineering Div. Summer Meeting*, 158, Washington, DC, June 20–24, pp. 29–38.

[7] Celik, I., and Karatekin, O., 1997, "Numerical Experiments on Application of Richardson Extrapolation With Nonuniform Grids," ASME J. Fluids Eng. **119**, pp. 584–590.

[8] Stern, F., Wilson, R. V., Coleman, H. W., and Paterson, E. G., 2001, "Comprehensive Approach to Verification and Validation of CFD Simulations: Part 1. Methodology and Procedures," ASME J. Fluids Eng. **123**, pp. 793–802.

[9] Cadafalch, J., Perez-Segarra, C. D., Consul, R., and Oliva, A., 2002, "Verification of Finite Volume Computations on Steady-State Fluid Flow and Heat Transfer," ASME J. Fluids Eng. **124**, pp. 11–21.

[10] Eca, L., and Hoekstra, M., 2002, "An Evaluation of Verification Procedures for CFD Applications," *24th Symp. on Naval Hydrodynamics*, Fukuoka, Japan, July 8–13.

[11] Celik, I., and Li, J., 2004, "Assessment of Numerical Uncertainty for the Calculations of Turbulent Flow over a Backward Facing Step," *Workshop on Uncertainty Estimation*, Lisbon, Oct. 21–22.

[12] Roy, C. J., 2003, private communication.

[13] Klein, M., 2004, private communication.

[14] Fox, L., 1957, *The Numerical Solution of Two-point Boundary Value Problems in ODE's*, Clarendon Press, Oxford, pp. 332.

[15] Phillips, G. M., and Taylor, P. J., 1973, *Theory and Applications of Numerical Analysis*, Academic Press, New York, pp. 345.

J. U. Schlüter
X. Wu
S. Kim
S. Shankaran
J. J. Alonso
H. Pitsch

Center for Turbulence Research and Aerospace Computing Lab,
Stanford University,
Stanford, CA 94305-3030

A Framework for Coupling Reynolds-Averaged With Large-Eddy Simulations for Gas Turbine Applications

Full-scale numerical prediction of the aerothermal flow in gas turbine engines are currently limited by high computational costs. The approach presented here intends the use of different specialized flow solvers based on the Reynolds-averaged Navier-Stokes equations as well as large-eddy simulations for different parts of the flow domain, running simultaneously and exchanging information at the interfaces. This study documents the development of the interface and proves its accuracy and efficiency with simple test cases. Furthermore, its application to a turbomachinery application is demonstrated.
[DOI: 10.1115/1.1994877]

1 Introduction

In the design of gas turbine engines computational fluid dynamics (CFD) is often used to predict the flow in single components of the engine, such as the compressor, the combustor, or the turbine. The simulation of the entire flow path of a gas turbine engine using high-fidelity CFD is deemed impossible by the enormous computational costs that it entails. However, the increasing availability of massively parallel computational resources and the improved algorithmic efficiency of future flow solvers puts the simulation of an entire engine within reach. In order for such a simulation to be useful in the design process it has to deliver accurate results with reasonable turnaround.

The goal of the advanced simulation and computing (ASC) program of the Department of Energy (DoE) at Stanford is to develop high-performance flow solvers that are able to use highly parallel supercomputers for the simulation of an entire engine. Although the development of new supercomputers is one of the main tasks in the overall ASC effort of the DoE, the physics part of the ASC project at Stanford investigates the development of flow solvers for gas turbine engines in order to improve efficiency, scalability, and modeling of physical effects. However, looking at the wide variety of flow phenomena, which have to be simulated in the flow path of an engine, it is clear that only the use of multiple specialized flow solvers (one for the turbomachinery portions and one for the combustor) can guarantee efficiency and accuracy of such a simulation: the flow regimes and the physical phenomena, which have to be modeled vary dramatically in these two components. Most flow solvers used nowadays in the design process are specialized for either of these two tasks.

The flow field in the turbomachinery portions of the domain is characterized by both high Reynolds and high Mach numbers. The accurate prediction of the flow requires the precise description of the turbulent boundary layers around the rotor and stator blades, including tip gaps and leakage flows. A number of flow solvers that have been developed to deal with this kind of problem have been in use in industry for many years. These flow solvers are typically based on the Reynolds-averaged Navier-Stokes (RANS) approach. Here, the unsteady flow field is ensemble averaged, removing all dependence on the details of the small-scale turbulence. A turbulence model becomes necessary to represent the portion of the physical stresses that has been removed during the averaging process. Because of the complexity of the flows in turbomachinery, various parameters in these turbulence models have to be adapted in order to deliver accurate solutions. Since this kind of flow has been the subject of a large number of investigations, these parameters are usually well known and, hence, the flow solvers deliver reasonably good results.

The flow in the combustor, on the other hand, is characterized by detached flows, chemical reactions, and heat release. The prediction of detached flows and free turbulence is greatly improved using flow solvers based on large-eddy simulations (LES). Although the use of LES increases the computational costs, it has been the only predictive tool that is able to simulate consistently these complex flows. LES resolves the large-scale turbulent motions in time and space and only the influence of smallest scales, which are generally more universal and hence, easier to represent has to be modeled [1,2]. Since the energy containing part of the turbulent scales is resolved, the modeling of turbulent combustion is facilitated by additional data that are provided by the LES solution [3]. LES flow solvers have been shown in the past to be able to model simple flames and are currently adapted for use in gas turbine combustors [4,5].

In order to predict multicomponent effects, such as compressor-combustor instabilities, combustor-turbine hot-streak migration, and combustion instabilities, the flow solvers that describe different components in the gas turbine have to run simultaneously, each computing its part of the domain, and periodically exchange flow information at the interface (Fig. 1). The simultaneous execution of multiple parallel flow solvers requires the definition of an interface that allows the exchange of flow information and a framework for well-posed boundary conditions in order to process the exchanged data.

The approach to couple multiple simulation codes has been used already in other areas of application, most notably in global climate simulations [6], and found recently more attention in other areas of mechanical engineering [7]. However, the idea to couple RANS and LES flow solvers is a very recent approach and a unique method to construct an LES-RANS hybrid.

Other LES-RANS hybrid approaches, such as detached-eddy simulations (DES) [8] and limited-numerical scales (LNS) [9] combine LES and RANS in a single flow solver. This requires a sensor that determines when to switch from one approach to the other. In our approach the domains are defined as zones by the computational domains of both codes. The use of two separate codes allows one to employ the optimal combination of a math-

Contributed by the Fluids Engineering Division for publication in the ASME JOURNAL OF FLUIDS ENGINEERING. Manuscript received by the Fluids Engineering Division April 14, 2004. Final revision February 16, 2005. Associate Editor: Thomas B. Gatski.

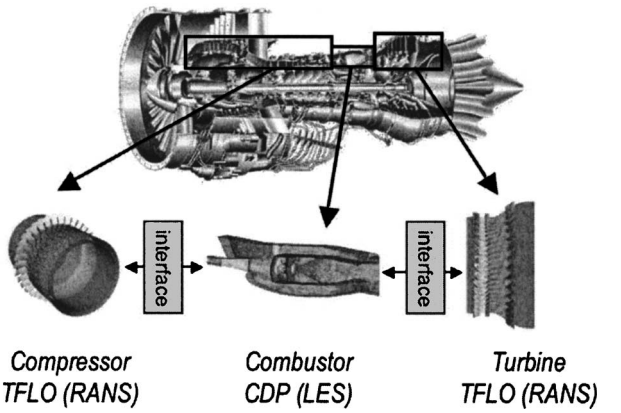

Fig. 1 Computation of the flow path of an entire gas turbine: decomposition of the engine. Compressor and turbine with RANS; combustor with LES (combustor and turbine images from [34,5])

ematical approach, numerical method, and models in each domain (e.g., the modeling of combustion requires the solution of additional transport equations). Here, we can limit the solution of these transport equations to the combustor. Furthermore, the time step in each domain can be chosen to fulfill the local requirements, which means that usually the RANS domain can be computed with a larger time step than the LES domain. The approach to couple two existing flow solvers also has the distinct advantage to build on the experience and validation that has been put into the individual codes during their development. Furthermore, once the procedures to couple independent simulation codes are in place, the extension of this concept to multiphysics simulations using other simulation tools can be done [10].

The current study describes the framework for the simultaneous execution of RANS and LES flow solvers and addresses the following points:

1. Description of the RANS and LES flow solvers (Sec. 2)
2. Presentation of the interface, which enables contact and information exchange between the simultaneously executed flow solvers (Sec. 3)
3. Description of the boundary conditions used by the flow solvers at the interfaces (Sec. 4)
4. Validation of the communication routines and the boundary conditions using simple test cases (Sec. 5)
5. Demonstration of coupled RANS-LES of complex geometries (Sec. 6)

2 Flow Solvers

This section describes the flow solvers used in the current study and emphasizes the differences between the RANS and LES approaches.

2.1 RANS Flow Solver. RANS flow solvers solve the classical Reynolds-averaged Navier-Stokes equations for turbulent flows. With this approach, the flow variables are split into mean and fluctuating portions $u_i=\bar{u}_i+u_i'$ and the Navier-Stokes equations are time averaged. This averaging process results in a set of equations for the mean flow quantities, but leaves an undetermined term $\overline{u_i'u_j'}$, which has to be modeled with a turbulence model. Turbulence models are commonly based on an eddy viscosity approach, which can be modeled with varying levels of complexity. The most commonly used models for RANS flow solvers are two-equation models, such as the $k-\epsilon$ or $k-\omega$ models, where two additional transport equations are solved in order to determine values and distribution of the eddy viscosity field. These models are typically accepted as a good compromise between efficiency and accuracy for turbomachinery applications.

The RANS flow solver used for this investigation is the TFLO code developed in the Aerospace Computing Lab (ACL) at Stanford. The flow solver computes the unsteady Reynolds-averaged Navier-Stokes equations using a cell-centered discretization on arbitrary multiblock meshes [11]. The convective terms are discretized using central differences (second-order accurate on smooth meshes). In order to maintain numerical stability artificial dissipation is added. The solution procedure is based on efficient explicit modified Runge-Kutta methods with several convergence acceleration techniques, such as multigrid, residual averaging, and local time stepping. These techniques, multigrid, in particular, provide excellent numerical convergence and fast solution turnaround. The turbulent viscosity is computed with the Wilcox $k-\omega$ two-equation turbulence model [12]. The dual-time stepping technique [13–15] is used for time-accurate simulations that account for the relative motion of moving parts as well as other sources of flow unsteadiness.

2.2 LES Flow Solver. LES flow solvers solve a filtered version of the Navier-Stokes equations. The filter ensures that the large-scale turbulence is resolved in time and space, which results in a decomposition of the flow variables into a resolved and a subgrid portion, $u_i=\tilde{u}_i+u_i''$. For practical purposes, a mesh filter is applied, implying that the local cell size defines the filter at each point in the mesh. Applying the filter to the Navier-Stokes equation leaves an undetermined term, $\widetilde{u_i''u_j''}$, which defines the subgrid turbulence that must be modeled. As opposed to the Reynolds stress term $\overline{u_i'u_j'}$ in the RANS equations, which includes the turbulent motions of all scales, the LES term describes only the subgrid turbulence. With sufficiently high mesh resolution, the LES solution can be very robust with respect to the chosen subgrid model. Most models use an eddy viscosity approach for the description of the subgrid stresses. Typically the eddy viscosity is determined by algebraic models, such as the Smagorinsky model [16], or, as used in this study, by a dynamic procedure, where the solution of the high-frequency resolved flow field is used to determine the subgrid stresses [17].

For the initial development of the interface two separate LES flow solvers are used. The first one is a structured LES flow solver, which has the advantage of very fast execution speeds. The second LES flow solver used is the unstructured CDP code, which is used for its ability to resolve complex geometries.

The structured LES flow solver chosen for this work is a code developed at the Center for Turbulence Research (CTR) at Stanford by Pierce and Moin [18]. It solves the filtered momentum equations with a low-Mach-number assumption on an axisymmetric, structured, single-block mesh. A second-order finite-volume scheme on a staggered grid is used [19]. Centerline boundary conditions for the radial velocity and its gradients are obtained by averaging corresponding values across the centerline [20]. The approach is designed to allow radial flow communication through the centerline. The low-Mach-number approximation allows one to circumvent the acoustic Courant-Fredriechs-Lewey (CFL) condition for compressible flows and increases the permissible timestep by at least 1/Ma. In return, the pressure field has to be determined by solving the Poisson equation. The subgrid stresses are approximated with an eddy viscosity approach, where the eddy viscosity is determined by a dynamic procedure [17,21].

The unstructured LES flow solver CDP has been developed at the Center for Turbulence Research at Stanford [22]. The filtered momentum equations are solved on a cell-centered unstructured mesh with a second-order accurate central differences spatial discretization [23]. An implicit time-advancement procedure is applied. As in the structured flow solver, a low-Mach-number approximation is used and the Poisson equation is solved in order to

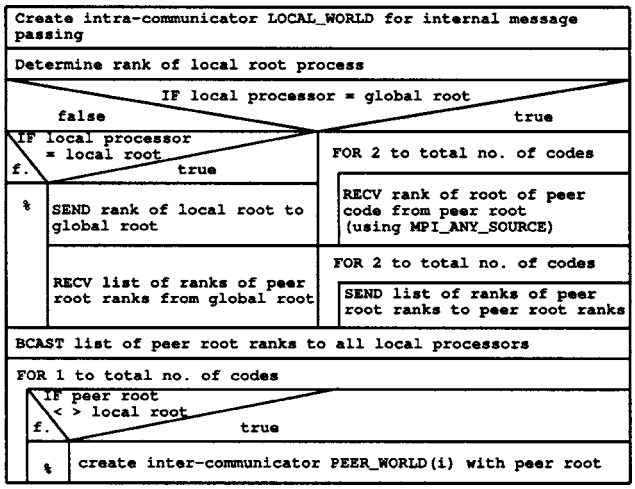

Fig. 2 Structure chart: exchange of root ranks needed for creation of intercommunicators

determine the pressure field. The subgrid stresses are modeled with a dynamic procedure.

3 Interface

The role of the interface is to establish the communication between two or more simultaneously executed flow solvers and to enable the efficient transfer of flow variables among all of them. In the following sections, the interface routines are described together with their implementation in the previously described RANS and LES flow solvers. Careful attention is paid to the fact that all flow solvers are parallelized using the message-passing interface (MPI) and that the execution of these codes is usually carried out on massively parallel supercomputers [24].

3.1 Peer-to-Peer Message Passing. The messages between two separate flow solvers (peer-to-peer message passing) is very similar to the information exchange between processors of a parallel computation. Many flow solvers are parallelized and use MPI for process-to-process message passing. MPI can be used for communication between different flow solvers as well.

Before establishing the contact between two flow solvers, one must make sure that the commands for message passing that are internal to each of the two codes do not interfere with the communication between codes. With MPI it is possible to define the scope of the message passing using communicators. The most commonly used communicator in MPI is the standard communicator MPI_COMM_WORLD, which includes all processors of all codes started from the same MPIRUN command. Using this communicator for internal message passing will inevitably result in confusion for communication between the two codes. Hence, each code creates its own local communicator (intracommunicator) to encapsulate the internal message passing. All codes have to use their own intracommunicator for all MPI commands concerning the internal parallelization of the code instead of MPI_COMM_WORLD.

In the next step, a communicator is created for the peer-to-peer message passing (intercommunicator). For example, assume a case with three flow solvers is to be run with a first instance of a RANS code using two processors (ranks 0 and 1, local root process 0), an LES code using four processors (ranks 2, 3, 4, and 5, local root process 2), and a second instance of a RANS code using three processors (ranks 6, 7, and 8, local root process 6). In order to create the intercommunicator, it is necessary that every processor knows the rank of the root processes of the other codes. A global root process is appointed (rank 0) that collects the ranks of the root processes of all codes (here: ranks 0, 2, and 6), compiles them into a list, and sends them back to the local root processes. A chart with the structure of this procedure is shown in Fig. 2. Since there is no intercommunicator available yet, this communication has to be done using the standard communicator MPI_COMM_WORLD. With the knowledge of the ranks of all root processes it is then possible to create the intercommunicators.

3.2 Handshake and Communication.

3.2.1 Handshake. The efficient parallelization of a flow solver seeks to limit the information exchange between parallel processes to a minimum, since the information exchange requires considerable time compared to the actual computation and can, therefore, limit parallel scalability. For similar reasons, it is desirable to minimize the communication between flow solvers running simultaneously. Since the flow solvers have to exchange flow information rather often, either after each iteration or after a chosen time step, the aim is to minimize the amount of information communicated at each synchronization point by including an initial handshake step, which serves to optimize the communication during the actual flow computation.

The simplest way to organize the information exchange between solvers would be to let only the root processes in each solver communicate. However, this would mean that prior to the peer-to-peer communication, the root processes would have to gather the flow information to transfer from their own processes, and after the peer-to-peer communication process is complete, they would have to distribute the obtained information back to their processes. This creates an obvious bottleneck in the communication pattern, which must be avoided. The solution reported here avoids this bottleneck by direct communication among the neighboring processors on the interface.

The initial handshake routine establishes the direct communication pattern described above (Fig. 3). First, each processor of each participating code must identify all the points for which it needs flow information from its peers to define its interface boundary conditions. The location of each of these points has to be stored in a data structure containing three integers and three double-precision values. The three integers are an *ip* number, which determines what kind of flow variables are requested for this point; an *id* number, which contains a unique identification number for each point; and a *flow solver* number denoting the flow solver requesting this point. The three double precision numbers contain the *x*-, *y*-, *z*-coordinates of the point in Cartesian coordinates using SI units.

The initial handshake takes place in four steps. First, each processor sends the number of points in its own domain for which flow data will be requested to each processor of the peer code. This allows each code to dynamically allocate memory to store the information received. In the second step, each processor receives information containing the location in space of the requested points from each of the peer processors that request a nonzero number of points.

In an intermediate step, each processor identifies whether a requested point lies within its own domain and data can be provided for it. During this step, the interpolation schemes required to obtain the data for this point are determined and stored for later use.

In the third communication step, each processor communicates the number of points found within its domain to all peer-processes requesting data. Again, this allows the dynamic allocation of arrays for the last step. In the fourth communication step, each processor sends out an array to each peer processor it can serve. The array consists of two integers containing the *ip* and *id* of the point. Finally, each processor determines whether all of its requested points can be served by peer processors. If not all points can be served, appropriate errors are flagged.

3.2.2 Communication. The communication of flow data between iterations is rather straight forward once the initial handshake is completed (Fig. 4). Since it is known to every processor what kind of data has to be provided to which peer processor, and from which peer processor data is expected, the data packages can

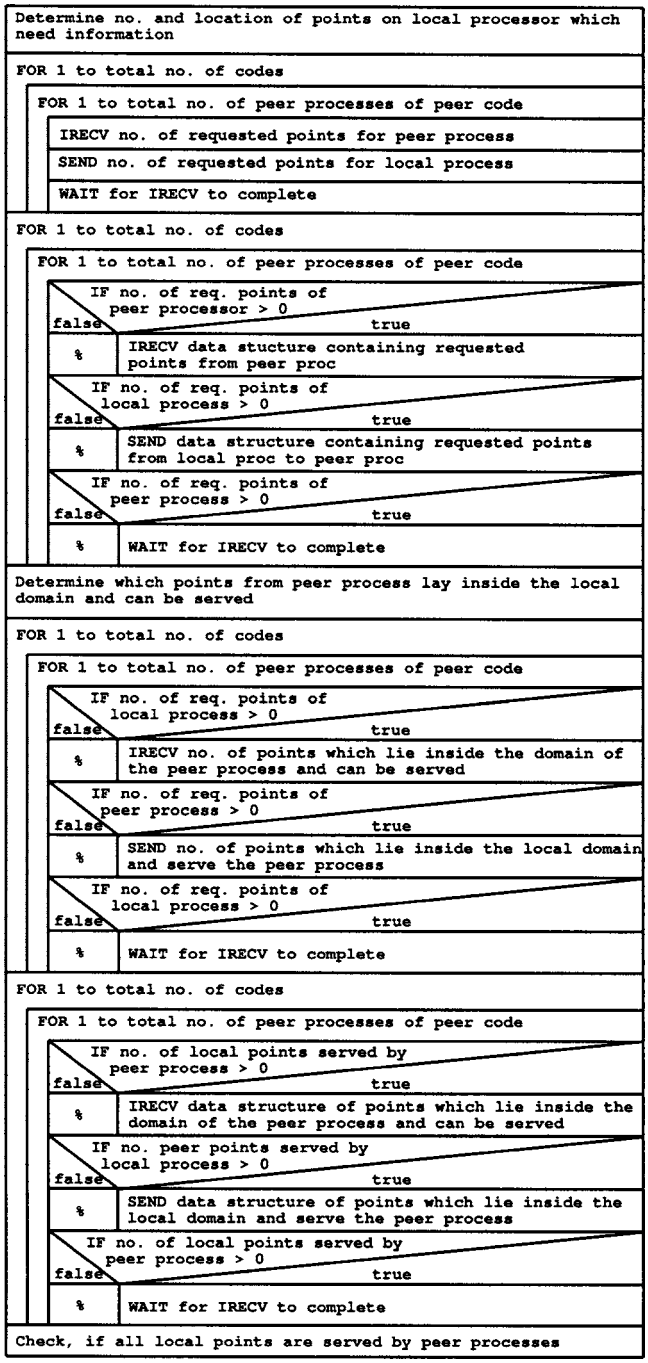

Fig. 3 Structure chart: initial handshake to establish direct communication between interface processors

be sent directly without going through the root processes. After the initialization step, all communication is carried out in the most efficient possible pattern.

Each processor has to compile the data to be sent into a send buffer. The contents of this buffer may vary for different flow solvers and has to be defined beforehand. Although our communication procedure allows for flexible contents of the communication buffers, a standard data structure made up of seven variables has been established. These variables contain ρ, ρu_1, ρu_2, ρu_3, ρE, k, and ν_t, in this order, with ρ being the density, u_1, u_2, u_3 the Cartesian velocity components, E the total energy of the fluid, k the turbulent kinetic energy, and ν_t the eddy viscosity. This set of variables provides the freedom to chose between several RANS

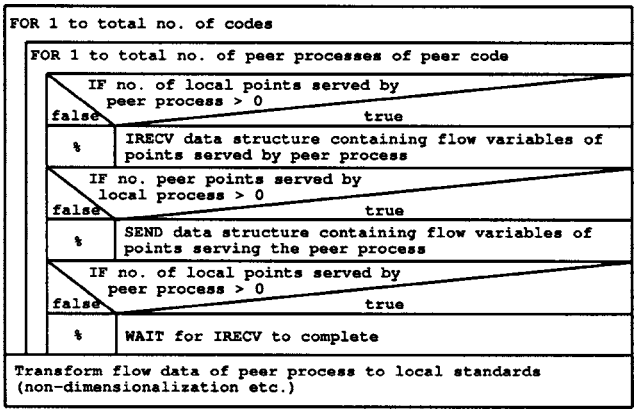

Fig. 4 Structure chart: communication of flow data during flow computations

turbulence models without changing the interface routines, e.g. boundary conditions can be defined from this set of data for both the $k-\epsilon$ and $k-\omega$ turbulence models.

4 Boundary Conditions

4.1 LES Boundary Conditions. The definition of the boundary conditions requires special attention on the LES side due to the different modeling approach used when compared to the RANS solver. Since on the LES side we resolve a part of the turbulent energy spectrum, the challenge is to regenerate and preserve the resolved turbulent motions at the boundaries.

4.1.1 LES Inflow Boundary Conditions. At the LES inflow boundary, the challenge is to prescribe transient turbulent velocity profiles from ensemble-averaged RANS data. A simple addition of random fluctuations to the RANS profiles misses the temporal and spatial correlations of real turbulence, and the fluctuations dissipate very quickly. Instead, we have chosen to create a database of turbulent fluctuations using an auxiliary LES computation of a periodic turbulent pipe flow. The LES inflow boundary condition can then be described as

$$u_{i,\mathrm{LES}}(t) = \underbrace{\bar{u}_{i,\mathrm{RANS}}(t)}_{I} + \underbrace{(u_{i,\mathrm{DB}}(t) - \bar{u}_{i,\mathrm{DB}})}_{II} \cdot \underbrace{\frac{\sqrt{\overline{u'^2_{(i)}}_{\mathrm{RANS}}(t)}}{\sqrt{\overline{u'^2_{(i)}}_{\mathrm{DB}}}}}_{III} \tag{1}$$

where the subscript RANS denotes the solution obtained from the RANS computation, and quantities with subscript DB are provided from the database. Here, t is the time, u_i stands for the Cartesian velocity components, and $\bar{u}_i$ is the ensemble average of the velocity component u_i.

Term II of Eq. (1) is the velocity fluctuation of the database. This turbulent fluctuation is scaled to the desired value through the multiplication by term III, which ensures that the correct level of velocity fluctuation is recovered.

Since the RANS flow solver using a two-equation turbulence model cannot provide all Reynolds stresses, the normal stresses are approximated by

$$\overline{u'^2_{(i)}}_{\mathrm{RANS}} = \tfrac{2}{3}k \quad \text{with} \quad i = 1,2,3 \tag{2}$$

with (i) denoting that no summation of the components is made.

This boundary condition has been validated thoroughly in a previous study [25].

4.1.2 LES Outflow Boundary Conditions. In order to take into account upstream effects of the downstream flow development, the LES outflow conditions have to be defined so that the mean flow properties of the unsteady LES solution can be specified to match the statistical properties delivered by a downstream RANS

simulation. A method that has been tested in the past employs virtual body forces in the momentum equations to drive the mean velocity field of the LES solution to a RANS target velocity field. The virtual body force is given by

$$F_i(\mathbf{x},\mathbf{t}) = \sigma[\bar{u}_{i,\mathrm{RANS}}(\mathbf{x},\mathbf{t}) - \bar{u}_{i,\mathrm{LES}}(\mathbf{x},\mathbf{t})] \tag{3}$$

where $\bar{u}_{i,\mathrm{RANS}}$ is the solution provided by the RANS flow solver, which is computed in an overlap region between the LES and RANS domains, and $\bar{u}_{i,\mathrm{LES}}$ is a time average of the LES solution over a trailing time window. The time variable t is the time according to the LES (changes with every LES time step), and τ is the time according to the RANS time step (changes with every RANS time step). The body force constant σ determines the strength of the body force. Its value can be estimated by a one-dimensional (1D) Euler analysis [26] and its minimum is given by

$$\sigma_{\min} = \frac{u_B}{l_F} \ln\left(\frac{|u_0 - u_t|}{\epsilon u_t}\right) \tag{4}$$

with u_B the bulk velocity, l_F the length of the forcing region, u_0 an estimate for the unforced solution, and u_t the target solution.

This body force ensures that the velocity profiles at the outlet of the LES domain fulfill the same statistical properties as the velocity profiles in the overlap region computed by a downstream RANS simulation. This makes it possible to take upstream effects of downstream flow alterations into account. This LES outflow condition has been validated in previous work [27].

The numerical outflow conditions at the LES outflow are determined by the so-called convective outflow condition

$$\frac{\partial \phi}{\partial t} + u_c \frac{\partial \phi}{\partial n} = 0 \tag{5}$$

where ϕ is any scalar or velocity component, u_c is the convective velocity, and n is the coordinate in the direction of the outward normal at the boundary. The pressure at the outlet adjusts, accordingly, to the velocity distribution determined by the Poisson equation and, hence, it cannot be prescribed. Instead, the proper pressure conditions are adjusted using Eq. (3).

4.2 RANS Boundary Conditions. The specification of RANS boundary conditions from LES data is essentially straightforward. The unsteady LES flow data are time averaged over the time step used by the RANS flow solver and can be employed directly as a boundary condition.

In the current study, the compressible formulation of the RANS flow solver and the low-Mach-number formulation of the LES code posed a challenge. Although the RANS code allows for acoustic waves to propagate within the limits of its domain, the density field of the LES solution is entirely defined by mixing and the combustion process and not by acoustics. This leads to the need for RANS inflow and outflow conditions that allow acoustic waves to leave the domain without spurious reflections. The construction of these boundary conditions is nontrivial, particularly for viscous flows, and must allow for variations of the flow variables at the interface locations. Currently, the local one-dimensional inviscid (LODI) relations [28] are applied.

In the case of the LES domain upstream of the RANS domain, the RANS flow solver has to define its inflow conditions from the LES data. For every point of the inlet plane the mass-flux vector $(\rho u, \rho v, \rho w)$ is imposed, delivered by the LES computation. This allows the density ρ to fluctuate to account for the passing of acoustic waves. The velocity components u, v, w are adjusted accordingly in order to conserve the mass flux. Variations of ρ are in the order of $<2\%$ for typical Mach numbers.

For the RANS turbulence model, k is delivered by the LES solution as the turbulent kinetic energy of the resolved turbulence. The second variable ω is currently set constant at the interfaces, since it was found that it is difficult to retrieve a meaningful approximation of this variable from the LES solution.

In the other case, where the LES domain is downstream of the RANS, at the outlet the static pressure is defined by the LES and applied as the outflow boundary condition to account for the influence of a downstream LES flow solution.

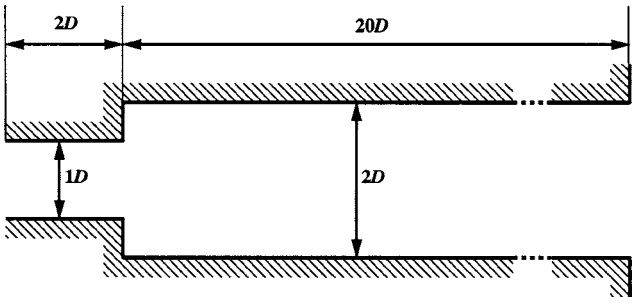

Fig. 5 Interface validation: geometry of the experimental test section [29]

5 Interface Validation

In order to validate the interface for gas turbine applications, two different scenarios have to be validated. The first one corresponds to the upstream interface between the compressor and the combustor. Then, the upstream flow solver is the RANS flow solver (for the compressor geometry), while the downstream domain (the combustor) is solved using an LES solver, which has to define its inflow boundary condition from the upstream RANS solution. The RANS flow solver obtains its outflow boundary condition from the LES solution. The second scenario corresponds to the downstream interface between the combustor and the turbine. Conversely, the LES flow solver is now upstream and has to define its outflow conditions according to the solution of the RANS solver downstream. The RANS flow solver obtains its inflow conditions from the upstream LES.

5.1 Upstream Interface: RANS-LES. In order to validate the upstream interface and the LES inflow boundary condition, a coupled RANS-LES computation of an axisymmetric expansion has been performed. The geometry is shown in Fig. 5 and has an expansion ratio of 1:2 leading to an area ratio of 1:4. The Reynolds number based on the upstream diameter and the bulk velocity is Re=30,000. This test case corresponds to a well-documented experimental configuration [29], and extensive experimental data are available upstream and downstream of the expansion. This allows for an accurate definition of the inflow flow parameters and an assessment of the simulated flow development.

Although this flow has been computed earlier using LES [25], here an additional level of complexity is added by using a coupled RANS-LES approach. While this has no particular advantage for the current test case, it allows one to validate the communication routines and the boundary conditions on both sides of the interface. A part of the flow domain upstream of the expansion is computed with the RANS code TFLO, whereas the flow at the expansion is computed by the LES flow solver CDP (Fig. 6).

With the origin of the coordinate system at the center of the expansion, the inlet velocity profiles in the RANS section are

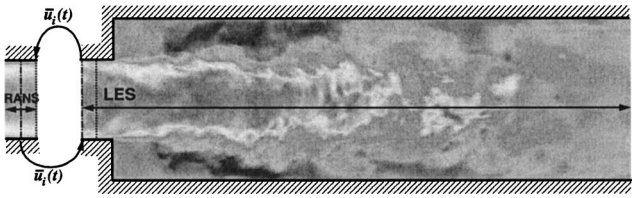

Fig. 6 Interface validation: integrated RANS-LES of a confined jet

specified at $x/D=-0.75D$ according to the experimental data interpolated between $x/D=-2.0$ and $x/D=-0.5$. The variation of these two measured velocity profiles is minimal. The RANS flow solver TFLO computes the flow through the upstream pipe and transfers the data at its outlet to the subsequent LES flow solver. The RANS domain is relatively short ($0.5D$, with D being the diameter of the pipe upstream of the expansion) in order to reproduce the experimental flow field at the inlet of the LES domain as closely as possible. At the RANS outlet the static pressure delivered by the LES solution is imposed.

The LES domain starts at $x/D=-0.5D$, which results in an overlap region between the RANS and LES of $\Delta x/D=0.25$. The LES flow solver CDP obtains its inflow velocity profiles from the RANS flow solver and specifies its LES inflow boundary conditions according to Eq. (1). An overlap region between the two domains was used in order to ensure that the data collection for the communication of flow variables is far enough from the boundary of the computed domain, where the results are influenced by the convective boundary condition.

The RANS mesh contains 350,000 mesh points and is refined near the wall. The LES mesh contains 1.1 million mesh points with the mesh points concentrated near the spreading region of the jet. The mesh has an H–O topology over the pipe cross section: an O mesh near the pipe walls allows for the proper resolution of the wall, while an H-mesh in the center is used to ensure the resolution of the centerline. The far field of the jet is intentionally left relatively coarse in order to decrease computational costs.

The simulation was run for approximately five flow-through times before collecting flow statistics for another five flow-through times. The integrated simulation was computed using five processors for the RANS domain and 24 processors for the LES domain. The exchange of flow information between the two flow solvers was performed with the interface frequency $f_{\mathrm{INTERFACE}}=1/\Delta t_{\mathrm{RANS}}$ using a RANS time step of $\Delta t_{\mathrm{RANS}}=0.1\times D/U_{\mathrm{BULK}}$. The LES time step was determined by the convective CFL condition and was set to $\Delta t_{\mathrm{LES}}=0.01\times D/U_{\mathrm{BULK}}$. This results in a time-step ratio of $\Delta t_{\mathrm{RANS}}/\Delta t_{\mathrm{LES}}=10$. The computation of a single flow through time on an IBM SP3 using 29 processors requires $\sim$2.5 h of wall-clock time, adding up to a total wall-clock time of 25 h for the entire simulation.

The quality of the results of the integrated RANS-LES computation has been assessed by two means. First, the numerical results have been compared against the experimental data. Second, a LES of the entire domain using only the LES code has been performed, where the inflow parameters have been specified according to the measurements at $x=-0.5$. This allows a comparison of the integrated RANS-LES results with a LES computation and the assessment, whether errors have been introduced by uncertainties of the LES approach in the region of the jet or by the coupled RANS-LES approach.

Figure 7 shows the velocity profiles obtained from this computation. The mean velocity distribution of the integrated RANS-LES computation agrees very well with the experimental data and the LES computation. The spreading of the jet and the reattachment of the flow are well predicted by both simulations.

The axial velocity fluctuations are also well predicted in the near field of the jet by both simulations. The far field of the jet is underresolved, and hence the numerical predictions underpredict the turbulence levels. Since the error appears in both simulations, this error can be associated to the mesh resolution and is not caused by the coupling of the RANS and LES flow solver.

This computation validates the coupled RANS-LES approach for the case, where the RANS domain is upstream of the LES calculation.

5.2 Downstream Interface: LES-RANS. In order to verify the interface for this second scenario where the LES domain is upstream of the RANS domain, a swirl flow is considered. The computation of a swirl flow presents a challenging test case for

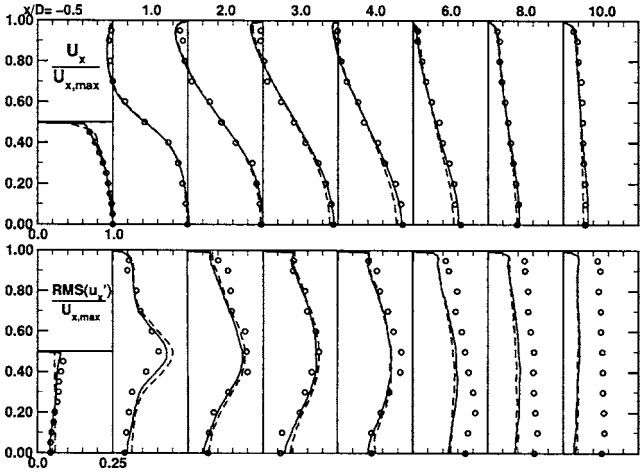

Fig. 7 Results of interface validation. Above: axial velocity profiles. Below: axial velocity fluctuations. Circles: experiments. Solid lines: LES with inflow from experimental data. Dashed lines: integrated RANS-LES, RANS with inflow from experimental data, LES inflow derived from simultaneously running RANS solver.

the validation of the interface and the boundary conditions because of the complexity of the flow and its sensitivity to inflow and outflow parameters. The sensitivity of the upstream flow field allows for a fair assessment of the interface because it ensures that the downstream RANS solution is of relevance for the upstream flow development computed by LES. Yet, this test case is simple enough to perform a LES computation of the entire domain in order to obtain a solution, which serves as a reference to assess the accuracy of integrated computations. Here, the structured LES flow solver and RANS flow solver TFLO are used.

A swirl flow at an expansion with a subsequent contraction three diameters D downstream of the expansion is considered (Fig. 8(*a*)). The inlet velocity profiles are taken from an the experiment described in the previous test case [29,30]. The swirl number of the flow is $S=0.3$, which is just supercritical, meaning that vortex breakdown takes place and a recirculation zone develops. The Reynolds number for this flow configuration was set to $\mathrm{Re}=20{,}000$. The flow conditions were chosen for maximum sensitivity to boundary conditions in order to create a challenging test case for the validation of the interface and the LES outflow boundary conditions.

The extension and strength of this recirculation zone is strongly influenced by the presence of the downstream contraction, which is to be resolved by the RANS flow solver. Unless the effect of the RANS solution is correctly transferred by the interface boundary conditions, the details of the recirculation region in the LES do-

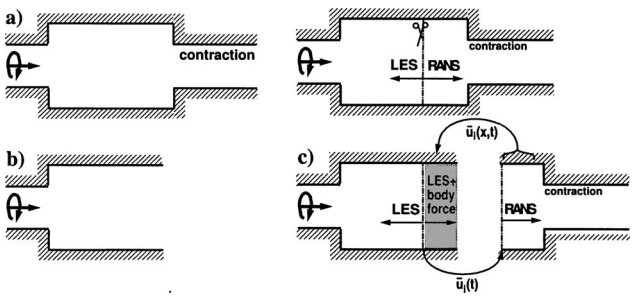

Fig. 8 Geometry for integrated LES/RANS computations: (*a*) full geometry, (*b*) reduced LES domain, and (*c*) schematic splitting of domain to two computational domains

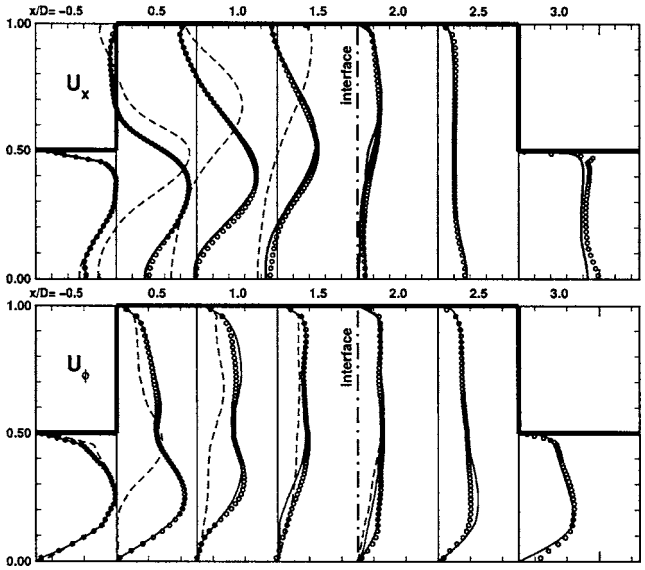

Fig. 9 Integrated LES/RANS computations. Velocity components for different downstream positions. Circles: LES of full geometry (Fig. 8(*a*)) dashed line: LES of expansion (Fig. 8(*b*)) solid line: integrated LES-RANS computation (Fig. 8(*c*)).

main will not be computed correctly.

The first calculation of this study is carried out using the LES solver for the entire domain, including the expansion and the contraction. This computation is considered the reference solution, and the accuracy of all subsequent computations is measured against these results. The following computations consider that this domain is to be computed by two or more separate flow solvers. The geometry is divided into two computational domains with a short overlap region. The expansion is computed with the LES code, whereas the contraction is computed by the RANS solver (Fig. 8(*c*)). If the coupling of the two codes is done appropriately, then this coupled simulation should recover the solution of the LES performed for the entire domain.

The mesh of the LES domain computing the entire domain contains $386\times64\times64$ ($\approx$1.5 million) cells and is refined near the walls and shear layers of the swirl flow. The mesh for the LES domain for the coupled LES-RANS computations consists of $256\times64\times64$ ($\approx$1.0 million) cells and closely resembles the LES mesh for the entire domain. The flow was computed for ten flow-through times before collecting flow statistics for another five flow-through times. The LES of the entire domain computes one flow-through time in 2 h wall-clock time on 12 processors on an SGI Origin 2000. The coupled LES-RANS computation computes the same physical time span in 1.4 h using eight processors for the LES domain and five processors for the RANS domain.

The RANS time step was chosen to $\Delta t_{\mathrm{RANS}}=0.1\times D/U_{\mathrm{BULK}}$, which defines the interface frequency. The LES time step in this computation was varying between different iterations in order to allow for a maximum time step according to the CFL condition. In order to ensure an accurate synchronization of the two flow solvers, the LES time step preceding the communication was adjusted to match the RANS time. The ratio of the time steps was approximately $\Delta t_{\mathrm{RANS}}/\Delta t_{\mathrm{LES}}\approx 12-15$.

Figure 9 shows the velocity profiles for three different computations. The velocity profiles denoted by the circles represent the LES computation of the entire domain (Fig. 8(*a*)) and hence, the target for the integrated computations.

In order to demonstrate the influence of the contraction on the swirl flow at the expansion, the dashed lines show the velocity profiles of a LES computation of the expansion without the computation of the contraction (Fig. 8(*b*)). Convective outflow conditions (Eq. (5)) are used without a body-force treatment. It can be seen that the obtained velocity field differs substantially from the first simulation, and hence the influence of the downstream contraction cannot be neglected.

The solid lines in Fig. 9 show the integrated LES-RANS computation using two flow solvers for the two domains (Fig. 8(*c*)). The location of the interface is denoted with a dotted-dashed line. The velocity profiles on the left-hand side of the interface are computed with LES and the profiles on the right-hand side with RANS. The RANS computation of the subsequent contraction delivers a mean flow field, which is used to correct the outflow conditions of the upstream LES. As a result, the velocity profiles of the integrated LES-RANS computation tend toward the velocity profiles of the LES of the entire domain. Because of the large RANS time step, in the RANS domain the energy of resolved turbulence is negligible compared to the energy of the modeled turbulence.

This test case demonstrates that the downstream development of the flow can have a substantial influence on the upstream flow development. The coupled RANS-LES approach is able to predict the downstream flow development with a RANS flow solver and transfer its effect to the upstream LES. Although in this particular test case a LES of the entire domain was feasible, the value of coupled LES-RANS is apparent in more complex applications such as gas turbines, where LES is not always feasible and some components might have to be computed with RANS.

6 Demonstration of Integrated RANS-LES in Complex Geometries

In order to demonstrate the applicability of coupled RANS-LES computations in realistic gas turbine geometries, a turbomachinery case has been investigated [31]. The goal of this study is to test the interface routines for the flow between the compressor and the combustor and to study the influence of possible unsteady interactions between the compressor and the combustor inlet diffuser. The test case consists of a compressor geometry computed by a RANS flow solver and a prediffuser (the component upstream of the injector to the combustor) computed by a LES flow solver.

The computational study of such cases is relevant and important, since typically these two components are developed in isolation and combined tests are typically done only in a final prototype assembly. Yet, the upstream compressor has a substantial influence on the diffuser performance [32,33]. The numerical prediction of this flow configuration will allow for an assessment of the interactions of the components during the design phase. One of the most important questions for compressor-prediffuser flows is whether separation in the diffuser takes place. Since the inflow of the prediffuser is inhomogeneous and periodically perturbed by blade passings, the integrated computation of this geometry can offer insight into how to modify the geometry in order to develop a more compact, attached diffuser.

The drawback of the choice of this configuration is that no experimental data are available to validate the computation. The quality of the computed results can only be guaranteed on the basis of the separate validation process that the component codes have undergone and the detailed testing of the interface routines that has been presented in this and previous work. Some validation studies of the individual flow solvers are given in Yao et al. [11] and Davis et al. [34,35] for the TFLO code and in Constantinescu et al. [5], Ham et al. [36] and Moin and Apte [22] for the CDP code. The interface has been developed and tested, in detail, in previous sections. Although many of the techniques necessary for the coupling of these two flow solvers are still under development, all necessary elements, such as the coupling procedure and the boundary conditions on both sides, are currently in place for the chosen test case.

The goal of this computation is to demonstrate the feasibility of integrated RANS-LES computations in a turbomachinery environment and to identify practical issues involved in these calculations.

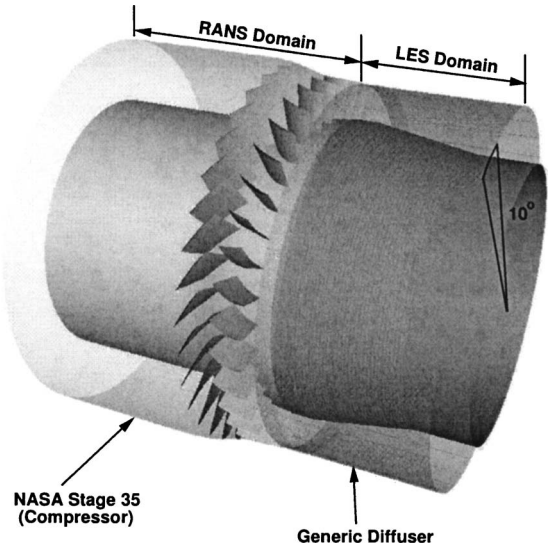

Fig. 10 Geometry of coupled NASA stage 35/prediffuser. RANS domain includes inflow channel, one rotor, and one stator. LES domain includes the diffuser. A 10 deg axisymmetric sector is computed.

6.1 Geometry. The compressor geometry for this test case corresponds to that of a modified version of the NASA Stage 35 experimental rig. The one-stage experimental rig consists of 46 rotors followed by 36 stators. In order to simplify this geometry, the rotor row has been rescaled to have only 36 blades, which allows us to compute an axisymmetric segment of 10 deg using periodic boundary conditions at the corresponding azimuthal planes (Fig. 10).

For this integrated computation, the rotor tip gap has been closed in order to decrease the overall computational cost. The inclusion of the tip gap can be addressed in the TFLO flow solver and poses no additional problems from the integration point of view. The RANS time step was chosen to resolve one blade passing with 50 intervals.

The RANS mesh is a structured multiblock mesh consisting of ~1.5 million control volumes. The speed of the rotor was set to a relatively low 5000 rpm in order to keep the flow at the interface within the low-Mach-number regime that the LES solver is able to handle. This decrease in rotational speed had to be done for the current case. In a real engine, the compressor consists of multiple stages resulting in a higher pressure and higher temperature at the compressor exit. The high temperature of the air in this section of the flow path will ensure that the low-Mach-number approximation is not violated, even when the engine is at full load.

For the RANS domain, the flow solver TFLO has been used. On the LES side, the LES flow solver CDP has been applied.

The diffuser expansion begins one stator chord length behind the stator. The LES domain starts $\frac{1}{3}$ chord behind the stator. The RANS domain reaches $\frac{2}{3}$ of the chord length into the LES domain, which essentially means that the RANS outlet plane is right at the beginning of the expansion of the diffuser.

The diffuser geometry has been chosen with a relatively wide opening such that separation may occur. The diffuser opens toward the centerline of the compressor. Over three chord lengths, the diffuser opens up 0.5 chord lengths. The outer wall of the diffuser is straight.

The LES mesh for the CDP flow solver consists of 500,000 control volumes and is concentrated near the walls. The cell size near the wall is approximately $y^+=30$, and while recent studies show that this resolution may not be enough to characterize a diffuser flow [37], we consider it sufficient for the purpose of the demonstration of the RANS-LES approach.

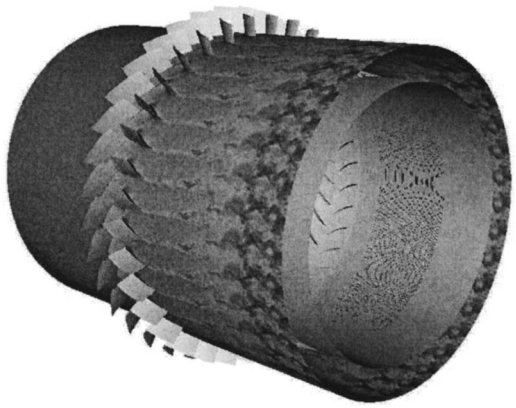

Fig. 11 Integrated RANS-LES of compressor/prediffuser: velocity distribution at the 50% plane

LES inflow boundary conditions were defined corresponding to Eq. (1). The turbulence database needed for this inflow boundary condition was created by a periodic annular pipe flow using the same mean flow characteristics as estimated for this flow configuration.

The load balancing between the two flow solvers has to be done manually. A variety of factors play a role in the efficient allocation of available resources to the two flow solvers. These factors are the number of control volumes in each domain, the ratio of time steps (here: $\Delta t_{\mathrm{RANS}}/\Delta t_{\mathrm{LES}}=7$), the convergence speeds, the numerical methods, parallel efficiencies, and partitioning limits. The variety of factors requires a practical approach to address the load balancing. Here, we performed simulations of the separate domains and assessed the computational needs for each flow solver. As it turned out, for the current case an equal amount of computational resources were necessary for both domains. This allows one to minimize the idle times at the synchronization points.

6.2 Results. The computations using the unstructured LES flow solver CDP and the multiblock structured RANS solver TFLO were carried out using 64 processors for TFLO and 64 processors for CDP. Here, eight blade passings were computed in 60 h of wall-clock time using an IBM Power3 system.

The actual Mach number at the interface was Ma=0.1 ensuring the validity of the low-Mach-number approximation in the LES domain. With these flow conditions, the Reynolds number in the compressor, based on the inlet velocity and the chord length, is approximately Re=60,000. The mass flux over the interface was conserved with an error of ≈0.5%.

Since no experimental data are available for this test case, the interpretation of the results has to be done qualitatively. Figures 11 and 12 show the axial velocity distributions at 50% of the span of the compressor blades for an instantaneous snapshot of the computation. The upstream RANS solution corresponds to a phase-averaged solution, whereas the downstream LES solution is truly unsteady.

The wakes of the stators can clearly be identified in the RANS domain downstream of the stators. The communication of the flow solvers at the interface ensures that the full three-dimensional (3D) flow features are transferred from the upstream flow solver to the downstream domain. The boundary conditions of the LES flow solver are defined according to these data. Hence, the wake of the stator correctly propagates across the interface and can still be found far downstream in the diffuser. It can also be seen that the turbulence, which is resolved in the LES domain, creates more evenly distributed velocity profiles.

The differences in the description of turbulence are more apparent in Fig. 13, which shows the vorticity distribution at 50% of the span of the stator. Here the magnitude of the vorticity is depicted

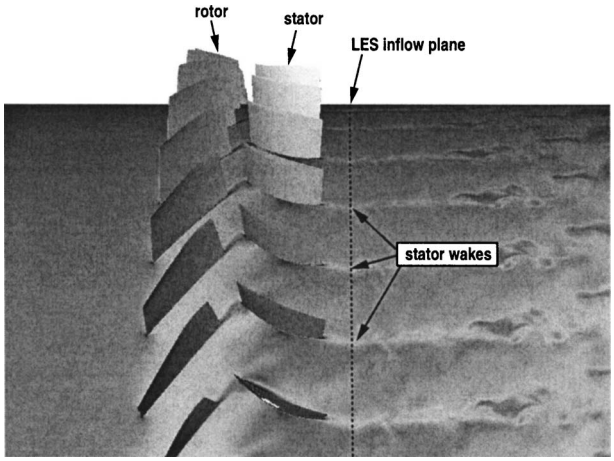

Fig. 12 Integrated RANS-LES of compressor/prediffuser: velocity distribution at the 50% plane. Close-up of the interface.

and is computed according to the unsteady flow field of both domains. In the RANS domain, the vorticity is mainly created because of the mean flow features, such as the wall boundary layers, and secondary flows and vortices. The stator creates two vorticity sheets, one on the extrado and one on the intrado. Both vorticity sheets propagate downstream across the interface.

The vorticity distribution in the LES domain is characterized by small-scale turbulence. Turbulence, present in the upstream RANS domain and modeled by a RANS turbulence model, has to be regenerated. The small-scale turbulence has been reconstructed at the interface using the LES inflow boundary condition (Eq. (1)). It can be seen that the small-scale turbulence interferes with the stator wakes. The turbulent diffusion of the stator wakes in the RANS domain is modeled with an eddy viscosity model, which gives these a very smooth appearance. In the LES domain, the turbulent transport is given by the resolved turbulence, and hence vortical turbulent structures can be identified.

7 Conclusions

The current study describes an approach to combine RANS and LES flow solvers for integrated simulations. Here, for gas turbine applications, a framework has been established that allows one to simulate the multicomponent effects between the turbomachinery and the combustor. The RANS flow solver is used to compute turbomachinery portions, whereas the LES is intended for the combustor. The main motivation is to reduce the overall computational cost of this kind of simulations by using the appropriate models for each of the portions of the flow path.

Part of the efforts to integrate RANS and LES flow solvers was devoted to the setup of an efficient communication pattern between the flow solvers in a parallel environment. Algorithms have been developed and implemented in several flow solvers that allow for an arbitrary number of flow solvers to be run simultaneously and exchange flow information at the interfaces of their domains.

Furthermore, it has to be ensured that the received flow information is used in meaningful boundary conditions to take the flow physics computed by the peer flow solvers into account. For this reason, appropriate boundary conditions have been developed and implemented.

The interface and boundary conditions have been validated on two test cases, one where the RANS flow solver is upstream of the LES, and one where the RANS flow solver is downstream of the LES. Both validation studies show very good results. Additionally, the computation of the coupled modified NASA stage 35/ prediffuser geometry demonstrates the concept of integrated RANS-LES computations in complex geometries.

The current study renders the integrated RANS-LES approach available to study multicomponent effects in gas turbines. Recent studies showed that the present approach can be applied to realistic gas turbine geometries with reasonable computational costs [29]. Ultimately, this approach will allow one to simulate the flow through entire gas turbines using RANS for the turbomachinery and LES for the combustor.

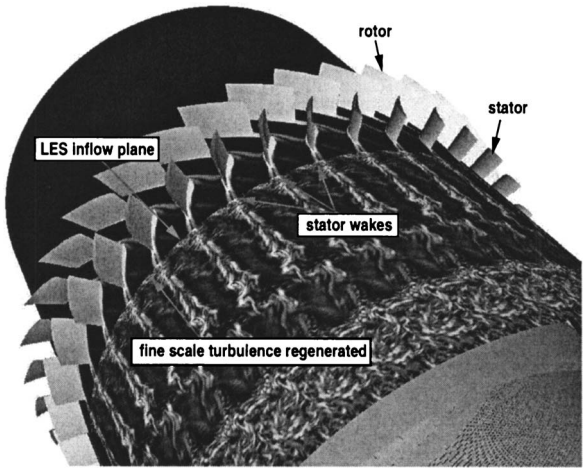

Fig. 13 Integrated RANS-LES of compressor/prediffuser: vorticity magnitude distribution at the 50% plane. Vorticity created on the surfaces of the stators can be found in the LES domain.

Acknowledgments

The support by the US Department of Energy within the ASC program is gratefully acknowledged.

References

[1] Ferziger, J. H., 1996, *New Tools in Turbulence Modelling*, Springer, New York, *Les edition physique*, Chap. 2, pp. 29–47.
[2] Sagaut, P., 2002, *Large Eddy Simulation for Incompressible Flows*, 2nd Edition, Springer, Berlin.
[3] Veynante, D., and Poinsot, T., 1996, *New Tools in Turbulence Modelling*, Les edition physique, Chap. 5, pp. 105–140.
[4] Poinsot, T., Schlüter, J., Lartigue, G., Selle, L., Krebs, W., and Hoffmann, S., 2001, "Using Large Eddy Simulations to Understand Combustion Instabilities in Gas Turbines," *IUTAM Symposium on Turbulent Mixing and Combustion*, Kingston, Canada pp. 1–8.
[5] Constantinescu, G., Mahesh, K., Apte, S., Iaccarino, G., Ham, F., and Moin, P., 2003, "A New Paradigm for Simulation of Turbulent Combustion in Realistic Gas Turbine Combustors Using LES," *ASME Turbo Expo 2003*, ASME Paper No. GT2003-38356.
[6] Trenberth, K. E., 1992, *Climate System Modeling*, Cambridge, New York, Chap. 9.
[7] Adamidis, P., Beck, A., Becker-Lemgau, U., Ding, Y., Franzke, M., Holthoff, H., Laux, M., Müller, A., Münch, M., Reuter, A., Steckel, B., and Tilch, R., 1998, "Steel Strip Production—A Pilot Application for Coupled Simulation With Several Calculation Systems," J. Mater. Process. Technol., **80–81**, pp. 330–336.
[8] Spalart, P. R., 2000, "Trends in Turbulence Treatments," *Fluids 2000*, June, Denver, AIAA Paper No. 2000-2306.
[9] Batten, P., Goldberg, U., and Chakravarthy, S., 2002, "LNS—An Approach Towards Embedded LES," *40th AIAA Aerospace Sciences Meeting and Exhibit*, Jan., Reno, AIAA Paper No. AIAA 2002-0427.
[10] Doi, H., and Alonso, J. J., 2002, "Fluid/Structure Couples aeroelastic computations for Transsonic flows in Turbomachinery," *ASME Turbo Expo 2002*, ASME Paper No. GT-2002-30313.
[11] Yao, J., Jameson, A., Alonso, J. J., and Liu, F., 2000, "Development and Validation of a Massively Parallel Flow Solver for Turbomachinery Flows," AIAA Paper No. 00-0882.
[12] Wilcox, D. C., 1998, *Turbulence Modeling in CFD*, 2nd Edition, DCW Industries, La Canada, CA.
[13] Jameson, A., 1991, "Time Dependent Calculations Using Multigrid, With Applications to Unsteady Flows Past Airfoils and Wings," *AIAA 10th Computational Fluid Dynamics Conference*, Honolulu, AIAA Paper No. 91-1596.
[14] Alonso, J. J., Martinelli, L., and Jameson, A., 1995, "Multigrid Unsteady Navier-Stokes Calculations With Aeroelastic Applications," *AIAA Paper, AIAA 33rd Aerospace Sciences Meeting and Exhibit*, Reno, AIAA Paper No. 95-0048.

[15] Belov, A., Martinelli, L., and Jameson, A., 1996, "Three-Dimensional Computations of Time-Dependent Incompressible Flows With an Implicit Multigrid-Driven Algorithm on Parallel Computers," *Proc. of 15th Int. Conference on Numerical Methods in Fluid Dynamics, Monterey, CA*, Springer-Verlag, Berlin, Lecture Notes in Physics, No. 490.
[16] Smagorinsky, J., 1963, "General Circulation Experiments With the Primitive Equations, I. The Basic Experiment," Mon. Weather Rev., **91**(3), pp. 99–152.
[17] Germano, M., Piomelli, U., Moin, P., and Cabot, W., 1991, "A Dynamic Subgrid-Scale Eddy Viscosity Model," Phys. Fluids A, **3**(7), pp. 1760–1765.
[18] Pierce, C., and Moin, P., 1998, "Large Eddy Simulation of a Confined Coaxial Jet With Swirl and Heat Release," AIAA Paper No. 98-2892, June.
[19] Akselvoll, K., and Moin, P., 1996, "Large-Eddy Simulation of Turbulent Confined Coannular Jets," J. Fluid Mech., **315**, pp. 387–411.
[20] Pierce, C. D., 2001, "Progress-Variable Approach for Large-Eddy Simulation of Turbulent Combustion," Ph.D. thesis, Stanford University, Stanford, June.
[21] Moin, P., Squires, K., Cabot, W., and Lee, S., 1991, "A Dynamic Subgrid-Scale Model for Compressible Turbulence and Scalar Transport," Phys. Fluids A, **3**(11), pp. 2746–2757.
[22] Moin, P., and Apte, S., 2004, "Large-Eddy Simulation of Realistic Gas Turbine Combustors," AIAA Paper No. 2004-0330, Jan.
[23] Mahesh, K., Constantinescu, G., and Moin, P., 2004, "A Numerical Method for Large-Eddy Simulation in Complex Geometries," J. Comput. Phys., **197**(1), pp. 215–240.
[24] Schlüter, J. U., Shankaran, S., Kim, S., Pitsch, H., Alonso, J. J., and Moin, P., 2003, "Towards Multi-Component Analysis of Gas Turbines by CFD: Integration of RANS and LES Flow Solvers," *ASME Turbo Expo 2003*, June 16–19, Atlanta, ASME Paper No. GT2003-38350.
[25] Schlüter, J. U., Pitsch, H., and Moin, P., 2004, "Large Eddy Simulation In-Flow Conditions for Coupling With Reynolds-Averaged Flow Solvers," AIAA J., **42**(3), pp. 478–484.
[26] Schlüter, J. U., Pitsch, H., and Moin, P., 2004, "Outflow Conditions for Integrated Large Eddy Simulation/Reynolds-Averaged Navier-Stokes Simulations," AIAA J., **43**(1), pp. 156–164.
[27] Schlüter, J. U., Wu, X., Kim, S., Alonso, J. J., and Pitsch, H., 2004, "Coupled RANS-LES Computation of a Compressor and Combustor in a Gas Turbine Engine," *40th AIAA/ASME/SAE/ASEE Joint Propulsion Conference and Exhibit*, July, AIAA Paper No. 2004-3417.
[28] Poinsot, T. J., and Lele, S. K., 1992, "Boundary Conditions for Direct Simulations of Compressible Viscous Reacting Flows," J. Comput. Phys., **101**, pp. 104–129.
[29] Dellenback, P. A., Metzger, D. E., and Neitzel, G. P., 1988, "Measurements in Turbulent Swirling Flow Through an Aprupt Axisymmetric Expansion," AIAA J., **26**(6), pp. 669–681.
[30] Dellenback, P. A., 1986, "Heat Transfer and Velocity Measurements in Turbulent Swirling Flows Through an Aprupt Axisymmetric Expansion," Ph.D. thesis, Arizona State University, Dec.
[31] Schlüter, J. U., Wu, X., Kim, S., Alonso, J. J., and Pitsch, H., 2004, "Integrated RANS-LES Computations of Gas Turbines: Compressor-Diffuser," Jan. AIAA Paper No. 2004-0369.
[32] Barker, A. G., and Carrotte, J. F., 2001, "Influence of Compressor Exit Conditions on Combustor Annular Diffusers, Part 1: Diffuser Performance," J. Propul. Power, **17**(3), pp. 678–686.
[33] Barker, A. G., and Carrotte, J. F., 2001, "Influence of Compressor Exit Conditions on Combustor Annular Diffusers, Part 2: Flow Redistribution," J. Propul. Power, **17**(3), pp. 687–694.
[34] Davis, R., Yao, J., Clark, J. P., Stetson, G., Alonso, J. J., Jameson, A., Haldeman, C., and Dunn, M., 2002, "Unsteady Interaction Between a Transsonic Turbine Stage and Downstream Components," *ASME Turbo Expo 2002*, ASME Paper No. GT-2002-30364.
[35] Davis, R., Yao, J., Alonso, J. J., Paolillo, R., and Sharma, O. P., 2003, "Prediction of Main/Secondary-Air System Flow Interaction in a High Pressure Turbine," AIAA Paper No. AIAA-2003-4833.
[36] Ham, F., Apte, S., Iaccarino, G., Wu, X., Herrmann, M., Constantinescu, G., Mahesh, K., and Moin, P., 2004, "Unstructured LES of Reacting Multiphase Flows in Realistic Gas Turbine Combustors," *CTR Annual Research Briefs*, Center for Turbulence Research, Stanford, pp. 139–160.
[37] Wu, X., Schlüter, J. U., Moin, P., Pitsch, H., Iaccarino, G., and Ham, F., "Identification of an Internal Layer in a Diffuser," Stanford University/NASA Ames, Center for Turbulence Research, Annual Research Briefs 2004, pp. 169–182.

Effect of Perforated Plate Open Area on Gas Holdup in Rayon Fiber Suspensions

Xuefeng Su

Theodore J. Heindel[1]
e-mail: theindel@iastate.edu

Department of Mechanical Engineering,
Ames, Iowa 50011-2161

Three different aeration plates are used to study their effect on gas holdup and flow regime transition in fiber suspensions. The aeration plates differ by their open-area ratios (A=0.57%, 0.99%, and 2.14%), where the hole diameter remains the same while the number of holes increase. Experiments are performed using three different Rayon fiber lengths (L=3, 6, and 12 mm) over a range of superficial gas velocities ($U_g \leqslant 18$ cm/s) and fiber mass fractions ($0 \leqslant C \leqslant 1.8\%$) in a 15.24 cm dia semi-batch bubble column. Experimental results show that the aeration plate with A=0.99% produces the highest gas holdup in an air-water system and low fiber mass fraction suspensions, and the plate with A=2.14% yields the lowest gas holdup in these systems. In medium fiber mass fraction suspensions, the plate with A=0.57% produces slightly higher gas holdup values, while the other two plates yield similar results. The effect of the aeration plate open area on gas holdup diminishes at high fiber mass fractions ($C \geqslant 1.2\%$). All aeration plates generate homogeneous, transitional, and heterogeneous flow regimes over the range of superficial gas velocities for air-water and low fiber mass fraction suspensions. However, the aeration plate with A=2.14% enhances the flow regime transition, i.e., the superficial gas velocity at which transitional flow appears is lower. Additionally, the fiber mass fraction at which pure heterogeneous flow is observed is lower when A=2.14%. [DOI: 10.1115/1.1994878]

Keywords: Aeration, Bubble Column, Drift Flux, Gas Holdup, Fiber Suspension, Flow Regime

Introduction

Bubble columns are commonly used to affect gas-liquid (GL) or gas-liquid-solid (GLS) heat and/or mass transfer operations. Considerable attention has been paid to the study of liquid (slurry) properties, the gas distributor, and bubble column dimensions on bubble column gas holdup, also termed the volumetric gas fraction or void fraction. Selected studies on the liquid (slurry) property effects include surface tension [1,2], viscosity [3–6], and solid type and loading [7–11].

Gas-liquid-fiber (GLF) systems, where flexible fibers comprise the solid phase, have grown in interest because of their applications in the pulp and paper industry, including paper recycling (i.e., flotation deinking), fiber bleaching, direct-contact steam heating, and deaeration. Several gas-liquid-fiber studies have been devoted to gas holdup [12–17], flow regimes [14,18,19], and bubble size distribution [20].

The gas distributor is a key factor that ensures an even inlet gas distribution, which provides the highest gas holdup and, thus, the largest possible interfacial area for heat and mass transfer. Hence, the geometric properties of the distributor plate are very important to bubble column performance. Open-area ratio, defined as the ratio of the total plate hole area to column cross-sectional area, is related to the size and number of aeration holes in a perforated plate distributor and is one parameter that may have a significant effect on gas holdup.

Contradictive phenomena of the effect of open area are observed in the literature. Zahradnik et al. [3], Ohki and Inoue [21], Tsuchiya and Nakanishi [22], and Zahradnik and Kastanek [23] found that gas holdup increases with increasing plate open area (i.e., by increasing the number of holes). This was attributed to the lower bubble velocity at the gas inlet hole with increasing open area, resulting in a lower liquid circulation, which had a favorable effect on the stability of the homogeneous flow regime. On the contrary, Shnip et al. [24] numerically showed that the critical gas holdup decreased with increasing open area, implying a similar relationship with overall gas holdup.

Assuming holes are uniformly distributed over the entire aeration plate and the hole diameters remain the same, a change in open area leads to a change in hole spacing, which has an impact on bubble-bubble interaction and the resulting gas holdup. Kawasaki and Tanaka [25] investigated the effect of hole pitch with a constant number of holes on gas holdup and observed that gas holdup decreased with decreasing hole pitch. This was attributed to the fact that when the hole pitch was small, bubbles tended to coalesce together as soon as they left the hole, resulting in larger bubble sizes and a lower gas holdup. Bubble formation at closely spaced holes was studied by Solanki et al. [26]. They pointed out that close spacing enhanced bubble coalescence at the gas inlet.

Hole spacing plays an important role at the inlet and directly influences the interfacial area and transport rate in bubble column reactors [23]. Zahradnik and Kastanek [27] found that a uniform gas distribution led to higher gas holdup compared to a nonuniform gas distribution.

Hole spacing influences the inlet gas distribution through affecting bubble formation at the hole. Ruzicka et al. [28] found that there were two bubble formation modes when bubbles were formed from two holes: (i) synchronous, where bubbles are formed simultaneously through each hole, producing a uniform gas holdup profile in the bottom of the column; and (ii) asynchronous, where the active holes work either out of phase (bubbles are in different stages of formation at the same time) or alternate (only one of the two holes is active at one time). Ruzicka et al. [29]

[1]Corresponding author.

Contributed by the Fluids Engineering Division for publication in the ASME JOURNAL OF FLUIDS ENGINEERING. Manuscript received by the Fluids Engineering Division July 7, 2004. Final revision April 14, 2005. Associate Editor: Georges Chahine.

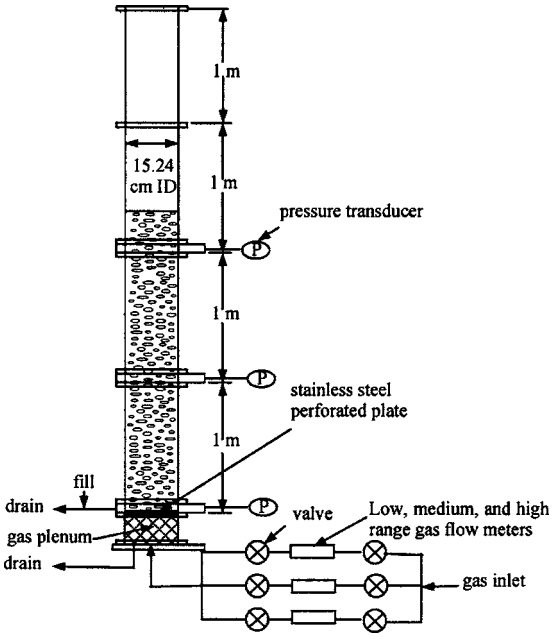

Fig. 1 Schematic of experimental bubble column

found that these two modes were also observed for multihole bubbling, and they demonstrated that hole spacing played a key role in the modes of bubble formation. Bubble formation modes were also influenced by the gas flow rate. Ruzicka et al. [28] showed that there was a critical gas flow rate beyond which the synchronous regime lost its stability and promoted the transition from homogeneous flow to heterogeneous flow. This critical gas flow rate was a function of hole spacing and decreased with decreasing hole spacing.

Additionally, open area combined with gas flow rate is a decisive factor that ensures the stable performance of the gas distributor, leading to a uniform gas distribution. Haug [30] investigated the stability of perforated plates and claimed that in order to get an even gas distribution, the plate pressure drop must be above some critical value (the pressure drop is related to the gas flow rate and the plate open area). There was a limiting gas flow rate below which the gas distribution was nonuniform and liquid weeping occurred. This caused the gas distribution to change from even to uneven as the plate open area increased.

The effect of aeration plate open area on gas holdup in gas-liquid systems has been studied extensively, but little information is available for gas-liquid-solid systems. This study addresses the effect of aeration plate open-area ratio ($A=0.57\%$, 0.99%, and 2.14%) on gas holdup in gas-liquid-fiber systems.

Experimental Procedures

The bubble column experimental facility used in this study is schematically represented in Fig. 1. The bubble column consists of four 1 m sections of 15.24 cm ID cast acrylic, yielding a total column height of 4 m. Gas is injected at the base of the column through one of three stainless-steel perforated plates with open areas $A=0.57\%$, 0.99%, and 2.14% (Fig. 2). For each plate, 1 mm dia holes are uniformly distributed over the entire plate; this is accomplished using a MATLAB program that equated the radial hole pitch with the azimuthal hole pitch. Additional design criteria included open areas as close as possible to 0.5%, 1%, and 2%, and aeration holes spanning the column diameter. Hence, the change in open area is produced by changing the number of uniformly distributed holes. A gas plenum is located below the perforated plate and is filled with glass beads to promote uniform gas distribution into the test facility. Three mass flow meters are used to measure the gas flow rate to encompass a low, medium, and high gas flow rate range. Three pressure transducers are installed along the column, one located at the column base, one at $H=1$ m, and one at $H=2$ m, where H is the column height from the perforated plate. The mass flow meters and pressure transducers are interfaced to a data acquisition system. Average gas flow rate and pressures are recorded from 4000 individual readings sampled at a frequency of 200 Hz.

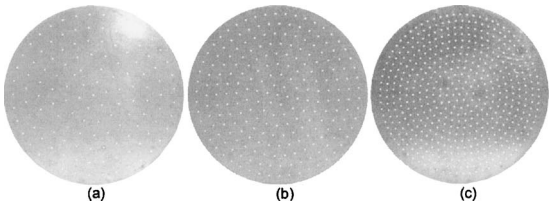

Fig. 2 Gas distributor plates: (*a*) *A*=0.57%, (*b*) *A*=0.99%, and (*c*) *A*=2.14%

The GLF system is composed of air, water, and Rayon fiber. Three nominal Rayon fiber lengths are studied in this paper ($L=3$, 6, and 12 mm), and the fiber diameter is 20.6 μm. Various fiber mass fractions ($0\leq C\leq 1.8\%$) and superficial gas velocities ($U_g\leq 18$ cm/s) are investigated. The superficial liquid velocity in this study is held constant at zero.

The gas holdup (ε) is measured in the upper column section ($1\leq H\leq 2$ m). The gas holdup is determined from the column pressure drop. In a semi-batch system, the frictional pressure drop is negligible, so the total pressure drop corresponds to the hydrostatic head; in this case,

$$\varepsilon = 1 - \frac{\Delta P}{\Delta P_o} \tag{1}$$

where ΔP is the difference between the average local pressure at any two pressure transducers with $U_g>0$, and ΔP_o is the corresponding average value with $U_g=0$. For the GL system, ΔP_o equals the liquid hydrostatic head; for the GLF systems, ΔP_o corresponds to the fiber slurry hydrostatic head.

Experiments are performed at specified fiber mass fractions (C), where the actual fiber mass added to the system is determined from

$$M_f = CM_t \tag{2}$$

The total mass of the fiber-water mixture M_t is determined from $M_t=\rho_{\text{eff}}V$, where ρ_{eff} is the effective slurry density determined from

$$\frac{1}{\rho_{\text{eff}}} = \frac{C}{\rho_f} + \frac{1-C}{\rho_w} \tag{3}$$

and the moisture-free Rayon fiber density is $\rho_f=1500$ kg/m^3 and V is the total volume of the fiber-water mixture.

Before an experiment is initiated, the dry fiber mass calculated from Eq. (2) is soaked in tap water for 2–3 days during which it is washed 2–3 times to remove any residual contaminants and additives absorbed on the fiber surface. The soaked fiber is then added to a small container of water and mixed at low speed using an electronic mixer equipped with a propeller blade. The resulting mixture is then added to the bubble column, which is partially filled with water. Additional water is added to fill the column to a height of 2.13 m (14 column diameters). All experiments are initiated with this slurry volume. The column is then operated at a high gas flow rate for ~35 min to ensure the slurry is well mixed throughout the column. The gas flow rate is then reduced to the lowest value of interest to begin data collection and then incremented sequentially for additional data points. Note that data are collected ~15 min after each gas flow-rate adjustment. The gas used in all experiments is filtered compressed air.

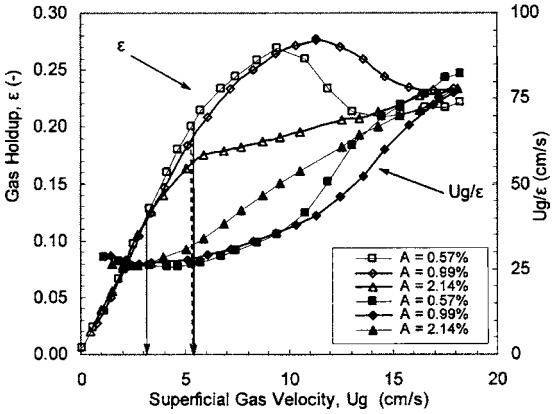

Fig. 3 Gas holdup and flow regime transition using different aeration plates in an air-water system

Although fiber settling did occur with no air injection, the mixing caused by air injection is generally sufficient to maintain a well-mixed system when $C \lesssim 0.4\%$. At higher fiber mass fractions, some bulk fiber settling is observed, but only at the lowest superficial gas velocities, and once the air injection produces sufficient mixing, the fiber slurry is uniformly dispersed throughout the bubble column.

The uncertainty in the superficial gas velocity measurements is estimated to be ±2–4%, and the absolute uncertainty in gas holdup is estimated to be $\Delta\varepsilon = \pm 0.006 - 0.008$.

Results and Discussion

Air-Water. The effect of the aeration plate open area on gas holdup in an air-water system is shown in Fig. 3 (open symbols). At low and high gas flow rates, where the corresponding flow regime is homogeneous and heterogeneous, respectively, the open area has a negligible effect on gas holdup. This phenomenon agrees with the observations of Zahradnik et al. [3] and Zahradnik and Kastanek [23] who observed that gas holdup began to deviate among different open-area ratio plates after a maximum value was recorded and then converged in the heterogeneous flow regime. In the heterogeneous flow regime, gas holdup is determined primarily by bulk liquid circulation and hardly affected by bubble formation modes [3], leading to little gas holdup difference among the three plates in this regime. At medium gas flow rates, where the gas flow is in the transitional regime, gas holdup behavior deviates among the three plates. Gas holdup increases with increasing open-area ratio from $A = 0.57 - 0.99\%$; this agrees well with the results of Zahradnik et al. [3], Ohki and Inoue [21], Tsuchiya and Nakanishi [22], and Zahradnik and Kastanek [23] in which A has a favorable effect on gas holdup. Note, however, that all of these studies were based on $A \leqslant 1\%$. When A is further increased to 2.14%, the gas holdup decreases dramatically. In the transitional flow regime for both $A = 0.57\%$ and 0.99%, gas holdup increases with increasing superficial gas velocity until a maximum gas holdup is reached, and then gas holdup decreases with increasing superficial gas velocity to a minimum value which indicates the end of the transitional flow regime. For $A = 2.14\%$, no maximum gas holdup is observed, and the gas holdup continuously increases with superficial gas velocity.

Combining the observations in this study and Zahradnik et al. [3], Ohki and Inoue [21], Tsuchiya and Nakanishi [22], and Zahradnik and Kastanek [23], we can conclude that the favorable effect of plate open area on gas holdup is valid only within a certain range ($A \lesssim 1\%$); when open area is beyond this range, gas holdup decreases. The following will provide possible explanations of the latter phenomenon.

For a given superficial gas velocity, the gas velocity through the aeration holes is reduced with increasing open area when the number of holes is increased with a constant hole diameter, leading to smaller bubble sizes [31], lower bubble rise velocities, a lower degree of liquid circulation, and more bubbles, all which result in a higher gas holdup and a delay in the flow regime transition. This causes gas holdup to be higher when $A = 0.99\%$ than when $A = 0.57\%$. However, further increasing open area beyond a critical value by increasing the number of holes with a constant hole diameter enhances bubble coalescence near the aeration plate because of a reduced hole spacing; this leads to a reduction in gas holdup. Solanki et al. [26] proposed that coalescence of adjacent bubbles formed at closely spaced holes may occur and depends on three time factors: (i) time of bubble formation t_f, (ii) time required for a bubble to grow to a diameter equal to the hole separation distance to begin bubble-bubble interaction t_i, and (iii) time to drain the liquid film between bubbles to a critical thickness for rupture t_s. For $t_f > t_i + t_s$, coalescence occurs. Smaller hole spacing leads to a smaller bubble size required for the occurrence of interaction with adjacent bubbles. Thus, provided the bubble growth rate is constant, smaller hole spacing results in smaller t_i and $t_i + t_s$, which leads to a higher probability of bubble coalescence compared to a larger hole spacing. Enhanced bubble-bubble interaction with decreasing hole spacing was observed by Xie and Tan [32]. Additionally, when formed through holes, bubble diameter increases with increasing gas flow rate [33]; hence, the probability of bubble-bubble interaction increases with increasing gas flow rate. Therefore, when the superficial gas velocity is increased, the likelihood of bubble coalescence is higher for $A = 2.14\%$ than for $A = 0.57\%$ and 0.99%. As a result, the gas holdup for $A = 2.14\%$ is lower than that of $A = 0.57\%$ and 0.99%. This is not observed when $A = 0.99\%$ because the holes are not close enough to encourage bubble-bubble interaction.

A lower gas holdup for $A = 2.14\%$ when compared to $A = 0.57\%$ and 0.99% may also be ascribed to the fact that for $A = 2.14\%$, the open area is too large to produce a stable gas inlet for the range of superficial gas velocities addressed in this study. Zahradnik and Kastanek [23] and Haug [30] determined that when the plate pressure drop is less than a critical value, bubble formation is influenced by pressure fluctuations in the gas-liquid layer (i.e., bubbling bed), and the plate works in unstable operation. Unstable distributor operation leads to partial aeration, a nonuniform gas distribution, large-scale liquid circulation, and an unstable flow pattern [30]. The critical gas flow rate at which the plate works in stable operation is estimated by the Weber number We. As suggested by Zahradnik and Kastanek [23], stable plate operation occurs when

$$\mathrm{We} = \frac{v_o^2 d_o \rho_g}{\sigma} \geqslant 2 \tag{4}$$

where v_o is the aeration hole gas velocity, d_o is the aeration hole diameter, ρ_g is the gas density, and σ is the surface tension. To achieve the critical Weber number, a higher gas flow rate is required for a larger open area. If We=2, $d_o = 1$ mm, $\rho_g = 1.57$ kg/m^3, and $\sigma = 72.7$ mN m^{-1}, the critical v_o is 9.62 m/s. Thus, the corresponding superficial gas velocities in our system are 5.4, 9.4, and 20.6 cm/s for $A = 0.57\%$, 0.99%, and 2.14%, respectively. It is clear that the plate with $A = 2.14\%$ will not operate in stable operation for the entire superficial gas velocity range of this study, which may contribute to the lower gas holdup. The gas holdup of $A = 0.99\%$ is greater than that of $A = 0.57\%$ after $U_g = 9.5$ cm/s, verifying the importance of stable plate operation.

Hole spacing also changes with open area, and this affects the bubble formation mode, thus influencing the inlet gas distribution and the resulting gas holdup and flow regime transition. In addition to bubble jetting, Ruzicka et al. [29] and Xie and Tan [32] identified two basic bubble formation modes for multihole aeration plates, synchronous and asynchronous. The synchronous mode produces a uniform gas holdup profile and low liquid cir-

culation. This is favorable for the homogeneous flow regime in bubble column operation. In the asynchronous mode, bubble formation at adjacent holes is either out of phase, or they form at alternating holes. Some active holes tend to produce liquid circulation that makes the other holes passive, resulting in a nonuniform inlet gas distribution. This further enhances liquid circulation and leads to flow regime transition. They also observed that hole spacing plays an important role in the bubble formation modes. When the hole spacing is large, the synchronous mode occurs at gas flow rates below a critical value. When hole spacing is small, the close proximity prevents the gas flow through adjacent holes from being in phase and no synchronous mode is observed. The critical gas flow rate at which the transition from the synchronous to asynchronous mode occurs decreases with decreasing hole spacing (i.e., increasing open area) [28]. Therefore, the critical gas flow rate for $A=2.14\%$ is lower than that of $A=0.57\%$ and 0.99%. It is possible that at the same superficial gas velocity, the tendency of the synchronous regime for $A=0.57\%$ and 0.99% is higher than that of $A=2.14\%$. This would produce a more uniform gas distribution for $A=0.57\%$ and 0.99% than 2.14%. Zahradnik and Kastanek [27] demonstrated that a nonuniform gas distribution will induce liquid circulation and an unstable flow pattern; this results in enhanced bubble-bubble interaction and bubble coalescence, leading to a reduced gas holdup when compared to a uniform gas distribution at the same gas flow rate. From Fig. 3 it is plausible that the aeration plates with $A=0.57\%$ and 0.99% produce a more uniform inlet gas distribution than that from $A=2.14\%$.

Figure 3 also shows the flow regime transitions for $A=0.57\%$, 0.99%, and 2.14% by applying the Zuber-Findlay drift flux model [34] (solid symbols), a detailed explanation is provided by others [3,16,35]. In this model, U_g/ε represents the mean bubble rise velocity. All three plates produce homogeneous, transitional, and heterogeneous flow regimes. For the homogeneous flow regime, U_g/ε slightly decreases with increasing U_g and reaches a minimum value denoted as the critical superficial gas velocity at which transitional flow appears. Similar observations were obtained by Tsuchiya and Nakanishi [22]. The negative slope of the plot of U_g/ε versus U_g in the homogeneous regime for all aeration plates may be the result of downward liquid flow between bubbles, compensating for the amount of liquid carried by the bubble wake to ensure conservation of mass [36]. This downward liquid flow has a hindrance effect on the bubble rise velocity leading to a bubble rise velocity less than the terminal rise velocity. This reduction in bubble rise velocity increases with increasing gas holdup (i.e., increasing superficial gas velocity) [24,37].

When the superficial gas velocity is further increased, bubble-bubble interaction is enhanced, and bubble coalescence occurs, which indicates the flow regime transition. In the transitional flow regime, gross liquid circulation, increasing with increasing superficial gas velocity, changes the slope of U_g/ε versus U_g to increase with increasing U_g.

The transitional superficial gas velocity, identified by the down arrows in Fig. 3, is similar when $A=0.57\%$ and 0.99%. This is because the two plates produce similar gas holdup results until a maximum gas holdup is reached for $A=0.57\%$. This observation indicates that increasing the open-area ratio may increase the maximum gas holdup, but it may not delay the flow regime transition. The transitional superficial gas velocity is $\sim$3.4 cm/s for $A=2.14\%$, which is less than $\sim$5.7 cm/s for $A=0.57\%$ and 0.99%. The lower superficial gas velocity at which transition occurs when $A=2.14\%$ may be attributed to two affects. First, bubble coalescence is enhanced with closer hole spacing (large open area), and this induces liquid circulation and triggers flow regime transition. Second, a large open area (close hole spacing) results in a partially activated aeration plate [29], leading to a nonuniform gas distribution and liquid circulation, promoting flow regime transition.

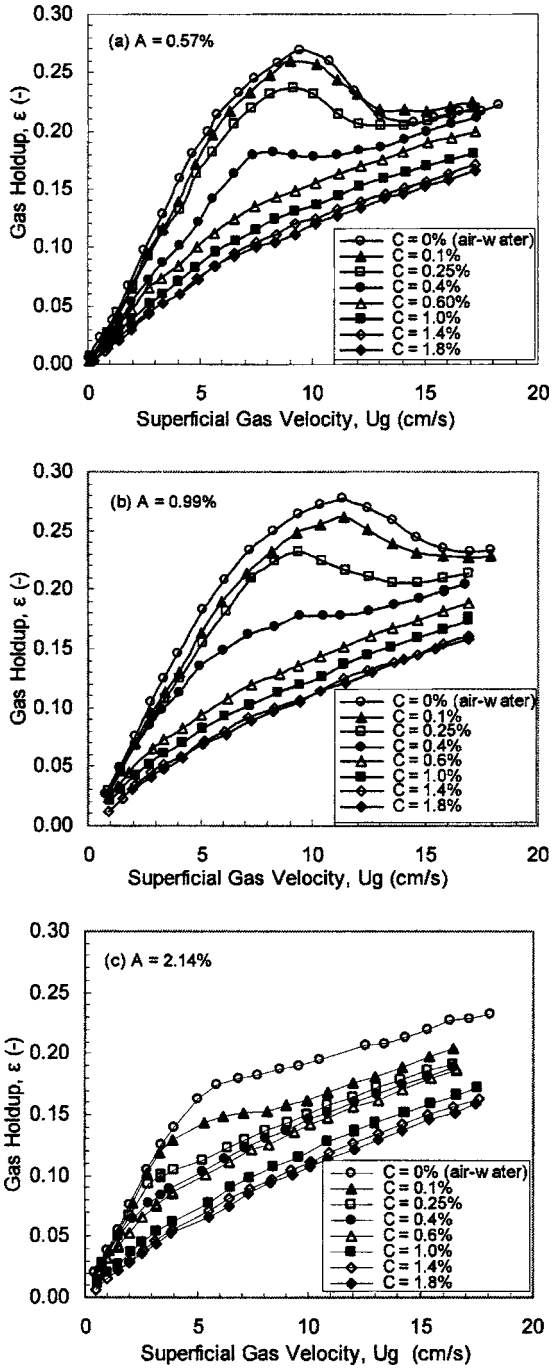

Fig. 4 Effect of fiber mass fraction on gas holdup with different aeration plates for $L=3$ mm Rayon fiber suspensions: (*a*) $A=0.57\%$, (*b*) $A=0.99\%$, and (*c*) $A=2.14\%$

Fiber Suspensions.

Effect of Fiber Mass Fraction. Typical trends of the effect of fiber mass fraction on gas holdup using three different gas aeration plates ($A=0.57\%$, 0.99%, and 2.14%) are shown in Fig. 4 for $L=3$ mm long Rayon fiber. For all three aeration plates, gas holdup decreases with increasing fiber mass fraction. This phenomenon is attributed to the promotion of bubble coalescence and/or reduction of bubble breakup due to the increase in the effective suspension viscosity with increasing fiber mass fraction, and the increasing large bubble sizes due to the increasing yield stress of the fiber suspension; this has been explained by Su and Heindel [16]. The reduction in gas holdup with increasing fiber

mass fraction is more pronounced at low fiber mass fractions. When fiber mass fraction is high ($C \geq 1.4\%$), fiber addition does not significantly affect gas holdup. The trends of gas holdup variation with fiber mass fraction of $A=0.57\%$ and 0.99% are similar. At low fiber mass fractions ($C \leq 0.4\%$, Figs. 4(*a*) and 4(*b*)), gas holdup behavior is similar to that of an air-water system: there is a maximum gas holdup, indicating homogeneous, transitional, and heterogeneous flow regimes exist over the range of superficial gas velocities. The effect of fiber mass fraction is more significant in the transitional flow regime, while little influence is observed in the homogeneous flow regime. At $C>0.4\%$, gas holdup continuously increases with increasing superficial gas velocity and pure heterogeneous flow [38] is observed.

For $A=2.14\%$ (Fig. 4(*c*)), gas holdup increases with increasing superficial gas velocity monotonically for all fiber mass fractions. At low fiber mass fractions ($C \leq 0.25\%$), the homogeneous flow regime exists at low superficial gas velocities, and when $C>0.25\%$, pure heterogeneous flow appears over the range of superficial gas velocities. Similar to $A=0.57\%$ and 0.99%, gas holdup is not influenced by fiber mass fraction in the homogeneous flow regime, whereas the transitional flow regime is affected by fiber addition. Similar trends are obtained for Rayon fiber with $L=6$ and 12 mm for all three aeration plates.

Effect of Aeration Plate Open Area. Figure 5 depicts the effect of aeration plate open area on gas holdup in $L=3$ mm long Rayon fiber suspensions. At low superficial gas velocities ($U_g \leq 3$ cm/s), the open-area ratio has a negligible effect on gas holdup. This phenomenon is similar to that of the air-water system. When $U_g>3$ cm/s, the effect of aeration plate open area ratio on gas holdup is pronounced. At low fiber mass fractions (e.g., $C=0.1\%$), where homogeneous, transitional, and heterogeneous flow regimes exist, the aeration plate open area has a significant effect on gas holdup behavior in the transitional gas flow regime; a higher gas holdup is observed when $A=0.57\%$ and 0.99% than that recorded with $A=2.14\%$. This was also observed in the air-water system (i.e., Fig. 3). In the heterogeneous flow regime, open area influences gas holdup in fiber suspensions, which was not observed in the air-water system (see Fig. 3). This may be because, for the air-water system, there is a significant amount of liquid turbulence at high superficial gas velocities, leading to a negligible effect of the aeration plate on bubble behavior. In contrast, fiber addition results in a decrease in turbulence intensity because the effective suspension viscosity increases with increasing fiber mass fraction, and the effect of bubble formation on gas holdup becomes important. The reasons that the aeration plate with $A=2.14\%$ decreases the gas holdup in fiber suspensions compared to that of $A=0.57\%$ and 0.99% is ascribed to the same reasons as that of the air-water system.

The effect of aeration plate open area on gas holdup for $A=0.99\%$ is influenced by fiber mass fraction. With increasing fiber mass fraction, the performance of $A=0.99\%$ changes from similar to $A=0.57\%$ to that similar to $A=2.14\%$. At low fiber mass fraction ($C=0.1\%$), the gas holdup when $A=0.99\%$ has similar behavior to that of the air-water system, i.e., it is higher than that of $A=0.57\%$. As the fiber mass fraction is further increased ($C=0.25\%$), the gas holdup of $A=0.99\%$ drops faster than $A=0.57\%$ and the two are very similar. At $C=0.60\%$, the gas holdup of $A=0.99\%$ is lower than that of $A=0.57\%$, but almost the same as that of $C=2.14\%$. The larger decrease in gas holdup when $A=0.99\%$ with increasing fiber mass fraction than that of $A=0.57\%$ may be attributed to the increase in the bubble formation size with increasing fiber mass fraction; when the bubble formation size is large enough, adjacent bubbles near the aeration plate begin to coalesce, which is enhanced when $A=0.99\%$ because of its smaller hole spacing compared to that of $A=0.57\%$. This leads the performance of $A=0.99\%$ to be closer to that of $A=2.14\%$ with increasing fiber mass fraction.

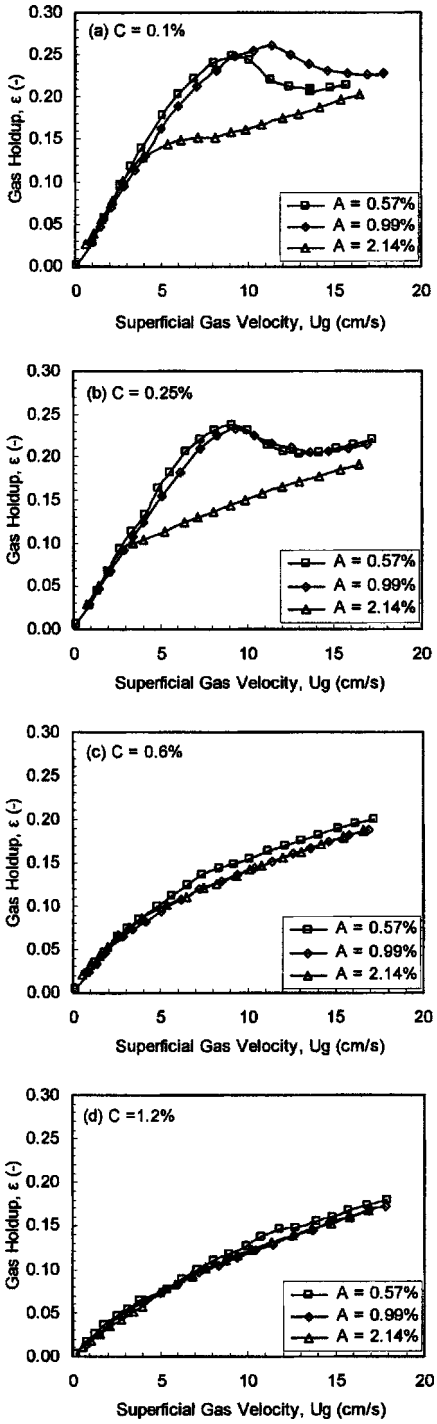

Fig. 5 Effect of aeration plate open area on gas holdup at various fiber mass fractions ($L=3$ mm): (*a*) $C=0.1\%$, (*b*) $C=0.25\%$, (*c*) $C=0.6\%$, and (*d*) $C=1.2\%$

Figure 5 also demonstrates that the effect of aeration plate open area is less significant with increasing fiber mass fraction when the fiber mass fraction is high. The difference of gas holdup of the three aeration plates disappears when the fiber mass fraction is $C \geq 1.2\%$. Similar trends are observed for $L=6$ and 12 mm Rayon fiber. Consequently, the aeration plate open area has an effect on gas holdup in low fiber mass fraction suspensions, which depend on the gas flow regime. However, in high fiber mass fraction suspensions, the aeration plate open area has a negligible effect on gas holdup.

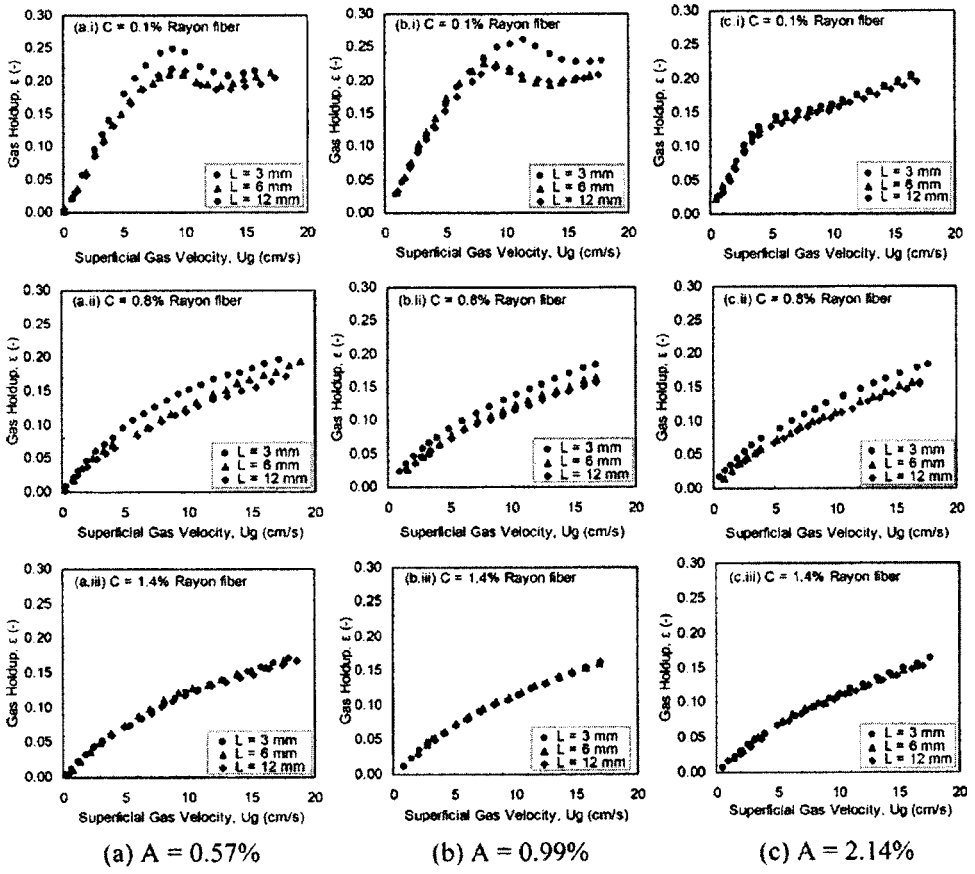

Fig. 6 Effect of fiber length on gas holdup: (*a*) *A*=0.57%, (*b*) *A*=0.99%, and (*c*) *A*=2.14%

It can be concluded that increasing aeration plate open area may enhance or reduce gas holdup in air-water and air-water-fiber systems, and the results are influenced by bubble formation size, hole diameter and spacing, superficial gas velocity, and fiber mass fraction. Increasing aeration plate open area tends to increase gas holdup when the hole spacing is large enough that a bubble formed at the inlet hole has no interaction with adjacent bubbles. Otherwise, increasing the open area tends to reduce gas holdup when bubble formation size is increased by either increasing hole diameter [39], superficial gas velocity, or fiber mass fraction.

Effect of Fiber Length. The effect of fiber length on gas holdup behavior for the three open area ratios are shown in Fig. 6. The trends of $A=0.57\%$ and 0.99% are similar, and for low and medium fiber mass fractions, gas holdup decreases significantly when the fiber length is increased from $L=3$ mm to $L=6$ mm, but a negligible change is observed when the fiber length is further increased to $L=12$ mm. In contrast, there is a negligible effect of fiber length on gas holdup when $A=2.14\%$ at low fiber mass fractions (e.g., $C=0.1\%$). At medium fiber mass fractions (e.g., $C=0.8\%$), a decrease is observed between $L=3$ mm and $L=6$ mm, which is similar to that of $A=0.57\%$ and 0.99%.

In general, increasing fiber length tends to reduce gas holdup in fiber suspensions. However, for long fiber (e.g., $L=6$ and 12 mm), the effect of fiber length on gas holdup is not significant. This phenomenon is analogous to that of a viscous liquid. When liquid viscosity is high, a further increase in viscosity has little effect on gas holdup [10]. This may be attributed to two competing effects: (i) bubble rise velocity of small bubbles is reduced in highly viscous liquids [40], leading to an increase in gas holdup; and (ii) bubble coalescence is enhanced, reducing gas holdup. In fiber suspensions, the longer the fiber, the larger the effective viscosity at the same fiber mass fraction. Therefore, long fiber suspensions tend to hinder bubble rise and enhance bubble coalescence. In addition, the yield stress increases with fiber length [41], which further reduces bubble rise velocity and traps more bubbles. These factors may be the reasons that gas holdup does not reduce significantly with increasing fiber length for long fibers.

Figure 6 also shows that at high fiber mass fractions ($C=1.4\%$), the three aeration plates produce similar gas holdup results for all three fiber lengths. To more clearly depict the effect of open area and fiber length at high fiber mass fractions, Fig. 7 provides all results for $C=1.4\%$, which shows that when the fiber

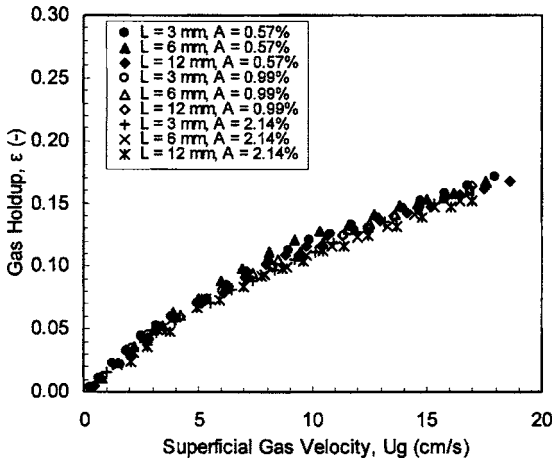

Fig. 7 Effect of fiber length and aeration plate open area on gas holdup at *C*=1.4%

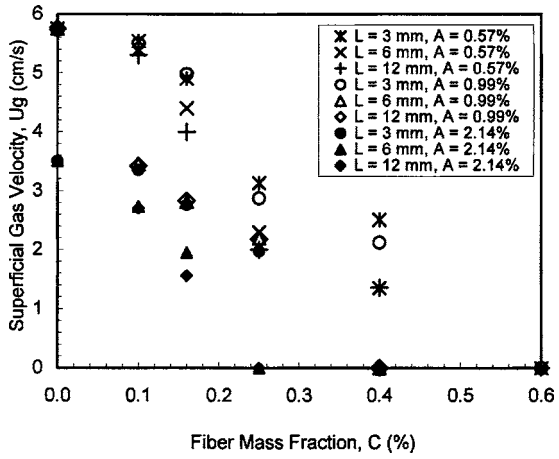

Fig. 8 Effect of aeration plate open area, fiber mass fraction, and fiber length on the superficial gas velocity at which flow regime transition is initiated

mass fraction is high, gas holdup has only a weak dependence on fiber length and aeration plate open area. It also implies that the gas holdup in a high fiber mass fraction suspension is mainly determined by slurry mixing.

Flow Regime Transition. Figure 8 shows the effect of fiber mass fraction, length, and open area on the superficial gas velocity at which transitional flow is observed for the three distributor plates. The superficial gas velocity at which transitional flow begins is determined by the Zuber-Findlay drift flux model [34] and shown by the arrows in Fig. 3. Additional details in this determination can be found in [3,16,35]. In general, fiber addition tends to destabilize the homogeneous flow regime, and when the fiber mass fraction is beyond a critical value, pure heterogeneous flow is observed over the entire range of superficial gas velocities. This phenomenon is ascribed to the increase in effective suspension viscosity with increasing fiber mass fraction. Zahradnik et al. [3] have shown that the flow pattern will change from that of the existence of three flow regimes (homogeneous, transitional, and heterogeneous) to pure heterogeneous flow as the liquid viscosity increases. The fiber length has an effect on flow regime transition where the longer the fiber, the lower the superficial gas velocity at which transition begins. This effect is more significant when fiber length increases from 3 to 6 mm. There is not a pronounced difference between $L=6$ and 12 mm in either the superficial gas velocity or the critical fiber mass fraction at which transitional flow begins. This is consistent with the trends shown in Fig. 6 that the effect of fiber length on gas holdup is not significant when fiber length is increased from 6 to 12 mm for all three aeration plates.

It is apparent that in fiber suspensions, increasing aeration plate open area is not favorable to the homogeneous flow stabilization. The aeration plate with $A=2.14\%$ obviously encourages the flow regime transition and the transitional superficial velocities for the three fiber lengths are lower than those of $A=0.57\%$ and 0.99%. $A=0.99\%$ produces very similar results to that of $A=0.57$ for all three fiber lengths. The critical fiber mass fraction beyond which a pure heterogeneous flow regime exists is also dependent on the aeration plate open area and decreases with increasing open area. When $A=0.57\%$, pure heterogeneous flow appears when $C \geqslant 0.6\%$, and the dependence of the critical fiber mass fraction on fiber length is negligible. For the other two plates, the critical fiber mass fraction is affected by fiber length between $L=3$ and 6 mm. $A=0.99\%$ does not affect the critical fiber mass fraction for $L=3$ mm, and homogeneous flow also can be observed when $C<0.6\%$. For $L=6$ and 12 mm, homogeneous flow exists when $C<0.4\%$. When $A=2.14\%$, the critical fiber mass fraction further decreases. For $L=3$ mm, homogeneous flow is observed when $C \leqslant 0.25\%$, and for $L=6$ and 12 mm, this critical value reduces to 0.16%.

Conclusions

Three aeration plates with different open areas ($A=0.57\%$, 0.99%, and 2.14%) and the same hole diameter ($d_o=1$ mm) were used to study their effect on gas holdup and flow regime transition in Rayon fiber suspensions. When $A=0.57\%$ and 0.99%, a pronounced maximum gas holdup was recorded for the air-water and low fiber mass fraction systems; this was not observed when $A=2.14\%$. For an air-water system, gas holdup did not depend on open area in the homogeneous or heterogeneous flow regime, but open area influenced the transitional flow regime. Gas holdup was higher when $A=0.99\%$ than that of $A=0.57\%$; it reduced significantly when $A=2.14\%$ from that of $A=0.57\%$. For fiber suspensions with $C \leqslant 1.2\%$, aeration plate open area had no effect on gas holdup in the homogeneous flow regime, but differences were observed in the transitional and heterogeneous flow regimes. Gas holdup decreased with increasing fiber length when $C \leqslant 1.4\%$ for all three aeration plates. At high fiber mass fractions, no dependence of gas holdup on fiber length or aeration plate was observed.

Homogeneous, transitional, and heterogeneous flow conditions were observed at low fiber mass fractions for all three aeration plates. However, the aeration plate with $A=2.14\%$ tended to destabilize the homogeneous flow regime, and the transitional superficial gas velocity decreased from that recorded when $A=0.57\%$ and 0.99%. In addition, the critical fiber mass fraction at which the flow pattern changed from homogeneous, transitional and heterogeneous flow to pure heterogeneous flow was lower when $A=2.14\%$.

Finally, increasing aeration plate open area is favorable to gas holdup when $A \lesssim 1\%$. The effect depends on the bubble formation, hole spacing, and liquid (slurry) properties.

Acknowledgment

Financial support of this work by the National Science Foundation under Grant No. CTS-0209928 is greatly appreciated.

Nomenclature

A = open area, %
C = fiber mass fraction, %
d_o = hole diameter, mm
H = column height, m
L = fiber length, mm
M_f = dry fiber mass, kg
M_t = total mass of fiber-water mixture, kg
P = average pressure of the air-water-fiber suspension, Pa
P_o = average pressure of the water-fiber suspension, Pa
t_f = time of bubble formation
t_i = time for a bubble, growing to a diameter equal to the hole separation distance, to begin bubble-bubble interaction
t_s = time to drain the liquid film between bubbles to a critical thickness for rupture
U_g = superficial gas velocity, cm/s
V = volume of the fiber-water mixture, m^3
v_o = aeration hole gas velocity, cm/s
We = Weber number

Greek Letters

ε = gas holdup
ρ_{eff} = effective density of the fiber-water mixture, kg/m^3
ρ_g = gas density, kg/m^3

ρ_f = dry fiber density, kg/m^3
ρ_w = water density, kg/m^3
σ = surface tension, mNm^{-1}
Δ = difference

References

[1] Zahradnik, J., Kuncova, G., and Fialova, M., 1999, "The Effect of Surface Active Additives on Bubble Coalescence and Gas Holdup in Viscous Aerated Batches," Chem. Eng. Sci., **54**(13–14), pp. 2401–2408.

[2] Kluytmans, J. H. J., van Wachem, B. G. M., Kuster, B. M., and Schouten, J. C., 2001, "Gas Holdup in a Slurry Bubble Column: Influence of Electrolyte and Carbon Particles," Ind. Eng. Chem. Res., **40**(23), pp. 5326–5333.

[3] Zahradnik, J., Fialova, M., Ruzicka, M., Drahos, J., Kastanek, F., and Thomas, N. H., 1997, "Duality of the Gas-Liquid Flow Regimes in Bubble Column Reactors," Chem. Eng. Sci., **52**(21–22), pp. 3811–3826.

[4] Krishna, R., Urseanu, M. I., de Swart, J. W. A., and Ellenberger, J., 2000, "Gas Hold-up in Bubble Columns: Operation With Concentrated Slurries Versus High Viscosity Liquid," Can. J. Chem. Eng., **78**(3), pp. 442–448.

[5] Al-Masry, W. A., 2001, "Gas Holdup in Circulating Bubble Columns With Pseudoplastic Liquids," Chem. Eng. Technol., **24**(1), pp. 71–76.

[6] Schafer, R., Merten, C., and Eigenberger, G., 2002, "Bubble Size Distributions in a Bubble Column Reactor Under Industrial Conditions," Exp. Therm. Fluid Sci., **26**(6–7), pp. 595–604.

[7] Jamialahmadi, M., and Muller-Steinhagen, H., 1991, "Effect of Solid Particles on Gas Hold-up in Bubble-Columns," Can. J. Chem. Eng., **69**(1), pp. 390–393.

[8] Banisi, S., Finch, J. A., Laplante, A. R., and Weber, M. E., 1995, "Effect of Solid Particles on Gas Holdup in Flotation Columns. 1. Measurement," Chem. Eng. Sci., **50**(14), pp. 2329–2334.

[9] Krishna, R., De Swart, J. W. A., Ellenberger, J., Martina, G. B., and Maretto, C., 1997, "Gas Holdup in Slurry Bubble Columns: Effect of Column Diameter and Slurry Concentrations," AIChE J., **43**(2), pp. 311–316.

[10] Gandhi, B., Prakash, A., and Bergougnou, M. A., 1999, "Hydrodynamic Behavior of Slurry Bubble Column at High Solids Concentrations," Powder Technol., **103**(2), pp. 80–94.

[11] Chen, C. M., and Leu, L. P., 2002, "Flow Regimes and Radial Gas Holdup Distribution in Three-Phase Magnetic Fluidized Beds," Ind. Eng. Chem. Res., **41**(7), pp. 1877–1884.

[12] Walmsley, M. R. W., 1992, "Air Bubble Motion in Wood Pulp Fiber Suspension," Appita J., **45**, pp. 509–515.

[13] Went, J., Jamialahmadi, M., and Muller-Steinhagen, H., 1993, "Effect of Wood Pulp Fiber Concentration on Gas Holdup in Bubble Column," Chem.-Ing.-Tech., **63**(3), pp. 306–308.

[14] Lindsay, J. D., Ghiaasiaan, S. M., and Abdel-Khalik, S. I., 1995, "Macroscopic Flow Structures in a Bubbling Paper Pulp-Water Slurry," Ind. Eng. Chem. Res., **34**(10), pp. 3342–3354.

[15] Schulz, T. H., and Heindel, T. J., 2000, "A Study of Gas Holdup in Cocurrent Air/Water/Fiber System," Tappi J., **83**(6), pp. 58–69.

[16] Su, X., and Heindel, T. J., 2003, "Gas Holdup in a Fiber Suspension," Can. J. Chem. Eng., **81**(3–4), pp. 412–418.

[17] Xie, T., Ghiaasiaan, S. M., Karrila, S., and McDonough, T., 2003, "Flow Regimes and Gas Holdup in Paper Pulp-Water-Gas Three-Phase Slurry Flow," Chem. Eng. Sci., **58**(8), pp. 1417–1430.

[18] Bennington, C. P. J., 1993, "Mixing Gases into Medium Consistency Pulp Suspensions Using Rotary Devices," Tappi J., **76**(7), pp. 77–86.

[19] Heindel, T. J., 2000, "Gas Flow Regime Changes in a Bubble Column Filled With a Fiber Suspension," Can. J. Chem. Eng., **78**(5), pp. 1017–1022.

[20] Heindel, T. J., 2002, "Bubble Size in a Cocurrent Fiber Slurry," Ind. Eng. Chem. Res., **41**(3), pp. 632–641.

[21] Ohki, Y., and Inoue, H., 1970, "Longitudinal Mixing of the Liquid Phase in Bubble Columns," Chem. Eng. Sci., **25**(1), pp. 1–16.

[22] Tsuchiya, K., and Nakanishi, O., 1992, "Gas Holdup Behavior in a Tall Bubble Column With Perforated Plate Distributors," Chem. Eng. Sci., **47**(13–14), pp. 3347–3354.

[23] Zahradnik, J., and Kastanek, F., 1979, "Gas Holdup in Uniformly Aerated Bubble Column Reactors," Chem. Eng. Commun., **3**, pp. 413–429.

[24] Shnip, A. I., Kolhatkar, R. V., Swamy, D., and Joshi, J. B., 1992, "Criteria for the Transition From the Homogeneous to the Heterogeneous Regime in 2-Dimensional Bubble Column Reactors," Int. J. Multiphase Flow, **18**(5), pp. 705–726.

[25] Kawasaki, H., and Tanaka, H., 1995, "Effects of Geometric Properties for a Perforated Plate on Gas Holdup in a Bubble Column," J. Chem. Eng. Jpn., **28**(6), pp. 715–720.

[26] Solanki, M. K. S., Mukherjee, A. K., and Das, T. R., 1992, "Bubble Formation at Closely Spaced Orifices in Aqueous-Solutions," Chem. Eng. J., **49**(1), pp. 65–71.

[27] Zahradnik, J., and Kastanek, F., 1978, "Effect of Gas-Distribution on Hydrodynamic Parameters of a Bubble Bed," Collect. Czech. Chem. Commun., **43**(1), pp. 216–223.

[28] Ruzicka, M., Drahos, J., Zahradnik, J., and Thomas, N. H., 2000, "Structure of Gas Pressure Signal at Two-Orifice Bubbling from a Common Plenum," Chem. Eng. Sci., **55**(2), pp. 421–429.

[29] Ruzicka, M., Drahos, J., Zahradnik, J., and Thomas, N. H., 1999, "Natural Modes of Multi-Orifice Bubbling From a Common Plenum," Chem. Eng. Sci., **54**(21), pp. 5223–5229.

[30] Haug, H. F., 1976, "Stability of Sieve Trays With High Overflow Weirs," Chem. Eng. Sci., **31**(4), pp. 295–307.

[31] Miyahara, T., Haga, H., and Takahashi, T., 1983, "Bubble Formation From an Orifice at High Gas Flow Rates," Int. Chem. Eng., **23**(3), pp. 524–531.

[32] Xie, S. Y., and Tan, R. B. H., 2003, "Bubble Formation at Multiple Orifices: Bubbling Synchronicity and Frequency," Chem. Eng. Sci., **58**(20), pp. 4639–4647.

[33] Li, H. A. Z., 1999, "Bubbles in Non-Newtonian Fluids: Formation, Interactions and Coalescence," Chem. Eng. Sci., **54**(13–14), pp. 2247–2254.

[34] Zuber, N., and Findlay, J. D., 1965, "Average Volumetric Concentration in Two Phase Flow Systems," ASME J. Heat Transfer, **87**, pp. 453–468.

[35] Vial, C., Camarasa, E., Poncin, S., Wild, G., Midoux, N., and Bouillard, J., 2000, "Study of Hydrodynamic Behaviour in Bubble Columns and External Loop Airlift Reactors Through Analysis of Pressure Fluctuations," Chem. Eng. Sci., **55**(15), pp. 2957–2973.

[36] Chen, R. C., Reese, J., and Fan, L. S., 1994, "Flow Structure in a 3-Dimensional Bubble-Column and 3-Phase Fluidized-Bed," AIChE J., **40**(7), pp. 1093–1104.

[37] Shen, G., and Finch, J. A., 1996, "Bubble Swarm Velocity in a Column," Chem. Eng. Sci., **51**(14), pp. 3665–3674.

[38] Ruzicka, M. C., Zahradnik, J., Drahos, J., and Thomas, N. H., 2001, "Homogeneous-Heterogeneous Regime Transition in Bubble Columns," Chem. Eng. Sci., **56**(15), pp. 4609–4626.

[39] Valencia, A., Cordova, M., and Ortega, J., 2002, "Numerical Simulation of Gas Bubbles Formation at a Submerged Orifice in a Liquid," Int. Commun. Heat Mass Transfer, **29**(6), pp. 821–830.

[40] Li, H., and Prakash, A., 2000, "Influence of Slurry Concentrations on Bubble Population and Their Rise Velocities on a Three-Phase Slurry Bubble Column," Powder Technol., **113**, pp. 158–167.

[41] Bennington, C. P. J., Kerekes, R. J., and Grace, J. R., 1990, "The Yield Stress of Fiber Suspensions," Can. J. Chem. Eng., **68**(5), pp. 748–757.

Journal of Fluids Engineering

Technical Brief

Influence of Lateral Walls on Peristaltic Flow in a Rectangular Duct

M. V. Subba Reddy
Department of Mathematics, Sri Venkateswara University, Tirupati-517502, India

Manoranjan Mishra
Institut Non Linéaire de Nice, UMR 6618 CNRS, Sophia Antipolis, 1361 route des Lucioles 06560, Valbonne, France

S. Sreenadh
Department of Mathematics, Sri Venkateswara University, Tirupati-517502, India

A. Ramachandra Rao[1]
e-mail: ramchand@math.iisc.ernet.in
Department of Mathematics, Indian Institute of Science, Bangalore-560012, India

The flow of a viscous fluid due to symmetric peristaltic waves propagating on the horizontal sidewalls of a rectangular duct is studied under the assumptions of long wavelength and low Reynolds number. The effect of aspect ratio β, ratio of height to width, on the pumping characteristics is discussed in detail. The results are compared to with those corresponding to Poiseuille flow. [DOI: 10.1115/1.1994876]

Keywords: Peristalsis, Peristaltic Pumping, Rectangular Duct

1 Introduction

Peristaltic pumping is a form of fluid transport generated by a progressive wave of area contraction or expansion along a length of a distensible tube containing fluid. In the living systems peristalsis is the mechanism used to propel foodstuffs through esophagus and alimentary canal, urine in ureter, and semen in vas deferens ducts. Engineers developed pumps having industrial and physiological applications adopting the principle of peristalsis. Shapiro et al. [1] and Fung and Yih [2] were some of the first to mathematically model peristaltic transport to explain the basic fluid mechanics aspects using wave and fixed frame analyses respectively. The experimental works of De Vries et al. [3] and Chalubinski et al. [4] reveal that the intrauterine fluid motion is due to peristalsis. In view of this, Eytan and Elad [5] have studied the peristaltic flow in an asymmetric two-dimensional channel to explain the motion of intrauterine fluid in a sagittal cross section of the uterus. In fact, the sagittal cross section of the uterus may be better approximated by a tube of rectangular cross section than a two-dimensional channel. Tsangaris and Vlachakis [6] have obtained an exact solution of the Navier-Stokes equations for a pulsating flow in a rectangular duct in order to explain the blood flow in fiber membranes used for the artificial kidney. The effects of sidewalls on axial flow in rectangular ducts with suction and injection have been investigated by Erdogan [7].

The aim of the present study is to investigate the effects of aspect ratio $\beta(=a/d)$ on the peristaltic pumping by introducing lateral walls separated by a distance $2d$ in a channel of height $2a$. Symmetric peristaltic waves are assumed to propagate on two opposite horizontal sidewalls with constant velocity of the channel, and the remaining lateral walls are not subjected to peristalsis. Aspect ratio $\beta<1$ means that height is less compared to width, and $\beta=0$ corresponds to a two-dimensional channel. When $\beta=1$, the rectangular duct becomes a square duct and for $\beta>1$, the height is more compared to width. Pumping characteristics are discussed for different values of β in detail.

2 Mathematical Formulation and Solution

Consider the motion of an incompressible viscous fluid in a duct of rectangular cross section with width $2d$ and height $2a$ as shown in Fig. 1. Cartesian coordinate system (X,Y,Z) is with X, Y, and Z axes corresponding to axial, lateral, and vertical directions, respectively, of a rectangular duct. The duct walls are flexible, and an infinite train of sinusoidal waves propagate with constant velocity c only along the walls parallel to the XY plane in the axial direction. The peristaltic waves on the walls are given by

$$Z = H(X,t) = \pm a \pm b\cos\frac{2\pi}{\lambda}(X-ct) \tag{1}$$

where b is the wave amplitude and λ is the wavelength. The walls parallel to XZ plane remain undisturbed and are not subjected to any peristaltic wave motion. We assume that the lateral velocity is zero as there is no change in lateral direction of the duct's cross section. Under the assumptions that the pressure difference across a wavelength is constant and the length of the tube is an integral multiple of the wavelength, the flow becomes steady in a wave frame (x,y,z) moving with velocity c away from the fixed frame (X,Y,Z). The transformation between the two frames is given by

$$x = X-ct, \quad y = Y, \quad z = Z, \quad u = U-c, \quad w = W, \qquad p(x,z) = P(X,Z,t) \tag{2}$$

where $(u,0,w)$ and $(U,0,W)$ are the velocity components, and p and P are the pressures in wave and fixed frames of reference, respectively.

Using the nondimensional quantities

[1]Corresponding author

Contributed by the Fluids Engineering Division for publication in the ASME JOURNAL OF FLUIDS ENGINEERING. Manuscript received by the Fluids Engineering Division August 3, 2004; Final revision March 10, 2005. Associate Editor: S. Balachandar.

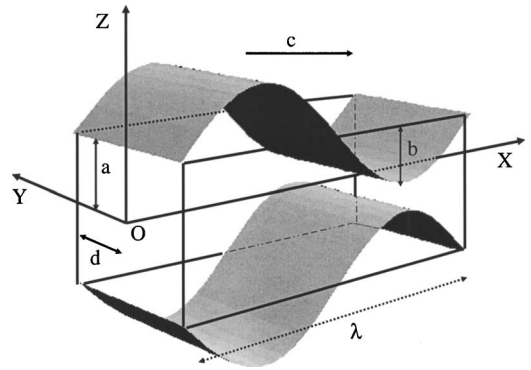

Fig. 1 Schematic diagram of peristaltic flow with waves propagating on horizontal walls in a rectangular duct

$$\bar{x}=\frac{x}{\lambda},\quad \bar{y}=\frac{y}{d},\quad \bar{z}=\frac{z}{a},\quad \delta=\frac{a}{\lambda},\quad \bar{u}=\frac{u}{c},\quad \bar{\omega}=\frac{\omega}{c\delta},$$

$$\bar{t}=\frac{ct}{\lambda},\quad h=\frac{H}{a},\quad \phi=\frac{b}{a},\quad \bar{p}=\frac{a^2p}{\mu c\lambda}$$

in the Navier-Stokes equations and equation of continuity, which governs the flow, we get (dropping the bars)

$$\mathrm{Re}\left(u\frac{\partial u}{\partial x}+w\frac{\partial u}{\partial z}\right)=-\frac{\partial p}{\partial x}+\delta^2\frac{\partial^2 u}{\partial x^2}+\beta^2\frac{\partial^2 u}{\partial y^2}+\frac{\partial^2 u}{\partial z^2} \tag{3}$$

$$\mathrm{Re}\,\delta^2\left(u\frac{\partial w}{\partial x}+w\frac{\partial w}{\partial z}\right)=-\frac{\partial p}{\partial z}+\delta^2\left(\delta^2\frac{\partial^2 w}{\partial x^2}+\beta^2\frac{\partial^2 w}{\partial y^2}+\frac{\partial^2 w}{\partial z^2}\right) \tag{4}$$

$$\frac{\partial p}{\partial y}=0 \tag{5}$$

$$\frac{\partial u}{\partial x}+\frac{\partial w}{\partial z}=0 \tag{6}$$

where $\beta=a/d$ (aspect ratio) and $\mathrm{Re}=\rho ac\delta/\mu$ (Reynolds number).

Under lubrication approach (negligible inertia $\mathrm{Re}\to 0$ and long wavelength $\delta\ll 1$), the Eqs. (3)–(6) reduce to

$$\beta^2\frac{\partial^2 u}{\partial y^2}+\frac{\partial^2 u}{\partial z^2}=\frac{dp}{dx} \tag{7}$$

$$\frac{\partial u}{\partial x}+\frac{\partial w}{\partial z}=0 \tag{8}$$

The corresponding no-slip boundary conditions are

$$u=-1 \quad \text{at} \quad y=\pm 1 \tag{9}$$

$$u=-1 \quad \text{at} \quad z=\pm h(x)=\pm 1\pm\phi\cos 2\pi x \tag{10}$$

where $0\le\phi\le 1$, $\phi=0$ for straight duct and $\phi=1$ corresponds to total occlusion. Introducing $x=x'$, $y=\beta y'$, $z=z'$ in Eq. (7), we get

$$\frac{\partial^2 u}{\partial y'^2}+\frac{\partial^2 u}{\partial z'^2}=\frac{dp}{dx'} \tag{11}$$

substituting $u=u'-1-\frac{1}{2}(dp/dx')(h^2-z'^2)$ in (11), we get

$$\frac{\partial^2 u'}{\partial y'^2}+\frac{\partial^2 u'}{\partial z'^2}=0 \tag{12}$$

The corresponding boundary conditions are

$$u'=\frac{1}{2}\frac{dp}{dx'}(h^2-z'^2) \quad \text{at} \quad y'=\pm\frac{1}{\beta} \tag{13}$$

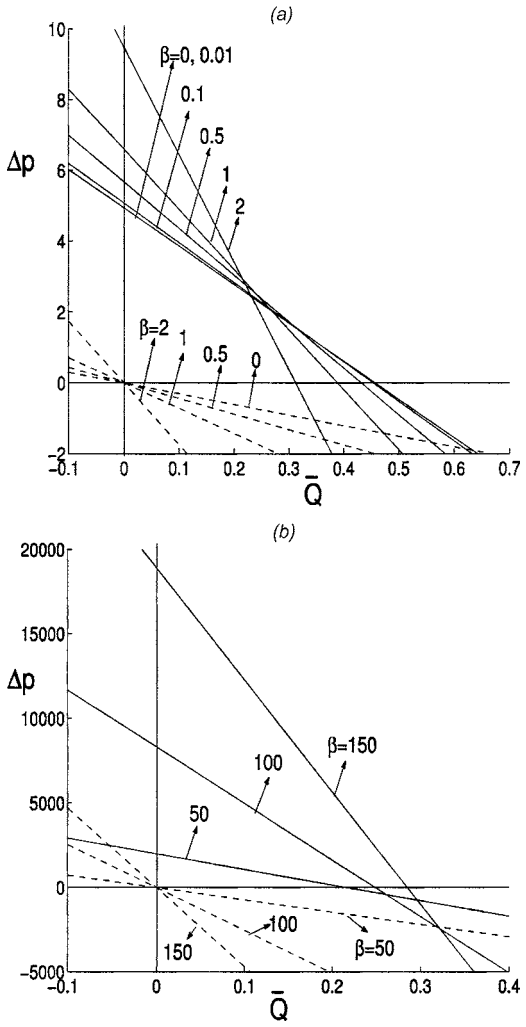

Fig. 2 Variation of Δp versus $\bar{Q}$ with $\phi=0.6$, (*a*) for small values of β, (*b*) for large β, and the corresponding graphs for Poiseuille flow are given in dashed lines.

$$u'=0 \quad \text{at} \quad z'=\pm h(x') \tag{14}$$

The solution of (7), using Eqs. (11)–(14), valid in $-1\le y\le 1$, $-h(x)\le z\le h(x)$, satisfying the corresponding boundary conditions (9) and (10) is given by

$$u=-1-\frac{h^2(x)}{2}\frac{dp}{dx}\left\{1-\frac{z^2}{h^2(x)}-4\sum_{n=1}^{\infty}\frac{(-1)^n\cosh\alpha_n y/\beta h(x)\cos\alpha_n z/h(x)}{\alpha_n^3\cosh\alpha_n/\beta h(x)}\right\} \tag{15}$$

where $\alpha_n=(2n-1)\pi/2$.

The volumetric flow rate in the rectangular duct in the wave frame (in one quadrant) is given by

$$q=\int_0^1\int_0^{h(x)}u\,dy\,dz=-h(x)-\frac{h^3(x)}{3}\frac{dp}{dx}\left\{1-6h(x)\beta\sum_{n=1}^{\infty}\frac{1}{\alpha_n^5}\tanh\alpha_n/\beta h(x)\right\} \tag{16}$$

The instantaneous flux $Q(x,t)$ in the laboratory frame is

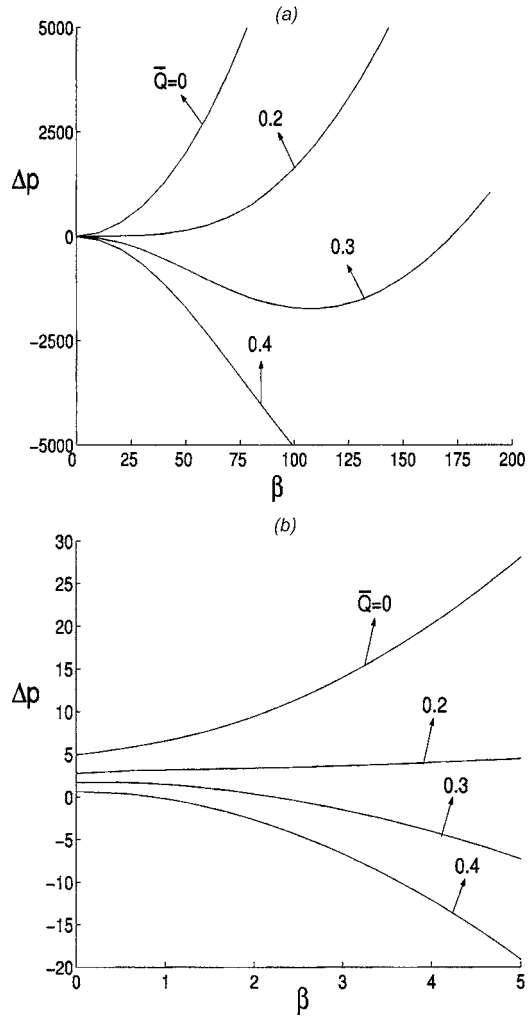

Fig. 3 Variation of Δp versus β with $\phi=0.6$, (*a*) for different values of flux $\bar{Q}$ and (*b*) enlargement of (*a*) near $\beta=0$

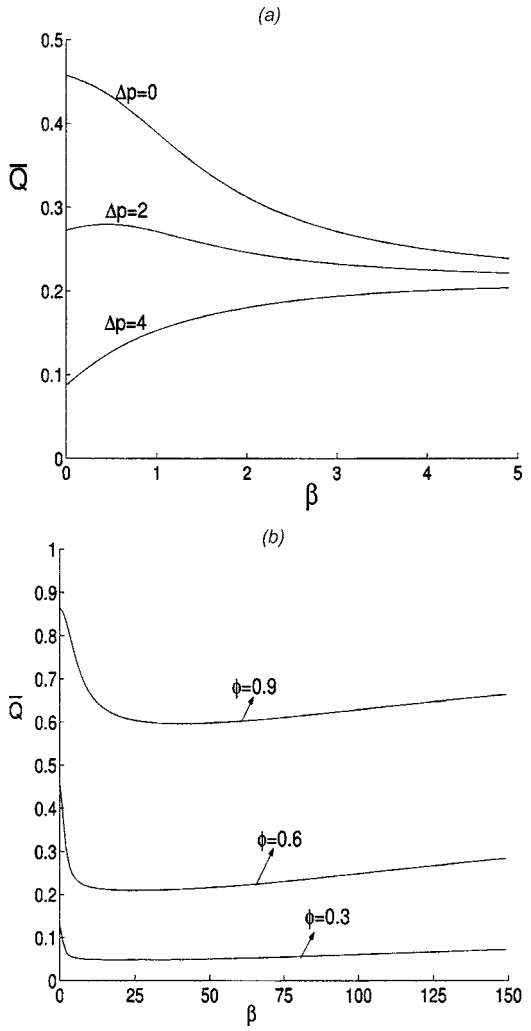

Fig. 4 (*a*) Variation of $\bar{Q}$ versus β with $\phi=0.6$, for different value of Δp, and (*b*) variation of free pumping flux with β for different ϕ

$$Q = \int_0^1 \int_0^{h(x)} (u+1)\,dy\,dz = q + h(x) \tag{17}$$

The average flux $\bar{Q}$ over one period ($T=\lambda/c$) of the peristaltic wave is

$$\bar{Q} = \frac{1}{T}\int_0^T Q\,dt = q + 1 \tag{18}$$

From Eqs. (16) and (18), the pressure gradient is obtained as

$$\frac{dp}{dx} = \frac{-3(\bar{Q} - 1 + h(x))}{h^3(x)\left\{1 - 6h(x)\beta\sum_{n=1}^{\infty}\frac{1}{\alpha_n^5}\tanh\alpha_n/\beta h(x)\right\}} \tag{19}$$

Integrating Eq. (19) with respect to x over one wavelength, we get the pressure rise(drop) over one cycle of the wave as

$$\Delta p = -3(\bar{Q} - 1)I_1 - 3I_2 \tag{20}$$

where $I_1=\int_0^1\{dx/[h^3(x)(1-k)]\}$, $I_2=\int_0^1\{dx/[h^2(x)(1-k)]\}$, and $k=6h(x)\beta\Sigma_{n=1}^{\infty}(1/\alpha_n^5)\tanh\alpha_n/\beta h(x)$.

In the limit $\beta\to 0$ (keeping a fixed and $d\to\infty$), the rectangular duct reduces to a two-dimensional channel and our results reduce to those given by Shapiro et al. [1].

3 Discussion of Results

In order to understand the influence of lateral walls on the pumping characteristics one has to analyze the pressure-flux relation given in Eq. (20) for different values of β. Physically, as β increases from small value to a value greater than one, a transition takes place from a rectangular duct with domination of width to the one with height passing through a cross section of a square duct. The integrals and the series in Eq. (20) are evaluated numerically by built-in routines of MATLAB. Figure 2 depicts the pumping curves with a fixed value of $\phi=0.6$ for different values of β. For small values of β, any two pumping curves intersect at a point in the first quadrant as seen in Fig. 2(*a*). As long as this point remains in the first quadrant, to the left of this point pumping increases and to the right both pumping and free pumping ($\Delta p=0$) decreases with increasing β, i.e., vertical dimension a is large compared to horizontal dimension d. This point of intersection moves to the fourth quadrant for large values of β as depicted in Fig. 2(*b*). As a consequence, both pumping and free pumping increase with increasing β. These results indicate how the finite extent of the width of the duct alters the pumping characteristics, which is not captured by earlier theories existing in the literature [1]. It has been observed that for $\beta=0.01$, the pumping graph overlaps the one with $\beta=0$, indicating that when the width of the duct is 100 times the height, the assumption of the two-

dimensional channel for a rectangular duct is quite satisfactory. In order to compare our results to the Poiseuille flow, i.e., without peristalsis ($\phi=0$), we have plotted the pumping characteristics given by Δp versus $\bar{Q}$ in dashed lines in Fig. 2. Here Δp is the externally imposed pressure gradient on the flow. In Poiseuille flow, flux rate $\bar{Q}$ decreases with increasing β for a favorable pressure gradient Δp (<0), where as this behavior is achieved for $\Delta p>0$ in peristaltic flow (see Fig. 2(a)). For large values of β, there exist a range of favorable pressure gradients in which the flux rate increases in peristaltic flow, whereas it decreases in a Poiseuille flow as seen in Fig. 2(b).

In order to understand the effect of β more clearly, we have considered the variation of Δp versus β for different values of flux rates $\bar{Q}$ with $\phi=0.6$ in Fig. 3. It is observed from the Fig. 3(a) that Δp strictly increases for small values of $\bar{Q}=0,0.2$ and strictly decreases for larger flux $\bar{Q}=0.4$ for all values of β. But the curve corresponding to $\bar{Q}=0.3$ shows a decrease in ΔP as β increases and attains a minimum around $\beta=100$ before it starts increasing for a further increase in β. Figure 3(b) is an enlargement of Fig. 3(a), showing that the curves for various $\bar{Q}$ do not meet at a single point near $\beta=0$. The variation $\bar{Q}$ with β for different Δp and ϕ is depicted in Fig. 4. Flow rate $\bar{Q}$ decreases for $\Delta p=0$ and increases for $\Delta p=4$ only for small values of β, as shown in Fig. 4(a). Whereas Fig. 4(b) shows that the free pumping flux rate $\bar{Q}$ attains a minimum around $\beta=25$ and starts increasing for a further increase in β. Furthermore, we observe pumping flux increases with increasing ϕ, and also the minimum free pumping flux rate attained at β increases with increasing ϕ. We observe that even though the pumping increases with increasing β, free pumping starts decreasing until a certain limiting value of β, and thereafter it increases with an increase in β but never attains the free pumping limit for a channel (corresponding to $\beta=0$). The peristalsis works as a pump against higher pressure for a given $\phi(=b/a)$ at large values of β as they give rise to a peristaltic wave with a large amplitude.

The two nonzero components of velocity u and w are functions of x, y, and z, and this motion is a pseudo plane motion of the first kind. The stream function associated with the flow depends on all the three coordinates. The regions of reflux and trapping can be studied through the streamlines in the xz plane fixing a lateral station y. This is not done here, as the main emphasis is to bring out the effects of the presence of lateral walls on pumping characteristics.

Acknowledgment

Authors M. V. Subba Reddy and S. Sreenadh thank IISc-TIFR short-term visitors' program for providing an opportunity to carry out this work in the Department of Mathematics, I.I.Sc., Bangalore, INDIA. The author M. Mishra gratefully acknowledges the financial support from the National Board of Higher Mathematics (NBHM), Department of Atomic Energy, Government of India through a postdoctoral fellowship. The authors also thank the referees for their valuable comments.

References

[1] Shapiro, A. H., Jaffrin, M. Y., and Weinberg, S. L., 1969, "Peristaltic Pumping With Long Wavelengths at Low Reynolds Number," J. Fluid Mech., **37**, pp. 799–825.
[2] Fung, Y. C., and Yih, C. S., 1968, "Peristaltic Transport," ASME J. Appl. Mech., **35**, pp. 669–675.
[3] De Vries, K., Lyons, E. A., Ballard, J., Levi, C. S., and Lindsay, D. J., 1990, "Contraction of the Inner Third of Myometrium," Am. J. Obstet. Gynecol., **162**, pp. 679–682.
[4] Chalubinski, K., Deutinger, J., and Bernaschek, G., 1993, "Vaginosonography for Recording of Cycle-Related Myometrial Contractions," Fertil. Steril., **59**, pp. 225–228.
[5] Eytan, O., and Elad, D., 1999, "Analysis of Intra-Uterine Fluid Motion Induced by Uterine Contractions," Bull. Math. Biol., **61**, pp. 221–238.
[6] Tsangaris, S., and Vlachakis, N. W., 2003, "Exact Solution of the Navier-Stokes Equations for the Fully Developed, Pulsating Flow in a Rectangular Duct With Constant Cross-Sectional Velocity," ASME J. Fluids Eng., **125**, pp. 382–385.
[7] Erdogan, M. E., 2003, "The Effects of Side Walls on Axial Flow in Rectangular Ducts With Suction and Injection," Acta Mech., **162**, pp. 157–166.